MECHANO-CALCIUM, MECHANO-ELECTRIC, AND MECHANO-METABOLIC FEEDBACK LOOPS: CONTRIBUTION TO THE MYOCARDIUM CONTRACTION IN HEALTH AND DISEASES

EDITED BY: Leonid Katsnelson, Gentaro Iribe, Remi Peyronnet and
Olga Solovyova
PUBLISHED IN: Frontiers in Physiology

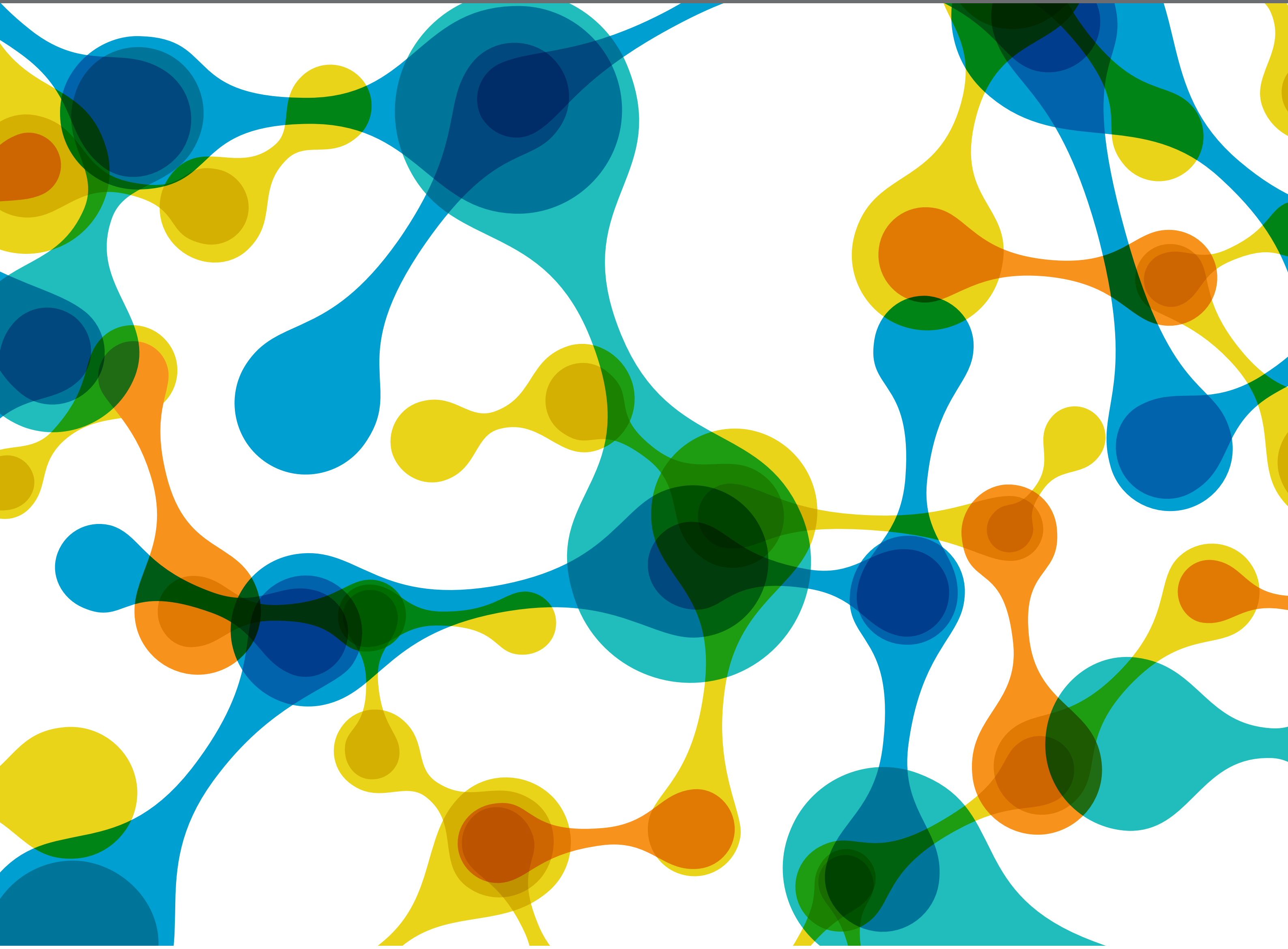

frontiers Research Topics

ISSN 1664-8714
ISBN 978-2-88966-834-2
DOI 10.3389/978-2-88966-834-2

About Frontiers

Frontiers is more than just an open-access publisher of scholarly articles: it is a pioneering approach to the world of academia, radically improving the way scholarly research is managed. The grand vision of Frontiers is a world where all people have an equal opportunity to seek, share and generate knowledge. Frontiers provides immediate and permanent online open access to all its publications, but this alone is not enough to realize our grand goals.

Frontiers Journal Series

The Frontiers Journal Series is a multi-tier and interdisciplinary set of open-access, online journals, promising a paradigm shift from the current review, selection and dissemination processes in academic publishing. All Frontiers journals are driven by researchers for researchers; therefore, they constitute a service to the scholarly community. At the same time, the Frontiers Journal Series operates on a revolutionary invention, the tiered publishing system, initially addressing specific communities of scholars, and gradually climbing up to broader public understanding, thus serving the interests of the lay society, too.

Dedication to Quality

Each Frontiers article is a landmark of the highest quality, thanks to genuinely collaborative interactions between authors and review editors, who include some of the world's best academicians. Research must be certified by peers before entering a stream of knowledge that may eventually reach the public - and shape society; therefore, Frontiers only applies the most rigorous and unbiased reviews.
Frontiers revolutionizes research publishing by freely delivering the most outstanding research, evaluated with no bias from both the academic and social point of view. By applying the most advanced information technologies, Frontiers is catapulting scholarly publishing into a new generation.

What are Frontiers Research Topics?

Frontiers Research Topics are very popular trademarks of the Frontiers Journals Series: they are collections of at least ten articles, all centered on a particular subject. With their unique mix of varied contributions from Original Research to Review Articles, Frontiers Research Topics unify the most influential researchers, the latest key findings and historical advances in a hot research area! Find out more on how to host your own Frontiers Research Topic or contribute to one as an author by contacting the Frontiers Editorial Office: frontiersin.org/about/contact

MECHANO-CALCIUM, MECHANO-ELECTRIC, AND MECHANO-METABOLIC FEEDBACK LOOPS: CONTRIBUTION TO THE MYOCARDIUM CONTRACTION IN HEALTH AND DISEASES

Topic Editors:
Leonid Katsnelson, Institute of Immunology and Physiology (RAS), Russia
Gentaro Iribe, Asahikawa Medical University, Japan
Remi Peyronnet, University of Freiburg, Germany
Olga Solovyova, Institute of Immunology and Physiology (RAS), Russia

Citation: Katsnelson, L., Iribe, G., Peyronnet, R., Solovyova, O., eds. (2021). Mechano-Calcium, Mechano-Electric, and Mechano-Metabolic Feedback Loops: Contribution to the Myocardium Contraction in Health and Diseases. Lausanne: Frontiers Media SA. doi: 10.3389/978-2-88966-834-2

Table of Contents

05 ***Editorial: Mechano-Calcium, Mechano-Electric, and Mechano-Metabolic Feedback Loops: Contribution to the Myocardial Contraction in Health and Diseases***
Rémi Peyronnet, Olga Solovyova, Gentaro Iribe and Leonid B. Katsnelson

09 ***Length-Dependent Activation of Contractility and Ca-Transient Kinetics in Auxotonically Contracting Isolated Rat Ventricular Cardiomyocytes***
Oleg Lookin and Yuri Protsenko

19 ***Energetics Equivalent of the Cardiac Force-Length End-Systolic Zone: Implications for Contractility and Economy of Contraction***
Kenneth Tran, Andrew J. Taberner, Denis S. Loiselle and June-Chiew Han

27 ***Heart Plasticity in Response to Pressure- and Volume-Overload: A Review of Findings in Compensated and Decompensated Phenotypes***
Fotios G. Pitoulis and Cesare M. Terracciano

43 ***Modulation of Calcium Transients in Cardiomyocytes by Transient Receptor Potential Canonical 6 Channels***
Azmi A. Ahmad, Molly E. Streiff, Chris Hunter and Frank B. Sachse

56 ***Disruption of Transverse-Tubules Eliminates the Slow Force Response to Stretch in Isolated Rat Trabeculae***
Amelia Power, Sarbjot Kaur, Cameron Dyer and Marie-Louise Ward

65 ***The Degree of t-System Remodeling Predicts Negative Force-Frequency Relationship and Prolonged Relaxation Time in Failing Human Myocardium***
Maha Abu-Khousa, Dominik J. Fiegle, Sophie T. Sommer, Ghazali Minabari, Hendrik Milting, Christian Heim, Michael Weyand, Roland Tomasi, Andreas Dendorfer, Tilmann Volk and Thomas Seidel

75 ***Stretch-Induced Biased Signaling in Angiotensin II Type 1 and Apelin Receptors for the Mediation of Cardiac Contractility and Hypertrophy***
Kinya Seo, Victoria N. Parikh and Euan A. Ashley

89 ***The Effects of Mechanical Preload on Transmural Differences in Mechano-Calcium-Electric Feedback in Single Cardiomyocytes: Experiments and Mathematical Models***
Anastasia Khokhlova, Pavel Konovalov, Gentaro Iribe, Olga Solovyova and Leonid Katsnelson

104 ***May the Force Not Be With You During Culture: Eliminating Mechano-Associated Feedback During Culture Preserves Cultured Atrial and Pacemaker Cell Functions***
Noa Kirschner Peretz, Sofia Segal and Yael Yaniv

113 ***Arrhythmogenic Interaction Between Sympathetic Tone and Mechanical Stretch in Rat Pulmonary Vein Myocardium***
Yuriy V. Egorov, Leonid V. Rosenshtraukh and Alexey V. Glukhov

121 ***An Equivocal Final Link – Quantitative Determination of the Thermodynamic Efficiency of ATP Hydrolysis – Sullies the Chain of Electric, Ionic, Mechanical and Metabolic Steps Underlying Cardiac Contraction***
Christopher John Barclay and Denis Scott Loiselle

132 ***Ischemia Enhances the Acute Stretch-Induced Increase in Calcium Spark Rate in Ventricular Myocytes***
Breanne A. Cameron, Hiroaki Kai, Keiko Kaihara, Gentaro Iribe and T. Alexander Quinn

142 ***The Lectin LecA Sensitizes the Human Stretch-Activated Channel TREK-1 but Not Piezo1 and Binds Selectively to Cardiac Non-myocytes***
Elisa Darkow, Eva A. Rog-Zielinska, Josef Madl, Annette Brandel, Lina Siukstaite, Ramin Omidvar, Peter Kohl, Ursula Ravens, Winfried Römer and Rémi Peyronnet

158 ***High-Resolution Optical Measurement of Cardiac Restitution, Contraction, and Fibrillation Dynamics in Beating vs. Blebbistatin-Uncoupled Isolated Rabbit Hearts***
Vineesh Kappadan, Saba Telele, Ilija Uzelac, Flavio Fenton, Ulrich Parlitz, Stefan Luther and Jan Christoph

176 ***Insights From Computational Modeling Into the Contribution of Mechano-Calcium Feedback on the Cardiac End-Systolic Force-Length Relationship***
Megan E. Guidry, David P. Nickerson, Edmund J. Crampin, Martyn P. Nash, Denis S. Loiselle and Kenneth Tran

188 ***Sinoatrial Node Structure, Mechanics, Electrophysiology and the Chronotropic Response to Stretch in Rabbit and Mouse***
Eilidh A. MacDonald, Josef Madl, Joachim Greiner, Ahmed F. Ramadan, Sarah M. Wells, Angelo G. Torrente, Peter Kohl, Eva A. Rog-Zielinska and T. Alexander Quinn

203 ***Multiscale Modeling of Cardiovascular Function Predicts That the End-Systolic Pressure Volume Relationship Can Be Targeted via Multiple Therapeutic Strategies***
Kenneth S. Campbell, Brianna Sierra Chrisman and Stuart G. Campbell

215 ***Mechano-Electric Coupling and Arrhythmogenic Current Generation in a Computational Model of Coupled Myocytes***
Viviane Timmermann and Andrew D. McCulloch

frontiers in Physiology

EDITORIAL
published: 06 April 2021
doi: 10.3389/fphys.2021.676826

Editorial: Mechano-Calcium, Mechano-Electric, and Mechano-Metabolic Feedback Loops: Contribution to the Myocardial Contraction in Health and Diseases

Rémi Peyronnet[1,2], *Olga Solovyova*[3], *Gentaro Iribe*[4] *and Leonid B. Katsnelson*[3*]

[1] Institute for Experimental Cardiovascular Medicine, University Heart Center Freiburg Bad Krozingen, Freiburg, Germany, [2] Medical Center and Faculty of Medicine, University of Freiburg, Freiburg, Germany, [3] Institute of Immunology and Physiology, Russian Academy of Sciences, Ekaterinburg, Russia, [4] Department of Physiology, Asahikawa Medical University, Asahikawa, Japan

Keywords: myocardium contraction, electromechanical coupling, mechano-electric coupling, mechano-mechanical feedback, calcium transient, action potential, frank-starling law

Editorial on the Research Topic

Mechano-Calcium, Mechano-Electric, and Mechano-Metabolic Feedback Loops: Contribution to the Myocardium Contraction in Health and Diseases

Edited and reviewed by:
Peter J. Reiser,
The Ohio State University,
United States

****Correspondence:***
Leonid B. Katsnelson
leonidkatsnelson51@gmail.com

Specialty section:
This article was submitted to
Striated Muscle Physiology,
a section of the journal
Frontiers in Physiology

Received: *06 March 2021*
Accepted: *10 March 2021*
Published: *06 April 2021*

Citation:
Peyronnet R, Solovyova O, Iribe G and Katsnelson LB (2021) Editorial: Mechano-Calcium, Mechano-Electric, and Mechano-Metabolic Feedback Loops: Contribution to the Myocardial Contraction in Health and Diseases. Front. Physiol. 12:676826. doi: 10.3389/fphys.2021.676826

Sensing of and adaptation to mechanical forces in the heart are allowed in part by Mechano-Electric Coupling (MEC), including mechano-electric, -calcium, and -mechanical feedback mechanisms interrelating with each other. Mechanosensitivity of healthy and diseased hearts has been a focus of research interests for decades (Lab, 1982, 1996, 1999; Kohl et al., 1999; Kohl and Sachs, 2001; Takahashi et al., 2013). Many mechanisms underlying MEC are still unclear. The works presented in this Research Topic involve state-of-the-art experimental approaches, computational modeling and focused reviews, aimed at shedding light on some specific aspects of MEC which can be subdivided as follow.

MEC AND CARDIAC REMODELING

Cardiac metabolic, mechanical, electrical, and structural remodeling allows the heart to adapt its function to the demand. Such plasticity of the cardiac tissue and cells in response to hemodynamic loads is comprehensively reviewed by Pitoulis and Terraciano. Two more articles presented in the Research Topic also relate to remodeling (Abu-Khousa et al., Seo et al.).

FRANK-STARLING LAW AND UNDERLYING MECHANISMS

Three articles deal with “Force-Length” and “Pressure-Volume” relationships in single cardiomyocytes, multicellular preparations, and whole ventricle. Using a mathematical model of cardiac excitation-contraction, Guidry et al. compared end-systolic force-length relationships (ESFLR) simulated in isometric and work-loop contractions. These simulations show that the isometric ESFLR curve lies significantly higher than its work-loop counterpart, being in good agreement with the data of numerous experiments on muscle preparations and the whole heart. The authors attribute these results to the mechanosensitive kinetics of Ca^{2+} -TnC, while further analysis seems necessary.

The same team of researchers discovered close correlations between the stress-length and heat-stress relations in both isometric and work-loop contractions over wide ranges of preloads and afterloads in experiments on rat trabeculae (Tran et al.). Both relations changed in codirectional manner depending on mechanical loading. These data demonstrate tight interdependence between mechano-mechanical and mechano-energetic feedback loops.

To predict how perturbations of molecular level mechanisms in myocardium will scale up to modulate system-level properties, Campbell et al. developed a multiscale hemodynamic mathematical model using a single contractile element to drive a single hemisphere ventricle that pumps blood around a closed circulation. They found that the End-Systolic Pressure Volume Relationship was the most sensitive to small changes in molecular-level parameters compared to other system-level properties. The results suggested that a subtle deficit in nearly any aspect of sarcomere-level function could compromise contractility.

LOCATION MATTERS FOR MEC

Not only ventricle mechanosensitivity, but also that of other heart regions has been studied in the articles presented in this Topic. The pulmonary veins (PV) have been targeted as the source of the atrial arrhythmogenic activity. Egorov et al. investigated stretch-induced MEC to the development of arrhythmogenic ectopic beats from pulmonary veins. They found that pathological stretch facilitates the development of arrhythmogenic ectopic activity induced by high concentrations of adrenaline in pulmonary veins resulting in intra-PV conduction, frequent episodes of unstable reentrant activity, and atrial extra beats. These findings highlight an arrhythmogenic impact of pulmonary vein stretch in the development of atrial arrhythmias under elevated autonomic tone which could play a critical role in patients with elevated blood pressure.

Comparison of the chronotropic response of the isolated sinoatrial node (SAN) to stretch in rabbit and mouse allowed better understanding of interplay between structural, mechanical, and electrophysiological properties of the SAN as highlighted by MacDonald et al. Importantly, pharmacological interventions aimed to prolong mouse SAN action potential plateau duration resulted in stable positive chronotropic response similar to that of rabbit and other species.

Khokhlova et al. showed that preload might be a source for mechano-calcium-electric modulation in myocyte electrophysiological and contractile function across the wall. They experimentally studied the effect of stretch on the force characteristics of rat subendocardial and subepicardial single ventricular cardiomyocytes and analyzed the results using mathematical models. They concluded that greater myofilament length-dependent activation in subendocardial cells compared to subepicardial cells via MEC led to the reduction in the transmural differences in action potential duration at a higher preload.

CALCIUM, T-SYSTEM, AND TRANSIENT RECEPTOR POTENTIAL (TRP) CHANNELS IN MEC

Simulations carried out in one-dimensional computational model of electro-mechanics in rabbit ventricular cardiomyocyte with mechanically non-uniform sarcomeres (Timmermann and McCulloch) showed that myocyte stretch sequences may contribute significantly to the delayed after-depolarizations due to mechanically-triggered calcium waves in myocytes overloaded with calcium. In 1D multi-cellular chain models where such myocytes were coupled via gap junctions, the mechanically-induced waves contributed to synchronizing arrhythmogenic calcium waves and afterdepolarizations (*ibidem*).

This work seems to be in line with earlier studies, although those were focused on various mechanisms underlying the studied phenomena: one dealt with contribution of mechano-calcium feedbacks to arrhythmogenesis in cardiomyocytes overloaded with Ca^{2+} analyzed in a mathematical model (Sulman et al., 2008); the second reported on calcium waves triggered by heterogeneous contractions (Ter Keurs et al., 2005).

Lookin and Protsenko investigated how the extent of length-dependent activation (LDA) in cardiac cells may relate to the diastolic level of calcium and calcium-transient peak rest and/or activator calcium in rat cardiomyocytes. They have found that the extent of LDA is not determined by actual peak systolic tension but regulated by the Ca^{2+}-transient peak magnitude of activator calcium and the kinetics of the Ca^{2+}-transient decline. Their findings suggest that complex mechanisms of mechano-calcium feedback are involved with LDA.

Ahmad et al. describe the location and effects of transient receptor potential canonical 6 (TRPC6) channels in neonatal rat ventricular myocytes (NRVM) induced with an adenoviral vector to express enhanced-green fluorescent protein (eGFP) or TRPC6-eGFP. Induced NRVM exhibited increased sarcoplasmic reticulum calcium load compared to eGFP cells. These experimental findings were supported by ionic model simulations. Obtained results deepen the understanding of the processes underlying the stretch-induced activation of TRPC6 channels. Overexpression of TRPC6 channels may be involved in development of cardiac hypertrophy. This opens a new target for pharmacological therapies based on TRPC6 inhibitors.

Positive force-frequency relationship (FFR) is a characteristic of the healthy human heart. In chronically failing hearts the FFR becomes flat or negative. Reasons for this are not clearly established. Abu-Khousa et al. investigated whether remodeling of the transverse tubular system (t-system) could explain the alteration of the FFR. They show using human cardiac tissue slices that the remodeling of the t-system can predict FFR alterations.

Complementary to the analysis of the t-system alteration on the FFR, the impact of transverse tubule loss was next assessed on the slow force response. The latter and the β-adrenergic activation are shown to critically require transverse tubules (Power et al.).

Ischemic tissue exhibits altered mechanics and is more prone to arrhythmias. A better understanding of the mechanisms underlying such pro-arrhythmic substrate is the focus of the work from Cameron et al.. Ischemia is shown to enhance both stretch-induced increase of Ca^{2+} spark rate and the associated ROS production. Such mechanism may contribute to the generation of Ca^{2+}-induced arrhythmias.

STRETCH-INDUCED INTRACELLULAR SIGNALING

Molecular adaptations to mechanical overload during hypertrophy and heart failure is a subject of the review presented by Seo et al.. In response to overload, cardiac tissue adaptation processes are multifaceted and involve a large number of molecules. It has been suggested that angiotensin II type 1 receptor (AT_1R) and apelin receptor (APJ) are primary upstream actors with indirect mechano-sensing capacities contributing to both Ca^{2+}-dependent and Ca^{2+}-independent inotropic effects. Seo et al. review the impact of AT_1R and APJ signaling pathway activation by ligand *vs.* mechanical stimuli on inotropy and cardiac hypertrophy. The relevance of these receptors as therapeutical targets in the context of heart failure is also discussed.

TOOLS AND METHODS FOR MEC INVESTIGATION

Articles presented in the Research Topic Collection involve and describe various methodical approaches relevant in the area under consideration.

In particular, Darkow et al. present a cell-selective pharmacological tool to study cardiac mechano-sensors. Such tools are important to recognize various mechanisms underlying MEC. All cells in the heart sense their mechanical environment and adapt to it. To do so, mechano-sensors such as stretch-activated channels are believed to be important players. Modulating their activity in a selective manner has always been a target and a challenge. Lectin A may offer an original way to sensitize TREK-1 but not Piezo1 to stretch. Interestingly, this curvature-inducing protein binds only to non-myocytes in the heart and not to cardiomyocytes.

A further noteworthy aspect of the impact of mechanical conditions on contractility and electrical activity of the cardiomyocytes is disclosed in the review dealing with preconditioning of cultured cells (Peretz et al.). It turns out that elimination of contraction during culturing preserves important MEC properties of cultured myocytes, in particular, cultured pacemaker, and atrial cells.

Elimination of contraction was implemented also by Kappadan et al. in Langendorff experiments with whole hearts. Particular effects of contractions on myocardial electrical activity are still a matter of debate. Different studies demonstrated either shortening or lengthening, or no response of action potentials in isolated cells or myocardial tissue to the mechanical perturbations. Kappadan et al. utilized optical mapping techniques to compare ventricular electrophysiology in beating *vs.* contraction-inhibited isolated rabbit hearts. They observed shorter action potential durations in contracting hearts. The results do not allow one to distinguish pure effects of contraction from possible effects of mild hypoxia in contracting hearts during Langendorff-perfusion (Garrot et al., 2017). Further studies might elucidate the matter.

ENERGETICS

Last but not least, two studies focus on mechano-energetic coupling. In addition to the above-cited article by Tran et al. dealing with the energetics equivalent of the Cardiac FLR, there is the article by Barclay and Loiselle studying quantitative determination of the thermodynamic efficiency of ATP hydrolysis. This work was initiated by a mismatch between ATP yield per mole of glucose inferred from thermal studies compared to that seen in mitochondria oxidation [see *e.g.,* Rich (2003) or Salway (2004)]. The authors tried to probe this discrepancy using a thermodynamically constrained algebraic model of cardiac mechano-energetics. They conclude that the mismatch is due to different techniques between myothermic and mitochondrial experiments. Future improvement of technology in the field may reconcile them and further the understanding of cardiac mechano-energetics.

Considering long-term perspectives, it would be interesting to study other manifestations of the mechano-energetic coupling, *e.g.,* investigating whether different mechanical loading conditions of the cardiomyocyte are associated with differences in energy consumption. Are there intracellular mechanisms that might allow maintaining the necessary level of ATP in the cytosol under any mechanical loading, and if so, what are these mechanisms? Perhaps, this topic will be explored in the future along with a host of other subjects from the exciting field of cardiac mechano-sensitivity and adaptation. The interesting results reported and discussed within this Research Topic will hopefully stimulate future studies in this area.

AUTHOR CONTRIBUTIONS

All authors contributed to the first draft of the manuscript, manuscript revision, and read and approved the submitted version.

ACKNOWLEDGMENTS

We would like to thank all contributing authors for their time and effort.

REFERENCES

Garrot, K., Kuzmiak-Glancy, S., Wengrowski, A., Zhang, H., Rogers, J. M., and Kay, M. W. (2017). Katp channel inhibition blunts electromechanical decline during hypoxia in left ventricular working rabbit hearts. *J. Physiol.* 595, 3799–3813. doi: 10.1113/JP273873

Kohl, P., Hunter, P., and Noble, D. (1999). Stretch-induced changes in heart rate and rhythm: clinical observations, experiments and mathematical models. *Prog. Biophys. Mol. Biol.* 71, 91–138. doi: 10.1016/S0079-6107(98)00038-8

Kohl, P., and Sachs, F. (2001). Mechanoelectric feedback in cardiac cells. *Philos. Trans. R. Soc. Math. Phys. Eng. Sci.* 359, 1173–1185. doi: 10.1098/rsta.2001.0824

Lab, M. J. (1982). Contraction-excitation feedback in myocardium. Physiological basis and clinical relevance. *Circ. Res.* 50, 757–766. doi: 10.1161/01.RES.50.6.757

Lab, M. J. (1996). Mechanoelectric feedback (transduction) in heart: concepts and implications. *Cardiovasc. Res.* 32, 3–14. doi: 10.1016/S0008-6363(96)00088-0

Lab, M. J. (1999). Mechanosensitivity as an integrative system in heart: an audit. *Prog. Biophys. Mol. Biol.* 71, 7–27. doi: 10.1016/S0079-6107(98)00035-2

Rich, P. R. (2003). The molecular machinery of Keilin's respiratory chain. *Biochem. Soc. Trans.* 31, 1095–1105. doi: 10.1042/bst0311095

Salway, J. S. (2004). *Metabolism at a Glance*, 3rd Edn. Oxford: Blackwell Publishing Ltd.

Sulman, T., Katsnelson, L. B., Solovyova, O., and Markhasin, V. S. (2008). Mathematical modeling of mechanically modulated rhythm disturbances in homogeneous and heterogeneous myocardium with attenuated activity of $Na+$-$K+$ pump. *Bull. Math. Biol.* 70, 910–949. doi: 10.1007/s11538-007-9285-y

Takahashi, K., Kakimoto, Y., Toda, K., and Naruse, K. (2013). Mechanobiology in cardiac physiology and diseases. *J. Cell. Mol. Med.* 17, 225–232. doi: 10.1111/jcmm.12027

Ter Keurs, H. E. D. J., Wakayama, Y., Miura, M., Stuyvers, B. D., Boyden, P. A., and Landesberg, A. (2005). Spatial nonuniformity of contraction causes arrhythmogenic $Ca2^+$ waves in rat cardiac muscle. *Ann. N. Y. Acad. Sci.* 1047, 345–365. doi: 10.1196/annals.1341.031

Conflict of Interest: The authors declare that the research was conducted in the absence of any commercial or financial relationships that could be construed as a potential conflict of interest.

frontiers in Physiology

ORIGINAL RESEARCH
published: 11 December 2019
doi: 10.3389/fphys.2019.01473

Length-Dependent Activation of Contractility and Ca-Transient Kinetics in Auxotonically Contracting Isolated Rat Ventricular Cardiomyocytes

Oleg Lookin[1,2] and Yuri Protsenko[1]*

[1]Laboratory of Biological Motility, Institute of Immunology and Physiology, Ural Branch of Russian Academy of Sciences, Yekaterinburg, Russia, [2]Center for Fundamental Biotechnology and Bioengineering, Institute of Natural Sciences and Mathematics, Ural Federal University, Yekaterinburg, Russia

Edited by:
Gentaro Iribe,
Asahikawa Medical University, Japan

Reviewed by:
Olivier Cazorla,
Université de Montpellier, France
Denis Scott Loiselle,
The University of Auckland,
New Zealand

****Correspondence:***
Oleg Lookin
o.lookin@iip.uran.ru

Specialty section:
This article was submitted to Biophysics,
a section of the journal
Frontiers in Physiology

Received: *03 September 2019*
Accepted: *14 November 2019*
Published: *11 December 2019*

Citation:
Lookin O and Protsenko Y (2019) Length-Dependent Activation of Contractility and Ca-Transient Kinetics in Auxotonically Contracting Isolated Rat Ventricular Cardiomyocytes.
Front. Physiol. 10:1473.
doi: 10.3389/fphys.2019.01473

Length-dependent activation (LDA) of contraction is an important mechanism of proper myocardial function that is often blunted in diseases accompanied by deficient contractility and impaired calcium homeostasis. We evaluated how the extent of LDA is related to the decreased force in healthy rat myocardium under negative inotropic conditions that affect the calcium cycle. The length-dependent effects on auxotonic twitch and Ca-transient were compared in isolated rat ventricular cardiomyocytes at room temperature ("25C") and near-physiological temperature ("35C") in normal Tyrode and at 25°C with thapsigargin-depleted sarcoplasmic reticulum ("25C + Thap"). At the slack length, a similar negative inotropy in "35C" and "25C + Thap" was accompanied by totally different changes in Ca-transient amplitude, time-to-peak, and time-to-decline from peak to 50% amplitude. End-systolic/end-diastolic tension-sarcomere length relationships were obtained for each individual cell, and the ratio of their slopes, the dimensionless Frank-Starling Gain index, was 2.32 ± 0.16, 1.78 ± 0.09, and 1.37 ± 0.06 in "25C," "35C" and "25C + Thap," respectively (mean ± S.E.M.). Ca-transient diastolic level and amplitude did not differ between "25C" and "35C" at any SL, but in "35C" it developed and declined significantly faster. In contrast, thapsigargin-induced depletion of SERCA2a significantly attenuated and retarded Ca-transient. The relative amount of Ca^{2+} utilized by troponin C, evaluated by the integral magnitude of a short-lived component of Ca-transient decline ("bump"), increased by ~25% per each 0.05 μm increase in SL in all groups. The kinetics of the Ca-TnC dissociation, evaluated by the bump time-to-peak, was significantly faster in "35C" and slower in "25C + Thap" vs. "25C" (respectively, 63.7 ± 5.3 and 253.6 ± 8.3% of the value in "25C," mean ± S.E.M.). In conclusion, a similar inotropic effect can be observed in rat ventricular myocardium under totally different kinetics of free cytosolic calcium. The extent of LDA is not determined by actual peak systolic tension but is regulated by the level of peak systolic calcium and the kinetics of Ca-transient decline which, in turn, are governed by Ca-TnC dissociation and Ca^{2+} reuptake by the sarcoplasmic reticulum. Altogether, these findings constitute new evidence about the role of the length-dependent modulation of Ca^{2+} homeostasis in the mechanisms of calcium regulation of contraction and mechano-calcium feedback in the myocardium.

Keywords: rat myocardium, isolated cardiomyocyte, auxotonic contraction, Ca-transient, length-dependent activation, Frank-Starling mechanism

INTRODUCTION

The length-dependent activation (LDA) of myocardial contractility plays an important role in the adaptation of ventricular systolic pressure to the changes in end-diastolic ventricular volume. LDA constitutes the Frank-Starling Mechanism (FSM) and in normal myocardium is regulated by numerous well-tuned mechanisms, including myofilamental Ca^{2+} sensitivity (Dobesh et al., 2002), coordinated actomyosin interaction (Farman et al., 2011; Milani-Nejad et al., 2015; Zhang et al., 2017), giant protein titin (Cazorla et al., 2001; Fukuda and Granzier, 2004; Li et al., 2019), and the phosphorylation of myosin binding protein C and regulatory protein troponin (Korte et al., 2012; Wijnker et al., 2014; Kumar et al., 2015).

The availability of Ca^{2+} ions to interact with regulatory units of thin filaments is a primary condition for the initiation of a contractile response. While the cooperative activation of contractile filaments itself is independent of the sarcomere length, the Ca^{2+} sensitivity of myofilaments increases with longer sarcomere length (de Tombe et al., 2010). Therefore, dynamic changes of free cytosolic calcium in electrically stimulated cardiac cells (Ca-transient) are vital to how calcium ions will communicate with myofilaments. In contrast, the mechanical state of sarcomeres like prestretch will strongly affect these changes. Environmental factors, both physical ones like temperature and biochemical ones like treatment with a drug, may affect the level of diastolic and/or cytosolic Ca^{2+}, for example *via* the ATP-dependent Ca^{2+} pump of the sarcoplasmic reticulum (SERCA2a). These changes in Ca^{2+} homeostasis lead to modifications in the length-dependent activation of contraction (ter Keurs, 2012; Smith and Eisner, 2019). While the FSM can be easily assessed from the force-length relationship under different inotropic conditions, it is still questionable how substantial changes in diastolic or peak systolic Ca^{2+} can modulate LDA.

The length-dependent activation (LDA) of contraction was evaluated in auxotonically contracting rat ventricular cardiomyocytes under three environmental conditions: in normal saline at 25°C (the referent condition), in normal saline at 35°C, and in thapsigargin-containing saline at 25°C. An increase in temperature from 25 to 35°C was chosen to accelerate Ca^{2+} uptake by SERCA2a, which is a main contributor to Ca^{2+} extrusion from the interfilament space (Bassani et al., 1994; Mackiewicz and Lewartowski, 2006). Thapsigargin, in contrast, inhibits SERCA2a (Bassani et al., 1994; Treiman et al., 1998; Bassani and Bassani, 2003) and has an opposite effect on the kinetics of free cytosolic Ca^{2+}. It is assumed that both conditions have a minor direct effect on the intrinsic properties of contractile machinery compared to Ca^{2+}-induced modulation of contraction. In this study, we compared the extent of LDA in cardiac cells with substantially different levels of Ca^{2+} to answer two main questions: (1) which changes in Ca-transient characteristics underlie length-dependent effects on force generation and (2) is force deficiency under negative inotropic conditions accompanied by the loss of LDA.

MATERIALS AND METHODS

This study was carried out in accordance with the principles of the Basel Declaration and recommendations of The Animal Care and Use Committee of the Institute of Immunology and Physiology UB RAS (IIP). The experimental protocol was approved by The Animal Care and Use Committee of IIP. The animals were obtained from the Institutional Animal House and maintained under standard conditions.

Isolation of Ventricular Cardiomyocytes

Two-month-old male and female Wistar rats were used in this study. The rats were anesthetized with 15 mg/kg zolazepam (Zoletil100®; Virbac, Carros, France), injected by heparin (1,000 U/kg), and were euthanized 15 min later. The isolated heart was cannulated through the aorta to the Whole Heart Perfusion System (Radnoti, AD Instruments, Australia) and Langendorff-perfused by modified Krebs-Henseleit Buffer (KHB, in mM: NaCl 118, KCl 4.7, $MgSO_4$ 1.2, KH_2PO_4 1.2, $NaHCO_3$ 25, HEPES 10, $CaCl_2$ 1.25, glucose 11.1) at 37°C and saturated with 95% O_2 + 5% CO_2. After equilibration at the rate of 90–180 beats/min, the perfusion was switched to nominally Ca^{2+}-free KHB (25 μM $CaCl_2$), and the heart was perfused for 25–30 min more. After that, enzymatic digestion of extracellular tissue was performed by adding collagenase (1 mg/ml Collagenase Type 2, Worthington Biochemical Corporation, USA) to the nominally Ca^{2+}-free KHB and perfusion by this media for another 20 min. The digested ventricles were fragmented in nominally Ca^{2+}-free and collagenase-free KHB. The cell suspension was transferred to Tyrode (in mM: NaCl 140, KCl 4.7, $MgSO_4$ 1.2, HEPES 10, glucose 11.1) and slowly saturated by Ca^{2+} up to the final concentration of 1.25 mM. Ca^{2+}-tolerant, well-striated, rod-shaped cells were stained using Ca^{2+}-sensitive fluorophore rhod-2 (5 μM in final Tyrode) in its esterified AM-form. All chemicals were purchased from Sigma-Aldrich (St Louis, MO, USA) except for collagenase (Collagenase Type 2, Worthington Biochemical Corporation, USA).

Carbon Fiber Technique

Auxotonic contraction of a cardiomyocyte was measured by a pair of thin carbon fibers (Tsukuba Materials Information

Laboratory Ltd., Japan) attached to both ends of a cell and controlled by precise micromanipulators (MP285, Sutter Instrument, USA) and a command unit (ROE200, Sutter Instrument, USA). Contraction and Ca-transient were simultaneously measured by a laser confocal scanning microscope (LSM 710, Carl Zeiss, Germany). Prior to the measurement, a narrow region of scanning was selected on the cell image, assuming it contained both CFs (**Figure 1A**). Within the region, the intensity profile was reconstructed as a function of distance from the left edge of the image (**Figure 1B**). The distance between CFs, not the distance between the cell edges, was assumed to be the cell length. Dynamic changes in the CFs' positions were easily detected by the intensity profile as the areas with minimal intensity and were then converted to cell shortening traces (**Figure 1C**). Similarly, the mean sarcomere length was derived from the striation pattern of the cell *between* the fibers based on Discrete Fourier Transform, using custom-made software. In this study, only diastolic values of sarcomere length were used further in the analysis of length-related effects on cell mechanics and free cytosolic calcium. The amount of force produced by a cell was calculated as a product of cell shortening and mean stiffness coefficients of the two fibers (**Figure 1D**) and was converted to tension by dividing by the elliptical cross-sectional area of a cell ($S = \pi d^2/12$, where d is cell width), according to a common assumption that the cell width-to-depth ratio is about 3:1 (Nishimura et al., 2004). Simultaneous with the mechanical measurements, calcium transients (CaT) in the same cell were acquired (**Figure 1E**).

Force-Length Protocol

The distance between carbon fibers without any external load being applied was assumed to be the slack end-diastolic cell length (EDL_0). A step-by-step increase in length by several microns (2–5% of EDL_0) was applied until cell detachment occurred from the carbon fibers. Steady-state auxotonic twitches and Ca-transients (obtained as the F/F_0 ratio; F_0 is the fluorescence intensity in the quiescent cell at slack length) were recorded at each new length and ~10 individual twitches were averaged for further analysis. The characteristics of tension/CaT were analyzed as a function of relative end-diastolic cell length (% of EDL_0) or sarcomere length.

Force-length protocols were implemented for separate sets of cells incubated under different environmental conditions: at room temperature (25°C) and near-physiological (35°C) temperatures in normal Tyrode and at 25°C with specific depletion of sarcoplasmic reticulum Ca^{2+}-APTase (SERCA2a) by 1 μM thapsigargin in Tyrode. Thapsigargin is a non-competitive inhibitor of SERCA and prevents Ca^{2+} reuptake. For simplicity, these conditions are identified throughout the manuscript as "25C," "35C," and "25C + Thap." The twitches were elicited by electrical stimulation at 1 Hz pacing rate. Each cell was tested only in one condition because it was completely damaged after implementation of the force-length protocol and its removal from the carbon fibers.

Statistical Analysis

One-way ANOVA was used to evaluate the significance of difference in mean values between environmental conditions (between-group analysis): (1) twitch/Ca-transient characteristics obtained at slack length, and (2) slopes of linear approximation of tension-length relationships and Frank-Starling Gain values. Mann-Whitney *U*-test was used to evaluate the significance of difference between mean values of twitch characteristics measured under three environmental conditions at the same sarcomere length. The differences were considered significant at $p < 0.05$. Data are presented either as mean ± S.D. or

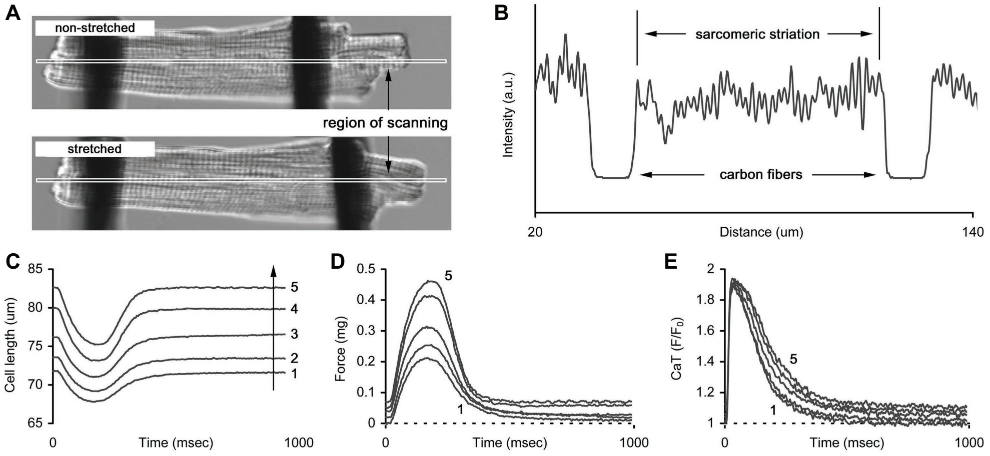

FIGURE 1 | The technique of carbon fibers (CFs) applied to manipulate the length of cardiomyocyte. **(A)** Two images of a cell without and with stretch applied by CFs. The long and narrow region of scanning indicates the area where image acquisition is performed to retrieve cell mechanics and sarcomeric striation. **(B)** The example of intensity profile obtained from a region of scanning. Two areas with lowest intensity correspond to the positions of CFs and the striation pattern *between* the areas is used to retrieve mean sarcomere length. **(C)** The series of auxotonic shortenings obtained at different cell lengths (numbered from 1 to 5, arrow indicates the increase in length). **(D)** The series of auxotonic forces calculated as a product of auxotonic shortening and mean stiffness coefficient of the carbon fibers used in this measurement. **(E)** The series of Ca-transients (CaT, presented as *F/F0* ratio) measured simultaneously with auxotonic shortenings shown in **(C)**. Numbers in **(C–E)** indicate cell length (1 – slack length, 2…4 – gradual increase in length, 5 – maximal length).

mean ± S.E.M. and are stated accordingly. The number of animals involved in the given group is indicated by "*N*," and the total number of cells in the group is indicated by "*n*."

RESULTS

Auxotonic Twitch and Ca-Transient at Slack Length

Figure 2 shows averaged auxotonic shortening and tension as well as the Ca-transient measured in rat ventricular cells at slack length under different conditions. The twitch developed and relaxed faster in cells of "35C" and slower in cells of "25C + Thap" compared to the group "25C" (**Figures 2A,B,D,E**), for example the maximal rate of tension rise, normalized to active tension, was 16.8 ± 3.3 1/s in "35C" and 7.5 ± 2.2 1/s in "25C + Thap," compared to 12.2 ± 1.8 1/s in "25C" (mean ± S.D.; all values were significantly different from each other, $p < 0.05$). However, both "35C" and "25C + Thap" cells showed less than one-half of the twitch amplitude in "25C" cells (**Figure 2B**). Also, a typical effect of an increase in temperature was a substantial acceleration of the Ca-transient in both the rise and decline without changing its amplitude, while SERCA2a depletion led to significant retardation and attenuation of the Ca-transient (**Figures 2C,F**).

Length-Dependent Effect on Mechanical Response in Auxotonic Twitch

To assess length-dependent changes in contractility under different inotropic conditions, auxotonic twitches were measured in cardiomyocytes subjected to a protocol of length change. Sarcomere length (SL) was measured in the diastolic phase. **Figure 3A** represents the plots of end-diastolic/end-systolic tension vs. end-diastolic sarcomere length (EDT-EDSL, the top row of panels, and EST-EDSL, the bottom row of panels, respectively) obtained in individual cells under different experimental conditions, as indicated in the panels. Linear approximation of each individual EDT-EDSL relationship (**Figure 3A**, top row of panels) gave mean slope values of 40.3 ± 4.8, 29.4 ± 3.2, and 29.3 ± 3.2 (units are mN/mm^2 per one μm of SL) for "25C," "35C," and "25C + Thap" groups, respectively, in which no significant difference was observed between any of the two groups. SL-dependent potentiation of end-systolic tension was significantly higher in cells of "25C" (**Figure 3A**, bottom row of panels; the mean slope for the involved EST-EDSL relationships was 96.0 ± 13.0 mN/mm^2 per one μm of SL) compared to cells of "35C" (mean slope = 53.6 ± 6.8, p = 0.004) or "25C + Thap" (mean slope = 42.1 ± 5.9, p = 0.001). On the other hand, the mean slopes for "35C" and "25C + Thap" were not significantly different (p = 0.234).

As we proposed in our previous study (Bollensdorff et al., 2011), the ratio of slope coefficients of end-systolic/end-diastolic tension-length relationships, or dimensionless Frank-Starling Gain (FSG), is a useful index for evaluating length-dependent activation of contraction. Higher FSG values correspond to a greater length-dependent increase in peak force, i.e., a greater length-induced activation of contraction. This index amounted to 2.32 ± 0.74, 1.78 ± 0.47 and 1.37 ± 0.25 in cells of "25C," "35C," and "25C + Thap," respectively (**Figure 3B**), in which the mean values were significantly different between any two

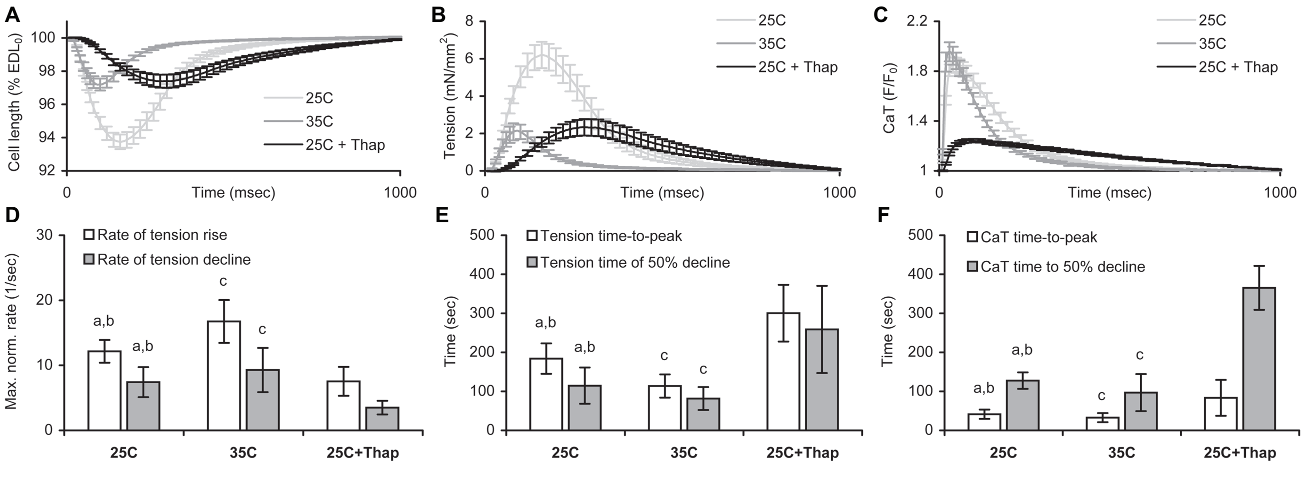

FIGURE 2 | The comparison of shortening, tension, and Ca-transient (CaT) characteristics obtained for isolated rat ventricular cells auxotonically contracting at slack length under different conditions: at room temperature in normal saline ("25C," *N* = 4 animals, *n* = 34 cells for mechanics, *n* = 32 cells for CaT); at near-physiological temperature in normal saline ("35C," *N* = 3 animals, *n* = 29 cells for mechanics/CaT); and at room temperature with depleted SERCA2a ("25C + Thap," *N* = 3 animals, *n* = 27 cells for mechanics/CaT). **(A)** The averaged relative shortening traces. **(B)** The averaged tension traces. **(C)** The averaged CaT traces, presented as the *F*/*F0* ratio, where *F0* is the fluorescence intensity measured in a quiescent cell at slack length. All traces shown as mean ± S.E.M. **(D)** The maximal rates of tension rise and decline, normalized to active tension. **(E)** The time-to-peak tension and time-to-decline of tension from peak to 50% amplitude (*T50*). **(F)** The time-to-peak CaT and time-to-decline of CaT from peak to 50% amplitude (CaT *T50*). *EDL0* – end-diastolic cell length. Data in **(D–F)** shown as mean ± S.D. ^{a} – significant difference between "25C" and "35C"; ^{b} – significant difference between "25C" and "25C + Thap"; ^{c} – significant difference between "35C" and "25C + Thap" (Mann-Whitney *U*-test, $p < 0.05$).

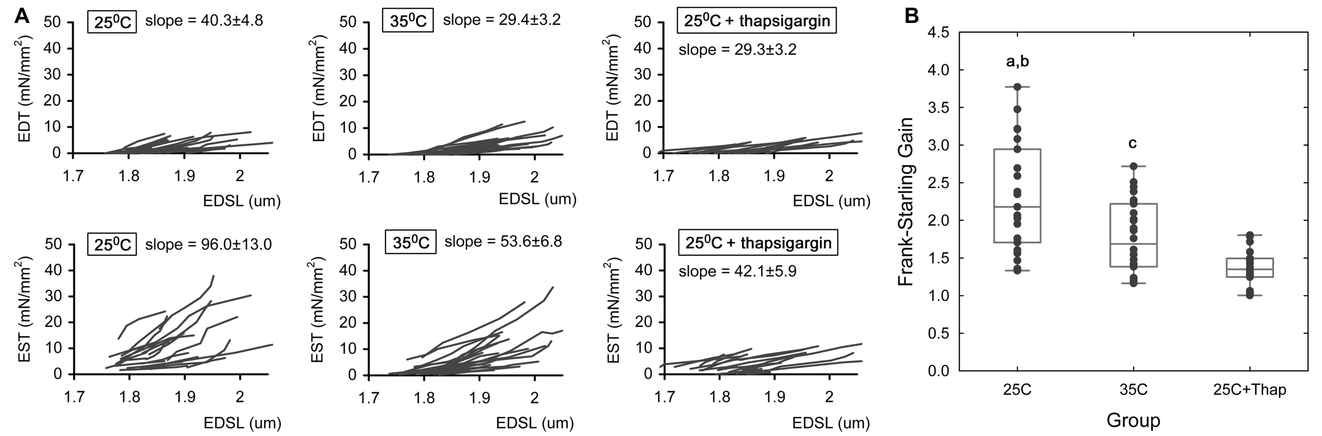

FIGURE 3 | The length-dependent change in active and passive tension in auxotonically contracting isolated rat ventricular cardiomyocytes under different experimental conditions. **(A)** The individual end-diastolic tension – end-diastolic sarcomere length relationships (the top row of panels) and end-systolic tension – end-diastolic sarcomere length relationships (the bottom row of panels) at room temperature in normal saline ("25C," *N* = 4 animals, *n* = 21 cells); at near-physiological temperature in normal saline ("35C," *N* = 3 animals, *n* = 26 cells); and at room temperature with depleted SERCA2a by thapsigargin ("25C + Thap," *N* = 3 animals, *n* = 18 cells). *EDT* – end-diastolic tension, *EST* – end-systolic tension, *EDSL* – end-diastolic sarcomere length. The slopes derived from linear approximation of each individual relationship were averaged and indicated as mean ± S.E.M., units are mN/mm^2 per one µm of SL. All scales are the same throughout. **(B)** The dimensionless Frank-Starling Gain obtained for the same cells of these groups as a ratio of slopes of EST-EDSL and EDT-EDSL relationships. Scatter-plots of raw data (dots), median value (central horizontal line in the boxes), and 25–75% percentiles are shown. [a] – significant difference between "25C" and "35C"; [b] – significant difference between "25C" and "25C + Thap"; [c] – significant difference between "35C" and "25C + Thap" (Student's two-sided *t*-test, $p < 0.05$).

groups (values given as mean ± S.D., $p < 0.05$). The results show that length-dependent increase in peak systolic tension, according to the Frank-Starling Mechanism, was extremely (roughly 2-fold) attenuated only in cells with depleted SERCA2a ("25C + Thap"), even though the similar extent of negative inotropic effect was observed in "35C" and "25C + Thap" under slack length (see **Figure 2B**).

As is evident from the data presented in **Figure 2**, an equivalent depression of systolic tension in "35C" and "25C + Thap" at slack length (compared to the value in "25C") was not followed by identical changes in timing properties of cell contraction. Similar findings were obtained in the cells subjected to length change protocol, e.g., at any sarcomere length (in the range of 1.8–1.95 µm), the values of time-to-peak tension were substantially smaller in "35C," but they increased in "25C + Thap," compared to the values of "25C." The time-to-decline from peak to 50% of amplitude (T_{50}) was significantly higher in "25C + Thap" vs. "25C" over the whole range of tested SL, but the significant difference between "25C" and "35C" was found only for SL = 1.8 and 1.85 µm. Nonetheless, neither time-to-peak nor T_{50} in any group of cells showed dependence on diastolic sarcomere length, so the quantitative difference remained virtually constant during the force-length protocol in which SL was increased from 1.8 to 1.95 µm. On average for this SL range and being compared to the values in "25C" group taken as 100%, the cells of "35C" and "25C + Thap" had, respectively, (1) time-to-peak value of 68.8 ± 4.2 and 157.5 ± 12.6% (values are given here as mean ± S.D.; both are significantly different from "25C," $p < 0.05$), and (2) T_{50} value of 90.6 ± 8.0 and 245.0 ± 8.6% (the last value is significantly different from "25C," $p < 0.05$).

Length-Dependent Effect on Ca-Transient

The deficiency in peak auxotonic shortening/tension observed in "35C" is thought to be related to faster Ca^{2+} removal from cytosol, since the amplitude of Ca-transient (CaT) at any end-diastolic SL was not changed vs. "25C" (**Figure 4B**), while the diastolic level of Ca-transient was significantly smaller in "35C" vs. "25C" at the sarcomere length of 1.9–1.95 µm (**Figure 4A**). In contrast, significant depression of active tension in the cells of "25C + Thap" correlates well to the substantially diminished Ca-transient amplitude, which constitutes, on average for SL between 1.8 and 1.95 µm, only 33.0 ± 1.8% of the value of "25C" (mean ± S.D., $p < 0.05$). The diastolic level of Ca-transient was found to gradually increase with SL in "25C" and "25C + Thap" (on average, by ~5.5 and ~2.6% of a value at SL = 1.8 µm per each 0.05 µm increase in sarcomere length), although a minor effect of SL on Ca-transient diastolic level was found in "35C" (**Figures 4A,B**). This possibly indicates a shallower end-diastolic tension-length relationship under near-physiological temperature vs. those obtained under 25°C (compare the mean slopes in **Figure 3A**). Note that Ca-transient amplitude did not change with SL in either condition (**Figure 4B**).

The Ca-transient decline from peak to 50% amplitude was found to be SL-independent in each group of cells (**Figure 4D**). This possibly reflects the length-independence of Ca^{2+} uptake by SR. However, Ca-transient time-to-peak values were affected by SL in the cells bathed in thapsigargin-free saline (**Figure 4C**). Both "25C" and "35C" groups showed gradual prolongation of Ca-transient time-to-peak (respectively, by 13.1 ± 11.8 and 10.3 ± 4.2% of the value at SL = 1.8 µm per each 0.05 µm increase in SL, mean ± S.D.), but no such tendency was found in the cells of "25C + Thap" (−1.6 ± 5.0%). This may relate to the different extent of Ca-TnC interaction in cells with

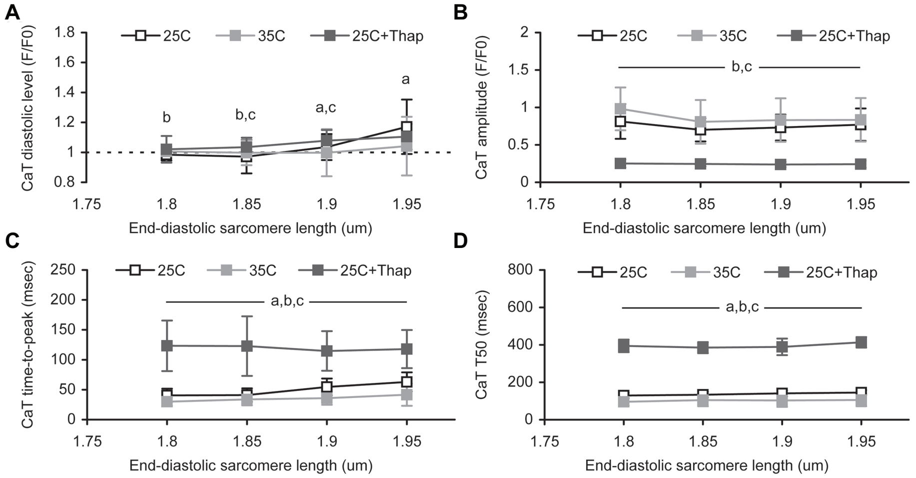

FIGURE 4 | The sarcomere length dependences of Ca-transient (CaT) characteristics obtained in auxotonically contracting isolated rat ventricular cells at room temperature in normal saline ("25C," *N* = 4 animals, *n* = 21 cells); at near-physiological temperature in normal saline ("35C," *N* = 3 animals, *n* = 24 cells); and at room temperature with depleted SERCA2a ("25C + Thap," *N* = 3 animals, *n* = 18 cells). **(A)** The diastolic level. **(B)** The amplitude. **(C)** The time-to-peak. **(D)** The time-to-decline from peak to 50% amplitude (*T50*). Data shown as mean ± S.D. Horizontal lines with the significance symbol(s) show the range where this significance is found. ^{a} – significant difference between "25C" and "35C"; ^{b} – significant difference between "25C" and "25C + Thap"; ^{c} – significant difference between "35C" and "25C + Thap" (Mann–Whitney *U*-test, $p < 0.05$).

normal and reduced peak systolic Ca^{2+} levels, which is discussed below. Interestingly, the mean value of relative peak shortening at slack length in "25C" was >2-fold higher vs. "25C + Thap," in contrast to Ca-transient amplitude, which was >3-fold higher. Therefore, while the lower extent of shortening-induced inactivation in the cells of the "25C + Thap" group would result in more prolonged Ca-transient at higher SL, as is expected from the length-dependent augmentation of Ca-TnC interaction, the veritable picture is quite the opposite due to the dramatically decreased total Ca^{2+} content in the thapsigargin-bathed cells. Also, absolute values of Ca-transient time-to-peak and T_{50}, gathered at SL between 1.8 and 1.95 μm, were significantly higher in "25C + Thap" and significantly lower in "35C" compared to the cells of the "25C" group, e.g., because the average for SL in 1.8–1.95 μm, Ca-transient time-to-peak was 71.3 ± 9.5 and 232.1 ± 59.1% of value for "25C" (mean ± S.D.; both are significantly different vs. "25C," $p < 0.05$).

To evaluate the length-dependent changes in the kinetics of Ca-TnC interaction in different environmental conditions, an extended analysis of Ca-transient was undertaken. Briefly, a progressive increase in the length of isometrically contracting rat cardiac muscle is accompanied by a concomitant short-lived component over monotonic decline of its Ca-transient [the so-called "bump" (Jiang et al., 1998; Kentish and Wrzosek, 1998)]. Previously, we showed a length-dependence of the bump extent in isometrically contracting rat trabeculae (Lookin and Protsenko, 2019). This analysis of Ca-transient bump characteristics was implemented in this study as well (**Figure 5A**). The (relative) amplitude of bump was obtained as a % of Ca-transient amplitude, and the (relative) integral magnitude (area) of bump was obtained as a % of the area under Ca-transient trace minus bump area. The time-to-peak of bump was obtained in raw milliseconds calculated from Ca-transient time-to-peak.

The relative amplitude of the bump was significantly higher in cells of "25C + Thap" compared to the "25C" and "35C" groups (**Figure 5B**) and displayed a gradual SL-dependent change. If the integral level of Ca-TnC interaction was evaluated by the integral magnitude of the bump, there was no significant difference between all groups for any SL (**Figure 5C**) except SL = 1.85 μm, in which "35C" was significantly higher vs. "25C + Thap" ($p = 0.025$). This indicates that integral Ca-TnC interaction in rat myocardium is highly proportional to sarcoplasmic Ca^{2+} content. Therefore, if contractile machinery of a cardiomyocyte is unchanged (e.g., thapsigargin-inhibited SERCA2a), the relative amount of Ca^{2+} utilized by TnC during the whole twitch is virtually independent of the Ca^{2+} available in cytosol. However, strongly in accordance with the molecular mechanisms of the Frank-Starling Law, the relative bump integral magnitude substantially increased with SL in "25C," "35C," and "25C + Thap," on average by 25.5 ± 12.3, 22.2 ± 22.0, and 26.6 ± 3.8%, respectively, per 0.05 μm increase in SL (values are given as mean ± S.D.; no significant difference was found between any two values). This result shows that acceleration or depletion of SERCA2a has a minor effect on the length-dependent increase of the relative amount of Ca^{2+} utilized by TnC.

Similar to the Ca-transient decline, the rate of bump development was accelerated ~1.5 times in cells of "35C" and decelerated ~2.5 times in cells of "25C + Thap" compared to "25C" (**Figure 5D**). On average for the tested SL (1.8–1.95 μm), the bump time-to-peak was, respectively, 63.7 ± 9.2 and 253.6 ± 14.4% of the value obtained in "25C" (values are given as mean ± S.D. and significantly differ from the mean value for "25C"). Note that the bump time-to-peak values in actively shortened cells were either SL-independent (as in "25C + Thap") or showed an SL-dependent *decrease*

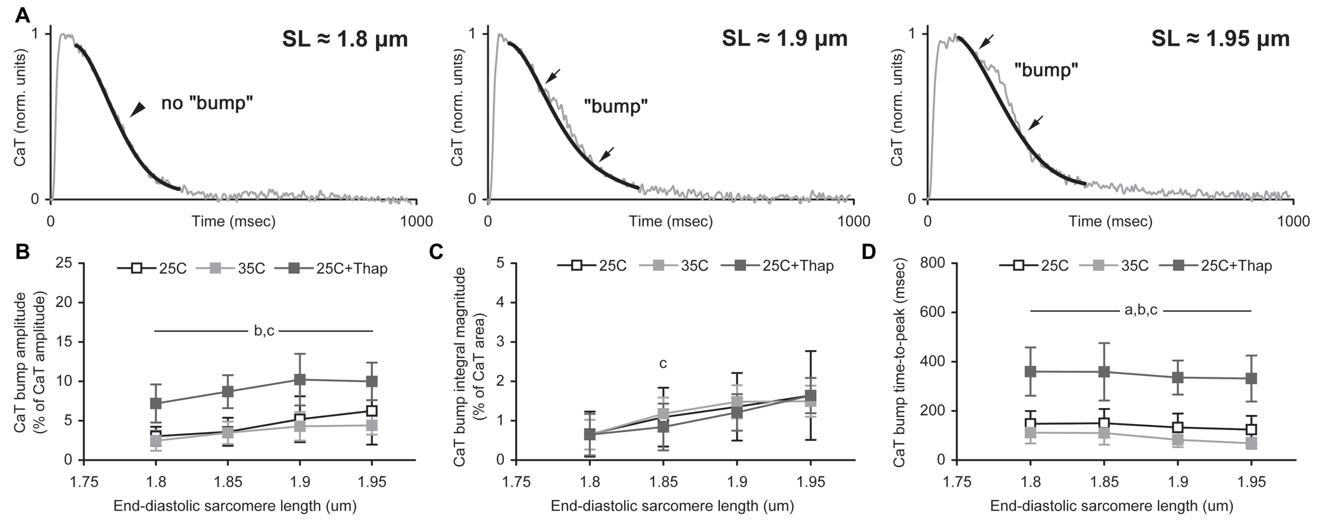

FIGURE 5 | The sarcomere length dependence of Ca-transient (CaT) bump. **(A)** The representative record of CaT traces demonstrating the effect of sarcomere length on the bump extent. Thin gray line shows original CaT trace, thick black line follows the monotonic decline, the bump is the difference between these two lines. Arrows indicate the points of beginning and ending of the bump. Corresponding sarcomere lengths are shown. **(B–D)** The CaT bump characteristics obtained in auxotonically contracting isolated rat ventricular cells at room temperature in normal saline ("25C," $N = 4$ animals, $n = 21$ cells); at near-physiological temperature in normal saline ("35C," $N = 3$ animals, $n = 18$ cells); and at room temperature with depleted SERCA2a ("25C + Thap," $N = 3$ animals, $n = 18$ cells). **(B)** The bump amplitude, as a % of CaT amplitude. **(C)** The bump integral magnitude (the bump area), as a % of area under complete CaT minus this bump area. **(D)** The bump time-to-peak, in msec. Data shown as mean ± S.D. Horizontal lines with the significance symbol(s) show the range where this significance is found. [a] – significant difference between "25C" and "35C"; [b] – significant difference between "25C" and "25C + Thap"; [c] – significant difference between "35C" and "25C + Thap" (Mann-Whitney *U*-test, $p < 0.05$).

(as in "35C"), in contrast to the previously observed length-related *increase* in the bump time-to-peak in isometrically contracting muscles (Lookin and Protsenko, 2019).

DISCUSSION

The length-dependent activation (LDA) of contraction was evaluated in auxotonically contracting rat ventricular cardiomyocytes under three environmental conditions: in normal saline at 25°C (assumed to be the referent state of SERCA2a), in normal saline at 35°C (accelerated Ca^{2+} uptake by SERCA2a), and in thapsigargin-containing saline at 25°C (depleted Ca^{2+} uptake by SERCA2a). The increase in temperature of thapsigargin-free saline affects the rate of Ca^{2+} uptake by sarcoplasmic reticulum (SR) and therefore accelerates Ca^{2+} removal from cytosolic space, thereby providing faster relaxation. Also, it may affect the relative contribution of SERCA, NCX, and PMCA to Ca^{2+} (Mackiewicz and Lewartowski, 2006) and therefore is involved in the regulation of diastolic Ca^{2+} level and contractile function (Shutt et al., 2006). Application of thapsigargin at 25°C had a similar negative inotropic effect but principally different lusitropic effect as well as effects on Ca-transient kinetics, compared to 35°C in normal saline. Thapsigargin, a non-competitive inhibitor of SERCA, prevents Ca^{2+} repletion of SR and markedly attenuates and prolongs Ca-transient (Bassani and Bassani, 2003). These changes in intracellular Ca^{2+} kinetics strongly modulate the contractile response of cardiac cell *via* EC-coupling and mechano-calcium feedback (Eisner et al., 2017). Partial inhibition of SERCA2a by 1 μM thapsigargin was needed to investigate LDA in cells with substantially altered Ca-handling while they were still able to contract.

Length-Dependent Effect on Mechanical Response and Ca-Transient

The main conclusions of this study are (1) similar negative inotropic effects of certain conditions do not necessarily correspond to the same changes in the level of peak systolic Ca^{2+}, (2) the negative inotropic effect is not necessarily accompanied by a deficiency in LDA, and (3) the extent of LDA deficiency is modulated by both the level of peak systolic Ca^{2+} in cytosol and the kinetics of Ca-transient decline. Indeed, an increase in temperature from 25 to 35°C led to a prominent negative inotropic effect with a substantial acceleration of both force and Ca-transient decline. This agrees with previously published findings in rat myocardium (Janssen et al., 2002), but we did not observe accompanying temperature-dependent changes in Ca-transient amplitude. Application of thapsigargin at 25°C led to a negative inotropic effect similar to that found at 35°C in thapsigargin-free saline, but the cells with depleted SERCA2a did show a dramatic decrease in Ca-transient amplitude. Therefore, we conclude that the extent of inotropy is not directly related to the level of peak systolic Ca^{2+}, but rather to the dynamic changes in cytosolic Ca^{2+}, e.g., the rate of Ca-transient decline. Moreover, although peak tension was attenuated to a highly similar extent in the "35C" and "25C + Thap" groups, LDA was affected by temperature to a modest extent (the Frank-Starling Gain index decreased by <20% of the value at 25°C) compared to the SERCA2a-inhibited cells (the Frank-Starling Gain index decreased 2-fold). Note also that auxotonic contraction is accompanied by shortening-induced inactivation of contractility. It might be expected that the lesser shortening found in the cells of the "35C" and "25C + Thap" groups would intensify their LDA, as measured by Frank-Starling Gain, because these cells contracted under mechanical conditions that are somewhat "closer" to isometric. However, both showed smaller Frank-Starling Gains.

In contrast to length-dependent prolongation of the isometric twitch in healthy rat myocardium (Kentish and Wrzosek, 1998; Janssen et al., 2002; Lookin et al., 2015), the timing characteristics of auxotonic twitch/Ca-transient revealed moderate or minor SL-dependence (for SL = 1.8–1.95 μm) under any experimental condition. This might be closely related to the progressively increased amplitude of auxotonic shortening in a stretched cell and the enhanced shortening-induced attenuation and acceleration of the twitch (Hanft et al., 2008; Iribe et al., 2014). Also, this shortening-induced inactivation of myofilaments may be linked to titin-based modulation of Ca^{2+}-troponin interaction (Li et al., 2019) and/or force-dependent recruitment of strong-bound myosin cross-bridges (Campbell et al., 2018). As a result, a positive effect of increased preload and a negative effect of shortening counteract and provide little SL-related variation of timing characteristics in auxotonically beating cells. Indeed, tension and Ca-transient decline times were not affected by SL under all conditions tested in this study, thus supporting the finding that Ca^{2+} removal from cytosol *via* SERCA2a, the dominant player in rat myocardium, is not modulated by SL (Kentish and Wrzosek, 1998). It is interesting that cells with inhibited SERCA2a showed the smallest SL-dependence of Ca-transient timing properties. This may relate to the phenomenon of length-dependent modulation of interaction between Ca^{2+} and troponin C (TnC), e.g., *via* changes in Ca^{2+} sensitivity of the thin filament (Dobesh et al., 2002) or due to the contribution of titin (Fukuda and Granzier, 2004). At normal levels of cytosolic and SR Ca^{2+}, Ca-TnC interaction is more intense at larger SL and therefore affects Ca-transient to a greater extent. In cells with reduced Ca^{2+} load to SR (e.g., by thapsigargin), this Ca-dependent modulation of cooperative activation of myofilaments is attenuated, thereby giving negligible SL-dependence of Ca-TnC dissociation. Also, the relatively small effect of SL on Ca-transient decline time supports that SERCA2a can effectively uptake the full amount of Ca^{2+} released from TnC during active shortening. However, such an amount may modulate Ca^{2+} signaling pathways, e.g., nucleoplasmic Ca-transient regulating (Kiess and Kockskämper, 2019) or Ca^{2+}-dependent mechanisms essential for LDA in the myocardium (Neves et al., 2016).

The Ca-transient diastolic level was slightly elevated at 25 vs. 35°C at SL = 1.95 μm. Such a discrepancy may be related to the temperature-dependence of SR Ca^{2+} uptake. Ca^{2+} sensitivity of myofilaments is increased with SL and affects the diastolic level of Ca^{2+}. Ca^{2+} removal by SERCA2a is accelerated by temperature in rat myocardium (Mackiewicz and Lewartowski, 2006) and prevents a length-dependent shift in diastolic Ca^{2+}. The decreased rate of SR Ca^{2+} uptake, e.g. at low temperature or SERCA2a inhibition (Bassani et al., 1994), does not prevent it, similarly to guinea pig myocytes (Le Guennec et al., 1991). This finding contradicts other reports that found length-independence of diastolic Ca^{2+} in rat myocytes at 22–25°C. However, these studies used ~20% lower $[Ca^{2+}]_o$ (White et al., 1995; Hongo et al., 1996).

Our finding that the relative amplitude and relative integral magnitude of the bump may not follow the changes in the inotropic state in a similar manner (see section "Length-Dependent Effect on Ca-Transient" and **Figure 5**) indicates that careful interpretation of the bump characteristics is needed to speculate about Ca-TnC interaction and its dependence on SL and Ca^{2+} levels. For instance, if a putative Ca-TnC interaction is evaluated during a complete twitch, the integral magnitude of the bump is more reliable vs. the bump amplitude, which reflects a momentary Ca-TnC interaction. A promising finding of this study is that a rate of Ca^{2+} utilization by TnC in auxotonically contracting cells, indirectly obtained from the bump time-to-peak value, shows rather the opposite length-dependence compared to isometrically contracting muscles (Lookin et al., 2015; Lookin and Protsenko, 2019). This is very likely attributed to the shortening-induced inactivation of contraction: increased amplitude of auxotonic shortening in a pre-stretched cell induces more inactivation and faster release of Ca^{2+} from TnC. In contrast, sarcomeres do not shorten during an isometric twitch, and their contractility is regulated mainly by cooperative activation of contractile proteins. Therefore, dynamic changes in length and load continuously regulate Ca^{2+} utilization and redistribution between (intra) cellular components (Hanft et al., 2008; Cazorla and Lacampagne, 2011; ter Keurs, 2012) in which Ca-TnC interaction and Ca^{2+} reuptake by SR are thought to be mostly important in Ca-handling, at least due to their great potency to buffer Ca^{2+} ions (Eisner et al., 2017; Smith and Eisner, 2019). Importantly, the opposite length-related changes in the bump time-to-peak in isometric and auxotonic contractions convincingly support that the bump can be used for indirect evaluation of the kinetics of Ca^{2+} release from TnC during cardiac relaxation.

The Limitations of the Study

The mechanical response in isolated cardiomyocyte was measured by a carbon fiber technique that was introduced ~30 years ago (Le Guennec et al., 1990) and that is now extensively used (White et al., 1995; Hongo et al., 1996; Iribe et al., 2007; Prosser et al., 2013; Fowler et al., 2015; Helmes et al., 2016; Yamaguchi et al., 2017). The conventional method of two carbon fibers used in this study allowed sarcomere stretch by ~8%. Use of rigid carbon fiber to fix one of the cell ends may provide >10% stretch (Sugiura et al., 2006). Recently, an innovative modification was proposed to pinch each end of a cell using two fibers (Iribe et al., 2014). This improvement gives sarcomere stretch by >15% of the slack length, which is comparable to the effectiveness of biological adhesives like MyoTak™ (IonOptix, USA), which is used to attach a cell to the stretching device (Cazorla et al., 2005; Ait Mou et al., 2008; Prosser et al., 2013). To overcome the problem of the stretch-induced partial detachment of carbon fibers, we used a dimensionless Frank-Starling Gain index to evaluate length-dependent changes in contractility (Bollensdorff et al., 2011).

Another limitation concerns the uncontrollable extent of shortening-induced inactivation in auxotonically contracting cells. Also, since shortening is accompanied by a dynamic change in passive tension, special correction is needed to retrieve the real systolic force (King et al., 2011); similar approach was implemented here. A relatively small extent of shortening-induced inactivation can be achieved during isometric contraction (Iribe et al., 2007). Alternatively, controllable cell shortening, i.e., isotonic/physiological mode, can be used to compare two cells. Therefore, isometric/isotonic/physiological modes are more reasonable for force-length protocols in single cells, although their implementation requires special approaches. At present, only a few studies are available on isolated cells with flow length/load control are available (Iribe et al., 2007, 2014; Helmes et al., 2016) in which fast optical tracking of fibers' displacement is coordinated with tuned feedback control of their new positions according to the desired mode of contraction.

CONCLUSION

The inotropic effects in mammalian myocardium do not correlate simply with the level of peak systolic Ca^{2+} but are governed by dynamic changes in cytosolic Ca^{2+}. Totally different kinetics of Ca-transient may be accompanied by negative inotropism to the same extent. Similarly, the extent of length-dependent activation of contraction does not correspond simply to peak systolic tension but is regulated by the level of peak systolic Ca^{2+} and the kinetics of Ca-transient decline. The latter, in turn, is governed by Ca-TnC dissociation and Ca^{2+} reuptake by the sarcoplasmic reticulum. Our data indicate that, at least in healthy rat ventricular myocardium, the integral kinetics of Ca-TnC interaction (association plus dissociation) during a twitch is proportional to the sarcoplasmic Ca^{2+} content. The findings constitute new evidence about the role of length-dependent modulation of Ca-TnC interaction in the mechanisms of calcium regulation of contraction and mechano-calcium feedback in the myocardium.

DATA AVAILABILITY STATEMENT

The original raw records and datasets generated for this study are available on request to the corresponding author (as well as custom-made software needed to work with raw data).

ETHICS STATEMENT

This study was carried out in accordance with the recommendations of the regulations of the Animal Welfare Act, the National Institutes of Health Guide for the Care and Use of Laboratory Animals, "The Guiding Principles in the Care and Use of Animals" approved by the Council of the American Physiological Society. The experimental protocol was approved by The Animal Care and Use Committee of the Institute of Immunology and Physiology UB RAS.

AUTHOR CONTRIBUTIONS

OL and YP contributed to the conception and design of the study. OL performed experiments and data analysis. Both authors prepared the first draft of the manuscript, contributed to manuscript revision, read and approved the submitted version.

FUNDING

The study was carried out within the framework of the IIF UrB RAS theme No AAAA-A18-118020590031-8, supported by RFBR (grant #18-04-00572-a) and by RF Government Act #211 of March 16, 2013 (agreement 02.A03.21.0006).

REFERENCES

Ait Mou, Y., Le Guennec, J. Y., Mosca, E., de Tombe, P. P., and Cazorla, O. (2008). Differential contribution of cardiac sarcomeric proteins in the myofibrillar force response to stretch. *Pflugers Arch.* 457, 25–36. doi: 10.1007/s00424-008-0501-x

Bassani, R. A., and Bassani, J. W. M. (2003). Inhibition of the sarcoplasmic reticulum Ca2+ pump with thapsigargin to estimate the contribution of Na+-Ca2+ exchange to ventricular myocyte relaxation. *Braz. J. Med. Biol. Res.* 36, 1717–1723. doi: 10.1590/s0100-879x2003001200014

Bassani, J. W. M., Bassani, R. A., and Bers, D. M. (1994). Relaxation in rabbit and rat cardiac cells: species-dependent differences in cellular mechanisms. *J. Physiol. Lond.* 476, 279–293. doi: 10.1113/jphysiol.1994.sp020130

Bollensdorff, C., Lookin, O., and Kohl, P. (2011). Assessment of contractility in intact ventricular cardiomyocytes using the dimensionless 'Frank–Starling gain' index. *Pflugers Arch.* 462, 39–48. doi: 10.1007/s00424-011-0964-z

Campbell, K. S., Janssen, P. M. L., and Campbell, S. G. (2018). Force-dependent recruitment from the myosin off state contributes to length-dependent activation. *Biophys. J.* 115, 543–553. doi: 10.1016/j.bpj.2018.07.006

Cazorla, O., and Lacampagne, A. (2011). Regional variation in myofilament length-dependent activation. *Pflugers Arch.* 462, 15–28. doi: 10.1007/s00424-011-0933-6

Cazorla, O., Szilagyi, S., Le Guennec, J. Y., Vassort, G., and Lacampagne, A. (2005). Transmural stretch-dependent regulation of contractile properties in rat heart and its alteration after myocardial infarction. *FASEB J.* 19, 88–90. doi: 10.1096/fj.04-2066fje

Cazorla, O., Wu, Y., Irving, T. C., and Granzier, H. (2001). Titin-based modulation of calcium sensitivity of active tension in mouse skinned cardiac myocytes. *Circ. Res.* 88, 1028–1035. doi: 10.1161/hh1001.090876

de Tombe, P. P., Mateja, R. D., Tachampa, K., Ait Mou, Y., Farman, G. P., and Irving, T. C. (2010). Myofilament length dependent activation. *J. Mol. Cell. Cardiol.* 48, 851–858. doi: 10.1016/j.yjmcc.2009.12.017

Dobesh, D. P., Konhilas, J. P., and de Tombe, P. P. (2002). Cooperative activation in cardiac muscle: impact of sarcomere length. *Am. J. Physiol. Heart Circ. Physiol.* 282, H1055–H1062. doi: 10.1152/ajpheart.00667.2001

Eisner, D. A., Caldwell, J. L., Kistamás, K., and Trafford, A. W. (2017). Calcium and excitation-contraction coupling in the heart. *Circ. Res.* 121, 181–195. doi: 10.1161/CIRCRESAHA.117.310230

Farman, G. P., Gore, D., Allen, E., Schoenfelt, K., Irving, T. C., and de Tombe, P. P. (2011). Myosin head orientation: a structural determinant for the Frank-Starling relationship. *Am. J. Physiol. Heart Circ. Physiol.* 300, H2155–H2160. doi: 10.1152/ajpheart.01221.2010

Fowler, E. D., Benoist, D., Drinkhill, M. J., Stones, R., Helmes, M., Wüst, R. C., et al. (2015). Decreased creatine kinase is linked to diastolic dysfunction in rats with right heart failure induced by pulmonary artery hypertension. *J. Mol. Cell. Cardiol.* 86, 1–8. doi: 10.1016/j.yjmcc.2015.06.016

Fukuda, N., and Granzier, H. (2004). Role of the giant elastic protein titin in the Frank-Starling mechanism of the heart. *Curr. Vasc. Pharmacol.* 2, 135–139. doi: 10.2174/1570161043476357

Hanft, L. M., Korte, F. S., and McDonald, K. S. (2008). Cardiac function and modulation of sarcomeric function by length. *Cardiovasc. Res.* 77, 627–636. doi: 10.1093/cvr/cvm099

Helmes, M., Najafi, A., Palmer, B. M., Breel, E., Rijnveld, N., Iannuzzi, D., et al. (2016). Mimicking the cardiac cycle in intact cardiomyocytes using diastolic and systolic force clamps; measuring power output. *Cardiovasc. Res.* 111, 66–73. doi: 10.1093/cvr/cvw072

Hongo, K., White, E., Le Guennec, J. Y., and Orchard, C. H. (1996). Changes in [Ca2+]i, [Na+]i and Ca2+ current in isolated rat ventricular myocytes following an increase in cell length. *J. Physiol.* 491, 609–619. doi: 10.1113/jphysiol.1996.sp021243

Iribe, G., Helmes, M., and Kohl, P. (2007). Force-length relations in isolated intact cardiomyocytes subjected to dynamic changes in mechanical load. *Am. J. Physiol. Heart Circ. Physiol.* 292, H1487–H1497. doi: 10.1152/ajpheart.00909.2006

Iribe, G., Kaneko, T., Yamaguchi, Y., and Naruse, K. (2014). Load dependency in force-length relations in isolated single cardiomyocytes. *Prog. Biophys. Mol. Biol.* 115, 103–114. doi: 10.1016/j.pbiomolbio.2014.06.005

Janssen, P. M. L., Stull, L. B., and Marbán, E. (2002). Myofilament properties comprise the rate-limiting step for cardiac relaxation at body temperature in the rat. *Am. J. Physiol. Heart Circ. Physiol.* 282, H499–H507. doi: 10.1152/ajpheart.00595.2001

Jiang, Y., Patterson, M. F., Morgan, D. L., and Julian, F. J. (1998). Basis for late rise in fura 2 R signal reporting [Ca2+]i during relaxation in intact rat ventricular trabeculae. *Am. J. Phys.* 274, C1273–C1282

Kentish, J. C., and Wrzosek, A. (1998). Changes in force and cytosolic Ca2+ concentration after length changes in isolated rat ventricular trabeculae. *J. Physiol.* 506, 431–444. doi: 10.1111/j.1469-7793.1998.431bw.x

Kiess, T., and Kockskämper, J. (2019). SERCA activity controls the systolic calcium increase in the nucleus of cardiac myocytes. *Front. Physiol.* 10:56. doi: 10.3389/fphys.2019.00056

King, N. M., Methawasin, M., Nedrud, J., Harrell, N., Chung, C. S., Helmes, M., et al. (2011). Mouse intact cardiac myocyte mechanics: cross-bridge and titin-based stress in unactivated cells. *J. Gen. Physiol.* 137, 81–91. doi: 10.1085/jgp.201010499

Korte, F. S., Feest, E. R., Razumova, M. V., Tu, A. Y., and Regnier, M. (2012). Enhanced Ca2+ binding of cardiac troponin reduces sarcomere length dependence of contractile activation independently of strong crossbridges. *Am. J. Physiol. Heart Circ. Physiol.* 303, H863–H870. doi: 10.1152/ajpheart.00395.2012

Kumar, M., Govindan, S., Zhang, M., Khairallah, R. J., Martin, J. L., Sadayappan, S., et al. (2015). Cardiac myosin-binding protein C and troponin-I phosphorylation independently modulate myofilament length-dependent activation. *J. Biol. Chem.* 290, 29241–29249. doi: 10.1074/jbc.M115.686790

Le Guennec, J. Y., Peineau, N., Argibay, J. A., Mongo, K. G., and Garnier, D. (1990). A new method of attachment of isolated mammalian ventricular myocytes for tension recording: length dependence of passive and active tension. *J. Mol. Cell. Cardiol.* 22, 1083–1093. doi: 10.1016/0022-2828(90)90072-A

Le Guennec, J. Y., White, E., Gannier, F., Argibay, J. A., and Garnier, D. (1991). Stretch-induced increase of resting intracellular calcium concentration in single Guinea-pig ventricular myocytes. *Exp. Physiol.* 76, 975–978. doi: 10.1113/expphysiol.1991.sp003560

Li, K. L., Methawasin, M., Tanner, B. C. W., Granzier, H. L., Solaro, R. J., and Dong, W. J. (2019). Sarcomere length-dependent effects on Ca2+-troponin regulation in myocardium expressing compliant titin. *J. Gen. Physiol.* 151, 30–41. doi: 10.1085/jgp.201812218

Lookin, O., Balakin, A., Kuznetsov, D., and Protsenko, Y. (2015). The length-dependent activation of contraction is equally impaired in impuberal male and female rats in monocrotaline-induced right ventricular failure. *Clin. Exp. Pharmacol. Physiol.* 42, 1198–1206. doi: 10.1111/1440-1681.12471

Lookin, O., and Protsenko, Y. (2019). The lack of slow force response in failing rat myocardium: role of stretch-induced modulation of Ca-TnC kinetics. *J. Physiol. Sci.* 69, 345–357. doi: 10.1007/s12576-018-0651-3

Mackiewicz, U., and Lewartowski, B. (2006). Temperature dependent contribution of Ca2+ transporters to relaxation in cardiac myocytes: important role of sarcolemmal Ca2+-ATPase. *J. Physiol. Pharmacol.* 57, 3–15.

Milani-Nejad, N., Canan, B. D., Elnakish, M. T., Davis, J. P., Chung, J. H., Fedorov, V. V., et al. (2015). The Frank-Starling mechanism involves deceleration of cross-bridge kinetics and is preserved in failing human right ventricular myocardium. *Am. J. Physiol. Heart Circ. Physiol.* 309, H2077–H2086. doi: 10.1152/ajpheart.00685.2015

Neves, J. S., Leite-Moreira, A. M., Neiva-Sousa, M., Almeida-Coelho, J., Castro-Ferreira, R., and Leite-Moreira, A. F. (2016). Acute myocardial response to stretch: what we(don't) know. *Front. Physiol.* 6:408. doi: 10.3389/fphys.2015.00408

Nishimura, S., Yasuda, S., Katoh, M., Yamada, K. P., Yamashita, H., Saeki, Y., et al. (2004). Single cell mechanics of rat cardiomyocytes under isometric, unloaded, and physiologically loaded conditions. *Am. J. Physiol. Heart Circ. Physiol.* 287, H196–H202. doi: 10.1152/ajpheart.00948.2003

Prosser, B. L., Khairallah, R. J., Ziman, A. P., Ward, C. W., and Lederer, W. J. (2013). X-ROS signaling in the heart and skeletal muscle: stretch-dependent local ROS regulates [Ca2+]i. *J. Mol. Cell. Cardiol.* 58, 172–181. doi: 10.1016/j.yjmcc.2012.11.011

Shutt, R. H., Ferrier, G. R., and Howlett, S. E. (2006). Increases in diastolic [Ca2+] can contribute to positive inotropy in Guinea pig ventricular myocytes in the absence of changes in amplitudes of Ca2+ transients. *Am. J. Physiol. Heart Circ. Physiol.* 291, H1623–H1634. doi: 10.1152/ajpheart.01245.2005

Smith, G. L., and Eisner, D. A. (2019). Calcium buffering in the heart in health and disease. *Circulation* 139, 2358–2371. doi: 10.1161/CIRCULATIONAHA.118.039329

Sugiura, S., Nishimura, S., Yasuda, S., Hosoya, Y., and Katoh, K. (2006). Carbon fiber technique for the investigation of single-cell mechanics in intact cardiac myocytes. *Nat. Protoc.* 1, 1453–1457. doi: 10.1038/nprot.2006.241

ter Keurs, H. E. D. J. (2012). The interaction of Ca2+ with sarcomeric proteins: role in function and dysfunction of the heart. *Am. J. Physiol. Heart Circ. Physiol.* 302, H38–H50. doi: 10.1152/ajpheart.00219.2011

Treiman, M., Caspersen, C., and Christensen, S. B. (1998). A tool coming of age: thapsigargin as an inhibitor of sarco-endoplasmic reticulum Ca2+-ATPases. *Trends Pharmacol. Sci.* 19, 131–135. doi: 10.1016/S0165-6147(98)01184-5

White, E., Boyett, M. R., and Orchard, C. H. (1995). The effects of mechanical loading and changes of length on single Guinea-pig ventricular myocytes. *J. Physiol.* 482, 93–107. doi: 10.1113/jphysiol.1995.sp020502

Wijnker, P. J., Sequeira, V., Foster, D. B., Li, Y., Dos Remedios, C. G., Murphy, A. M., et al. (2014). Length-dependent activation is modulated by cardiac troponin I bisphosphorylation at Ser23 and Ser24 but not by Thr143 phosphorylation. *Am. J. Physiol. Heart Circ. Physiol.* 306, H1171–H1181. doi: 10.1152/ajpheart.00580.2013

Yamaguchi, Y., Iribe, G., Kaneko, T., Takahashi, K., Numaga-Tomita, T., Nishida, M., et al. (2017). TRPC3 participates in angiotensin II type 1 receptor-dependent stress-induced slow increase in intracellular Ca2+ concentration in mouse cardiomyocytes. *J. Physiol. Sci.* 68, 153–164. doi: 10.1007/s12576-016-0519-3

Zhang, X., Kampourakis, T., Yan, Z., Sevrieva, I., Irving, M., and Sun, Y. B. (2017). Distinct contributions of the thin and thick filaments to length-dependent activation in heart muscle. *elife* 6:e24081. doi: 10.7554/eLife.24081

Conflict of Interest: The authors declare that the research was conducted in the absence of any commercial or financial relationships that could be construed as a potential conflict of interest.

frontiers in Physiology

ORIGINAL RESEARCH
published: 21 January 2020
doi: 10.3389/fphys.2019.01633

Energetics Equivalent of the Cardiac Force-Length End-Systolic Zone: Implications for Contractility and Economy of Contraction

Kenneth Tran[1], Andrew J. Taberner[1,2], Denis S. Loiselle[1,3] and June-Chiew Han[1]*

[1] Auckland Bioengineering Institute, The University of Auckland, Auckland, New Zealand, [2] Department of Engineering Science, The University of Auckland, Auckland, New Zealand, [3] Department of Physiology, The University of Auckland, Auckland, New Zealand

We have recently demonstrated the existence of a region on the cardiac mechanics stress-length plane, which we have designated "The cardiac end-systolic zone." The zone is defined as the area on the pressure-volume (or stress-length) plane within which all stress-length contraction profiles reach their end-systolic points. It is enclosed by three boundaries: the isometric end-systolic relation, the work-loop (shortening) end-systolic relation, and the zero-active stress isotonic end-systolic relation. The existence of this zone reflects the contraction-mode dependence of the cardiac end-systolic force-length relations, and has been confirmed in a range of cardiac preparations at the whole-heart, tissue and myocyte levels. This finding has led us to speculate that a comparable zone prevails for cardiac metabolism. Specifically, we hypothesize the existence of an equivalent zone on the energetics plane (heat vs. stress), and that it can be attributed to the recently-revealed heat of shortening in cardiac muscle. To test these hypotheses, we subjected trabeculae to both isometric contractions and work-loop contractions over wide ranges of preloads and afterloads. We found that the heat-stress relations for work-loop contractions were distinct from those of isometric contractions, mirroring the contraction mode-dependence of the stress-length relation. The zone bounded by these contraction-mode dependent heat-stress relations reflects the heat of shortening. Isoproterenol-induced enhancement of contractility led to proportional increases in the zones on both the mechanics and energetics planes, thereby supporting our hypothesis.

Keywords: cardiac energetics, shortening heat, cardiac mechanics, force-length relation, cardiac end-systolic zone

Edited by:
Leonid Katsnelson,
Institute of Immunology
and Physiology (RAS), Russia

Reviewed by:
Kerry S. McDonald,
University of Missouri, United States
P. Bryant Chase,
Florida State University, United States

Correspondence:
June-Chiew Han
j.han@auckland.ac.nz

Specialty section:
This article was submitted to
Biophysics,
a section of the journal
Frontiers in Physiology

Received: *30 October 2019*
Accepted: *26 December 2019*
Published: *21 January 2020*

Citation:
Tran K, Taberner AJ, Loiselle DS
and Han J-C (2020) Energetics
Equivalent of the Cardiac
Force-Length End-Systolic Zone:
Implications for Contractility
and Economy of Contraction.
Front. Physiol. 10:1633.
doi: 10.3389/fphys.2019.01633

INTRODUCTION

The force produced by an isometrically contracting muscle can be varied over a range of initial lengths or preloads. Contractility is illustrated on the force-length plane as the slope of the isometric end-systolic force-length relation. As first revealed by Frank in his cardiac pressure-volume diagram (Frank, 1899), a separate relation in the plane exists for a series of afterloaded shortening (work-loop) contractions. These two force-length relations (isometric and work-loop) are distinct – that for isometric contractions lying above its work-loop counterpart. The divergence of these two force-length relations, exemplified particularly under conditions of either high preloads or low afterloads, reveals a region that encompasses all possible end-systolic force-length points. This zone has been coined the "cardiac end-systolic zone," and is applicable to preparations ranging from the whole-heart (Frank, 1899; Kissling et al., 1985) to isolated cardiac tissues (Gülch and Jacob, 1975; Han et al., 2019) and myocytes (Iribe et al., 2014), as illustrated in Figure 7 of Han et al. (2019). For over a century, it was unclear why some experimentalists observed a single end-systolic relation for both isometric and afterloaded shortening contractions while others observed two separate relations. The demonstration of the existence of a cardiac end-systolic zone by Han et al. (2019) has resolved this long-standing puzzle in the field of cardiac mechanics.

The mechanical properties of cardiac muscle described above are intimately linked with its energetics characteristics. We therefore hypothesize that there exists an equivalent zone for energetics, specifically on the heat-force plane. An isometrically-contracting muscle transduces chemical energy entirely into heat, whereas an afterloaded shortening muscle captures some of that energy as work (Gibbs, 1978). When assessed on the heat-force plane, the mechanoenergetics of cardiac muscle likewise displays contraction-mode dependence (Pham et al., 2017; Tran et al., 2017). Explicitly, for a given force, the heat arising from an isometric contraction is less than that from a work-loop contraction, resulting in the isometric heat-force relation lying below its work-loop counterpart. We further hypothesize that the region lying between these two contraction mode-dependent heat-force relations reflects the existence of "heat of shortening" in cardiac muscle (Tran et al., 2017). That is, the energetics equivalent of the end-systolic zone (ESZ) on the mechanics plane is the "heat of shortening" region, and this region is also expected to encompass all possible heat-force points resulting from isometric and work-loop contractions. We tested this proposed equivalence by simultaneously measuring force, length, and heat under both isometric and work-loop modes of contraction and over a wide range of preloads and afterloads. We further challenged their equivalence by the use of an inotropic agent that increases cardiac contractility.

MATERIALS AND METHODS

This study was carried out in accordance with the principles of the Basel Declaration. The protocol was approved by the University of Auckland Animal Ethics Committee under the Approval Number R2006. Following anesthesia with isoflurane (5% in O_2), each rat (8–10 week-old male Wistar strain of weights ranging from 300 to 350 g) was injected with heparin (1000 IU kg^{-1}) and killed via cervical dislocation. The heart was excised and immediately arrested by submergence in chilled Tyrode solution. The aorta was rapidly cannulated and Langendorff-perfused with low-Ca^{2+} Tyrode solution (in mmol l^{-1}: 130 NaCl, 6 KCl, 1 $MgCl_2$, 0.5 NaH_2PO_4, 0.3 $CaCl_2$, 10 Hepes, 10 glucose, 20 2,3-butanedione monoxime, pH adjusted to 7.4 using Tris), and vigorously gassed with 100% O_2 at room temperature.

Experiments were performed on $n = 12$ trabeculae dissected from the left ventricle. Six trabeculae from four rats were randomly assigned to a Control group, where they were exposed to Tyrode solution with composition as listed above except for a higher concentration of $CaCl_2$ (1.5 mmol l^{-1}) and in the absence of 2,3-butanedione monoxime. The other six trabeculae from the other four rats were assigned to an Isoproterenol group, where they were exposed to the same Tyrode solution with addition of the inotropic agent isoproterenol (0.5 μmol l^{-1}). The isoproterenol dose-response curve for active force development saturates at concentrations above 0.1 μmol l^{-1} (Monasky et al., 2008). We chose a concentration of 0.5 μmol l^{-1} to ensure that the maximum inotropic response is elicited, which is within the typical range, 0.1 μmol l^{-1} (Barclay et al., 1979) to 1 μmol l^{-1} (Power et al., 2018), used for cardiac muscle experiments.

Each trabecula was mounted in our flow-through work-loop calorimeter (Taberner et al., 2011, 2018) and superfused with Tyrode solution. After a period of about 1 h of continuous 2 Hz electrical stimulation, during which mechanical performance of the trabecula and thermal equilibration of the apparatus were reached, the muscle was slowly lengthened to optimal length (L_o) where twitch force was maximal. Muscle dimensions (L_o, and the top and perpendicular views of diameter) were measured with a microscope graticule. There were no statistically significant differences in trabecula dimensions between the Control group and the Isoproterenol group in either cross-sectional area (0.08 ± 0.01 and 0.06 ± 0.01 mm^2, respectively) or length (3.2 ± 0.2 and 2.8 ± 0.2 mm, respectively).

The entire calorimeter apparatus was enclosed within a hood to diminish external optical and thermal disturbances. Ambient temperature within the hood was maintained at 32°C by temperature controllers installed on the top and at the bottom of the measurement chamber, and a separate system heating the optical table upon which the entire calorimeter system is mounted.

Experiments commenced when a stable thermal environment was reached. Stimulus frequency was then increased to 3 Hz. The trabecula was first subjected to a series of five shortening contractions at progressively diminishing afterloads, thereby performing a series of afterloaded work-loops (see Taberner et al., 2011 for details). This series of five afterloaded work-loop contractions was further performed at two reduced muscle lengths (0.95 L_o and 0.90 L_o). At all three lengths (preloads), isometric contractions were interspersed between each of the five afterloaded work-loop contractions. Following the three preloaded, five afterloaded, work-loop contractions, muscle length was further reduced to 0.85 L_o, 0.81 L_o, and 0.77 L_o to perform additional isometric contractions. Completion of the experimental protocol thus included isometric twitches obtained at six muscle lengths.

The rate of heat production (measured in units of W) was recorded simultaneously alongside twitch force and muscle length, and subsequently converted to heat per twitch (expressed in units of J) by dividing by the stimulus frequency. Upon completion of an experiment, two sources of heat artifact were quantified while the trabecula was unstimulated, thereby remaining in its quiescent state. The heat artifact arising from the cyclic movement of the upstream hook (required for muscle shortening during work-loop contractions) was quantified with the muscle quiescent by oscillating the hook at a frequency of 3 Hz over the extent of muscle shortening achieved at the lowest afterload. The heat artifact resulting from electrical stimulation was quantified by electronically relocating the muscle downstream, away from the measurement chamber and into the mounting chamber. Both heat artifacts were subtracted from the measured heat signal before further data analyses.

Statistical Analyses

Data were fitted using polynomial regression (up to third order) and the regression lines were averaged within groups using the "random coefficient model" within PROC MIXED of the SAS software package. The significance of differences among regression lines, or between mean values, of the two groups was tested and declared when $P < 0.05$.

RESULTS

Figure 1 shows a subset of experimental records of simultaneous measurements of muscle length, muscle stress and heat signal. At each initial length (preload), isometric stress and heat were the highest compared with those achieved in the work-loop contractions where reducing afterload resulted in decreasing heat but increasing extent of shortening. With decreasing initial length (preload), both isometric stress and heat reduced.

Figure 2 shows results from a single, representative, trabecula in the Control group. Panel A shows the isometric end-systolic (upper thick line) and end-diastolic (passive; lower thick line) stress-length relations. Both relations were obtained by fitting to their respective six end-systolic points (black circles) and end-diastolic points (open circles) of the isometric contractions at steady state (vertical gray lines). These isometric stress-length relations are replicated in panels B–E of **Figure 2**. Panels B–D show, respectively, the work-loop contractions and their corresponding end-systolic stress-length relations (ESSLRs) at three initial muscle lengths (preloads): L_o, 0.95 L_o, and 0.90 L_o (blue, green, and magenta curves). Note that these work-loop ESSLRs each terminated at its own unique lowest achievable afterload. These lowest afterloads fell in the vicinity of their respective passive stresses. These results reveal that the ESSLR is indeed *dependent* on the mode of contraction as the three work-loop ESSLRs each diverged from the isometric ESSLR. The magnitude of their divergence from the isometric ESSLR decreased with decreasing preload, as is evident in **Figure 2E** where the three work-loop ESSLRs (colored) are superimposed, along with the isometric stress-length relations (black). The curvatures of each of the three work-loop ESSLRs were not significantly different from one another, as more clearly revealed in the inset of panel E where they have been self-normalized to both the isometric stress and the initial length. Using the curvature, we interpolated the work-loop ESSLR for any given initial muscle length, resulting in the shaded area which we have coined the "cardiac end-systolic zone" in the stress-length plane.

In panel F of **Figure 2**, a zone equivalent to the "cardiac end-systolic zone" in the stress-length plane (panel E) was obtained. This heat-stress zone (HSZ) shaded in gray on the heat-stress plane, likewise, contains the work-loop heat-stress relations where, again, their slopes were not significantly different from one another (as illustrated in the inset of panel F). Qualitatively similar results were obtained in a trabecula subjected to isoproterenol (**Figure 3**).

Figure 4 shows the average results from six trabeculae in the Control group (panels A and B) and from a different set of six trabeculae in the Isoproterenol group (panels C and D). The equivalence between the ESZ in the stress-length plane and the zone in the heat-stress plane was preserved under the isoproterenol challenge.

Figure 5 shows the effects of isoproterenol on mechanoenergetics under both preloaded isometric contractions and afterloaded work-loop contractions at L_o. Trabeculae exposed to isoproterenol had elevated isometric ESSLR and work-loop ESSLR, with no difference in their passive stress-length relations (panel A). In panel B, both the isometric heat-stress relation and the work-loop heat-stress relation were significantly higher in the Isoproterenol group, as evident by the higher heat-intercepts and higher isometric active stress and isometric heat. The Isoproterenol group had greater shortening kinetics, producing higher velocities of shortening across all three initial muscle lengths (**Figure 6**).

DISCUSSION

In this study, we extended the ESZ framework developed for cardiac mechanics to encompass energetics. The ESZ framework revealed the existence of a zone on the force-length plane within which all end-systolic points are situated. The zone is bounded above by the isometric ESSLR, and below by work-loop contractions at L_o and work-loops resulting from zero-active force. Within these three boundaries exists an infinite number of work-loop ESFLRs, each unique to a given preload. We show in **Figure 2F** that these features, observed in the mechanics plane, are mirrored on the energetics plane in the form of an equivalent HSZ. As is the case with mechanics, the heat-stress relations are dependent on the mode of contraction. The isometric heat-stress relation (black line) sits below all those arising from work-loop contractions (colored lines). For work-loop contractions at reduced preloads, their heat-stress relations are located progressively closer to the isometric heat-stress relation. The entire HSZ is bounded above by work-loop contractions at L_o, and below by isometric contractions at different muscle lengths. The HSZ encompasses all possible heat-stress points for a given level of contractility, consistent with the property of the ESZ of encompassing all end-systolic points. When muscle contractility was increased via addition of isoproterenol, new commensurate zones for ESZ and HSZ were established, demonstrating an inotropic dependence inherent in

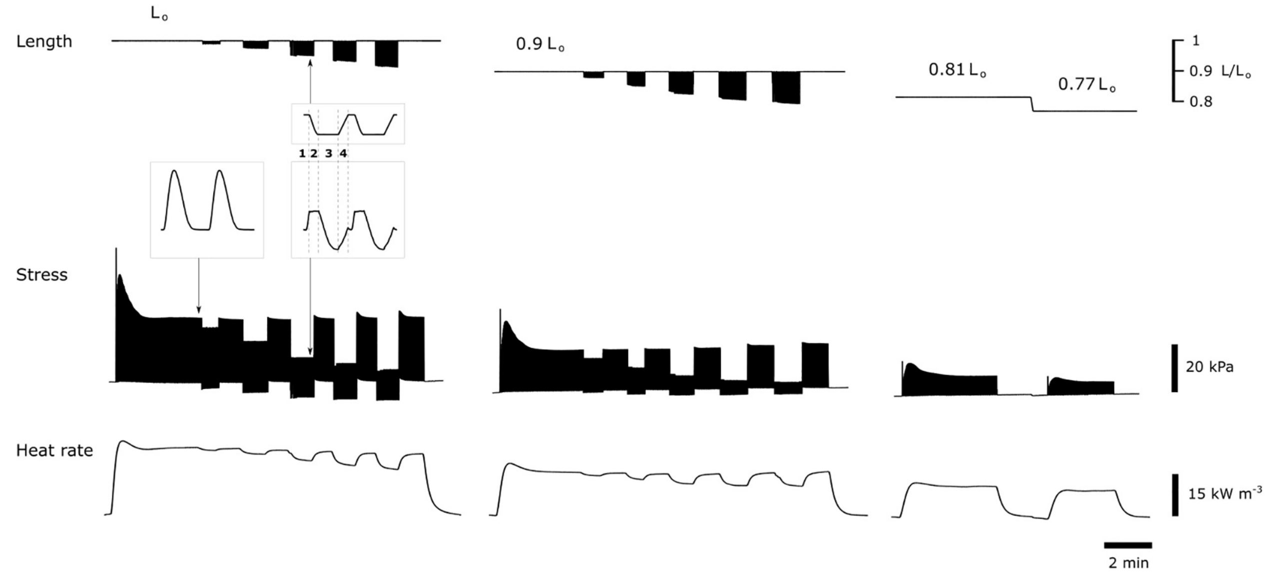

FIGURE 1 | Subset of experimental records. Muscle length, muscle stress, and associated heat signal were simultaneously recorded. The **left panel** shows records of combined isometric and work-loop contractions, with the former mode interposed with latter, from an initial length at L_o. Work-loop contractions with the five decreasing afterloads are concomitant with increasing extent of shortening and decreasing output of heat. The **middle panel** shows records at an initial length of 0.9 L_o. The **right panel** shows records of two isometric contractions at 0.81 L_o and 0.77 L_o. Electrical stimulation was paused between interventions required for the reduction of initial length. Insets show expanded traces for two individual twitches at steady state, indicated by the arrows. The work-loop twitch consists of four phases: (1) isometric contraction, (2) isotonic shortening, (3) isometric relaxation, and (4) passive re-stretch back to initial muscle length.

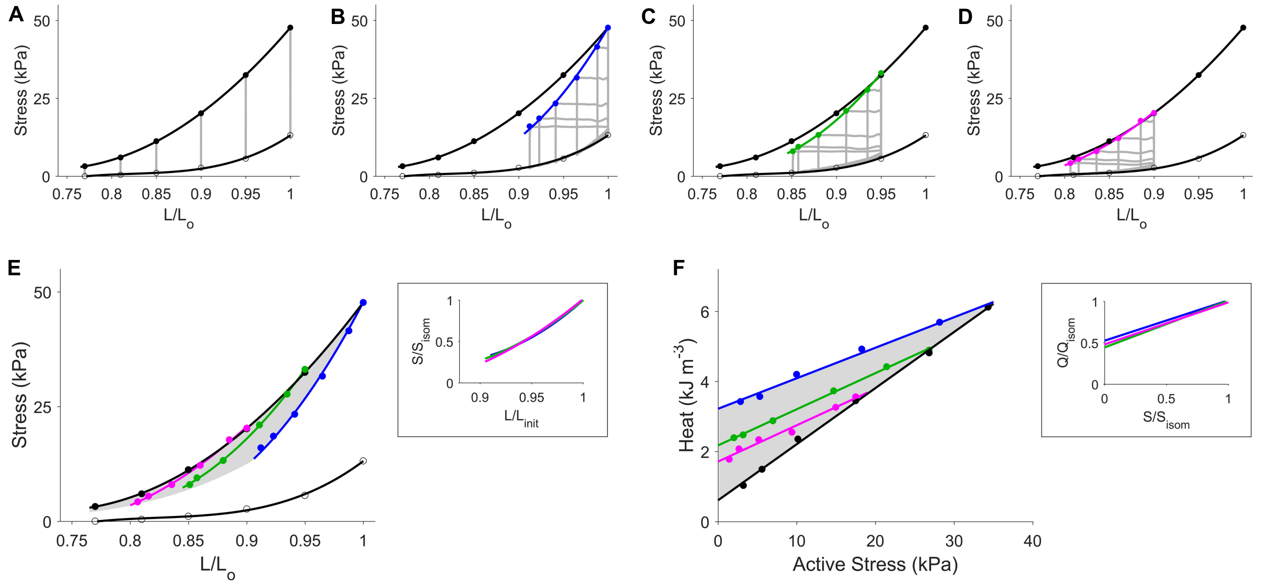

FIGURE 2 | Steady-state data from a representative trabecula superfused with Tyrode solution. In panel **(A)**, the isometric end-systolic stress-length relation (upper thick line) and the isometric passive stress-length relation (lower thick line) have been fitted to the six isometric contractions (gray lines) at end-systole (black circles) and at end-diastole (open circles), respectively. These two relations have been transcribed to panels **(B–E)**. The work-loop end-systolic stress-length relation, obtained by fitting to the end-systolic points (filled circles), is dependent on the initial length (lines: blue, green, and magenta, respectively): at L_o **(B)**, 0.95 L_o **(C)**, and 0.90 L_o **(D)**. In panel **(E)**, all stress-length relations are superimposed, where the shaded area indicates the zone of the end-systolic points as interpolated using the self-normalized work-loop stress-length relations in the inset, in which L_{init} refers to the three initial muscle lengths (L_o, 0.95 L_o, and 0.90 L_o). In panel **(F)**, the shaded area indicates the zone of the heat-stress relations obtained from the three preloaded work-loop contractions and the isometric contractions. The inset shows the three relations between work-loop heat (Q) and stress (S) normalized to their isometric values (subscripted as "isom").

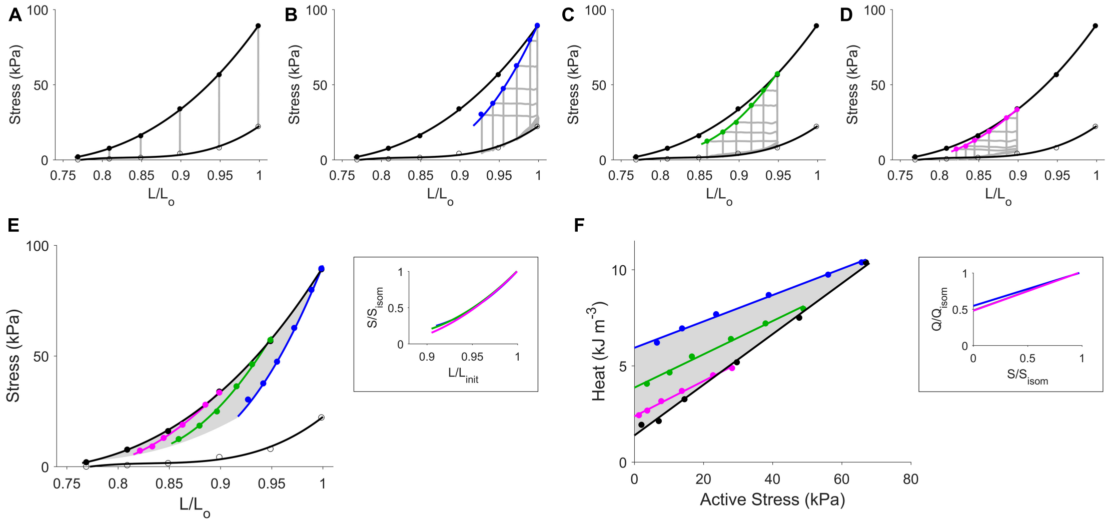

FIGURE 3 | Steady-state data from a representative trabecula superfused with Tyrode solution and isoproterenol. Figure caption is the same as that in **Figure 2**. In panel **(A)**, the isometric end-systolic stress-length relation (upper thick line) and the isometric passive stress-length relation (lower thick line) have been fitted to the six isometric contractions (gray lines) at end-systole (black circles) and at end-diastole (open circles), respectively. These two relations have been transcribed to panels **(B–E)**. The work-loop end-systolic stress-length relation, obtained by fitting to the end-systolic points (filled circles), is dependent on the initial length (lines: blue, green, and magenta, respectively): at L_o **(B)**, 0.95 L_o **(C)**, and 0.90 L_o **(D)**. In panel **(E)**, all stress-length relations are superimposed, where the shaded area indicates the zone of the end-systolic points as interpolated using the self-normalized work-loop stress-length relations in the inset, in which L_{init} refers to the three initial muscle lengths (L_o, 0.95 L_o, and 0.90 L_o). In panel **(F)**, the shaded area indicates the zone of the heat-stress relations obtained from the three preloaded work-loop contractions and the isometric contractions. The inset shows the three relations between work-loop heat (Q) and stress (S) normalized to their isometric values (subscripted as "isom").

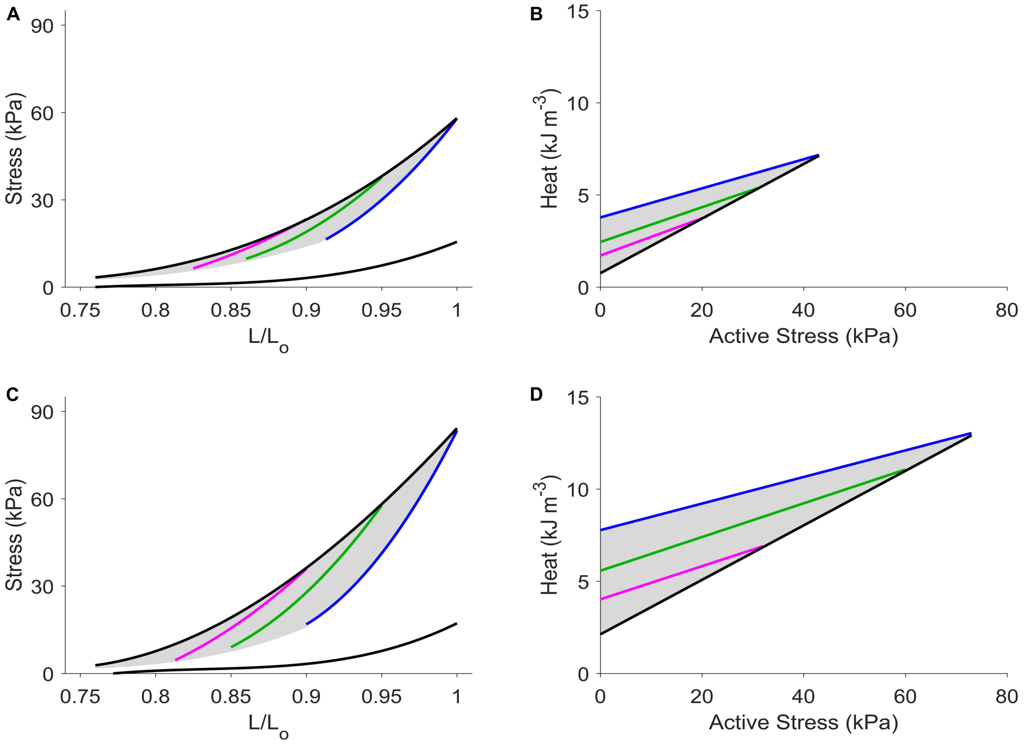

FIGURE 4 | Average regression lines from six trabeculae per group. Average lines from the Control group are presented in panels **(A,B)**, and those from the Isoproterenol group are depicted in panels **(C,D)**. Black lines denote isometric contraction. Blue, green, and magenta, respectively, denote work-loop contractions at L_o, 0.95 L_o, and 0.90 L_o. The shaded areas in **A** and **C** denote the end-systolic zones, whereas those in **B** and **D** denote the heat-stress zones.

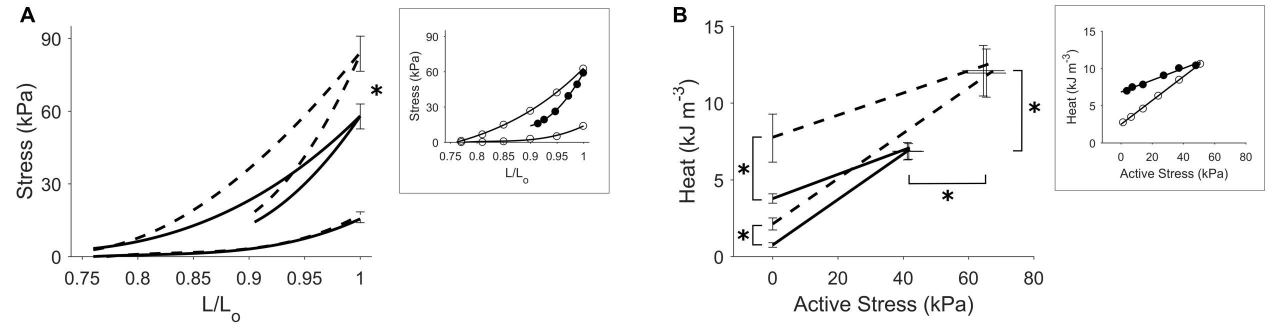

FIGURE 5 | Effects of increased contractility. Average regression lines from trabeculae in the Control group (continuous lines) and those in the Isoproterenol group (broken lines) undergoing preloaded isometric contractions and afterloaded work-loop contractions at L_o are shown in each panel. The asterisk in panel **(A)** indicates a statistically significant difference between the regression lines. The asterisks in panel **(B)** signify effects of isoproterenol on the heat-intercepts as well as on the peak active stress and muscle heat output. Standard errors of means at peak values are superimposed in all panels. The insets depict regression lines fitted to the data from a representative Control trabecula where open circles denote isometric contractions and filled circles denote work-loop contractions at L_o.

both zones, thereby further strengthening our claim of their equivalence (**Figure 4**).

Shortening Heat

In skeletal muscle, the hydrolysis of ATP associated with muscle shortening leads to the production of work and the liberation of heat above that of isometric contractions. This "extra" heat above the isometric heat was termed the "heat of shortening" by Hill (1938). Until recently, it was thought that the heat of shortening is a property unique to skeletal muscle (Gibbs and Chapman, 1979; Holroyd and Gibbs, 1992). However, a recent experimental and modeling study (Tran et al., 2017) has provided compelling evidence that the heat of shortening also exists in cardiac tissues. At any given force, more heat is produced from a shortening contraction than from an isometric contraction owing to the liberation of heat from muscle shortening. In this study, we find that the HSZ describes the liberation of heat which is in excess of heat produced by isometric contractions, consistent with the heat of shortening. Given that the ESZ arises from the difference between the end-systolic points of isometric and shortening contractions on the mechanics plane, it is not surprising that its energetic equivalent is the difference in heat liberated by these two modes of contraction. The ESZ and HSZ represent two orthogonal quantifications of particular characteristics in a cardiac muscle twitch. That is, a point within the ESZ marks the moment of end-systole of a twitch on the stress-length plane, while a point within the HSZ quantifies the heat liberated over the course of the twitch on the heat-stress plane.

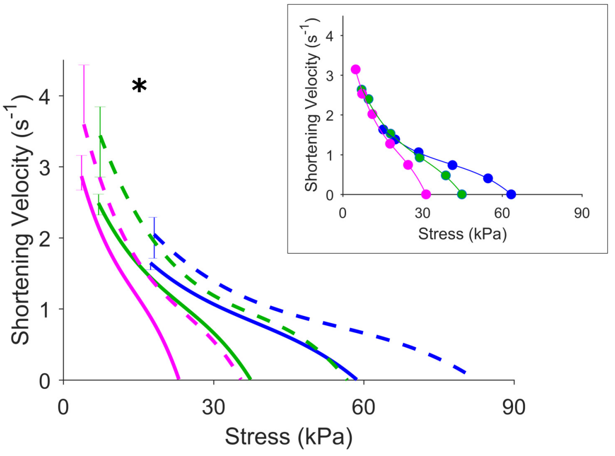

FIGURE 6 | Effects of increased contractility on velocity of shortening. Inset shows representative data for a Control muscle. The asterisk indicates that the velocity of shortening at the lowest afterload of work loop contraction for the three initial muscle lengths is greater for the Isoproterenol group (dashed lines) compared with the Control group (solid lines). Blue, green, and magenta colored lines represent work-loop contractions starting at L_o, 0.95 L_o, and 0.90 L_o, respectively.

Implications for Economy of Contraction

The inverse of the slope of the heat-stress relation is a measure of the economy of contraction (Gibbs, 1978). It is typically quantified from isometric contractions in order to relate muscle force production to its energetic cost (Gibbs, 1978; Alpert and Mulieri, 1982; Han et al., 2010; Johnston et al., 2016). **Figure 4B** shows that the slope of the heat-stress relation for isometric contractions is steeper than its work-loop counterpart, giving the impression of a higher economy of contraction under work-loop contractions. But this impression is misleading because the work-loop heat-stress relation contains heat that is in excess of isometric cross-bridge heat ($Q_{XB(Isom)}$), in accord with Figure 10 of Tran et al. (2017). The partitioning of cross-bridge heat in is this manner demonstrates that more heat is liberated for a shortening contraction than an isometric contraction at a given level of force (Rall, 1982). However, this is not to say that in a shortening muscle, there are a subset of cross-bridges that cycle isometrically while another subset is involved in sarcomere shortening. $Q_{XB(Isom)}$ can be measured only from muscles undergoing isometric contractions. In our opinion, economy of contraction should be strictly derived from $Q_{XB(Isom)}$ and therefore be purely a property of isometric contractions.

We also observed that the economy of contraction is independent of an increase in contractility induced by the addition of the beta-adrenergic stimulant, isoproterenol. The slopes of the isometric heat-stress relations for the control and isoproterenol cases were the same despite an increase in force in the isoproterenol case (**Figure 5B**). This suggests that isoproterenol has no direct effect on the chemo-mechanical energy transduction of cardiac myofilaments and that the augmentation of contractility arises indirectly from an increase in the peak of the cytosolic Ca^{2+} transient (Tamura et al., 1992; Kassiri et al., 2000; Power et al., 2018). Our measurement of a null effect of isoproterenol on economy, but a higher activation heat in the presence of isoproterenol, is consistent with earlier observations reported in the literature (Gibbs, 1967; Gibbs and Gibson, 1972; Barclay et al., 1979).

The preservation of the economy of contraction in the presence of an isoproterenol-induced increase in contractility suggests that the efficiency of the myofibrillar energy transduction step has not been altered (Gibbs and Gibson, 1972). That is, the efficiency of ATP hydrolysis by myosin ATPase is unaffected by isoproterenol despite an increase in the velocity of shortening (**Figure 6**). The faster shortening kinetics is consistent with reported effects of the beta-adrenergic stimulant increasing cross-bridge cycling rates in both intact (Hoh et al., 1988; Kentish et al., 2001) and skinned cardiac preparations (Strang et al., 1994; Saeki et al., 1997). On the surface, these results appears to be at odds with reports that slowing of cross-bridge kinetics is a compensatory mechanism that increases economy of contraction in hypertrophic (Alpert and Mulieri, 1982), diabetic (Rundell et al., 2004), and aging (van der Velden et al., 1998; Kiriazis and Gibbs, 2001) hearts. Slowing of cross-bridge cycling kinetics is typically associated with a shift of myosin isoforms. The two types of myosin heavy chains (MHC) in the heart (α-MHC and β-MHC) carry the site for ATPase activity (Hoh et al., 1978). Their formation of homo- or heterodimers give rise to, in order of decreasing ATPase activity, V1, V2, and V3 myosin isoforms (Pope et al., 1980). In aging and diseased hearts, remodeling of the tissue leads to replacement of the myosin V1 isoform with the kinetically slower V3 isoform. Given the difference in ATPase activity between these myosin isoforms, we speculate that the myosin profile of the tissue is the key determinant of contraction economy (Rundell et al., 2004; Narolska et al., 2005a,b), rather than cycling kinetics *per se*.

Implications for Contractility

The effect of isoproterenol to increase cardiac contractility has typically been demonstrated in intact isolated tissues contracting at a single fixed muscle length (Kassiri et al., 2000; Layland and Kentish, 2000; Power et al., 2018). Our isometric ESSLR protocol characterizes the peak stress development of twitching trabeculae over a range of muscle lengths in response to isoproterenol (**Figure 5**). An important implication of our ESZ framework is that an accurate assessment of changes in contractility requires identical loading conditions to be applied (Han et al., 2019). In **Figure 5A**, the change of contractility can be assessed by comparing either the isometric ESSLR or the work-loop ESSLR between the control and isoproterenol cases. Note that in each contraction mode the associated loading conditions were kept the same – i.e., isometric ESSLR up to L_o or work-loop ESSLR at an initial length of L_o. Making these comparisons appropriately reveals steeper ESSLRs for muscles superfused with isoproterenol, indicative of an increase in contractility.

CONCLUSION

In cardiac muscle, the ESZ is an area on the stress-length plane that encompasses all possible end-systolic points arising from isometric and work-loop contractions. The associated heat liberated from these two modes of contraction is circumscribed by a zone (HSZ) on an orthogonal heat-stress plane. These two zones are equivalent in that they are bounded by isometric contractions on one side and work-loop contractions at L_o on the other, and expand in the presence of an inotropic agent. The HSZ represents the heat of shortening associated with work-loop contractions. The equivalence between the mechanical and energetic properties of cardiac tissues has allowed us to comment on appropriate methods for comparing muscle contractility and assessing economy of contraction. We conclude that meaningful comparisons of contractility require parity in loading conditions, and suggest that economy of contraction should be calculated only from muscles undergoing isometric contractions.

DATA AVAILABILITY STATEMENT

The datasets generated for this study are available on request to the corresponding author.

ETHICS STATEMENT

The animal study was reviewed and approved by The University of Auckland Animal Ethics Committee under the Approval Number R2006.

AUTHOR CONTRIBUTIONS

J-CH performed the experiments and analyzed the data. All authors contributed to the conception and design of the study, interpretation and discussion of the data, drafting of the manuscript, and approved the final version of the manuscript.

FUNDING

This work was supported in part by the Marsden Fund Fast-Start grants (UOA1504 and UOA1703) from the Royal Society of New Zealand (awarded to J-CH and KT, respectively), Emerging Researcher First Grant (16/510) from the Health Research Council of New Zealand (awarded to J-CH), and Research Fellowship grant (1692) from the National Heart Foundation of New Zealand (awarded to KT).

REFERENCES

Alpert, N. R., and Mulieri, L. A. (1982). Increased myothermal economy of isometric force generation in compensated cardiac hypertrophy induced by pulmonary artery constriction in the rabbit. a characterization of heat liberation in normal and hypertrophied right ventricular papillary muscles. *Circ. Res.* 50, 491–500. doi: 10.1161/01.res.50.4.491

Barclay, J. K., Gibbs, C. L., and Loiselle, D. S. (1979). Stress as an index of metabolic cost in papillary muscle of the cat. *Basic Res. Cardiol.* 74, 594–603. doi: 10.1007/bf01907501

Frank, O. (1899). Die grundform des arteriellen pulses. *Z. Biol.* 37, 483–526.

Gibbs, C. L. (1967). Changes in cardiac heat production with agents that alter contractility. *Aust. J. Exp. Biol. Med. Sci.* 45, 379–392. doi: 10.1038/icb.1967.37

Gibbs, C. L. (1978). Cardiac energetics. *Physiol. Rev.* 58, 174–254.

Gibbs, C. L., and Chapman, J. B. (1979). Cardiac heat production. *Ann. Rev. Physiol.* 41, 507–519. doi: 10.1146/annurev.ph.41.030179.002451

Gibbs, C. L., and Gibson, W. R. (1972). Isoprenaline, propranolol, and the energy output of rabbit cardiac muscle. *Cardiovasc. Res.* 6, 508–515. doi: 10.1093/cvr/6.5.508

Gülch, R. W., and Jacob, R. (1975). Length-tension diagram and force-velocity relations of mammalian cardiac muscle under steady-state conditions. *Pflügers Arch.* 355, 331–346. doi: 10.1007/bf00579854

Han, J.-C., Pham, T., Taberner, A. J., Loiselle, D. S., and Tran, K. (2019). Solving a century-old conundrum underlying cardiac force-length relations. *Am. J. Physiol. Heart Circ. Physiol.* 316, H781–H793. doi: 10.1152/ajpheart.00763.2018

Han, J.-C., Taberner, A. J., Nielsen, P. M. F., Kirton, R. S., Ward, M.-L., and Loiselle, D. S. (2010). Energetics of stress production in isolated cardiac trabeculae from the rat. *Am. J. Physiol. Heart Circ. Physiol.* 299, H1382–H1394. doi: 10.1152/ajpheart.00454.2010

Hill, A. V. (1938). The heat of shortening and the dynamic constants of muscle. *Proc. R. Soc. Lond. B.* 126, 136–195. doi: 10.1098/rspb.1938.0050

Hoh, J. F., Rossmanith, G. H., Kwan, L. J., and Hamilton, A. M. (1988). Adrenaline increases the rate of cycling of crossbridges in rat cardiac muscle as measured by pseudo-random binary noise-modulated perturbation analysis. *Circ. Res.* 62, 452–461. doi: 10.1161/01.res.62.3.452

Hoh, J. F. Y., Mcgrath, P. A., and Hale, P. T. (1978). Electrophoretic analysis of multiple forms of rat cardiac myosin: effects of hypophysectomy and thyroxine replacement. *J. Mol. Cell Cardiol.* 10, 1053–1076.

Holroyd, S. M., and Gibbs, C. L. (1992). Is there a shortening-heat component in mammalian cardiac muscle contraction? *Am. J. Physiol. Heart Circ. Physiol.* 262, H200–H208.

Iribe, G., Kaneko, T., Yamaguchi, Y., and Naruse, K. (2014). Load dependency in force-length relations in isolated single cardiomyocytes. *Prog. Biophys. Mol. Biol.* 115, 103–114. doi: 10.1016/j.pbiomolbio.2014.06.005

Johnston, C. M., Han, J.-C., Loiselle, D. S., Nielsen, P. M. F., and Taberner, A. J. (2016). Cardiac activation heat remains inversely dependent on temperature over the range 27–37°C. *Am. J. Physiol. Heart Circ. Physiol.* 310, H1512–H1519.

Kassiri, Z., Myers, R., Kaprielian, R., Banijamali, H. S., and Backx, P. H. (2000). Rate-dependent changes of twitch force duration in rat cardiac trabeculae: a property of the contractile system. *J. Physiol.* 524, 221–231. doi: 10.1111/j.1469-7793.2000.t01-3-00221.x

Kentish, J. C., Mccloskey, D. T., Layland, J., Palmer, S., Leiden, J. M., Martin, A. F., et al. (2001). Phosphorylation of troponin I by protein kinase a accelerates relaxation and crossbridge cycle kinetics in mouse ventricular muscle. *Circ. Res.* 88, 1059–1065. doi: 10.1161/hh1001.091640

Kiriazis, H., and Gibbs, C. L. (2001). Effects of ageing on the activation metabolism of rat papillary muscles. *Clin. Exp. Pharmacol. Physiol.* 28, 176–183. doi: 10.1046/j.1440-1681.2001.03416.x

Kissling, G., Takeda, N., and Vogt, M. (1985). Left ventricular end-systolic pressure-volume relationships as a measure of ventricular performance. *Basic Res. Cardiol.* 80, 594–607. doi: 10.1007/bf01907858

Layland, J., and Kentish, J. C. (2000). Effects of α1- or β-adrenoceptor stimulation on work-loop and isometric contractions of isolated rat cardiac trabeculae. *J. Physiol.* 524, 205–219. doi: 10.1111/j.1469-7793.2000.t01-1-00205.x

Monasky, M. M., Varian, K. D., and Janssen, P. M. L. (2008). Gender comparison of contractile performance and beta-adrenergic response in isolated rat cardiac trabeculae. *J. Comp. Physiol. B* 178, 307–313. doi: 10.1007/s00360-007-0223-y

Narolska, N. A., Eiras, S., Van Loon, R. B., Boontje, N. M., Zaremba, R., Spiegelen Berg, S. R., et al. (2005a). Myosin heavy chain composition and the economy of contraction in healthy and diseased human myocardium. *J. Muscle Res. Cell Motil.* 26, 39–48. doi: 10.1007/s10974-005-9005-x

Narolska, N. A., Loon, V. R. B., Boontje, N. M., Zaremba, R., Penas, S. E., Russell, J., et al. (2005b). Myocardial contraction is 5-fold more economical in ventricular than in atrial human tissue. *Cardiovasc. Res.* 65, 221–229. doi: 10.1016/j.cardiores.2004.09.029

Pham, T., Han, J.-C., Taberner, A., and Loiselle, D. (2017). Do right-ventricular trabeculae gain energetic advantage from having a greater velocity of shortening? *J. Physiol.* 595, 6477–6488. doi: 10.1113/JP274837

Pope, B., Hoh, J. F. Y., and Weeds, A. (1980). The ATPase activities of rat cardiac myosin isoenzymes. *FEBS Lett.* 118, 205–208. doi: 10.1016/0014-5793(80)80219-5

Power, A. S., Hickey, A. J., Crossman, D. J., Loiselle, D. S., and Ward, M.-L. (2018). Calcium mishandling impairs contraction in right ventricular hypertrophy prior to overt heart failure. *Pflügers Arch.* 470, 1115–1126. doi: 10.1007/s00424-018-2125-0

Rall, J. A. (1982). Sense and nonsense about the Fenn effect. *Am. J. Physiol.* 242, H1–H6.

Rundell, V. L. M., Geenen, D. L., Buttrick, P. M., and De Tombe, P. P. (2004). Depressed cardiac tension cost in experimental diabetes is due to altered myosin heavy chain isoform expression. *Am. J. Physiol. Heart Circ. Physiol.* 287, H408–H413.

Saeki, Y., Kobayashi, T., Minamisawa, S., and Sugi, H. (1997). Protein kinase a increases the tension cost and unloaded shortening velocity in skinned rat cardiac muscle. *J. Mol. Cell Cardiol.* 29, 1655–1663. doi: 10.1006/jmcc.1997.0401

Strang, K. T., Sweitzer, N. K., Greaser, M. L., and Moss, R. L. (1994). Beta-adrenergic receptor stimulation increases unloaded shortening velocity of skinned single ventricular myocytes from rats. *Circ. Res.* 74, 542–549. doi: 10.1161/01.res.74.3.542

Taberner, A. J., Han, J.-C., Loiselle, D. S., and Nielsen, P. M. F. (2011). An innovative work-loop calorimeter for in vitro measurement of the mechanics and energetics of working cardiac trabeculae. *J. Appl. Physiol.* 111, 1798–1803. doi: 10.1152/japplphysiol.00752.2011

Taberner, A. J., Johnston, C. M., Pham, T., Han, J.-C., Uddin, R., Loiselle, D. S., et al. (2018). A flowthrough infusion calorimeter for measuring muscle energetics: design and performance. *IEEE Trans. Instrum. Meas.* 67, 1690–1699. doi: 10.1109/tim.2018.2800838

Tamura, K., Yoshida, S., Iwai, T., and Watanabe, I. (1992). Effects of isoprenaline and ouabain on cytosolic calcium and cell motion in single rat cardiomyocytes. *Cardiovasc. Res.* 26, 179–185. doi: 10.1093/cvr/26.2.179

Tran, K., Han, J.-C., Crampin, E. J., Taberner, A. J., and Loiselle, D. S. (2017). Experimental and modelling evidence of shortening heat in cardiac muscle. *J. Physiol.* 595, 6313–6326. doi: 10.1113/JP274680

van der Velden, J., Moorman, A. F., and Stienen, G. J. (1998). Age-dependent changes in myosin composition correlate with enhanced economy of contraction in guinea-pig hearts. *J. Physiol.* 507, 497–510. doi: 10.1111/j.1469-7793.1998.497bt.x

Conflict of Interest: The authors declare that the research was conducted in the absence of any commercial or financial relationships that could be construed as a potential conflict of interest.

frontiers
in Physiology

REVIEW
published: 13 February 2020
doi: 10.3389/fphys.2020.00092

Heart Plasticity in Response to Pressure- and Volume-Overload: A Review of Findings in Compensated and Decompensated Phenotypes

*Fotios G. Pitoulis**† *and Cesare M. Terracciano**†

Myocardial Function, National Heart and Lung Institute, Imperial College London, London, United Kingdom

Edited by:
Remi Peyronnet,
University of Freiburg, Germany

Reviewed by:
Han-Zhong Feng,
Wayne State University School of Medicine, United States
Nazareno Paolocci,
Johns Hopkins University, United States

****Correspondence:***
Fotios G. Pitoulis
fp1314@ic.ac.uk
Cesare M. Terracciano
c.terracciano@imperial.ac.uk

†ORCID:
Fotios G. Pitoulis
orcid.org/0000-0001-9814-9046
Cesare M. Terracciano
orcid.org/0000-0003-2761-0696

Specialty section:
This article was submitted to Striated Muscle Physiology, a section of the journal Frontiers in Physiology

Received: *10 October 2019*
Accepted: *27 January 2020*
Published: *13 February 2020*

Citation:
Pitoulis FG and Terracciano CM (2020) Heart Plasticity in Response to Pressure- and Volume-Overload: A Review of Findings in Compensated and Decompensated Phenotypes. Front. Physiol. 11:92. doi: 10.3389/fphys.2020.00092

The adult human heart has an exceptional ability to alter its phenotype to adapt to changes in environmental demand. This response involves metabolic, mechanical, electrical, and structural alterations, and is known as cardiac plasticity. Understanding the drivers of cardiac plasticity is essential for development of therapeutic agents. This is particularly important in contemporary cardiology, which uses treatments with peripheral effects (e.g., on kidneys, adrenal glands). This review focuses on the effects of different hemodynamic loads on myocardial phenotype. We examine mechanical scenarios of pressure- and volume overload, from the initial insult, to compensated, and ultimately decompensated stage. We discuss how different hemodynamic conditions occur and are underlined by distinct phenotypic and molecular changes. We complete the review by exploring how current basic cardiac research should leverage available cardiac models to study mechanical load in its different presentations.

Keywords: myocardial remodeling, pressure overload, volume overload, mechanical load, heart failure, concentric hypertrophy, eccentric hypertrophy, myocardial slices

INTRODUCTION

The heart is a terminally differentiated organ aimed at maintaining cardiac output (CO) to the rest of the body. Changing metabolic demands require systems and signaling pathways in place to allow the heart to (a) operate across a range of contractile profiles in the short term, and (b) chronically alter its function and structure when these are of enduring nature. The latter process, whereby the heart changes its phenotype chronically, is termed cardiac remodeling or plasticity.

Cardiac plasticity is a complex and multifactorial process. It is driven by mechanical load, the neurohormonal axis (Cohn et al., 2000; Yang et al., 2016), inflammation (Anzai, 2018), as well as autocrine and paracrine mediators (Gnecchi et al., 2008). Within the context of a whole organism these remodeling actors are interconnected and directly or indirectly influence one another. A decrease in systolic blood pressure decreases systolic load, and is met with hormonal release, including angiotensin II and catecholamines. These not only modulate the function of the heart, but that of the vasculature as well, which in turn has mechanical consequences on the operation of the heart. Complex feedback loops are established in this manner, fine tuning the acute functional outputs of the heart while simultaneously driving remodeling.

There are numerous reviews (de Tombe, 1998; Burchfield et al., 2013) on pathological remodeling as seen in end-stage heart failure (HF). Here, we focus less on the terminal phenotypes and more on the process of ventricular remodeling as it occurs during pressure- and volume-overload. When the information allows it, we attempt to temporally track remodeling from initial event and its immediate effects on heart function, to changes seen in the compensated, and ultimately decompensate stage. Emphasis is placed on contractile and metabolic remodeling, and the interaction of these. The electrical apparatus is discussed vis-à-vis its capacity to induce sustained mechanical dysfunction.

Basis for Cardiac Remodeling

Cardiac remodeling is adaptive and has evolutionary underpinnings. A fight-or-flight event elicits acute physiological responses, such as β-adrenergic activation, to increase CO. These are beneficial in the short-term as they take us away from danger; yet persistent stressor exposure drives maladaptive remodeling leading to decompensation (Swynghedauw, 2006; Hill and Olson, 2008). Still, the ability to remodel is evolutionary advantageous (Shave et al., 2019). When compared to sister taxa species (e.g., chimpanzees), human hearts are comparatively longer, thinner, and less trabeculated and so optimized to maintain CO during low-to-moderate intensity endurance activities (e.g., farming) (Shave et al., 2019). Such phenotypes are not fail-proof and when short bursts of resistance-dominated activities (fight, lift, flight) are needed, failure to increase CO can have dire consequences for survival (Shave et al., 2019). As such, conservation of cardiac phenotypic plasticity permits stimuli-driven cardiac adaptations and survival.

Changes in heart structure and function of rowers and skiers were recognized by pioneering investigators as early as late 19th century, and the concept of exercise-induced cardiac remodeling is now widely accepted (Weiner and Baggish, 2012). Likewise, left ventricular mass increases during pregnancy, a physiological state of chronic volume-overload, but regresses to normal levels post-partum (Mesa et al., 1999; Hill and Olson, 2008). It is hypothesized that under physiological stimulation the heart remodels without subsequent decompensation. In contrast, arterial hypertension, myocardial infarction, and valvular disease lead to cardiac hypertrophy, albeit in different forms, which if not corrected progresses to overt decompensation. At least in the initial phases, phenotypic overlap exists between physiological and pathological remodeling (Hill and Olson, 2008). Binary categorization may be too simplistic and it is more likely that remodeling occurs across a continuum (Dorn, 2007). This is supported by clinical and pre-clinical observations of not only progressive pathological- but also reverse-remodeling (Gheorghiade et al., 2016), as seen for example with implantation of mechanical assist devices (Ibrahim and Terracciano, 2013; Kormos et al., 2017) or when the cause of adverse remodeling is corrected (Lamb et al., 2002).

PRESSURE-OVERLOAD

An increase in arterial blood pressure represents an increase in afterload. Cardiac physiology dictates that for the same inotropic state, a reduction in stroke volume (SV), and by extension CO ensues (**Figure 1**). Compensatory release of catecholamines, among other hormones as well as intrinsic myocardial responses, increase contractility to preserve CO. However, persistent exposure to growth factors results in hypertrophic cardiac growth. If left uncorrected, contractile, electrophysiological, metabolic, and structural abnormalities occur. Together, these orchestrate the progressive decline in cardiac pump function (Schirone et al., 2017).

Cardiac Hypertrophy

Sustained elevated systolic stress via thoracic aortic constriction (TAC) in mice, increases the rate of protein synthesis as soon as 4 days post-op and results in cardiac hypertrophy (Wang et al., 2017) (**Figure 2**). The putative hypothesis of stress normalization, proposed by Grossman et al. (1975), argues that elevations in systolic stress are offset by an increase in wall thickness. This results in normalization of stress according to LaPlace's law[1] (**Figure 3**). In pressure-overload, it is generally accepted that ventricular wall thickening occurs by growth of cardiomyocytes via addition of sarcomeres in parallel within myofibrils. At the level of the whole heart, this leads to concentric hypertrophy, and chamber geometry of increased ventricular wall-thickness *(h)* to radius *(r)* ratio (Grossman and Paulus, 2013). However, this hypothesis has been questioned. Rat right ventricular papillary muscles cultured under isometric- (supraphysiological systolic stress) or isometric-load with the contraction uncoupler BDM (reduced systolic stress) both develop increased cardiomyocyte diameter and decreased length in comparison to physiologically loaded muscle, suggestive of parallel rearrangement of sarcomeres (Guterl et al., 2007). As very high and very low systolic stresses both lead to similar sarcomeric rearrangement, muscle shortening profiles (rate and amount of muscle shortening or equally changes in volume; e.g., isometric twitches do not shorten) have been proposed to be more decisive than stress in driving the hypertrophic response (Guterl et al., 2007). More importantly, irrespective of the driver of wall thickening it is still unclear whether this initial compensatory phase is required and whether it is in fact beneficial.

Cardiac hypertrophy is an independent and the single most important risk factor for cardiovascular morbidity and mortality (Manyari et al., 1990; Balke, 1998). In TAC-induced pressure-overloaded mice, inhibition of calcineurin, a hypertrophic signal transduction molecule (**Figure 2**), abolishes development of compensatory cardiac hypertrophy without deterioration of LV function and structure, or progression to HF (Hill et al., 2000).

Other studies show that hypertrophic adaptations are necessary. Stromal interaction molecule 1 (STIM1) is a regulator of cardiomyocyte growth (Schirone et al., 2017). In pressure-overload, STIM1 silencing prevents cardiac hypertrophy but results in rapid deterioration to HF (Benard et al., 2016; Schirone et al., 2017). Moreover, studies on isolated cardiomyocytes from patients on mechanical assist devices show that regression of hypertrophy *per se* is not associated with clinical recovery (Terracciano et al., 2004). Instead, both patients who recover and those who do not recover show decreased cell size but the former demonstrate renormalization of excitation-contraction

---

[1] Laplace's law: $\sigma = r^{*}P/2h$ where σ is systolic wall stress, r is LV cavity radius, P is left ventricular pressure, and h is LV wall thickness.

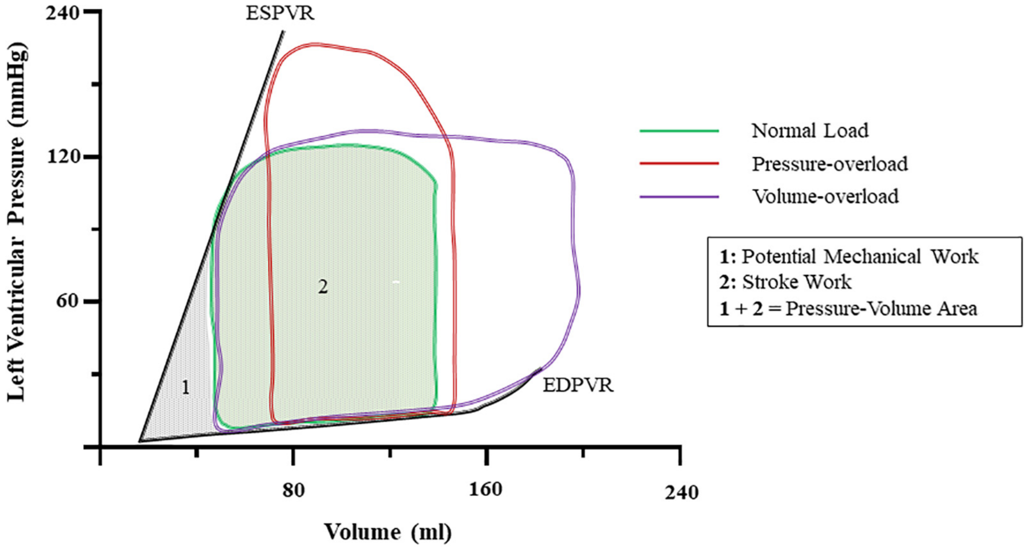

FIGURE 1 | Ventricular pressure-volume dynamics under normal and at onset of pressure-, and volume-overload. Notice that increases in pressure increase left-ventricular pressure and abbreviate stroke volume. Volume-overload shifts the EDV to the right, and SV increases due to higher preload. The sum of the area encompassed by the PV-loop of normal (Cohn et al., 2000) and the ESPVR and EDPVR (Yang et al., 2016) is known as pressure-volume area (PVA) and it correlates with myocardial oxygen consumption. ESPVR, end-systolic pressure-volume relationship; EDPVR, end-diastolic pressure-volume relationship; SV, stroke volume; EDV, end-diastolic volume.

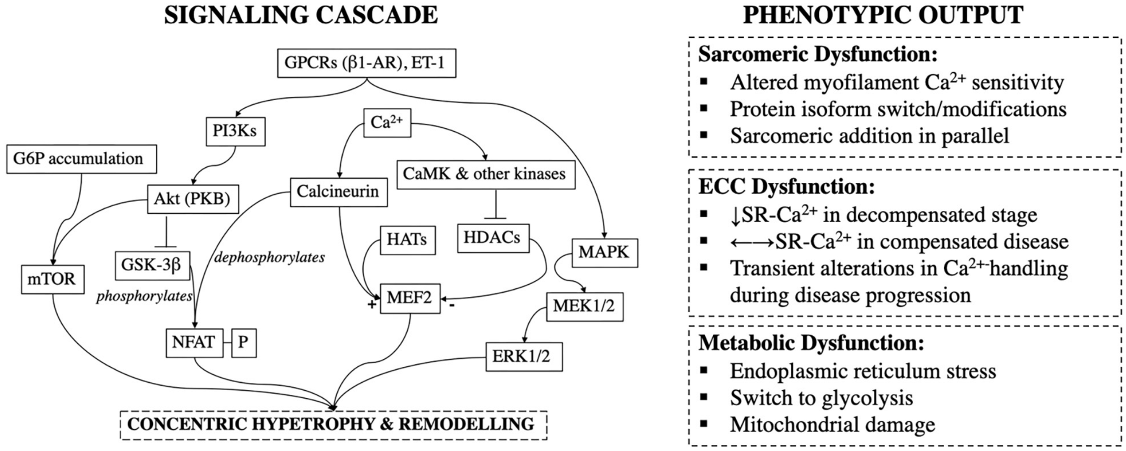

FIGURE 2 | Signaling cascade and phenotypic outcomes during pressure-overload induced cardiac remodeling; GPCRs, G-Protein Couple Receptors; β1-AR, β1-Adrenoceptor; ET-1, Endothelin-1; PI3Ks, Phosphoinositide-3-Kinases; Akt (PKB), Akt/Protein Kinase B; G6P, Glucose-6-Phosphate; GSK-3β, Glycogen Synthase Kinase-3β; mTOR, Mammalian Target of Rapamycin; NFAT-P, Phosphorylated Nuclear Factor Activated T-cells; CaMK, Calmodulin Kinase; HATs, Histone Acetylases; HDACs, Histone Deacetylases; MEF2, Myocyte Enhancer Factor-2; MAPK, Mitogen Activated Protein Kinase; SR, Sarcoplasmic Reticulum.

features, such as sarcoplasmic reticulum Ca^{2+}-content, and L-type Ca^{2+} current (Terracciano et al., 2004). More, concentric hypertrophy is a physiological response to strength exercise, where activation of vasopressor systems and increases in peripheral resistance can elevate the aortic pressure up to 320/225 mmHg (Mihl et al., 2008).

Such polarizing findings muddle our understanding of the protective and/or detrimental effects of hypertrophy. Part of the explanation for this stems from incomplete mapping of responsible pathways. Not all hypertrophic pathways are maladaptive. For example, mice dominant-negative for phosphoinositide 3-kinase (PI3Ks) p110α-isoform, develop hypertrophy after aortic constriction but not exercise (McMullen et al., 2003) (**Figure 2**). This suggests that in contrast to harmful effects of calcineurin activation (Sussman et al., 1998), PI3Ks may be cardioprotective and promote beneficial adaptations to stress (McMullen et al., 2003; Crozatier and Ventura-Clapier, 2015). However, others have reported that calcineurin mediates physiological responses (Wilkins and Molkentin, 2002). It is likely that overlap exists in signaling pathways of physiological, adaptive, and pathological reactive hypertrophy (Dorn, 2007), and sharp distinctions may not be possible. Clinically, this perturbs the therapeutic line of what we can and cannot safely manipulate. Inhibition of protective or sustained elevation of pathological pathways may lead to the same net deleterious outcome.

Contractile Remodeling

Sarcomeric Dysfunction

Sarcomeric protein isoform expression and post-translational modifications are key determinants of sarcomeric function (Yin et al., 2015). The healthy human adult heart is β-myosin heavy chain (MHC) dominant (Miyata et al., 2000), with α-MHC density suggested to range from less than 10% (Taegtmeyer et al., 2010) up to 30% (Hamdani et al., 2008). A switch from α- to β-MHC has been reported during pressure-overload (Crozatier and Ventura-Clapier, 2015) but whether this is happening in humans remains controversial (de Tombe, 1998). β-MHC is more energetically efficient in developing force, whereas α-MHC has faster tension kinetics and power output (Herron and McDonald, 2002; Taegtmeyer et al., 2010). Isoform switch may thus be beneficial in the face of increased oxygen demand due to elevated systolic wall stress, but at the expense of contractile speed (Hamdani et al., 2008; Stelzer et al., 2008). As twitch duration impacts SV, α-MHC may be better equipped to maintain CO when the heart is overloaded. Consequently, the heart may struggle to cope with workload following isoform switch and this may contribute to pathological remodeling in a positive-feedback fashion.

If isoform switch does happen, the magnitude of switch appears related to the originally dominant isoform; in the healthy rat heart, where α-MHC expression is high, the shift to β-MHC can be quantitatively bigger than in the human heart (Schwartz et al., 1992). This is particularly relevant given that MHC isoform composition varies within the ventricular wall. α-MHC shows a transmural gradient highest in subepicardial than subendocardial fibers (Stelzer et al., 2008). Transmural heterogeneity in other sarcomeric proteins and their post-translational status, such regulatory light chain phosphorylation (RLC-p), has also been reported (Davis et al., 2001). In healthy hearts, intricate protein isoform and phosphorylation patterns across the wall together with electrical heterogeneity (Cordeiro et al., 2004) facilitate efficient mechanical performance by optimizing the complex three-dimensional twisting and compressing motion of the whole heart (Davis et al., 2001). Yet, transmural protein profiles create margins for these to be regionally disrupted. This could lead to mechano-electrical mismatch across the ventricular wall and contribute to disease development and progression. As thorough assessment of transmural mechanical properties has not been yet performed, the consequences of this warrant further study.

Changes in myofilament Ca^{2+} sensitivity have been reported in TAC-induced hypertrophy and linked to systolic dysfunction (Belin et al., 2006). However, systolic dysfunction is not typically evident during the initial compensatory stages of remodeling to pressure-overload (Franklin et al., 1975; de Tombe, 1998) and the temporal progression of changes in myofilament Ca^{2+} sensitivity have only recently been illuminated. Rupert et al. examined ventricular function and structure in relation to sarcomeric function after 6, 12, and 16 weeks of TAC in rats. At 6-weeks post-op, myofilament Ca^{2+}-sensitivity was significantly increased, whereas it normalized back to sham-group levels at 12- and 18-weeks post-op. These findings correlated temporally with an increased ESPVR at 6-weeks post-op, suggesting increased inotropic state (Suga et al., 1973; Ruppert et al., 2019). Early compensatory response to pressure-overload may therefore be predicated upon favorable adaptations in myofilament Ca^{2+}-sensitivity, which are eventually lost in later stages of hypertrophy. Likewise, the Frank-Starling mechanism – that is, an increase in contractile output per unit of preload, seems to be preserved in compensated disease. In isolated papillary muscles from rats with compensated ventricular hypertrophy, maximum developed active tension is preserved (Okoshi et al., 2004). Similarly, in spontaneously hypertensive rats with ventricular hypertrophy, cardiac performance is maintained at 11- and 24-weeks when assessed with *in vivo* preload stress (by venous infusion), but falls sharply at 83-weeks of age (Pfeffer et al., 1979). Whether the Frank-Starling response is preserved at later stages of disease remains an open question.

In human hearts, Schwinger et al. (1994) suggested that the terminally failing heart is unable to employ the Frank-Starling mechanism due to loss of length-dependent activation. Exhaustion of the Frank-Starling reserve has similarly been reported in dogs with congestive HF (Komamura et al., 1993) and spontaneously hypertensive rats (Hallbäck et al., 1975). More, in right-ventricular pressure-overload hypertrophy that has progressed to decompensation, tension development in skinned isolated myocytes is reduced (Fan et al., 1997). As hypertrophy can impact the content of ECM, these experiments suggest that intrinsic changes in contractile protein function may underlie the altered contractile phenotype. However, others have shown preserved Frank-Starling in end-stage HF (Holubarsch et al., 1996; Pieske et al., 1997; Weil et al., 1998) with a leftward shift in the force-pCa curve suggesting increased Ca^{2+} sensitivity at higher sarcomere lengths (preload), and thus maintained length-dependent activation (Holubarsch et al., 1996).

As mentioned herein, pressure-overload induces concentric hypertrophy, reflected by parallel addition of sarcomeres at the level of the cardiomyocyte. Given the simultaneous incessant motion of the heart, mediated by sarcomeric shortening, and cyclic stresses, it is remarkable how new elements can be added without disruption of active cardiac mechanics. Live imaging of neonatal rat cardiomyocytes illustrates that upon stretch, parallel sarcomeric addition occurs by using pre-existing sarcomeres as templates (Yang et al., 2016). It is hypothesized that resident sarcomeres act as templates and allow for the sequential addition of "Z-bodies" that initially look like beads (Sanger et al., 2010) and progressively build up to form linear Z-disks (Yang et al., 2016). Subsequently, assembly and introduction of sarcomeric proteins (e.g., myosin, actin, titin, etc.), and the formation of new sarcomeres takes place (Russell et al., 2010; Yang et al., 2016) leading to the concentric hypertrophic geometry.

Ca^{2+} Handling

In decompensated disease with systolic dysfunction, there is decreased ability to sequester Ca^{2+} in the sarcoplasmic reticulum (SR) and/or release it (de Tombe, 1998). Ca^{2+}-uptake in the SR is carried out by the SR Ca^{2+}-ATPase (SERCA). Reductions in SERCA density and/or its Ca^{2+} uptake rates (De la Bastie et al., 1990; Sharma et al., 1994; de Tombe, 1998) can thus compromise SR Ca^{2+}-availability. This can diminish the magnitude of the next and the relaxation kinetics of the preceding contraction.

There is an arsenal of evidence that this is happening (Limas et al., 1987; Hasenfuss et al., 1990; Beuckelmann et al., 1995; Flesch et al., 1996). However, most studies have been performed in dilated cardiomyopathy (Limas et al., 1987; Hasenfuss et al., 1990; Flesch et al., 1996) or end-stage HF (Beuckelmann et al., 1995; Flesch et al., 1996) samples. What is less clear is the progressive change in SERCA density and function following initial trigger. Guinea-pigs with compensated cardiac phenotype (increased LV mass with normal function) 4- and 8-weeks post-TAC, do not show changes in SERCA protein expression or function whereas animals with decompensated phenotypes (increased LV mass with depressed function) do (Kiss et al., 1995). Coupled with increased myofilament Ca^{2+} sensitivity preserved SERCA function may uphold ventricular performance during the early compensated phases of remodeling.

SERCA activity is tonically inhibited by phospholamban (PLB). PLB phosphorylation by cAMP- or Ca^{2+}/calmodulin-dependent (CaMKII) protein kinases, lifts the inhibition and the SR Ca^{2+} uptake rate is increased (Bers, 2002). Hyperphosphorylation of PLB has been recorded in severe but compensated LV canine hypertrophy following aortic banding (Song et al., 2005). PKCα decreases PLB-phosphorylation via a pathway involving protein phosphatase-1, resulting in decreased SR-Ca^{2+} uptake, Ca^{2+} transient, and contractility (Braz et al., 2004). As such, PKCα deletion has been proposed to be cardioprotective against pressure-overload, yet mice without PKCα demonstrate cardiac hypercontractility (Braz et al., 2004). Given the potential of positive inotropic agents for long-term deleterious consequences, whether PKCα inhibition is of therapeutic benefit remains to be seen (Packer, 1993; Swynghedauw and Charlemagne, 2002). In contrast, nitroxyl (HNO), a product of nitric oxide (NO) reduction, is a positive inotropic agent that increases SR-Ca^{2+} content without raising intracellular Ca^{2+}-content that may be deleterious. Recently, it was suggested that the mechanism underlying HNO-mediated SR-Ca^{2+} content increases is attained by keeping PLB in its oligomerized form (pentameric), which is less inhibitory than the monomeric PLB counterpart when associated with SERCA (Sivakumaran et al., 2013).

Excitation Contraction Coupling (ECC)

During calcium-induced calcium release (CICR) Ca^{2+} influx (I_{Ca}) through sarcolemmal L-type Ca^{2+} channels (LTCCs) causes release of Ca^{2+} from the SR via SR Ca^{2+} release channels. Spatial proximity between LTCCs and SR Ca^{2+} release units is necessary for efficient CICR. This is accomplished by the highly organized network of T-tubules running throughout the entire cardiomyocyte. Rat isolated cardiomyocytes, examined during a period of hypertension before development of compensated hypertrophy have myocytes with longer action potential duration, Ca^{2+} transients, and increased ECC gain (that is I_{Ca} can trigger greater SR Ca^{2+} release) compared to non-hypertensive rats (Chen-Izu et al., 2007). Initial alterations in Ca^{2+} homeostasis thus seem to precede hypertrophy and may promote it (e.g., by activation of calcineurin and CaMKII) (Chen-Izu et al., 2007) (see below and **Figure 2**). In contrast, during the compensated phase, Ca^{2+}-transient, and % shortening of unloaded cardiomyocytes is preserved but not elevated compared to control (Nagata et al., 1998). It is likely that an initiation window exists before compensatory remodeling where cardiomyocytes become hyperfunctional, driving disease progression.

ECC gain is reduced in decompensated disease (Gomez et al., 1997). Geometrical abnormalities in t-tubular architecture can reduce the coupling between LTCCs and SR Ca^{2+} release units and hamper ECC (Santana et al., 1996; Gomez et al., 1997). T-tubular system remodeling begins prior to the onset of heart failure in pressure-overload (Guo et al., 1996; Wei et al., 2010). Although the temporal details are not known, it is possible that during compensation maladaptive changes in t-tubule structure exist, but overall function is preserved as a result of increased myofilament sensitivity and/or improved Ca^{2+} handling (see above).

CaMKII is an intracellular serine/threonine protein kinase that acts as a Ca^{2+}-dependent hypertrophic pathway (Backs et al., 2009; Maier, 2012). Under basal conditions CaMKII activity is minimal because its catalytic domain is blocked by its regulatory domain (Anderson et al., 2011). Binding of calcified calmodulin (Ca-CaM) to the regulatory domain frees the catalytic site, increasing CaMKII activity (Anderson et al., 2011). Pharmacological inhibition (Zhang et al., 2005) and genetic knockouts (Ling et al., 2009) of CaMKII, prevent progression of pressure-overload to pathological remodeling. Spontaneous diastolic Ca^{2+}-leak from SR Ca^{2+}-release channels (Ca^{2+}-sparks) can regulate CaMKII activity (Heineke and Molkentin, 2006; Van Oort et al., 2010). In compensated LV hypertrophy increased Ca^{2+}-sparks have been reported (Song et al., 2005) and TAC pressure-overload causes increased Ca^{2+} spark frequency associated with CaMKII activation (Toischer et al., 2010). The hypertrophic response in mice with leaky RyR2 channels (R176Q knock-in mutation), is accelerated and there is propensity for progression to dilated cardiomyopathy compared to wild-type (Van Oort et al., 2010). These findings are in line with clinical evidence showing that genetically defective RyRs are associated with hypertrophic cardiomyopathy predisposition (Fujino et al., 2006; Chiu et al., 2007).

CaMKII also regulates histone deacetylases (HDACs), which bind to specific transcription factors such as myocyte enhancer factor 2 (MEF-2) to control hypertrophic gene pathways (Hulot et al., 2011). HDACs are post-translational modifying enzymes that deacetylate histones and repress transcription. In contrast, histone acetylases (HATs) acetylate histones and promote transcriptional activation; HDACs and HATs have antagonistic effects. Phosphorylation of HDACs by CaMKII impairs their association with MEF-2 and other transcription factors and enhances transcriptional activation (i.e., de-represses) (Frey et al., 2004) (**Figure 2**). At least three classes of HDACs have been identified with class I HDACs considered to be pro-hypertrophic, whereas class II & III HDACs suggested to negatively regulate the hypertrophic gene program (Kehat and Molkentin, 2010).

Metabolic Dysfunction

Heart function is energetically demanding and requires constant supply of ATP. As ATP stock is limited to a few beats, continuous replenishment is critical (Ingwall, 2009). Typically, in the healthy adult heart, ATP supply is maintained by oxidative phosphorylation. When acute surges in energetic demand occur highly efficient glycolytic and phosphotransferase pathways are employed to boost ATP production (Ingwall, 2009). The latter involves conversion of ADP and phosphocreatine (PCr) to ATP and creatine by creatine-kinase (CK). Physiologically, high energy-demand and oxygen consumption (VO_2) are predicted by the pressure-volume area (PVA) – that is, the area enclosed by the end-systolic and end-diastolic pressure volume relationships and systolic work (Suga et al., 1981; Nozawa et al., 1994) (**Figure 1**). Correspondingly, changes in inotropy, systolic work, and diastolic function all impact cardiac energetics.

Increased afterload increases cardiac work per beat, and leads to an imbalance in the contribution of glycolytic and oxidative pathways in maintaining ATP levels (Nguyen et al., 1990; Young et al., 2007; Ingwall, 2009; Taegtmeyer et al., 2010). In particular, the heart switches from a fatty-acid dominant metabolism to the use of glucose as a primary source of energy, associated with an increase in the rate of glucose uptake (Kundu et al., 2015).

Because glucose uptake rate can exceed rate of glucose utilization, particularly within the overloaded myocardium (Nguyen et al., 1990), glucose accumulation, in the form of glucose-6-phosphate (G6P) occurs (Kundu et al., 2015). This precedes the development of hypertrophy and has been reported to occur as early as 1-day post-TAC surgery (Kundu et al., 2015), and before LVH in spontaneously hypertensive rats (Hernandez et al., 2013). G6P accumulation contributes to pathological progression in two ways. First, it can activate the mechanistic target of rapamycin complex 1 (mTORC1), a major pathway of cardiac remodeling (Proud, 2004) (**Figure 2**). Sustained mTORC1 activation induces protein synthesis rates that cannot be matched by the endoplasmic reticulum's (ER) protein folding capacity. This can lead to ER stress, misfolded proteins and ultimately cell death and diminished contractile output (Proud, 2004; Glembotski, 2008). Secondly, high G6P levels may directly activate the fetal gene program, by activation of the hexosamine biosynthetic pathway and subsequent glycosylation of transcription factors (Young et al., 2007). Metabolic shifts can thus precede, trigger, and maintain the reinduction to the fetal gene program (Taegtmeyer et al., 2010). In TAC-rats, low-carbohydrate/high-fat diet minimizes α- to β-MHC isoform switch (Young et al., 2007). Furthermore treatment with propranolol decreases glucose uptake rates, G6P accumulation, and rescues the decrease in ejection fraction observed in vehicle-treated rats (Zhong et al., 2013).

The consequences of a fetal energetic state are reductions in [ATP] by as much as 30% in diseased compared to healthy hearts (Ingwall, 2009). Because ATP is necessary for normal contraction, reduced ATP levels means that the failing heart is energetically starved. Until recently it was unclear whether this was one of the many failing phenotypic consequences or contributes directly to disease progression (Gupta et al., 2012). In TAC pressure-overloaded mice, overexpression of creatinine kinase-M (CK-M) improves LV contractile function and augments contractile reserve compared to TAC-controls. Importantly, these functional effects are lost when CK-M overexpression ceases (Gupta et al., 2012). These findings suggest that energy starvation, in this case attributed to CK levels and activity, can directly contribute to mechanical dysfunction and the development of disease.

Pressure-overload also causes mitochondrial damage. This leads to mitochondrial dysfunction, disturbances in substrate utilization and mitochondrial respiration, a decrease of fatty acids and an increase of glucose oxidizing proteins (Dai et al., 2012). The majority of proteins are imported into mitochondria, where they undergo folding and assembly (Smyrnias et al., 2019). Production of reactive-oxygen species in pressure-overload (ROS) (Goh et al., 2019) promotes mitochondrial protein misfolding, dysfunction, and a perpetual cycle of progressively worsening mitochondrial damage (Smyrnias et al., 2019). A major source of ROS production are monoamine oxidases (MAOs), and in particular MAO-A (Kaludercic et al., 2014). MAOs are mitochondrial flavoenzymes that catabolize neurotransmitters, such as norepinephrine and epinephrine. H_2O_2 is produced during this catalytic pathway resulting in oxidative stress (Kaludercic et al., 2010). In TAC, MAO-A expression and activity increases causing oxidative stress and adverse chamber dilatation (Kaludercic et al., 2010). Remarkably, mice dominant negative for MAO-A exposed to TAC, despite a slight shift in the PV relationship, have preserved cardiac function 9 weeks post TAC (Kaludercic et al., 2010). Protein misfolding due to ROS may also contribute to activation of the mitochondrial unfolded protein response (UPR^{mt}) pathway (Smyrnias et al., 2019). This is an evolutionary conserved pathway activated in response to compromised mitochondrial folding capacity. Pharmacological enhancement of UPR^{mt} ameliorates mitochondrial dysfunction (Smyrnias et al., 2019).

Last but not least, compromised mitochondria can directly impair sarcomeric function and regulation. In adult cardiomyocytes, mitochondria are located close to sarcomeres in what are considered 'energetic couplons' (Saks et al., 2001), units primed for optimal ATP exchange. Impaired mitochondrial energetic output may constrain sarcomeric function and encourage adaptive sarcomeric responses such as isoform switch to energetically favorable β-MHC. Increases in cardiomyocyte volume during hypertrophy can also decouple these units and impose energetic diffusional barriers (Crozatier and Ventura-Clapier, 2015) further facilitating sarcomeric remodeling. Yet, the extent of the latter is not clear, as simultaneous mitochondrial biogenesis has been reported to occur during parallel sarcomeric addition (Yang et al., 2016).

Debrief

(1) Pressure-overload causes concentric hypertrophy. This can happen in response to physiological and pathological triggers. Within the context of disease, whether hypertrophy confers protection or is deleterious remains elusive.

(2) An initial window characterized by functional and structural changes exists before overt compensated hypertrophy. Changes that occur during this window may directly contribute to the initiation of hypertrophy. In particular:

(i) Increased energetic demand is offset by changes in sarcomeric protein composition (economical isoform switches), and changes in utilization of energetic substrates (fatty acid to glucose). It is possible that energetic-contractile signaling exists, mediated (a) directly due to proximity of energy-producing and energy-consuming units, and (b) indirectly by glycosylation of transcription factors that regulate sarcomeric apparatus.

(ii) Changes in ECC function and structure such as Ca^{2+}-handling precede development of hypertrophy and initiate it (e.g., via Ca^{2+}-dependent hypertrophic pathways).

(3) Compensation does not preclude maladaptive remodeling. T-tubular loss, mitochondrial dysfunction, and sarcomeric dysfunction may all be present but masked by countering hyperfunctional cardiomyocyte elements, such as increased myofilament Ca^{2+} sensitivity. If the trigger is not corrected, the balance tilts, loss of hyperfunction occurs, and this is manifested macroscopically as overt decompensation.

VOLUME-OVERLOAD

End-diastolic volume corresponds to ventricular preload. In volume-overload, such as aortic and mitral valve insufficiency and certain congenital abnormalities, excessive preload is imposed on the heart. For example, in mitral valve regurgitation, following LV ejection a volume of blood is displaced back into the lower-pressure left atrial chamber; ventricular filling of the next contraction is increased causing volume-overload. In such settings, patterns of ventricular remodeling can be very different to pressure-overload.

Eccentric hypertrophy is the hallmark of volume-overload, whereby the chamber dilates while wall thickness decreases or is maintained. Wall thickness is particularly important. As a compensatory response, eccentric hypertrophy develops to preserve SV in the face of excess volume (Carabello et al., 1992). According to LaPlace's law chamber enlargement would lead to acute increases in systolic stress (caused by decreased h/r ratio) that would be subsequently normalized by thickening of the LV wall so that mass-to-volume ratio is preserved (Grossman et al., 1975; Opie et al., 2006) (**Figure 3**). However, although LV mass has been reported to increase (Grossman et al., 1975), many have found a decrease in mass-to-volume ratio (Corin et al., 1987; Carabello et al., 1992; de Giovanni, 2004), and so uncompensated stress leading to maladaptive remodeling (Carabello et al., 1992; Toischer et al., 2010). In contrast, physiological eccentric hypertrophy occurs in endurance athletes where LV mass closely mirrors increases in volume (Hoogsteen et al., 2003; Mihl et al., 2008).

During progression to heart failure from compensated pressure-overload, significant ventricular dilatation is observed resembling eccentric geometry (Randhawa and Singal, 1992). This is different from the eccentric hypertrophy seen during the compensated phases of volume-overload, where SV is maintained despite increased chamber size (Carabello, 2002).

Contractile Remodeling

Sarcomeres and Cardiomyocyte Morphology

The initiating trigger for eccentric hypertrophy is postulated to be excess end-diastolic wall stress or preload (Grossman et al., 1975; Urabe et al., 1992). Preload is the mechanical stretch and tension encountered by the myocardium during the diastolic phase. It represents the passive component of twitch tension, or passive tension. High preload causes cardiomyocytes to lengthen and thin as sarcomeric apparatus is rearranged and sarcomeres are added in series (Kehat and Molkentin, 2010).

This type of sarcomeric remodeling is mediated by specific signaling pathways. Gp130 is a transmembrane protein of cytokine receptors and a critical component for signal transduction following cytokine engagement (Giese et al., 2005). Cardiotrophin-1, a cytokine, has been shown to cause gp130 homodimerisation or heterodimerization with leukemia inhibitory factor receptor β (LIFRβ) and trigger sarcomeric addition in series, and cardiomyocyte lengthening in volume-overload (Wollert et al., 1996) (**Figure 4**).

Optimal force generation occurs across a narrow spectrum of SLs (Hibberd and Jewell, 1982; Allen and Kentish, 1985) meaning that resting SL must be maintained (Urabe et al., 1992; Mansour et al., 2004). This ensures that when preload increases and cardiomyocytes are stretched, the SL-force relationship is preserved. Accordingly, though cardiomyocytes elongate under increased diastolic stress, their resting SL remains normal, reflecting sarcomeric addition in series (Gerdes et al., 1992). Uniaxial strain in isolated neonatal rat cardiomyocytes causes an acute ∼6% increase in SL, which however renormalizes back to resting SL after 6 h in culture (Mansour et al., 2004). The mechanical sensors that orchestrate this are still unclear. Protein kinase C ε-subtype (PKCε) and focal adhesion kinase (FAK) have been reported (Mansour et al., 2004). These colocalize in costameres and cardiomyocyte focal adhesions, where they sense and mediate initiation of sarcomerogenesis in response to changes in stress and strain (Russell et al., 2010). Myofibril elongation is then suggested to take place by two mechanisms.

Firstly, insertion of new sarcomeres close to the cell-membranes, and most likely at intercalated disks (ID) (Wilson et al., 2014). IDs are complex folded structures where adjacent cardiomyocytes come in contact. Adherens junctions at the ID connect to the terminal thin filaments of sarcomeres sensing tension (Wilson et al., 2014). A special region within IDs

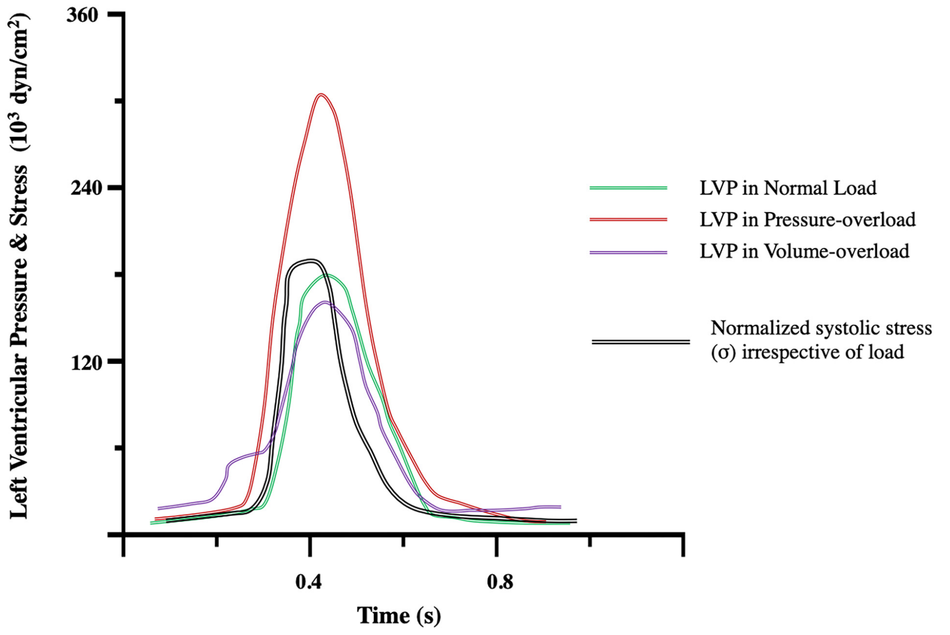

FIGURE 3 | Left ventricular pressure (LVP) and stress (σ) transients during the compensatory phase of pressure-, and volume-overload and compared to normal load. Notice that hemodynamic profiles differ in terms of cardiac LVP generation. The ventricular chamber must generate pressure greater than that in the aorta to eject blood. An increase in afterload in pressure-overload results in increased LVP. In the compensated state, stress is normalized by thickening of the ventricular wall according to LaPlace's law. Modified from Figure 5 of Grossman et al. (1975).

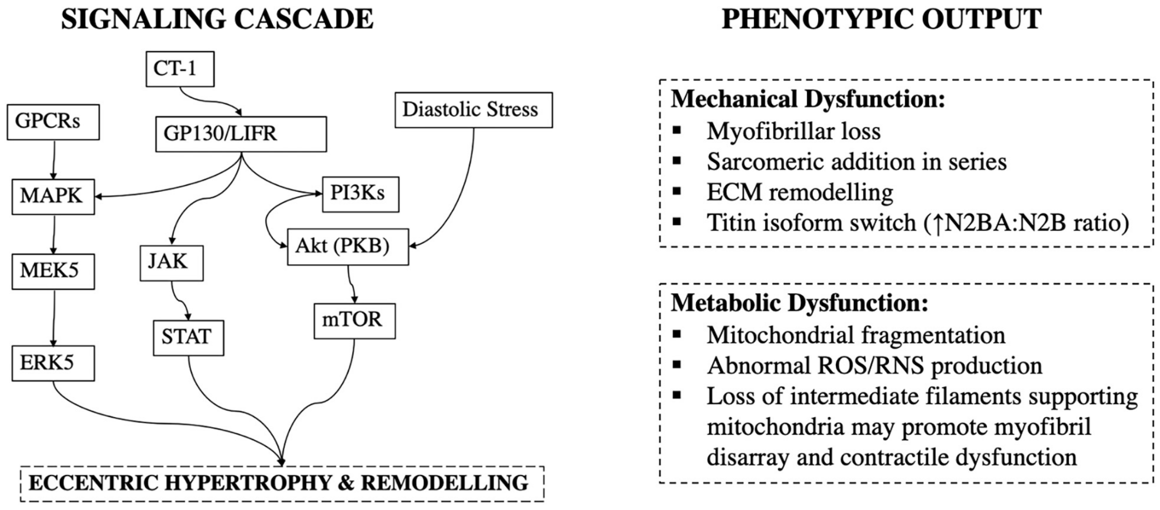

FIGURE 4 | Signaling cascade and phenotypic output in volume-overload. CT-1, Cardiotrophin-1; GP130/LIFR, Glycoprotein-130/Leukemia Inhibitory Factor Receptor; JAK, Janus Kinases; STAT, Signal Transducer and Activator of Transcription Proteins.

known as transitional junction, can act as a "proto Z-disk" where new sarcomeres can be added (Yoshida et al., 2010). The second mechanism is insertion within an existing myofibril via splitting. This occurs when a myofibril splits open to allow for insertion of a new sarcomere at the cleaved site (Yang et al., 2016).

Myocyte elongation may put them at a mechanical disadvantage when generating force (Gerdes and Capasso, 1995). It is possible that in eccentric remodeling the same amount of preload causes a different SL change; put simply, longer cardiomyocytes may need to be stretched more, compared to their normal counterparts, to reach a given SL. Thus, although the SL-force relationship may be preserved, force production may be compromised because myocardial tissue would require a greater (and perhaps supraphysiological) preload to reach the same SL.

Mechanical Dysfunction

In volume-overload from surgically induced aorto-caval shunts in rats, isoform switch from α- to β-MHC has been noted (Guggilam et al., 2013). Isolated cardiomyocytes from these rats demonstrate impaired contractile function with reduced amplitude and velocity of shortening (Guggilam et al., 2013). However, these experiments carried out 21-week post-op may reflect end-stage HF and may occur irrespective of the original volume-overload event. For example, others have not reported isoform switch in a similar experimental model of volume-overload at 24 h (Toischer et al., 2010). Without temporal tracking of functional and molecular changes during compensated and decompensated stages it is difficult to attribute observations to volume-overload or simply a common decompensated phenotype that has originated from volume-overload. Furthermore, no differences in shortening amplitude, velocity, and relaxation of isolated cardiomyocytes 4–15 weeks (Ryan et al., 2007) and 7-days post (Toischer et al., 2010) aorto-caval shunt surgery compared to control have been reported. Myofibrillar loss has been shown to occur extensively in volume-overload in both experimental mitral valve regurgitation (Urabe et al., 1992), and in biopsies from patients undergoing repair surgery (Ahmed et al., 2010; Gladden et al., 2011) and may contribute to mechanical dysfunction.

The extracellular matrix (ECM) regulates contractile performance via direct manipulation of myocardial stiffness as well as by coordinating myocardial remodeling (Baharvand et al., 2005). In volume-overload, ECM is degraded with reductions in collagen fractional volume, and increases in elastin (Ryan et al., 2007; Wilson and Lucchesi, 2014; Hutchinson et al., 2015). Collagen reductions occur due to increased matrix metalloproteinases (MMPs) activity and a concurrent decrease in their inhibitors, tissue inhibitors of MMPs (TIMPs) (Levick et al., 2008; Wilson and Lucchesi, 2014). This is in stark contrast to pressure-overload, whereby increased collage synthesis occurs (Bishop et al., 1994) and is associated with perivascular fibrosis (Toischer et al., 2010). Elastin is more compliant than collagen and decreased elastin-to-collagen ratio contributes to arterial stiffening with age (Fomovsky et al., 2010); therefore, an increase in elastin coupled with collagen reduction may lead to a more compliant ventricle in volume-overload.

In addition to collagen, passive myocardial mechanical properties are regulated by titin. Titin is a giant protein that forms part of the sarcomeric apparatus, and within the adult heart is typically found in either a longer more compliant N2BA or a shorter and stiffer N2B isoform (Lewinter and Granzier, 2010). The N2BA:N2B ratio increases after 4-weeks of volume-overload by aorto-caval shunt in rats, and this corresponds functionally to an increase in the passive tension of skinned myofibers (Hutchinson et al., 2015) (**Figure 4**). This is hypothesized to be a beneficial adaptation, as increased stiffness may limit excessive eccentric remodeling (Hutchinson et al., 2015).

Metabolic Remodeling

In volume-overload, elevated LV end-diastolic stress increases cardiac work, myocardial oxygen and ATP demand, haemodynamically reflected by a greater PVA (Suga et al., 1981; Gladden et al., 2011). Disruptions in mitochondrial function can impair energy generation and contribute to pathological remodeling. Indeed, mitochondria fragmentation has been observed in volume-overload, and this has been linked with bioenergetic deficit (Gladden et al., 2011).

One implicated pathway has been abnormal generation of reactive oxygen and nitrogen species (RNS). Mitochondria are major producers and consumers of ROS/RNS due to their high content in reactive proteins (Gutierrez et al., 2006). ROS/RNS reactions damage mitochondrial DNA, resulting in further ROS production and harmful positive feedback loops (Gladden et al., 2011; Yancey et al., 2015). Xanthine oxidase (XO) activity, involved in ROS production, is increased in the LV within the first 24 h in rats following aorto-caval shunt surgery (Gladden et al., 2011). This is accompanied by a decrease in mitochondrial oxidative function (Gladden et al., 2011), and suggests early metabolic abnormalities in volume-overload.

Mitochondrial dysfunction has also been linked to ECM remodeling (Ulasova et al., 2011). 24 h after aorto-caval shunt there is disruption of subsarcolemmal mitochondria structure, and interstitial collagen decrease, attributed to increased MMP activity (Ulasova et al., 2011). These abnormalities are corrected by pharmacological MMP inhibition (+PD166793) and mitochondrial respiration is significantly increased (Ulasova et al., 2011).

Emerging evidence also shows that increased MMP activity can have intracellular consequences, namely myofibril proteolysis (Kandasamy et al., 2010). For example, MMP-2 increases troponin-I, and myosin light chain 1 degradation in ischemia-reperfusion injury (Sawicki et al., 2005). Moreover, MMP activation is speculated to digest intermediate filaments supporting intermyofibrillar mitochondria (Ulasova et al., 2011). It is possible that this leads to contractile dysfunction by promoting myofibril disarray and loss, while disrupting the energetic coupling between mitochondria and sarcomeres.

More, similar to pressure-overload, glycemic control may impact development and progression of volume-overload by activation of hypertrophic pathways. In rats with aortic-regurgitation, high fructose intake results in worsening of eccentric remodeling (Bouchard-Thomassin et al., 2011). In pressure-overload activation of the Akt/mTOR signaling cascade is enhanced with hyperglycemia (Hernandez et al., 2013), but this pathway was not found to be upregulated in high-fructose aortic regurgitation (Bouchard-Thomassin et al., 2011). However, aortic-regurgitation does not produce pure volume-overload (Wilson and Lucchesi, 2014), and others have reported that activation of Akt/mTORC1 pathway has a central role in promoting eccentric hypertrophy in aorto-caval shunts with the level of pathway activation being a function of LV end-diastolic stress (Ikeda et al., 2015) (**Figure 4**).

Debrief

(1) Volume-overload results in eccentric hypertrophy. The decreased *h/r* ratio elevates stress and is normalized by increases in wall thickness; the chamber size remains elongated. Pattern of

remodeling is generally agreed to be driven by diastolic and not systolic stress.

(2) Sarcomeric addition occurs in series. This allows SL to be restored back to normal resting length following acute diastolic stretch. Though the force-SL relationship may be maintained, greater amount of stretch may be required to reach a given SL in elongated cardiomyocytes, which may impair the Frank-Starling response.

(3) Although the extent of isoform switches remains unclear, myofibrillar loss is a common feature of volume-overload, diminishing contractile performance and disrupting energetic couplons (mitochondria-sarcomeres). Mitochondrial oxidative stress may also directly cause myofibrillar loss, disrupt energetic coupling, and establish damaging feedback loops.

CONVERGENCE AND DIVERGENCE IN HEMODYNAMIC OVERLOAD

Volume and pressure-overload apply distinct hemodynamic load profiles (**Figures 1**, **3**) and molecular responses (**Figures 2**, **4**) on the myocardium. Generally, these are characterized by increased end-diastolic and end-systolic stress respectively. Myocardial adaptions then follow in line with intrinsic phenotypic plasticity. However, are these isolated and distinct responses and if not, is there overlap?

If they are different responses, remodeling would diverge and lead to distinct phenotypes. In contrast, overlap would result in convergence and shared phenotypes (**Figure 5**).

Activation of CAMKII, and calcineurin has been shown in pressure-, but not volume-overload (Toischer et al., 2010). Likewise, titin N2BA:N2B isoform ratio is decreased in volume-overload whereas it is increased in patients with aortic stenosis (Borbély et al., 2009). In pressure-overload excess collagen deposition and fibrosis are mediated by TGF-β and contribute to mechanical dysfunction (Dobaczewski et al., 2011), whereas inhibition of TGF-β in volume-overload accelerates LV dilatation (Frantz et al., 2008; Ulasova et al., 2011). Different biochemical and gene expression profiles have been suggested to be modulated in pressure- vs. volume-overload (Miyazaki et al., 2006; Toischer et al., 2010; You et al., 2018) correspondent with different signaling pathways (**Figures 2**, **4**). These findings support divergent pathways resulting in distinct morphological, structural, and functional myocardial properties in each load profile.

However, whether these experimental results where hemodynamic and environmental control is strictly and finely imposed are adequately representative of human pathophysiology is unclear. In patients with symptomatic aortic stenosis, eccentric hypertrophy has been noted (Villari et al., 1995). Likewise, titin N2BA:N2B ratio has been found to increase not only in compensated volume (Hutchinson et al., 2015), but also in pressure-overload (Williams et al., 2009).

It therefore seems that despite distinct signaling pathways mediating responses to load, convergence promoters must also be at play, shifting the myocardium toward common phenotypes. Identification of points of convergence and divergence is important as many of the properties of therapeutic agents for pressure-overload may not be shared in volume-overload and vice-versa (You et al., 2018). Patterns of convergence and divergence may be underlined by quantitative and qualitative agents: namely *time*, and *nature and spectrum of stimulus*.

The first obvious convergence promoter is *time*. Temporal phenotypic heterogeneity is often seen at first in cardiac disease, and as we have described herein, early adaptive phases following insult result in stark phenotypic differences in volume- and pressure-overload. Yet terminal HF phenotype share many similarities irrespective of initial trigger. It is possible that *compensated* remodeling is associated with *divergence* whereas *decompensated* remodeling with *convergence*. Clinically, this may be important as treatment during divergence may (a) be more likely to work, and (b) be more likely to be tailored to the phenotype being treated.

Secondly, the *nature and spectrum* of initiating stimulus. For example, arterial hypertension comprises a large range of volume- and pressure-load profiles (de Giovanni, 2004). In myocardial infarction there is both pressure- and volume-overload and remodeling includes both early LV dilation and hypertrophy (Opie et al., 2006). Likewise, aortic regurgitation has components of both volume- and pressure-overload (Carabello, 2002). In the presence of multiple and overlapping stimuli *convergence* will be favored. Similarly, with progression to decompensation, multiple signaling pathways that were previously quiescent now become active, and *convergence* dominates.

When initial events have distinct hemodynamic profiles, divergent phenotypes appear during the initial compensatory phases. With time, activation of multiple overlapping pathways leads to decompensation and phenotype convergence. Mixed phenotypes are possible in real-life where elements from both pressure- and volume-overload are likely to exist in sync.

EXPERIMENTAL MODELS TO STUDY LOAD-INDUCED REMODELING

In preclinical *in vivo* cardiac research, mechanical load cannot be studied in isolation to the neurohormonal axis. This is because, irrespective of complexity of experimental design to minimize neurohormonal activation (Swynghedauw, 2006), disrupting one inadvertently disrupts the other (Russell et al., 2010). Mechanical load and the neurohormonal axis can both drive cardiac remodeling, and can activate different gene programs (Frank et al., 2008). For example, many studies on RV volume-overload do not show deterioration of chamber contractility, yet when autonomic activity blockade is employed, RV contractile performance shows an immediate and persistent decline (Shah et al., 2000). Without model reduction, attained with utilization of simpler *in vitro* systems, pinpointing the contribution of the hormonal and mechanical axis, the activation of specific pathway mediators and their therapeutic potential is not only challenging but potentially misleading.

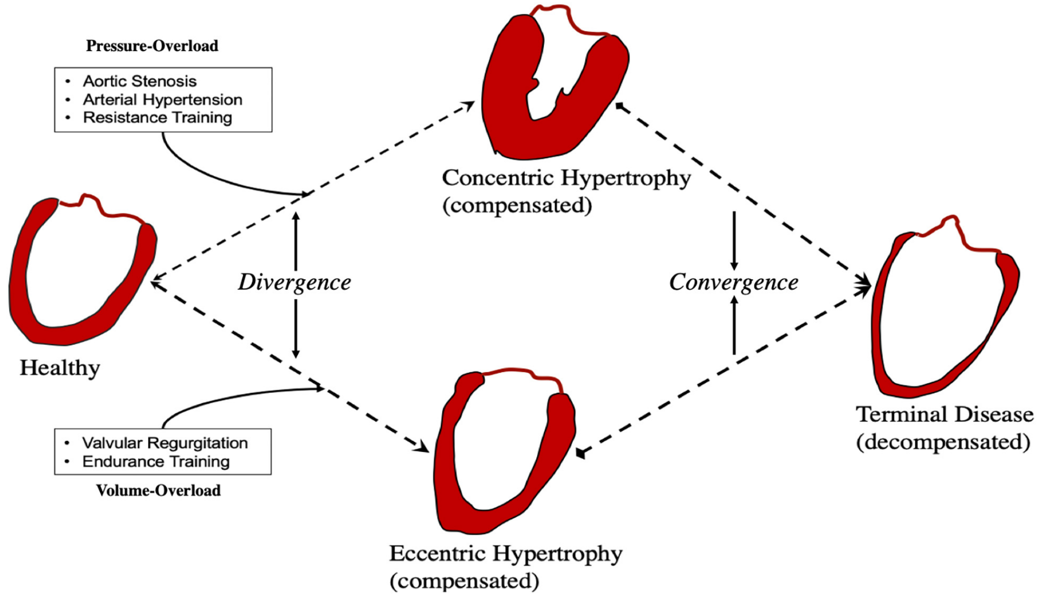

FIGURE 5 | Convergence and divergence in cardiac remodeling.

Although each cardiac model has unique advantages and limitations, many contemporary *in vitro* assays are oversimplified, and/or have low experimental throughput (Pitoulis F. G. et al., 2019). For example, isolated cardiomyocytes lack extracellular matrix (Watson et al., 2017). The relevance of engineered heart tissue (EHT) constructs to adult myocardium needs to be validated (Dhahri et al., 2018), and papillary muscles, whole hearts, and trabecula may suffer from low experimental throughput (Schechter et al., 2014). Additionally, appropriate protocols to simulate physiological and pathological mechanical load *in vitro* are not in widespread use. Sine-wave cyclic stretch in isolated cardiomyocytes (Yancey et al., 2015), and isotonic or isometric protocols in engineered heart tissues (Weinberger et al., 2017; Leonard et al., 2018) do not reflect the complexity of *in vivo* cardiac mechanics. Given the importance of pressure-volume and stress-strain relationships, at different times during the cardiac cycle in directing remodeling, physiology-inspired approaches are needed to simulate mechanical load *in vitro* and study its phenotypic consequences reliably.

In our lab we have pioneered the development of a novel *in vitro* cardiac model known as myocardial slices (Perbellini et al., 2017; Watson et al., 2017, 2019; Pitoulis F. et al., 2019). Myocardial slices are living organotypic preparations that can be prepared from mammalian hearts including human biopsies (Watson et al., 2017). The nature of the preparation means that myocardial functional (contractility, electrophysiology) and structural properties (ECM, hetero- and multi-cellularity) of the original tissue are preserved. Additionally, multiple slices can be prepared from a single specimen allowing for high-throughput experimentation. We and others have shown that slices can be kept in *in vitro* culture for prolonged periods of time with minimal loss of the adult myocardial phenotype (Kang et al., 2016; Fischer et al., 2019; Watson et al., 2019). As such, myocardial slices are uniquely positioned for interrogation of effects of chronic load on the myocardium away from the confounding influences of the neurohormonal arm.

CONCLUDING REMARKS

More Work on Progression of Disease and Volume-Overload

The past decades have seen massive strides in enhancing our understanding of the terminal myocardial phenotype. Experimentally, this may be easier to study. Less is known about the progression of disease from insult, to compensation, and then decompensation. Furthermore, despite much work on pressure-overload, our literature search supports that volume-overload induced remodeling is not as well documented.

Differential Therapies in Phenotypic Convergence and Divergence

Experimental evidence, mostly from animal research, demonstrates divergent phenotypes in pressure- and volume-overload. However, the situation is probably more complicated in human pathology where multiple convergent pathways may be simultaneously activated. Using this framework, much of the heterogeneity in presentation during the compensatory phases of cardiac remodeling converges toward more homogeneous phenotypes in end-stage HF. Divergent phenotypes are more likely to benefit from tailored treatments, whereas convergence is more likely to benefit from one-size fits all approaches.

In Need of Novel *in vitro* Cardiac Models to Study Mechanical Load

Advances in disease modeling and new methodologies have made the study of mechanical load possible in *in vitro* cardiac research; yet, fine manipulation of load is missing. The basic cardiac landscape is rapidly changing. The advent of new models coupled with new technologies is bound to open new research avenues. This will help uncover novel mediators of mechanical load in physiology, pathology, and at different stages of disease and will encourage their manipulation for therapeutic applications.

AUTHOR CONTRIBUTIONS

FP performed the literature search and wrote the manuscript. CT reviewed and edited the manuscript.

ACKNOWLEDGMENTS

We thank the British Heart Foundation (BHF) for grant to FP under the MBBS-Ph.D. studentship scheme (FS/18/37/33642).

REFERENCES

Ahmed, M. I., Gladden, J. D., Litovsky, S. H., Lloyd, S. G., Gupta, H., Inusah, S., et al. (2010). Increased oxidative stress and cardiomyocyte myofibrillar degeneration in patients with chronic isolated mitral regurgitation and ejection fraction >60%. *J. Am. Coll. Cardiol.* 55, 671–679. doi: 10.1016/j.jacc.2009.08.074

Allen, D. G., and Kentish, J. C. (1985). The cellular basis of the length-tension relation in cardiac muscle. *J. Mol. Cell. Cardiol.* 17, 821–840. doi: 10.1016/s0022-2828(85)80097-3

Anderson, M. E., Brown, J. H., and Bers, D. M. (2011). CaMKII in myocardial hypertrophy and heart failure. *J. Mol. Cell. Cardiol.* 51, 468–473. doi: 10.1016/j.yjmcc.2011.01.012

Anzai, T. (2018). Inflammatory mechanisms of cardiovascular remodeling. *Circ. J.* 82, 629–635. doi: 10.1253/circj.CJ-18-0063

Backs, J., Backs, T., Neef, S., Kreusser, M. M., Lehmann, L. H., Patrick, D. M., et al. (2009). The δ isoform of CaM kinase II is required for pathological cardiac hypertrophy and remodeling after pressure overload. *Proc. Natl. Acad. Sci. U.S.A.* 106, 2342–2347. doi: 10.1073/pnas.0813013106

Baharvand, H., Azarnia, M., Parivar, K., and Ashtiani, S. K. (2005). The effect of extracellular matrix on embryonic stem cell-derived cardiomyocytes. *J. Mol. Cell. Cardiol.* 38, 495–503. doi: 10.1016/j.yjmcc.2004.12.011

Balke, C. (1998). Alterations in calcium handling in cardiac hypertrophy and heart failure. *Cardiovasc. Res.* 37, 290–299. doi: 10.1016/s0008-6363(97)00272-1

Belin, R. J., Sumandea, M. P., Kobayashi, T., Walker, L. A., Rundell, V. L., Urboniene, D., et al. (2006). Left ventricular myofilament dysfunction in rat experimental hypertrophy and congestive heart failure. *Am. J. Physiol. Heart Circ. Physiol.* 291, H2344–H2353.

Benard, L., Oh, J. G., Cacheux, M., Lee, A., Nonnenmacher, M., Matasic, D. S., et al. (2016). Cardiac Stim1 silencing impairs adaptive hypertrophy and promotes heart failure through inactivation of mTORC2/Akt signaling. *Circulation* 133, 1458–1471; discussion 1471. doi: 10.1161/CIRCULATIONAHA.115.020678

Bers, D. M. (2002). Cardiac excitation-contraction coupling. *Nature* 415, 198–205.

Beuckelmann, D. J., Näbauer, M., Krüger, C., and Erdmann, E. (1995). Altered diastolic [Ca2+]i handling in human ventricular myocytes from patients with terminal heart failure. *Am. Heart J.* 129, 684–689. doi: 10.1016/0002-8703(95)90316-x

Bishop, J. E., Rhodes, S., Laurent, G. J., Low, R. B., and Stirewalt, W. S. (1994). Increased collagen synthesis and decreased collagen degradation in right ventricular hypertrophy induced by pressure overload. *Cardiovasc. Res.* 28, 1581–1585. doi: 10.1093/cvr/28.10.1581

Borbély, A., Falcao-Pires, I., Van Heerebeek, L., Hamdani, N., Édes, I., Gavina, C., et al. (2009). Hypophosphorylation of the stiff N2B titin isoform raises cardiomyocyte resting tension in failing human myocardium. *Circ. Res.* 104, 780–786. doi: 10.1161/CIRCRESAHA.108.193326

Bouchard-Thomassin, A. A., Lachance, D., Drolet, M. C., Couet, J., and Arsenault, M. (2011). A high-fructose diet worsens eccentric left ventricular hypertrophy in experimental volume overload. *Am. J. Physiol. Heart Circ. Physiol.* 300, H125–H134. doi: 10.1152/ajpheart.00199.2010

Braz, J. C., Gregory, K., Pathak, A., Zhao, W., Sahin, B., Klevitsky, R., et al. (2004). PKC-α regulates cardiac contractility and propensity toward heart failure. *Nat. Med.* 10, 248–254. doi: 10.1038/nm1000

Burchfield, J. S., Xie, M., and Hill, J. A. (2013). Pathological ventricular remodeling: mechanisms: part 1 of 2. *Circulation* 128, 388–400. doi: 10.1161/circulationaha.113.001878

Carabello, B. A. (2002). Concentric versus eccentric remodeling. *J. Card. Fail.* 8(Part B), S258–S263.

Carabello, B. A., Zile, M. R., Tanaka, R., and Cooper, G. (1992). 4th Left ventricular hypertrophy due to volume overload versus pressure overload. *Am. J. Physiol.* 263(4 Pt 2), H1137–H1144.

Chen-Izu, Y., Chen, L., Bányász, T., McCulle, S. L., Norton, B., Scharf, S. M., et al. (2007). Hypertension-induced remodeling of cardiac excitation-contraction coupling in ventricular myocytes occurs prior to hypertrophy development. *Am. J. Physiol. Heart Circ. Physiol.* 293, H3301–H3310.

Chiu, C., Tebo, M., Ingles, J., Yeates, L., Arthur, J. W., Lind, J. M., et al. (2007). Genetic screening of calcium regulation genes in familial hypertrophic cardiomyopathy. *J. Mol. Cell. Cardiol.* 43, 337–343. doi: 10.1016/j.yjmcc.2007.06.009

Cohn, J. N., Ferrari, R., and Sharpe, N. (2000). Cardiac remodeling-concepts and clinical implications: a consensus paper from an International Forum on Cardiac Remodeling. *J. Am. Coll. Cardiol.* 35, 569–582. doi: 10.1016/s0735-1097(99)00630-0

Cordeiro, J. M., Greene, L., Heilmann, C., Antzelevitch, D., and Antzelevitch, C. (2004). Transmural heterogeneity of calcium activity and mechanical function in the canine left ventricle. *Am. J. Physiol. Circ. Physiol.* 286, H1471–H1479.

Corin, W. J., Monrad, E. S., Murakami, T., Nonogi, H., Hess, O. M., and Krayenbuehl, H. P. (1987). The relationship of afterload to ejection performance in chronic mitral regurgitation. *Circulation* 76, 59–67. doi: 10.1161/01.cir.76.1.59

Crozatier, B., and Ventura-Clapier, R. (2015). Inhibition of hypertrophy, per se, may not be a good therapeutic strategy in ventricular pressure overload: other approaches could be more beneficial. *Circulation* 131, 1448–1457. doi: 10.1161/circulationaha.114.013895

Dai, D. F., Hsieh, E. J., Liu, Y., Chen, T., Beyer, R. P., Chin, M. T., et al. (2012). Mitochondrial proteome remodelling in pressure overload-induced heart failure: the role of mitochondrial oxidative stress. *Cardiovasc. Res.* 93, 79–88. doi: 10.1093/cvr/cvr274

Davis, J. S., Hassanzadeh, S., Winitsky, S., Lin, H., Satorius, C., Vemuri, R., et al. (2001). The overall pattern of cardiac contraction depends on a spatial gradient of myosin regulatory light chain phosphorylation. *Cell* 107, 631–641. doi: 10.1016/s0092-8674(01)00586-4

de Giovanni, S. (2004). Concentric or eccentric hypertrophy: how clinically relevant is the difference? *Hypertension* 43, 714–715. doi: 10.1161/01.hyp.0000121363.08252.a7

De la Bastie, D., Levitsky, D., Rappaport, L., Mercadier, J. J., Marotte, F., Wisnewsky, C., et al. (1990). Function of the sarcoplasmic reticulum and expression of its Ca2+-ATPase gene in pressure overload-induced cardiac hypertrophy in the rat. *Circ. Res.* 66, 554–564. doi: 10.1161/01.res.66.2.554

de Tombe, P. P. (1998). Altered contractile function in heart failure. *Cardiovasc. Res.* 37, 367–380. doi: 10.1016/s0008-6363(97)00275-7

Dhahri, W., Romagnuolo, R., and Laflamme, M. A. (2018). Training heart tissue to mature. *Nat. Biomed. Eng.* 2, 351–352. doi: 10.1038/s41551-018-0253-7

Dobaczewski, M., Chen, W., and Frangogiannis, N. G. (2011). Transforming growth factor (TGF)-β signaling in cardiac remodeling. *J. Mol. Cell. Cardiol.* 51, 600–606. doi: 10.1016/j.yjmcc.2010.10.033

Dorn, G. W. (2007). The fuzzy logic of physiological cardiac hypertrophy. *Hypertension* 49, 962–970. doi: 10.1161/hypertensionaha.106.079426

Fan, D., Wannenburg, T., and De Tombe, P. P. (1997). Decreased myocyte tension development and calcium responsiveness in rat right ventricular pressure overload. *Circulation* 95, 2312–2317. doi: 10.1161/01.cir.95.9.2312

Fischer, C., Milting, H., Fein, E., Reiser, E., Lu, K., Seidel, T., et al. (2019). Long-term functional and structural preservation of precision-cut human myocardium under continuous electromechanical stimulation in vitro. *Nat. Commun.* 10:117. doi: 10.1038/s41467-018-08003-1

Flesch, M., Schwinger, R. H. G., Schnabel, P., Schiffer, F., Van Gelder, I., Bavendiek, U., et al. (1996). Sarcoplasmic reticulum Ca^{2+}ATPaSe and phospholamban mRNA and protein levels in end-stage heart failure due to ischemic or dilated cardiomyopathy. *J. Mol. Med.* 74, 321–332. doi: 10.1007/s001090050033

Fomovsky, G. M., Thomopoulos, S., and Holmes, J. W. (2010). Contribution of extracellular matrix to the mechanical properties of the heart. *J. Mol. Cell. Cardiol.* 48, 490–496. doi: 10.1016/j.yjmcc.2009.08.003

Frank, D., Kuhn, C., Brors, B., Hanselmann, C., Lüdde, M., Katus, H. A., et al. (2008). Gene expression pattern in biomechanically stretched cardiomyocytes: evidence for a stretch-specific gene program. *Hypertension* 51, 309–318. doi: 10.1161/hypertensionaha.107.098046

Franklin, D., Bloor, C. M., and Dilley, R. B. (1975). Adaptations of the left ventricle to chronic pressure overload. *Circ. Res.* 38, 172–178. doi: 10.1161/01.res.38.3.172

Frantz, S., Hu, K., Adamek, A., Wolf, J., Sallam, A., Maier, S. K. G., et al. (2008). Transforming growth factor beta inhibition increases mortality and left ventricular dilatation after myocardial infarction. *Basic Res. Cardiol.* 103, 485–492. doi: 10.1007/s00395-008-0739-7

Frey, N., Katus, H. A., Olson, E. N., and Hill, J. A. (2004). Hypertrophy of the heart: a new therapeutic target? *Circulation* 109, 1580–1589. doi: 10.1161/01.cir.0000120390.68287.bb

Fujino, N., Ino, H., Hayashi, K., Uchiyama, K., Nagata, M., Konno, T., et al. (2006). A novel missense mutation in cardiac ryanodine receptor gene as a possible cause of hypertrophic cardiomyopathy: evidence from familial analysis. *Circulation* 114, II–165.

Gerdes, A. M., and Capasso, J. M. (1995). Structural remodeling and mechanical dysfunction of cardiac myocytes in heart failure. *J. Mol. Cell. Cardiol.* 27, 849–856. doi: 10.1016/0022-2828(95)90000-4

Gerdes, A. M., Kellerman, S. E., Moore, J. A., Muffly, K. E., Clark, L. C., Reaves, P. Y., et al. (1992). Structural remodeling of cardiac myocytes in patients with ischemic cardiomyopathy. *Circulation* 86, 426–430. doi: 10.1161/01.cir.86.2.426

Gheorghiade, M., Larson, C. J., Shah, S. J., Greene, S. J., Cleland, J. G. F., Colucci, W. S., et al. (2016). Developing new treatments for heart failure. *Circ. Heart Fail.* 9:e002727.

Giese, B., Roderburg, C., Sommerauer, M., Wortmann, S. B., Metz, S., Heinrich, P. C., et al. (2005). Dimerization of the cytokine receptors gp130 and LIFR analysed in single cells. *J. Cell Sci.* 118, 5129–5140. doi: 10.1242/jcs.02628

Gladden, J. D., Zelickson, B. R., Wei, C. C., Ulasova, E., Zheng, J., Ahmed, M. I., et al. (2011). Novel insights into interactions between mitochondria and xanthine oxidase in acute cardiac volume overload. *Free Radic. Biol. Med.* 51, 1975–1984. doi: 10.1016/j.freeradbiomed.2011.08.022

Glembotski, C. C. (2008). The role of the unfolded protein response in the heart. *J. Mol. Cell. Cardiol.* 44, 453–459.

Gnecchi, M., Zhang, Z., Ni, A., and Dzau, V. J. (2008). Paracrine mechanisms in adult stem cell signaling and therapy. *Circ. Res.* 103, 1204–1219. doi: 10.1161/CIRCRESAHA.108.176826

Goh, K. Y., He, L., Song, J., Jinno, M., Rogers, A. J., Sethu, P., et al. (2019). Mitoquinone ameliorates pressure overload-induced cardiac fibrosis and left ventricular dysfunction in mice. *Redox Biol.* 21:101100. doi: 10.1016/j.redox.2019.101100

Gomez, A. M., Valdivia, H. H., Cheng, H., Lederer, M. R., Santana, L. F., Cannell, M. B., et al. (1997). Defective excitation-contraction coupling in experimental cardiac hypertrophy and heart failure. *Science* 276, 800–806. doi: 10.1126/science.276.5313.800

Grossman, W., Jones, D., and McLaurin, L. P. (1975). Wall stress and patterns of hypertrophy in the human left ventricle. *J. Clin. Invest.* 56, 56–64. doi: 10.1172/jci108079

Grossman, W., and Paulus, W. J. (2013). Myocardial stress and hypertrophy: a complex interface between biophysics and cardiac remodeling. *J. Clin. Invest.* 123, 3701–3703. doi: 10.1172/JCI69830

Guggilam, A., Hutchinson, K. R., West, T. A., Kelly, A. P., Galantowicz, M. L., Davidoff, A. J., et al. (2013). In vivo and in vitro cardiac responses to beta-adrenergic stimulation in volume-overload heart failure. *J. Mol. Cell. Cardiol.* 57, 47–58. doi: 10.1016/j.yjmcc.2012.11.013

Guo, A., Zhang, C., Wei, S., Chen, B., and Song, L. S. (1996). Emerging mechanisms of T-tubule remodelling in heart failure. *Cardiovasc. Res.* 98, 204–215. doi: 10.1093/cvr/cvt020

Gupta, A., Akki, A., Wang, Y., Leppo, M. K., Chacko, V. P., Foster, D. B., et al. (2012). Creatine kinase-Mediated improvement of function in failing mouse hearts provides causal evidence the failing heart is energy starved. *J. Clin. Invest.* 122, 291–302. doi: 10.1172/JCI57426

Guterl, K. A., Haggart, C. R., Janssen, P. M., and Holmes, J. W. (2007). Isometric contraction induces rapid myocyte remodeling in cultured rat right ventricular papillary muscles. *Am. J. Physiol. Heart Circ. Physiol.* 293, 3707–3712.

Gutierrez, J., Ballinger, S. W., Darley-Usmar, V. M., and Landar, A. (2006). Free radicals, mitochondria, and oxidized lipids: the emerging role in signal transduction in vascular cells. *Circ. Res.* 99, 924–932. doi: 10.1161/01.res.0000248212.86638.e9

Hallbäck, M., Isaksson, O., and Noresson, E. (1975). Consequences of myocardial structural adaptation on left ventricular compliance and the frank-starling relationship in spontaneously hypertensive rats. *Acta Physiol. Scand.* 94, 259–270. doi: 10.1111/j.1748-1716.1975.tb05885.x

Hamdani, N., Kooij, V., Van Dijk, S., Merkus, D., Paulus, W. J., Remedios, C. D., et al. (2008). Sarcomeric dysfunction in heart failure. *Cardiovasc. Res.* 77, 649–658.

Hasenfuss, G., Mulieri, L. A., Leavitt, B. J., Allen, P. D., Haeberle, J. R., and Alpert, N. R. (1990). Alteration of contractile function and excitation-contraction coupling in dilated cardiomyopathy. *Circ. Res.* 70, 1225–1232. doi: 10.1161/01.res.70.6.1225

Heineke, J., and Molkentin, J. D. (2006). Regulation of cardiac hypertrophy by intracellular signalling pathways. *Nat. Rev. Mol. Cell Biol.* 7, 589–600. doi: 10.1038/nrm1983

Hernandez, A. M., Huber, J. S., Murphy, S. T., Janabi, M., Zeng, G. L., Brennan, K. M., et al. (2013). Longitudinal evaluation of left ventricular substrate metabolism, perfusion, and dysfunction in the spontaneously hypertensive rat model of hypertrophy using small-animal PET/CT imaging. *J. Nucl. Med.* 54, 1938–1945. doi: 10.2967/jnumed.113.120105

Herron, T. J., and McDonald, K. S. (2002). Small amounts of α-myosin heavy chain isoform expression significantly increase power output of rat cardiac myocyte fragments. *Circ. Res.* 90, 1150–1152. doi: 10.1161/01.res.0000022879.57270.11

Hibberd, M. G., and Jewell, B. R. (1982). Calcium- and length-dependent force production in rat ventricular muscle. *J. Physiol.* 329, 527–540. doi: 10.1113/jphysiol.1982.sp014317

Hill, J. A., Karimi, M., Kutschke, W., Davisson, R. L., Zimmerman, K., Wang, Z., et al. (2000). Cardiac hypertrophy is not a required compensatory response to short- term pressure overload. *Circulation* 101, 2863–2869. doi: 10.1161/01.cir.101.24.2863

Hill, J. A., and Olson, E. N. (2008). Cardiac plasticity. *N. Engl. J. Med.* 358, 1370–1380.

Holubarsch, C., Ruf, T., Goldstein, D. J., Ashton, R. C., Nicki, W., Pieske, B., et al. (1996). Existence of the Frank-Starling mechanism in the failing human heart: investigations on the organ, tissue, and sarcomere levels. *Circulation* 94, 683–689. doi: 10.1161/01.cir.94.4.683

Hoogsteen, J., Hoogeveen, A., Schaffers, H., Wijn, P. F. F., and Van Der Wall, E. E. (2003). Left atrial and ventricular dimensions in highly trained cyclists. *Int. J. Cardiovasc. Imaging* 19, 211–217.

Hulot, J. S., Fauconnier, J., Ramanujam, D., Chaanine, A., Aubart, F., Sassi, Y., et al. (2011). Critical role for stromal interaction molecule 1 in cardiac hypertrophy. *Circulation* 124, 796–805. doi: 10.1161/CIRCULATIONAHA.111.031229

Hutchinson, K. R., Saripalli, C., Chung, C. S., and Granzier, H. (2015). Increased myocardial stiffness due to cardiac titin isoform switching in a mouse model of volume overload limits eccentric remodeling. *J. Mol. Cell. Cardiol.* 79, 104–114. doi: 10.1016/j.yjmcc.2014.10.020

Ibrahim, M., and Terracciano, C. M. (2013). Reversibility of T-tubule remodelling in heart failure: mechanical load as a dynamic regulator of the T-tubules. *Cardiovasc. Res.* 98, 225–232. doi: 10.1093/cvr/cvt016

Ikeda, M., Ide, T., Fujino, T., Matsuo, Y., Arai, S., Saku, K., et al. (2015). The Akt-mTOR axis is a pivotal regulator of eccentric hypertrophy during volume overload. *Sci. Rep.* 5:15881. doi: 10.1038/srep15881

Ingwall, J. S. (2009). Energy metabolism in heart failure and remodelling. *Cardiovasc. Res.* 81, 412–419. doi: 10.1093/cvr/cvn301

Kaludercic, N., Carpi, A., Nagayama, T., Sivakumaran, V., Zhu, G., Lai, E. W., et al. (2014). Monoamine Oxidase b prompts mitochondrial and cardiac dysfunction in pressure overloaded hearts. *Antioxidants Redox Signal.* 20, 267–280. doi: 10.1089/ars.2012.4616

Kaludercic, N., Takimoto, E., Nagayama, T., Feng, N., Lai, E. W., Bedja, D., et al. (2010). Monoamine oxidase a-mediated enhanced catabolism of norepinephrine contributes to adverse remodeling and pump failure in hearts with pressure overload. *Circ. Res.* 106, 193–202. doi: 10.1161/CIRCRESAHA.109.198366

Kandasamy, A. D., Chow, A. K., Ali, M. A. M., and Schulz, R. (2010). Matrix metalloproteinase-2 and myocardial oxidative stress injury: beyond the matrix. *Cardiovasc. Res.* 85, 413–423. doi: 10.1093/cvr/cvp268

Kang, C., Qiao, Y., Li, G., Baechle, K., Camelliti, P., Rentschler, S., et al. (2016). Human organotypic cultured cardiac slices: new platform for high throughput preclinical human trials. *Sci. Rep.* 6:28798. doi: 10.1038/srep28798

Kehat, I., and Molkentin, J. D. (2010). Molecular pathways underlying cardiac remodeling during pathophysiological stimulation. *Circulation* 122, 2727–2735. doi: 10.1161/circulationaha.110.942268

Kiss, E., Ball, N. A., Kranias, E. G., and Walsh, R. A. (1995). Differential changes in cardiac phospholamban and sarcoplasmic reticular Ca^{2+}-ATPase protein levels: effects on Ca^{2+} transport and mechanics in compensated pressure-overload hypertrophy and congestive heart failure. *Circ. Res.* 77, 759–764. doi: 10.1161/01.res.77.4.759

Komamura, K., Shannon, R. P., Ihara, T., Shen, Y. T., Mirsky, I., Bishop, S. P., et al. (1993). Exhaustion of Frank-Starling mechanism in conscious dogs with heart failure. *Am. J. Physiol. Heart Circ. Physiol.* 265(4 Pt 2), H1119–H1131.

Kormos, R. L., McCall, M., Althouse, A., Lagazzi, L., Schaub, R., Kormos, M. A., et al. (2017). Left ventricular assist device malfunctions: it's more than just the pump. *Circulation* 136, 1714–1725. doi: 10.1161/circulationaha.117.027360

Kundu, B. K., Zhong, M., Sen, S., Davogustto, G., Keller, S. R., and Taegtmeyer, H. (2015). Remodeling of glucose metabolism precedes pressure overload-induced left ventricular hypertrophy: review of a hypothesis. *Cardiology* 130, 211–220. doi: 10.1159/000369782

Lamb, H. J., Beyerbacht, H. P., De Roos, A., Van Der Laarse, A., Vliegen, H. W., Leujes, F., et al. (2002). Left ventricular remodeling early after aortic valve replacement: differential effects on diastolic function in aortic valve stenosis and aortic regurgitation. *J. Am. Coll. Cardiol.* 40, 2182–2188. doi: 10.1016/s0735-1097(02)02604-9

Leonard, A., Bertero, A., Powers, J. D., Beussman, K. M., Bhandari, S., Regnier, M., et al. (2018). Afterload promotes maturation of human induced pluripotent stem cell derived cardiomyocytes in engineered heart tissues. *J. Mol. Cell. Cardiol.* 118, 147–158. doi: 10.1016/j.yjmcc.2018.03.016

Levick, S. P., Gardner, J. D., Holland, M., Hauer-Jensen, M., Janicki, J. S., and Brower, G. L. (2008). Protection from adverse myocardial remodeling secondary to chronic volume overload in mast cell deficient rats. *J. Mol. Cell. Cardiol.* 45, 56–61. doi: 10.1016/j.yjmcc.2008.04.010

Lewinter, M. M., and Granzier, H. (2010). Cardiac titin: a multifunctional giant. *Circulation* 121, 2137–2145. doi: 10.1161/circulationaha.109.860171

Limas, C. J., Olivari, M. T., Goldenberg, I. F., Levine, T. B., Benditt, D. G., and Simon, A. (1987). Calcium uptake by cardiac sarcoplasmic reticulum in human dilated cardiomyopathy. *Cardiovasc. Res.* 21, 601–605. doi: 10.1093/cvr/21.8.601

Ling, H., Zhang, T., Pereira, L., Means, C. K., Cheng, H., Gu, Y., et al. (2009). Requirement for Ca^{2+}/calmodulin-dependent kinase II in the transition from pressure overload-induced cardiac hypertrophy to heart failure in mice. *J. Clin. Invest.* 119, 1230–1240. doi: 10.1172/JCI38022

Maier, L. S. (2012). "Ca^{2+}/calmodulin-dependent protein kinase II (CaMKII) in the heart BT," in *Calcium Signaling*, ed. M. S. Islam, (Dordrecht: Springer), 685–702. doi: 10.1007/978-94-007-2888-2_30

Mansour, H., De Tombe, P. P., Samarel, A. M., and Russell, B. (2004). Restoration of resting sarcomere length after uniaxial static strain is regulated by protein kinase Cε and focal adhesion kinase. *Circ. Res.* 94, 642–649. doi: 10.1161/01.res.0000121101.32286.c8

Manyari, D. E., Levy, D., Garrison, R. J., Kannel, W. B., and Castelli, W. P. (1990). Prognostic implications of echocardiographically determined left ventricular mass in the Framingham heart study. *N. Engl. J. Med.* 322, 1561–1566. doi: 10.1056/nejm199005313222203

McMullen, J. R., Shioi, T., Zhang, L., Tarnavski, O., Sherwood, M. C., Kang, P. M., et al. (2003). Phosphoinositide 3-kinase(p110α) plays a critical role for the induction of physiological, but not pathological, cardiac hypertrophy. *Proc. Natl. Acad. Sci. U.S.A.* 100, 12355–12360. doi: 10.1073/pnas.1934654100

Mesa, A., Jessurun, C., Hernandez, A., Adam, K., Brown, D., Vaughn, W. K., et al. (1999). Left ventricular diastolic function in normal human pregnancy. *Circulation* 99, 511–517. doi: 10.1161/01.cir.99.4.511

Mihl, C., Dassen, W. R. M., and Kuipers, H. (2008). Cardiac remodelling: concentric versus eccentric hypertrophy in strength and endurance athletes. *Neth. Heart J.* 16, 129–133. doi: 10.1007/bf03086131

Miyata, S., Minobe, W., Bristow, M. R., and Leinwand, L. A. (2000). Myosin heavy chain isoform expression in the failing and nonfailing human heart. *Circ. Res.* 86, 386–390. doi: 10.1161/01.res.86.4.386

Miyazaki, H., Oka, N., Koga, A., Ohmura, H., Ueda, T., and Imaizumi, T. (2006). Comparison of gene expression profiling in pressure and volume overload - Induced myocardial hypertrophies in rats. *Hypertens. Res.* 29, 1029–1045. doi: 10.1291/hypres.29.1029

Nagata, K., Liao, R., Eberli, F. R., Satoh, N., Chevalier, B., Apstein, C. S., et al. (1998). Early changes in excitation-contraction coupling: transition from compensated hypertrophy to failure in Dahl salt-sensitive rat myocytes. *Cardiovasc. Res.* 37, 467–477. doi: 10.1016/s0008-6363(97)00278-2

Nguyen, V. T., Mossberg, K. A., Tewson, T. J., Wong, W. H., Rowe, R. W., Coleman, G. M., et al. (1990). Temporal analysis of myocardial glucose metabolism by 2-[18F]fluoro-2-deoxy-D-glucose. *Am. J. Physiol.* 259(4 Pt 2), H1022–H1031.

Nozawa, T., Cheng, C. P., Noda, T., and Little, W. C. (1994). Relation between left ventricular oxygen consumption and pressure-volume area in conscious dogs. *Circulation* 89, 810–817. doi: 10.1161/01.cir.89.2.810

Okoshi, K., Ribeiro, H. B., Okoshi, M. P., Matsubara, B. B., Gonçalves, G., Barros, R., et al. (2004). Improved systolic ventricular function with normal myocardial mechanics in compensated cardiac hypertrophy. *Jpn. Heart J.* 45, 647–656. doi: 10.1536/jhj.45.647

Opie, L. H., Commerford, P. J., Gersh, B. J., and Pfeffer, M. A. (2006). Controversies in ventricular remodelling. *Lancet* 367, 356–367. doi: 10.1016/s0140-6736(06)68074-4

Packer, M. (1993). The development of positive inotropic agents for chronic heart failure: how have we gone astray? *J. Am. Coll. Cardiol.* 22(4 Suppl. A), 119A–126A.

Perbellini, F., Watson, S. A., Scigliano, M., Alayoubi, S., Tkach, S., Bardi, I., et al. (2017). Investigation of cardiac fibroblasts using myocardial slices. *Cardiovasc. Res.* 114, 77–89. doi: 10.1093/cvr/cvx152

Pfeffer, J. M., Pfeffer, M. A., and Fishbein, M. C. (1979). Cardiac function and morphology with aging in the spontaneously hypertensive rat. *Am. J. Physiol. Heart Circ. Physiol.* 237, H461–H468.

Pieske, B., Schlotthauer, K., Schattmann, J., Beyersdorf, F., Martin, J., Just, H., et al. (1997). Ca^{2+}-dependent and Ca^{2+}-independent regulation of contractility in isolated human myocardium. *Basic Res. Cardiol.* 92, 75–86. doi: 10.1007/bf00794071

Pitoulis, F., Perbellini, F., Harding, S. E., De Tombe, P., and Terracciano, C. M. (2019). P5373Mechanical heterogeneity across the left ventricular wall - a study using intact multicellular preparations. *Eur. Heart J.* 40(Suppl._1):ehz746.0336.

Pitoulis, F. G., Watson, S. A., Perbellini, F., and Terracciano, C. M. (2019). Myocardial slices come to age: an intermediate complexity in vitro cardiac model for translational research. *Cardiovasc. Res.* cvz341. doi: 10.1093/cvr/cvz341 [Epub ahead of print].

Proud, C. G. (2004). Ras, PI3-kinase and mTOR signaling in cardiac hypertrophy. *Cardiovasc. Res.* 63, 403–413. doi: 10.1016/j.cardiores.2004.02.003

Randhawa, A. K., and Singal, P. K. (1992). Pressure overload-induced cardiac hypertrophy with and without dilation. *J. Am. Coll. Cardiol.* 20, 1569–1575. doi: 10.1016/0735-1097(92)90452-s

Ruppert, M., Bódi, B., Korkmaz-Icöz, S., Loganathan, S., Jiang, W., Lehmann, L., et al. (2019). Myofilament Ca $^{2+}$ sensitivity correlates with left ventricular contractility during the progression of pressure overload-induced left ventricular myocardial hypertrophy in rats. *J. Mol. Cell. Cardiol.* 129, 208–218. doi: 10.1016/j.yjmcc.2019.02.017

Russell, B., Curtis, M. W., Koshman, Y. E., and Samarel, A. M. (2010). Mechanical stress-induced sarcomere assembly for cardiac muscle growth in length and width. *J. Mol. Cell. Cardiol.* 48, 817–823. doi: 10.1016/j.yjmcc.2010.02.016

Ryan, T. D., Rothstein, E. C., Aban, I., Tallaj, J. A., Husain, A., Lucchesi, P. A., et al. (2007). Left ventricular eccentric remodeling and matrix loss are mediated by bradykinin and precede cardiomyocyte elongation in rats with volume overload. *J. Am. Coll. Cardiol.* 49, 811–821. doi: 10.1016/j.jacc.2006.06.083

Saks, V. A., Kaambre, T., Sikk, P., Eimre, M., Orlova, E., Paju, K., et al. (2001). Intracellular energetic units in red muscle cells. *Biochem. J.* 356(Pt 2), 643–657. doi: 10.1042/bj3560643

Sanger, J. W., Wang, J., Fan, Y., White, J., and Sanger, J. M. (2010). Assembly and dynamics of myofibrils. *J. Biomed. Biotechnol.* 2010:858606. doi: 10.1155/2010/858606

Santana, L. F., Cheng, H., Gómez, A. M., Cannell, M. B., Lederer, W. J., Scott, J. D., et al. (1996). Relation between the sarcolemmal Ca^{2+} current and Ca^{2+} sparks and local control theories for cardiac excitation-contraction coupling. *Circ. Res.* 78, 166–171. doi: 10.1161/01.res.78.1.166

Sawicki, G., Leon, H., Sawicka, J., Sariahmetoglu, M., Schulze, C. J., Scott, P. G., et al. (2005). Degradation of myosin light chain in isolated rat hearts subjected to ischemia-reperfusion injury: a new intracellular target for matrix metalloproteinase-2. *Circulation* 112, 544–552. doi: 10.1161/circulationaha.104.531616

Schechter, M. A., Southerland, K. W., Feger, B. J., Linder, D., Ali, A. A., Njoroge, L., et al. (2014). An isolated working heart system for large animal models. *J. Vis. Exp.* 88:51671.

Schirone, L., Forte, M., Palmerio, S., Yee, D., Nocella, C., Angelini, F., et al. (2017). A review of the molecular mechanisms underlying the development and progression of cardiac remodeling. *Oxid. Med. Cell. Longev.* 2017:3920195. doi: 10.1155/2017/3920195

Schwartz, K., Boheler, K. R., De la Bastie, D., Lompre, A. M., and Mercadier, J. J. (1992). Switches in cardiac muscle gene expression as a result of pressure and volume overload. *Am. J. Physiol. Regul. Integr. Comp. Physiol.* 262, R364–R369.

Schwinger, R. H. G., Böhm, M., Koch, A., Schmidt, U., Morano, I., Eissner, H. J., et al. (1994). The failing human heart is unable to use the Frank-Starling mechanism. *Circ. Res.* 74, 959–969. doi: 10.1161/01.res.74.5.959

Shah, A. S., Atkins, B. Z., Hata, J. A., Tai, O., Kypson, A. P., Lilly, R. E., et al. (2000). Early effects of right ventricular volume overload on ventricular performance and β-adrenergic signaling. *J. Thorac. Cardiovasc. Surg.* 120, 342–349. doi: 10.1067/mtc.2000.107278

Sharma, H. S., Verdouw, P. D., and Lamers, J. M. J. (1994). Involvement of the sarcoplasmic reticulum calcium pump in myocardial contractile dysfunction: comparison between chronic pressure-overload and stunning. *Cardiovasc. Drugs Ther.* 8, 461–468. doi: 10.1007/bf00877923

Shave, R. E., Lieberman, D. E., Drane, A. L., Brown, M. G., Batterham, A. M., Worthington, S., et al. (2019). Selection of endurance capabilities and the trade-off between pressure and volume in the evolution of the human heart. *Proc. Natl. Acad. Sci. U.S.A.* 116, 19905–19910. doi: 10.1073/pnas.1906902116

Sivakumaran, V., Stanley, B. A., Tocchetti, C. G., Ballin, J. D., Caceres, V., Zhou, L., et al. (2013). HNO enhances SERCA2a activity and cardiomyocyte function by promoting redox-dependent phospholamban oligomerization. *Antioxidants Redox Signal.* 19, 1185–1197. doi: 10.1089/ars.2012.5057

Smyrnias, I., Gray, S. P., Okonko, D. O., Sawyer, G., Zoccarato, A., Catibog, N., et al. (2019). Cardioprotective effect of the mitochondrial unfolded protein response during chronic pressure overload. *J. Am. Coll. Cardiol.* 73, 1795–1806. doi: 10.1016/j.jacc.2018.12.087

Song, L. S., Pi, Y. Q., Kim, S. J., Yatani, A., Guatimosim, S., Kudej, R. K., et al. (2005). Paradoxical cellular Ca^{2+} signaling in severe but compensated canine left ventricular hypertrophy. *Circ. Res.* 97, 457–464. doi: 10.1161/01.res.0000179722.79295.d4

Stelzer, J. E., Norman, H. S., Chen, P. P., Patel, J. R., and Moss, R. L. (2008). Transmural variation in myosin heavy chain isoform expression modulates the timing of myocardial force generation in porcine left ventricle. *J. Physiol.* 586, 5203–5214. doi: 10.1113/jphysiol.2008.160390

Suga, H., Hayashi, T., and Shirahata, M. (1981). Ventricular systolic pressure-volume area as predictor of cardiac oxygen consumption. *Am. J. Physiol.* 240, H39–H44.

Suga, H., Sagawa, K., and Shoukas, A. A. (1973). Load independence of the instantaneous pressure-volume ratio of the canine left ventricle and effects of epinephrine and heart rate on the ratio. *Circ. Res.* 32, 314–322. doi: 10.1161/01.res.32.3.314

Sussman, M. A., Lim, H. W., Gude, N., Taigen, T., Olson, E. N., Robbins, J., et al. (1998). Prevention of cardiac hypertrophy in mice by calcineurin inhibition. *Science* 281, 1690–1693. doi: 10.1126/science.281.5383.1690

Swynghedauw, B. (2006). Phenotypic plasticity of adult myocardium: molecular mechanisms. *J. Exp. Biol.* 209(Pt 12), 2320–2327. doi: 10.1242/jeb.02084

Swynghedauw, B., and Charlemagne, D. (2002). What is wrong with positive inotropic drugs? Lessons from basic science and clinical trials. *Eur. Heart J. Suppl.* 4(Suppl._D), D43–D49.

Taegtmeyer, H., Sen, S., and Vela, D. (2010). Return to the fetal gene program: a suggested metabolic link to gene expression in the heart. *Ann. N. Y. Acad. Sci.* 1188, 191–198. doi: 10.1111/j.1749-6632.2009.05100.x

Terracciano, C. M. N., Hardy, J., Birks, E. J., Khaghani, A., Banner, N. R., and Yacoub, M. H. (2004). Clinical recovery from end-stage heart failure using left-ventricular assist device and pharmacological therapy correlates with increased sarcoplasmic reticulum calcium content but not with regression of cellular hypertrophy. *Circulation* 109, 2263–2265. doi: 10.1161/01.cir.0000129233.51320.92

Toischer, K., Rokita, A. G., Unsöld, B., Zhu, W., Kararigas, G., Sossalla, S., et al. (2010). Differential cardiac remodeling in preload versus afterload. *Circulation* 122, 993–1003. doi: 10.1161/CIRCULATIONAHA.110.943431

Ulasova, E., Gladden, J. D., Chen, Y., Zheng, J., Pat, B., Bradley, W., et al. (2011). Loss of interstitial collagen causes structural and functional alterations of cardiomyocyte subsarcolemmal mitochondria in acute volume overload. *J. Mol. Cell. Cardiol.* 50, 147–156. doi: 10.1016/j.yjmcc.2010.10.034

Urabe, Y., Mann, D. L., Kent, R. L., Nakano, K., Tomanek, R. J., Carabello, B. A., et al. (1992). Cellular and ventricular contractile dysfunction in experimental canine mitral regurgitation. *Circ. Res.* 70, 131–147. doi: 10.1161/01.res.70.1.131

Van Oort, R. J., Respress, J. L., Li, N., Reynolds, C., De Almeida, A. C., Skapura, D. G., et al. (2010). Accelerated development of pressure overload-induced cardiac hypertrophy and dysfunction in an RyR2-R176Q knockin mouse model. *Hypertension* 55, 932–938. doi: 10.1161/HYPERTENSIONAHA.109.146449

Villari, B., Vassaili, G., Monrad, E. S., Chiariello, M., Turina, M., and Hess, O. M. (1995). Normalization of diastolic dysfunction in aortic stenosis late after valve replacement. *Circulation* 91, 2353–2358. doi: 10.1161/01.cir.91.9.2353

Wang, Y., Zhang, Y., Ding, G., May, H. I., Xu, J., Gillette, T. G., et al. (2017). Temporal dynamics of cardiac hypertrophic growth in response to pressure overload. *Am. J. Physiol. Heartt Circ. Physiol.* 313, H1119–H1129. doi: 10.1152/ajpheart.00284.2017

Watson, S. A., Duff, J., Bardi, I., Zabielska, M., Atanur, S. S., Jabbour, R. J., et al. (2019). Biomimetic electromechanical stimulation to maintain adult myocardial slices in vitro. *Nat. Commun.* 10:2168. doi: 10.1038/s41467-019-10175-3

Watson, S. A., Scigliano, M., Bardi, I., Ascione, R., Terracciano, C. M., and Perbellini, F. (2017). Preparation of viable adult ventricular myocardial slices from large and small mammals. *Nat. Protoc.* 12, 2623–2639. doi: 10.1038/nprot.2017.139

Wei, S., Guo, A., Chen, B., Kutschke, W., Xie, Y. P., Zimmerman, K., et al. (2010). T-tubule remodeling during transition from hypertrophy to heart failure. *Circ. Res.* 107, 520–531. doi: 10.1161/circresaha.109.212324

Weil, J., Eschenhagen, T., Hirt, S., Magnussen, O., Mittmann, C., Remmers, U., et al. (1998). Preserved Frank–Starling mechanism in human end stage heart failure. *Cardiovasc. Res.* 37, 541–548. doi: 10.1016/s0008-6363(97)00227-7

Weinberger, F., Mannhardt, I., and Eschenhagen, T. (2017). Engineering cardiac muscle tissue: a maturating field of research. *Circ. Res.* 120, 1487–1500. doi: 10.1161/CIRCRESAHA.117.310738

Weiner, R. B., and Baggish, A. L. (2012). Exercise-induced cardiac remodeling. *Prog. Cardiovasc. Dis.* 9:e005321.

Wilkins, B. J., and Molkentin, J. D. (2002). Calcineurin and cardiac hypertrophy: where have we been? Where are we going? *J. Physiol.* 541(Pt 1), 1–8. doi: 10.1113/jphysiol.2002.017129

Williams, L., Howell, N., Pagano, D., Andreka, P., Vertesaljai, M., Pecor, T., et al. (2009). Titin isoform expression in aortic stenosis. *Clin. Sci.* 117, 237–242. doi: 10.1042/CS20080248

Wilson, A. J., Schoenauer, R., Ehler, E., Agarkova, I., and Bennett, P. M. (2014). Cardiomyocyte growth and sarcomerogenesis at the intercalated disc. *Cell. Mol. Life Sci.* 71, 165–181. doi: 10.1007/s00018-013-1374-5

Wilson, K., and Lucchesi, P. A. (2014). Myofilament dysfunction as an emerging mechanism of volume overload heart failure. *Pflugers Arch. Eur. J. Physiol.* 466, 1065–1077. doi: 10.1007/s00424-014-1455-9

Wollert, K. C., Taga, T., Saito, M., Narazaki, M., Kishimoto, T., Glembotski, C. C., et al. (1996). Cardiotrophin-1 activates a distinct form of cardiac muscle cell hypertrophy. *J. Biol. Chem.* 271, 9535–9545. doi: 10.1074/jbc.271.16.9535

Yancey, D. M., Guichard, J. L., Ahmed, M. I., Zhou, L., Murphy, M. P., Johnson, M. S., et al. (2015). Cardiomyocyte mitochondrial oxidative stress and cytoskeletal breakdown in the heart with a primary volume overload. *Am. J. Physiol. Heart Circ. Physiol.* 308, H651–H663. doi: 10.1152/ajpheart.00638.2014

Yang, H., Schmidt, L. P., Wang, Z., Yang, X., Shao, Y., Borg, T. K., et al. (2016). Dynamic myofibrillar remodeling in live cardiomyocytes under static stretch. *Sci. Rep.* 6:20674. doi: 10.1038/srep20674

Yin, Z., Ren, J., and Guo, W. (2015). Sarcomeric protein isoform transitions in cardiac muscle: a journey to heart failure. *Biochim. Biophys. Acta Mol. Basis Dis.* 1852, 47–52. doi: 10.1016/j.bbadis.2014.11.003

Yoshida, M., Sho, E., Nanjo, H., Takahashi, M., Kobayashi, M., Kawamura, K., et al. (2010). Weaving hypothesis of cardiomyocyte sarcomeres: discovery of periodic broadening and narrowing of intercalated disk during volume-load change. *Am. J. Pathol.* 176, 660–678. doi: 10.2353/ajpath.2010.090348

You, J., Wu, J., Zhang, Q., Ye, Y., Wang, S., Huang, J., et al. (2018). Differential cardiac hypertrophy and signaling pathways in pressure versus volume overload. *Am. J. Physiol. Heart Circ. Physiol.* 314, H552–H562. doi: 10.1152/ajpheart.00212.2017

Young, M. E., Yan, J., Razeghi, P., Cooksey, R. C., Guthrie, P. H., Stepkowski, S. M., et al. (2007). Proposed regulation of gene expression by glucose in rodent heart. *Gene Regul. Syst. Bio.* 1, 251–262.

Zhang, R., Khoo, M. S. C., Wu, Y., Yang, Y., Grueter, C. E., Ni, G., et al. (2005). Calmodulin kinase II inhibition protects against structural heart disease. *Nat. Med.* 11, 409–417. doi: 10.1038/nm1215

Zhong, M., Alonso, C. E., Taegtmeyer, H., and Kundu, B. K. (2013). Quantitative PET imaging detects early metabolic remodeling in a mouse model of pressure-overload left ventricular hypertrophy in vivo. *J. Nucl. Med.* 54, 609–615. doi: 10.2967/jnumed.112.108092

Conflict of Interest: The authors declare that the research was conducted in the absence of any commercial or financial relationships that could be construed as a potential conflict of interest.

ORIGINAL RESEARCH
published: 14 February 2020
doi: 10.3389/fphys.2020.00044

Modulation of Calcium Transients in Cardiomyocytes by Transient Receptor Potential Canonical 6 Channels

*Azmi A. Ahmad[1,2†], Molly E. Streiff[1,2†], Chris Hunter[1] and Frank B. Sachse[1,2]**

[1]*Nora Eccles Harrison Cardiovascular Research and Training Institute, University of Utah, Salt Lake City, UT, United States,* [2]*Department of Biomedical Engineering, University of Utah, Salt Lake City, UT, United States*

Edited by:
Olga Solovyova,
Institute of Immunology and
Physiology (RAS), Russia

Reviewed by:
José Javier López Barba,
University of Extremadura, Spain
Isaac Jardin,
University of Extremadura, Spain

Correspondence:
Frank B. Sachse
frank.sachse@utah.edu

†These authors have contributed equally to this work

Specialty section:
This article was submitted to
Membrane Physiology and
Membrane Biophysics,
a section of the journal
Frontiers in Physiology

Received: *09 October 2019*
Accepted: *20 January 2020*
Published: *14 February 2020*

Citation:
Ahmad AA, Streiff ME, Hunter C and Sachse FB (2020) Modulation of Calcium Transients in Cardiomyocytes by Transient Receptor Potential Canonical 6 Channels. Front. Physiol. 11:44. doi: 10.3389/fphys.2020.00044

Transient receptor potential canonical 6 (TRPC6) channels are non-selective cation channels that are thought to underlie mechano-modulation of calcium signaling in cardiomyocytes. TRPC6 channels are involved in development of cardiac hypertrophy and related calcineurin-nuclear factor of activated T cells (NFAT) signaling. However, the exact location and roles of TRPC6 channels remain ill-defined in cardiomyocytes. We used an expression system based on neonatal rat ventricular myocytes (NRVMs) to investigate the location of TRPC6 channels and their role in calcium signaling. NRVMs isolated from 1- to 2-day-old animals were cultured and infected with an adenoviral vector to express enhanced-green fluorescent protein (eGFP) or TRPC6-eGFP. After 3 days, NRVMs were fixed, immunolabeled, and imaged with confocal and super-resolution microscopy to determine TRPC6 localization. Cytosolic calcium transients at 0.5 and 1 Hz pacing rates were recorded in NRVMs using indo-1, a ratio-metric calcium dye. Confocal and super-resolution microscopy suggested that TRPC6-eGFP localized to the sarcolemma. NRVMs infected with TRPC6-eGFP exhibited higher diastolic and systolic cytosolic calcium concentration as well as increased sarcoplasmic reticulum (SR) calcium load compared to eGFP infected cells. We applied a computer model comprising sarcolemmal TRPC6 current to explain our experimental findings. Altogether, our studies indicate that TRPC6 channels play a role in sarcolemmal and intracellular calcium signaling in cardiomyocytes. Our findings support the hypothesis that upregulation or activation of TRPC6 channels, e.g., in disease, leads to sustained elevation of the cytosolic calcium concentration, which is thought to activate calcineurin-NFAT signaling and cardiac hypertrophic remodeling. Also, our findings support the hypothesis that mechanosensitivity of TRPC6 channels modulates cytosolic calcium transients and SR calcium load.

Keywords: transient receptor potential canonical channels, transient receptor potential canonical 6, cardiomyocyte, calcium transient, mechanosensitivity

INTRODUCTION

Transient receptor potential canonical (TRPC) 6 channels are non-selective cation channels expressed in the mammalian heart (Bon and Beech, 2013). The channels are permeable to Na^+ and Ca^{2+}, with six-fold higher permeability for Ca^{2+} than Na^+ (Dietrich and Gudermann, 2014). TRPC6 channels can be activated by diacylglycerol (DAG) (Hofmann et al., 1999), a product of phospholipase C, and other DAG analogues (Aires et al., 2007). Other studies suggested that the level of TRPC6 at the plasma membrane increases upon muscarinic receptor stimulation and depletion of intracellular Ca^{2+} pool (Cayouette et al., 2004). TRPC6 channels are thought to be stretch-activated channels (SACs). SACs convert mechanical stimuli into electrical or chemical signals used in various mechanosensitive pathways (Martinac and Kloda, 2003; Sachs, 2010). SACs and mechanosensitive channels contribute to mechano-regulation of Ca^{2+} signaling in the normal and diseased heart (Friedrich et al., 2012). Stretch activation of TRPC6 channels was linked to increases in cytosolic Ca^{2+} concentration ($[Ca^{2+}]_i$) (Dyachenko et al., 2008). Also, TRPC6 was found to be a contributor to the adaptive stretch-induced slow force response, a slow increase in $[Ca^{2+}]_i$ and twitch force that develops during stretch (Yamaguchi et al., 2017). Furthermore, TRPC6 was suggested to be involved in cardiac systolic mechanosignaling (Seo et al., 2014). Despite these findings, the precise role of TRPC6 channels in Ca^{2+} signaling and its mechanical modulation in cardiomyocytes remains unclear. It is also unclear if in cardiomyocytes TRPC6 channels contribute to mechano-electrical feedback (MEF), i.e., alter cell electrophysiology in response to mechanical stimuli (Franz, 2000).

In cardiac disease, TRPC6 is a positive regulator of calcineurin-NFAT signaling and plays a critical role in angiotensin II-induced cardiac hypertrophy (Kuwahara et al., 2006; Onohara et al., 2006; Wu et al., 2010). TRPC6 was upregulated in response to activated calcineurin and pressure overload, further indicating a role in cardiac disease (Kuwahara et al., 2006). In pathological conditions, TRPC6 were suggested to underlie dysregulated $[Ca^{2+}]_i$ and force, as well as arrhythmogenicity (Seo et al., 2014). TRPC6 is thought to be a key contributor to the initiation of hypertrophy and heart failure (Yamaguchi et al., 2017). Endothelin-treated neonatal rat cardiomyocytes showed hypertrophy along with increased TRPC6 mRNA expression (Kiso et al., 2013). A study in mouse cardiomyocytes revealed that overexpression of TRPC6 causes spontaneous cardiac hypertrophy and remodeling (Xie et al., 2012).

The involvement of TRPC6 in cardiac diseases has made it a target for treatment. Deletion of TRPC6 prevented stress-induced remodeling in mice (Xie et al., 2012). The enzyme Klotho reduced TRPC6 currents in cardiomyocytes. Also, Klotho inhibited TRPC6 currents in HEK293 and L6 cell lines independently of fibroblast growth factors (Wright et al., 2019). Studies on human cardiac fibroblasts suggested that knockdown of TRPC6 reduces 1-oleoyl-2-acetyl-sn-glycerol-induced Ca^{2+} entry (Ikeda et al., 2013). Drug blockade of TRPC6 reversed the excessive slow force response in dystrophic myocardium (Seo et al., 2014).

Localization of TRPC6 within cardiomyocytes is dependent on developmental stages and species (Ahmad et al., 2017). A study in rat ventricular myocytes suggested that in neonates TRPC6 localizes in the cytoplasm and nuclear envelope, and in adult animals to z-lines, intercalated discs and the nucleus (Jiang et al., 2014). TRPC6 expression was highest during the fetal stage and decreased after birth, with similar levels in neonatal and adult animals. In contrast, studies on mouse ventricular myocytes suggested TRPC6 location in the t-system and plasma membrane (Dyachenko et al., 2008; Mohl et al., 2011). These differences stress the importance of understanding TRPC6 localization when interpreting functional measurements.

In this study, we aimed at understanding effects of upregulation of TRPC6 on Ca^{2+} signaling in cardiac myocytes. We studied neonatal rat ventricular myocytes (NRVMs) infected with adenoviral constructs to modulate TRPC6 expression. We applied confocal microscopy and super-resolution imaging to identify TRPC6 localization. We measured $[Ca^{2+}]_i$ transients and Ca^{2+} load of sarcoplasmic reticulum (SR) using Ca^{2+}-sensitive dyes and spinning disk confocal microscopy. We applied computational modeling to qualitatively reproduce experimental findings and predict effects of upregulation or increased activity of TRPC6 on Ca^{2+} signaling.

METHODS

All studies were conducted at the University of Utah in accordance with National Institute of Health Guidelines for the Care and Use of Animals and reviewed by the Institutional Animal Care and Use Committee.

Preparation, Adenoviral Infection, and Culture of NRVMs

Sprague Dawley rat dams were obtained from Charles River (Wilmington, MA, USA). Ventricular myocytes were enzymatically isolated from 1-day old rats (NCIS, Worthington Biochemical Corporation, Lakewood, NJ, USA). NRVMs were separated from fibroblasts by cell suspension to take advantage of fibroblast rapid adhesion and recovering myocyte suspension. Myocytes were counted and plated at 75,000 cells per 0.95 cm^2 in a 48 well tissue culture plate containing No. 0 coverslips treated with fibronectin. NRVMs were infected 24 h after plating with an adenoviral vector containing human TRPC6 attached to enhanced green fluorescent protein (eGFP) fused to the C-terminal and 6X HIS tag fused to the N-terminal (TRPC6-eGFP) at 10 multiplication of infection (MOI). We applied also an eGFP vector (Cat No. 1060) at 20 MOI as control. Furthermore, we infected NRVMs with shRNA TRPC6 with eGFP tag (shRNA-TRPC6-eGFP, Cat No. shADV-226,546) at 100 MOI to silence native TRPC6 expression. The virus was removed 24 h after infection. Infected and washed cells were maintained and cultured for an additional 24–48 h in a humidity and CO_2-controlled incubator at 37°C. All viral vectors were produced by Vector Biolabs (Malvern, PA, USA) with a backbone of type 5 (dE1/E3). All eGFP tags were under a CMV promoter.

Western Blotting

Cultured cells were lysed in RIPA buffer. Protein concentration in each sample was determined using Pierce BCA protein assay kit (23227, ThermoFisher). RIPA buffer, 2-Mercaptoethanol (BME), and 6x gel loading dye were added to the protein lysate to create gel ready samples at 1 μg/μl. Samples were heated at 70°C for 10 min to reduce protein. Protein was loaded on an 8% Bis-Tris Plus Gel (NW00082, Thermo Fisher) and electrophoresed in MOPS running buffer (B001, Invitrogen) at 200 V for 35 min. Protein was transferred onto 0.45 μm nitrocellulose membrane in Tris-Glycine-Methanol buffer at 250 mA for 1 h. The transferred blot was blocked in 5% (w/v) non-fat milk in Tris-Buffered Saline with Tween 20 (TBS-T) for 60–90 min at room temperature. Blots were incubated with primary anti-TRPC6 (LS-C19628) or anti-eGFP (AB6556) antibodies in blocking solution @1:1000 dilution and left overnight at 4°C. After washing in TBS-T, goat anti-rabbit secondary antibody was applied at 1:50 k in TBS-T, while Precision Protein StrepTactin-HRP (1610380, BioRad) was applied at 1:100 k to stain for the molecular weight ladder. Blots were incubated in WesternBright ECL HRP substrate kit (K012045, Advansta, San Jose, CA, USA) for 2 min and imaged on Bio-Rad Image (Bio-Rad).

Immunolabeling of NRVMs

Coverslip plated NRVMs were fixed with 1% paraformaldehyde (PFA) for 15 min at room temperature and then washed in phosphate-buffered saline (PBS) and stored at 4°C for immunolabeling. NRVMs were permeabilized with 0.3% Triton X-100 (VWR International, Radnor, PA, USA) for 18 min and bathed in image-iT Fx Signal Enhancer (I36933, Thermo Fisher) for 30 min. Cells were blocked in 10% normal donkey serum (D9663, Millipore, Billerica, MA, USA) for 60 min at room temperature. Primary antibody for TRPC6 (LS-C19628, LifeSpan BioSciences, Seattle, WA, USA) was incubated overnight in 2% normal donkey serum incubation solution at 4°C. The next day primary antibodies were triple-washed in PBS for 15 min. Secondary antibodies were applied for 60 min at room temperature. For confocal microscopy, the secondary antibody used was a donkey anti-rabbit conjugated to Alexa Fluor 647 (A31573, Thermo Fisher). Non-specific secondary labeling was controlled by similarly labeling NRVMs while omitting primary antibody. Cells were then incubated with DAPI (D3571, Thermo Fisher) for 15 min to stain the nuclei and rinsed in PBS to be held at 4°C for imaging. For super-resolution microscopy, an anti-GFP nanobody conjugated to Alexa Fluor 647 was applied (gb2AF647, Chromotek, Planegg-Martinsried, Germany).

Confocal Microscopy, Image Acquisition, and Image Processing

Fixed and labeled NRVM coverslips were placed in PBS and imaged using a Leica SP8 confocal microscope (Leica Microsystems, Wetzlar, Germany). Two dimensional images were acquired using a GaAsP-HyD detector and a 40x oil immersion lens (numerical aperture 1.2) with a 0.1 × 0.1 μm pixel size. DAPI was excited with a 405 nm laser and emission collected at 410–550 nm. Fluorescence of eGFP was excited with a 488 nm laser and emission collected at 491–610 nm. Alexa Fluor 647 conjugated antibody was excited with a 633 nm laser and emission collected at 638–775 nm. All samples were imaged with identical imaging parameters. We used sequential framing to avoid simultaneous excitation of fluorophores and minimize cross-talk. Images were processed for noise reduction and background correction, then visualized with the same intensity ranges for comparison.

Super-resolution Microscopy

Three-dimensional single-molecule localization microscopy was performed using a Vutara 352 (Bruker Corporation, Middleton, WI). Fixed and labeled TRPC6-eGFP NRVM coverslips were immersed in a blinking solution containing 20 mM MEA, 1% (v/v) 2-Mercaptoethanol, and an oxygen scavenging system (glucose oxidase and catalase) in a buffer of 50 mM Tris, 10 mM NaCl, and 10% (w/v) glucose. We applied a 640 nm excitation laser and 405 nm activation laser. A 60x water immersion lens (numerical aperture: 1.2) was used to collect 10,000 images with 20 ms exposure. We acquired image stacks with a size of approximately 18 μm × 18 μm × 2 μm. Localizations with less than median photon count and greater than median radial precision were filtered out.

Measurement of $[Ca^{2+}]_i$ in NRVMs

$[Ca^{2+}]_i$ in infected NRVMs 48–72 h post-infection was measured using the ratiometric Ca^{2+} fluorescent dye indo-1 (I1203, Thermo Fisher). We applied an X-Light V2 spinning disk equipped with a Photometrics Prime 95B camera and an OptoSplit III LS (NCI Micro, Brooklyn Park, MN, USA). The spinning disk setup was built on a Zeiss confocal microscope (Carl Zeiss, Jena, Germany) equipped with a 40x oil lens and controlled with MetaMorph software (Molecular Devices, San Jose, CA, USA). We used a 365 ± 5 nm UV laser (ENTCII-653, Coherent, Santa Clara, CA, USA) for excitation of indo-1. Excitation and emission signals were split by a 387 nm long pass dichroic mirror (Chroma, Bellows Falls, VT, USA). Dual-wavelength emissions for the bound and unbound dye were split using a 440 nm dichroic mirror before band pass filtering (405 ± 15 and 485 ± 12.5 nm, respectively).

Cells were loaded with 20 μM indo-1 for 30 min at 37°C, then washed for 15–30 min before imaging. The cells were superfused with Tyrode solution (in mM: 126 NaCl, 4.4 KCl, 1 $MgCl_2$, 24 HEPES, 11 D-Glucose, 12.5 NaOH, 1 $CaCl_2$ and 0.7 probenecid) at room temperature (22 ± 1°C). We electrically paced the cells at 0.5 Hz until steady state was achieved. The image acquisition began with 10 s of 0.5 Hz pacing, followed by 10 s of 1 Hz pacing. We rapidly applied 20 mM caffeine to cause SR Ca^{2+} release after 10 s of 1 Hz pacing.

We obtained sequences of images at a rate of 50 Hz and with a pixel width and height of 0.278 µm. Images comprised dual-wavelength emissions for $F_{405,\text{camera}}$ and $F_{485,\text{camera}}$. The signals were registered for image processing and data extraction. Images from the camera $F_{405,\text{camera}}$ and $F_{485,\text{camera}}$ were corrected by subtraction of the camera background $F_{405,\text{bg}}$ and $F_{485,\text{bg}}$, respectively. We also corrected for cell autofluorescence and eGFP bleed-through for the two wavelength ranges, $F_{405,\text{cell}}$ and $F_{485,\text{cell}}$. We measured autofluorescence and eGFP bleed-through in NRVMs for all groups in the absence of indo-1. The corrected F_{405} and F_{485} images were calculated by:

$$F_{405} = F_{405,\text{camera}} - F_{405,bg} - F_{405,\text{cell}}$$

$$F_{485} = F_{485,\text{camera}} - F_{485,bg} - F_{485,\text{cell}}$$

Using our camera settings, $F_{405,bg}$ and $F_{485,bg}$ were 99.

Regions in the imaged cells were manually cropped to create a mask for calculation of F_{405} and F_{485} (**Supplementary Figure S1**). The ratio of signal from indo-1 with bound and unbound Ca^{2+} was determined:

$$F = \frac{F_{405}}{F_{485}}$$

Transients of $[Ca^{2+}]_i$ were calculated from F. We fit a first-order exponential function to measure the decay rate constant (T_{Decay}) of $[Ca^{2+}]_i$ transients under each pacing rate. SR load was determined by measuring the amplitude of the caffeine-induced peak (**Supplementary Figure S2**). Cells with multiple or delayed caffeine peaks were excluded from the analysis.

Calibration of $[Ca^{2+}]_i$ Measurements

NRVMs from the eGFP, TRPC6-eGFP, and shRNA-TRPC6-eGFP groups were loaded with indo-1 as described in Section "Measurement of $[Ca^{2+}]_i$ in Neonatal Rat Ventricular Myocytes." Cells were bathed in a 0 mM Ca^{2+} solution containing (in mM): 126 NaCl, 4.4 KCL, 1 $MgCl_2$, 11 D-Glucose, 24 HEPES, 12.9 NaOH, 10 EGTA, 0.7 probenecid, and 0.01 ionomycin (407,952, EDM MilliPore) for 15 min at 37°C and then rinsed in the same solution without ionomycin. Cells were imaged as described in Section "Measurement of $[Ca^{2+}]_i$ in Neonatal Rat Ventricular Myocytes," while in 0 mM Ca^{2+} solution containing 5 µM ionomycin and 40 mM 2,3-butanedione 2-monoxime (BDM) for 2–3 min before rapidly switching to a Tyrode solution containing 2 mM Ca^{2+} and 40 mM BDM. F at 0 and 2 mM Ca^{2+} determined $F_{\min}$ and $F_{\max}$, respectively, in the calibration equation (Grynkiewicz et al., 1985):

$$\left[Ca^{2+}\right]_i = K_d \frac{F - F_{\min}}{F_{\max} - F} \frac{S_{f2}}{S_{b2}}$$

Here, K_d is the equilibrium dissociation constant for Ca^{2+}, set to 250 nM based on literature (Grynkiewicz et al., 1985; Ikenouchi et al., 1991). S_{f2} and S_{b2} represent F_{485} during 0 and 2 mM Ca^{2+}, respectively. Traces for calibration were extracted with the same methods as for $[Ca^{2+}]_i$ measurements in paced cells.

Modeling of Sarcolemmal Ca^{2+} Leak in NRVMs

We used a mathematical model of NRVM electrophysiology for qualitative comparison to our experimental results (Korhonen et al., 2009). Current through TRPC6 channels (I_{TRPC6}) was modeled as an additional sarcolemmal leak Ca^{2+} current:

$$I_{\text{TRPC6}} = G_{\text{TRPC6}}\left(V_m - E_{\text{Ca}}\right)$$

where G_{TRPC6} is the Ca^{2+} conductance for TRPC6 channels in the sarcolemma, V_m is the membrane voltage and E_{Ca} is the Ca^{2+} Nernst voltage. E_{Ca} was determined by:

$$E_{Ca} = \frac{RT}{2F} ln \frac{\left[Ca^{2+}\right]_o}{\left[Ca^{2+}\right]_{\text{subSL}}}$$

with the gas constant R, temperature T, Faraday constant F, extracellular Ca^{2+} concentration $[Ca^{2+}]_o$ and subsarcolemmal Ca^{2+} concentration $[Ca^{2+}]_{\text{subSL}}$.

In our simulations with the revised model, we varied G_{TRPC6} to simulate increased TRPC6 expression. For pacing, i.e., triggering of action potentials, we applied intracellular current of −80 pA/pF for a duration of 0.5 ms at 0.5 Hz or 1 Hz for 1 min. $[Ca^{2+}]_i$ transients from the final beat were analyzed. T_{Decay} was calculated by fitting an exponential function to the decay phase of the transient. Application of caffeine was simulated 5 s following cessation of 1 Hz pacing. The effect of caffeine was modeled as previously described (Korhonen et al., 2009) by setting RyR Ca^{2+} flux to a large constant value and SERCA Ca^{2+} uptake to 0 µM/ms.

We also used the model to explore effects beyond those measured in our experiments. Ca^{2+} fluxes through other ion channels, exchanges, and pumps were calculated to evaluate how their contributions change of Ca^{2+} dynamics in response to changes in G_{TRPC6}. Currents (I_{channel}) through sarcolemmal Ca^{2+} channels and exchangers were converted to Ca^{2+} fluxes (J_{channel}):

$$J_{\text{channel}} = I_{\text{channel}} \frac{A_{\text{cap}} C_m}{2F \times 10^{-6} \mu\text{l/pl}}$$

where A_{cap} is the capacitive membrane area (1.38544×10^{-5} cm^2), C_m is the specific membrane capacitance (1 $\mu F/cm^2$), and F is Faradays constant of 96.5 C/mmol. The units of the resultant fluxes are µM/s, where the concentration is defined per cytosol volume. Fluxes through RyR and SERCA channels were converted to account for this definition. We integrated each flux over 2 and 1 s for 0.5 and 1 Hz pacing, respectively, to determine its effect on $[Ca^{2+}]_i$.

Statistical Analyses

Data are presented as mean ± standard error. Data analysis was performed in MATLAB version R2019a or higher (Mathworks Inc., Natick, MA, USA). Differences in experimental data were assessed using the t-test and considered significant for p less than 0.05.

RESULTS

Validation of Adenoviral Infection and Antibodies

We confirmed adenoviral infection and expression of eGFP, TRPC6-eGFP, and shRNA-TRPC6-eGFP constructs in live NRVMs using confocal microscopy (**Figures 1A–C**). Expression of TRPC6-eGFP concentrated along the sarcolemma and was also visible near the nucleus (**Figure 1B**, $n_{images} = 10$, $n_{cells} = 25$). Fluorescence in eGFP ($n_{images} = 5$, $n_{cells} = 20$) and shRNA-TRPC6-eGFP ($n_{images} = 3$, $n_{cells} = 10$) infected cells was present in the entire myocyte (**Figures 1A,C**). Western blotting with anti-eGFP antibody showed bands at ~30 kDa for eGFP and shRNA-TRPC6-eGFP infected cells (**Figure 1D**). Western blots of TRPC6-eGFP cells showed a band at ~135 kDa (**Figure 1E**), which was not present for eGFP or shRNA-TRPC6-eGFP cells (**Figure 1D**), even at higher exposure (**Supplementary Figure S3**). Probing NRVMs with anti-TRPC6 antibody LS-C19628 showed bands at ~135 kDa only for the TRPC-eGFP group (**Supplementary Figure S4**, $n_{litters} = 3$), similar to the anti-eGFP western blot (**Figure 1E**).

Localization of TRPC6 in NRVMs

We next studied fixed NRVMs from the experimental groups labeled with anti-TRPC6 antibody and DAPI. In the eGFP group ($n_{cells} = 40$, $n_{images} = 11$, $n_{litters} = 5$), eGFP signal exhibited a diffuse, in part sarcomeric pattern, and also localized to the nuclear membrane and nucleus (**Figure 2A**). Native TRC6 labeling with LS-C19628 yielded marginal signal (**Figure 2B**). DAPI labeling marked the nucleus of myocytes (**Figure 2C**). An overlay of the images from NRVMs expressing eGFP is shown in **Figure 2D**. In NRVM expressing TRPC6-eGFP ($n_{cells} = 40$, $n_{images} = 18$, $n_{litters} = 5$), the TRPC6-eGFP signal

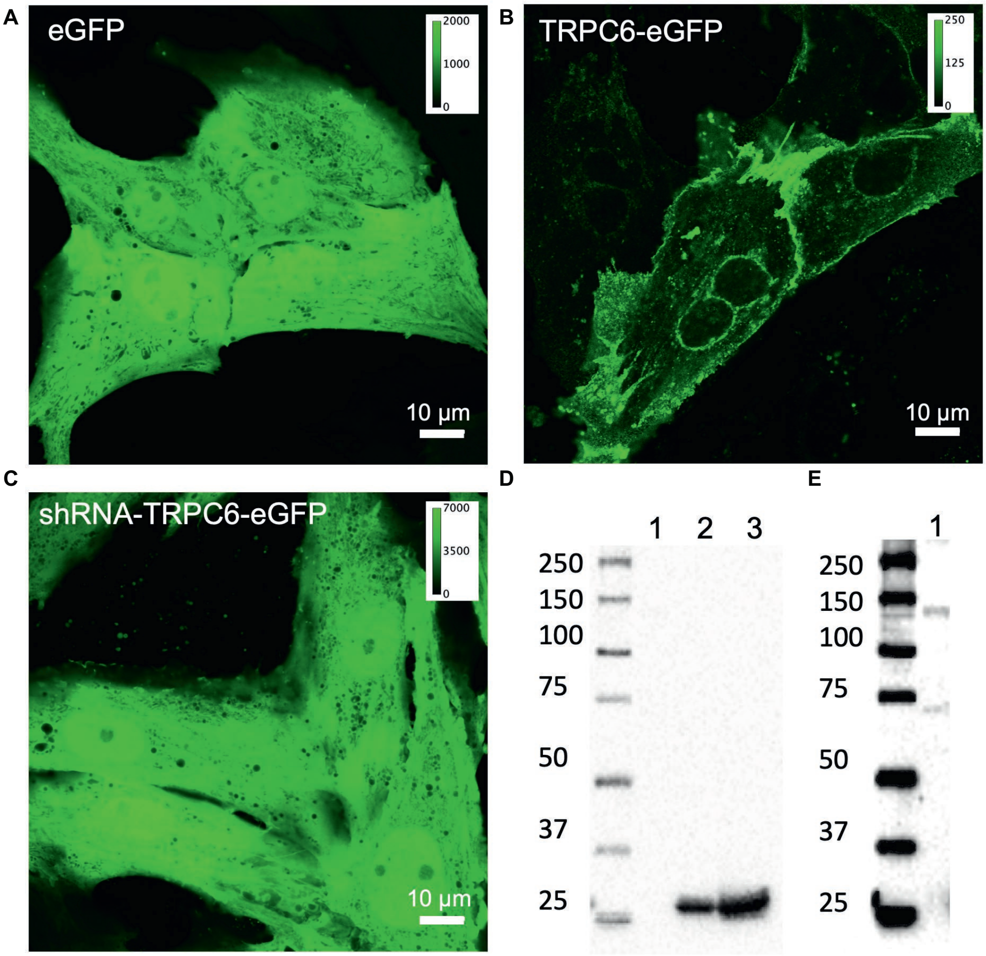

FIGURE 1 | Confocal microscopic images of living NRVMs infected with **(A)** eGFP at 20 MOI, **(B)** TRPC6-eGFP at 10 MOI, and **(C)** shRNA-TRPC6-eGFP at 100 MOI. eGFP and shRNA-TRPC6-eGFP infected cells exhibit a diffuse cytosolic signal. In TRPC6-eGFP cells, signal is localized to sarcolemma and nuclear membrane. Colormap for each signal is added for comparison of fluorescence intensities between groups. **(D)** Western blotting with anti-eGFP antibody (AB6556) of NRVMs expressing TRPC6-eGFP (lane 1), eGFP (lane 2), and shRNA-TRPC6-eGFP (lane 3). Expression of eGFP at ~30 kDa band was detected in eGFP and shRNA-TRPC6-eGFP cells. **(E)** Longer exposure of lane 1 confirms TRPC6-eGFP expression at the expected 135 kDa molecular weight of the construct.

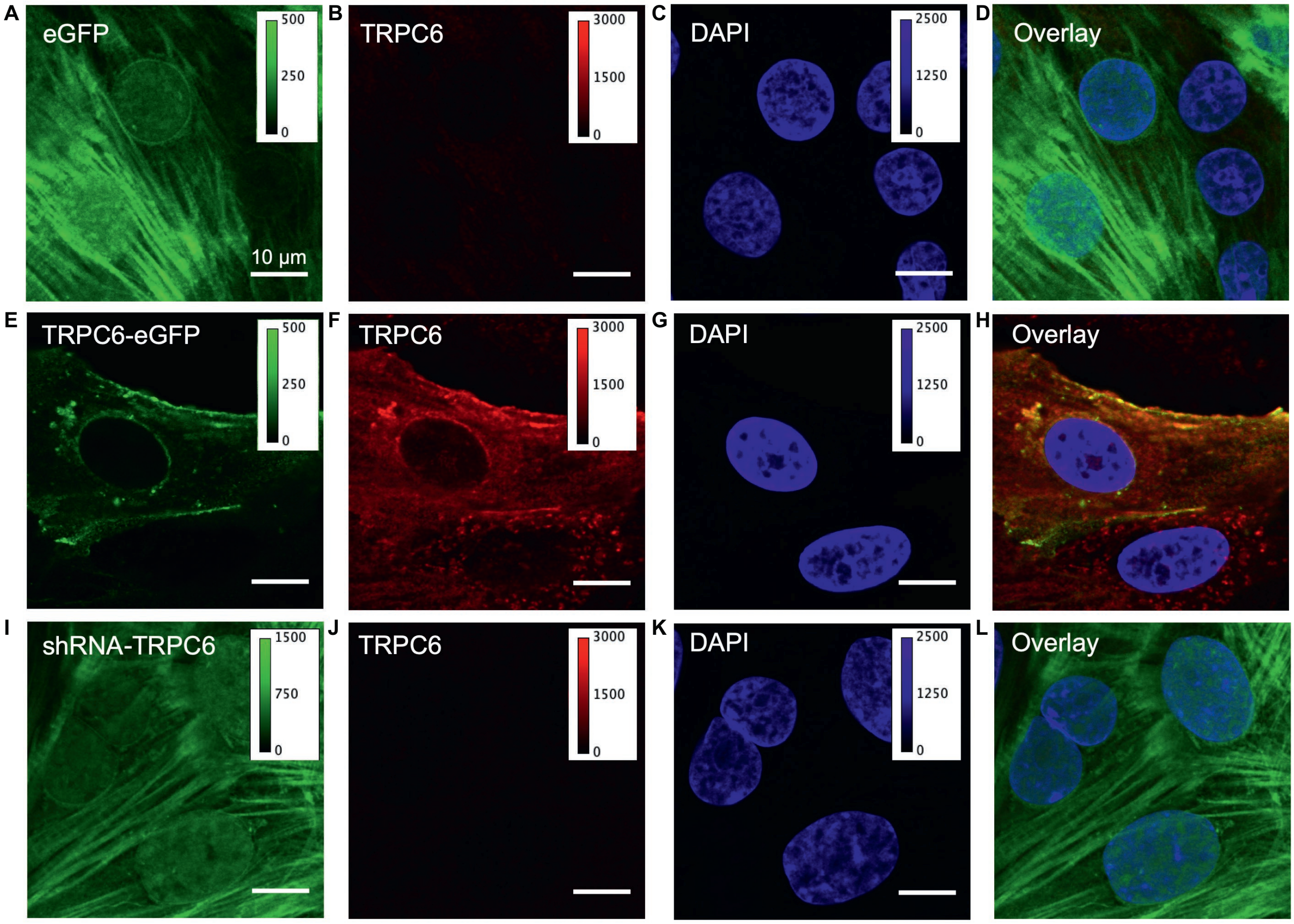

FIGURE 2 | Confocal microscopic images of fixed infected NRVMs. **(A)** NRVM infected with eGFP at 20 MOI present an intracellular eGFP distribution. **(B)** TRPC6 labeling with LS-C19628 antibody shows marginal signal. **(C)** DAPI used as a marker for the nucleus. **(D)** Overlay of **(A–C)**. **(E)** NRVMs infected with TRPC6-eGFP at 10 MOI present signal at the sarcolemma. **(F)** TRPC6 labeling shows high fluorescence signal at the sarcolemma and nuclear membrane. **(G)** DAPI as marker for the nucleus. **(H)** Overlay of **(E–G)** shows high colocalization of TRPC6-eGFP and anti-TRPC6 antibody labeling, suggesting successful detection of our vector by the antibody. **(I)** NRVM infected with shRNA-TRPC6-eGFP at 100 MOI present diffuse, very bright intracellular eGFP signal. **(J)** TRPC6 labeling shows marginal fluorescence. **(K)** DAPI as a marker for the nucleus. **(L)** Overlay of **(I–K)**. Imaging of eGFP, TRPC6, and DAPI in the three experimental groups was done with identical settings. Colormap for each signal is added for comparison of fluorescence intensities between groups. TRPC6 labeling had much higher fluorescence in TRPC6-eGFP than eGFP and shRNA-TRPC6-eGFP cells. Scale bar in **(A)** applies to **(B–L)**.

was associated with the sarcolemma and nuclear membrane as well as near the nucleus (**Figure 2E**). Anti-TRPC6 antibody signal was in the sarcolemma and irregularly distributed throughout the cell (**Figure 2F**). DAPI labeled the nuclei (**Figure 2G**). Overlay of TRPC6-eGFP and anti-TRPC6 images showed strong overlap of fluorescence in yellow (**Figure 2H**). In NRVMs expressing shRNA-TRPC6-eGFP ($n_{\text{cells}} = 50$, $n_{\text{images}} = 5$, $n_{\text{litters}} = 2$), eGFP signal was similar to signal in eGFP infected cells (**Figure 2I**). Labeling with anti-TRPC6 antibody yielded marginal signals (**Figure 2J**). DAPI marked the nuclei (**Figure 2K**). Overlay images were similar as in the eGFP group (**Figure 2L**). Brightness-adjusted images corresponding to **Figures 2B,F,J** are presented in **Supplementary Figures S5A–C**, respectively. Quantification of anti-TRPC6 antibody signal in these images is consistent with the visual impression that TRPC6-eGFP infection leads to a strong increase vs. eGFP infection (**Supplementary Figure S5D**). Marginal anti-TRPC6 antibody signal from eGFP infected NRVMs was further reduced in shRNA-TRPC6-eGFP infected NRVMs. Secondary antibody-only control showed negligible labeling in eGFP and TRPC6-eGFP NRVMs (**Supplementary Figure S6**).

We performed super-resolution microscopy using an anti-eGFP nanobody to further assess location of TRPC6-eGFP. An example image is shown in **Figure 3**. The images supported sarcolemmal localization of the TRPC6-eGFP construct.

Calibration of Indo-1

We assessed 30 regions in four images from eGFP, TRPC6-eGFP, and shRNA-TRPC6-eGFP infected cells without dye under indo-1 settings. $F_{405,\text{cell}}$ signal ranged from 3.3 to 3.7 ± 0.2 for all groups. $F_{485,\text{cell}}$ was 12.2 ± 0.2, 12.5 ± 0.2, and 20.8 ± 0.5 for eGFP, TRPC6-eGFP, and shRNA-TRPC6-eGFP cells.

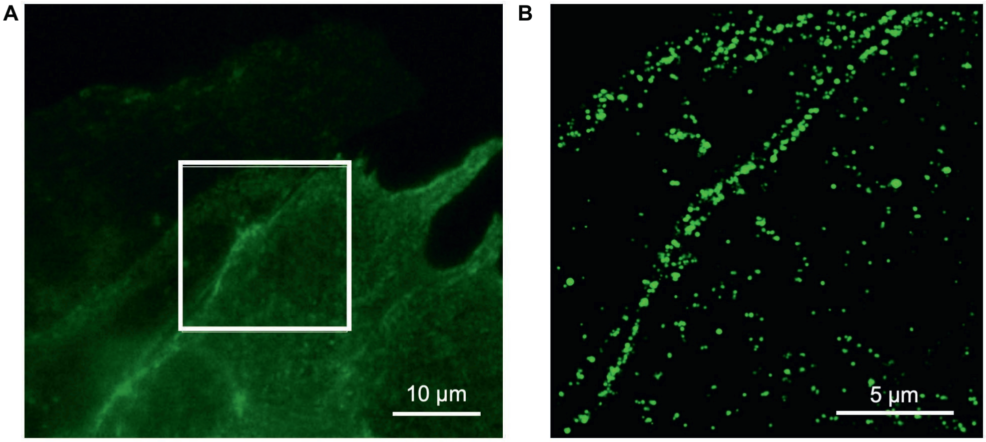

FIGURE 3 | Super-resolution microscopy of fixed NRVM infected with TRPC6-eGFP at 10 MOI and labeled with anti-eGFP nanobody. **(A)** Wide-field reference image of eGFP signal. **(B)** Super-resolution image of TRPC6-eGFP signal from box in **(A)**. The TRPC6-eGFP pattern suggests sarcolemmal localization.

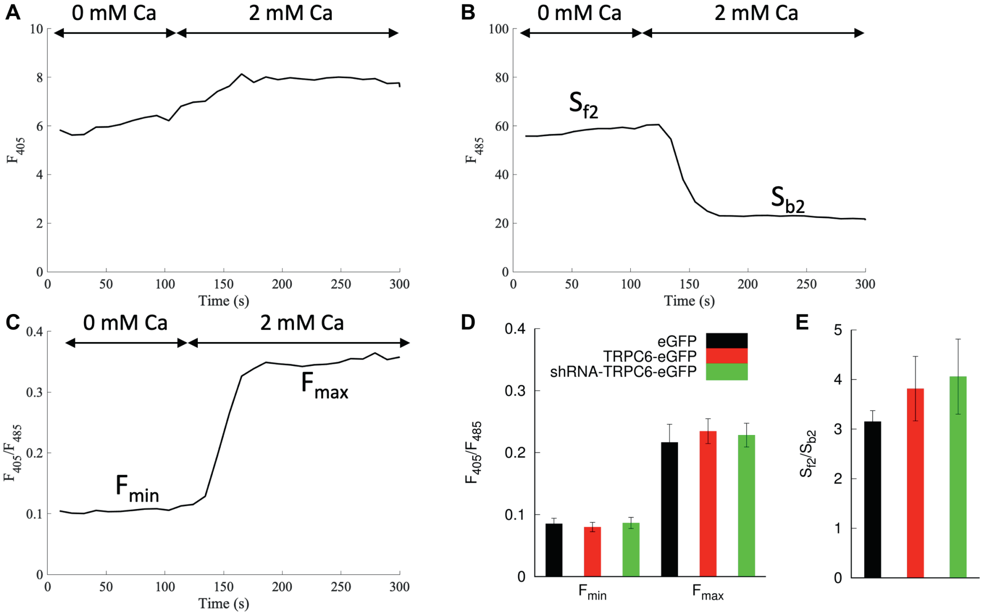

FIGURE 4 | Indo-1 calibration protocol in NRVMs bathed in 10 μM ionomycin. Example trace shows **(A)** F_{405}, **(B)** F_{485}, and **(C)** F_{405}/F_{485} during application of a bath solution with 0 and 2 mM Ca^{2+}. **(D)** F_{min} and F_{max} were calculated from F_{405}/F_{485} for 0 and 2 mM Ca^{2+} application, respectively. F_{min} and F_{max} for all groups were not significantly different. **(E)** Average S_{f2}/S_{b2} was calculated as the ratio from the F_{485} emission during the 0 Ca^{2+} and 2 mM Ca^{2+}. S_{f2}/S_{b2} in all groups was not significantly different.

We applied infected NRVMs loaded with indo-1 for calibration of $[Ca^{2+}]_i$ measurements. We applied ionomycin to measure indo-1 signals in NRVMs bathed in low and high calcium (**Figure 4**). Example traces of F_{405}, F_{485}, and F_{405}/F_{485} are presented in **Figures 4A–C**, respectively. F_{min} for eGFP, TRPC6-eGFP, and shRNA-TRPC6-eGFP was 0.085 ± 0.009 ($n_{cells} = 7$), 0.08 ± 0.008 ($n_{cells} = 8$), and 0.087 ± 0.009 ($n_{cells} = 5$), respectively (**Figure 4D**). F_{max} for eGFP, TRPC6-eGFP, and shRNA-TRPC6-eGFP was 0.22 ± 0.03, 0.24 ± 0.02, and 0.23 ± 0.02, respectively (**Figure 4D**). S_{f2}/S_{b2} measured from the F_{485} signal was 3.2 ± 0.2, 3.8 ± 0.7, and 4.1 ± 0.8 for the eGFP, TRPC6-eGFP, and shRNA-TRPC6-eGFP, respectively (**Figure 4E**). Since we did not find significant differences in any of the measurements between the three groups, we averaged measures of cells from all the groups and calculated F_{min}, F_{max}, and S_{f2}/S_{b2} to 0.084, 0.227, and 3.645, respectively.

Measurements of $[Ca^{2+}]_i$ in NRVMs

We measured F_{405}/F_{485} in NRVMs expressing eGFP ($n_{cells} = 19$, $n_{litters} = 6$), TRPC6-eGFP ($n_{cells} = 19$, $n_{litters} = 5$), and shRNA-TRPC6-eGFP ($n_{\text{cells}} = 16$, $n_{\text{litters}} = 4$). We present examples of F_{405}/F_{485} transients from NRVMs expressing eGFP and TRPC6-eGFP under 0.5 Hz (**Supplementary Figure S7A**) and 1 Hz (**Supplementary Figure S7B**). Diastolic F_{405}/F_{485} increased from 0.097 ± 0.004 in eGFP to 0.113 ± 0.005 in TRPC6-eGFP ($p = 0.03$) at 0.5 Hz, and from 0.105 ± 0.004 to 0.12 ± 0.005 at 1 Hz ($p = 0.02$) (**Supplementary Figure S7C**). Systolic F_{405}/F_{485} of TRPC6-eGFP cells increased to 0.144 ± 0.005 compared to eGFP 0.124 ± 0.005 ($p = 0.004$) at both 0.5 Hz and 1 Hz (**Supplementary Figure S7D**). The amplitude of $[Ca^{2+}]_i$ transient was not significantly different between eGFP and TRPC6-eGFP cells paced at 0.5 Hz (0.026 ± 0.003 vs. 0.031 ± 0.005, $p = 0.36$) or 1 Hz (0.019 ± 0.003 vs. 0.024 ± 0.004, $p = 0.35$). Also, SR load was not different before calibration (**Supplementary Figure S7E**).

We applied the calibration to the measured $F_{405}/F_{485.}$ NRVMs expressing TRPC6-eGFP cells exhibited a positive shift in cytosolic $[Ca^{2+}]_i$ transients compared to eGFP cells at both 0.5 and 1 Hz pacing rates (**Figures 5A,B**). Diastolic $[Ca^{2+}]_i$ levels increased in TRPC6-eGFP compared to eGFP cells at 0.5 Hz (278 ± 56 vs. 119 ± 34 nM, $p = 0.02$) and 1 Hz (375 ± 65 vs. 184 ± 43 nM, $p = 0.02$) (**Figure 5C**). Systolic $[Ca^{2+}]_i$ also increased in TRPC6-eGFP vs. eGFP cells at both 0.5 Hz (769 ± 106 vs. 430 ± 101 nM vs., $p = 0.03$) and 1 Hz (774 ± 103 vs. 420 ± 87 nM, $p = 0.01$) (**Figure 5D**). The amplitude of $[Ca^{2+}]_i$ transients was not significantly different between eGFP and TRPC6-eGFP at 0.5 or 1 Hz (data not shown). T_{Decay} was larger for eGFP than TRPC6-eGFP cells at 0.5 Hz (0.42 ± 0.02 vs. 0.35 ± 0.02 s^{-1}, $p = 0.02$), but not at 1 Hz (0.22 ± 0.03 vs. 0.24 ± 0.02 s^{-1}, $p = 0.5$) (**Figure 5E**). Furthermore, the SR Ca^{2+} load increased from 279 ± 44 nM in eGFP to 551 ± 121 nM in TRPC6-eGFP ($n_{\text{cells}} = 11$, $n_{\text{litters}} = 4–5$, $p = 0.048$) (**Figure 5F**).

NRVMs infected with shRNA-TRPC6-eGFP showed similar features as eGFP infected cells (**Supplementary Figure S8**) and differences were not significant. Diastolic F_{405}/F_{485} in shRNA-TRPC6 was 0.09 ± 0.004 ($p = 0.3$) and 0.104 ± 0.005 ($p = 0.89$) for 0.5 and 1 Hz, respectively (**Supplementary Figure S8A**). Systolic F_{405}/F_{485} was 0.125 ± 0.006 ($p = 0.82$) and 0.127 ± 0.006 ($p = 0.66$) at 0.5 and 1 Hz, respectively (**Supplementary Figure S8B**). Calibrated diastolic $[Ca^{2+}]_i$ for shRNA-TRPC6-eGFP was 76.5 ± 31.8 ($p = 0.37$) and 176.6 ± 48.1 ($p = 0.92$) for 0.5 and 1 Hz pacing, respectively (**Supplementary Figure S8C**). Systolic $[Ca^{2+}]_i$ was 447.9 ± 85.2 ($p = 0.9$) and 502.3 ± 107.8 ($p = 0.55$) for 0.5 and 1 Hz pacing, respectively (**Supplementary Figure S8D**). T_{Decay} was

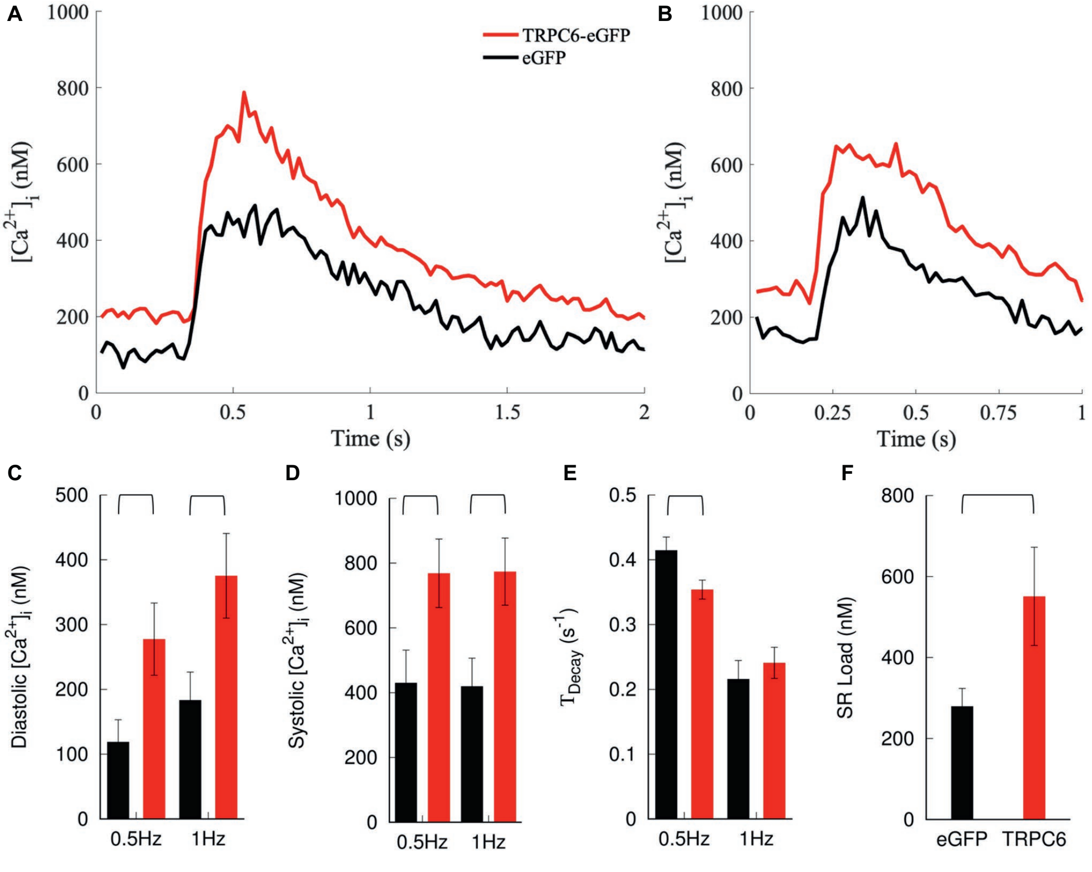

FIGURE 5 | Measurement and analysis of $[Ca^{2+}]_i$. Example traces for NRVMs expressing eGFP or TRPC6-eGFP and paced at **(A)** 0.5 and **(B)** 1 Hz. Expression of TRPC6-eGFP caused a positive shift in $[Ca^{2+}]_i$ transients vs. eGFP at both pacing rates. **(C)** Diastolic and **(D)** systolic $[Ca^{2+}]_i$ increased in TRPC6-eGFP vs. eGFP cells for both pacing rates. **(E)** T_{Decay} decreased in TRPC6-eGFP vs. eGFP cells for 0.5 Hz pacing. **(F)** SR load increased in NRVMs expressing TRPC6-eGFP vs. eGFP.

not significantly different at 0.5 Hz (0.43 ± 0.04, $p = 0.7$) or 1 Hz (0.2 ± 0.02, $p = 0.6$) vs. eGFP.

Modeling of Sarcolemmal Ca^{2+} Leak in NRVMs

We applied a mathematical model of NRVM electrophysiology to qualitatively reproduce findings of our experimental investigations. Increased TRPC6 expression was simulated by increasing G_{TRPC6} from 0 to 3 or 6 μS/μF. Increased G_{TRPC6} raised $[Ca^{2+}]_i$ during both diastole and systole (**Figures 6A–D**). For 0.5 Hz pacing, diastolic $[Ca^{2+}]_i$ was 159, 180, and 205 nM for G_{TRPC6} of 0, 3, and 6 μS/μF, respectively. Diastolic $[Ca^{2+}]_i$ increased for pacing with 1 Hz to 225, 245, and 267 nM for G_{TRPC6} of 0, 3, and 6 μS/μF, respectively (**Figure 6C**). Systolic $[Ca^{2+}]_i$ was 670, 707, and 754 nM for 0.5 Hz pacing and 740, 775, and 817 nM for 1 Hz pacing (**Figure 6D**) with G_{TRPC6} of 0, 3, and 6 μS/μF, respectively. The amplitude of $[Ca^{2+}]_i$ was 512, 528, and 550 nM for 0.5 Hz pacing, and 516, 530, and 550 nM for 1 Hz pacing. For both pacing rates, T_{Decay} decreased with increasing G_{TRPC6} (**Figure 6E**). T_{Decay} for 0.5 Hz pacing was 0.327, 0.319, and 0.307 s^{-1} for G_{TRPC6} of 0, 3, and 6 μS/μF, respectively. T_{Decay} for 1 Hz pacing was 0.227, 0.219, and 0.207 s^{-1} for G_{TRPC6} of 0, 3, and 6 μS/μF, respectively. The amplitude of $[Ca^{2+}]_i$ following simulation of caffeine application after 1 Hz pacing increased with increased G_{TRPC}, with 947, 1,052, and 1,222 nM for G_{TRPC6} of 0, 3, and 6 μS/μF, respectively (**Figure 6F**).

We used the model to predict effects of increased TRPC6 activity not explored in our experiments (**Supplementary Figures S9, S10**). Increased G_{TRPC6} resulted in an elevated resting V_m (**Supplementary Figure S9A**). For 0.5 Hz pacing, resting V_m was −69.95, −68.05, and − 66.03 mV for G_{TRPC6} of 0, 3, and 6 μS/μF, respectively. V_m for 1 Hz was −69.45, −67.91, and − 66.28 mV for G_{TRPC6} of 0, 3, and 6 μS/μF, respectively (**Supplementary Figure S9E**). Other major ion currents were assessed by calculating the integrated Ca^{2+} flux during a single beat. Integrated flux of Ca^{2+} through TRPC6 during 0.5 Hz was 7.4 and 14.6 μM for G_{TRPC6} of 3 and 6 μS/μF, respectively. Integrated Ca^{2+} through TRPC6 during 1 Hz was 3.4 and 6.8 μM (**Supplementary Figures S9B,F**). Integrated Ca^{2+} flux through L-type calcium channels (LCCs) was 30.2, 28.6, and 27.4 μM at 0.5 Hz and 24.4, 23.5, and 22.6 μM at 1 Hz (**Supplementary Figures S9C,G**). For 0.5 Hz pacing, integrated Ca^{2+} flux through NCX was 54.3, 60.5, and 66.9 μM for G_{TRPC6} of 0, 3, and 6 μS/μF, respectively. For 1 Hz pacing, the integrated flux of Ca^{2+} out of the cell through NCX was 35.6, 38.2, and 40.9 μM for G_{TRPC6} of 0, 3, and 6 μS/μF, respectively (**Supplementary Figures S9D,H**). The integrated Ca^{2+} release into the cytosol from the SR through RyRs was 8.5, 9.7, and 11.2 μM at 0.5 Hz and 7.5, 8.1, and

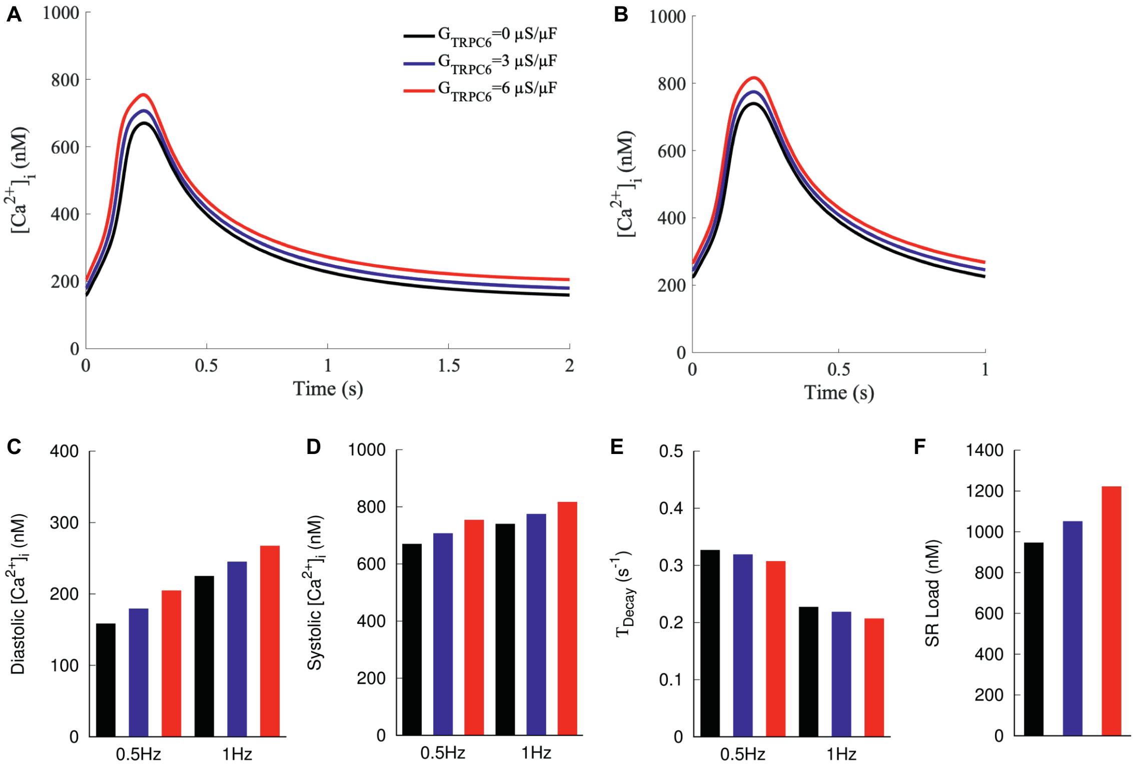

FIGURE 6 | Computer model of NRVM with currents through TRPC6 channels modeled as sarcolemmal leak with G_{TRPC6} at 0, 3, and 6 μS/μF. $[Ca^{2+}]_i$ at **(A)** 0.5 and **(B)** 1 Hz pacing. Increased G_{TRPC6} caused a positive shift in $[Ca^{2+}]_i$ transients at both 0.5 and 1 Hz pacing. **(C)** Diastolic and **(D)** systolic $[Ca^{2+}]_i$ at 0.5 and 1 Hz increased for increased G_{TRPC6}. **(E)** T_{Decay} decreased with increased G_{TRPC6}. **(F)** SR load increased with increasing G_{TRPC6}.

8.8 μM at 1 Hz, for G_{TRPC6} of 0, 3, and 6 μS/μF, respectively (**Supplementary Figures S10A,C**). The integrated Ca^{2+} pumped back into the SR through SERCA was 8.7, 9.9, and 11.4 μM at 0.5 Hz and 7.6, 8.2, and 8.9 μM at 1 Hz for G_{TRPC6} of 0, 3, and 6 μS/μF, respectively (**Supplementary Figures S10B,D**).

DISCUSSION

Our study supports a role of TRPC6 in sarcolemmal Ca^{2+} signaling in cardiomyocytes. Cells infected with eGFP vector served as control, while TRPC6-eGFP infected cells overexpressed TRPC6. Our primary findings are that TRPC6-eGFP was associated with the sarcolemma and, in paced myocytes, TRPC6 expression increased $[Ca^{2+}]_i$ and SR Ca^{2+} load in a pacing rate-dependent manner. We explored shRNA-TRPC6-eGFP constructs to reduce TRPC6 expression, but our structural and functional studies suggested that TRPC6 is only marginally expressed in NRVMs.

TRPC6-eGFP Localization

Our confocal and super-resolution imaging suggested that localization of TRPC6-eGFP is predominantly at the sarcolemma (**Figures 1B, 2E, 3**). We also found TRPC6-eGFP near the nuclear envelope, likely in the endoplasmic reticulum or Golgi apparatus, suggesting that the protein is on track for translocation and sarcolemmal integration. The eGFP and shRNA-TRPC6-eGFP constructs produced eGFP signals diffuse in the cytosol, indicating successful infection with the adenoviral vector (**Figures 1A,C**).

Western blotting with anti-eGFP antibody showed differences in the molecular weight detected in our experimental groups (**Figures 1D,E**). The TRPC6-eGFP group presented a band at ~135 kDa, which is explained by the TRPC6 molecular weight of ~105 kDa plus the weight of the conjugated eGFP of ~30 kDa. A 135 kDa band was not detected for eGFP or shRNA-TRPC6-eGFP, even at higher exposure (**Supplementary Figure S3**). The eGFP control and shRNA-TRPC6-eGFP groups only showed a band at 32 kDa for eGFP proteins. Differences of intensity of the bands between the groups are related to the difference in MOI for TRPC6-eGFP (10), eGFP (20), and shRNA-TRPC6-eGFP (100).

Fixation and immunolabeling led to changes in the eGFP patterns of eGFP and shRNA-TRPC6-eGFP infected NRVMs (**Figures 2A,I**), which are likely due to permeabilization of the sarcolemma and loss of eGFP from the cytosol, only leaving eGFP immobilized due to fixation. Similarities of TRPC6-eGFP patterns in fixed (**Figure 2E**) and living (**Figure 1B**) NRVMs further supported localization of the construct to the sarcolemma. Native TRPC6 signal in NRVMs infected with eGFP (**Figure 2B**) and shRNA-TRPC6-eGFP (**Figure 2J**) was marginal when compared under the same image settings used for TRPC6-eGFP NRVMs (**Figure 2F**) and in the brightness-adjusted images (**Supplementary Figure S5**). Secondary antibody only imaging presented even smaller signals (**Supplementary Figure S6**). The comparison indicates a pronounced expression of TRPC6-eGFP in the NRVMs in the context of marginal native TRPC6 expression.

Anti-TRPC6 Antibody Labeling in Infected NRVMs

The applied anti-TRPC6 antibody (LS-C19628) was developed from a 14 amino acid synthetic peptide from amino acids 50–100 of the human TRPC6 sequence. The antibody was validated by the manufacturer for western blot and immunofluorescence in human samples as well as immunochemistry in mouse samples. Comparison of the TRPC6 protein sequence from human and rat (Genbank Accession No. NP_004612 and NP_446011, respectively) shows 93.88% homology. Weak homology was in particular within the first 60 and last 100 amino acids. Comparison of the protein sequence from mouse and rat (Genbank Accession No. NP_03886 and NP_446011, respectively) exhibited 98.17% homology, with amino acids 50–100 being conserved in both species.

Successful detection of our TRPC1-eGFP construct in western blots supports sensitivity of the antibody for human TRPC6 (**Supplementary Figure S4**). However, the antibody did not show a band at the expected molecular weight of 106 kDa for the native rat TRPC6 (**Supplementary Figure S4**). In our immunofluorescence images, the antibody presented high colocalization with eGFP in TRPC6-eGFP infected cells (**Figure 2H**). Also, we noticed a marginal immunofluorescence signal in eGFP infected cells (**Supplementary Figure S5A**) that was reduced in shRNA-TRPC6-eGFP NRVMs (**Supplementary Figures S5C,D**). These findings indicate that the antibody is not sensitive for rat TRPC6 in western blotting but detects rat TRPC6 in both, human and rat in immunofluorescence (**Supplementary Figure S5D**). We evaluated further anti-TRPC6 antibodies for western blotting and immunofluorescence (**Supplementary Table S1**). **Supplementary Figure S11** presents a western blot using an antibody (AB-105845) that is capable of detecting rat TRPC6 and TRPC6-eGFP. However, this and another tested antibody (LS-B611) that targeted the region close to c-terminus were not capable of detecting TRPC6-eGFP in immunofluorescence. Our TRPC6-eGFP construct is based on fusion of eGFP to the TRPC6 c-terminus, which might interfere with antibody binding.

$[Ca^{2+}]_i$ Calibration of Indo-1 Signals in the Presence of eGFP

Quantification of $[Ca^{2+}]_i$ from indo-1 signals required correction for camera background, autofluorescence, and eGFP bleed-through. Contribution of eGFP to $F_{485,cell}$, but not $F_{405,cell}$ signal, varied across the NRVMs depending on MOI. The difference in $F_{485,cell}$ across our experimental groups strongly affected calculation of F. TRPC6-eGFP and eGFP infection at 10 and 20 MOI yielded similar levels of bleed-through as we found in uninfected NRVMs (data not shown). In contrast, shRNA-TRPC6-eGFP infection at 100 MOI almost doubled the bleed-through, suggesting that a high eGFP expression causes a fluorescence offset beyond the offset primarily explained by autofluorescence. We suggest that our approach for correction is useful in other studies with eGFP markers at high MOIs, where changes in the F_{485} signal must be accounted for.

Calibration using ionomycin and varying extracellular Ca^{2+} allowed us to calculate $[Ca^{2+}]_i$ accounting for the non-linear ratiometric fluorescence properties of indo-1. After corrections, eGFP, TRPC6-eGFP, and shRNA-TRPC6-eGFP infected cells yielded similar F_{min}, F_{max}, and S_{f2}/S_{b2} (**Figure 4**). This indicates that our corrections were successful. Averaging measures from all cells gave a uniform parameter set for calculating $[Ca^{2+}]_i$.

Comparison of $[Ca^{2+}]_i$ Measurements With Prior Work

In our eGFP NRVMs, diastolic $[Ca^{2+}]_i$ of 119 ± 34 nM at 0.5 Hz and 183 ± 43 nM at 1 Hz are close to previously measured diastolic $[Ca^{2+}]_i$ of 140 ± 11 nM for spontaneous beating 2- to 7-day-old NRVMs (Gomez et al., 1994). In these cells, systolic $[Ca^{2+}]_i$ ranged from 323 to 480 nM, comparable to the measurement of 430 ± 100 nM in our 4- to 5-day-old NRVMs. Other studies on paced rat cardiomyocytes reported systolic $[Ca^{2+}]_i$ in the range from 319 ± 37 to 454 ± 70 nM in 18-day fetal and rise to 743 ± 64 nM in adult rat (Seki et al., 2003). Previously reported T_{Decay} at 0.5 Hz pacing ranged from 0.47 ± 0.1 s^{-1} in the 18-day fetus to 0.2 ± 0.02 s^{-1} in the adult rat, similar to our measured T_{Decay} of 0.42 ± 0.02 s^{-1} at 0.5 Hz for eGFP NRVMs. Application of caffeine in our eGFP myocytes caused a 279 ± 44 nM rise in cytosolic Ca^{2+}, which is within the range of example responses for 2- and 7-day-old NRVMs (Gomez et al., 1994).

Increased TRPC6 Expression Leads to Increased $[Ca^{2+}]_i$ and SR Load in Paced Cells

Raw and calibrated measurements indicated an increase in $[Ca^{2+}]_i$ of TRPC6-eGFP compared to eGFP cells (**Figure 5, Supplementary Figure S7**). Diastolic and systolic $[Ca^{2+}]_i$ increased, but the amplitude did not, indicating only a offset in the overall transient. We qualitatively compared experimental findings with results from mathematical modeling assuming that TRPC6 causes sarcolemmal Ca^{2+} leak. In the model, diastolic and systolic $[Ca^{2+}]_i$ increased with increasing G_{TRPC6} (**Figures 6A,B**). The amplitude of $[Ca^{2+}]_i$ also increased, but to a small degree, which could explain why our measurements were not significantly different in the experimental groups.

We observed a pacing rate-dependent increase in diastolic $[Ca^{2+}]_i$ of NRVMs, which is in agreement with previous findings in adult rat (Dibb et al., 2007; Gattoni et al., 2016). In the model, 1 Hz pacing caused a 30, 36, and 42% increase in diastolic $[Ca^{2+}]_i$ vs. 0.5 Hz pacing for G_{TRPC6} of 0, 3, and 6 μS/μF, respectively (**Figure 6C**). Systolic $[Ca^{2+}]_i$ was also higher with 1 Hz pacing (**Figure 6D**), but interestingly, the amplitude of $[Ca^{2+}]_i$ transient remained mostly unchanged for both pacing rates for all G_{TRPC6} settings. Additionally, T_{Decay} reduced with increased TRPC6 in both, experiments (**Figure 5E**) and simulations (**Figure 6E**). Also, T_{Decay} was reduced for increased pacing rate.

Caffeine reduces the Ca^{2+} threshold for activation of RyR clusters and triggers release of the SR Ca^{2+} into the cytosol. The increase of $[Ca^{2+}]_i$ is often used as a measure of SR Ca^{2+} load. SR load was increased in TRPC6-eGFP vs. eGFP NRVMs (**Figure 5F**). Simulation of caffeine application also resulted in increased for increased G_{TRPC6} (**Figure 6F**).

Overall, the simulation results aligned with experimental findings, supporting the description of TRPC6 channels as sarcolemmal Ca^{2+} leak. The simulations also helped in mechanistic explanation of the experimental findings and predicted effects of TRPC6 activity not measured in our experiments. With the model, we evaluated Ca^{2+} flux through ion channels, pumps and exchangers. Ca^{2+} flux through TRPC6 channels was small (**Supplementary Figures S9B,F**) vs. LCC and NCX fluxes (**Supplementary Figures 9C,D,G,H**) but associated with notable changes of all Ca^{2+} fluxes. As a result of increased G_{TRPC6}, LCC fluxes decreased (**Supplementary Figures S9C,G**). The integral efflux of Ca^{2+} through NCX was increased, indicating increased activity of the exchanger (**Supplementary Figures S9D,H**). Integral Ca^{2+} flux through RyR and SERCA also increased with increased G_{TRPC6} (**Supplementary Figure S10**), which explains the increase in SR load in TRPC6-eGFP vs. eGFP cells (**Figure 5F**). Increased NCX and SERCA activity for increased TRPC6 expression explain the reduced T_{Decay} in both the model and experiments (**Figures 5E,6E**). Since NCX is electrogenic, its increased activity is also likely a driver of the observed slight depolarization of V_m. With increased I_{TRPC6} leading to elevated $[Ca^{2+}]_i$, NCX extrudes more Ca^{2+} (**Supplementary Figure S9H**), exchanging each Ca^{2+} ion for three Na^+ ions and resulting in a net increase of positive charge inside the cell (**Supplementary Figure S9C**). Resting V_m was marginally increased by increased G_{TRPC6} (**Supplementary Figures S9A,E**). Thus resting V_m is closer to Na^+ channel activation threshold, so less current is required to trigger an action potential.

Contribution of TRPC6 to Mechanical Feedback Mechanisms and Hypertrophic Remodeling

Our study shows direct effects of increased TRPC6 expression on $[Ca^{2+}]_i$ transients in cardiomyocytes. It was suggested that increased diastolic $[Ca^{2+}]_i$ increases diastolic tension and lowers the extent of cell relaxation (Louch et al., 2012). Due to the strong relationship of $[Ca^{2+}]_i$ and force in cardiomyocytes, we anticipate that the TRPC6-associated increase of $[Ca^{2+}]_i$ increases contraction. Similar effects can be expected in stretched cells, since TRPC6 is thought to be activated through membrane stretch (Spassova et al., 2006). TRPC6 knockout reduced stretch-induced slow force response by abolishing the slow increase in $[Ca^{2+}]_i$ (Yamaguchi et al., 2017). Our study with increased expression of TRPC6 supports their findings that the protein contributes to effects of the Frank-Starling mechanism by transiently increasing Ca^{2+} in response to stretch, thereby increasing contraction.

Previous studies linked TRPC6 to hypertrophy and increased calcineurin-NFAT signaling (Kuwahara et al., 2006; Onohara et al., 2006; Wu et al., 2010). NFAT was proposed to be a signal integrator of cumulative $[Ca^{2+}]_i$ load (Hannanta-Anan and Chow, 2016). It is thought that the role of TRPC6 in hypertrophic remodeling is through sustained and cumulative $[Ca^{2+}]_i$ increase that is sufficient to activate the calcineurin-NFAT pathway. A positive feedback in which Ca^{2+} influx through sarcolemmal TRPC6 channels activates calcineurin-NFAT leading to upregulation of TRPC6 and increased Ca^{2+} influx was suggested (Kuwahara et al., 2006). Our studies characterized the effects of upregulation of TRPC6 expression on $[Ca^{2+}]_i$, and we explain the effects by increased Ca^{2+} influx and SR load. Reduction of TRPC6 expression and/or activity is thus promising in disrupting the positive feedback loop as possible treatment for hypertrophic remodeling. Modulation of TRPC6 activity through pharmacological blockers is an active area of research (Bon and Beech, 2013). High-affinity potent inhibitors have been reported for TRPC6 including recent discoveries for orally available inhibitors (Washburn et al., 2013; Motoyama et al., 2018; Tang et al., 2018; Lin et al., 2019).

Limitations

We note several limitations related to our studies. We did not find differences of our TRPC6 functional measures between NRVMs infected with shRNA-TRPC6-eGFP and eGFP (**Figure 2, Supplementary Figure S8**). While our immunofluorescence images suggest reduced expression of TRPC6 in shRNA-TRPC6 compared to eGFP (**Supplementary Figure S5D**), the reduction of TRPC6 expression is small. It is possible is that our shRNA-TRPC6-eGFP construct, originally designed to silence human TRPC6, is not efficiently reducing expression of TRPC6 in NRVMs. However, even a more pronounced reduction is unlikely to result in functional differences due to marginal native TRPC6 expression. Our finding of marginal TRPC6 expression is consistent with previously reported gene expression in NRVMs (dataset GSE83228), which revealed that expression of this TRPC6 gene is small vs. Cav1.2 (27x larger) and RyR2 expression (70x larger) (Stratton et al., 2016). Also, Jiang et al. suggested that TRPC6 protein expression is small during postnatal development and adulthood vs. expression at fetal stages (Jiang et al., 2014).

Limitations of the applied mathematical model are discussed in (Korhonen et al., 2009). Most importantly, NRVMs are known to exhibit variable phenotypes, especially in different culture conditions and during development. The model was built from data from several different laboratories where culture conditions were presumably heterogeneous and different to the conditions in our laboratory. The model is based on data from cells cultured 3–5 days whenever possible to minimize age-related variance, which aligns with our duration of culture. A major difference is the temperature at which experiments were performed. Temperature strongly affects cell function. For instance, Ca^{2+} release from the SR of rat cardiomyocytes is highly temperature dependent (Fu et al., 2005). The model is for NRVMs at 32°C, but our experiments were performed at room temperature to allow us to control the pacing rate. The temperature difference causes alterations of ion transport, channel gating and ion concentrations, including $[Ca^{2+}]_i$. For this reason, we only used the model for qualitative comparison of trends rather than actual measurements.

DATA AVAILABILITY STATEMENT

The datasets generated for this study are available on request to the corresponding author.

ETHICS STATEMENT

The animal study was reviewed and approved by IACUC, University of Utah.

AUTHOR CONTRIBUTIONS

AA and FS designed the study. AA, FS, and MS drafted the manuscript. AS and MS acquired and analyzed image data. MS implemented the modeling and analyzed simulation data. CH isolated and infected cells. AA and CH performed western blotting. All authors critically revised the manuscript and approved the version to be published.

FUNDING

We acknowledge funding by the Nora Eccles Treadwell Foundation and the National Heart, Lung and Blood Institute of the National Institutes of Health (R01HL094464 and R01HL132067).

ACKNOWLEDGMENTS

We acknowledge molecular biology support and expert advice on adenoviral expression of the TRPC6 constructs from Dr. Michael Sanguinetti. We thank Dr. Boris Martinac for providing us with the TRPC6 construct.

SUPPLEMENTARY MATERIAL

The Supplementary Material for this article can be found online at: https://www.frontiersin.org/articles/10.3389/fphys.2020.00044/full#supplementary-material

REFERENCES

Ahmad, A. A., Streiff, M., Hunter, C., Hu, Q., and Sachse, F. B. (2017). Physiological and pathophysiological role of transient receptor potential canonical channels in cardiac myocytes. *Prog. Biophys. Mol. Biol.* 130, 254–263. doi: 10.1016/j.pbiomolbio.2017.06.005

Aires, V., Hichami, A., Boulay, G., and Khan, N. A. (2007). Activation of TRPC6 calcium channels by diacylglycerol (DAG)-containing arachidonic acid: a comparative study with DAG-containing docosahexaenoic acid. *Biochimie* 89, 926–937. doi: 10.1016/j.biochi.2006.10.016

Bon, R. S., and Beech, D. J. (2013). In pursuit of small molecule chemistry for calcium-permeable non-selective TRPC channels – mirage or pot of gold? *Br. J. Pharmacol.* 170, 459–474. doi: 10.1111/bph.12274

Cayouette, S., Lussier, M. P., Mathieu, E. L., Bousquet, S. M., and Boulay, G. (2004). Exocytotic insertion of TRPC6 channel into the plasma membrane upon Gq protein-coupled receptor activation. *J. Biol. Chem.* 279, 7241–7246. doi: 10.1074/jbc.M312042200

Dibb, K. M., Eisner, D. A., and Trafford, A. W. (2007). Regulation of systolic [Ca2+]i and cellular Ca2+ flux balance in rat ventricular myocytes by SR Ca2+, L-type Ca2+ current and diastolic [Ca2+]i. *J. Physiol.* 585, 579–592. doi: 10.1113/jphysiol.2007.141473

Dietrich, A., and Gudermann, T. (2014). TRPC6: physiological function and pathophysiological relevance. *Handb. Exp. Pharmacol.* 222, 157–188. doi: 10.1007/978-3-642-54215-2_7

Dyachenko, V., Husse, B., Rueckschloss, U., and Isenberg, G. (2008). Mechanical deformation of ventricular myocytes modulates both TRPC6 and Kir2.3 channels. *Cell Calcium* 45, 38–54. doi: 10.1016/j.ceca.2008.06.003

Franz, M. R. (2000). Mechano-electrical feedback. *Cardiovasc. Res.* 45, 263–266. doi: 10.1016/S0008-6363(99)00390-9

Friedrich, O., Wagner, S., Battle, A. R., Schurmann, S., and Martinac, B. (2012). Mechano-regulation of the beating heart at the cellular level--mechanosensitive channels in normal and diseased heart. *Prog. Biophys. Mol. Biol.* 110, 226–238. doi: 10.1016/j.pbiomolbio.2012.08.009

Fu, Y., Zhang, G. Q., Hao, X. M., Wu, C. H., Chai, Z., and Wang, S. Q. (2005). Temperature dependence and thermodynamic properties of Ca2+ sparks in rat cardiomyocytes. *Biophys. J.* 89, 2533–2541. doi: 10.1529/biophysj.105.067074

Gattoni, S., Roe, A. T., Frisk, M., Louch, W. E., Niederer, S. A., and Smith, N. P. (2016). The calcium-frequency response in the rat ventricular myocyte: an experimental and modelling study. *J. Physiol.* 594, 4193–4224. doi: 10.1113/JP272011

Gomez, J. P., Potreau, D., and Raymond, G. (1994). Intracellular calcium transients from newborn rat cardiomyocytes in primary culture. *Cell Calcium* 15, 265–275. doi: 10.1016/0143-4160(94)90066-3

Grynkiewicz, G., Poenie, M., and Tsien, R. Y. (1985). A new generation of Ca2+ indicators with greatly improved fluorescence properties. *J. Biol. Chem.* 260, 3440–3450.

Hannanta-Anan, P., and Chow, B. Y. (2016). Optogenetic control of calcium oscillation waveform defines NFAT as an integrator of calcium load. *Cell Syst.* 2, 283–288. doi: 10.1016/j.cels.2016.03.010

Hofmann, T., Obukhov, A. G., Schaefer, M., Harteneck, C., Gudermann, T., and Schultz, G. (1999). Direct activation of human TRPC6 and TRPC3 channels by diacylglycerol. *Nature* 397, 259–263. doi: 10.1038/16711

Ikeda, K., Nakajima, T., Yamamoto, Y., Takano, N., Tanaka, T., Kikuchi, H., et al. (2013). Roles of transient receptor potential canonical (TRPC) channels and reverse-mode Na+/Ca2+ exchanger on cell proliferation in human cardiac fibroblasts: effects of transforming growth factor beta1. *Cell Calcium* 54, 213–225. doi: 10.1016/j.ceca.2013.06.005

Ikenouchi, H., Peeters, G. A., and Barry, W. H. (1991). Evidence that binding of Indo-1 to cardiac myocyte protein does not markedly change Kd for Ca2+. *Cell Calcium* 12, 415–422. doi: 10.1016/0143-4160(91)90067-O

Jiang, Y., Huang, H., Liu, P., Wei, H., Zhao, H., Feng, Y., et al. (2014). Expression and localization of TRPC proteins in rat ventricular myocytes at various developmental stages. *Cell Tissue Res.* 355, 201–212. doi: 10.1007/s00441-013-1733-4

Kiso, H., Ohba, T., Iino, K., Sato, K., Terata, Y., Murakami, M., et al. (2013). Sildenafil prevents the up-regulation of transient receptor potential canonical channels in the development of cardiomyocyte hypertrophy. *Biochem. Biophys. Res. Commun.* 436, 514–518. doi: 10.1016/j.bbrc.2013.06.002

Korhonen, T., Hanninen, S. L., and Tavi, P. (2009). Model of excitation-contraction coupling of rat neonatal ventricular myocytes. *Biophys. J.* 96, 1189–1209. doi: 10.1016/j.bpj.2008.10.026

Kuwahara, K., Wang, Y., Mcanally, J., Richardson, J. A., Bassel-Duby, R., Hill, J. A., et al. (2006). TRPC6 fulfills a calcineurin signaling circuit during pathologic cardiac remodeling. *J. Clin. Invest.* 116, 3114–3126. doi: 10.1172/JCI27702

Lin, B. L., Matera, D., Doerner, J. F., Zheng, N., Del Camino, D., Mishra, S., et al. (2019). *In vivo* selective inhibition of TRPC6 by antagonist BI 749327 ameliorates fibrosis and dysfunction in cardiac and renal disease. *Proc. Natl. Acad. Sci. USA* 116, 10156–10161. doi: 10.1073/pnas.1815354116

Louch, W. E., Stokke, M. K., Sjaastad, I., Christensen, G., and Sejersted, O. M. (2012). No rest for the weary: diastolic calcium homeostasis in the normal and failing myocardium. *Physiology* 27, 308–323. doi: 10.1152/physiol.00021.2012

Martinac, B., and Kloda, A. (2003). Evolutionary origins of mechanosensitive ion channels. *Prog. Biophys. Mol. Biol.* 82, 11–24. doi: 10.1016/S0079-6107(03)00002-6

Mohl, M. C., Iismaa, S. E., Xiao, X. H., Friedrich, O., Wagner, S., Nikolova-Krstevski, V., et al. (2011). Regulation of murine cardiac contractility by activation of alpha(1A)-adrenergic receptor-operated Ca(2+) entry. *Cardiovasc. Res.* 91, 310–319. doi: 10.1093/cvr/cvr081

Motoyama, K., Nagata, T., Kobayashi, J., Nakamura, A., Miyoshi, N., Kazui, M., et al. (2018). Discovery of a bicyclo[4.3.0]nonane derivative DS88790512 as a potent, selective, and orally bioavailable blocker of transient receptor potential canonical 6 (TRPC6). *Bioorg. Med. Chem. Lett.* 28, 2222–2227. doi: 10.1016/j.bmcl.2018.03.056

Onohara, N., Nishida, M., Inoue, R., Kobayashi, H., Sumimoto, H., Sato, Y., et al. (2006). TRPC3 and TRPC6 are essential for angiotensin II-induced cardiac hypertrophy. *EMBO J.* 25, 5305–5316. doi: 10.1038/sj.emboj.7601417

Sachs, F. (2010). Stretch-activated ion channels: what are they? *Physiology* 25, 50–56. doi: 10.1152/physiol.00042.2009

Seki, S., Nagashima, M., Yamada, Y., Tsutsuura, M., Kobayashi, T., Namiki, A., et al. (2003). Fetal and postnatal development of Ca2+ transients and Ca2+ sparks in rat cardiomyocytes. *Cardiovasc. Res.* 58, 535–548. doi: 10.1016/S0008-6363(03)00255-4

Seo, K., Rainer, P. P., Lee, D. I., Hao, S., Bedja, D., Birnbaumer, L., et al. (2014). Hyperactive adverse mechanical stress responses in dystrophic heart are coupled to transient receptor potential canonical 6 and blocked by cGMP-protein kinase G modulation. *Circ. Res.* 114, 823–832. doi: 10.1161/CIRCRESAHA.114.302614

Spassova, M. A., Hewavitharana, T., Xu, W., Soboloff, J., and Gill, D. L. (2006). A common mechanism underlies stretch activation and receptor activation of TRPC6 channels. *Proc. Natl. Acad. Sci. USA* 103, 16586–16591. doi: 10.1073/pnas.0606894103

Stratton, M. S., Lin, C. Y., Anand, P., Tatman, P. D., Ferguson, B. S., Wickers, S. T., et al. (2016). Signal-dependent recruitment of BRD4 to cardiomyocyte super-enhancers is suppressed by a MicroRNA. *Cell Rep.* 16, 1366–1378. doi: 10.1016/j.celrep.2016.06.074

Tang, Q., Guo, W., Zheng, L., Wu, J. X., Liu, M., Zhou, X., et al. (2018). Structure of the receptor-activated human TRPC6 and TRPC3 ion channels. *Cell Res.* 28, 746–755. doi: 10.1038/s41422-018-0038-2

Washburn, D. G., Holt, D. A., Dodson, J., Mcatee, J. J., Terrell, L. R., Barton, L., et al. (2013). The discovery of potent blockers of the canonical transient receptor channels, TRPC3 and TRPC6, based on an anilino-thiazole pharmacophore. *Bioorg. Med. Chem. Lett.* 23, 4979–4984. doi: 10.1016/j.bmcl.2013.06.047

Wright, J. D., An, S. W., Xie, J., Lim, C., and Huang, C. L. (2019). Soluble klotho regulates TRPC6 calcium signaling *via* lipid rafts, independent of the FGFR-FGF23 pathway. *FASEB J.* 33, 9182–9193. doi: 10.1096/fj.201900321R

Wu, X., Eder, P., Chang, B., and Molkentin, J. D. (2010). TRPC channels are necessary mediators of pathologic cardiac hypertrophy. *Proc. Natl. Acad. Sci. USA* 107, 7000–7005. doi: 10.1073/pnas.1001825107

Xie, J., Cha, S. K., An, S. W., Kuro, O. M., Birnbaumer, L., and Huang, C. L. (2012). Cardioprotection by Klotho through downregulation of TRPC6 channels in the mouse heart. *Nat. Commun.* 3:1238. doi: 10.1038/ncomms2240

Yamaguchi, Y., Iribe, G., Nishida, M., and Naruse, K. (2017). Role of TRPC3 and TRPC6 channels in the myocardial response to stretch: linking physiology and pathophysiology. *Prog. Biophys. Mol. Biol.* 130, 264–272. doi: 10.1016/j.pbiomolbio.2017.06.010

Conflict of Interest: The authors declare that the research was conducted in the absence of any commercial or financial relationships that could be construed as a potential conflict of interest.

frontiers
in Physiology

ORIGINAL RESEARCH
published: 06 March 2020
doi: 10.3389/fphys.2020.00193

Disruption of Transverse-Tubules Eliminates the Slow Force Response to Stretch in Isolated Rat Trabeculae

*Amelia Power†, Sarbjot Kaur, Cameron Dyer† and Marie-Louise Ward**

Department of Physiology, Faculty of Medical and Health Sciences, University of Auckland, New Zealand

Edited by:
Remi Peyronnet,
University of Freiburg, Germany

Reviewed by:
Nazareno Paolocci,
Johns Hopkins University,
United States
Jens Kockskämper,
University of Marburg, Germany

***Correspondence:**
Marie-Louise Ward
m.ward@auckland.ac.nz

†Present address:
Amelia Power,
Department of Physiology, School of Biomedical Sciences, University of Otago, Dunedin, New Zealand
Cameron Dyer,
Whangarei Hospital, Northland District Health Board, Whangarei, New Zealand

Specialty section:
This article was submitted to Striated Muscle Physiology, a section of the journal Frontiers in Physiology

Received: *16 October 2019*
Accepted: *19 February 2020*
Published: *06 March 2020*

Citation:
Power A, Kaur S, Dyer C and Ward M-L (2020) Disruption of Transverse-Tubules Eliminates the Slow Force Response to Stretch in Isolated Rat Trabeculae. Front. Physiol. 11:193. doi: 10.3389/fphys.2020.00193

Ventricular muscle has a biphasic response to stretch. There is an immediate increase in force that coincides with the stretch which is followed by a second phase that takes several minutes for force to develop to a new steady state. The initial increase in force is due to changes in myofilament properties, whereas the second, slower component of the stretch response (known as the "slow force response" or SFR) is accompanied by a steady increase in Ca^{2+} transient amplitude. Evidence shows stretch-dependent Ca^{2+} influx during the SFR occurs through some mechanism that is continuously active for several minutes following stretch. Many of the candidate ion channels are located primarily in the t-tubules, which are consequently lost in heart disease. Our aim, therefore, was to investigate the impact of t-tubule loss on the SFR in non-failing cardiac trabeculae in which expression of the different Ca^{2+} handling proteins was not altered by any disease process. For comparison, we also investigated the effect of formamide detubulation of trabeculae on β-adrenergic activation (1 μM isoproterenol), since this is another key regulator of cardiac force. Measurement of intracellular calcium ($[Ca^{2+}]_i$) and isometric stress were made in RV trabeculae from rat hearts before, during and after formamide treatment (1.5 M for 5 min), which on washout seals the surface sarcolemmal t-tubule openings. Results showed detubulation slowed the time course of Ca^{2+} transients and twitch force, with time-to-peak, maximum rate-of-rise, and relaxation prolonged in trabeculae at optimal length (L_o). Formamide treatment also prevented development of the SFR following a step change in length from 90 to 100% L_o, and blunted the response to β-adrenergic activation (1 μM isoproterenol).

Keywords: slow force response, t-tubules, ventricular trabeculae, calcium, β-adrenergic activation

INTRODUCTION

Ventricular myocytes are the "working" cells of the heart, responsible for force generation. Their structure is characterized by regular invaginations of the surface sarcolemma (SL) that occur at the Z disc. These invaginations form a complex tubular system that is continuous with the extracellular environment, commonly referred to as the "transverse tubules" (or "t-tubules"). Linkages between t-tubules are also present in the longitudinal axis of myocytes (Sperelakis and Rubio, 1971), providing a highly branched tubular complex. The t-tubules have an important role during excitation-contraction (EC) coupling, ensuring that the action potential is propagated rapidly, and evenly, throughout the myocytes, which is essential for synchronized contraction.

During the cardiac action potential, influx of Ca^{2+} through voltage-gated, L-type, Ca^{2+} channels triggers Ca^{2+} release into the cytosol by activating ryanodine receptors (RyR) in the junctional membrane of the sarcoplasmic reticulum (SR), which is the myocyte intracellular Ca^{2+} store. This causes a ∼10-fold increase in cytosolic $[Ca^{2+}]_i$, during the "Ca^{2+} transient," which initiates cross-bridge cycling and force production. Many of the ion channels essential to EC coupling and Ca^{2+} transport are present in greater density in the t-tubule SL, which makes up 64% of the total sarcolemmal area of rat ventricular myocytes (Soeller and Cannell, 1999). These include the L-type Ca^{2+} channels which are in close apposition to the RyR clustered at the junctional SR (Forbes and Sperelakis, 1983). This specialized region, known as the "dyad," is critical to simultaneous Ca^{2+}-induced Ca^{2+}-release throughout the myocyte.

Relaxation of cardiac myocytes is brought about by the cytosolic $[Ca^{2+}]_i$ returning to resting (diastolic) levels. Although the main protein responsible for removal of cytosolic Ca^{2+} is the sarco-endoplasmic reticulum ATPase (SERCA), the Na^+-Ca^{2+} exchanger (NCX) also contributes. NCXs are also concentrated in the myocyte t-tubule SL (Thomas et al., 2003), and are important in Ca^{2+} removal from the junctional region of the dyad where Ca^{2+} reaches very high concentrations during RyR release. NCX is electrogenic, operating in "forward mode" to extrude 1 Ca^{2+} ion in exchange for 3 Na^+ ions (Hinata et al., 2002; Bers and Ginsburg, 2007), as well as in reverse mode to bring additional Ca^{2+} into the myocytes at positive membrane potentials (Litwin et al., 1996).

Disruption and/or loss of myocyte t-tubule structure has been reported in myocytes from human (Crossman et al., 2011) and many animal models (Wei et al., 2010; Ward and Crossman, 2014; Power et al., 2018) of heart disease in which contraction is compromised. The resulting increased t-tubule heterogeneity has been suggested as causing prolonged action potential duration (Beuckelmann et al., 1993; Tomaselli and Marban, 1999), asynchrony of subcellular Ca^{2+} release, and reduced force in diseased myocytes (Heinzel et al., 2011). However, the question remains as to what contribution t-tubule loss has on reduced contraction, since many of the pathologies associated with heterogenous t-tubules also exhibit alterations in Ca^{2+} cycling and myofilament proteins. This makes it difficult to assign the contractile dysfunction to t-tubule disruption, *per se*.

Therefore, our aim was (i) to examine the impact of acutely disrupting t-tubules on $[Ca^{2+}]_i$ and force in *multicellular* ventricular trabeculae, and (ii) to investigate the impact of detubulation on the slow force response to stretch which relies predominantly on transport of ions across the t-tubule SL. We also investigated the effects of detubulation on the β-adrenergic response which, along with stretch, is a key regulator of cardiac contraction. We hypothesized that pharmacological detubulation of trabeculae from healthy hearts would have an impact on both the magnitude of the SFR and on the response to β-adrenergic stimulation since both mechanisms augment force by receptor activation and/or ion transport across the t-tubule SL. However, β-adrenergic receptors are distributed throughout both the surface and t-tubule sarcolemma (Cros and Brette, 2013), therefore we anticipated the functional response to β-adrenergic stimulation would only be partially blunted by detubulation.

MATERIALS AND METHODS

Ethical Approval

This study was carried out in strict accordance with the recommendations in the Guide for the Care and Use of Laboratory Animals of the National Institutes of Health. The experimental protocol was approved by the Animal Ethics Committee of The University of Auckland (permit number AEC 001232). Animals were anaesthetized with isoflurane using 100% O_2 as the carrier gas until reflexive responses were lost and then killed by decapitation. Hearts were removed and perfusion of the coronary circulation with oxygenated solution (see below) maintained throughout dissection.

Isolation, Dissection, and Mounting of Trabeculae

Un-branched trabeculae (cross-sectional area: 0.057 ± 0.010 mm^2) were micro-dissected from the right ventricle (RV) of adult Wistar rats (weight: 287 ± 6 g, $n = 13$) with small blocks of ventricular wall at each end. Trabeculae were transferred to a bath (450 μl) on the stage of an inverted microscope (Nikon Eclipse TE2000-U, Japan) and continuously superfused with oxygenated physiological solution (see below). The small block of tissue at one end of the trabecula was held in a wire cradle extending from the beam of a force transducer (KX801 Micro Force Sensor, Kronex Technologies), while the tissue block at the other end was held in a nylon snare attached to a manipulator used to impose length changes. Field stimulation was provided at 0.2 Hz by electrical pulses of 5 ms duration at a voltage 10% above threshold (model D100, Digitimer^{TM}, United Kingdom). Once trabeculae were contracting at steady state, loading with fura-2/AM was commenced.

Measurement of $[Ca^{2+}]_i$

Intracellular calcium ($[Ca^{2+}]_i$) measurements were made as described previously (Ward et al., 2003). Briefly, trabeculae were loaded for 2 h at room temperature (21.0 ± 0.1°C) with 10 μM fura-2/AM (Teflabs, TX, United States) dissolved in 30 μl of anhydrous DMSO with 5% wt/vol of Pluronic F-127 (Teflabs, TX, United States). Fluorescence was measured at 510 nm for excitation wavelengths of 340, 360, and 380 nm. The 340/380 ratio of emitted fluorescence was obtained as a measure of $[Ca^{2+}]_i$. Emitted fluorescence at 360 nm did not vary with stimulation, or formamide treatment, confirming there was no movement artifact.

Experimental Interventions

Formamide exposure was carried out in trabeculae after baseline control data was obtained for each experimental intervention. 1.5 M formamide was added to the superfusate for 5 min whilst continually monitoring $[Ca^{2+}]_i$ and isometric force. Two experimental protocols were carried out that were known to have a high dependence on membrane channels and transporters predominantly located in the t-tubule SL.

The Slow Force Response to Stretch

Investigation of the slow force response to stretch was carried out before and 5 min after wash out of formamide. Trabeculae were first shortened to 90% of their optimal length (L_o) and allowed to reach steady state before rapidly lengthening to 100% L_o where they were held for 3 mins before decreasing again to 90% L_o. The Ca^{2+} transient and twitch force parameters immediately following the stretch were then compared with those after 3 min at 100% L_o.

ß-Adrenergic Activation

The response to ß-adrenergic activation was also investigated. One micrometer isoproterenol, a non-selective β adrenoreceptor agonist (Martin and Broadley, 1994), was added to the superfusate before (control) and after formamide treatment in trabeculae, with a return to isoproterenol-free steady state after each intervention.

Confocal Imaging of Trabeculae

Confocal imaging of trabeculae was carried out to confirm detubulation following formamide treatment by staining trabeculae with wheat germ agglutinin (WGA) and ryanodine receptor (RyR) antibodies. Control and formamide treated trabeculae (1.5 M formamide for 5 min followed by 10 min wash out) were held at L_o and fixed in 2% PFA for 10 min at room temperature. Trabeculae were then incubated for 2 h with Image-iT FX signal enhancer (Invitrogen Life Technologies, United States) followed by washing in phosphate buffer solution (PBS) 3 × 5 min. Next, trabeculae were immunolabeled with RyR monoclonal primary antibody (C3-33, catalog # MA3-916, Invitrogen Life Technologies, United States) (1:100, diluted in 1% bovine serum albumin with 0.1% Triton X-100 in PBS) followed by overnight incubation at 4°C. Next day, trabeculae were washed in PBS 3 × 5 min followed by 3 h incubation with goat anti-mouse Alexa Fluor 594 (catalog # A-11005, Invitrogen Life Technologies, United States) (1:200) and WGA conjugated Alexa Fluor 488 (1:200) at room temperature. Trabeculae were then washed in PBS, the tissue blocks at either end removed, and mounted on a slide with Prolong Gold antifade reagent (Invitrogen Life Technologies, United States). Confocal imaging of trabeculae was carried out to confirm detubulation in formamide treated trabeculae in comparison to control by viewing for t-tubular striations from WGA and RyR stains using 63 × objective with oil under Olympus FV1000 confocal microscope.

Chemicals and Solutions

Trabeculae were continuously superfused with a HCO_3^--free Tyrode's solution bubbled with 100% O_2, containing (in mM): 141.8 NaCl; 6 KCl; 1.2 $MgSO_4$; 1.2 Na_2HPO_4; 10 HEPES; 10 D-Glucose adjusted to pH 7.4. Extracellular calcium ($[Ca^{2+}]_o$) was set by adding $CaCl_2$ from a 1 M stock solution. The dissection and initial mounting solution contained 0.25 mM $[Ca^{2+}]_o$, and 20 mM 2,3-butanedione monoxime (BDM) for cardio-protection (Mulieri et al., 1989). Once mounted in the muscle chamber, trabeculae were superfused with a BDM-free solution. $[Ca^{2+}]_o$ was raised to 1.0 mM during fura-2 loading, and then to 1.5 mM during experiments (unless otherwise indicated). All chemicals were purchased from Sigma (Sigma Aldrich, Australia) unless stated otherwise.

Data Analysis

Data were acquired using LabVIEW (National Instruments, Austin, TX, United States) and analyzed off-line using a custom-written program (IDL Research Systems Inc., Boulder, CO, United States). Ca^{2+} transients were fitted by a five parameter function as described previously (Ward et al., 2003). All results were expressed as mean ± SEM. Statistical analysis was performed using paired or unpaired Student's *t*-tests, as well as two-way analysis of variance (ANOVA) followed by Sidak's multiple comparisons test using Prism 7.0c (GraphPad software, CA, United States) depending on the experimental protocol. A statistically significant difference was assumed at $P < 0.05$.

RESULTS

To demonstrate the effects of formamide on $[Ca^{2+}]_i$ and force throughout the whole detubulation process we show a continuous record of simultaneous Ca^{2+} transients (fura-2 340/380 fluorescence) and their corresponding twitch force from a representative trabecula before, during and after exposure to 1.5 M formamide. **Figure 1A** shows diastolic and peak $[Ca^{2+}]_i$ was increased during formamide exposure (ii), returning to pre-formamide control levels after ∼5 min of formamide washout (iv). Peak force also increased during formamide, with no discernible change in the diastolic force. Comparison of Ca^{2+} transient and twitch force kinetics before and after formamide treatment are shown in **Figure 1B**. Region (iv) showed lower amplitudes of both Ca^{2+} transients and twitch force in comparison to pre-formamide control (i), with a ∼20 ms delay in reaching peak force post-formamide treatment, as is illustrated by the gray lines on the force-time plot which are superimposed in time for comparison.

Table 1 shows mean ± SEM data from n = 9 trabeculae for the time points labeled in **Figure 1A**. The time to peak $[Ca^{2+}]_i$ was longer during and after formamide treatment, with the time constant of Ca^{2+} transient decay prolonged during the formamide exposure (ii), but not different to the pre-formamide control after washout. Active stress was decreased during and after formamide, with slower relaxation, although the maximum rate-of-rise of stress increased. An additional line (v) was added to **Table 1** for $n = 4$ trabeculae showing data 30 min after formamide washout. Although the Ca^{2+} transients in these trabeculae were not different to pre-formamide controls, the delay in time to peak $[Ca^{2+}]_i$ and time to 50% relaxation of force continued, suggesting the surface SL t-tubule openings remained sealed for this period of time.

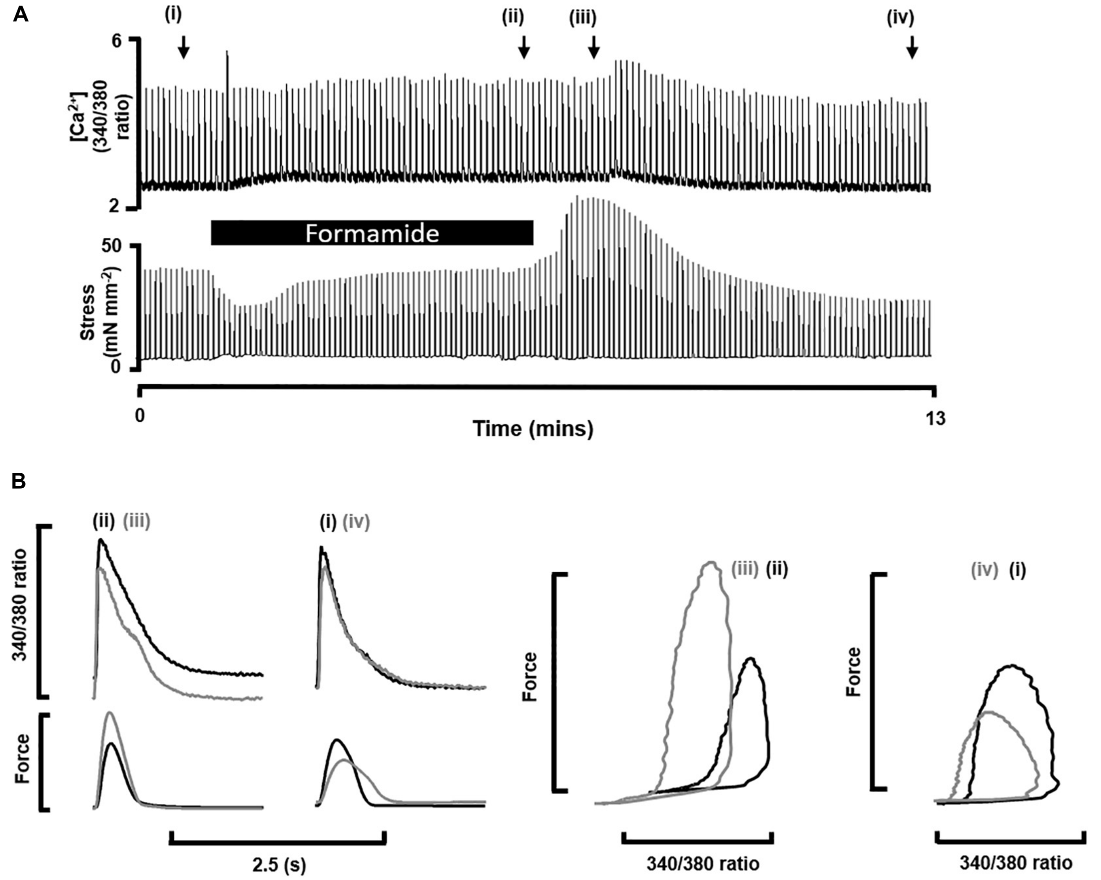

FIGURE 1 | Impact of formamide on multicellular trabeculae. **(A)** Shows continuous trace of $[Ca^{2+}]_i$ as fura-2 340/380 fluorescence (top) and isometric force (bottom) recorded from a representative trabecula stimulated at 0.2 Hz before (i), during (black bar, ii) and after (iii,iv) exposure to 1.5 M formamide. The x-axis shows time, and the black bar indicates 5 min of formamide exposure. **(B)** Shows examples of individual $[Ca^{2+}]_i$ and twitch force traces from the time points labeled in **(A)**.

TABLE 1 | Mean ± SEM $[Ca^{2+}]_i$ transient (340/380 fura-2 ratio) and twitch force for the time points shown in **Figure 1**: before (i), during (ii), immediately after (iii), 5 min after (iv), and 30 min after (v) formamide treatment.

Time point	n	Diastolic $[Ca^{2+}]_i$ (340/380 ratio)	Systolic $[Ca^{2+}]_i$ (340/380 ratio)	Time to peak $[Ca^{2+}]_i$ (s)	Tau $[Ca^{2+}]_i$ decay (s)	Max rate of rise in stress (mN mm^{-2} s^{-1})	Active stress (mN mm^{-2})	Time to 50% relaxation (s)	Peak $[Ca^{2+}]_i$ to peak force delay (s)
(i)	9	2.03 ± 0.13	3.60 ± 0.25	0.074 ± 0.004	0.24 ± 0.02	0.027 ± 0.002	40.3 ± 10.5	0.18 ± 0.01	0.145 ± 0.009
(ii)	9	2.18 ± 0.14*	3.94 ± 0.22**	0.092 ± 0.004**	0.40 ± 0.03**	0.043 ± 0.009**	28.1 ± 4.5**	0.14 ± 0.01*	0.102 ± 0.008***
(iii)	9	1.96 ± 0.14*	3.90 ± 0.31**	0.087 ± 0.003*	0.31 ± 0.04*	0.055 ± 0.012**	36.9 ± 5.8*	0.15 ± 0.01**	0.104 ± 0.007***
(iv)	9	2.06 ± 0.14	3.45 ± 0.23*	0.083 ± 0.005**	0.24 ± 0.02	0.032 ± 0.012**	31.6 ± 8.4*	0.22 ± 0.02**	0.159 ± 0.014
(v)	4	1.82 ± 0.07	2.78 ± 0.16	0.084 ± 0.003*	0.22 ± 0.01 (*P* = 0.06)	0.019 ± 0.004**	14.9 ± 5.1	0.20 ± 0.02**	0.144 ± 0.013*

*Data are from n = 9 trabeculae for time points (i) to (iv). Data n = 4 trabeculae are shown for time point (v). *P < 0.05, **P < 0.01, and ***P < 0.001. Two-tailed paired t-test in comparison to pre-formamide control (i).*

Slow Force Response to Stretch

Stretching cardiac muscle results in a biphasic increase in the force of contraction. There is an immediate increase in the force of contraction that coincides with the stretch, which is followed by a slower developing force increase that takes several minutes to reach a maximum, known as the "slow force response" or SFR. The SFR is accompanied by increasing Ca^{2+} transients that result from stretch-dependent Ca^{2+} influx via transport proteins thought to be located predominantly in the t-tubules. We therefore investigated whether detubulation would eliminate the SFR. Following trabeculae stretch there was an immediate increase in active stress, which was not affected by formamide treatment (Control: 148 ± 37% vs. Formamide: 129 ± 32%; $P = 0.45$, $n = 5$ trabeculae) suggesting detubulation had no impact on the Frank-Starling mechanism. Active stress increased in Control trabeculae stretched from 90 to 100% L_o showing a

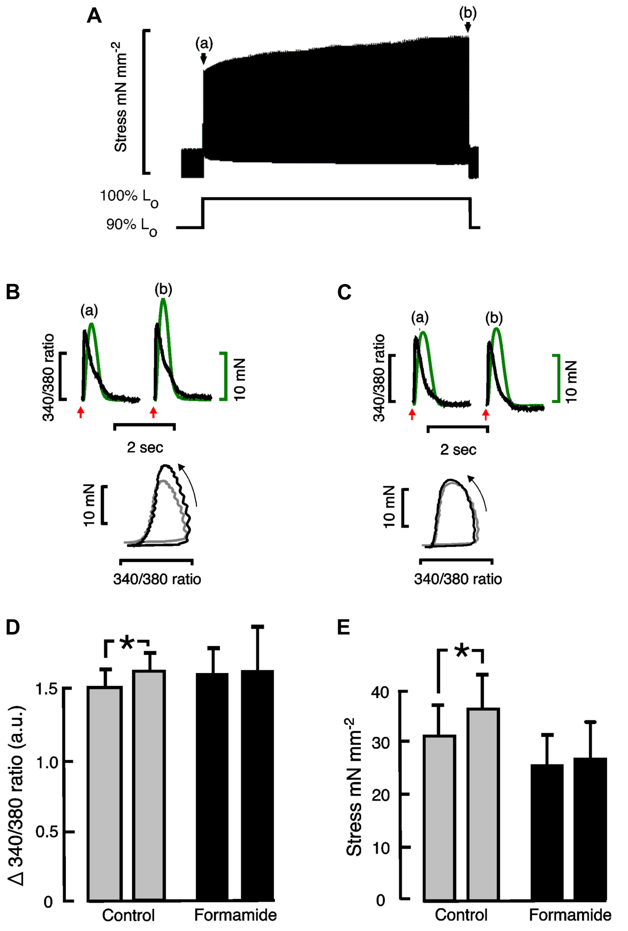

FIGURE 2 | Effect of formamide on slow force response to stretch. **(A)** Shows a representative slow force response from a rat trabecula stretched from 90 to 100% L_o. **(B)** (Control) and **(C)** (formamide) show Ca^{2+} transients (black) and twitch force (green) immediately after stretching a representative trabecula from 90 to 100% L_o on left (a), and after 3 min at 100% L_o on right (b). Red arrows indicate the time of stimulation. Phase plots of the force vs. Ca^{2+} data are shown beneath the Ca^{2+} transients and twitches with arrows indicating the direction of time. Phase plots immediately after the stretch are shown in gray, and after 3 min at 100% L_o are shown in black. **(D)** Shows mean ± SEM Ca^{2+} transient amplitudes ($n = 4$), and **(E)** shows mean ± SEM stress ($n = 6$) immediately after stretching trabeculae on left, and after 3 min at 100% L_o on right, for control (gray bars) and formamide treated (black bars) trabeculae. *$P < 0.05$. Two-tailed paired *t*-test. a.u, Arbitrary units.

SFR after 3 min of 114% (from 32.5 ± 5.7 mN mm^{-2} to 37.0 ± 6.9 mN mm^{-2}, $n = 6$, $P < 0.05$). An example SFR from a control trabecula is shown in **Figure 2A**.

Figure 2B shows calcium transients with their corresponding twitches superimposed and their phase plots below from a representative control trabecula immediately following the stretch (a) and after 3 min of stretch (b). Similar Ca^{2+} transients, twitches and phase plots from the same representative trabecula are shown after formamide treatment in **Figure 2C**. The relaxation part of the force-calcium phase plots provides an indication of myofilament Ca^{2+} sensitivity in intact trabeculae since the crossbridge cycling is in equilibrium at this point. **Figures 2B,C** show similar slopes for the relaxation section of the phase plots, providing further evidence that the SFR is not associated with a change in myofilament sensitivity, unlike the immediate response to stretch (Frank-Starling mechanism).

Figure 2D shows mean Ca^{2+} transient amplitude data from control and formamide treated trabeculae. There was a small but significant increase in Ca^{2+} transient amplitude during the SFR in control trabeculae that was not observed following formamide treatment. Consequently for formamide treated trabeculae, the SFR was reduced to 104% (from 25.6 ± 6.35 mN mm^{-2} to 26.6 ± 6.7 mN mm^{-2} after 3 min of stretch, $n = 6$, NS; **Figure 2E**).

Response to ß-Adrenergic Stimulation

Another important regulator of cardiac contractility is ß-adrenergic activation. Since myocyte ß-adrenergic receptors are found both on the surface, and t-tubule, sarcolemma, we hypothesized that the response to ß-adrenergic activation would be only partially depressed in formamide treated trabeculae. The ß-adrenergic effects were investigated by adding 1 μM isoproterenol to the superfusate. **Figure 3** shows mean ± SEM data from $n = 7$ control and $n = 8$ formamide treated trabeculae. No effect of isoproterenol was observed for either group on the time to peak of the Ca^{2+} transients (**Figure 3A**), or on the amplitude of the Ca^{2+} transients (control $P = 0.08$; formamide treated $P = 0.10$; **Figure 3C**), but there was a decrease in the time constant of Ca^{2+} transient decay (**Figure 3E**) for both control and formamide treated trabeculae. Isoproterenol decreased the time to peak stress (**Figure 3B**), and increased peak stress (**Figure 3D**), by similar amounts (although from different pre-isoproterenol values) in both groups. However, the time to 50% relaxation of stress was decreased only in control but not in formamide treated trabeculae (**Figure 3F**).

Evidence of Detubulation

Confocal imaging of trabeculae dual labeled with WGA and RyR antibodies was carried out to confirm that our formamide protocol effectively sealed the SL t-tubule openings. WGA binds to sialic acid residues on the surface SL and within the t-tubules and is commonly used as a label for the extracellular matrix and SL. Images from representative trabeculae in **Figure 4** show WGA labeled t-tubules in a control trabecula (**Figure 4A**) with an absence of t-tubule staining evident in the formamide treated preparation (**Figure 4D**). A similar RyR labeling pattern was observed in both control (**Figure 4B**) and detubulated trabeculae (**Figure 4E**), suggesting formamide treatment had no effect on the SR junctional ultrastructure.

DISCUSSION

The main goals of this project were to utilize multicellular ventricular trabeculae to (i) measure the changes in the time course of Ca^{2+} transients and isometric twitches following pharmacological removal of t-tubules; (ii) investigate the impact

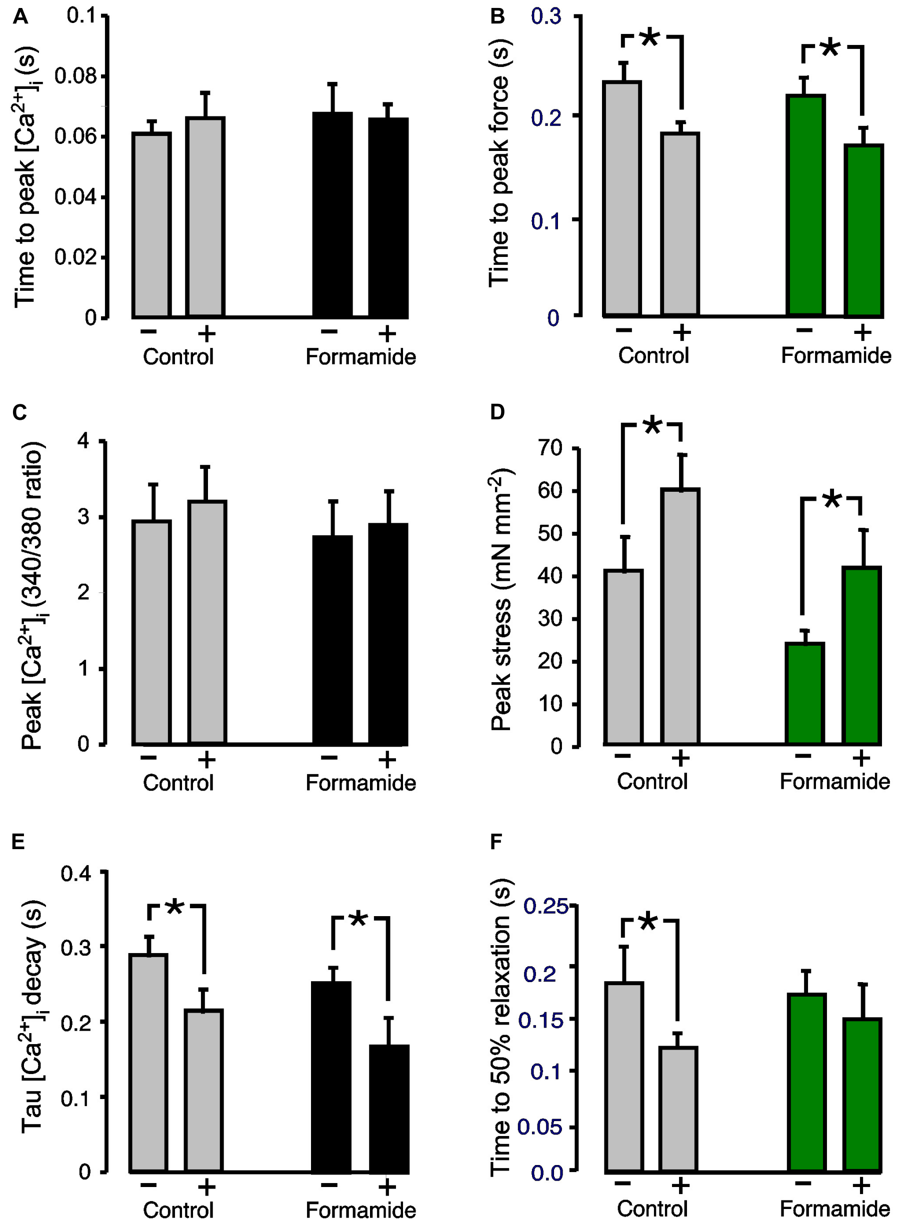

FIGURE 3 | Effect of formamide on response to ß-adrenergic stimulation. **(A,C,E)** Show Ca^{2+} transient parameters before (–) and during (+) 1 μM isoproterenol. **(B,D,F)** Show twitch force parameters before (–) and during (+) isoproterenol. Data are mean ± SEM. $^{*}P < 0.05$. Two-way ANOVA followed by Sidak's multiple comparisons test (Prism), $n = 7$ control and 8 formamide-treated trabeculae.

of detubulation on the slow force response to mechanical stretch; and (iii) determine whether detubulation modified the response to ß-adrenergic activation, since the ß1 receptors are not restricted to the t-tubule SL (Bhargava et al., 2013).

T-Tubule Loss Effects on Multicellular Trabeculae

Formamide has been used in the past to detubulate isolated ventricular myocytes (e.g., Kawai et al., 1999; Brette et al., 2002; Despa and Bers, 2007), and to a limited extent in multicellular trabeculae (Ferrantini et al., 2014). Exposure to physiological buffer solution containing 1.5 M formamide causes myocytes to shrink and equilibrate to a new cell volume (Kawai et al., 1999). Upon formamide wash off, the resulting rapid expansion of cells causes osmotic shock which disarticulates the t-tubular openings from the surface SL (Kawai et al., 1999). In our study, formamide was added to the superfusate of multicellular trabeculae held at fixed length (100% L_o). Simultaneous recordings of Ca^{2+} transients and isometric force were made before, during and after 5 min of formamide exposure. During formamide, we observed increased diastolic $[Ca^{2+}]_i$ and larger Ca^{2+} transients

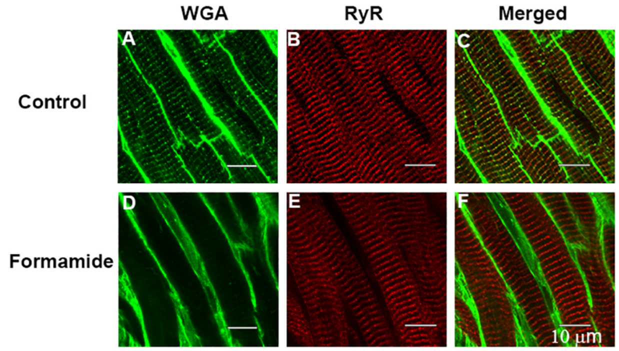

FIGURE 4 | Evidence of detubulation in response to formamide. Confocal images are shown of representative ventricular trabeculae labeled with t-tubule marker WGA (green) and anti-RyR antibody (red). Top row shows **A**: WGA, **B**: RyR, and **C**: merged labelling in a control trabecula. Bottom row shows **D**: WGA, **E**: RyR, and **F**: merged labelling in a formamide treated trabecula. Scale bar 10 μm.

in trabeculae, with reduced stress. We also observed a prolonged time to Ca^{2+} transient peak and a slower time constant of decay (**Table 1**). This is consistent with osmotic water loss effectively increasing the cytosolic $[Ca^{2+}]_i$ concentration, and impairing Ca^{2+} cycling, since measurements were made using a ratiometric Ca^{2+} indicator (fura-2).

Peak systolic $[Ca^{2+}]_i$ was decreased following formamide washout, and the time course of both the Ca^{2+} transients and twitch force were slower. This is consistent with impaired excitation-contraction coupling which has previously been reported after detubulation of isolated myocytes due to reduced L-type Ca^{2+} current (Gadeberg et al., 2017). This would also explain the reduced force after recovery from washout.

Measurements made 30 min after formamide washout [**Table 1**, (v)] suggests the surface SL t-tubule openings remained sealed since the time to peak systolic $[Ca^{2+}]_i$, and the time to 50% relaxation of force, remained prolonged. The Ca^{2+} transients were reduced in amplitude, and peak stress very much less after 30 mins of washout in comparison to pre-formamide treatment. Confocal imaging showed WGA had not penetrated the t-tubule system in formamide treated trabeculae, confirming that the t-tubule openings had remained sealed over (**Figure 4**). In contrast, no change in the RyR labeling pattern in formamide treated trabeculae was observed in comparison to control, suggesting that the junctional SR remained structurally intact and in close apposition to the t-tubule SL.

Loss of the Slow Force Response Following Detubulation

The slow force response is a physiological response to stretch that aids contractility. The magnitude of the slow force response is reduced in failing human myocardium, despite an increase in intracellular $[Na^+]$, suggesting that Na^+-contraction coupling is impaired in failing myocardium (von Lewinski et al., 2009). Since NCX resides largely in the t-tubules (Gadeberg et al., 2017), remodeling of the t-tubules could explain this lack of Na^+ mediated increase in intracellular $[Ca^{2+}]$.

A number of studies have implicated the Na^+-H^+ exchanger (NHE1) as contributing to Na^+ influx during the SFR (Calaghan and White, 2004; Kockskamper et al., 2008; von Lewinski et al., 2009; Shen et al., 2013), with an increase in intracellular $[Na^+]$ reported during sustained stretch— interventions (Calaghan and White, 2004; Caldiz et al., 2007). Blockade of NHE1 with pharmacological agents (Caldiz et al., 2007; Shen et al., 2013), or silencing NHE1 gene expression (Perez et al., 2011) blunts the SFR substantially in a number of species. Detubulation is unlikely to prevent stretch activation of NHE1 as these exchangers are restricted to the surface SL of cardiac myocytes (Garciarena et al., 2013). However, modeling studies attribute the stretch-dependent influx of Na^+ to be through stretch-activated, non-specific, cation channels (SAC_{NSC}), rather than via NHE1. TRPC channels are mechanosensitive, and have been implicated in the Ca^{2+} and/or Na^+ influx during the SFR (Yamaguchi et al., 2017). Antibody labeling of TRPC6 and TRPC3, likely candidates for stretch-dependent Ca^{2+} and Na^+ influx, shows they are abundant in isolated ventricular myocytes and apparently restricted to location in the t-tubule SL (Jiang et al., 2014). Since both NCX and TRPC channels are in the t-tubule SL, we speculate that detubulation would therefore prevent any stretch-dependent increase in $[Ca^{2+}]_i$, despite any possible activation of NHE1 in the surface sarcolemma.

Autocrine/paracrine factors released during stretch are also a component of the SFR and are important to consider. Others have shown that angiotensin II and endothelin are mediators of the SFR and consequently their receptors are reported to be found in the t-tubules (Chung et al., 2008). Therefore, it is plausible that their contribution to the SFR could be diminished following detubulation. However, under our experimental conditions we have found no contribution of Ang II to the SFR in rat ventricle (Shen et al., 2013). Instead, we have identified prostaglandin F2α as a stretch derived inotropic factor that contributes to the SFR (Shen et al., 2016). The distribution of F type prostaglandin receptors between the surface sarcolemma and t-tubules is unknown but could contribute to a lack of SFR in detubulated trabeculae.

ß-Adrenergic Activation of the Detubulated Myocardium

Isoproterenol had similar effects on control and formamide treated trabeculae (**Figure 3**), apart from the time to 50% stress relaxation which was slower in the formamide treated trabeculae. β1-adrenergic receptors are the most abundant of the β-adrenergic receptors in ventricular myocytes. They are distributed over both t-tubule and surface SL, which perhaps explains the lack of a difference between control and formamide treated groups. β2-adrenergic receptors are restricted to the t-tubule SL in ventricular tissue (Schobesberger et al., 2017), and can produce the same effects as β1-adrenergic receptors, although they can couple to both stimulatory and inhibitory G protein coupled receptors (Triposkiadis et al., 2009). We have previously shown that loss of t-tubules in right ventricle hypertrophy coincides with an attenuated inotropic response to β-adrenergic stimulation (Power et al., 2018). However, the results from this study suggest that detubulation *per se* does not explain the impaired β-adrenergic responsiveness observed in heart failure.

CONCLUSION

Our study tested the hypothesis that the slow force response to stretch requires an intact t-tubular system to enable stretch-dependent Ca^{2+} influx during the slow augmentation of force. We subjected multicellular trabeculae from healthy rat hearts to superfusion with 1.5 M formamide, which prevented establishment of the SFR. Confirmation that formamide treatment disarticulated t-tubules from the extracellular environment was obtained by WGA labeling and confocal microscopy. Our study shows for the first time that that removal of the t-tubules in healthy trabeculae impairs the response to ventricular stretch.

DATA AVAILABILITY STATEMENT

The datasets generated for this study are available on request to the corresponding author.

ETHICS STATEMENT

This study was carried out in strict accordance with the recommendations in the Guide for the Care and Use of Laboratory Animals of the National Institutes of Health. The experimental protocol was approved by the Animal Ethics Committee of The University of Auckland (permit number AEC 001232).

AUTHOR CONTRIBUTIONS

M-LW contributed to the conceptualization. AP, SK, and CD contributed to the experimental investigations. M-LW, SK, AP, and CD contributed to the data analysis. M-LW, SK, and AP contributed to the manuscript preparation. M-LW contributed to the funding acquisition and administration.

FUNDING

This work was funded by the Auckland Medical Research Foundation (Project Nos. 81555 and 1118006 to M-LW).

REFERENCES

Bers, D. M., and Ginsburg, K. S. (2007). Na:Ca stoichiometry and cytosolic Ca-dependent activation of NCX in intact cardiomyocytes. *Ann. N. Y. Acad. Sci.* 1099, 326–338. doi: 10.1196/annals.1387.060

Beuckelmann, D. J., Nabauer, M., and Erdmann, E. (1993). Alterations of K+ currents in isolated human ventricular myocytes from patients with terminal heart failure. *Circ. Res.* 73, 379–385. doi: 10.1161/01.res.73.2.379

Bhargava, A., Lin, X., Novak, P., Mehta, K., Korchev, Y., Delmar, M., et al. (2013). Super-resolution scanning patch clamp reveals clustering of functional ion channels in adult ventricular myocyte. *Circ. Res.* 112, 1112–1120. doi: 10.1161/CIRCRESAHA.111.300445

Brette, F., Komukai, K., and Orchard, C. H. (2002). Validation of formamide as a detubulation agent in isolated rat cardiac cells. *Am. J. Physiol. Heart Circ. Physiol.* 283, H1720–H1728.

Calaghan, S., and White, E. (2004). Activation of Na+-H+ exchange and stretch-activated channels underlies the slow inotropic response to stretch in myocytes and muscle from the rat heart. *J. Physiol.* 559(Pt 1), 205–214. doi: 10.1113/jphysiol.2004.069021

Caldiz, C. I., Garciarena, C. D., Dulce, R. A., Novaretto, L. P., Yeves, A. M., Ennis, I. L., et al. (2007). Mitochondrial reactive oxygen species activate the slow force response to stretch in feline myocardium. *J. Physiol.* 584(Pt 3), 895–905. doi: 10.1113/jphysiol.2007.141689

Chung, K. Y., Kang, M., and Walker, J. W. (2008). Contractile regulation by overexpressed ETA requires intact T tubules in adult rat ventricular myocytes. *Am. J. Physiol. Heart Circ. Physiol.* 294, H2391–H2399. doi: 10.1152/ajpheart.00011.2008

Cros, C., and Brette, F. (2013). Functional subcellular distribution of beta1- and beta2-adrenergic receptors in rat ventricular cardiac myocytes. *Physiol Rep.* 1:e00038. doi: 10.1002/phy2.38

Crossman, D. J., Ruygrok, P. N., Soeller, C., and Cannell, M. B. (2011). Changes in the organization of excitation-contraction coupling structures in failing human heart. *PLoS One* 6:e17901. doi: 10.1371/journal.pone.0017901

Despa, S., and Bers, D. M. (2007). Functional analysis of Na+/K+-ATPase isoform distribution in rat ventricular myocytes. *Am. J. Physiol. Cell Physiol.* 293, C321–C327.

Ferrantini, C., Coppini, R., Sacconi, L., Tosi, B., Zhang, M. L., Wang, G. L., et al. (2014). Impact of detubulation on force and kinetics of cardiac muscle contraction. *J. Gen. Physiol.* 143, 783–797. doi: 10.1085/jgp.201311125

Forbes, M. S., and Sperelakis, N. (1983). The membrane systems and cytoskeletal elements of mammalian myocardial cells. *Cell Muscle Motil.* 3, 89–155. doi: 10.1007/978-1-4615-9296-9_5

Gadeberg, H. C., Kong, C. H. T., Bryant, S. M., James, A. F., and Orchard, C. H. (2017). Sarcolemmal distribution of ICa and INCX and Ca(2+) autoregulation in mouse ventricular myocytes. *Am. J. Physiol. Heart Circ. Physiol.* 313, H190–H199. doi: 10.1152/ajpheart.00117.2017

Garciarena, C. D., Ma, Y. L., Swietach, P., Huc, L., and Vaughan-Jones, R. D. (2013). Sarcolemmal localisation of Na+/H+ exchange and Na+-HCO3- co-transport influences the spatial regulation of intracellular pH in rat ventricular myocytes. *J. Physiol.* 591, 2287–2306. doi: 10.1113/jphysiol.2012.249664

Heinzel, F. R., MacQuaide, N., Biesmans, L., and Sipido, K. (2011). Dyssynchrony of Ca2+ release from the sarcoplasmic reticulum as subcellular mechanism of cardiac contractile dysfunction. *J. Mol. Cell Cardiol.* 50, 390–400. doi: 10.1016/j.yjmcc.2010.11.008

Hinata, M., Yamamura, H., Li, L., Watanabe, Y., Watano, T., Imaizumi, Y., et al. (2002). Stoichiometry of Na+-Ca2+ exchange is 3:1 in guinea-pig ventricular myocytes. *J. Physiol.* 545, 453–461. doi: 10.1113/jphysiol.2002.025866

Jiang, Y., Huang, H., Liu, P., Wei, H., Zhao, H., Feng, Y., et al. (2014). Expression and localization of TRPC proteins in rat ventricular myocytes at various developmental stages. *Cell Tissue Res.* 355, 201–212. doi: 10.1007/s00441-013-1733-4

Kawai, M., Hussain, M., and Orchard, C. H. (1999). Excitation-contraction coupling in rat ventricular myocytes after formamide-induced detubulation. *Am. J. Physiol.* 277, H603–H609. doi: 10.1152/ajpheart.1999.277.2.H603

Kockskamper, J., von Lewinski, D., Khafaga, M., Elgner, A., Grimm, M., Eschenhagen, T., et al. (2008). The slow force response to stretch in atrial and ventricular myocardium from human heart: functional relevance and subcellular mechanisms. *Prog. Biophys. Mol. Biol.* 97, 250–267. doi: 10.1016/j.pbiomolbio.2008.02.026

Litwin, S., Kohmoto, O., Levi, A. J., Spitzer, K. W., and Bridge, J. H. (1996). Evidence that reverse Na-Ca exchange can trigger SR calcium release. *Ann. N. Y. Acad. Sci.* 779, 451–463. doi: 10.1111/j.1749-6632.1996.tb44820.x

Martin, S. W., and Broadley, K. J. (1994). Effects of chronic intravenous infusions of dopexamine and isoprenaline to rats on D1-, beta 1- and beta 2-receptor-mediated responses. *Br. J. Pharmacol.* 112, 595–603. doi: 10.1111/j.1476-5381.1994.tb13116.x

Mulieri, L. A., Hasenfuss, G., Ittleman, F., Blanchard, E. M., and Alpert, N. R. (1989). Protection of human left ventricular myocardium from cutting injury with 2,3-butanedione monoxime. *Circ. Res.* 65, 1441–1449. doi: 10.1161/01.res.65.5.1441

Perez, N. G., Nolly, M. B., Roldan, M. C., Villa-Abrille, M. C., Cingolani, E., Portiansky, E. L., et al. (2011). Silencing of NHE-1 blunts the slow force response to myocardial stretch. *J. Appl. Physiol.* 111, 874–880. doi: 10.1152/japplphysiol.01344.2010

Power, A. S., Hickey, A. J., Crossman, D. J., Loiselle, D. S., and Ward, M. L. (2018). Calcium mishandling impairs contraction in right ventricular hypertrophy prior to overt heart failure. *Pflugers. Arch.* 470, 1115–1126. doi: 10.1007/s00424-018-2125-0

Schobesberger, S., Wright, P., Tokar, S., Bhargava, A., Mansfield, C., Glukhov, A. V., et al. (2017). T-tubule remodelling disturbs localized beta2-adrenergic signalling in rat ventricular myocytes during the progression of heart failure. *Cardiovasc. Res.* 113, 770–782. doi: 10.1093/cvr/cvx074

Shen, X., Cannell, M. B., and Ward, M. L. (2013). Effect of SR load and pH regulatory mechanisms on stretch-dependent Ca(2+) entry during the slow force response. *J. Mol. Cell Cardiol.* 63, 37–46. doi: 10.1016/j.yjmcc.2013.07.008

Shen, X., Kaur, S., Power, A., Williams, L. Z., and Ward, M. L. (2016). Positive Inotropic Effect of Prostaglandin F2alpha in Rat Ventricular Trabeculae. *J. Cardiovasc. Pharmacol.* 68, 81–88. doi: 10.1097/FJC.0000000000000392

Soeller, C., and Cannell, M. B. (1999). Examination of the transverse tubular system in living cardiac rat myocytes by 2-photon microscopy and digital image-processing techniques. *Circ. Res.* 84, 266–275. doi: 10.1161/01.res.84.3.266

Sperelakis, N., and Rubio, R. (1971). An orderly lattice of axial tubules which interconnect adjacent transverse tubules in guinea-pig ventricular myocardium. *J. Mol. Cell Cardiol.* 2, 211–220.

Thomas, M. J., Sjaastad, I., Andersen, K., Helm, P. J., Wasserstrom, J. A., Sejersted, O. M., et al. (2003). Localization and function of the Na+/Ca2+-exchanger in normal and detubulated rat cardiomyocytes. *J. Mol. Cell Cardiol.* 35, 1325–1337. doi: 10.1016/j.yjmcc.2003.08.005

Tomaselli, G. F., and Marban, E. (1999). Electrophysiological remodeling in hypertrophy and heart failure. *Cardiovasc. Res.* 42, 270–283. doi: 10.1016/s0008-6363(99)00017-6

Triposkiadis, F., Karayannis, G., Giamouzis, G., Skoularigis, J., Louridas, G., and Butler, J. (2009). The sympathetic nervous system in heart failure physiology, pathophysiology, and clinical implications. *J. Am. Coll. Cardiol.* 54, 1747–1762. doi: 10.1016/j.jacc.2009.05.015

von Lewinski, D., Kockskamper, J., Zhu, D., Post, H., Elgner, A., and Pieske, B. (2009). Reduced stretch-induced force response in failing human myocardium caused by impaired Na(+)-contraction coupling. *Circ Heart Fail* 2, 47–55. doi: 10.1161/CIRCHEARTFAILURE.108.794065

Ward, M. L., and Crossman, D. J. (2014). Mechanisms underlying the impaired contractility of diabetic cardiomyopathy. *World J. Cardiol.* 6, 577–584. doi: 10.4330/wjc.v6.i7.577

Ward, M. L., Pope, A. J., Loiselle, D. S., and Cannell, M. B. (2003). Reduced contraction strength with increased intracellular [Ca2+] in left ventricular trabeculae from failing rat hearts. *J. Physiol.* 546(Pt 2), 537–550. doi: 10.1113/jphysiol.2002.029132

Wei, S., Guo, A., Chen, B., Kutschke, W., Xie, Y. P., Zimmerman, K., et al. (2010). T-tubule remodeling during transition from hypertrophy to heart failure. *Circ. Res.* 107, 520–531. doi: 10.1161/circresaha.109.212324

Yamaguchi, Y., Iribe, G., Nishida, M., and Naruse, K. (2017). Role of TRPC3 and TRPC6 channels in the myocardial response to stretch: linking physiology and pathophysiology. *Prog. Biophys. Mol. Biol.* 130(Pt B), 264–272. doi: 10.1016/j.pbiomolbio.2017.06.010

Conflict of Interest: The authors declare that the research was conducted in the absence of any commercial or financial relationships that could be construed as a potential conflict of interest.

frontiers
in Physiology

BRIEF RESEARCH REPORT
published: 13 March 2020
doi: 10.3389/fphys.2020.00182

The Degree of t-System Remodeling Predicts Negative Force-Frequency Relationship and Prolonged Relaxation Time in Failing Human Myocardium

Maha Abu-Khousa[1], Dominik J. Fiegle[1], Sophie T. Sommer[1], Ghazali Minabari[2], Hendrik Milting[3], Christian Heim[2], Michael Weyand[2,4], Roland Tomasi[5,6], Andreas Dendorfer[5,7], Tilmann Volk[1,4]* and Thomas Seidel[1,4]*

[1] Institute of Cellular and Molecular Physiology, Friedrich-Alexander-Universität Erlangen-Nürnberg, Erlangen, Germany, [2] Department of Cardiac Surgery, Friedrich-Alexander-Universität Erlangen-Nürnberg, Erlangen, Germany, [3] Erich and Hanna Klessmann Institute, Clinic for Thoracic and Cardiovascular Surgery, Heart and Diabetes Center NRW, Ruhr University Bochum, Bad Oeynhausen, Germany, [4] Muscle Research Center Erlangen (MURCE), Friedrich-Alexander-Universität Erlangen-Nürnberg, Erlangen, Germany, [5] Walter Brendel Centre of Experimental Medicine, University Hospital, LMU Munich, Munich, Germany, [6] Department of Anaesthesiology, University Hospital, LMU Munich, Munich, Germany, [7] German Center for Cardiovascular Research (DZHK), Partner Site Munich Heart Alliance, Munich, Germany

OPEN ACCESS

Edited by:
Remi Peyronnet,
University of Freiburg, Germany

Reviewed by:
Corrado Poggesi,
University of Florence, Italy
Theresia Kraft,
Hannover Medical School, Germany
Joachim Meißner,
Hannover Medical School, Germany
contributed to the review of TK

****Correspondence:***
Tilmann Volk
tilmann.volk@fau.de
Thomas Seidel
thomas.seidel@fau.de

Specialty section:
This article was submitted to
Striated Muscle Physiology,
a section of the journal
Frontiers in Physiology

Received: *22 November 2019*
Accepted: *17 February 2020*
Published: *13 March 2020*

Citation:
Abu-Khousa M, Fiegle DJ,
Sommer ST, Minabari G, Milting H,
Heim C, Weyand M, Tomasi R,
Dendorfer A, Volk T and Seidel T
(2020) The Degree of t-System
Remodeling Predicts Negative
Force-Frequency Relationship
and Prolonged Relaxation Time
in Failing Human Myocardium.
Front. Physiol. 11:182.
doi: 10.3389/fphys.2020.00182

The normally positive cardiac force-frequency relationship (FFR) becomes flat or negative in chronic heart failure (HF). Here we explored if remodeling of the cardiomyocyte transverse tubular system (t-system) is associated with alterations in FFR and contractile kinetics in failing human myocardium. Left-ventricular myocardial slices from 13 failing human hearts were mounted into a biomimetic culture setup. Maximum twitch force (F), 90% contraction duration (CD_{90}), time to peak force (TTP) and time to relaxation (TTR) were determined at 37°C and 0.2–2 Hz pacing frequency. $F_{1Hz}/F_{0\cdot5Hz}$ and $F_{2Hz}/F_{0\cdot5Hz}$ served as measures of FFR, intracellular cardiomyocyte t-tubule distance (ΔTT) as measure of t-system remodeling. Protein levels of SERCA2, NCX1, and PLB were quantified by immunoblotting. $F_{1Hz}/F_{0\cdot5Hz}$ (R^2 = 0.82) and $F_{2Hz}/F_{0\cdot5Hz}$ (R^2 = 0.5) correlated negatively with ΔTT, i.e., samples with severe t-system loss exhibited a negative FFR and reduced myocardial wall tension at high pacing rates. PLB levels also predicted $F_{1Hz}/F_{0\cdot5Hz}$, but to a lesser degree (R^2 = 0.49), whereas NCX1 was not correlated (R^2 = 0.02). CD_{90} correlated positively with ΔTT (R^2 = 0.39) and negatively with SERCA2/PLB (R^2 = 0.42), indicating that both the t-system and SERCA activity are important for contraction kinetics. Surprisingly, ΔTT was not associated with TTP (R^2 = 0) but rather with TTR (R^2 = 0.5). This became even more pronounced when interaction with NCX1 expression was added to the model (R^2 = 0.79), suggesting that t-system loss impairs myocardial relaxation especially when NCX1 expression is low. The degree of t-system remodeling predicts FFR inversion and contraction slowing in failing human myocardium. Moreover, together with NCX, the t-system may be important for myocardial relaxation.

Keywords: heart failure, cardiac excitation-contraction coupling, cardiac remodeling, human heart, force frequency relationship, transverse tubular system

INTRODUCTION

The myocardial force-frequency relationship (FFR), also referred to as staircase phenomenon, describes the frequency-dependent change of cardiac contractile force in the absence of other external stimuli and is therefore considered as an intrinsic regulatory mechanism of the heart. Most mammals, including humans, exhibit a positive FFR in the physiological range of heart rates (Janssen and Periasamy, 2007). Because heart rate is increased predominantly at the expense of ventricular filling time, end-diastolic volume decreases at high heart rates. Therefore, systolic force and contraction velocity must increase to maintain a high stroke volume during physical activity (Higginbotham et al., 1986), which, in addition to sympathetic activation, may be facilitated by a positive FFR.

It is widely accepted that dynamic changes in intracellular Ca^{2+} underlie the FFR. At high heart rates, increased influxes of Ca^{2+} and Na^+ due to more frequent action potentials cause respective rises in intracellular concentrations. This leads to increased Ca^{2+} load of the sarcoplasmic reticulum (SR), because more cytosolic Ca^{2+} is available for the SR Ca^{2+} ATPase (SERCA). Additionally, the increased amount of intracellular Na^+ reduces the driving force for the sodium-calcium exchanger (NCX). As a consequence, the relative contribution of SERCA to cytosolic Ca^{2+} removal increases. The overall effect is an increase in contractile force. However, while this is one common explanation for the positive FFR in healthy myocardium, additional mechanisms have been suggested (Endoh, 2004; Janssen and Periasamy, 2007), and it remains not completely understood how these mechanisms are altered in diseased myocardium.

The normally positive FFR becomes flat or negative in failing human myocardium (Mulieri et al., 1992). This is thought to contribute to poor cardiac function in heart failure patients, especially under conditions of cardiac stress (Hasenfuss et al., 1994a). It has been shown that altered expression levels and activities of Ca^{2+} cycling proteins, such as SERCA (Hasenfuss et al., 1994b; Munch et al., 2000), PLB (Hasenfuss et al., 1996; Brixius et al., 2003) and NCX (Hasenfuss et al., 1999) are associated with the negative FFR in human failing myocardium.

However, another important requirement for efficient Ca^{2+} cycling and excitation-contraction coupling in ventricular cardiomyocytes is the transverse tubular system (t-system). The t-system is formed by regularly arranged membrane tubules running from the surface into the cytosol, where they form close junctions with the SR. By bringing L-type Ca^{2+} channels close to ryanodine receptors in the SR, Ca^{2+}-induced Ca^{2+} release is largely facilitated. Additionally, t-tubules contain a high density of NCX, which may facilitate Ca^{2+} extrusion across the cell membrane (Thomas et al., 2003). A common feature of failing myocardium is remodeling and loss of the t-system (Kostin et al., 1998). The remodeling includes changes in t-tubule structure and reduced density of the t-system and has been associated with poor cardiac function and impaired recovery (Seidel et al., 2017a). Because t-system remodeling impairs intracellular Ca^{2+} cycling and causes slowed as well as reduced Ca^{2+} release (Louch et al., 2004; Seidel et al., 2019), we hypothesized that t-system remodeling may be associated with FFR inversion and altered contractile kinetics.

In this report we explored the correlation of t-system remodeling with the FFR and contraction kinetics in myocardial tissue slices from failing human hearts. We show that high degrees of t-system remodeling are associated with negative FFR and slowed contraction. Furthermore, we show that an interaction between NCX expression and t-system density may predict myocardial relaxation time.

METHOD

Methods are described in detail in the **Supplementary Material**.

Human Cardiac Samples

Transmural myocardial samples were collected from end-stage failing hearts with reduced ejection fraction from the left-ventricular (LV) apical core during implantation of mechanical assist devices or from the free LV wall of explanted hearts. An overview of the patients is displayed in **Supplementary Table S1**. Collection and use of human cardiac tissue samples was approved by the Institutional Review Boards of the University of Erlangen-Nürnberg, the Ruhr-University Bochum and the Ludwig-Maximilian University Munich. Studies were conducted according to Declaration of Helsinki principles. Patients gave their written informed consent prior to tissue collection.

Sample Preparation and Analysis of Contractile Parameters

Following a published method for stable cultivation of human myocardium (Fischer et al., 2019), myocardial slices of 300 μm thickness and approximately 5mm × 5mm length and width were cut with a high-precision vibratome (Leica VT1200S) and installed into biomimetic cultivation chambers at 37°C. Electrodes and a force-transducing wire included in the chambers allowed for continuous electrical stimulation and monitoring of contractile force during auxotonic (elastic) contraction (see **Supplementary Figure S1**). The sarcomere length at different degrees of preload was assessed in initial experiments by α-actinin staining. Preload was then set to 1.5 mN/mm^2 in all slices to obtain a resting sarcomere length between 2.0 and 2.1 μm (see **Supplementary Figure S2**), which is close to the optimum suggested for stable cultivation of myocardial tissue (Watson et al., 2019).

For all cultivated myocardial slices, the baseline stimulation rate was 0.5 Hz. The FFR and single-contraction parameters were assessed within 24 h after installation, using a protocol with intervals of 120 s duration and increasing stimulation frequencies of 0.2, 0.5, 1, and 2 Hz. Contractions during the last 30 s of each interval were analyzed with custom-written software scripts (Matlab 2019a). For each contraction, maximal force (F_{max}), time to peak (TTP), time to relaxation (TTR) and 90% contraction duration (CD_{90}) were analyzed and then averaged over the 30 s interval. Actively developed wall tension (T) was calculated by dividing the developed force (F) by the cross-sectional area (A): $T = F/A$. To estimate A, the width of the slices (5 mm) was multiplied with the nominal thickness (300 μm) minus 50 μm, assuming that the very top and bottom myocyte layers were damaged during the slicing: $A = 5\text{mm} \times 0.25\text{mm} = 1.25\text{mm}^2$.

Immunostaining and Confocal Imaging

Neighboring tissue slices of the functionally assessed slices were fixed with 2% PFA immediately after slicing and stained with AF647-conjugated wheat germ agglutinin (WGA, Thermo Fisher, W32466) to visualize the extracellular matrix, surface sarcolemma and t-tubules. RyR2 (Thermo Fisher, MA3-916) or α-actinin (A7811, Sigma) were co-stained with AF488 (A21121, Thermo Fisher). For the validation of the WGA staining, human tissue was co-stained with a mouse monoclonal anti-caveolin-3 antibody (sc-5310, Santa Cruz, CA, United States) and WGA (see **Supplementary Figure S3**).

The samples were mounted in Fluoromount G (Sigma, F4680) and 3D confocal image stacks (1280 × 1280 × 300 voxels, voxel size $0.1 \times 0.1 \times 0.1\ \mu\text{m}^3$) were acquired with a Zeiss LSM780 confocal microscope with a 63× oil immersion lens. At least 3 image stacks from each sample were recorded from randomly chosen regions. Additionally, two-dimensional confocal tile scans (1–5 mm^2) were acquired with a pixel size of $0.15 \times 0.15\ \mu\text{m}^2$. The researchers were blinded against functional parameters.

Image Analysis

Applying published methods (Seidel et al., 2013, 2016, 2017a,b), confocal image stacks were corrected for depth-dependent attenuation and then filtered, deconvolved and segmented, using histogram-based thresholds. By applying automated analysis scripts, the cardiomyocyte t-system could be distinguished from the outer sarcolemma and interstitial space, using either RyR or α-actinin as cardiomyocyte marker (Seidel et al., 2017a,b). Sarcomere length was determined by 2D Fourier transformation of α-actinin images and identification of the maximum in the power spectrum within a spatial frequency of 1/2.5 to 1/1.5 μm^{-1} (Seidel et al., 2017b). As a measure of t-system remodeling, we calculated the mean intracellular distance to the closest t-tubule (ΔTT), using the three-dimensional Euclidean distance transform of the extracted t-tubule signal and the cardiomyocyte mask (mean ΔTT from at least 3 image stacks per myocardial sample). To assess cardiomyocyte disarray, large area confocal tile scans (1–5 mm^2) were noise-filtered, deconvolved and then subjected to a watershed-based cardiomyocyte segmentation method published previously (Seidel et al., 2013). In brief, the watershed seeds were generated from the distance transform of the WGA image, followed by a morphological watershed segmentation with the distance transform as gradient image. Subsequently, segments with low contact area to the WGA signal were removed and the watershed run again. This process was iterated until most myocytes contained only one segment. The main axis orientation of myocytes was then determined by calculating the eigenvectors of the covariance matrix (2nd order central image moments) of each segment as described (Lackey et al., 2011).

Western Blotting

Small transmural tissue blocks from each sample were frozen at −80°C and used later for Western blot analysis. Primary antibodies against SERCA2, NCX1, PLB and phosphorylated PLB (pS16 and pT17) were used. Densitometric measurements were performed with ImageJ/Fiji software and normalized to the geometric means of Ponceau staining and GAPDH. To make samples from different blots comparable, we additionally normalized to a reference, which was added to each gel. A more detailed description of Western blotting, including antibody specifications, is available in the **Supplementary Material**.

Statistics

For each myocardial sample, contractile parameters (force, TTR, TTP, CD90, FFR) were assessed simultaneously in 2–8 neighboring tissue slices and the medians used as representative measures for subsequent statistical analyses. Correlation between parameters was tested by linear regression (fitlm function, Matlab version R2019a) with least squares fitting. *P*-values reported for linear models were obtained from an *F*-test against the corresponding constant model (intercept only, i.e., no effect of the predicting variable). *P*-values below 0.05 (type I error) were considered significant. The unpaired two-tailed student's *t*-test was used to compare means between different groups. The Holm-Bonferroni method was used to correct *P*-values for multiple comparisons. If not indicated otherwise, data are reported as mean ± standard error (SEM).

RESULTS

Variable t-System Density and Frequency Response Amongst Myocardial Samples

We obtained LV myocardial samples from 13 patients suffering from end-stage heart failure (LV ejection fraction 20.6 ± 7%, **Supplementary Table S1**) undergoing either LVAD implantation ($n = 5$) or heart transplantation ($n = 8$). In vibratome-cut myocardial slices of 300 μm thickness we assessed the FFR over a frequency range from 0.2 to 2 Hz and stained the extracellular matrix and cell membranes including the t-system with WGA. Reliable staining of t-tubules with WGA was verified by co-staining of caveolin-3, a commonly used membrane marker of cardiomyocytes (**Supplementary Figure S3**). Three-dimensional confocal microscopic images showed a substantial variability in the degree of t-tubular remodeling between samples from different patients (**Figures 1A–D**). While some samples presented with a dense and well-preserved t-system and, accordingly, low intracellular t-tubule distances (ΔTT) (**Figures 1A,B**), others displayed severe t-system loss, resulting in high ΔTT (**Figures 1C,D**). Inspection of the corresponding FFRs revealed positive relationships in samples with low ΔTT, i.e., preserved t-system (**Figure 1E**). In these samples the maximum twitch force increased with increasing stimulation frequency. In contrast, samples with high ΔTT, i.e., t-system loss, exhibited a flat response at lower frequencies and a clearly negative

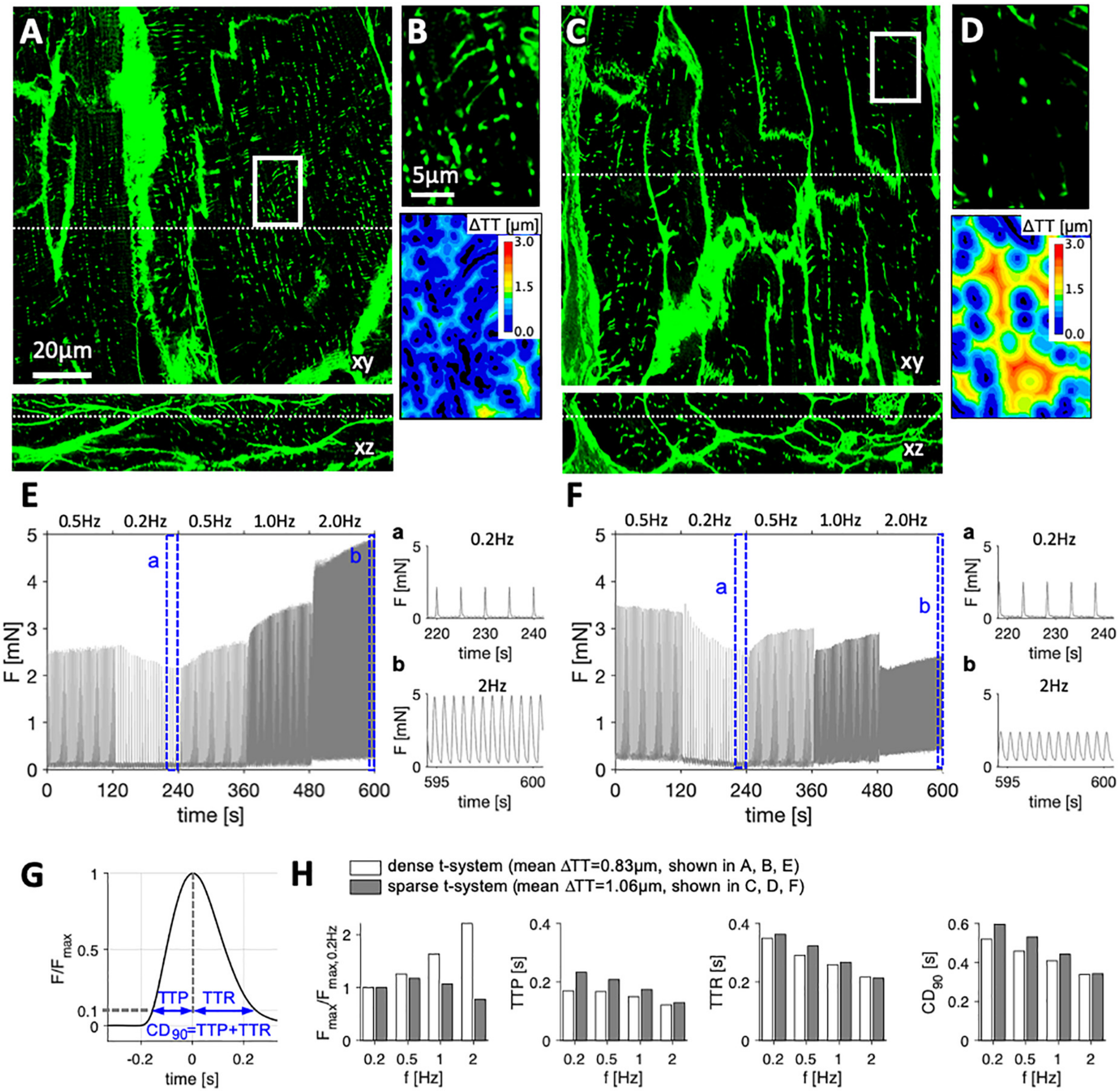

FIGURE 1 | Examples of tissue slices from myocardial specimens with high and low degree of t-system remodeling and corresponding force-frequency relationship. Three-dimensional confocal images in xy and xz views of left-ventricular myocardial tissue slices stained with wheat germ agglutinin from **(A,B)** specimen with dense t-system, and **(C,D)** specimen with sparse t-system. B and D show the respective magnifications of the boxed regions in A and C, and the corresponding 3D distance maps (color-coded distance to closest t-tubule, ΔTT). Dotted lines in A and C indicate the optical sections of the xy and xz views. **(E,F)** Twitch forces of myocardial slices from the specimens shown in A and C, respectively, stimulated with increasing pacing frequency. The highlighted intervals (a, b) are magnified. **(G)** Exemplary trace of one twitch, normalized to its maximum force (F_{max}) with schematic of assessed contraction parameters: time to peak (TTP), time to relaxation (TTR) and 90% contraction duration (CD_{90}). **(H)** Normalized F_{max}, TTP, TTR and CD_{90} at the assessed frequencies in the two examples shown in A (example with low ΔTT, i.e., dense t-system) and in C (example with high ΔTT, i.e., sparse t-system). Scale bar in A also applies to C, scale bar in B also applies to D.

response at higher frequencies (**Figure 1F**). We compared self-normalized forces and the following parameters of contraction kinetics: time to peak force (TTP), time to relaxation (TTR) and 90% contraction duration (CD_{90}, **Figure 1G**). **Figure 1H** shows that the maximum force in the sample with preserved t-system (low ΔTT) increased more than twofold from 0.2 to 2 Hz, but decreased by approximately 25% in the sample with reduced t-system density (high ΔTT). TTP, TTR, and CD_{90} fitted well to values reported in other studies (Mulieri et al., 1992; Rossman et al., 2004) and decreased consistently in both samples with increasing pacing frequency, but higher values of TTP, TTR, and CD_{90} indicated slowed contraction in the example with t-system loss, especially at low pacing frequencies. In conclusion, the results shown in **Figure 1** illustrate that the degree of t-system loss might be related to the FFR and contraction kinetics.

The Degree of t-System Remodeling Predicts the Degree of FFR Inversion

In order to evaluate if ΔTT may generally predict the FFR in failing human myocardium, we performed linear regression including the functional and histological data from all available samples. Mean ΔTT values, acquired from at least 3 confocal image stacks at randomly chosen regions of the tissue slices, ranged from approximately 0.8 to 1.5 μm. This most likely reflects the high regional heterogeneity of t-system loss across the left ventricle in failing hearts, as previously described (Crossman et al., 2015), see discussion. As measures of the FFR, we used the ratio between the maximum force amplitudes at 1 and 0.5 Hz ($F_{1Hz}/F_{0.5Hz}$) as well as 2 and 0.5 Hz ($F_{2Hz}/F_{0.5Hz}$). Values above or below 1 thus indicate a positive or negative FFR, respectively. **Figure 2A** shows the linear regression of $F_{1Hz}/F_{0.5Hz}$ over ΔTT, which yielded a negative and highly significant relationship between the both parameters. This means that with increasing ΔTT the FFR became more negative ($R^2 = 0.82$, $p < 0.0001$). The model predicted inversion of the FFR ($F_{1Hz}/F_{0.5Hz} \leq 1$) at ΔTT $\geq$ 1.05 μm. Thus, we divided the samples into two groups of similar size: samples with low to moderate t-system loss (ΔTT < 1.05 μm, $n = 6$), and samples with severe t-system loss (ΔTT $\geq$ 1.05 μm, $n = 7$). We performed a *t*-test to compare the corresponding means of $F_{1Hz}/F_{0.5Hz}$ (**Figure 2B**). Mean $F_{1Hz}/F_{0.5Hz}$ in the group with ΔTT < 1.05 μm was 1.08 ± 0.05, indicating a slightly positive FFR, whereas the group with ΔTT $\geq$ 1.05 μm exhibited a markedly negative FFR (0.80 ± 0.05, $p < 0.01$). When analyzing the relationship between ΔTT and $F_{2Hz}/F_{0.5Hz}$ (**Figures 2C,D**), we found very similar results, although the coefficient of determination was not as high ($R^2 = 0.5$, $p < 0.01$). In accordance with these findings, mean maximum wall tension did not differ between the two groups at 0.2 and 0.5 Hz pacing frequency, but was distinctively higher at 1 and 2 Hz in the group with ΔTT < 1.05 μm than with ΔTT $\geq$ 1.05 μm (2.01 ± 0.46 vs. 0.72 ± 0.16 and 1.93 ± 0.44 vs. 0.71 ± 0.2, respectively, in mN/mm^2, $p < 0.05$) (**Figure 2E**). In summary, these data indicate that in human failing myocardium a frequency-related increase in contractile force may require a dense t-system and that the degree of t-system remodeling predicts to a substantial extent a functional decline in FFR.

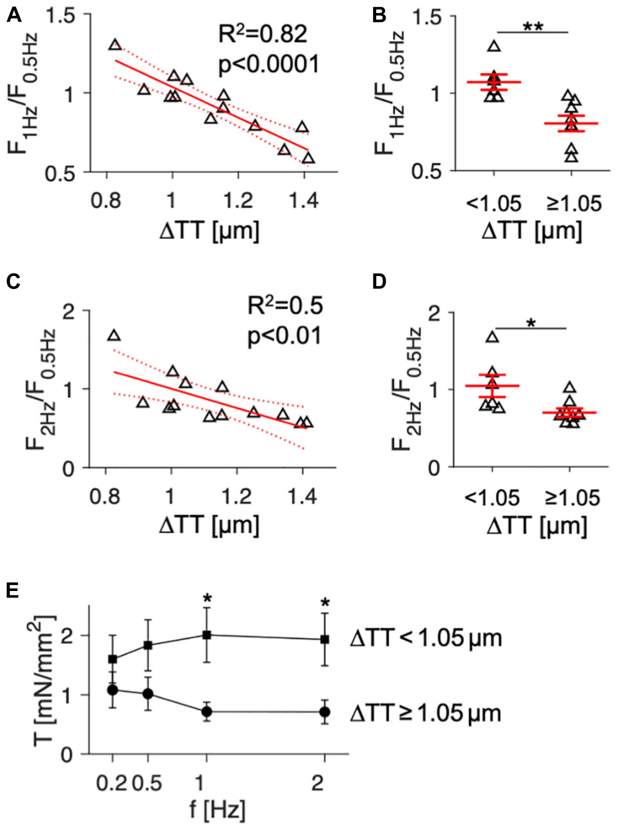

FIGURE 2 | Association of the force-frequency relationship and wall tension with cardiomyocyte t-tubule distance in tissue slices from human failing hearts ($n = 13$). **(A)** Linear model showing the correlation of force at 1 Hz relative to force at 0.5 Hz pacing rate ($F_{1Hz}/F_{0.5Hz}$) with t-tubule distance (ΔTT). R^2 is the coefficient of determination, p indicates the probability of type I error of linear regression. Dotted lines indicate 95% confidence intervals. **(B)** $F_{1Hz}/F_{0.5Hz}$ in specimens with low (<1.05 μm, $n = 7$) and high ΔTT ($\geq$1.05 μm, $n = 7$). Note that low ΔTT indicates high t-tubule density. **(C)** Correlation of force at 2 Hz relative to force at 0.5 Hz pacing rate ($F_{2Hz}/F_{0.5Hz}$) with ΔTT. **(D)** $F_{2Hz}/F_{0.5Hz}$ in specimens with low and high ΔTT. **(E)** Mean wall tension (T) developed actively during contraction in specimens with low (squares) and high ΔTT (circles) at 0.2–2 Hz pacing frequency (f). $^*p < 0.05$, $^{**}p < 0.01$ (unpaired, two-tailed *t*-test, multiple comparison adjustment in E), error bars indicate SEM.

Association of Ca^{2+} Cycling Proteins With FFR

Next, to investigate if Ca^{2+} cycling proteins reported to correlate with the FFR of human failing myocardium predict the FFR to a similar extent as the degree of t-system remodeling, we used Western blotting to quantify protein expression levels of NCX1, SERCA2, and PLB, including its phosphorylated forms pS16 and pT17 (**Figure 3A**). In 4 out of the 13 samples, the amount of available tissue was not sufficient for protein analysis. Probing for NCX1 yielded clear bands at 120kDa and 70kDa, as described in other studies using the same primary antibody. Because both bands have been shown to represent functional forms of NCX1, we included both in our analyses (McDonald et al., 2000). We found that the expression of Ca^{2+} cycling proteins varied considerably and that the FFR did not correlate with NCX1 or SERCA2 (**Figures 3B,C**). However, $F_{1Hz}/F_{0.5Hz}$ showed a significant negative correlation with total PLB. Samples with negative FFR displayed higher levels of PLB than samples with positive FFR ($R^2 = 0.49$, $p < 0.05$, **Figure 3D**). Using the SERCA2/PLB ratio improved the prediction only marginally ($R^2 = 0.52$, $p < 0.05$, **Figure 3E**). We also explored whether the extent of PLB inhibition by phosphorylation through PKA (PLBpS16) or CAMKII (PLBpT17) was associated with the FFR. While PLBpS16 and the PLBpS16/PLB ratio did not predict the FFR, the PLBpT17/PLB ratio showed a moderate positive association ($R^2 = 0.44$, $p < 0.05$, **Supplementary Table S2**). These results indicate that SERCA2 or NCX1 expression alone were poor predictors of the FFR and that proteins and measures reflecting SERCA2 activity (PLB, SERCA2/PLB ratio,

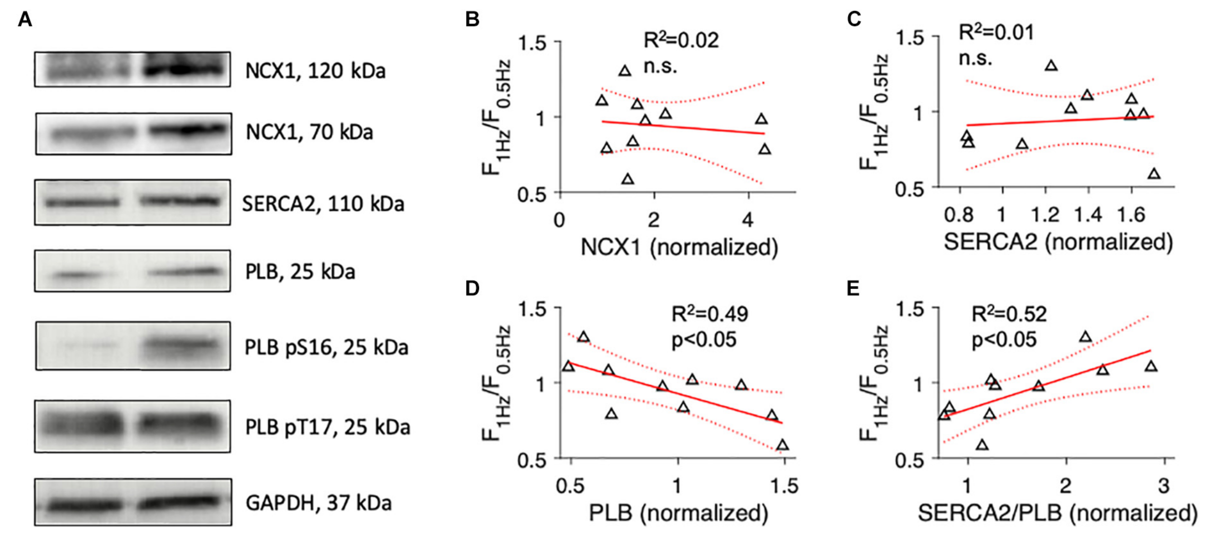

FIGURE 3 | Association of the force-frequency relationship with expression levels of proteins involved in cardiomyocyte Ca^{2+} cycling. **(A)** Example images of Western blots of cardiac sodium-calcium exchanger (NCX1), cardiac sarco/endoplasmic reticulum Ca^{2+}-ATPase (SERCA2), total phospholamban (PLB), phospho-S16 (pS16) PLB, phospho-T17 (pT17) PLB, and glyceraldehyde 3-phosphate dehydrogenase (GAPDH). **(B)** Linear model showing the correlation of force at 1 Hz relative to force at 0.5 Hz pacing rate ($F_{1Hz}/F_{0.5Hz}$) with NCX1 protein expression (normalized to a reference sample). R^2 is the coefficient of determination, p indicates the probability of type I error of linear regression. Dotted lines indicate 95% confidence intervals. **(C)** Correlation of $F_{1Hz}/F_{0.5Hz}$ with SERCA2 protein expression. **(D)** Correlation of $F_{1Hz}/F_{0.5Hz}$ with total PLB protein expression. **(E)** Correlation of $F_{1Hz}/F_{0.5Hz}$ with the ratio of SERCA2 to total PLB.

PLBpT17/PLB ratio) predicted the FFR significantly better, but not to the same extent as ΔTT (**Figure 2A**).

T-System Loss Is Associated With Slowed Myocardial Relaxation

We then sought to investigate parameters of contractile kinetics. Because contraction kinetics, especially relaxation time, may depend on diastolic sarcomere length (Janssen, 2010), we assessed the degree of cardiomyocyte disarray (Varnava et al., 2001) to rule out that differing fractions of non-aligned myocytes would affect the results (**Supplementary Figure S4**). Analyzing 2D confocal tile scans of 10 samples, we found that myocyte main axis orientation showed a standard deviation (dispersion) of 18.9 ± 1° and that 11.1 ± 1.8% of the myocytes deviated by more than 30° from the main fiber orientation. Both measures were similar in samples with high and low t-system density (**Supplementary Figures S4F,G**), allowing the conclusion that myocyte disarray did not bias contraction kinetics. We analyzed individual contractions recorded at 1 Hz stimulation frequency and determined the mean TTP, TTR, and CD_{90} for each sample during a 30 s interval. We then fitted linear models with TTP, TTR or CD_{90} as dependent variables and either SERCA2/PLB (**Figures 4A–C**) or ΔTT (**Figures 4D–F**) as predicting parameters. TTP and TTR showed a negative trend with increasing SERCA2/PLB ratio, but statistical significance was reached for CD_{90} only (**Figure 4C**, $R^2 = 0.42$, $p < 0.05$). This suggests that the trends on force increase and relaxation time add up and cause a prolonged contraction duration at low SERCA activity. Similar results were obtained for the PLBpT17/PLB ratio ($R^2 = 0.49$, data not shown). To our surprise, ΔTT did not correlate with TTP (**Figure 4D**), but rather with TTR and CD_{90} ($R^2 = 0.5$ and $R^2 = 0.39$, respectively, $p < 0.05$, **Figures 4E,F**). This prompted us to test for a relationship between NCX1 and TTR, and interactions between NCX1 and ΔTT, because the velocity of cytosolic Ca^{2+} extrusion via NCX1 may contribute to myocardial relaxation particularly in failing hearts (Hasenfuss et al., 1999). Moreover, NCX1 density has been reported to be high in t-tubules (Thomas et al., 2003). While NCX1 expression was not associated with relaxation time (**Figure 4G**) or ΔTT ($R^2 = 0.1$, n.s., data not shown), we found that a multivariate model including ΔTT and the interaction of ΔTT with NCX1 (ΔTT.NCX) predicted TTR significantly better than NCX1 expression or ΔTT alone ($R^2 = 0.79$, $p < 0.01$, **Figure 4H**). The data indicate that with increasing degrees of t-system loss contraction duration is prolonged, and that the prolongation is mainly due to an increased relaxation time, which not only depends on the t-system, but also on NCX expression. This can be interpreted as an increased influence of the t-system on relaxation time when NCX expression is low.

DISCUSSION

A reduced contractile reserve is a hallmark of chronic heart failure and leads to exacerbation of symptoms especially under conditions of cardiac stress, for example during physical activity. While in healthy myocardium, the FFR contributes to adaptation of cardiac output to increased demands, the intrinsic cardiac mechanisms are blunted or even inverted in failing myocardium (Mulieri et al., 1992; Schwinger et al., 1994). Furthermore, impaired myocardial relaxation may add to reduced diastolic filling in certain types of heart failure. Although the cellular and

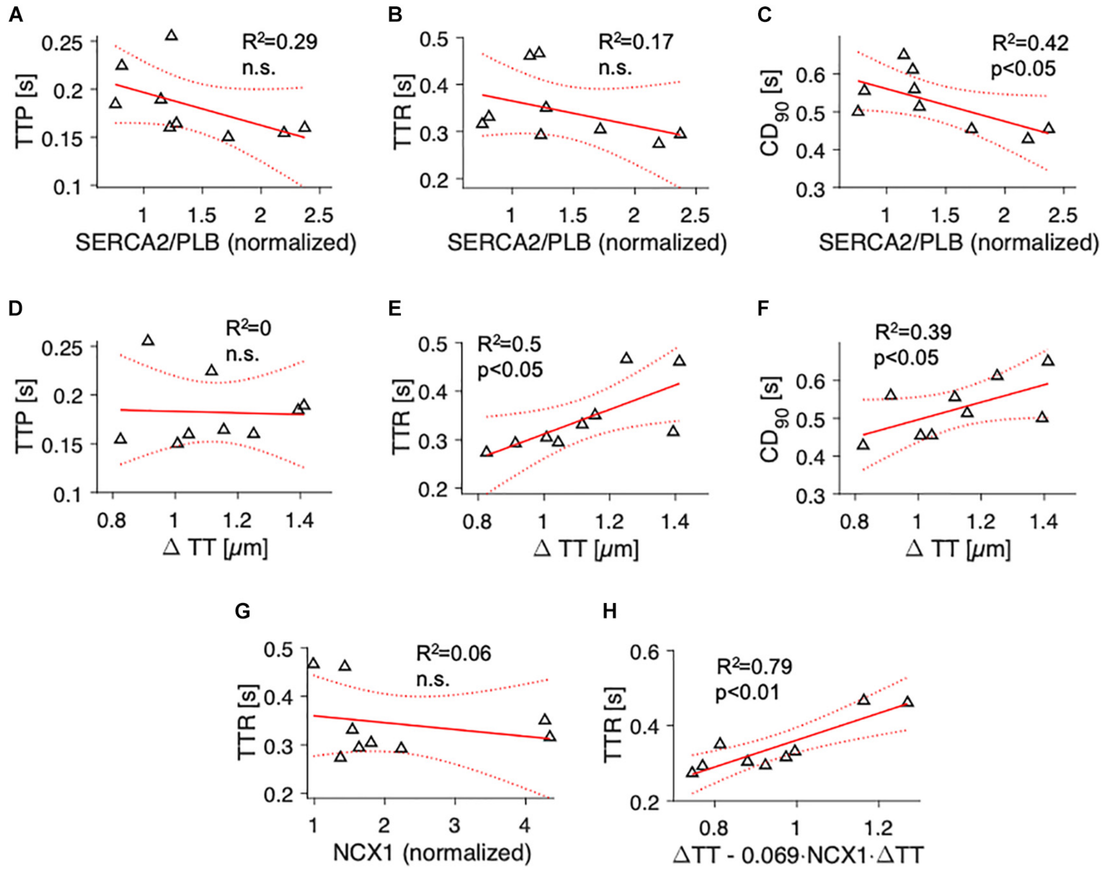

FIGURE 4 | Association of contraction parameters at 1 Hz pacing rate with SERCA2/PLB ratio, t-tubule distance and NCX1 expression. Linear models showing the correlation of **(A)** time to peak (TTP), **(B)** time to relaxation (TTR), and **(C)** 90% contraction duration (CD$_{90}$) with SERCA2/PLB, and of **(D)** TTP, **(E)** TTR and **(F)** CD$_{90}$ with t-tubule distance (ΔTT). R^2 is the coefficient of determination, p indicates the probability of type I error of linear regression. Dotted lines indicate 95% confidence intervals. **(G)** Correlation of TTR with NCX1. **(H)** Multivariate regression model combining ΔTT and the interaction of ΔTT with NCX (ΔTT + ΔTT:NCX) as predictors of TTR. The fitted model, $TTR = 0.36 \cdot (\Delta TT - 0.069 \cdot NCX1 \cdot \Delta TT)$, explains the variance in TTR significantly better than simple linear models with only NCX1 ($p < 0.001$) or ΔTT ($p = 0.01$, likelihood ratio test).

molecular mechanisms leading to these functional impairments have been intensively studied, they are still not entirely clear. It is unknown if remodeling of the t-system, which commonly occurs in chronic heart failure, contributes to FFR inversion and slowing of contraction in intact myocardium from failing human hearts. Here, we describe a close correlation of t-system loss with negative FFR and altered contractile kinetics in human myocardial tissue slices, using confocal microscopy and a recently published method for biomimetic assessment and culture of human myocardium (Fischer et al., 2019). With this, we provide additional evidence that t-system remodeling is an important pathomechanism in heart failure and may predict myocardial dysfunction on a very small spatial scale.

T-System and FFR

Our results show that there was a high variability in the functional myocardial response to increasing stimulation frequency. This may be surprising, because all patients suffered from end-stage heart failure with severely reduced LV ejection fraction (**Supplementary Table S1**), and it was shown that the FFR is blunted or reversed on the whole-heart level in heart failure patients (Hasenfuss et al., 1994a). One might therefore expect a negative FFR in all samples. However, considering the finding that myocardial contractility as well as t-system remodeling vary within failing hearts (Crossman et al., 2015), it becomes clear that samples taken randomly from the LV free wall as done in this study, show variations in structure and function. In fact, others also reported high variations in FFR amongst muscle strips obtained from failing hearts (Hasenfuss et al., 1994b). Here, we demonstrate that t-system distance, a histological parameter measuring the degree of t-system loss and remodeling (Seidel et al., 2017a), predicts the FFR with comparable or even higher accuracy than previously reported parameters of protein expression (Hasenfuss et al., 1994b). T-system remodeling may contribute to reduced force development at higher stimulation frequencies by causing decreased and slowed SR Ca^{2+} release due to impaired coupling between L-type Ca^{2+} channels and ryanodine receptors (Louch et al., 2004; Seidel et al., 2019). This may reduce the contractile reserve when fast Ca^{2+} cycling is required.

We also found that high PLB protein expression levels were associated with a negative FFR, suggesting that SERCA inhibition hindered the force increase at high pacing rates. Consistently, a high ratio of PLBpT17 to total PLB, which may reflect SERCA activity, correlated positively with the FFR, whereas SERCA expression levels did not. This is in accordance with a study in failing and non-failing human myocardium reporting a positive correlation of the FFR with SERCA activity, but not with SERCA protein levels (Munch et al., 2000). However, it appears to be in contrast with a study demonstrating that SERCA and PLB overexpression decreased and increased the frequency response, respectively, in isolated rabbit cardiomyocytes (Meyer et al., 1999) and another study reporting that PLB knockout blunts the FFR in mouse hearts (Wu et al., 2012). A possible explanation is that in the cases of SERCA overexpression or PLB knockout SR Ca^{2+} capacity is close to its maximum already at low pacing frequencies and therefore cannot increase at higher frequencies (Janssen and Periasamy, 2007). The degree of PLB phosphorylation at the CAMKII-specific site T17 may reflect CAMKII activity in a sample and therefore correlate positively with the FFR, as CAMKII has been implied as an important modulator of the frequency response (Zhao et al., 2004; Wu et al., 2012). However, considering that CAMKII is activated by cytosolic Ca^{2+}, it seems as well possible that increased fractions of PLBpT17 indicate higher intracellular Ca^{2+} levels, which in turn could result from higher t-system density. This becomes clear from the large contribution of the t-system to membrane surface area (Despa et al., 2003; Pasek et al., 2008) and a particularly high density of L-type Ca^{2+} channels in t-tubules (Brette et al., 2006; Seidel et al., 2019). Thus, assuming that L-type Ca^{2+} current density is unaltered or even decreased in samples with low t-system density, a reduction in membrane surface would result in diminished Ca^{2+} influx and might limit the accumulation of intracellular Ca^{2+} required for a positive FFR, especially when the contribution from SR Ca^{2+} is low (Stemmer and Akera, 1986; Endoh, 2004). This mechanism could link t-system density to CAMKII activity, but its investigation would require freezing of the tissue slices immediately after pacing with different frequencies. Here, we quantified PLBpT17 levels at rest only. PLB and the PLBp17/PLB ratio correlated moderately with ΔTT (R^2 = 0.48 and 0.37, respectively). However, dividing the cohort into samples with low and high PLB levels, using the corresponding median as threshold, still yielded high correlations of ΔTT with the FFR ($R^2 > 0.7$, $p < 0.05$), suggesting that the t-system and resting PLBpT17/PLB levels are independently related to the FFR.

The finding that t-system loss predicts negative FFR, which translates into reduced myocardial wall tension at high pacing rates (**Figure 1E**), fits well to results from other studies. Acutely detubulated rat myocardium showed a blunted FFR (Ferrantini et al., 2014). Assuming that SERCA and PLB are not affected by detubulation, this may additionally indicate that the dependence of a positive FFR on high t-system density is not confounded by altered SERCA activity in samples with t-system loss. Another study showed that the FFR is flat in human newborns and becomes positive in infants. At the same time, t-tubules develop in ventricular cardiomyocytes (Wiegerinck et al., 2009). Collectively, these findings support the hypothesis that the t-system is required for a positive FFR in human ventricular cardiomyocytes.

T-System and Contractile Kinetics

In addition to the relationship between the t-system and FFR, we found that t-system loss was associated with slowed contractile kinetics. TTP, however, did not correlate with ΔTT, although acute detubulation was reported to prolong the twitch peak time in rat ventricular trabeculae (Ferrantini et al., 2014). It is possible that due to slower contraction velocity in human than rat hearts (Milani-Nejad and Janssen, 2014), contraction velocity in the rat depends more steeply on the t-system. Moreover, t-system density in rat myocytes is markedly higher than in normal human myocytes (Jayasinghe et al., 2012). T-system loss in rat cardiomyocytes may thus lead to a more pronounced decrease in contraction velocity. Here, a relationship between ΔTT and TTP was not detectable, possibly because of varying age, underlying disease or drug therapy in the samples. Another factor that could affect contractile kinetics is resting sarcomere length (Janssen, 2010). Although we applied a defined diastolic preload to all samples, and found that the degree of myocyte disarray was similar in samples with low and high t-system density (**Supplementary Figures S2, S4**), we cannot fully exclude that variability stemming from tissue preparation may have masked a possible correlation between ΔTT and TTP. Nevertheless, we did find that ΔTT predicted relaxation time and overall contraction duration. This is consistent with slowed contraction as well as slowed relaxation time observed in acutely detubulated rat myocardium (Ferrantini et al., 2014). As an underlying mechanism we suggest a slowed decay of the intracellular Ca^{2+} transient, because Ca^{2+} removal via NCX is hindered when t-system density is low (Thomas et al., 2003; Ferrantini et al., 2014). This effect may be especially pronounced in human failing myocardium, where the relative contribution of NCX to Ca^{2+} removal seems to be increased because of SERCA downregulation (Hasenfuss et al., 1999). It is well possible that an intact t-system is required for efficient NCX function because the diffusion of intracellular Ca^{2+} ions to the surface sarcolemma may take much longer than to intracellularly located t-tubules. If these are lost, Ca^{2+} extrusion will consequently be slowed, leading to prolonged relaxation time. We provide some evidence for this idea by showing that a linear model taking into account the interaction of ΔTT with NCX predicted the relaxation time significantly better than ΔTT or NCX alone. The negative interaction term in the resulting model points to an increased influence of ΔTT on relaxation time when NCX expression is low. Thus, increased expression levels of NCX found in failing myocardium (Hasenfuss et al., 1996, 1999) might compensate not only for reduced SERCA activity, but also for t-system loss. Based on these exploratory findings we propose a role of the t-system in conjunction with NCX for myocardial relaxation. However, this hypothesis will have to be tested in future studies.

Limitations

The heart failure patients from whom samples were obtained in this study were heterogeneous regarding etiology, pharmacological treatments and concomitant diseases. Thus, although, the sample size used here ($n = 13$) was comparable to that of other studies (Mulieri et al., 1992; Hasenfuss et al., 1994b; Munch et al., 2000), a larger number of samples would be required to increase statistical power for subgroup analyses, to investigate the influence of clinical parameters on the functional and histological myocardial parameters, and to increase robustness against statistical outliers. However, despite the heterogeneity of the cohort, the main results, that is, correlation of t-system loss with negative FFR and, in conjunction with NCX1 expression, the prediction of slowed myocardial relaxation by t-system loss, showed high statistical significance. This was possibly reached because the structure-function relationships were assessed on a millimeter scale. It remains to be determined if t-system remodeling may predict cardiac function also on larger scales and how t-system remodeling varies across failing hearts.

DATA AVAILABILITY STATEMENT

The datasets generated for this study are available on request to the corresponding author.

ETHICS STATEMENT

The studies involving human participants were reviewed and approved by the Institutional Review Boards of the University of Erlangen-Nuremberg, the Ruhr-University Bochum and the Ludwig Maximilian University of Munich. The patients/participants provided their written informed consent to participate in this study.

AUTHOR CONTRIBUTIONS

TS, TV, AD, CH, MW, and HM contributed to the conception and design. MA-K, DF, SS, GM, RT, and TS contributed to the data acquisition and experiments. TS, MA-K, DF, and RT contributed to the data analysis. TS, TV, and MA-K contributed to the interpretation of the data. MA-K and TS contributed to the drafting of the manuscript. All authors revision and approval of the manuscript.

FUNDING

This work was supported by the DZHK (German Centre for Cardiovascular Research) and by the Interdisciplinary Centre for Clinical Research (IZKF) at the University Hospital of the University of Erlangen-Nuremberg.

ACKNOWLEDGMENTS

For excellent technical support we would like to thank Celine Grüninger and Lorenz McCargo from the Institute of Cellular and Molecular Physiology Erlangen as well as Caroline Stanasiuk and Desiree Gerdes from the Heart and Diabetes Center NRW. We also thank the Universitätsbund Erlangen-Nürnberg for financially supporting the vibratome.

SUPPLEMENTARY MATERIAL

The Supplementary Material for this article can be found online at: https://www.frontiersin.org/articles/10.3389/fphys.2020.00182/full#supplementary-material

REFERENCES

Brette, F., Salle, L., and Orchard, C. H. (2006). Quantification of calcium entry at the T-tubules and surface membrane in rat ventricular myocytes. *Biophys. J.* 90, 381–389. doi: 10.1529/biophysj.105.069013

Brixius, K., Wollmer, A., Bolck, B., Mehlhorn, U., and Schwinger, R. H. (2003). Ser16-, but not Thr17-phosphorylation of phospholamban influences frequency-dependent force generation in human myocardium. *Pflugers Arch.* 447, 150–157. doi: 10.1007/s00424-003-1163-3

Crossman, D. J., Young, A. A., Ruygrok, P. N., Nason, G. P., Baddelely, D., Soeller, C., et al. (2015). T-tubule disease: relationship between t-tubule organization and regional contractile performance in human dilated cardiomyopathy. *J. Mol. Cell Cardiol.* 84, 170–178. doi: 10.1016/j.yjmcc.2015.04.022

Despa, S., Brette, F., Orchard, C. H., and Bers, D. M. (2003). Na/Ca exchange and Na/K-ATPase function are equally concentrated in transverse tubules of rat ventricular myocytes. *Biophys. J.* 85, 3388–3396. doi: 10.1016/S0006-3495(03)74758-74754

Endoh, M. (2004). Force-frequency relationship in intact mammalian ventricular myocardium: physiological and pathophysiological relevance. *Eur. J. Harmacol.* 500, 73–86. doi: 10.1016/j.ejphar.2004.07.013

Ferrantini, C., Coppini, R., Sacconi, L., Tosi, B., Zhang, M. L., Wang, G. L., et al. (2014). Impact of detubulation on force and kinetics of cardiac muscle contraction. *J. Gen. Physiol.* 143, 783–797. doi: 10.1085/jgp.201311125

Fischer, C., Milting, H., Fein, E., Reiser, E., Lu, K., Seidel, T., et al. (2019). Long-term functional and structural preservation of precision-cut human myocardium under continuous electromechanical stimulation in vitro. *Nat. Commun.* 10:117. doi: 10.1038/s41467-018-08003-1

Hasenfuss, G., Holubarsch, C., Hermann, H. P., Astheimer, K., Pieske, B., and Just, H. (1994a). Influence of the force-frequency relationship on haemodynamics and left ventricular function in patients with non-failing hearts and in patients with dilated cardiomyopathy. *Eur. Heart. J.* 15, 164–170. doi: 10.1093/oxfordjournals.eurheartj.a060471

Hasenfuss, G., Reinecke, H., Studer, R., Meyer, M., Pieske, B., Holtz, J., et al. (1994b). Relation between myocardial function and expression of sarcoplasmic reticulum Ca(2+)-ATPase in failing and nonfailing human myocardium. *Circ. Res.* 75, 434–442. doi: 10.1161/01.res.75.3.434

Hasenfuss, G., Reinecke, H., Studer, R., Pieske, B., Meyer, M., Drexler, H., et al. (1996). Calcium cycling proteins and force-frequency relationship in heart failure. *Basic Res. Cardiol.* 91(Suppl. 2), 17–22. doi: 10.1007/bf00795357

Hasenfuss, G., Schillinger, W., Lehnart, S. E., Preuss, M., Pieske, B., Maier, L. S., et al. (1999). Relationship between Na+-Ca2+-exchanger protein levels and diastolic function of failing human myocardium. *Circulation* 99, 641–648. doi: 10.1161/01.cir.99.5.641

Higginbotham, M. B., Morris, K. G., Williams, R. S., McHale, P. A., Coleman, R. E., and Cobb, F. R. (1986). Regulation of stroke volume during submaximal and maximal upright exercise in normal man. *Circ. Res.* 58, 281–291. doi: 10.1161/01.res.58.2.281

Janssen, P. M. (2010). Myocardial contraction-relaxation coupling. *Am. J. Physiol. Heart Circ. Physiol.* 299, H1741–H1749. doi: 10.1152/ajpheart.00759.2010

Janssen, P. M., and Periasamy, M. (2007). Determinants of frequency-dependent contraction and relaxation of mammalian myocardium. *J. Mol. Cell. Cardiol.* 43, 523–531. doi: 10.1016/j.yjmcc.2007.08.012

Jayasinghe, I., Crossman, D., Soeller, C., and Cannell, M. (2012). Comparison of the organization of T-tubules, sarcoplasmic reticulum and ryanodine receptors in rat and human ventricular myocardium. *Clin. Exp. Pharmacol. Physiol.* 39, 469–476. doi: 10.1111/j.1440-1681.2011.05578.x

Kostin, S., Scholz, D., Shimada, T., Maeno, Y., Mollnau, H., Hein, S., et al. (1998). The internal and external protein scaffold of the T-tubular system in cardiomyocytes. *Cell Tissue Res.* 294, 449–460. doi: 10.1007/s004410051196

Lackey, D. P., Carruth, E. D., Lasher, R. A., Boenisch, J., Sachse, F. B., and Hitchcock, R. W. (2011). Three-dimensional modeling and quantitative analysis of gap junction distributions in cardiac tissue. *Ann. Biomed. Eng.* 39, 2683–2694. doi: 10.1007/s10439-011-0369-3

Louch, W. E., Bito, V., Heinzel, F. R., Macianskiene, R., Vanhaecke, J., Flameng, W., et al. (2004). Reduced synchrony of Ca2+ release with loss of T-tubules-a comparison to Ca2+ release in human failing cardiomyocytes. *Cardiovasc. Res.* 62, 63–73. doi: 10.1016/j.cardiores.2003.12.031

McDonald, R. L., Colyer, J., and Harrison, S. M. (2000). Quantitative analysis of Na+-Ca2+ exchanger expression in guinea-pig heart. *Eur. J. Biochem.* 267, 5142–5148. doi: 10.1046/j.1432-1327.2000.01579.x

Meyer, M., Bluhm, W. F., He, H., Post, S. R., Giordano, F. J., Lew, W. Y., et al. (1999). Phospholamban-to-SERCA2 ratio controls the force-frequency relationship. *Am. J. Physiol.* 276, H779–H785. doi: 10.1152/ajpheart.1999.276.3.H779

Milani-Nejad, N., and Janssen, P. M. (2014). Small and large animal models in cardiac contraction research: advantages and disadvantages. *Pharmacol. Ther.* 141, 235–249. doi: 10.1016/j.pharmthera.2013.10.007

Mulieri, L. A., Hasenfuss, G., Leavitt, B., Allen, P. D., and Alpert, N. R. (1992). Altered myocardial force-frequency relation in human heart failure. *Circulation* 85, 1743–1750. doi: 10.1161/01.cir.85.5.1743

Munch, G., Bolck, B., Brixius, K., Reuter, H., Mehlhorn, U., Bloch, W., et al. (2000). SERCA2a activity correlates with the force-frequency relationship in human myocardium. *Am. J. Physiol. Heart Circ. Physiol.* 278, H1924–H1932. doi: 10.1152/ajpheart.2000.278.6.H1924

Pasek, M., Brette, F., Nelson, A., Pearce, C., Qaiser, A., Christe, G., et al. (2008). Quantification of t-tubule area and protein distribution in rat cardiac ventricular myocytes. *Prog. Biophys. Mol. Biol.* 96, 244–257. doi: 10.1016/j.pbiomolbio.2007.07.016

Rossman, E. I., Petre, R. E., Chaudhary, K. W., Piacentino, V. III, Janssen, P. M., Gaughan, J. P., et al. (2004). Abnormal frequency-dependent responses represent the pathophysiologic signature of contractile failure in human myocardium. *J. Mol. Cell Cardiol.* 36, 33–42. doi: 10.1016/j.yjmcc.2003.09.001

Schwinger, R. H., Bohm, M., Koch, A., Schmidt, U., Morano, I., Eissner, H. J., et al. (1994). The failing human heart is unable to use the Frank-Starling mechanism. *Circ. Res.* 74, 959–969. doi: 10.1161/01.res.74.5.959

Seidel, T., Dräbing, T., Seemann, G., and Sachse, F. B. (2013). A semi-automatic approach for segmentation of three-dimensional microscopic image stacks of cardiac tissue. *Lect. Notes Comput. Sci.* 7945, 300–307. doi: 10.1007/978-3-642-38899-6_36

Seidel, T., Edelmann, J. C., and Sachse, F. B. (2016). Analyzing remodeling of cardiac tissue: a comprehensive approach based on confocal microscopy and 3D reconstructions. *Ann. Biomed. Eng.* 44, 1436–1448. doi: 10.1007/s10439-015-1465-6

Seidel, T., Fiegle, D. J., Baur, T. J., Ritzer, A., Nay, S., Heim, C., et al. (2019). Glucocorticoids preserve the t-tubular system in ventricular cardiomyocytes by upregulation of autophagic flux. *Basic Res. Cardiol.* 114:47. doi: 10.1007/s00395-019-0758-756

Seidel, T., Navankasattusas, S., Ahmad, A., Diakos, N. A., Xu, W. D., Tristani-Firouzi, M., et al. (2017a). Sheet-like remodeling of the transverse tubular system in human heart failure impairs excitation-contraction coupling and functional recovery by mechanical unloading. *Circulation* 135, 1632–1645. doi: 10.1161/CIRCULATIONAHA.116.024470

Seidel, T., Sankarankutty, A. C., and Sachse, F. B. (2017b). Remodeling of the transverse tubular system after myocardial infarction in rabbit correlates with local fibrosis: a potential role of biomechanics. *Prog. Biophys. Mol. Biol.* 130(Pt B), 302–314. doi: 10.1016/j.pbiomolbio.2017.07.006

Stemmer, P., and Akera, T. (1986). Concealed positive force-frequency relationships in rat and mouse cardiac muscle revealed by ryanodine. *Am. J. Physiol.* 251(6 Pt 2), H1106–H1110. doi: 10.1152/ajpheart.1986.251.6.H1106

Thomas, M. J., Sjaastad, I., Andersen, K., Helm, P. J., Wasserstrom, J. A., Sejersted, O. M., et al. (2003). Localization and function of the Na+/Ca2+-exchanger in normal and detubulated rat cardiomyocytes. *J. Mol. Cell Cardiol.* 35, 1325–1337. doi: 10.1016/j.yjmcc.2003.08.005

Varnava, A. M., Elliott, P. M., Mahon, N., Davies, M. J., and McKenna, W. J. (2001). Relation between myocyte disarray and outcome in hypertrophic cardiomyopathy. *Am. J. Cardiol.* 88, 275–279. doi: 10.1016/s0002-9149(01)01640-x

Watson, S. A., Duff, J., Bardi, I., Zabielska, M., Atanur, S. S., Jabbour, R. J., et al. (2019). Biomimetic electromechanical stimulation to maintain adult myocardial slices in vitro. *Nat. Commun.* 10:2168. doi: 10.1038/s41467-019-10175-3

Wiegerinck, R. F., Cojoc, A., Zeidenweber, C. M., Ding, G., Shen, M., Joyner, R. W., et al. (2009). Force frequency relationship of the human ventricle increases during early postnatal development. *Pediatr. Res.* 65, 414–419. doi: 10.1203/PDR.0b013e318199093c

Wu, Y., Luczak, E. D., Lee, E. J., Hidalgo, C., Yang, J., Gao, Z., et al. (2012). CaMKII effects on inotropic but not lusitropic force frequency responses require phospholamban. *J. Mol. Cell Cardiol.* 53, 429–436. doi: 10.1016/j.yjmcc.2012.06.019

Zhao, W., Uehara, Y., Chu, G., Song, Q., Qian, J., Young, K., et al. (2004). Threonine-17 phosphorylation of phospholamban: a key determinant of frequency-dependent increase of cardiac contractility. *J. Mol. Cell Cardiol.* 37, 607–612. doi: 10.1016/j.yjmcc.2004.05.013

Conflict of Interest: The authors declare that the research was conducted in the absence of any commercial or financial relationships that could be construed as a potential conflict of interest.

frontiers
in Physiology

REVIEW
published: 13 March 2020
doi: 10.3389/fphys.2020.00181

Stretch-Induced Biased Signaling in Angiotensin II Type 1 and Apelin Receptors for the Mediation of Cardiac Contractility and Hypertrophy

Kinya Seo[1]*, *Victoria N. Parikh*[1] *and Euan A. Ashley*[1,2]

[1] *Division of Cardiovascular Medicine, Department of Medicine, Stanford University, Stanford, CA, United States,*
[2] *Department of Genetics, Stanford University, Stanford, CA, United States*

The myocardium has an intrinsic ability to sense and respond to mechanical load in order to adapt to physiological demands. Primary examples are the augmentation of myocardial contractility in response to increased ventricular filling caused by either increased venous return (Frank–Starling law) or aortic resistance to ejection (the Anrep effect). Sustained mechanical overload, however, can induce pathological hypertrophy and dysfunction, resulting in heart failure and arrhythmias. It has been proposed that angiotensin II type 1 receptor (AT_1R) and apelin receptor (APJ) are primary upstream actors in this acute myocardial autoregulation as well as the chronic maladaptive signaling program. These receptors are thought to have mechanosensing capacity through activation of intracellular signaling via G proteins and/or the multifunctional transducer protein, β-arrestin. Importantly, ligand and mechanical stimuli can selectively activate different downstream signaling pathways to promote inotropic, cardioprotective or cardiotoxic signaling. Studies to understand how AT_1R and APJ integrate ligand and mechanical stimuli to bias downstream signaling are an important and novel area for the discovery of new therapeutics for heart failure. In this review, we provide an up-to-date understanding of AT_1R and APJ signaling pathways activated by ligand versus mechanical stimuli, and their effects on inotropy and adaptive/maladaptive hypertrophy. We also discuss the possibility of targeting these signaling pathways for the development of novel heart failure therapeutics.

Keywords: angiotensin II, AT_1R, apelin, APJ, β-arrestin, Frank–Starling law, Anrep effect, cardiac hypertrophy

Edited by:
Remi Peyronnet,
University of Freiburg, Germany

Reviewed by:
Lewis J. Watson,
University of Pikeville, United States
Sumanth D. Prabhu,
The University of Alabama at Birmingham, United States

***Correspondence:**
Kinya Seo
kseo1@stanford.edu

Specialty section:
This article was submitted to Striated Muscle Physiology, a section of the journal Frontiers in Physiology

Received: *29 November 2019*
Accepted: *17 February 2020*
Published: *13 March 2020*

Citation:
Seo K, Parikh VN and Ashley EA (2020) Stretch-Induced Biased Signaling in Angiotensin II Type 1 and Apelin Receptors for the Mediation of Cardiac Contractility and Hypertrophy. Front. Physiol. 11:181. doi: 10.3389/fphys.2020.00181

INTRODUCTION

The working heart adjusts cardiac output to changes in hemodynamic load in order to adapt to physiological demand. The first adaptation occurs immediately, on a beat-to-beat basis, after the ventricle is dilated by increased inflow. The relationship between end-diastolic volume and cardiac output, described by Ernest Henry Starling in a series of papers between 1912 and 1914, has been called “Starling’s Law of the Heart” or the “Frank–Starling relationship” which explains how the heart adapts to change in mechanical load by adjusting its contractile function (Katz Arnold, 2002). The main cellular mechanism that underlies the Frank–Starling relationship is enhanced myofilament sensitivity to Ca^{2+} at a longer sarcomere length, commonly referred to as length-dependent activation (Allen et al., 1974; de Tombe, 2003) (**Figure 1**, LDA). This length-dependent activation is modulated by posttranslational modification of myofilament proteins, such as cardiac troponin I (cTnI) (Tachampa et al., 2007; Wijnker et al., 2014), myosin-binding protein C (MyBPC) (Kumar et al., 2015), myosin regulatory light chain (Toepfer et al., 2016; Breithaupt et al., 2019) and titin (Hamdani et al., 2017). While the upstream molecular mechanisms that induce myofilament modifications and length-dependent activation had been poorly understood, recent studies suggest the roles of G protein-coupled receptors (GPCRs): angiotensin II type 1 receptor (AT_1R) (Abraham et al., 2016) and apelin receptor APJ (Peyronnet et al., 2017; Parikh et al., 2018).

The myocardium has another autoregulatory mechanism to gradually increase its contractility in the setting of increased systemic resistance. Gleb Von Anrep first described in 1912 that the heart exhibits progressive increases in contractility in response to left ventricular dilation induced by aortic clamping *in vivo* (von Anrep, 1912). This "Anrep effect" had been interpreted as secondary to a neurohormonal effect or increased oxygen consumption due to the change in coronary perfusion [known as the "Gregg phenomenon" (Gregg and Shipley, 1944)] until Stanley Sarnoff and his colleagues reproduced this phenomenon in pressure/flow controlled isolated hearts and defined it as an autoregulation of myocardium (Sarnoff et al., 1960; Sarnoff and Mitchell, 1961). Subsequently, in isolated ventricular muscle strips exposed to sudden myocardial stretch, a gradual secondary increase in isometric/isotonic force was observed to follow the initial rise in contractility induced by the Frank–Starling mechanism (Parmley and Chuck, 1973). It has since been proposed that this "Slow Force Response (SFR)" (**Figure 1**, SFR) is the *in vitro* equivalent of the Anrep effect (Alvarez et al., 1999). Unlike the Frank–Starling mechanism, SFR is induced by a gradual increase in Ca^{2+} transient amplitude (Allen and Kurihara, 1982; Kentish and Wrzosek, 1998) through the activation of multiple intracellular components and ion transporters (Cingolani et al., 2013). Notably, AT_1R may control this signaling pathway (Cingolani et al., 2013).

In response to sustained mechanical stress, the heart undergoes hypertrophic enlargement characterized by an increase in the size of individual cardiac myocytes. Although cardiac hypertrophy can initially be a compensatory response that temporarily augments and maintains cardiac output along with the Frank–Starling mechanism and the Anrep effect, prolonged hypertrophic stimuli can eventually lead to decompensation, heart failure, and arrhythmia (Levy et al., 1990; Ho et al., 1993). This pathological hypertrophy is induced by the activation of GPCRs by ligand or stretch stimulation, which in turn activates downstream signaling pathways, including mitogen-activated protein kinase (MAPK), protein kinase C (PKC), and calcineurin–nuclear factor of activated T cells (NFAT), leading to myocyte hypertrophy (Heineke and Molkentin, 2006). Candidates for control of this mechano-transduction of hypertrophic signaling include AT_1R (Zou et al., 2004) and APJ (Scimia et al., 2012).

The GPCR family is critical both at the bench and bedside, because the majority of current therapeutic drugs for heart failure target GPCRs (Lefkowitz, 2004). An expanding area of GPCR research is focused on the differential activation of G protein or β-arrestin signaling pathway in a "biased" manner to selectively promote cardiac beneficial pathways while preventing stimulation of cardiotoxic pathways. This biased agonism is achieved by ligands or mechanical stretch that can induce distinct active receptor conformations that in turn selectively activate only specific subsets of a given receptor (**Figure 2**) (Rakesh et al., 2010; Wisler et al., 2014). β-arrestin is a multifunctional scaffolding protein that desensitizes ligand-stimulated GPCRs but also can stimulate other signaling pathways distinct from G protein-dependent signaling (Reiter et al., 2012). Downstream of AT_1R, chronic G protein-dependent signaling is associated with adverse outcomes, while β-arrestin-dependent signaling is considered beneficial for heart failure (Kim et al., 2012). Importantly, mechanical stress has been proposed to activate both G protein- and β-arrestin-dependent AT_1R signaling pathways (Zou et al., 2004; Rakesh et al., 2010). In the APJ signaling system, in contrast, stretch stimulation selectively activates β-arrestin-dependent pathological pathway (Scimia et al., 2012), while apelin–APJ binding preferentially promotes G protein-dependent cardioprotective and prosurvival signaling. Because β-arrestins work as scaffolds that form complexes by binding to other proteins, it is conceivable that β-arrestins in AT_1R and APJ show different functions due to their different binding partners. Thus, the role of these interacting pathways downstream of GPCRs in myocardial physiology appears to be receptor-dependent, and further investigation of how AT_1R and APJ integrate ligand and mechanical stimuli to bias G protein or β-arrestin signaling, thus controlling cardioprotective versus cardiotoxic programs is important for the discovery of new therapeutics for heart failure.

This review aims to provide an up-to-date understanding of AT_1R and APJ signaling pathways activated by mechanical stimuli on cardiac function and pathological hypertrophy, with special emphasis on biased stretch-mediated engagement of both AT_1R and APJ and their potential roles in initiation or amelioration of heart diseases. The possibilities of targeting these pathways for the development of novel heart failure therapeutics will be discussed. Mechanistic insight will be provided through review of cell-based and animal models, and the areas of need for continued investigation will be highlighted.

ANGIOTENSIN II VERSUS STRETCH-INDUCED AT_1R SIGNALING

Angiotensin II type 1 receptor plays pivotal roles in the regulation of cardiovascular function, and is one of the major targets for the therapeutic treatment of heart failure (Violin et al., 2013). Angiotensin II (Ang II), the endogenous ligand for AT_1R, is well known for its action on vasoconstriction and aldosterone

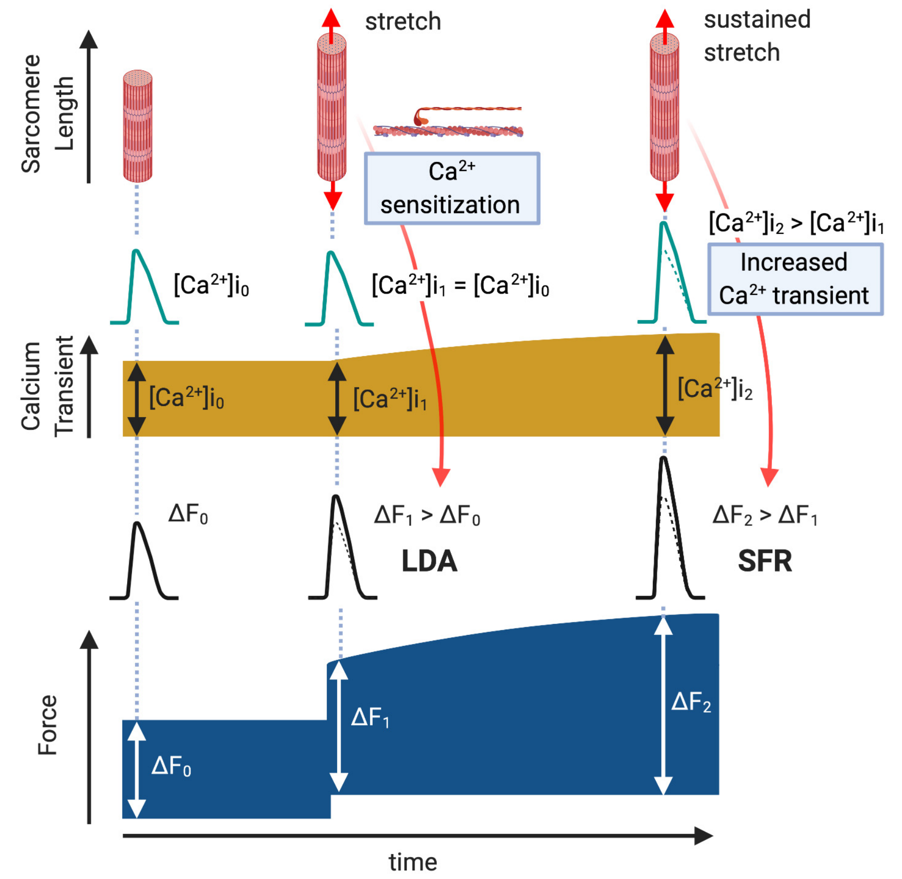

FIGURE 1 | Length-Dependent Activation (LDA) and Slow Force Response (SFR). Immediately after a cardiac muscle is stretched, there is a rapid Ca^{2+}-independent rise in developed force ($\Delta F_1 > \Delta F_0$, LDA) followed by a more gradual rise that is associated with an intracellular Ca^{2+} increase ($\Delta F_2 > \Delta F_1$, SFR).

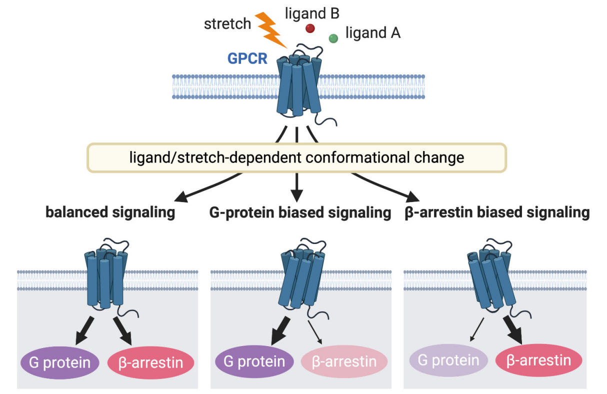

FIGURE 2 | GPCR signaling induced by different receptor activation. Different stimulations stabilize the receptors into distinct active conformational states that couples to a particular G protein or β-arrestin or both to activate diverse arrays of downstream signaling, resulting in different functional outcomes.

release, while its local action in the heart is also known to augment myocardial contraction (Petroff et al., 2000) and to activate hypertrophic signaling (Sadoshima and Izumo, 1993).

It is widely accepted that myocytes respond to mechanical stretch to release Ang II in an autocrine fashion to activate AT_1R and its intracellular signaling (Sadoshima et al., 1993). However, the receptor can also directly sense mechanical stress to activate its downstream signaling, even without Ang II binding (Zou et al., 2004; Yasuda et al., 2008; Rakesh et al., 2010). Komuro's group showed for the first time that the mechanical activation of AT_1R is agonist-independent in angiotensinogen-deficient mice (Zou et al., 2004). They also demonstrated that stretch stimulation of AT_1R induces a conformational change of the receptor that is distinct from the ligand-activated receptor conformation (Yasuda et al., 2008). Despite some commonalities between stretch- and ligand-induced AT_1R signaling pathways, recent studies have suggested that mechanical stress differentially activates β-arrestin-dependent AT_1R signaling, which is distinct from ligand-activated pathways (Rakesh et al., 2010; Wang et al., 2018). This section summarizes the current understanding of how AT_1R signaling regulates cardiac contractility and adaptive/maladaptive signaling when the heart is subjected to mechanical stress. In addition, the therapeutic possibility of targeting AT_1R signaling for mechanical stress-relevant heart diseases is discussed.

The Role of Ang II and AT_1R in Ca^{2+}-Independent Inotropic Response and the Frank–Starling Mechanism

Angiotensin II has a positive inotropic effect in cardiomyocytes both by myofilament Ca^{2+} sensitization and intracellular Ca^{2+} rise (Mattiazzi, 1997; Watanabe and Endoh, 1998). Experiments in isolated rabbit myocytes demonstrated that Ang II induced a positive inotropic effect without associated increases in either Ca^{2+} inward current or Ca^{2+} transients, but was accompanied by intracellular alkalosis that could potentially increase myofilament sensitivity to Ca^{2+} (Ikenouchi et al., 1994). It has also been shown that Ang II increases phosphorylation of myosin light chain 2 (MLC2) by the MLC–PKC pathway, thereby increasing myofilament Ca^{2+} responsiveness (Morano et al., 1988; Clement et al., 1992). This Ang II–AT_1R activation of myofilaments could, therefore, form the basis for length-dependent activation (Frank–Starling mechanism). Indeed, Rockman's group recently revealed that gene deletion or selective inhibition of AT_1R in mouse hearts abrogates the Frank–Starling relationship (Abraham et al., 2016).

Using β-arrestin1/2 deficient mice, they also found that the loss of β-arrestin proteins abrogates Frank–Starling relationship without activating PKC. It has been demonstrated that β-arrestin-biased AT_1R activation enhances myocyte contractility without increasing intracellular Ca^{2+} concentration (Rajagopal et al., 2006), and myofilament Ca^{2+} sensitivity associated with reduced TnI and MyBPC phosphorylation and enhanced tropomyosin phosphorylation (Monasky et al., 2013; Ryba et al., 2017). However, protein phosphorylation in the β-arrestin1/2 deficient mice does not differ compared to wildtype controls. This may be due to distinct β-arrestin signaling pathways downstream of stretch–AT_1R compared to ligand–AT_1R stimulation (Wang et al., 2018). Further detailed investigation of posttranslational modifications of myofilament proteins by proteomic analyses will identify novel proteins critical to the AT_1R-dependent modulation of the Frank–Starling relationship.

The Role of AT_1R in Ca^{2+}-Dependent Inotropic Response and Slow Force Response

In addition to the positive inotropic effect caused by myofilament Ca^{2+} sensitization, Ang II enhances contractility by a Ca^{2+} dependent mechanism. It has been proposed that Ang II–AT_1R binding triggers endothelin-1 (ET-1) production/release, which in turn activates endothelin type A receptor (ET_AR) to induce transactivation of epidermal growth factor receptor (EGFR) through ROS-induced ROS release (Cingolani et al., 2006; Yeves et al., 2015; Zhang et al., 2015). This results in NHE-1 activation to induce Na^+ influx that in turn triggers Ca^{2+} entry via reverse mode NCX, thereby enhancing contractility (Petroff et al., 2000; Pérez et al., 2003) (**Figure 3**, red arrows). It has been suggested that these mechanisms could be the basis for the SFR (the *in vitro* equivalent of the Anrep effect). Cingolani's group has described a similar complex signaling pathway upon stretch-induced Ang II production, involving autocrine/paracrine activation of AT_1R and ET_AR (Cingolani et al., 2011), ROS-induced ROS release (Caldiz et al., 2007), the transactivation of EGFR (Brea et al., 2016), ERK1/2 activation (Pérez et al., 2011), and NHE-1 and NCX activation (Pérez et al., 2001), thus increasing myocyte contraction (**Figure 3**, red arrows).

Recently, we demonstrated that transient receptor potential canonical (TRPC) 6 channel is an additional important upstream determinant of SFR. Our study demonstrated that gene deletion and selective blockade of TRPC6 channel abrogates SFR and the Anrep effect in physiologically loaded myocytes, muscle strips, and intact hearts (Seo et al., 2014a). More recently, it was found that TRPC3 is an equivalent contributor to this process (Yamaguchi et al., 2018) as supported by evidence that TRPC3 and 6 can form functional heterotetramers (Hofmann et al., 2002). The mechanosensitivity of TRPC6 had been demonstrated in smooth muscle cells (Spassova et al., 2006) and adult cardiomyocytes (Dyachenko et al., 2009) exposed to membrane stretch or shear stress. Some, however, have questioned the mechanosensing capacity of TRPC6 and attributed it to its upstream stretch-activated GPCRs and/or artifacts from TRPC6 overexpression in heterologous systems (Gottlieb et al., 2008). Importantly, TRPC3/6 is a downstream component of AT_1R, and Ang II stimulation is known to activate these channels via $G_{\alpha q}$ protein, PLC and diacylglycerol (DAG) signaling pathway (Onohara et al., 2006). Indeed, stretch-induced slow increase in Ca^{2+} was suppressed by either TRPC3/6 or AT_1R inhibition (Yamaguchi et al., 2018). Ca^{2+} influx through TRPC3/6 may directly stimulate SFR, while it is also conceivable that TRPC3/6 activates ERK1/2 (Yao et al., 2009; Chiluiza et al., 2013) upstream of NHE-1, thus inducing an inward Na^+ current that in turn triggers Ca^{2+} entry via NCX (Poburko et al., 2007, 2008; Louhivuori et al., 2010) (**Figure 3**, blue arrows). While many of these studies have suggested the involvement of AT_1R as an upstream component of SFR signaling pathways, there are several opposing reports describing that Ang II and AT_1R are not involved in the process because SFR was not suppressed by Ang II receptor blockers (ARBs) (Calaghan and White, 2001; von Lewinski et al., 2003; Shen et al., 2013). Despite the inverse agonistic effect of ARBs (Sato et al., 2016), mechanical stretch may differentially activate AT_1R even in the presence of ARBs which should normally suppress the ligand-stimulated signaling pathway. More direct evidence that links AT_1R to SFR, using AT_1R-deficient models, will be needed to clarify this mechanism.

Pathological AT_1R–TRPC3/6 and Cardioprotective AT_1R–β-Arrestin Signaling in Pressure-Overload Cardiac Hypertrophy

It is well established that Ang II can induce cardiomyocyte hypertrophy through the activation of multiple intracellular signaling pathways such as the mitogen-activated protein kinase (MAPK) signaling cascade (Thorburn et al., 1994; Zechner et al., 1997; Wang et al., 1998a), c-Jun *N*-terminal kinase (Sadoshima and Izumo, 1993; Ramirez et al., 1997; Wang et al., 1998b), Akt–mammalian target of rapamycin (mTOR) (Gorin et al., 2001; Diniz et al., 2009) and calcium–calmodulin-activated phosphatase calcineurin (Molkentin et al., 1998;

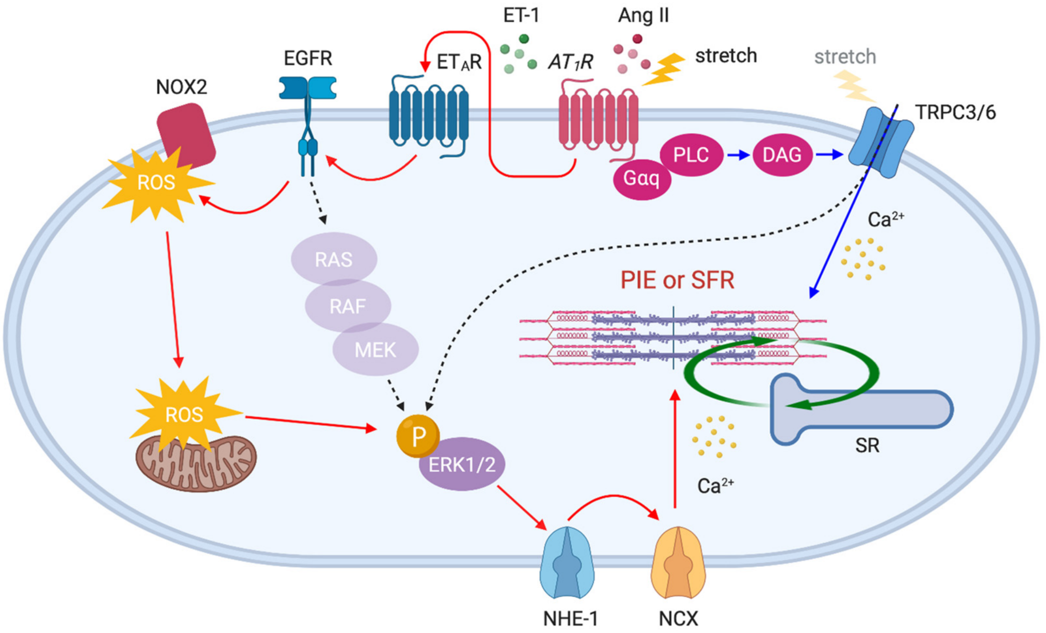

FIGURE 3 | AT_1R downstream signaling pathways activated by acute stretch or Ang II. Membrane stretch directly or indirectly (by the autocrine release of Ang II) stimulates AT_1R which in turn activates distinct downstream signaling pathways: (1) ET_AR–EGFR–ERK1/2–NHE-1–NCX axis (red arrows) and (2) PLC–DAG–TRPC3/6 axis (blue arrows). The gradual influx of Ca^{2+} through NCX and TRPC3/6 channels enhances myocardial contractility, thereby initiating SFR. Ang II-triggered positive inotropic effect (PIE) shares the same pathways.

Wilkins and Molkentin, 2004). In particular, calcineurin is a pivotal regulator of pathological cardiac hypertrophy preferentially activated by mechanical stress on GPCRs (Molkentin, 2004; Heineke and Molkentin, 2006). Once activated by increases in Ca^{2+}, calcineurin mediates the hypertrophic response through its downstream transcriptional effector NFAT (Crabtree and Olson, 2002). It has been accepted that a major source of Ca^{2+} for activation of calcineurin is Ca^{2+} influx through TPRC3 and 6 channels. Indeed, Ang II–AT_1R activation promotes calcineurin–NFAT signaling that requires the DAG-induced Ca^{2+} signaling pathway through TRPC3 and 6 (Onohara et al., 2006). Importantly, this signaling pathway can be activated by mechanical stress. TRPC3 overexpressed transgenic mice exhibit an increase in calcineurin–NFAT activation *in vivo*, and increased hypertrophy after Ang II/Phenylephrine and pressure-overload stimulation (Nakayama et al., 2006). In addition, TRPC6 transgenic mice also resulted in enhanced sensitivity to mechanical stress, with an increase in calcineurin–NFAT signaling, and severe cardiac hypertrophy and failure (Kuwahara et al., 2006). Although TRPC3/6 channels are linked to other $G_{\alpha q}$PCRs such as ET_AR and α-adrenergic receptors, AT_1R may be the putative central actor in stress-induced hypertrophy, considering the mechanosensing capacity of the receptor.

AT_1R activation by either Ang II or mechanical stress not only induces pathological signaling but also promotes physiological hypertrophy and prosurvival signaling. In embryonic, neonatal, and adult cardiomyocytes, Ang II–AT_1R activation promotes transactivation of EGFR, which in turn activates MAPK and Akt–mTOR pathways (Thomas et al., 2002; Diniz et al., 2009). Rockman's group recently demonstrated that mechanical stress in cells and the hearts activates AT_1R-induced prosurvival signaling in a β-arrestin-dependent manner that does not require Ang II release (Rakesh et al., 2010). The formation of an AT_1R–β-arrestin complex by mechanical stress induces EGFR transactivation and subsequent ERK and Akt signaling pathways, which suppresses cardiomyocyte injury (Rakesh et al., 2010). They later found that membrane stretch uniquely promotes the coupling of the inhibitory G protein ($G_{\alpha i}$) that is required for the recruitment of β-arrestin2 and activation of downstream signaling pathways, such as EGFR transactivation and ERK phosphorylation (Wang et al., 2018). $G_{\alpha i}$ proteins primarily inhibit the cAMP-dependent pathway by inhibiting adenylyl cyclase (AC) activity. Although previous studies have shown that Ang II may promote AT_1R–$G_{\alpha i}$ coupling to inhibit AC and to regulate Ca^{2+} channels in certain tissues or cell types (Hescheler et al., 1988; Maturana et al., 1999), it is not yet clear if the $G_{\alpha i}$–β-arrestin complex has the same function.

Taken together, chronic mechanical stress can induce both $G_{\alpha q}$–TRPC3/6 dependent and $G_{\alpha i}$–β-arrestin dependent signaling pathways to differentially promote pathological and prosurvival signaling (**Figure 4**). Although selective $G_{\alpha q}$–TRPC3/6 signaling initially works as an adaptive response to mechanical stress by enhancing myocardial contractility through SFR, prolonged signaling eventually worsens cardiac function. On the other hand, β-arrestin-dependent AT_1R signaling is proposed to enhance cardiac contractility by a Ca^{2+}-independent mechanism, and chronically activates prosurvival signaling,

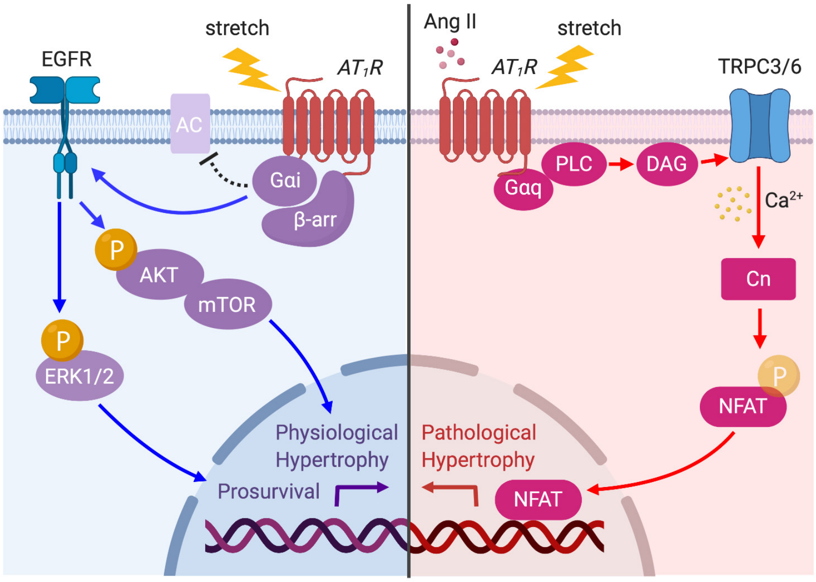

FIGURE 4 | AT$_1$R signaling pathways activated by prolonged mechanical load or Ang II. The AT$_1$R is principally coupled to $G_{\alpha q}$ protein but is also coupled to $G_{\alpha i}$ protein through β-arrestin (β-arr) recruitment when the myocyte is subjected to mechanical load. Ang II- or stretch-induced $G_{\alpha q}$ signaling activates TRPC3/6 to initiate Ca^{2+} influx, which in turn activates calcineurin (CN)–NFAT pathway to promote pathological cardiac hypertrophy (red arrows). AT$_1$R–$G_{\alpha i}$ coupling induces EGFR transactivation and Akt/ERK phosphorylation, which promotes physiological hypertrophy and prosurvival signaling (blue arrows).

TABLE 1 | Emerging drugs for heart failure therapeutics targeting AT$_1$R or APJ.

Name of drug	Drug class	Model studied/clinical trials
TRV120027	β-arrestin-biased AT$_1$R agonist	ADHF (Phase 2B BLAST-AHF, no benefit over placebo)
TRV120023	β-arrestin-biased AT$_1$R agonist	DCM (mice, improved contractility)
		ACI (mice/rats, improved contractility, reduced cell death)
TRV120067	β-arrestin-biased AT$_1$R agonist	DCM (mice, improved contractility and structure)
Sildenafil	PDE5 inhibitor	HFpEF (Phase 3 RELAX, no benefit over placebo)
		HFrEF (Phase 3 SIL-HF, recruiting)
BI 749327	TRPC6 inhibitor	CHF (mice, improved LV function and reduced fibrosis)
ML233	small molecule APJ agonist	No reports on HF
AMG 986	small molecule APJ agonist	CHF (Phase 1, terminated)
MM07	G-protein-biased peptide APJ agonist	No reports on HF
CLR325	peptide APJ agonist	CHF (Phase 2, completed)

ADHF, acute decompensated heart failure; DCM, dilated cardiomyopathy; ACI, acute cardiac injury; CHF, chronic heart failure.

making it a pathway of high clinical potential to ameliorate acute and chronic heart failure.

AT$_1$R Targeted Therapeutics for Mechanical Stress-Associated Heart Diseases (Table 1)

Pathological hypertrophy induced by the overstimulation of AT$_1$R by Ang II or mechanical stress can eventually lead to heart failure and sudden death associated with arrhythmia. One of the current therapeutics for these conditions is AT$_1$R blocking drugs, known as ARBs. Several ARBs are known to have inverse agonistic action which can inactivate the GPCR state, and thereby suppress the constitutive activity of receptors. Such drugs can suppress mechanical stretch-induced signals through AT$_1$R and may exhibit enhanced therapeutic effects for these disease states (Zou et al., 2004; Wei et al., 2011).

While endogenous Ang II activates both G protein and β-arrestin signaling pathways, several AT$_1$R ligands, such as [Sar1, Ile4, Ile8]-Ang II (SII), TRV120023, TRV120027, and TRV120067 have been shown to selectively activate β-arrestin-mediated pathways and therefore termed as β-arrestin-biased agonists (Rajagopal et al., 2010; Strachan et al., 2014). These β-arrestin-biased AT$_1$R agonists have been demonstrated to have beneficial effects on the disease condition caused by mechanical stress. For example, TRV120027 causes cardiac unloading action while preserving renal function in a canine model of acute heart failure (Boerrigter et al., 2011). However, a Phase 2B trial of TRV120027 in acute heart failure (BLAST-AHF) resulted in no benefit over placebo (De Vecchis et al., 2017). On the other hand, TRV120023 diminishes myocyte apoptosis caused by mechanical stress by selectively activating ERK1/2 cardioprotective signaling pathways in isolated mouse hearts (Kim et al., 2012). Long-term treatment with TRV120067 in the mouse model of dilated cardiomyopathy not only prevented maladaptive signaling but also improved cardiac function by altering the myofilament response to Ca^{2+} via β-arrestin signaling pathways (Ryba et al., 2017). Notably, TRV120023 and TRV120067 have shown better efficacy in cardiac function and cardioprotection compared to ARBs, suggesting their possibility to become novel therapeutic drugs for heart failure.

Targeting AT_1R downstream signals, such as protein kinase G (PKG) and TRPC3/6, could be another therapeutic strategy. Our study previously revealed that adverse myocardial responses induced by mechanical stimulation to these channels are suppressed by post-transcriptional modification of TRPC6 channel by activation of the cGMP–PKG pathway (Seo et al., 2014a). Indeed, there is growing evidence that stimulation of the cGMP–PKG pathway within cardiac myocytes dampens cardiac stress responses, and its activation can attenuate pathological hypertrophy, protect against ischemic injury and enhance cell survival (Zhang and Kass, 2011). One means to activate the cGMP–PKG pathway is to inhibit the degradation of cGMP by phosphodiesterase-5 (PDE5). PDE5 inhibitors [e.g., sildenafil (Viagra)] have proven their efficacy in treating pressure-overload cardiac hypertrophy and failure in animal models (Takimoto et al., 2005; Nagayama et al., 2009). Although the RELAX trial, a large clinical trial of PDE5 inhibition in heart failure with preserved ejection fraction (HFpEF), failed to show robust beneficial effects (Redfield et al., 2013), single-center trials in patients with heart failure with reduced ejection fraction (HFrEF) reported improved exercise capacity and quality of life (Lewis et al., 2007). Indeed, a meta-analysis of randomized controlled trials in heart failure shows statistically significant improvement of clinical outcomes in patients with HFrEF rather than HFpEF (De Vecchis et al., 2017). Our study demonstrated that sildenafil attenuates pathological hypertrophy by promoting TRPC6 phosphorylation by PKG in the mouse model of muscular dystrophy in which the heart is susceptible to mechanical load (Seo et al., 2014a). Direct antagonism of TRPC3/6 channels is also proven effective for preventing pathological hypertrophy in experiment levels (Seo et al., 2014b). Recently, the orally bioavailable selective TRPC6 inhibitor (BI 749327) was tested in mice, providing *in vivo* evidence of therapeutic efficacy for cardiac and renal stress-induced disease with fibrosis (Lin et al., 2019). Thus, direct inhibition of TRPC6 could be an alternative strategy to effectively suppress pathological cardiac hypertrophy and failure induced by adverse mechanical stress.

APELIN VERSUS STRETCH-INDUCED APJ SIGNALING

Apelin receptor is a GPCR that binds the endogenous peptide apelin (Tatemoto et al., 1998; Lee et al., 2000). This receptor is widely expressed in the cardiovascular system and is emerging as an important mediator of both cardiac and vascular function (Chandrasekaran et al., 2008). In the heart, apelin has been shown to increase myocardial contraction (Szokodi et al., 2002), reduce cardiac load (Ashley et al., 2005) and promote cardioprotective effects (Zhang et al., 2009). Recently, a peptide named ELABELA (Ryba et al., 2017) or Toddler (Pauli et al., 2014) was found to bind APJ, exhibiting a cardiac protective role comparable to apelin (Sato et al., 2017). In addition to this new ligand, it recently turned out that mechanical stretch can also directly activate this receptor. It has been proposed that APJ acts as a bifunctional receptor for both mechanical stress and apelin to activate separate signaling pathways directed to inotropic, cardiotoxic, and cardioprotective effects (Scimia et al., 2012). Intriguingly, unlike AT_1R, stretch-induced activation of APJ triggers pathological hypertrophy through β-arrestin, while β-arrestin-dependent signaling in AT_1R activates prosurvival signaling. This section summarizes the up-to-date findings of APJ signaling pathways stimulated by apelin or mechanical stress, and introduces how each stimulation can bring different cardiac outcomes. Therapeutic possibilities of biased agonists for heart failure targeting G protein versus β-arrestin-dependent signaling pathways are discussed.

The Role of Apelin–APJ in Ca^{2+}-Independent Positive Inotropic Effect and Frank–Starling Relationship

A potent inotropic effect of apelin has been demonstrated in cardiomyocytes (Farkasfalvi et al., 2007; Wang et al., 2008; Peyronnet et al., 2017), muscle strips (Dai et al., 2006), isolated hearts (Szokodi et al., 2002; Perjés et al., 2014) and *in vivo* heart disease models (Berry et al., 2004; Charo et al., 2009). It has been proposed that the increase in myocardial contractility is attributed to both Ca^{2+}-dependent (Dai et al., 2006; Wang et al., 2008) and Ca^{2+}-independent mechanisms (Farkasfalvi et al., 2007; Charo et al., 2009; Parikh et al., 2018). The latter is considered to rely on apelin's action on myofilament sensitivity to Ca^{2+}. It was first demonstrated by Farkasfalvi et al. (2007) in studies with normal and failing cardiomyocytes that displayed increased sarcomere shortening in the absence of increased Ca^{2+} transient amplitude after apelin administration. They suggested one of the mechanisms involves increased myofilament sensitivity to Ca^{2+} as apelin activates NHE-1 with consequent intracellular alkalinization. Subsequently, a study using isolated single left ventricular myocytes from apelin deficient and APJ deficient mice revealed that loss of apelin or APJ causes impaired contraction with no difference in intracellular Ca^{2+} kinetics, suggesting apelin and APJ affect either myofilament Ca^{2+} sensitivity or cross-bridge cycling kinetics (Charo et al., 2009). This may be attributable to the activation of MLC kinase through parallel and independent activation of PKCε and ERK1/2 signaling stimulated by apelin (Perjés et al., 2014).

The phosphorylation level of myofilament proteins can affect length-dependent activation, which positively regulates the Frank–Starling relationship. Recently, the direct effect of apelin on length-dependent activation was examined in mechanically preloaded cardiomyocytes; apelin increased compliance of the myocytes as indicated by the negative regulation of end-diastolic force-length relationship, which in turn enhanced contractility as indicated by increased Frank–Starling gain (dimensionless index for contractility) (Peyronnet et al., 2017). Increased cardiomyocyte compliance is presumably related to titin phosphorylation. However, the observed positive regulation of the Frank–Starling relationship by apelin must be dependent on other contractile proteins such as cTnI and MLC or alkalosis, because decreased titin-based stiffness is associated with reduced length-dependent activation of myocardium (Methawasin et al., 2014; Ait-Mou et al., 2016; Beqqali et al., 2016). Recently, we demonstrated that APJ-deficient cardiomyocytes showed negative regulation of the Frank–Starling relationship with no increase in Ca^{2+} transients in response to stretch (Parikh et al., 2018). Our study also provided mechanistic insights for apelin's positive inotropic and Frank–Starling effects. We demonstrated reduced protein kinase A (PKA) phosphorylation of cTnI at Ser^{22}/Ser^{23} in response to apelin. This is known to increase myofilament Ca^{2+} sensitivity, and is consistent with apelin-dependent AC–cAMP–PKA inhibition through $G_{\alpha i}$ activation (Szokodi et al., 2002; Scimia et al., 2012) (**Figure 5**).

The Role of Apelin–APJ in Ca^{2+}-Dependent Positive Inotropy and the Anrep Effect

In addition to this Ca^{2+}-independent mechanism, apelin is thought to exert its inotropic action by increasing the availability of intracellular Ca^{2+}. Apelin's inotropic effect in isolated hearts is dependent on PLC, PKC, NHE-1, and NCX activation (Szokodi et al., 2002). Notably, this inotropic response develops slowly to reach a plateau within 10–30 min and is then sustained, which is different from classical β-adrenergic receptor activation that develops rapidly over a matter of seconds. Although Ca^{2+} dynamics were not examined in this study, a later study proposed that apelin-induced increased contractility is the result of increased Ca^{2+} transients rather than changes in myofilament Ca^{2+} responsiveness (Dai et al., 2006). Most recently, these observations were consolidated in a report showing that apelin has positive inotropic and lusitropic actions on isolated myocytes with enhanced calcium-induced calcium release. This enhanced Ca^{2+} release is achieved through increased Ca^{2+} influx through NCX and increased rate of Ca^{2+} uptake to Ca^{2+} storage by sarcoplasmic reticulum Ca^{2+}-ATPase (SERCA), as controlled by PKC-directed phosphorylation (Wang et al., 2008). It is intriguing that the time course and the signaling pathways underlying the effect of apelin show some similarities to the mechanism of SFR (**Figure 6** compared to **Figure 3**), in which NHE-1 and NCX are the primary downstream actors. Although the role of APJ in SFR has yet to be fully explored, it is conceivable that this signaling pathway modulates this physiological phenomenon both through apelin–APJ binding and APJ's mechanosensing ability.

Integration of Apelin and Mechanical Stimuli in APJ to Differentially Activate Cardiac Prosurvival and Hypertrophic Signaling

We previously demonstrated a beneficial effect of chronic apelin supplementation on cardiac performance with reduced left ventricular preload and afterload, and increased contractile

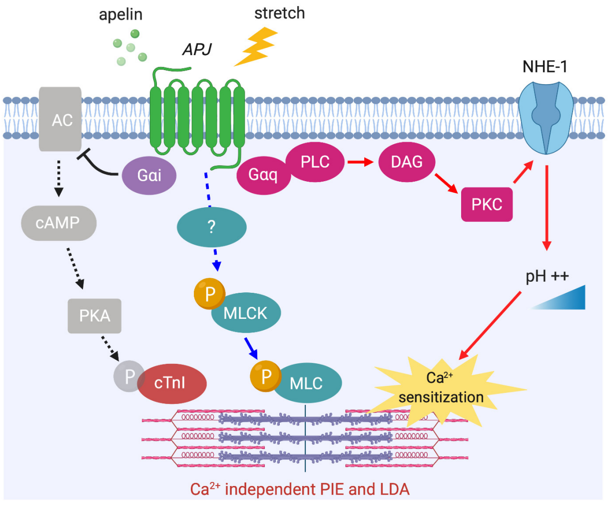

FIGURE 5 | APJ downstream signaling pathways for Ca^{2+} independent positive inotropic effect (PIE) and length-dependent activation (LDA). Apelin-induced activation of APJ enhances myofilament sensitivity to Ca^{2+}, which leads to the positive regulation of LDA. The mechanisms include intracellular alkalinization by $G_{\alpha q}$-dependent NHE-1 activation (red arrows), $G_{\alpha i}$-dependent dephosphorylation of cTnI (black dashed arrows), and the phosphorylation of MLC (blue arrows, mechanism unknown).

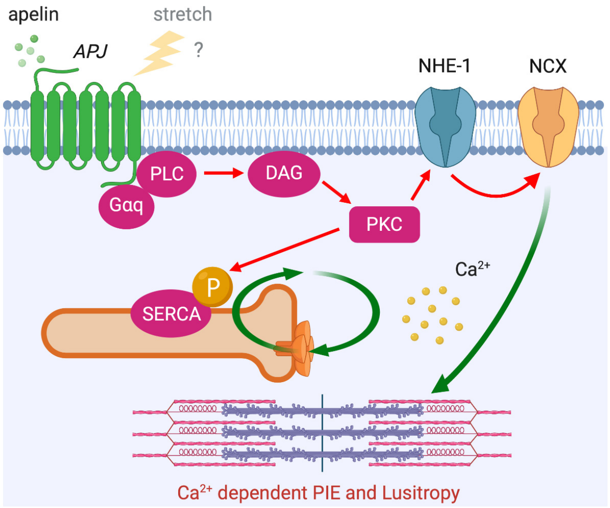

FIGURE 6 | APJ downstream signaling pathway for Ca^{2+} dependent positive inotropic effect (PIE). APJ activation by apelin also induces PIE that accompanies increased Ca^{2+} transient through $G_{\alpha q}$-dependent NCX activation (red arrows). Positive lusitropic effect (increased velocity of myocardial relaxation) is also induced via PKC-directed phosphorylation of SERCA.

function without evidence of hypertrophy (Ashley et al., 2005). Chronic stimulation of APJ by apelin not only increases cardiac performance but also attenuates the development of pressure-overload heart failure through the inhibition of TGF-β-driven profibrotic activity (Pchejetski et al., 2012) and NOX2-derived ROS production (Koguchi et al., 2012). In apelin-deficient mice, hypertrophic response to pressure overload was unchanged, but the progressive impairment of systolic function was observed (Kuba et al., 2007). Myocardial infarcted hearts in apelin deficient mice exhibit exacerbated postinfarction remodeling and impaired functional recovery with a significant reduction of prosurvival phospho-Akt and ERK1/2 signals in the infarct and peri-infarct regions (Wang et al., 2003). These studies clearly demonstrate the simultaneous inotropic and antihypertrophic effects of apelin in ischemia and pressure overload.

Conversely, cardiomyocyte-specific overexpression of APJ causes cardiac hypertrophy and contractile dysfunction in mice (Murata et al., 2016). This indicates that APJ has a capacity to activate multiple downstream signaling pathways such as $G_{\alpha i}$- and $G_{\alpha q}$-dependent pathways (Chapman et al., 2014), some of which may be independent of apelin's protective effects. It has also been shown that APJ can integrate chemical (apelin) and mechanical (stretch) stimuli and translates these into opposite cardiac outcomes by differentially activating downstream pathways (Scimia et al., 2012). Specifically, apelin activates APJ through $G_{\alpha i}$ protein to exert its cardioprotective effect, while stretch stimulates APJ to recruit β-arrestins, which promote pathological hypertrophy (**Figure 7**). At the cellular level, the mechanosensing capacity of APJ has been confirmed in H9c2 cardiomyocytes in which the increase in diameter, volume and protein content of cardiomyocytes under static pressure was ameliorated by APJ shRNA (Xie et al., 2014). Recently, our study provided supporting evidence that myocyte-specific deletion of APJ is protective against pressure-overload heart failure, showing the abrogation of mechanosensing capacity, reduced Ca^{2+} transient, and remarkable suppression of cellular hypertrophy and fibrosis (Parikh et al., 2018). These studies suggest that APJ integrates apelin and stretch stimuli, biasing the level of G protein versus β-arrestin signaling to attenuate or stimulate hypertrophy. While the downstream mechanisms of stretch-induced β-arrestin signaling remain undefined, the function of β-arrestins has also been observed to block the interaction of APJ with $G_{\alpha i}$ proteins (i.e., desensitization), which may contribute to the pro-hypertrophic program (Scimia et al., 2012). These studies have implications for the consideration of APJ as a drug target, because the greatest benefit may be obtained not simply by apelin stimulation, but rather by selectively activating the $G_{\alpha i}$-dependent signaling pathway or by inhibiting the ability of APJ to respond to mechanical stretch. For this purpose, further efforts are critical to clarify the intricacies

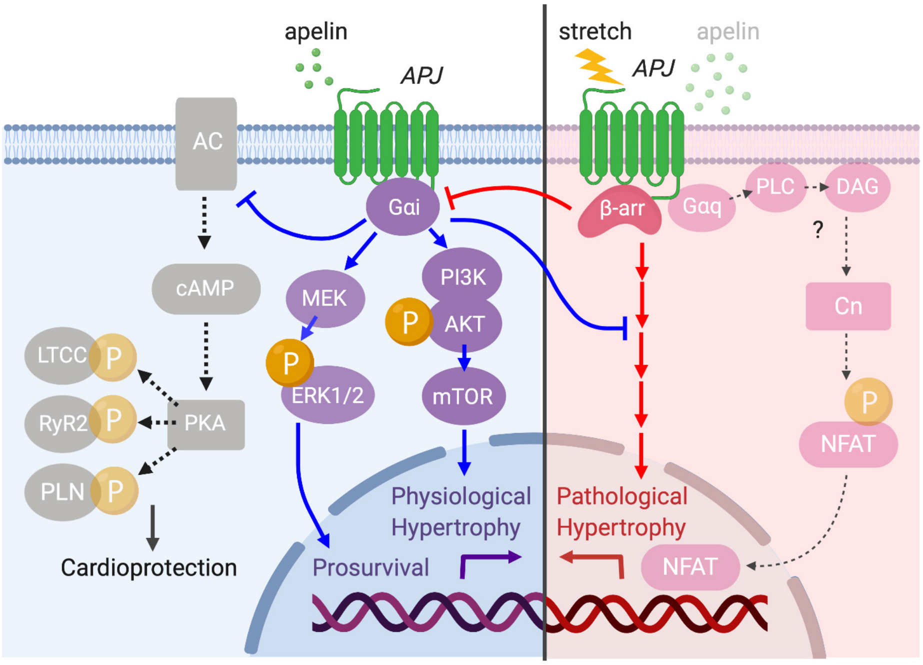

FIGURE 7 | Diverse APJ signaling pathways activated by prolonged mechanical load or apelin. APJ translates apelin and stretch stimuli into distinct downstream signaling pathways. Apelin stimulation induces $G_{\alpha i}$-dependent signaling to promote physiological hypertrophy and prosurvival signaling through the activation of Akt–mTOR and ERK1/2 (blue arrows). $G_{\alpha i}$ also inhibits deleterious cAMP–PKA pathway to serve a cardioprotective role (black dashed arrows). On the other hand, membrane stretch activates a β-arrestin-dependent program that results in pathological hypertrophy although the detailed downstream mechanisms are unresolved (red arrows). Importantly, there is a functional interplay between apelin- and stretch-dependent APJ signaling, in which apelin–APJ signaling blunts stretch-induced pathological signaling while stretch–APJ signaling interferes with apelin-induced $G_{\alpha i}$ activation. Although the apelin–APJ system involves $G_{\alpha q}$-dependent signaling pathway (**Figure 6**), the relevance of this pathway to pathological hypertrophy has not been examined.

of downstream integration of ligand and mechanosensitive signaling by APJ.

APJ Targeted Therapeutics for Mechanical Stress-Associated Heart Diseases (Table 1)

Apelin's positive inotropy and anti-hypertrophic effects support its therapeutic potential in preventing and treating cardiovascular disease. The majority of current heart failure therapies are targeted at the inhibition of deleterious neurohormonal axes that are upregulated in the later stages of the disease. In this aspect, the apelin–APJ system is attractive because it appears to be downregulated in heart failure (Japp and Newby, 2008), and stimulation of this pathway may have additive or even synergistic efficacy to current therapy by targeting complementary but separate pathways. Indeed, intravenous administration of [Pyr^1] apelin-13, an active fragment of apelin, in heart failure patients showed efficacy with peripheral and coronary vasodilatation and increases in cardiac output (Japp et al., 2010).

Nonetheless, the therapeutic application of apelin is limited because of its extremely short biological half-life and parenteral administration. This is attributed to the degradation by endogenous proteases circulating in the blood (Japp et al., 2008; Zhen et al., 2013). Furthermore, apelin is hydrolyzed and partially deactivated by angiotensin I converting enzyme 2 (ACE2) (Vickers et al., 2002; Wang et al., 2016). Thus, many efforts have been directed to the development of apelin analogs or novel agonists of APJ (Yamaleyeva et al., 2016). In particular, combinatorial screening of the NIH small molecule library identified a full non-peptide APJ agonist, ML233, at activating both $G_{\alpha i}$- and β-arrestin-dependent pathways (Khan et al., 2011). In addition, using molecular dynamics simulations, Brame et al. (2015) designed cyclic analogs and identified a biased agonist, MM07, which activates APJ by preferentially stimulating $G_{\alpha i}$-dependent pathways but not β-arrestin. Because stimulation of β-arrestin pathway could be deleterious, G protein-biased APJ ligand MM07 represents a potential new therapeutic for heart failure.

STRETCH-INDUCED CONFORMATIONAL CHANGE IN AT_1R AND APJ

G protein-coupled receptors adopt distinct conformations to selectively activate different arrays of downstream signaling (Rosenbaum et al., 2009; Vaidehi and Kenakin, 2010). Detailed analysis of the conformational changes is often performed by crystal structure analysis, but this only allows a static view of a given receptor conformation. Bioluminescence resonance energy transfer (BRET) and fluorescence resonance energy transfer (FRET) techniques allow insight into the kinetics and amplitudes of agonist- and stretch-induced receptor conformations. Using these techniques, stretch-induced conformational changes of AT_1R have been studied. BRET revealed that membrane stretch induces an active AT_1R conformation allowing for G protein activation and subsequent β-arrestin recruitment (y Schnitzler et al., 2008). More recently, a study using BRET and FRET demonstrated that G protein activation is not necessary for β-arrestin recruitment and that mechanical stretch induces a particular β-arrestin conformation that is distinct from the agonist-stimulated conformation (Rakesh et al., 2010). Another approach was also taken to examine the conformational change of AT_1R in response to stretch. Using the substituted cysteine accessibility method (SCAM) and molecular modeling approach, Yasuda et al. (2008) showed that stretch stimulation of AT_1R induces a dislocation and a counterclockwise rotation of transmembrane domain 7 toward the ligand-binding pocket, a conformation that is distinct from the ligand-activated receptor conformation. These fascinating data suggest that conformational change is responsible for biased signaling in AT_1R. Such studies of APJ and examination of the differential effect of novel AT_1R ligands on its conformation could eventually lead to structure-based drug design focused on selective inhibition of adverse remodeling via stretch-dependent pathways.

INTERACTION BETWEEN ANG-II–AT_1R AND APELIN–APJ

Neurohormonal interaction between AT_1R and APJ systems has been well-studied. Infusion of Ang II in rats causes an acute reduction of apelin and APJ levels in the heart, which is abolished by treatment with an ARB (Iwanaga et al., 2006). The left ventricular dysfunction observed in apelin deficient mice is restored to normal levels either by the treatment with an ARB or by AT_1R gene deletion (Sato et al., 2013). Furthermore, apelin overexpression abolishes Ang II-induced cardiac hypertrophy in cultured myocytes (Ye et al., 2015). While a growing literature suggests the antagonistic interplay between AT_1R and APJ systems through neurohormonal interactions, direct physical interaction between AT_1R and APJ has also been reported. Co-immunoprecipitation and FRET analysis revealed heterodimerization of AT_1R and APJ, in which the interaction appears to induce the inhibition of the AT_1R signaling pathway (Chun et al., 2008). More recently, it was revealed that AT_1R–APJ heterodimerization is induced by apelin, but is not affected by Ang II (Siddiquee et al., 2013). To date, the downstream effects of ligand and stretch stimulation on heterodimeric AT_1R–APJ have not been examined. It is conceivable that AT_1R–APJ heterodimers activate distinct signaling pathways compared to monomeric receptors, or that the multiple reported downstream pathways of AT_1R and APJ may be partially dependent on the activation of the heterodimeric receptor. Understanding of this may lead to the identification of novel ligands with optimal effects on heart failure pathobiology.

CONCLUSION

Angiotensin II type 1 receptor and APJ are mechanosensitive GPCRs in the heart, playing vital roles in cardiac physiological adaptation to changes in mechanical load. However, when a mechanical load is excessive and sustained, it can induce maladaptive hypertrophic signaling. Enormous effort has been invested in understanding the physiological and pathophysiological roles of AT_1R and APJ signaling to identify novel therapeutic strategies. Selective activation or inhibition of mechanically stimulated signaling components by biased agonists may yield more precise molecular enhancers of desired inotropic or cardioprotective effects while avoiding detrimental signaling. In addition, by gaining an improved understanding of the signaling mechanisms of these receptors in the heart, it is likely that complementary downstream targets will be identified to modulate cardiac function and ameliorate disease.

AUTHOR CONTRIBUTIONS

KS took the lead in writing the manuscript with input from VP and EA.

FUNDING

This work was supported by the American Heart Association (Career Development Award 18CDA34020088 to KS), NIH (K08-HL143185 to VP), and the Sarnoff Cardiovascular Research and John Taylor Babbitt Foundation (VP).

REFERENCES

Abraham, D. M., Davis, R. T. III, Warren, C. M., Mao, L., Wolska, B. M., Solaro, R. J., et al. (2016). β-Arrestin mediates the Frank-Starling mechanism of cardiac contractility. *Proc. Natl. Acad. Sci. U.S.A.* 113, 14426–14431. doi: 10.1073/pnas.1609308113

Ait-Mou, Y., Hsu, K., Farman, G. P., Kumar, M., Greaser, M. L., Irving, T. C., et al. (2016). Titin strain contributes to the Frank-Starling law of the heart by structural rearrangements of both thin- and thick-filament proteins. *Proc. Natl. Acad. Sci. U.S.A.* 113, 2306–2311. doi: 10.1073/pnas.1516732113

Allen, D. G., Jewell, B. R., and Murray, J. W. (1974). The contribution of activation processes to the length–tension relation of cardiac muscle. *Nature* 248, 606–607. doi: 10.1038/248606a0

Allen, D. G., and Kurihara, S. (1982). The effects of muscle length on intracellular calcium transients in mammalian cardiac muscle. *J. Physiol.* 327, 79–94. doi: 10.1113/jphysiol.1982.sp014221

Alvarez, B. V., Pérez, N. G., Ennis, I. L., Camilión de Hurtado, M. C., and Cingolani, H. E. (1999). Mechanisms underlying the increase in force and Ca(2+) transient that follow stretch of cardiac muscle: a possible explanation of the Anrep effect. *Circ. Res.* 85, 716–722. doi: 10.1161/01.res.85.8.716

Ashley, E. A., Powers, J., Chen, M., Kundu, R., Finsterbach, T., Caffarelli, A., et al. (2005). The endogenous peptide apelin potently improves cardiac contractility and reduces cardiac loading *in vivo*. *Cardiovasc. Res.* 65, 73–82. doi: 10.1016/j.cardiores.2004.08.018

Beqqali, A., Bollen, I. A. E., Rasmussen, T. B., van den Hoogenhof, M. M., van Deutekom, H. W. M., Schafer, S., et al. (2016). A mutation in the glutamate-rich region of RNA-binding motif protein 20 causes dilated cardiomyopathy through missplicing of titin and impaired Frank–Starling mechanism. *Cardiovasc. Res.* 112, 452–463. doi: 10.1093/cvr/cvw192

Berry, M. F., Pirolli, T. J., Jayasankar, V., Burdick, J., Morine, K. J., Gardner, T. J., et al. (2004). Apelin has in vivo inotropic effects on normal and failing hearts. *Circulation* 110, II187–II193.

Boerrigter, G., Lark, M. W., Whalen, E. J., Soergel, D. G., Violin, J. D., and Burnett, J. C. Jr. (2011). Cardiorenal actions of Trv120027, a Novel ß-arrestin–biased ligand at the angiotensin Ii TYPE I RECEPTOR, in healthy and heart failure canines: a novel therapeutic strategy for acute heart failure. *Circ. Heart Fail.* 4, 770–778. doi: 10.1161/circheartfailure.111.962571

Brame, A. L., Maguire, J. J., Yang, P., Dyson, A., Torella, R., Cheriyan, J., et al. (2015). Design, characterization, and first-in-human study of the vascular actions of a novel biased apelin receptor agonist. *Hypertension* 65, 834–840. doi: 10.1161/hypertensionaha.114.05099

Brea, M. S., Díaz, R. G., Escudero, D. S., Caldiz, C. I., Portiansky, E. L., Morgan, P. E., et al. (2016). Epidermal growth factor receptor silencing blunts the slow force response to myocardial stretch. *J. Am. Heart Assoc.* 5:e004017. doi: 10.1161/JAHA.116.004017

Breithaupt, J. J., Pulcastro, H. C., Awinda, P. O., DeWitt, D. C., and Tanner, B. C. W. (2019). Regulatory light chain phosphorylation augments length-dependent contraction in PTU-treated rats. *J. Gen. Physiol.* 151, 66–76. doi: 10.1085/jgp.201812158

Calaghan, S. C., and White, E. (2001). Contribution of angiotensin II, endothelin 1 and the endothelium to the slow inotropic response to stretch in ferret papillary muscle. *Pflugers Arch.* 441, 514–520. doi: 10.1007/s004240000458

Caldiz, C. I., Garciarena, C. D., Dulce, R. A., Novaretto, L. P., Yeves, A. M., Ennis, I. L., et al. (2007). Mitochondrial reactive oxygen species activate the slow force response to stretch in feline myocardium. *J. Physiol.* 584, 895–905. doi: 10.1113/jphysiol.2007.141689

Chandrasekaran, B., Dar, O., and McDonagh, T. (2008). The role of apelin in cardiovascular function and heart failure. *Eur. J. Heart Fail.* 10, 725–732. doi: 10.1016/j.ejheart.2008.06.002

Chapman, N. A., Dupré, D. J., and Rainey, J. K. (2014). The apelin receptor: physiology, pathology, cell signalling, and ligand modulation of a peptide-activated class A GPCR. *Biochem. Cell Biol.* 92, 431–440. doi: 10.1139/bcb-2014-0072

Charo, D. N., Ho, M., Fajardo, G., Kawana, M., Kundu, R. K., Sheikh, A. Y., et al. (2009). Endogenous regulation of cardiovascular function by apelin-APJ. *Am. J. Physiol. Heart Circ. Physiol.* 297, H1904–H1913.

Chiluiza, D., Krishna, S., Schumacher, V. A., and Schlöndorff, J. (2013). Gain-of-function mutations in transient receptor potential C6 (TRPC6) activate extracellular signal-regulated kinases 1/2 (ERK1/2). *J. Biol. Chem.* 288, 18407–18420. doi: 10.1074/jbc.m113.463059

Chun, H. J., Ali, Z. A., Kojima, Y., Kundu, R. K., Sheikh, A. Y., Agrawal, R., et al. (2008). Apelin signaling antagonizes Ang II effects in mouse models of atherosclerosis. *J. Clin. Invest.* 118, 3343–3354.

Cingolani, H. E., Ennis, I. L., Aiello, E. A., and Pérez, N. G. (2011). Role of autocrine/paracrine mechanisms in response to myocardial strain. *Pflugers Arch.* 462, 29–38. doi: 10.1007/s00424-011-0930-9

Cingolani, H. E., Pérez, N. G., Cingolani, O. H., and Ennis, I. L. (2013). The Anrep effect: 100 years later. *Am. J. Physiol. Heart Circ. Physiol.* 304, H175–H182.

Cingolani, H. E., Villa-Abrille, M. C., Cornelli, M., Nolly, A., Ennis, I. L., Garciarena, C., et al. (2006). The positive inotropic effect of angiotensin II: role of endothelin-1 and reactive oxygen species. *Hypertension* 47, 727–734. doi: 10.1161/01.hyp.0000208302.62399.68

Clement, O., Puceat, M., Walsh, M. P., and Vassort, G. (1992). Protein kinase C enhances myosin light-chain kinase effects on force development and ATPase activity in rat single skinned cardiac cells. *Biochem. J.* 285(Pt 1), 311–317. doi: 10.1042/bj2850311

Crabtree, G. R., and Olson, E. N. (2002). NFAT signaling: choreographing the social lives of cells. *Cell* 109(Suppl.), S67–S79.

Dai, T., Ramirez-Correa, G., and Gao, W. D. (2006). Apelin increases contractility in failing cardiac muscle. *Eur. J. Pharmacol.* 553, 222–228. doi: 10.1016/j.ejphar.2006.09.034

de Tombe, P. P. (2003). Cardiac myofilaments: mechanics and regulation. *J. Biomech.* 36, 721–730. doi: 10.1016/s0021-9290(02)00450-5

De Vecchis, R., Cesaro, A., Ariano, C., Giasi, A., and Cioppa, C. (2017). Phosphodiesterase-5 inhibitors improve clinical outcomes, exercise capacity and pulmonary hemodynamics in patients with heart failure with reduced left ventricular ejection fraction: a meta-analysis. *J. Clin. Med. Res.* 9, 488–498. doi: 10.14740/jocmr3008w

Diniz, G. P., Carneiro-Ramos, M. S., and Barreto-Chaves, M. L. M. (2009). Angiotensin type 1 receptor mediates thyroid hormone-induced cardiomyocyte hypertrophy through the Akt/GSK-3beta/mTOR signaling pathway. *Basic Res. Cardiol.* 104, 653–667. doi: 10.1007/s00395-009-0043-1

Dyachenko, V., Husse, B., Rueckschloss, U., and Isenberg, G. (2009). Mechanical deformation of ventricular myocytes modulates both TRPC6 and Kir2.3 channels. *Cell Calcium* 45, 38–54. doi: 10.1016/j.ceca.2008.06.003

Farkasfalvi, K., Stagg, M. A., Coppen, S. R., Siedlecka, U., Lee, J., Soppa, G. K., et al. (2007). Direct effects of apelin on cardiomyocyte contractility and electrophysiology. *Biochem. Biophys. Res. Commun.* 357, 889–895. doi: 10.1016/j.bbrc.2007.04.017

Gorin, Y., Kim, N. H., Feliers, D., Bhandari, B., Choudhury, G. G., and Abboud, H. E. (2001). Angiotensin II activates Akt/protein kinase B by an arachidonic acid/redox-dependent pathway and independent of phosphoinositide 3-kinase. *FASEB J.* 15, 1909–1920. doi: 10.1096/fj..01-0165com

Gottlieb, P., Folgering, J., Maroto, R., Raso, A., Wood, T. G., Kurosky, A., et al. (2008). Revisiting TRPC1 and TRPC6 mechanosensitivity. *Pflugers Arch.* 455, 1097–1103. doi: 10.1007/s00424-007-0359-3

Gregg, D. E., and Shipley, R. E. (1944). Augmentation of left coronary inflow with elevation of left ventricular pressure and observations on the mechanism for increased coronary inflow with increased cardiac load. *Am. J. Physiol.* 142:44 doi: 10.1152/ajplegacy.1944.142.1.44

Hamdani, N., Herwig, M., and Linke, W. A. (2017). Tampering with springs: phosphorylation of titin affecting the mechanical function of cardiomyocytes. *Biophys. Rev.* 9, 225–237. doi: 10.1007/s12551-017-0263-9

Heineke, J., and Molkentin, J. D. (2006). Regulation of cardiac hypertrophy by intracellular signalling pathways. *Nat. Rev. Mol. Cell Biol.* 7, 589–600. doi: 10.1038/nrm1983

Hescheler, J., Rosenthal, W., Hinsch, K. D., Wulfern, M., Trautwein, W., and Schultz, G. (1988). Angiotensin II-induced stimulation of voltage-dependent Ca2+ currents in an adrenal cortical cell line. *EMBO J.* 7, 619–624. doi: 10.1002/j.1460-2075.1988.tb02855.x

Ho, K. K., Pinsky, J. L., Kannel, W. B., and Levy, D. (1993). The epidemiology of heart failure: the Framingham study. *J. Am. Coll. Cardiol.* 22, 6A–13A.

Hofmann, T., Schaefer, M., Schultz, G., and Gudermann, T. (2002). Subunit composition of mammalian transient receptor potential channels in living cells. *Proc. Natl. Acad. Sci. U.S.A.* 99, 7461–7466. doi: 10.1073/pnas.102596199

Ikenouchi, H., Barry, W. H., Bridge, J. H., Weinberg, E. O., Apstein, C. S., and Lorell, B. H. (1994). Effects of angiotensin II on intracellular Ca2+ and pH in isolated beating rabbit hearts and myocytes loaded with the indicator indo-1. *J. Physiol.* 480(Pt 2), 203–215. doi: 10.1113/jphysiol.1994.sp020353

Iwanaga, Y., Kihara, Y., Takenaka, H., and Kita, T. (2006). Down-regulation of cardiac apelin system in hypertrophied and failing hearts: possible role of angiotensin II–angiotensin type 1 receptor system. *J. Mol. Cell. Cardiol.* 41, 798–806. doi: 10.1016/j.yjmcc.2006.07.004

Japp, A. G., Cruden, N. L., Amer, D. A. B., Li, V. K. Y., Goudie, E. B., Johnston, N. R., et al. (2008). Vascular effects of apelin *in vivo* in man. *J. Am. Coll. Cardiol.* 52, 908–913. doi: 10.1016/j.jacc.2008.06.013

Japp, A. G., Cruden, N. L., Barnes, G., van Gemeren, N., Mathews, J., Adamson, J., et al. (2010). Acute cardiovascular effects of apelin in humans: potential role in patients with chronic heart failure. *Circulation* 121, 1818–1827. doi: 10.1161/circulationaha.109.911339

Japp, A. G., and Newby, D. E. (2008). The apelin-APJ system in heart failure: pathophysiologic relevance and therapeutic potential. *Biochem. Pharmacol.* 75, 1882–1892. doi: 10.1016/j.bcp.2007.12.015

Katz Arnold, M. (2002). Ernest Henry starling, his predecessors, and the "Law of the HEART.". *Circulation* 106, 2986–2992. doi: 10.1161/01.cir.0000040594.96123.55

Kentish, J. C., and Wrzosek, A. (1998). Changes in force and cytosolic Ca2+ concentration after length changes in isolated rat ventricular trabeculae. *J. Physiol.* 506(Pt 2), 431–444. doi: 10.1111/j.1469-7793.1998.431bw.x

Khan, P., Maloney, P. R., Hedrick, M., Gosalia, P., Milewski, M., Li, L., et al. (2011). "Functional agonists of the apelin (APJ) receptor. *Probe Reports from the NIH Molecular Libraries Program*, (Bethesda, MD: National Center for Biotechnology Information).

Kim, K.-S., Abraham, D., Williams, B., Violin, J. D., Mao, L., and Rockman, H. A. (2012). β-Arrestin-biased AT1R stimulation promotes cell survival during acute cardiac injury. *Am. J. Physiol. Heart Circ. Physiol.* 303, H1001–H1010.

Koguchi, W., Kobayashi, N., Takeshima, H., Ishikawa, M., Sugiyama, F., and Ishimitsu, T. (2012). Cardioprotective effect of apelin-13 on cardiac performance and remodeling in end-stage heart failure. *Circ. J.* 76, 137–144. doi: 10.1253/circj.cj-11-0689

Kuba, K., Zhang, L., Imai, Y., Arab, S., Chen, M., Maekawa, Y., et al. (2007). Impaired heart contractility in Apelin gene-deficient mice associated with aging and pressure overload. *Circ. Res.* 101, e32–e42.

Kumar, M., Govindan, S., Zhang, M., Khairallah, R. J., Martin, J. L., Sadayappan, S., et al. (2015). Cardiac myosin-binding protein C and Troponin-I phosphorylation independently modulate myofilament length-dependent activation. *J. Biol. Chem.* 290, 29241–29249. doi: 10.1074/jbc.m115.686790

Kuwahara, K., Wang, Y., McAnally, J., Richardson, J. A., Bassel-Duby, R., Hill, J. A., et al. (2006). TRPC6 fulfills a calcineurin signaling circuit during pathologic cardiac remodeling. *J. Clin. Invest.* 116, 3114–3126. doi: 10.1172/jci27702

Lee, D. K., Cheng, R., Nguyen, T., Fan, T., Kariyawasam, A. P., Liu, Y., et al. (2000). Characterization of apelin, the ligand for the APJ receptor. *J. Neurochem.* 74, 34–41.

Lefkowitz, R. J. (2004). Historical review: a brief history and personal retrospective of seven-transmembrane receptors. *Trends Pharmacol. Sci.* 25, 413–422. doi: 10.1016/j.tips.2004.06.006

Levy, D., Garrison, R. J., Savage, D. D., Kannel, W. B., and Castelli, W. P. (1990). Prognostic implications of echocardiographically determined left ventricular mass in the Framingham heart study. *N. Engl. J. Med.* 322, 1561–1566. doi: 10.1056/nejm199005313222203

Lewis, G. D., Shah, R., Shahzad, K., Camuso, J. M., Pappagianopoulos, P. P., Hung, J., et al. (2007). Sildenafil improves exercise capacity and quality of life in patients with systolic heart failure and secondary pulmonary hypertension. *Circulation* 116, 1555–1562. doi: 10.1161/circulationaha.107.716373

Lin, B. L., Matera, D., Doerner, J. F., Zheng, N., del Camino, D., Mishra, S., et al. (2019). In vivo selective inhibition of TRPC6 by antagonist BI 749327 ameliorates fibrosis and dysfunction in cardiac and renal disease. *Proc. Natl. Acad. Sci.* 116, 10156–10161. doi: 10.1073/pnas.1815354116

Louhivuori, L. M., Jansson, L., Nordström, T., Bart, G., Näsman, J., and Akerman, K. E. O. (2010). Selective interference with TRPC3/6 channels disrupts OX1 receptor signalling via NCX and reveals a distinct calcium influx pathway. *Cell Calcium* 48, 114–123. doi: 10.1016/j.ceca.2010.07.005

Mattiazzi, A. (1997). Positive inotropic effect of angiotensin II. Increases in intracellular Ca2+ or changes in myofilament Ca2+ responsiveness? *J. Pharmacol. Toxicol. Methods* 37, 205–214. doi: 10.1016/s1056-8719(97)00020-8

Maturana, A. D., Casal, A. J., Demaurex, N., Vallotton, M. B., Capponi, A. M., and Rossier, M. F. (1999). Angiotensin II negatively modulates L-type calcium channels through a pertussis toxin-sensitive G protein in adrenal glomerulosa cells. *J. Biol. Chem.* 274, 19943–19948. doi: 10.1074/jbc.274.28.19943

Methawasin, M., Hutchinson, K. R., Lee, E.-J., Smith, J. E. III, Saripalli, C., Hidalgo, C. G., et al. (2014). Experimentally increasing titin compliance in a novel mouse model attenuates the Frank-Starling mechanism but has a beneficial effect on diastole. *Circulation* 129, 1924–1936. doi: 10.1161/circulationaha.113.005610

Molkentin, J. D. (2004). Calcineurin-NFAT signaling regulates the cardiac hypertrophic response in coordination with the MAPKs. *Cardiovasc. Res.* 63, 467–475. doi: 10.1016/j.cardiores.2004.01.021

Molkentin, J. D., Lu, J. R., Antos, C. L., Markham, B., Richardson, J., Robbins, J., et al. (1998). A calcineurin-dependent transcriptional pathway for cardiac hypertrophy. *Cell* 93, 215–228. doi: 10.1016/s0092-8674(00)81573-1

Monasky, M. M., Taglieri, D. M., Henze, M., Warren, C. M., Utter, M. S., Soergel, D. G., et al. (2013). The β-arrestin-biased ligand TRV120023 inhibits angiotensin II-induced cardiac hypertrophy while preserving enhanced myofilament response to calcium. *Am. J. Physiol. Heart Circ. Physiol.* 305, H856–H866.

Morano, I., Bächle-Stolz, C., Katus, A., and Rüegg, J. C. (1988). Increased calcium sensitivity of chemically skinned human atria by myosin light chain kinase. *Basic Res. Cardiol.* 83, 350–359. doi: 10.1007/bf02005820

Murata, K., Ishida, J., Ishimaru, T., Mizukami, H., Hamada, J., Saito, C., et al. (2016). Lactation is a risk factor of postpartum heart failure in mice with cardiomyocyte-specific apelin receptor (APJ) overexpression. *J. Biol. Chem.* 291, 11241–11251. doi: 10.1074/jbc.m115.699009

Nagayama, T., Hsu, S., Zhang, M., Koitabashi, N., Bedja, D., Gabrielson, K. L., et al. (2009). Sildenafil stops progressive chamber, cellular, and molecular remodeling and improves calcium handling and function in hearts with pre-existing advanced hypertrophy caused by pressure overload. *J. Am. Coll. Cardiol.* 53, 207–215. doi: 10.1016/j.jacc.2008.08.069

Nakayama, H., Wilkin, B. J., Bodi, I., and Molkentin, J. D. (2006). Calcineurin-dependent cardiomyopathy is activated by TRPC in the adult mouse heart. *FASEB J.* 20, 1660–1670. doi: 10.1096/fj.05-5560com

Onohara, N., Nishida, M., Inoue, R., Kobayashi, H., Sumimoto, H., Sato, Y., et al. (2006). TRPC3 and TRPC6 are essential for angiotensin II-induced cardiac hypertrophy. *EMBO J.* 25, 5305–5316. doi: 10.1038/sj.emboj.7601417

Parikh, V. N., Liu, J., Shang, C., Woods, C., Chang, A. C., Zhao, M., et al. (2018). Apelin and APJ orchestrate complex tissue-specific control of cardiomyocyte hypertrophy and contractility in the hypertrophy-heart failure transition. *Am. J. Physiol. Heart Circ. Physiol.* 315, H348–H356.

Parmley, W. W., and Chuck, L. (1973). Length-dependent changes in myocardial contractile state. *Am. J. Physiol.* 224, 1195–1199. doi: 10.1152/ajplegacy.1973.224.5.1195

Pauli, A., Norris, M. L., Valen, E., Chew, G.-L., Gagnon, J. A., Zimmerman, S., et al. (2014). Toddler: an embryonic signal that promotes cell movement via apelin receptors. *Science* 343:1248636. doi: 10.1126/science.1248636

Pchejetski, D., Foussal, C., Alfarano, C., Lairez, O., Calise, D., Guilbeau-Frugier, C., et al. (2012). Apelin prevents cardiac fibroblast activation and collagen production through inhibition of sphingosine kinase 1. *Eur. Heart J.* 33, 2360–2369. doi: 10.1093/eurheartj/ehr389

Pérez, N. G., de Hurtado, M. C., and Cingolani, H. E. (2001). Reverse mode of the Na+-Ca2+ exchange after myocardial stretch: underlying mechanism of the slow force response. *Circ. Res.* 88, 376–382. doi: 10.1161/01.res.88.4.376

Pérez, N. G., Nolly, M. B., Roldan, M. C., Villa-Abrille, M. C., Cingolani, E., Portiansky, E. L., et al. (2011). Silencing of NHE-1 blunts the slow force response to myocardial stretch. *J. Appl. Physiol.* 111, 874–880. doi: 10.1152/japplphysiol.01344.2010

Pérez, N. G., Villa-Abrille, M. C., Aiello, E. A., Dulce, R. A., Cingolani, H. E., and Camilión de Hurtado, M. C. (2003). A low dose of angiotensin II increases inotropism through activation of reverse Na+/Ca2+ exchange by endothelin release. *Cardiovasc. Res.* 60, 589–597. doi: 10.1016/j.cardiores.2003.09.004

Perjés, Á, Skoumal, R., Tenhunen, O., Kónyi, A., Simon, M., Horváth, I. G., et al. (2014). Apelin increases cardiac contractility via protein kinase Cε- and extracellular signal-regulated kinase-dependent mechanisms. *PLoS One* 9:e93473. doi: 10.1371/journal.pone.0093473

Petroff, M. G., Aiello, E. A., Palomeque, J., Salas, M. A., and Mattiazzi, A. (2000). Subcellular mechanisms of the positive inotropic effect of angiotensin II in cat myocardium. *J. Physiol.* 529(Pt 1), 189–203. doi: 10.1111/j.1469-7793.2000.00189.x

Peyronnet, R., Bollensdorff, C., Capel, R. A., Rog-Zielinska, E. A., Woods, C. E., Charo, D. N., et al. (2017). Load-dependent effects of apelin on murine cardiomyocytes. *Prog. Biophys. Mol. Biol.* 130, 333–343. doi: 10.1016/j.pbiomolbio.2017.09.013

Poburko, D., Fameli, N., Kuo, K.-H., and van Breemen, C. (2008). Ca2+ signaling in smooth muscle: TRPC6, NCX and LNats in nanodomains. *Channels* 2, 10–12. doi: 10.4161/chan.2.1.6053

Poburko, D., Liao, C.-H., Lemos, V. S., Lin, E., Maruyama, Y., Cole, W. C., et al. (2007). Transient receptor potential channel 6–mediated, localized cytosolic [Na+] transients drive Na+/Ca2+ exchanger–mediated Ca2+ entry in purinergically stimulated aorta smooth muscle cells. *Circ. Res.* 101, 1030–1038. doi: 10.1161/circresaha.107.155531

Rajagopal, K., Whalen, E. J., Violin, J. D., Stiber, J. A., Rosenberg, P. B., Premont, R. T., et al. (2006). β-Arrestin2-mediated inotropic effects of the angiotensin II type 1A receptor in isolated cardiac myocytes. *Proc. Natl. Acad. Sci. U.S.A.* 103, 16284–16289. doi: 10.1073/pnas.0607583103

Rajagopal, S., Rajagopal, K., and Lefkowitz, R. J. (2010). Teaching old receptors new tricks: biasing seven-transmembrane receptors. *Nat. Rev. Drug Discov.* 9, 373–386. doi: 10.1038/nrd3024

Rakesh, K., Yoo, B., Kim, I.-M., Salazar, N., Kim, K.-S., and Rockman, H. A. (2010). β-arrestin–biased agonism of the angiotensin receptor induced by mechanical stress. *Sci. Signal.* 3:ra46. doi: 10.1126/scisignal.2000769

Ramirez, M. T., Sah, V. P., Zhao, X.-L., Hunter, J. J., Chien, K. R., and Brown, J. H. (1997). The MEKK-JNK pathway is stimulated by α1-adrenergic receptor and ras activation and is associated with in Vitroand *in vivo* cardiac hypertrophy. *J. Biol. Chem.* 272, 14057–14061. doi: 10.1074/jbc.272.22.14057

Redfield, M. M., Chen, H. H., Borlaug, B. A., Semigran, M. J., Lee, K. L., Lewis, G., et al. (2013). Effect of phosphodiesterase-5 inhibition on exercise capacity and clinical status in heart failure with preserved ejection fraction: a randomized clinical trial. *JAMA* 309, 1268–1277.

Reiter, E., Ahn, S., Shukla, A. K., and Lefkowitz, R. J. (2012). Molecular mechanism of β-arrestin-biased agonism at seven-transmembrane receptors. *Annu. Rev. Pharmacol. Toxicol.* 52, 179–197. doi: 10.1146/annurev.pharmtox.010909.105800

Rosenbaum, D. M., Rasmussen, S. G. F., and Kobilka, B. K. (2009). The structure and function of G-protein-coupled receptors. *Nature* 459, 356–363.

Ryba, D. M., Li, J., Cowan, C. L., Russell, B., Wolska, B. M., and Solaro, R. J. (2017). Long-Term Biased β-arrestin signaling improves cardiac structure and function in dilated cardiomyopathy. *Circulation* 135, 1056–1070. doi: 10.1161/circulationaha.116.024482

Sadoshima, J., and Izumo, S. (1993). Molecular characterization of angiotensin II–induced hypertrophy of cardiac myocytes and hyperplasia of cardiac fibroblasts. Critical role of the AT1 receptor subtype. *Circ. Res.* 73, 413–423. doi: 10.1161/01.res.73.3.413

Sadoshima, J., Xu, Y., Slayter, H. S., and Izumo, S. (1993). Autocrine release of angiotensin II mediates stretch-induced hypertrophy of cardiac myocytes *in vitro*. *Cell* 75, 977–984. doi: 10.1016/0092-8674(93)90541-w

Sarnoff, S. J., and Mitchell, J. H. (1961). The regulation of the performance of the heart. *Am. J. Med.* 30, 747–771.

Sarnoff, S. J., Mitchell, J. H., Gilmore, J. P., and Remensnyder, J. P. (1960). Homeometric autoregulation in the heart. *Circ. Res.* 8, 1077–1091. doi: 10.1161/01.res.8.5.1077

Sato, J., Makita, N., and Iiri, T. (2016). Inverse agonism: the classic concept of GPCRs revisited [Review]. *Endocr. J.* 63, 507–514. doi: 10.1507/endocrj.ej16-0084

Sato, T., Sato, C., Kadowaki, A., Watanabe, H., Ho, L., Ishida, J., et al. (2017). ELABELA-APJ axis protects from pressure overload heart failure and angiotensin II-induced cardiac damage. *Cardiovasc. Res.* 113, 760–769. doi: 10.1093/cvr/cvx061

Sato, T., Suzuki, T., Watanabe, H., Kadowaki, A., Fukamizu, A., Liu, P. P., et al. (2013). Apelin is a positive regulator of ACE2 in failing hearts. *J. Clin. Invest.* 123, 5203–5211. doi: 10.1172/jci69608

Scimia, M. C., Hurtado, C., Ray, S., Metzler, S., Wei, K., Wang, J., et al. (2012). APJ acts as a dual receptor in cardiac hypertrophy. *Nature* 488, 394–398. doi: 10.1038/nature11263

Seo, K., Rainer, P. P., Lee, D.-I., Hao, S., Bedja, D., Birnbaumer, L., et al. (2014a). Hyperactive adverse mechanical stress responses in dystrophic heart are coupled to transient receptor potential canonical 6 and blocked by cGMP-protein kinase G modulation. *Circ. Res.* 114, 823–832. doi: 10.1161/circresaha.114.302614

Seo, K., Rainer, P. P., Shalkey Hahn, V., Lee, D.-I., Jo, S.-H., Andersen, A., et al. (2014b). Combined TRPC3 and TRPC6 blockade by selective small-molecule or genetic deletion inhibits pathological cardiac hypertrophy. *Proc. Natl. Acad. Sci. U.S.A.* 111, 1551–1556. doi: 10.1073/pnas.1308963111

Shen, X., Cannell, M. B., and Ward, M.-L. (2013). Effect of SR load and pH regulatory mechanisms on stretch-dependent Ca(2+) entry during the slow force response. *J. Mol. Cell. Cardiol.* 63, 37–46. doi: 10.1016/j.yjmcc.2013.07.008

Siddiquee, K., Hampton, J., McAnally, D., May, L., and Smith, L. (2013). The apelin receptor inhibits the angiotensin II type 1 receptor via allosteric trans-inhibition. *Br. J. Pharmacol.* 168, 1104–1117. doi: 10.1111/j.1476-5381.2012.02192.x

Spassova, M. A., Hewavitharana, T., Xu, W., Soboloff, J., and Gill, D. L. (2006). A common mechanism underlies stretch activation and receptor activation of TRPC6 channels. *Proc. Natl. Acad. Sci. U.S.A.* 103, 16586–16591. doi: 10.1073/pnas.0606894103

Strachan, R. T., Sun, J.-P., Rominger, D. H., Violin, J. D., Ahn, S., Rojas Bie Thomsen, A., et al. (2014). Divergent transducer-specific molecular efficacies generate biased agonism at a G protein-coupled receptor (GPCR). *J. Biol. Chem.* 289, 14211–14224. doi: 10.1074/jbc.m114.548131

Szokodi, I., Tavi, P., Földes, G., Voutilainen-Myllylä, S., Ilves, M., Tokola, H., et al. (2002). Apelin, the novel endogenous ligand of the orphan receptor APJ, regulates cardiac contractility. *Circ. Res.* 91, 434–440. doi: 10.1161/01.res.0000033522.37861.69

Tachampa, K., Wang, H., Farman, G. P., and de Tombe, P. P. (2007). Cardiac troponin I threonine 144: role in myofilament length–dependent activation. *Circ. Res.* 101, 1081–1083. doi: 10.1161/circresaha.107.165258

Takimoto, E., Champion, H. C., Li, M., Belardi, D., Ren, S., Rodriguez, E. R., et al. (2005). Chronic inhibition of cyclic GMP phosphodiesterase 5A prevents and reverses cardiac hypertrophy. *Nat. Med.* 11, 214–222. doi: 10.1038/nm1175

Tatemoto, K., Hosoya, M., Habata, Y., Fujii, R., Kakegawa, T., Zou, M. X., et al. (1998). Isolation and characterization of a novel endogenous peptide ligand for the human APJ receptor. *Biochem. Biophys. Res. Commun.* 251, 471–476. doi: 10.1006/bbrc.1998.9489

Thomas, W. G., Brandenburger, Y., Autelitano, D. J., Pham, T., Qian, H., and Hannan, R. D. (2002). Adenoviral-directed expression of the type 1A angiotensin receptor promotes cardiomyocyte hypertrophy via transactivation of the epidermal growth factor receptor. *Circ. Res.* 90, 135–142. doi: 10.1161/hh0202.104109

Thorburn, J., Frost, J. A., and Thorburn, A. (1994). Mitogen-activated protein kinases mediate changes in gene expression, but not cytoskeletal organization associated with cardiac muscle cell hypertrophy. *J. Cell Biol.* 126, 1565–1572. doi: 10.1083/jcb.126.6.1565

Toepfer, C. N., West, T. G., and Ferenczi, M. A. (2016). Revisiting Frank-Starling: regulatory light chain phosphorylation alters the rate of force redevelopment (ktr) in a length-dependent fashion. *J. Physiol.* 594, 5237–5254. doi: 10.1113/jp272441

Vaidehi, N., and Kenakin, T. (2010). The role of conformational ensembles of seven transmembrane receptors in functional selectivity. *Curr. Opin. Pharmacol.* 10, 775–781. doi: 10.1016/j.coph.2010.09.004

Vickers, C., Hales, P., Kaushik, V., Dick, L., Gavin, J., Tang, J., et al. (2002). Hydrolysis of biological peptides by human angiotensin-converting enzyme-related carboxypeptidase. *J. Biol. Chem.* 277, 14838–14843. doi: 10.1074/jbc.m200581200

Violin, J. D., Soergel, D. G., Boerrigter, G., Burnett, J. C. Jr., and Lark, M. W. (2013). GPCR biased ligands as novel heart failure therapeutics. *Trends Cardiovasc. Med.* 23, 242–249. doi: 10.1016/j.tcm.2013.01.002

von Anrep, G. (1912). On the part played by the suprarenals in the normal vascular reactions of the body. *J. Physiol.* 45, 307–317. doi: 10.1113/jphysiol.1912.sp001553

von Lewinski, D., Stumme, B., Maier, L. S., Luers, C., Bers, D. M., and Pieske, B. (2003). Stretch-dependent slow force response in isolated rabbit myocardium is Na+ dependent. *Cardiovasc. Res.* 57, 1052–1061. doi: 10.1016/s0008-6363(02)00830-1

Wang, C., Du, J.-F., Wu, F., and Wang, H.-C. (2008). Apelin decreases the SR Ca2+ content but enhances the amplitude of [Ca2+]i transient and contractions during twitches in isolated rat cardiac myocytes. *Am. J. Physiol. Heart Circ. Physiol.* 294, H2540–H2546.

Wang, J., Hanada, K., Gareri, C., and Rockman, H. A. (2018). Mechanoactivation of the angiotensin II type 1 receptor induces β-arrestin-biased signaling through Gαi coupling. *J. Cell. Biochem.* 119, 3586–3597. doi: 10.1002/jcb.26552

Wang, W., McKinnie, S. M., Farhan, M., Paul, M., McDonald, T., McLean, B., et al. (2016). Angiotensin-converting enzyme 2 metabolizes and partially inactivates pyr-apelin-13 and apelin-17. *Hypertension* 68, 365–377. doi: 10.1161/hypertensionaha.115.06892

Wang, W., McKinnie, S. M., Patel, V. B., Haddad, G., Wang, Z., Zhabyeyev, P., et al. (2003). Loss of apelin exacerbates myocardial infarction adverse remodeling and ischemia-reperfusion injury: therapeutic potential of synthetic apelin analogues. *J. Am. Heart Assoc.* 2:e000249.

Wang, Y., Huang, S., Sah, V. P., Ross, J. Jr., Brown, J. H., Han, J., et al. (1998a). Cardiac muscle cell hypertrophy and apoptosis induced by distinct members of the p38 mitogen-activated protein kinase family. *J. Biol. Chem.* 273, 2161–2168. doi: 10.1074/jbc.273.4.2161

Wang, Y., Su, B., Sah, V. P., Brown, J. H., Han, J., and Chien, K. R. (1998b). Cardiac hypertrophy induced by mitogen-activated protein kinase kinase 7, a specific activator for c-Jun NH2-terminal kinase in ventricular muscle cells. *J. Biol. Chem.* 273, 5423–5426. doi: 10.1074/jbc.273.10.5423

Watanabe, A., and Endoh, M. (1998). Relationship between the increase in Ca2+ transient and contractile force induced by angiotensin II in aequorin-loaded rabbit ventricular myocardium. *Cardiovasc. Res.* 37, 524–531. doi: 10.1016/s0008-6363(97)00287-3

Wei, F., Jia, X.-J., Yu, S.-Q., Gu, Y., Wang, L., Guo, X.-M., et al. (2011). Candesartan versus imidapril in hypertension: a randomised study to assess effects of anti-AT1 receptor autoantibodies. *Heart* 97, 479–484. doi: 10.1136/hrt.2009.192104

Wijnker, P. J. M., Sequeira, V., Foster, D. B., Li, Y., Dos Remedios, C. G., Murphy, A. M., et al. (2014). Length-dependent activation is modulated by cardiac troponin I bisphosphorylation at Ser23 and Ser24 but not by Thr143 phosphorylation. *Am. J. Physiol. Heart Circ. Physiol.* 306, H1171–H1181.

Wilkins, B. J., and Molkentin, J. D. (2004). Calcium-calcineurin signaling in the regulation of cardiac hypertrophy. *Biochem. Biophys. Res. Commun.* 322, 1178–1191. doi: 10.1016/j.bbrc.2004.07.121

Wisler, J. W., Xiao, K., Thomsen, A. R. B., and Lefkowitz, R. J. (2014). Recent developments in biased agonism. *Curr. Opin. Cell Biol.* 27, 18–24. doi: 10.1016/j.ceb.2013.10.008

Xie, F., Liu, W., Feng, F., Li, X., Yang, L., Lv, D., et al. (2014). A static pressure sensitive receptor APJ promote H9c2 cardiomyocyte hypertrophy via PI3K-autophagy pathway. *Acta Biochim. Biophys. Sin.* 46, 699–708. doi: 10.1093/abbs/gmu046

y Schnitzler, M. M., Storch, U., Meibers, S., Nurwakagari, P., Breit, A., Essin, K., et al. (2008). Gq-coupled receptors as mechanosensors mediating myogenic vasoconstriction. *EMBO J.* 27, 3092–3103. doi: 10.1038/emboj.2008.233

Yamaguchi, Y., Iribe, G., Kaneko, T., Takahashi, K., Numaga-Tomita, T., Nishida, M., et al. (2018). TRPC3 participates in angiotensin II type 1 receptor-dependent stress-induced slow increase in intracellular Ca2+ concentration in mouse cardiomyocytes. *J. Physiol. Sci.* 68, 153–164. doi: 10.1007/s12576-016-0519-3

Yamaleyeva, L. M., Shaltout, H. A., and Varagic, J. (2016). Apelin-13 in blood pressure regulation and cardiovascular disease. *Curr. Opin. Nephrol. Hypertens.* 25, 396–403. doi: 10.1097/mnh.0000000000000241

Yao, H., Peng, F., Fan, Y., Zhu, X., Hu, G., and Buch, S. J. (2009). TRPC channel-mediated neuroprotection by PDGF involves Pyk2/ERK/CREB pathway. *Cell Death Differ.* 16, 1681–1693. doi: 10.1038/cdd.2009.108

Yasuda, N., Miura, S.-I., Akazawa, H., Tanaka, T., Qin, Y., Kiya, Y., et al. (2008). Conformational switch of angiotensin II type 1 receptor underlying mechanical stress-induced activation. *EMBO Rep.* 9, 179–186. doi: 10.1038/sj.embor.7401157

Ye, L., Ding, F., Zhang, L., Shen, A., Yao, H., Deng, L., et al. (2015). Serum apelin is associated with left ventricular hypertrophy in untreated hypertension patients. *J. Transl. Med.* 13:290.

Yeves, A. M., Caldiz, C. I., Aiello, E. A., Villa-Abrille, M. C., and Ennis, I. L. (2015). Reactive oxygen species partially mediate high dose angiotensin II-induced positive inotropic effect in cat ventricular myocytes. *Cardiovasc. Pathol.* 24, 236–240. doi: 10.1016/j.carpath.2015.01.002

Zechner, D., Thuerauf, D. J., Hanford, D. S., McDonough, P. M., and Glembotski, C. C. (1997). A role for the p38 mitogen-activated protein kinase pathway in myocardial cell growth, sarcomeric organization, and cardiac-specific gene expression. *J. Cell Biol.* 139, 115–127. doi: 10.1083/jcb.139.1.115

Zhang, M., and Kass, D. A. (2011). Phosphodiesterases and cardiac cGMP: evolving roles and controversies. *Trends Pharmacol. Sci.* 32, 360–365. doi: 10.1016/j.tips.2011.02.019

Zhang, M., Prosser, B. L., Bamboye, M. A., Gondim, A. N. S., Santos, C. X., Martin, D., et al. (2015). Contractile function during angiotensin-II activation: increased nox2 activity modulates cardiac calcium handling via phospholamban phosphorylation. *J. Am. Coll. Cardiol.* 66, 261–272.

Zhang, Z., Yu, B., and Tao, G.-Z. (2009). Apelin protects against cardiomyocyte apoptosis induced by glucose deprivation. *Chin. Med. J.* 122, 2360–2365.

Zhen, E. Y., Higgs, R. E., and Gutierrez, J. A. (2013). Pyroglutamyl apelin-13 identified as the major apelin isoform in human plasma. *Anal. Biochem.* 442, 1–9. doi: 10.1016/j.ab.2013.07.006

Zou, Y., Akazawa, H., Qin, Y., Sano, M., Takano, H., Minamino, T., et al. (2004). Mechanical stress activates angiotensin II type 1 receptor without the involvement of angiotensin II. *Nat. Cell Biol.* 6, 499–506. doi: 10.1038/ncb1137

Conflict of Interest: The authors declare that the research was conducted in the absence of any commercial or financial relationships that could be construed as a potential conflict of interest.

frontiers
in Physiology

ORIGINAL RESEARCH
published: 17 March 2020
doi: 10.3389/fphys.2020.00171

The Effects of Mechanical Preload on Transmural Differences in Mechano-Calcium-Electric Feedback in Single Cardiomyocytes: Experiments and Mathematical Models

Anastasia Khokhlova[1,2]*, Pavel Konovalov[1], Gentaro Iribe[3,4], Olga Solovyova[1,2] and Leonid Katsnelson[1,2]

[1] Institute of Immunology and Physiology, Russian Academy of Sciences, Yekaterinburg, Russia, [2] Institute of Natural Sciences and Mathematics, Ural Federal University, Yekaterinburg, Russia, [3] Department of Physiology, Asahikawa Medical University, Hokkaido, Japan, [4] Department of Cardiovascular Physiology, Okayama University, Okayama, Japan

Edited by:
Jose Renato Pinto,
Florida State University, United States

Reviewed by:
Laurin Michelle Hanft,
University of Missouri, United States
Sabine J. van Dijk,
University of California, Davis,
United States

***Correspondence:**
Anastasia Khokhlova
a.d.khokhlova@urfu.ru;
a.khokhlova@iip.uran.ru

Specialty section:
This article was submitted to
Striated Muscle Physiology,
a section of the journal
Frontiers in Physiology

Received: 30 November 2019
Accepted: 13 February 2020
Published: 17 March 2020

Citation:
Khokhlova A, Konovalov P, Iribe G,
Solovyova O and Katsnelson L (2020)
The Effects of Mechanical Preload on
Transmural Differences
in Mechano-Calcium-Electric
Feedback in Single Cardiomyocytes:
Experiments and Mathematical
Models. Front. Physiol. 11:171.
doi: 10.3389/fphys.2020.00171

Transmural differences in ventricular myocardium are maintained by electromechanical coupling and mechano-calcium/mechano-electric feedback. In the present study, we experimentally investigated the influence of preload on the force characteristics of subendocardial (Endo) and subepicardial (Epi) single ventricular cardiomyocytes stretched by up to 20% from slack sarcomere length (SL) and analyzed the results with the help of mathematical modeling. Mathematical models of Endo and Epi cells, which accounted for regional heterogeneity in ionic currents, Ca^{2+} handling, and myofilament contractile mechanisms, showed that a greater slope of the active tension–length relationship observed experimentally in Endo cardiomyocytes could be explained by greater length-dependent Ca^{2+} activation in Endo cells compared with Epi ones. The models also predicted that greater length dependence of Ca^{2+} activation in Endo cells compared to Epi ones underlies, via mechano-calcium-electric feedback, the reduction in the transmural gradient in action potential duration (APD) at a higher preload. However, the models were unable to reproduce the experimental data on a decrease of the transmural gradient in the time to peak contraction between Endo and Epi cells at longer end-diastolic SL. We hypothesize that preload-dependent changes in viscosity should be involved alongside the Frank–Starling effects to regulate the transmural gradient in length-dependent changes in the time course of contraction of Endo and Epi cardiomyocytes. Our experimental data and their analysis based on mathematical modeling give reason to believe that mechano-calcium-electric feedback plays a critical role in the modulation of electrophysiological and contractile properties of myocytes across the ventricular wall.

Keywords: single cardiomyocytes, mechanical preload, length-dependent activation, transmural differences, electromechanical coupling, mechano-calcium-electric feedback

INTRODUCTION

Over the past 30 years, the main concept of the studies on regional heterogeneity in the healthy heart has maintained that transmural differences are required in the myocyte function to effectively optimize the ejection of blood by the heart (Katz and Katz, 1989; Solovyova et al., 2016). Transmural differences in action potential (AP) properties have been reported at the single-cell level in humans (Johnson et al., 2018), and large (Cordeiro et al., 2004) and small (Chen et al., 2017) animals. Endocardial and subendocardial (Endo) cardiomyocytes across species have a higher AP upstroke velocity, longer AP duration (APD) and smaller phase-1 repolarization rate as compared with epicardial and subepicardial (Epi) myocytes. A larger Na^+ current, I_{Na}, in the subendocardium underlies the higher AP upstroke velocity in Endo cells, whereas a greater transient outward current, I_{to}, and a smaller L-type Ca^{2+} current, I_{CaL}, and Na^+–Ca^{2+} exchanger current, I_{NaCa}, both (Wan et al., 2005; Xu et al., 2012) underlie the higher repolarization rate and shorter APD in Epi cells (Veerman et al., 2017).

These differences in repolarization duration lead to Endo-Epi differences in the Ca^{2+} transient and force developed. On the other hand, regional heterogeneity in the expression and function of Ca^{2+} cycling and sarcomere proteins, including L-type Ca^{2+} channels (Wang and Cohen, 2003; Wan et al., 2005), SERCA2a (Lou et al., 2011), Na^+–Ca^{2+} exchanger (Dilly et al., 2006), and myosin isoform (Cazorla et al., 2005), also contribute to regional variations in the Ca^{2+} transient and sarcomere shortening. Experiments on single cells showed that Endo myocytes had a higher diastolic Ca^{2+} level, greater amplitude of the Ca^{2+} transient and sarcomere shortening, and slower rising and decline phases of the Ca^{2+} transient and sarcomere shortening (Cordeiro et al., 2004; Pan et al., 2018). Moreover, single studies on mechanically loaded cardiomyocytes demonstrated that the Frank–Starling mechanisms depended on cell location with a steeper sarcomere length (SL)–active tension relationship (Cazorla et al., 1997, 2000) and a larger increase in Ca^{2+} sensitivity following stretch (Cazorla et al., 2005) in endocardium than in epicardium. They also revealed a positive gradient of cellular stiffness in intact cardiomyocytes across the ventricular wall from Epi to Endo. Our previous results suggested that heterogeneity in the parameters of Ca^{2+} handling and myofilament mechanics between Endo and Epi cardiomyocytes via cooperative mechanisms of mechano-calcium-electric feedback modulates transmural differences in AP properties between the cells (Khokhlova et al., 2018a). Thus, there are several cross-links, electromechanical, mechano-calcium, and mechano-electric, that underlie the manifestation of transmural heterogeneity in the cellular function.

In the intact heart, the transmural gradient in both diastolic stretch and systolic contraction was revealed in the canine ventricle, with the greatest stretch and contraction in the Endo layer (Waldman et al., 1985). Experiments *in vivo* showed that myofiber shortening in the intact canine ventricle started earliest at the Endo layer and was progressively delayed toward the Epi one, whereas the onset of myofiber relaxation occurred earlier in epicardium than endocardium (Ashikaga et al., 2007).

Although the authors discovered a regional dispersion of myofiber shortening in the intact heart, they found no evidence of significant transmural gradient in electrical repolarization (Ashikaga et al., 2007). It was suggested that the transmural activation pattern compensates for the intrinsic transmural difference in APD, resulting in more homogeneous repolarization of the intact ventricular wall (Opthof et al., 2007; Myles et al., 2010; Boukens et al., 2015). Moreover, some studies showed no transmural gradients in APD in intact hearts (Taggart et al., 2001; Mačianskienė et al., 2018). Thus, the link between the intracellular mechanisms of transmural heterogeneity at the cellular level and its role in the whole heart function are poorly understood.

Previously, we showed that mechanical preload affects the transmural gradient in cell contractile properties, and even a small diastolic stretch (∼3.5% from slack SL) reduces transmural differences in the time to peak contraction and decay time of the Ca^{2+} transient between Endo and Epi cardiomyocytes (Khokhlova et al., 2018b). In the present study, we investigate the force characteristics of Endo and Epi single ventricular cardiomyocytes from the mouse heart using an original single-cell stretch technique (Iribe et al., 2014) to stretch cells by up to 20% from slack SL. To test the hypothesis that mechanical preload may influence the transmural gradient in the electrophysiological function of Endo and Epi cells, we present here detailed mathematical models of Endo and Epi cardiomyocytes, which account for regional heterogeneity in ionic currents, Ca^{2+} handling, and myofilament contractile mechanisms.

MATERIALS AND METHODS

Isolation of Mouse Ventricular Myocytes

All procedures involving animal use were performed in accordance with the Guiding Principles for the Care and Use of Animals approved by the Council of the Physiological Society of Japan. All protocols involving animals were approved by the Animal Subjects Committee of Okayama University, Graduate School of Medicine, Dentistry and Pharmaceutical Sciences.

Endo and Epi myocytes were isolated from healthy adult (8- to 10-week-old) male C57BL6/J mice by enzymatic dissociation and mechanical dispersion as described previously (Khokhlova et al., 2018b). Briefly, hearts were excised from mice sacrificed by an overdose of isoflurane (DS Pharma Animal Health, Osaka, Japan), mounted on a Langendorff perfusion apparatus, and perfused retrogradely through the aorta with oxygenated Ca^{2+}-free solution supplemented with 10 mM 2,3-butanedione monoxime (Sigma-Aldrich, St. Louis, MO, United States) for 4–6 min, followed by the same solution containing 0.093 mg/ml Liberase TM (Roche, Basel, Switzerland) and 12.5 μM $CaCl_2$ for 6–7 min at 37°C. Following the perfusion, the central region of left ventricular (LV) free wall was separated in the latter solution using fine forceps and scissors and then tissue pieces from the Endo and Epi layers of the LV free wall were dissected under a microscope. All separation procedures were carried out at room temperature (22–24°C). Then, the Endo and Epi tissue pieces were separately minced and incubated at 37°C for

5 min in fresh enzyme buffer, subsequently dispersed by gentle trituration and placed into Ca^{2+}-free solution supplemented with 12.5 μM $CaCl_2$ and 10% fetal bovine serum (FBS; Sigma-Aldrich, United States). The resulting cell suspensions were filtered and centrifuged once for 3 min at $15 \times g$ (Kubota, Tokyo, Japan). Then, cardiomyocytes were consistently resuspended in Ca^{2+}-containing solution (0.6, 1.2, and 1.8 mM) and harvested by gravity sedimentation. Finally, single myocytes were stored in Hepes-buffered Tyrode solution containing (in mM): NaCl (140), KCl (5.4), $CaCl_2$ (1.8), $MgCl_2$ (1.0), Hepes (5), and glucose (11) (pH adjusted to 7.4 using NaOH) at room temperature until used within 8 h of cell isolation. The cardiomyocytes selected for study showed clear sarcomere patterns and were quiescent when not stimulated.

Measurements of Single Cell Length and Force

The detailed method to provide length and force measurements on single cardiomyocytes is described elsewhere (Iribe et al., 2014; Khokhlova et al., 2018b). In brief, two pairs of carbon fibers (CF) (~10 μm in diameter, Tsukuba Materials Information Laboratory, Ltd., Tsukuba, Japan) were attached to the top and bottom surfaces of the left and right cell end, while both CFs on the left side were mounted on computer-controlled piezoelectric transducers (PZT). To change the mechanical preload (to apply end-diastolic axial stretch to a cell), both left CFs received the same movement command (in our protocol, 2 μm per 300 ms for a step) using LabVIEW (National Instruments Corp., Austin, TX, United States), while both right CFs rigidly fixed the right cell end, preventing it from moving. The distance between left and right CF tips ("cell length") and SL changes were recorded during uncontrolled auxotonic contraction (when a cell contracted under mechanical loading by CFs) using the IonOptix equipment and software (IonOptix Corporation, Milton, MA, United States). All experiments were performed at a stimulation frequency of 1 Hz at room temperature. After all CFs were set, a cell was paced at 1 Hz for 3 min before recordings to enhance cell–CF adhesion (Iribe et al., 2007, 2014).

Cellular force was calculated as follows: $F = K \cdot (\Delta L_{PZT} - \Delta L_{CF})$, where K is the combined stiffness of the left CFs (0.07–0.09 μN/μm in this study), ΔL_{PZT} is the change in PZT position, and ΔL_{CF} is the change in distance between left and right CF tips. Then, force was normalized to effective cross-sectional area, assuming an elliptical shape of the cross section with a 3:1 ratio of long (measured cell width, y-direction) and short axes (estimated cell height, *z*-direction) (Nishimura et al., 2004).

The SL range across the ventricular wall and its changes during the cardiac cycle are still unknown. Chung and Granzier reported that end-diastolic SL (EDSL) varied in a transmural-dependent manner in the contracted isolated mouse heart (2.08 ± 0.01 μm in epicardium and 1.98 ± 0.02 μm in endocardium) (Chung and Granzier, 2011). Under physiological settings at high heartbeat frequencies in mice *in vivo*, the EDSL value in the epicardial surface was 1.97 ± 0.20 μm (Kobirumaki-Shimozawa et al., 2016). In this study, we stretched single cardiomyocytes by up to 20% from slack SL, i.e., up to ~2.16 μm to cover the physiological range of EDSL in cardiomyocytes found in the above studies.

Analysis of Length-Dependent Changes in Cellular Force and Time Characteristics

To analyze length-dependent changes in cellular force, we measured the slopes of the end-diastolic force–length relationship curve (EDFLR), end-systolic force–length relationship curve (ESFLR), and active force–length relationship curve (F_{active}LR). The amplitudes of passive (end-diastolic), total (end-systolic), and active (total minus passive) tension were fitted by linear regression ($R^2 > 0.9$) for relative changes in cell length (see **Supplementary Material** and **Supplementary Figure S1**). We also used an index called "Frank–Starling Gain" (FSG), calculated as the ratio of ESFLR and EDFLR slopes (Bollensdorff et al., 2011). Being a dimensionless and cross-section independent parameter, it is not sensitive to errors in force normalization and supports improved inter-individual comparison of cells.

Time to peak contraction ($T_{\max}$) was measured from stimulation onset to the peak of auxotonic tension. Time to 50% relaxation (TR_{50}) was measured as the time interval from $T_{\max}$ to the time of 50% relaxation. To analyze the effects of preload on the time characteristics of contraction and relaxation, we assessed the dependence of $T_{\max}$ and TR_{50} on the relative changes in the end-diastolic cell length. We found that only $T_{\max}$LR ($T_{\max}$–length relation) curve could be fitted well by linear regression ($R^2 > 0.8$). No correlation was found between TR_{50} and changes in the end-diastolic cell length.

Statistical Analysis

Data analysis was carried out with Origin 8.0 (Origin Lab, Northampton, MA, United States) and GraphPrism 7.0 (GraphPad Software, San Diego, CA, United States). The data are expressed as the mean ± standard error of the mean (SEM). A Student's unpaired *t* test was used for statistical analysis. Differences between means with $p < 0.05$ were considered statistically significant.

Mathematical Modeling

Previously, we developed mathematical models of Endo and Epi cells based on the Yekaterinburg–Oxford mathematical model (Sulman et al., 2008). These models reproduce transmural differences in the contractile function of mouse single ventricular cardiomyocytes at room temperature (Khokhlova et al., 2018b). To mimic Endo–Epi differences in the electrophysiological parameters and mechano-calcium-electric feedback, we have incorporated our contraction model into the models of electrical activity (Pandit et al., 2001) and Ca^{2+} handling (Hinch et al., 2004). After analysis of several available models for the electrophysiological characteristics of rodent cardiomyocytes, the models that we had adopted gave us the best fit to literature and our experimental data. The Pandit model was initially developed for rat Endo and Epi cardiomyocytes. We have therefore adjusted the model parameters (**Table 1**) to fit literature

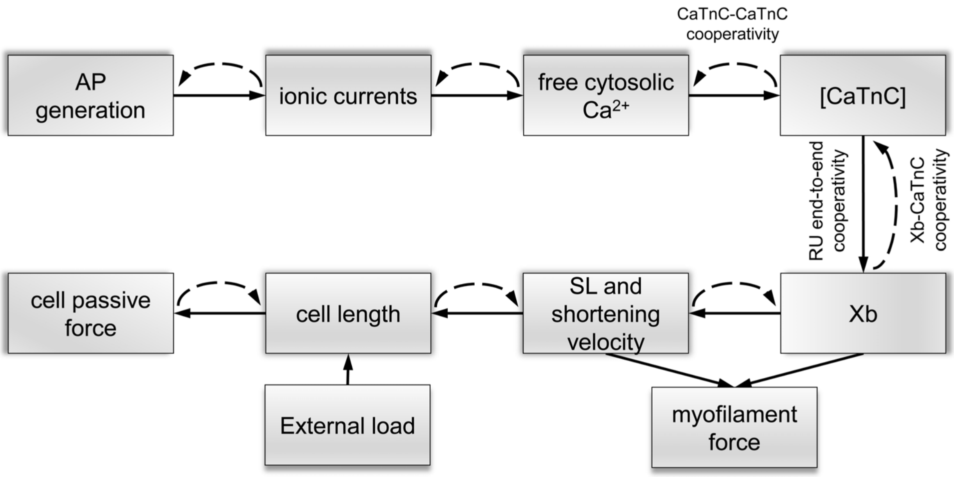

FIGURE 1 | Schematic links between mechanisms of electromechanical coupling and mechano-calcium-electric feedback in the mathematical Endo and Epi models. Solid lines show direct links between the mechanisms of excitation–contraction coupling and dashed lines show feedback links. Cooperative mechanisms of Ca^{2+} activation of myofilaments [Xb–CaTnC, CaTnC–CaTnC, and regulatory unit (RU) end-to-end cooperativity] are described in the text.

TABLE 1 | Literature and experimental data on the Endo/Epi differences taken into account in the mathematical models.

Target	Endo	Epi	Animal	Source
Na^+ current (I_{Na}) amplitude	Bigger	Smaller	Mouse	Veerman et al., 2017
Transient outward K^+ current (I_t) amplitude	Smaller	Bigger	Mouse	Rossow et al., 2006; Liu et al., 2015; Veerman et al., 2017
Na^+–Ca^{2+} exchanger current (I_{NaCa}) amplitude	Smaller	Bigger	Mouse	Dilly et al., 2006; Xu et al., 2012
Ca^{2+} release flux from sarcoplasmic reticulum (J_{RyR}) amplitude	Bigger	Smaller	Mouse	Dilly et al., 2006
SERCA2a Ca^2 pump flux (J_{SERCA}) amplitude	Bigger	Smaller	Mouse	Pan et al., 2018
Rate constant of Xb cycling	Smaller	Bigger	Guinea pig Pig	Le Guennec et al., 2008 Stelzer et al., 2008
Passive stiffness	Bigger	Smaller	Mouse	Experimental data
Probability $n_1(l_1)$ of Xb attachment to the actin filament	Bigger	Smaller	Mouse	Experimental data

data on AP generation and Ca^{2+} transient and our experimental data on Endo/Epi myocyte contraction obtained for mice at room temperature.

A key feature of our single-cell models is that it includes mechano-calcium-electric cross-links. The cooperative mechanisms of Ca^{2+} activation of myofilament regulatory units (RUs) were formulated and justified in our previous papers (Katsnelson et al., 2004; Khokhlova et al., 2018b). Here, we describe them briefly (**Figure 1**):

Xb–CaTnC Cooperativity

The rate of CaTnC dissociation decreases with an increase in the fraction of force generating cross-bridges (Xbs) per single CaTnC complex.

CaTnC–CaTnC Cooperativity

The rate of CaTnC complex dissociation decreases with increasing numbers of CaTnC complexes.

RU End-to-End Cooperativity

Ca^{2+} binding by TnC, located within one RU on a thin filament affects the neighboring RUs through tropomyosin end-to-end conformational interaction, thus contributing to the opening of the active actin sites for myosin head attachment.

The non-linear dependence of the on-rate for Xb attachment on the concentration of CaTnC complexes [CaTnC] (via RU end-to-end cooperativity, see **Supplementary Material** 2.5.9, M_A) and the off-rate for CaTnC dissociation on the fraction of Xbs (via Xb–CaTnC cooperative mechanism, see **Supplementary Material** 2.4.12, π_{NA}) and [CaTnC] (via CaTnC–CaTnC cooperative mechanism, see Supplementary Material 2.4.13, $e^{kA*CaTnC}$) formalize the key cooperative mechanisms of myofilament Ca^{2+} activation in the models (**Figure 1**). These three mechanisms underlie a number of essential properties of the cardiac muscle, such as the dependence of contraction and relaxation on myofilament length and load (Katsnelson et al., 2004).

In our cell models, the key link that ties the mechano-calcium feedback together with the cooperativity mechanisms is the mechanosensitive probability $n_1(l_1)$ of Xb attachment to the actin filament depending on the instantaneous SL: the bigger l_1 (the deformation of the sarcomere against its slack length), the higher n_1 (see **Supplementary Material** 2.5.9, n_1). In short, $n_1(l_1)$ accounts for the effect of length on Xb fraction, while Xb–CaTnC cooperativity accounts for the effect of Xb fraction on [CaTnC]. The other two types of cooperativity amplify this effect. Note that our phenomenological dependence $n_1(l_1)$ is invariant with respect to the underlying intracellular mechanisms, which are still debated (see section "Discussion").

The rheological scheme of the models consists of a cardiomyocyte attached to an extra-series element (see **Supplementary Material** and **Supplementary Figure S2**, XSE), which corresponds to CFs in experiments. The elastance of the extra-series element corresponds to CF stiffness in experimental settings. The sum of the cell and extra-series element lengths is set to be constant, while the cell length dynamically changes

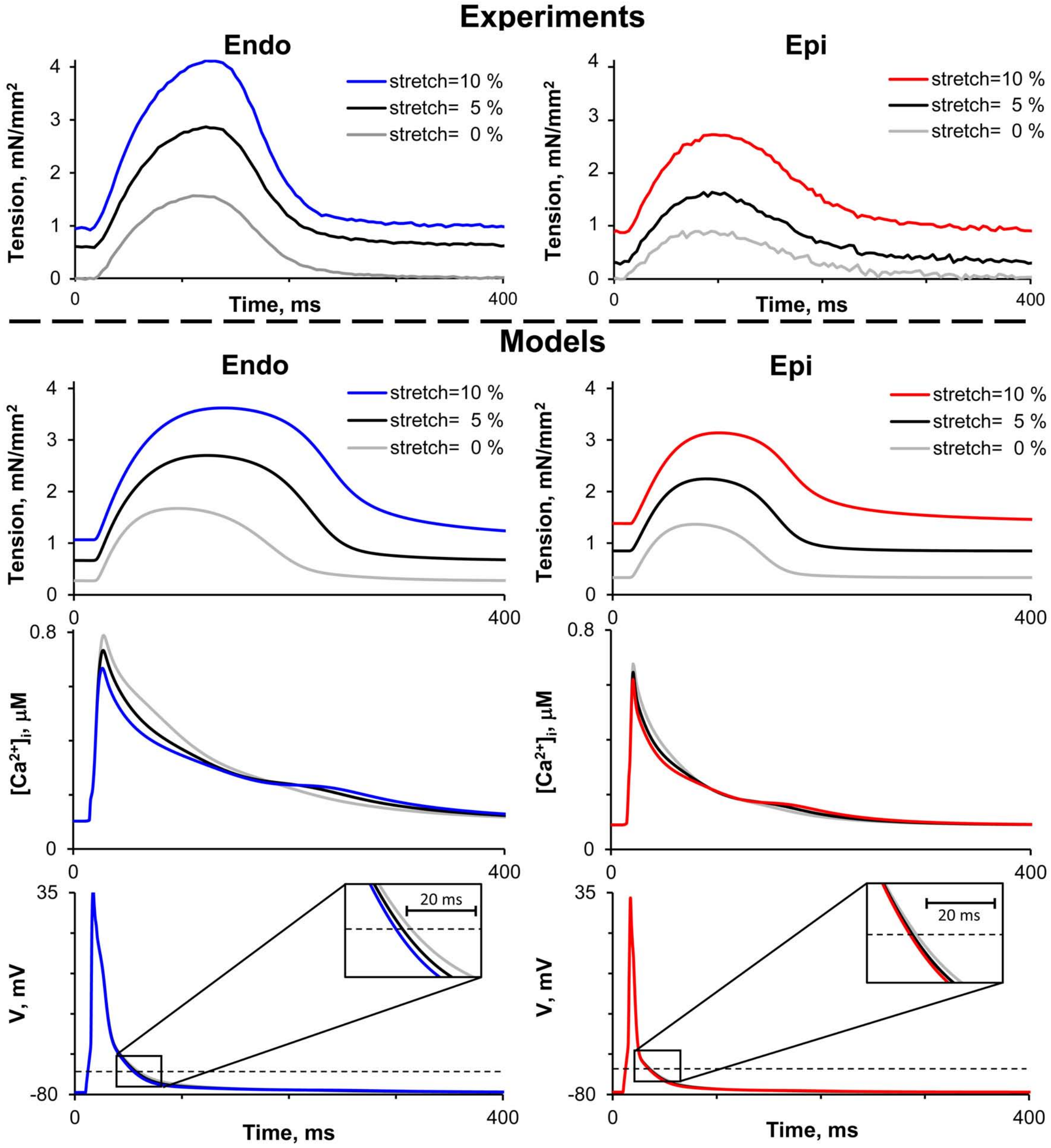

FIGURE 2 | Representative recordings of auxotonic tension in experiments (top panel) and mathematical model simulations of tension, cytosolic Ca^{2+} concentration ([Ca^{2+}]$_i$) and action potential (V) during the cardiac cycle (bottom panel) of Endo and Epi isolated cardiomyocytes at varying preload (cell stretch 5 and 10% relative to the initial end-diastolic length).

during the cardiac cycle under the loading of the extra-series elastic element, i.e., under the auxotonic condition.

Euler integration with a time step of 0.01 ms and the Newton method for solving algebraic equations were used for simulations. All the results are shown in their steady state, achieved by allowing the models to run for 30 s at a stimulation frequency of 1 Hz.

To compare model simulation with experimental data, we fitted passive, total, and active tension amplitudes as well as the $T_{\max}$, amplitude of the Ca^{2+} transient, time from peak to 50% and 90% Ca^{2+} decay (CaT_{50}, CaT_{90}), and APD at 90% repolarization (APD_{90}) at varying preload by linear regression lines for relative changes in cell length.

RESULTS

The Transmural Gradient in AP, Ca^{2+} Transient, Force Development and the Cell Morphology

We found no differences in the morphological parameters between unstretched single Endo and Epi cells. Cell length (Endo: 120.0 ± 2.0 μm, *n* = 56 vs. Epi: 120.7 ± 1.8 μm, *n* = 57), width (22.75 ± 0.33 μm, *n* = 56 vs. 22.21 ± 0.28 μm, *n* = 57), and slack EDSL (Endo: 1.78 ± 0.01 μm, *n* = 34 vs. Epi: 1.77 ± 0.01 μm, *n* = 28) were similar between the groups.

Figure 2 shows representative recordings of auxotonic tension in the experiments and mathematical model simulations at varying preload. Comparing the parameters of cell contractions at slack EDSL, we found the amplitude of auxotonic tension to be higher and the time to peak contraction ($T_{\max}$) to be greater in Endo cells compared with Epi ones (**Figures 2**, **3**). No significant difference was found in the time to 50% relaxation (TR_{50}) between the cells (**Figure 3**).

The Endo and Epi mathematical models described above were able to reproduce the experimental data on transmural differences in contraction parameters (**Figure 3**). A comparison of the AP and Ca^{2+} transient characteristics in the models with literature data obtained for unloaded mouse single cardiomyocytes showed good consistency (**Table 2**). Resting membrane potential was similar in Endo and Epi cells. APD was greater in Endo than in Epi cardiomyocytes. Endo cardiomyocytes also showed a slower Ca^{2+} transient. Consistently with literature data (Dilly et al., 2006; Rossow et al., 2006; Pan et al., 2018), the Endo model had a higher Ca^{2+} transient amplitude (15% relative to the Endo model) and a higher diastolic Ca^{2+} level (12% relative to the Epi model) compared with the Epi model (**Table 2**).

The Effects of Preload on the Transmural Gradient in Length-Dependent Activation and Time Course of Contraction

To estimate length-dependent activation in Endo and Epi cardiomyocytes, we analyzed the slopes of the end-diastolic force–length relationship curve (EDFLR), end-systolic force–length relationship curve (ESFLR), active force–length relationship curve (F_{active}LR), and FSG index expressed as the ratio of ESFLR and EDFLR slopes (see **Supplementary Material**

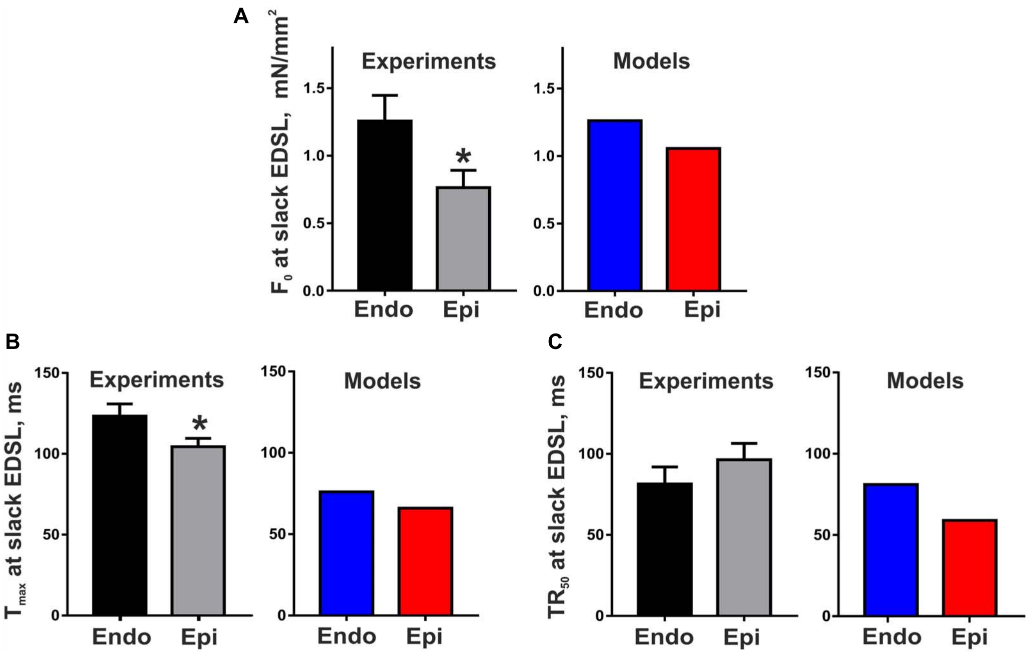

FIGURE 3 | Transmural gradient in the parameters of mouse cardiomyocyte contraction at slack end-diastolic sarcomere length (EDSL) in experiments [Endo: *n* = 8 (*N* = 3), Epi: *n* = 9 (*N* = 5)] and mathematical models. **(A)** Tension amplitude (F_0), **(B)** Time to peak contraction ($T_{\max}$), **(C)** Time to 50% relaxation (TR_{50}). $^{*}p < 0.05$ Endo vs. Epi, Student's unpaired *t* test. *N* = number of animals, *n* = number of cells.

TABLE 2 | Experimental and simulated parameters of action potential, Ca^{2+} transient, and contraction for Endo and Epi mouse ventricular myocytes.

	Experiment, RT 1 Hz	**Simulation, RT 1 Hz**	**Shi et al. (2013), RT 1 Hz**	**Brunet et al. (2004), RT 1 Hz**	**Khokhlova et al. (2018b), RT 1 Hz**	**Kondo et al. (2006), RT 1 Hz**	**Dilly et al. (2006), 37°C 1 Hz**	**Pan et al. (2018), 37°C 1 Hz**	**Chen et al. (2017), 37°C 8 Hz**
Endo									
RP (mV)		−78.80 (0.2%)		−70 ± 2 (0%)					
APD$_{90}$ (ms)		52 (40%)	36.0 ± 2.0 (58%)	18.0 ± 2.8 (12%)			93.1 ± 5.4 (53%)		56.2 ± 6.4 (9%)
Diastolic $[Ca^{2+}]_i$ (μM or F_{340}/F_{380} ratio)		0.101 μM (12%)					0.256 ± 0.020 μM (42%)	0.52 ± 0.023 ratio (13%)	
Ca amplitude (μM or F_{340}/F_{380} ratio)		0.705 μM (15%)			0.105 ± 0.017 ratio (24%)		0.630 ± 0.088 μM (43%)	0.241 ± 0.014 ratio (16%)	
CaTR$_{50}$ (ms)		65 (57%)			137.0 ± 4.4 (8%)		194.3 ± 8.2 (6%)		
CaTR$_{90}$ (ms)		215 (38%)						469.6 ± 22.4 (18%)	
Tension amplitude (mN/mm^2)	1.26 ± 0.19 (39%)	1.12 (18%)							
T_{max} (ms)	123 ± 7 (15%)	76 (13%)						58.4 ± 3.7 (18%)	
TR$_{50}$ (ms)	81 ± 10 (-18%)	81 (19%)				98 ± 3 (-5%)			
TR$_{90}$ (ms)		138 (34%)						215.5 ± 39.8 (46%)	
Epi									
RP (mV)		−78.6		−70 ± 2					
APD$_{90}$ (ms)		31	15.1 ± 1.2	15.8 ± 2.5			43.8 ± 6.1		51.2 ± 5.8
Diastolic $[Ca^{2+}]_i$ (μM or F_{340}/F_{380} ratio)		0.089 μM					0.148 ± 0.18 μM	0.45 ± 0.022 ratio	
Ca amplitude (μM or F_{340}/F_{380} ratio)		0.599 μM			0.080 ± 0.012 ratio		0.358 ± 0.91 μM	0.203 ± 0.011 ratio	
CaTR$_{50}$ (ms)		28			126.0 ± 4.9		183.1 ± 4.8		
CaTR$_{90}$ (ms)		133						384.4 ± 19.7	
Tension amplitude (mN/mm^2)	0.77 ± 0.11	0.919							
T_{max} (ms)	104 ± 5	66						47.6 ± 2.2	
TR$_{50}$ (ms)	96 ± 10	59				103 ± 3			
TR$_{90}$ (ms)		91						115.8 ± 18.5	

RP, resting potential; APD$_{90}$, action potential duration at 90% repolarization; $[Ca^{2+}]_i$, cytosolic Ca^{2+} concentration; CaT$_{50}$ and CaT$_{90}$, time from peak to 50% and 90% Ca^{2+} decay; T_{max}, time to peak contraction; TR$_{50}$ and TR$_{90}$, time to 50% and 90% relaxation. The relative percentage of differences between the Endo and Epi models relative to the Endo model is shown in parentheses.

and **Supplementary Figure S1**). We found no significant difference in the slope of EDFLR between Endo and Epi cells, demonstrating their similar passive stiffness (**Figure 4**). The parameters of the mathematical models for passive force description were fitted to mimic experimental values (**Supplementary Table S2.2** in **Supplementary Material**, **Figure 4**).

Neither did we find any significant difference in the ESFLR slope between the groups; however, the FSG index and F_{active}LR slope were significantly higher in Endo cells than in Epi cells,

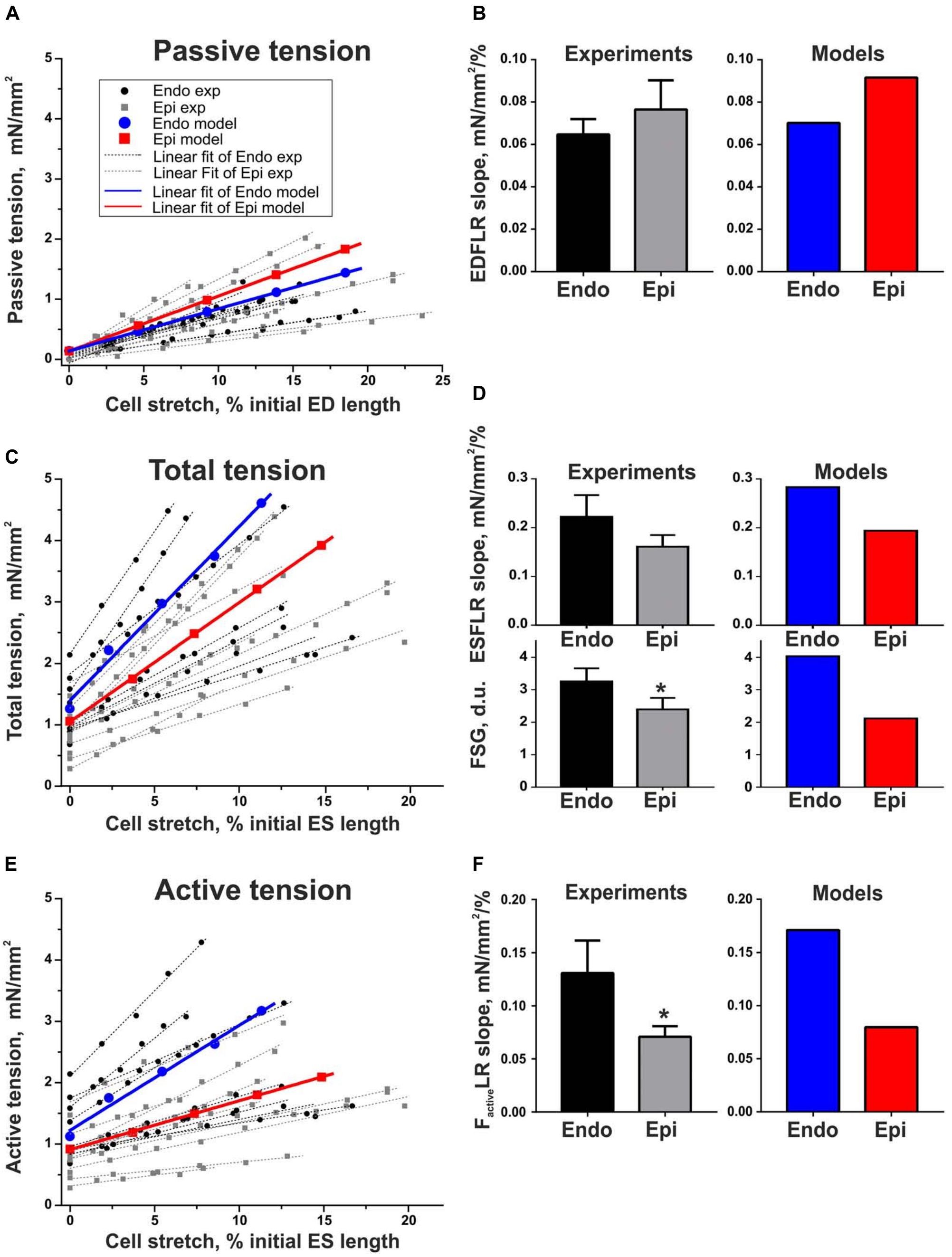

FIGURE 4 | Length-dependent changes in passive, total, and active (total minus passive) tension of single mouse ventricular Endo and Epi cardiomyocytes in experiments [Endo: $n = 8$ ($N = 3$), Epi: $n = 9$ ($N = 5$)] and mathematical models. **(A)** End-diastolic force–length relation curves (EDFLR) from experimental (exp) data set and model simulations. **(B)** EDFLR slopes as the stiffness index in experiments and mathematical models. **(C)** End-systolic force–length relation curves (ESFLR) from experimental (exp) data set and model simulations. **(D)** ESFLR slopes and FSG index (the ratio of ESFLR and EDFLR slopes) in experiments and mathematical models. **(E)** Active force–length relation curves (F_{active}LR) from experimental (exp) data set and model simulations. **(F)** F_{active}LR slopes in experiments and mathematical models. $p < 0.05$ Endo vs. Epi, Student's unpaired *t* test. *N* = number of animals, *n* = number of cells. ED, end-diastolic; ES, end-systolic.

pointing to greater myofilament length-dependent activation in Endo cardiomyocytes (**Figure 4**). By setting the mechanosensitive probability $n_1(l_1)$ of Xb attachment to the actin filament in the Endo model greater than in the Epi one, we were able to reproduce the experimental data (**Supplementary Table S2.2** in **Supplementary Material** and **Figure 4**).

Analyzing the effects of preload on the time course of contraction, we found that $T_{\max}$ increased with preload in Epi cells significantly greater that in Endo ones, resulting in a decrease in the transmural gradient in $T_{\max}$ at high preload (**Figure 5**). Previously, we had suggested that a greater deceleration of CaTnC dissociation at increased preload in Epi cells may contribute to a steeper preload dependence of $T_{\max}$ in these cells (Khokhlova et al., 2018b). In the present study, our mathematical models, accounting for new experimental data on transmural differences in length-dependent activation (F_{active}LR slope and FSG index), failed to reproduce the steeper $T_{\max}$–length relationship in Epi cells (**Figure 5**). Possible explanations will be discussed below. In contrast to $T_{\max}$, the experiments did not reveal any significant change in TR_{50} with an increase in preload in either Endo or Epi cells; however, both the Endo and Epi mathematical models predicted a monotonic rise in TR_{50}.

It is also interesting that in the analysis of the tension–length relationship, the two populations of cells from the same Endo or Epi region were visually distinguishable (**Figures 4**, **5**).

The Effects of Preload on the Transmural Gradient in Excitation–Contraction Coupling

To test the hypothesis that mechanical preload affects the transmural gradient in excitation–contraction coupling between Endo and Epi cells, we estimated the parameters of Ca^{2+} transient and AP in the mathematical models of Endo and Epi cardiomyocytes. An increase in preload (20% diastolic stretch) decreased the amplitude of the Ca^{2+} transient in both the Endo and Epi models, the decrease being more pronounced for Endo cells (24% in the Endo model vs. 12% in the Epi model, **Figure 6**). No effect of stretch on the AP amplitude was found in both cell-type models. Regarding the time course parameters, stretch had almost no effect on the time to peak of the Ca^{2+} transient in both models, but a greater decrease in CaT_{50} with a greater increase in Ca_{90} was found in the Endo model compared with the Epi one at high preload (**Figure 6**). These steeper length-dependent changes with an increase in preload in the cytosolic Ca^{2+} decay were accompanied by a greater decrease in APD_{90} in the Endo model in comparison with the Epi one (17% in the Endo model vs. 10% in the Epi model), providing a reduction of the transmural gradient in APD_{90} at high preload between Endo and Epi cardiomyocytes (**Figure 6**). Analysis of the models showed that a decrease in the Ca^{2+} transient amplitude and acceleration of the fast phase of the cytosolic Ca^{2+} decay with an increase in preload resulted in Na^+–Ca^{2+} exchanger activity modulation. The outward Na^+–Ca^{2+} exchange current increased (0.7% in Endo vs. 0.1% in Epi for peak amplitudes), while the inward Na^+–Ca^{2+} exchange current decreased (21% in Endo vs. 17% in Epi for peak amplitudes). These changes led to an acceleration of repolarization, which, in turn, slightly increased voltage-dependent outward K^+ currents (~2% in Endo vs. ~0.5% in Epi for peak amplitudes) and accelerated its activation. Thus, greater changes in cytosolic Ca^{2+} with an increase in preload in the Endo model resulted in greater modulation of the Na^+–Ca^{2+} exchange current and voltage-dependent outward K^+ currents compared with the Epi model causing greater shortening of APD in Endo cardiomyocytes.

DISCUSSION

This study was designed to examine the effects of mechanical preload on mechano-calcium-electric feedback in single cardiomyocytes isolated from the Endo and Epi layers of the central region of mouse free LV wall. Using an original single-cell stretch technique (Iribe et al., 2014), we stretched single cardiomyocytes by up to 20% from slack SL to confirm the results of our previous study suggesting steeper length-dependent changes in $T_{\max}$ in Epi cells compared with Endo cells under small preloads (Khokhlova et al., 2018b). For the purposes of the study, we developed detailed mathematical models of electromechanical coupling in mouse Endo and Epi cardiomyocytes, which reproduced our experimental data on smaller active tension–length relationship (F_{active}LR) in Epi cardiomyocytes compared with Endo ones. The models showed that this effect could be explained by greater length-dependent Ca^{2+} activation in Endo cells. However, the Epi model failed to reproduce the bigger slope of the $T_{\max}$–length relationship simultaneously with the smaller slope of F_{active}LR compared with the Endo model. We speculate that preload-dependent changes in viscosity should be involved alongside the Frank–Starling effects to regulate the transmural gradient in length-dependent changes in the time course of contraction between Endo and Epi cardiomyocytes.

Using our Endo and Epi mathematical models, we studied the effects of preload on the transmural gradient in APD between the Endo and Epi cardiomyocytes. The models predicted that greater length-dependent activation in Endo cells *via* mechano-calcium-electric feedback gives a greater decrease in APD with stretch compared with Epi cells, providing a reduction in the transmural gradient in APD at longer end-diastolic SL.

The Transmural Gradient in Myocyte Morphology and Contractile Function

Our findings of similar length, width, and EDSL for mouse LV Endo and Epi cardiomyocytes are consistent with data obtained for rats (Cazorla et al., 2000; Natali et al., 2002; McCrossan et al., 2004).

Consistent with findings on mouse unloaded single-cell shortening (Kondo et al., 2006; Pan et al., 2018), our data showed that the amplitude of auxotonic tension was higher and $T_{\max}$ was greater in single Endo cells compared with Epi ones. The Endo and Epi mathematical models that we developed for the study reproduced the experimental data on transmural differences in contraction and literature data on the transmural gradient in AP and Ca^{2+} parameters (**Table 2**).

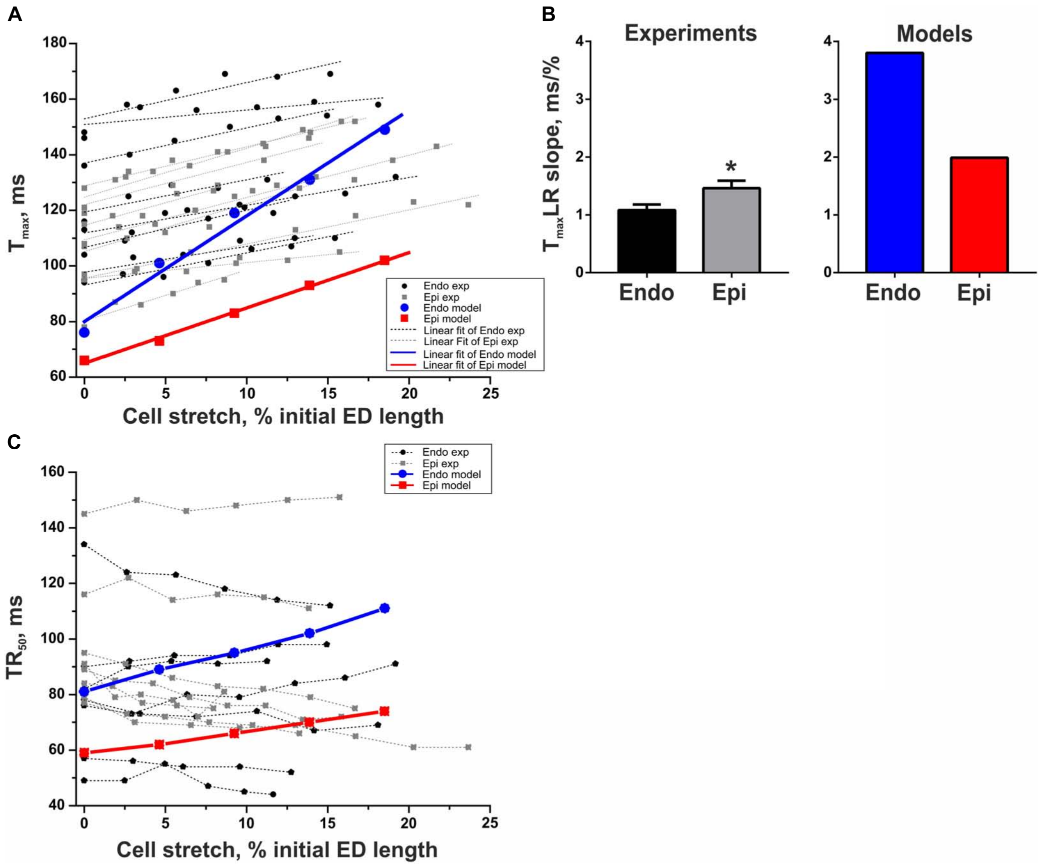

FIGURE 5 | Length-dependent changes in the time to peak contraction (T_{max}) and time to 50% relaxation (TR_{50}) of single mouse ventricular Endo and Epi cardiomyocytes in experiments [Endo: $n = 8$ ($N = 3$), Epi: $n = 9$ ($N = 5$)] and mathematical models. **(A)** T_{max}–length relation curves (T_{max}LR) from experimental (exp) data set and model simulations. **(B)** T_{max}LR slopes in experiments and mathematical models. **(C)** No correlation was found between TR_{50} and changes in the end-diastolic cell length in experiments. $^*p < 0.05$ Endo vs. Epi, Student's unpaired *t* test. *N* = number of animals, *n* = number of cells. ED, end-diastolic.

The discrepancies in the time of cytosolic Ca^{2+} decay between the models and experiments could also be explained by the binding characteristics of the fluorescent dyes used for Ca^{2+} measurements. These dyes may have contributed to cytosolic Ca^{2+} kinetics that is not accounted for in the mathematical models.

We also found that the time of tension decay was longer in the Endo model (negligibly for TR_{50}) but shorter in the Epi model compared with the experimental data. These discrepancies could be explained in two ways. First, the models overlooked the additional mechanism of intracellular transmural heterogeneity, which mostly affected the relaxation phase. The second explanation can be associated with the substantial variation of relaxation time with a standard deviation of 28% of the mean for Endo cells and 26% for Epi cells despite the fact that we used only the central part of the LV avoiding edge effects from the base and apex. Interestingly, in earlier studies, the variation of contractile properties among cardiomyocytes within small regions was also found to be significant (Clark and Campbell, 2019; Clark et al., 2019). Thus, within a rat Epi myocardial tissue volume of 7 mm^3, RT_{50} was found to have a standard deviation of 28% of the mean, and this degree of variation persisted even within tissue volumes as small as 1 mm^3 (Clark and Campbell, 2019). The authors discovered that RT_{50} was directly related to TnI phosphorylation levels and correlated significantly with end-diastolic cell length, suggesting a link between cell morphology and intrinsic relaxation behavior.

In our study, we observed two populations of cardiomyocytes with regard to their force–length properties between cells from the same region, i.e., within the endocardium and within the epicardium. Previously, Hanft and McDonald found that cells isolated from the rat LV exhibited two populations of force–length relationships (Hanft and McDonald, 2010). Thus, our findings are in agreement with the observation that functional variability among individual myocytes at the microscale may contribute to the contractile properties of the myocardium (Clark and Campbell, 2019; Clark et al., 2019). However, in the intact heart, the electrotonic coupling of cardiomyocytes via gap junctions and mechanical connections between cells at costameres and intercalated discs may attenuate these cell-to-cell differences at the macroscale (McCain and Parker, 2011; Quinn et al., 2016).

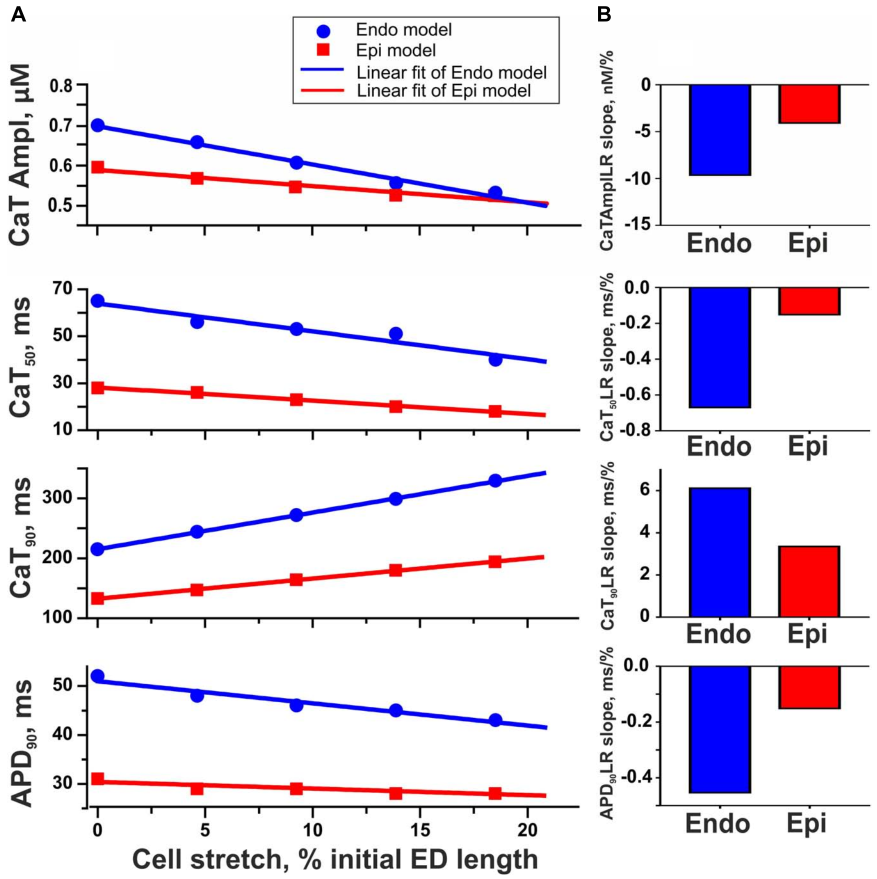

FIGURE 6 | Model predictions of length-dependent changes in the amplitude of Ca^{2+} transient (CaT Ampl), time from peak to 50% and 90% Ca^{2+} decay (CaT_{50}, CaT_{90}), and action potential duration at 90% repolarization (APD_{90}) in Endo and Epi cells. **(A)** CaAmplLR, CaT_{50}LR, Ca_{90}LR, and APD_{90}LR—Ca^{2+} transient amplitude–length relation, CaT_{50}–length relation, CaT_{90}–length relation, and APD_{90}–relation curves, respectively. **(B)** The slopes of CaAmplLR, CaT_{50}LR, CaT_{90}LR, and APD_{90}LR. ED, end-diastolic.

In this study, we used a parametrically modified Pandit model, which initially described the electrophysiological activity of Endo and Epi rat cardiomyocytes (Pandit et al., 2001), and a simplified model of Ca^{2+} handling in ventricular myocytes (Hinch et al., 2004). The choice of the models was determined by good coupling with our contractile model of Endo and Epi mouse cardiomyocytes (Khokhlova et al., 2018b) and best fit to literature and experimental data. To our knowledge, there are models (Bondarenko and Rasmusson, 2010; Mullins and Bondarenko, 2013) that account for transmural differences in electromechanical coupling in mice. In contrast to those models, our study takes into account not only literature data on transmural differences in intracellular ionic mechanisms and Ca^{2+} cycling but also intrinsic differences in acto-myosin interaction that may underlie Endo/Epi differences in mice (**Table 1**). We failed to find direct data on regional differences in murine Xb cycling kinetics and so had to use data obtained for guinea pigs and pigs (Le Guennec et al., 2008; Stelzer et al., 2008), which together with other target mechanisms allowed us to reproduce the functional electromechanical behavior of mouse Endo and Epi cardiomyocytes.

The Effects of Preload on the Transmural Gradient in Mechano-Calcium-Electric Feedback

To analyze changes in force amplitude and time course of contraction in a wide range of preloads, we used a modified CF technique where two pairs of CFs are used like two forceps for fixing and stretching a cell along the long axis (Iribe et al., 2014).

To analyze length-dependent changes in the force of Endo and Epi cardiomyocytes, we measured the slopes of the EDFLR as an index of myocardial passive stiffness and the slopes of the ESFLR, F_{active}LR, and FSG index as indices of a cell's ability to generate force under mechanical load. Consistently with our previous results (Khokhlova et al., 2018b), we found that there was no significant difference in the slope of the EDFLR and ESFLR between Endo and Epi cells. However, an assessment of the active tension–length relationship and the FSG index showed that the slope of F_{active}LR and the FSG index were significantly higher in Endo cardiomyocytes than in Epi ones, indicating greater myofilament length-dependent activation in Endo cells. Observations of rat cardiomyocytes also revealed a steeper active tension–SL relationship in Endo cells against Epi ones (Cazorla et al., 2000). Experiments on rat skinned cells demonstrated a larger increase in myofibrillar Ca^{2+} sensitivity following stretch due to a higher phosphorylation level of myosin-light chain 2 after stretch in Endo cells than in Epi cells (Cazorla et al., 2005, 2006).

There are still debates going concerning the mechanisms underlying increased contractility upon preload/stretch (length-dependent activation). It has been suggested that a decrease in myofilament lattice spacing between thin and thick filaments (McDonald and Moss, 1995; Irving et al., 2000; Fukuda et al., 2003) due to an increase in SL results in an increased number of attached Xbs, which, in turn, cooperatively increases the affinity of troponin C for Ca^{2+} (Hofmann and Fuchs, 1987) enhancing thin filament activation. Recent studies have shown that other mechanisms may be involved in this order of events instead of myofilament lattice spacing, e.g., changes in myosin head orientation relative to thin filaments (Farman et al., 2011) and titin-based structural rearrangements within both thin and thick filaments (Ait-Mou et al., 2016). In our models, the phenomenologically described length-dependent probability $n_1(l_1)$ of Xb binding to actin (see **Supplementary Material**, 2.5.9, n_1) is invariant with respect to a particular mechanism providing an increase in n_1 in response to an increase in l_1; this mechanism may be involved in addition to or instead of lattice spacing. The setting of $n_1(l_1)$ in the Endo model greater than in the Epi one enabled us to reproduce the experimental data on transmural differences in the slope of F_{active}LR and the FSG index.

In our mathematical models, an increase in preload increases the Xb formation probability $n_1(l_1)$. An increase in the concentration of force-generating Xbs brings about an increase in TnC affinity for Ca^{2+} (the first type of cooperativity implemented through a decrease in the rate constant of Ca^{2+} dissociation from Ca^{2+}–TnC complexes). Furthermore, the higher the concentration of [CaTnC], the lower the off-rate (the second type of cooperativity), which leads to a subsequent slowing down of the Ca^{2+}–TnC decay. As a consequence, Ca^{2+}–TnC binding has a higher peak and decreases slowly at longer SL (Solovyova et al., 2003). The slowing down of Ca^{2+}–TnC dissociation leads to a slight decrease in the amplitude and acceleration of the fast phase of the cytosolic Ca^{2+} decay (**Figure 6**, CaT_{50}).

By stretching single cardiomyocytes by up to 20% from slack SL, we have now confirmed the finding obtained in our previous study for small stretch (Khokhlova et al., 2018b): Epi cardiomyocytes demonstrate steeper length-dependent changes in T_{max} compared with Endo cardiomyocytes. Previously, we suggested that a greater slowing down of CaTnC dissociation at increased preload in Epi cells may contribute to a steeper preload dependence of T_{max} in Epi ones (Khokhlova et al., 2018b). In this study, while accounting for new experimental data on transmural differences in F_{active}LR and FSG index, our mathematical models failed to reproduce the bigger slope of the T_{max}–length relationship simultaneously with the smaller slope of F_{active}LR in Epi cells. As model analysis showed, a greater deceleration of CaTnC dissociation in Epi cells that could give a steeper T_{max}–length relationship with stretching would lead to a bigger slope of F_{active}LR in these cells. The latter would directly contradict the experimentally obtained steeper F_{active}LR in Endo cells. Thus, the models suggest that the deceleration of CaTnC dissociation at increased preload should be greater in Endo cells rather than in Epi ones. This means that other mechanisms should be involved in the regulation of the transmural gradient in length-dependent changes in the time course of contraction of Endo and Epi cardiomyocytes. For example, stretch-hold experiments involving mice and pigs showed that viscosity based on interaction between titin and actin depends on stretch velocity and EDSL, being greater at longer SL (Chung and Granzier, 2011; Chung et al., 2011a,b). In our previous modeling study, an increase in viscosity decreased T_{max} of contraction but did not affect length-dependent activation (Katsnelson et al., 2004). It has been shown on rats that the amount of titin differed between the subendocardium and subepicardium, with Endo cells expressing more titin per half-sarcomere than Epi cells (Cazorla et al., 2005). Our preliminary simulations have confirmed that a greater viscosity response to an increase in preload in the Endo model accounts for a smaller increase in T_{max} at longer SL, i.e., for a smaller slope of the T_{max}–length relationship in Endo cardiomyocytes. At the same time, F_{active}LR remains unaffected by a change in viscosity, i.e., remains greater in Endo cardiomyocytes due to the greater slowing down of CaTnC dissociation at high preload in Endo cells. These preliminary findings should be verified in future studies.

It is still unclear how an increase in preload affects the transmural gradient in AP characteristics. The only study available on isolated rat Endo and Epi cardiomyocytes showed that transmural electrophysiological responses to stretch are different (Saint et al., 2010). The authors suggested that a greater expression of TREK-1, a mechanosensitive K^+ channel, may be accountable for a greater decrease in the APD in Endo cells compared with Epi ones upon stretch, providing a decrease of the transmural gradient in APD. Our models predict one more possible mechanism of this phenomenon mediated via mechano-calcium-electric feedback.

In the Endo model, a greater Xb formation probability $n_1(l_1)$ provides a greater increase in TnC affinity for Ca^{2+} compared with the Epi model and a greater acceleration of CaT_{50}, respectively (**Figure 6**, CaT_{50}). This, in turn, leads to a greater modulation of the Na^+–Ca^{2+} exchange current and outward K^+ currents causing a greater shortening of APD in the Endo model at longer SL (**Figure 6**, APD). Thus, we suggest that Endo/Epi heterogeneity in length-dependent activation via mechano-calcium-electric feedback provides a reduction in the transmural gradient in APD at longer SL, which may partially explain the difficulties of determination of transmural gradients in APD in the intact heart (Taggart et al., 2001; Mačianskienė et al., 2018).

In conclusion, transmural heterogeneity is a major characteristic of the healthy LV. We have demonstrated that a change in preload might be a source for mechano-calcium-electric modulation of electrophysiological and contractile properties of myocytes across the wall.

Mathematical Model Limitation

In the mathematical models, we did not aim to precisely mimic the mean values of experiments or literature data. Our goal was to ensure falling into the correct parameter range to be able to explain the molecular and cellular mechanisms that underlie transmural heterogeneity in the heart. However, some output parameters, such as $T_{\max}$, turned out to be out of the range. The tuning mathematical model parameters should be continued in further studies.

DATA AVAILABILITY STATEMENT

The datasets generated for this study are available on request to the corresponding author.

ETHICS STATEMENT

All procedures involving animal use were performed in accordance with the Guiding Principles for the Care and Use of Animals approved by the Council of the Physiological Society of Japan. All protocols involving animals were approved by the Animal Subjects Committee of Okayama University, Graduate School of Medicine, Dentistry and Pharmaceutical Sciences.

AUTHOR CONTRIBUTIONS

AK and GI contributed to the design of wet experiments, analysis, and interpretation of the results. PK contributed to the mathematical model simulations and analysis. OS and LK contributed to the conception of the mathematical models, design, analysis, and interpretation of the results and simulations. The manuscript was written by AK, with the assistance of GI, OS, and LK. All authors approved the final version of the manuscript.

FUNDING

Wet experiments were supported by the Russian Science Foundation (#18-74-10059). The development of mouse ventricular cardiomyocyte model was supported by the Russian Foundation for Basic Research (#18-01-00059), IIF UrB RAS theme (AAAA-A18-118020590031-8), and by RF Government Act #211 of March 16, 2013 (agreement 02.A03.21.0006).

SUPPLEMENTARY MATERIAL

The Supplementary Material for this article can be found online at: https://www.frontiersin.org/articles/10.3389/fphys.2020.00171/full#supplementary-material

REFERENCES

Ait-Mou, Y., Hsu, K., Farman, G. P., Kumar, M., Greaser, M. L., Irving, T. C., et al. (2016). Titin strain contributes to the Frank–Starling law of the heart by structural rearrangements of both thin-and thick-filament proteins. *Proc. Natl. Acad. Sci. U.S.A.* 113, 2306–2311. doi: 10.1073/pnas.1516732113

Ashikaga, H., Coppola, B. A., Hopenfeld, B., Leifer, E. S., McVeigh, E. R., and Omens, J. H. (2007). Transmural dispersion of myofiber mechanics: implications for electrical heterogeneity in vivo. *J. Am. Coll. Cardiol.* 49, 909–916. doi: 10.1016/j.jacc.2006.07.074

Bollensdorff, C., Lookin, O., and Kohl, P. (2011). Assessment of contractility in intact ventricular cardiomyocytes using the dimensionless 'Frank–Starling Gain'index. *Pflügers Arch. Eur. J. Physiol.* 462, 39–48. doi: 10.1007/s00424-011-0964-z

Bondarenko, V. E., and Rasmusson, R. L. (2010). Transmural heterogeneity of repolarization and Ca2+ handling in a model of mouse ventricular tissue. *Am. J. Physiol. Heart Circ. Physiol.* 299, H454–H469.

Boukens, B. J., Sulkin, M. S., Gloschat, C. R., Ng, F. S., Vigmond, E. J., and Efimov, I. R. (2015). Transmural APD gradient synchronizes repolarization in the human left ventricular wall. *Cardiovasc. Res.* 108, 188–196. doi: 10.1093/cvr/cvv202

Brunet, S., Aimond, F., Li, H., Guo, W., Eldstrom, J., Fedida, D., et al. (2004). Heterogeneous expression of repolarizing, voltage-gated K+ currents in adult mouse ventricles. *J. Physiol.* 559, 103–120. doi: 10.1113/jphysiol.2004.063347

Cazorla, O., Ait Mou, Y., Goret, L., Vassort, G., Dauzat, M., Lacampagne, A., et al. (2006). Effects of high-altitude exercise training on contractile function of rat skinned cardiomyocyte. *Cardiovasc. Res.* 71, 652–660. doi: 10.1016/j.cardiores.2006.06.020

Cazorla, O., Le Guennec, J.-Y., and White, E. (2000). Length–tension relationships of sub-epicardial and sub-endocardial single ventricular myocytes from rat and ferret hearts. *J. Mol. Cell. Cardiol.* 32, 735–744. doi: 10.1006/jmcc.2000.1115

Cazorla, O., Pascarel, C., Garnier, D., and Le Guennec, J.-Y. (1997). Resting tension participates in the modulation of active tension in isolated guinea pig ventricular myocytes. *J. Mol. Cell. Cardiol.* 29, 1629–1637. doi: 10.1006/jmcc.1997.0402

Cazorla, O., Szilagyi, S., Le Guennec, J.-Y., Vassort, G., and Lacampagne, A. (2005). Transmural stretch-dependent regulation of contractile properties in rat heart and its alteration after myocardial infarction. *FASEB J.* 19, 88–90. doi: 10.1096/fj.04-2066fje

Chen, X., Qin, M., Jiang, W., Zhang, Y., and Liu, X. (2017). Electrophysiological characteristics of pressure overload-induced cardiac hypertrophy and its influence on ventricular arrhythmias. *PLoS One* 12:e0183671. doi: 10.1371/journal.pone.0183671

Chung, C. S., Bogomolovas, J., Gasch, A., Hidalgo, C. G., Labeit, S., and Granzier, H. L. (2011a). Titin-actin interaction: PEVK-actin-based viscosity in a large animal. *Biomed Res. Int.* 2011:310791.

Chung, C. S., and Granzier, H. L. (2011). Contribution of titin and extracellular matrix to passive pressure and measurement of sarcomere length in the mouse left ventricle. *J. Mol. Cell. Cardiol.* 50, 731–739. doi: 10.1016/j.yjmcc.2011.01.005

Chung, C. S., Methawasin, M., Nelson, O. L., Radke, M. H., Hidalgo, C. G., Gotthardt, M., et al. (2011b). Titin based viscosity in ventricular physiology: an integrative investigation of PEVK–actin interactions. *J. Mol. Cell. Cardiol.* 51, 428–434. doi: 10.1016/j.yjmcc.2011.06.006

Clark, J. A., and Campbell, S. G. (2019). Diverse relaxation rates exist among rat cardiomyocytes isolated from a single myocardial region. *J. Physiol.* 597, 711–722. doi: 10.1113/jp276718

Clark, J. A., Weiss, J. D., and Campbell, S. (2019). A microwell cell capture device reveals variable response to dobutamine in isolated cardiomyocytes. *BioRxiv* [preprint]. doi: 10.1101/636852

Cordeiro, J. M., Greene, L., Heilmann, C., Antzelevitch, D., and Antzelevitch, C. (2004). Transmural heterogeneity of calcium activity and mechanical function in the canine left ventricle. *Am. J. Physiol. Heart Circ. Physiol.* 286, H1471–H1479.

Dilly, K. W., Rossow, C. F., Votaw, V. S., Meabon, J. S., Cabarrus, J. L., and Santana, L. F. (2006). Mechanisms underlying variations in excitation–contraction coupling across the mouse left ventricular free wall. *J. Physiol.* 572, 227–241. doi: 10.1113/jphysiol.2005.102020

Farman, G. P., Gore, D., Allen, E., Schoenfelt, K., Irving, T. C., and de Tombe, P. P. (2011). Myosin head orientation: a structural determinant for the Frank-Starling relationship. *Am. J. Physiol. Heart Circ. Physiol.* 300, H2155–H2160.

Fukuda, N., Wu, Y., Farman, G., Irving, T. C., and Granzier, H. (2003). Titin isoform variance and length dependence of activation in skinned bovine cardiac muscle. *J. Physiol.* 553, 147–154. doi: 10.1113/jphysiol.2003.049759

Hanft, L. M., and McDonald, K. S. (2010). Length dependence of force generation exhibit similarities between rat cardiac myocytes and skeletal muscle fibres. *J. Physiol.* 588, 2891–2903. doi: 10.1113/jphysiol.2010.190504

Hinch, R., Greenstein, J., Tanskanen, A., Xu, L., and Winslow, R. (2004). A simplified local control model of calcium-induced calcium release in cardiac ventricular myocytes. *Biophys. J.* 87, 3723–3736. doi: 10.1529/biophysj.104.049973

Hofmann, P. A., and Fuchs, F. (1987). Effect of length and cross-bridge attachment on Ca2+ binding to cardiac troponin C. *Am. J. Physiol. Cell Physiol.* 253, C90–C96.

Iribe, G., Helmes, M., and Kohl, P. (2007). Force-length relations in isolated intact cardiomyocytes subjected to dynamic changes in mechanical load. *Am. J. Physiol. Heart Circ. Physiol.* 292, H1487–H1497.

Iribe, G., Kaneko, T., Yamaguchi, Y., and Naruse, K. (2014). Load dependency in force–length relations in isolated single cardiomyocytes. *Prog. Biophys. Mol. Biol.* 115, 103–114. doi: 10.1016/j.pbiomolbio.2014.06.005

Irving, T. C., Konhilas, J., Perry, D., Fischetti, R., and De Tombe, P. P. (2000). Myofilament lattice spacing as a function of sarcomere length in isolated rat myocardium. *Am. J. Physiol. Heart Circ. Physiol.* 279, H2568–H2573.

Johnson, E. K., Springer, S. J., Wang, W., Dranoff, E. J., Zhang, Y., Kanter, E. M., et al. (2018). Differential expression and remodeling of transient outward potassium currents in human left ventricles. *Circulation* 11:e005914.

Katsnelson, L. B., Nikitina, L. V., Chemla, D., Solovyova, O., Coirault, C., Lecarpentier, Y., et al. (2004). Influence of viscosity on myocardium mechanical activity: a mathematical model. *J. Theor. Biol.* 230, 385–405. doi: 10.1016/j.jtbi.2004.05.007

Katz, A. M., and Katz, P. B. (1989). Homogeneity out of heterogeneity. *Circulation* 79, 712–717. doi: 10.1161/01.cir.79.3.712

Khokhlova, A., Balakina-Vikulova, N., Katsnelson, L., Iribe, G., and Solovyova, O. (2018a). Transmural cellular heterogeneity in myocardial electromechanics. *J. Physiol. Sci.* 68, 387–413. doi: 10.1007/s12576-017-0541-0

Khokhlova, A., Iribe, G., Katsnelson, L., Naruse, K., and Solovyova, O. (2018b). The effects of load on transmural differences in contraction of isolated mouse ventricular cardiomyocytes. *J. Mol. Cell. Cardiol.* 114, 276–287. doi: 10.1016/j.yjmcc.2017.12.001

Kobirumaki-Shimozawa, F., Oyama, K., Shimozawa, T., Mizuno, A., Ohki, T., Terui, T., et al. (2016). Nano-imaging of the beating mouse heart in vivo: Importance of sarcomere dynamics, as opposed to sarcomere length per se, in the regulation of cardiac function. *J. Gen. Physiol.* 147, 53–62. doi: 10.1085/jgp.201511484

Kondo, R. P., Dederko, D. A., Teutsch, C., Chrast, J., Catalucci, D., Chien, K. R., et al. (2006). Comparison of contraction and calcium handling between right and left ventricular myocytes from adult mouse heart: a role for repolarization waveform. *J. Physiol.* 571, 131–146. doi: 10.1113/jphysiol.2005.101428

Le Guennec, J.-Y., Mosca, E., de Tombe, P. P., and Cazorla, O. (2008). Differential contribution of cardiac sarcomeric proteins in the myofibrillar force response to stretch. *Pflügers Arch. Eur. J. Physiol.* 457, 25. doi: 10.1007/s00424-008-0501-x

Liu, J., Kim, K.-H., Morales, M. J., Heximer, S. P., Hui, C.-C., and Backx, P. H. (2015). Kv4. 3-encoded fast transient outward current is presented in Kv4. 2 knockout mouse cardiomyocytes. *PLoS One* 10:e0133274. doi: : 10.1371/journal.pone.0133274

Lou, Q., Fedorov, V. V., Glukhov, A. V., Moazami, N., Fast, V. G., and Efimov, I. R. (2011). Transmural heterogeneity and remodeling of ventricular excitation-contraction coupling in human heart failure. *Circulation* 123, 1881–1890. doi: 10.1161/circulationaha.110.989707

Mačianskienė, R., Martišienė, I., Navalinskas, A., Treinys, R., Andriulė, I., and Jurevičius, J. (2018). Mechanism of action potential prolongation during metabolic inhibition in the whole rabbit heart. *Front. Physiol.* 9:1077. doi: 10.3389/fphys.2018.01077

McCain, M. L., and Parker, K. K. (2011). Mechanotransduction: the role of mechanical stress, myocyte shape, and cytoskeletal architecture on cardiac function. *Pflügers Arch. Eur. J. Physiol.* 462, 89–104. doi: 10.1007/s00424-011-0951-4

McCrossan, Z. A., Billeter, R., and White, E. (2004). Transmural changes in size, contractile and electrical properties of SHR left ventricular myocytes during compensated hypertrophy. *Cardiovasc. Res.* 63, 283–292. doi: 10.1016/j.cardiores.2004.04.013

McDonald, K. S., and Moss, R. L. (1995). Osmotic compression of single cardiac myocytes eliminates the reduction in Ca2+ sensitivity of tension at short sarcomere length. *Circ. Res.* 77, 199–205. doi: 10.1161/01.res.77.1.199

Mullins, P. D., and Bondarenko, V. E. (2013). A mathematical model of the mouse ventricular myocyte contraction. *PLoS One* 8:e63141. doi: 10.1371/journal.pone.0063141

Myles, R. C., Bernus, O., Burton, F. L., Cobbe, S. M., and Smith, G. L. (2010). Effect of activation sequence on transmural patterns of repolarization and action potential duration in rabbit ventricular myocardium. *Am. J. Physiol. Heart Circ. Physiol.* 299, H1812–H1822.

Natali, A., Wilson, L., Peckham, M., Turner, D., Harrison, S., and White, E. (2002). Different regional effects of voluntary exercise on the mechanical and electrical properties of rat ventricular myocytes. *J. Physiol.* 541, 863–875. doi: 10.1113/jphysiol.2001.013415

Nishimura, S., Yasuda, S.-I., Katoh, M., Yamada, K. P., Yamashita, H., Saeki, Y., et al. (2004). Single cell mechanics of rat cardiomyocytes under isometric, unloaded, and physiologically loaded conditions. *Am. J. Physiol. Heart Circ. Physiol.* 287, H196–H202.

Opthof, T., Coronel, R., Wilms-Schopman, F. J., Plotnikov, A. N., Shlapakova, I. N., and Danilo, P. Jr. (2007). Dispersion of repolarization in canine ventricle and the electrocardiographic T wave: Tp-e interval does not reflect transmural dispersion. *Heart Rhythm* 4, 341–348. doi: 10.1016/j.hrthm.2006.11.022

Pan, W., Yang, Z., Cheng, J., Qian, C., and Wang, Y. (2018). Contractile heterogeneity in ventricular myocardium. *J. Cell. Physiol.* 233, 6273–6279. doi: 10.1002/jcp.26512

Pandit, S. V., Clark, R. B., Giles, W. R., and Demir, S. S. (2001). A mathematical model of action potential heterogeneity in adult rat left ventricular myocytes. *Biophys. J.* 81, 3029–3051. doi: 10.1016/s0006-3495(01)75943-7

Quinn, T. A., Camelliti, P., Rog-Zielinska, E. A., Siedlecka, U., Poggioli, T., O'Toole, E. T., et al. (2016). Electrotonic coupling of excitable and nonexcitable cells in the heart revealed by optogenetics. *Proc. Natl. Acad. Sci. U.S.A.* 113, 14852–14857. doi: 10.1073/pnas.1611184114

Rossow, C. F., Dilly, K. W., and Santana, L. F. (2006). Differential calcineurin/NFATc3 activity contributes to the I to transmural gradient in the mouse heart. *Circ. Res.* 98, 1306–1313. doi: 10.1161/01.res.0000222028.92993.10

Saint, D. A., Kelly, D., and Mackenzie, L. (2010). "The contribution of MEF to electrical heterogeneity and arrhythmogenesis," in *Mechanosensitivity of the Heart*, eds A. Kamkin, and I. Kiseleva (Cham: Springer), 275–300. doi: 10.1007/978-90-481-2850-1_11

Shi, C., Wang, X., Dong, F., Wang, Y., Hui, J., Lin, Z., et al. (2013). Temporal alterations and cellular mechanisms of transmural repolarization during progression of mouse cardiac hypertrophy and failure. *Acta Physiol.* 208, 95–110. doi: 10.1111/apha.12071

Solovyova, O., Katsnelson, L. B., Kohl, P., Panfilov, A. V., Tsaturyan, A. K., and Tsyvian, P. B. (2016). Mechano-electric heterogeneity of the myocardium as a paradigm of its function. *Prog. Biophys. Mol. Biol.* 120, 249–254. doi: 10.1016/j.pbiomolbio.2015.12.007

Solovyova, O., Vikulova, N., Katsnelson, L. B., Markhasin, V. S., Noble, P., Garny, A., et al. (2003). Mechanical interaction of heterogeneous cardiac muscle segments in silico: effects on Ca 2+ handling and action potential. *Int. J. Bifurcat. Chaos* 13, 3757–3782. doi: 10.1142/s0218127403008983

Stelzer, J. E., Norman, H. S., Chen, P. P., Patel, J. R., and Moss, R. L. (2008). Transmural variation in myosin heavy chain isoform expression modulates the timing of myocardial force generation in porcine left ventricle. *J. Physiol.* 586, 5203–5214. doi: 10.1113/jphysiol.2008.160390

Sulman, T., Katsnelson, L. B., Solovyova, O., and Markhasin, V. S. (2008). Mathematical modeling of mechanically modulated rhythm disturbances in homogeneous and heterogeneous myocardium with attenuated activity of Na+–K+ pump. *Bull. Math. Biol.* 70, 910–949. doi: 10.1007/s11538-007-9285-y

Taggart, P., Sutton, P. M., Opthof, T., Coronel, R., Trimlett, R., Pugsley, W., et al. (2001). Transmural repolarisation in the left ventricle in humans during normoxia and ischaemia. *Cardiovasc. Res.* 50, 454–462. doi: 10.1016/s0008-6363(01)00223-1

Veerman, C. C., Podliesna, S., Tadros, R., Lodder, E. M., Mengarelli, I., de Jonge, B., et al. (2017). The Brugada syndrome susceptibility gene HEY2 modulates cardiac transmural ion channel patterning and electrical heterogeneity. *Circ. Res.* 121, 537–548. doi: 10.1161/circresaha.117.310959

Waldman, L. K., Fung, Y., and Covell, J. W. (1985). Transmural myocardial deformation in the canine left ventricle. Normal in vivo three-dimensional finite strains. *Circ. Res.* 57, 152–163. doi: 10.1161/01.res.57.1.152

Wan, X., Laurita, K. R., Pruvot, E. J., and Rosenbaum, D. S. (2005). Molecular correlates of repolarization alternans in cardiac myocytes. *J. Mol. Cell. Cardiol.* 39, 419–428. doi: 10.1016/j.yjmcc.2005.06.004

Wang, H. S., and Cohen, I. S. (2003). Calcium channel heterogeneity in canine left ventricular myocytes. *J. Physiol.* 547, 825–833. doi: 10.1113/jphysiol.2002.035410

Xu, L., Chen, J., Li, X.-Y., Ren, S., Huang, C.-X., Wu, G., et al. (2012). Analysis of Na+/Ca 2+ exchanger (NCX) function and current in murine cardiac myocytes during heart failure. *Mol. Biol. Rep.* 39, 3847–3852. doi: 10.1007/s11033-011-1163-x

Conflict of Interest: The authors declare that the research was conducted in the absence of any commercial or financial relationships that could be construed as a potential conflict of interest.

frontiers
in Physiology

MINI REVIEW
published: 20 March 2020
doi: 10.3389/fphys.2020.00163

May the Force Not Be With You During Culture: Eliminating Mechano-Associated Feedback During Culture Preserves Cultured Atrial and Pacemaker Cell Functions

Noa Kirschner Peretz†, **Sofia Segal**† and **Yael Yaniv***

Biomedical Engineering Faculty, Technion Israel Institute of Technology, Haifa, Israel

Edited by:
Leonid Katsnelson,
Institute of Immunology
and Physiology (RAS), Russia

Reviewed by:
Alexey V. Glukhov,
University of Wisconsin–Madison,
United States
Denis Abramochkin,
Lomonosov Moscow State University,
Russia

***Correspondence:**
Yael Yaniv
yaely@bm.technion.ac.il;
yanivyael@gmail.com

†*These authors have contributed equally to this work*

Specialty section:
This article was submitted to
Striated Muscle Physiology,
a section of the journal
Frontiers in Physiology

Received: *29 November 2019*
Accepted: *12 February 2020*
Published: *20 March 2020*

Citation:
Kirschner Peretz N, Segal S and Yaniv Y (2020) May the Force Not Be With You During Culture: Eliminating Mechano-Associated Feedback During Culture Preserves Cultured Atrial and Pacemaker Cell Functions. Front. Physiol. 11:163. doi: 10.3389/fphys.2020.00163

Cultured cardiomyocytes have been shown to possess significant potential as a model for characterization of mechano-Ca^{2+}, mechano-electric, and mechano-metabolic feedbacks in the heart. However, the majority of cultured cardiomyocytes exhibit impaired electrical, mechanical, biochemical, and metabolic functions. More specifically, the cells do not beat spontaneously (pacemaker cells) or beat at a rate far lower than their physiological counterparts and self-oscillate (atrial and ventricular cells) in culture. Thus, efforts are being invested in ensuring that cultured cardiomyocytes maintain the shape and function of freshly isolated cells. Elimination of contraction during culture has been shown to preserve the mechano-Ca^{2+}, mechano-electric, and mechano-metabolic feedback loops of cultured cells. This review focuses on pacemaker cells, which reside in the sinoatrial node (SAN) and generate regular heartbeat through the initiation of the heart's electrical, metabolic, and biochemical activities. In parallel, it places emphasis on atrial cells, which are responsible for bridging the electrical conductance from the SAN to the ventricle. The review provides a summary of the main mechanisms responsible for mechano-electrical, Ca^{2+}, and metabolic feedback in pacemaker and atrial cells and of culture methods existing for both cell types. The work concludes with an explanation of how the elimination of mechano-electrical, mechano-Ca^{2+}, and mechano-metabolic feedbacks during culture results in sustained cultured cell function.

Keywords: 2,3-butanedione-monoxime, blebbistatin, mechanics, sinoatrial node, ventricular

INTRODUCTION

Cardiac physiology research aims to understand how the heart works under both healthy and pathophysiological conditions, since the prevention and treatment of cardiovascular abnormalities, including arrhythmias, is the most critical goal of biomedical researchers. A top-to-bottom approach, i.e., parallel performance of *in vivo* experiments and *in vitro* cardiac tissue and single-cell experiments, is often taken to achieve these goals. Animals are the most favorable model, as the production of human-like cells and tissues remains a challenge. In order to understand true cardiac physiology, the mammalian cells and tissues must be maintained under conditions similar to those prevailing in the body, with temperature and extracellular conditions being crucial for physiological cell and tissue functioning. More specifically, to explore the mechano-electrical, mechano-Ca^{2+}, and mechano-metabolic feedbacks that determine heart function (e.g., Braunwald, 1971; Bers, 2008; Quinn, 2014; Kamoun et al., 2018), one of the most fascinating branches of cardiac physiology, the ability of spontaneously beating cells to self-contract at their physiological frequency or of electrically triggered cells to remain quiescent in the absence of electrical stimulation and to respond to posed physiological frequency stimuli, must be preserved.

Recently, new genetic manipulation techniques, including Förster resonance energy transfer (FRET), have been applied to measure contractile filament activity, Ca^{2+} cycling, and metabolite dynamics (Warrier et al., 2005; Lu et al., 2013; Kioka et al., 2014; Li et al., 2016; Musheshe et al., 2018). Most of these experiments can only be performed in culture. Thus, a sustainable, viable and physiological-like culture method is crucial. Cardiac cell culture protocols ensuring maintenance of cell morphology, cell quiescence in culture, response to electrical stimulation at a physiological rate (or spontaneously beating under physiological conditions), and preservation of Ca^{2+} cycling and bioenergetic function are viewed as successful protocols. However, currently, the majority of cultured cardiomyocytes exhibit impaired electrical, mechanical, biochemical, and metabolic functions.

This review focuses on pacemaker cells, which reside in the sinoatrial node (SAN) and generate the heartbeat by initiating the heart's electrical, metabolic, and biochemical activities. In parallel, it places emphasis on atrial cells, which are responsible for bridging the electrical conductance from the SAN to the ventricle. More specifically, the review provides a summary of the main mechanisms responsible for mechano-electrical, Ca^{2+}, and metabolic feedback in pacemaker and atrial cells (**Figure 1**) and of the existing culture methods for each cell type. The work concludes with an explanation of how the elimination of mechano-electrical, mechano-Ca^{2+}, and mechano-metabolic feedbacks during culture leads to sustained cultured cell function.

ELECTRO-Ca^{2+}-METABOLIC-MECHANICAL FEEDBACK IN PACEMAKER AND ATRIAL CELLS

The heart is assembled from different cell types that, together, determine its function. The atria are comprised of two of the four chambers of the heart and are situated above the two ventricles. The right atrium contains the SAN, the heart's primary pacemaker, which initiates heart electrical activity (Monfredi et al., 2010) by generating an action potential (AP) that spreads across both atria, inducing their contraction and forcing the blood they hold into their corresponding ventricles. The pacemaker cell beating rate is controlled by internal pacemaker cell clocks and through brain signaling that activates receptors on the pacemaker cell membrane (Vinogradova et al., 2002). During early depolarization, prior to the burst of an AP in the pacemaker cell, Ca^{2+} is spontaneously released from the sarcoplasmic reticulum (SR) through the ryanodine receptor channels (RyR2), close to the cell membrane, subsequently activating the Na^{+}/Ca^{2+} exchanger (NCX) (Bogdanov et al., 2001). The inward current through the NCX, together with the funny current channels (I_f), which are highly expressed in pacemaker cells (DiFrancesco and Ojeda, 1980), prompts the surface M-clock, an ensemble of sarcolemmal electrogenic molecules, to generate an AP (Lyashkov et al., 2018). The AP stimulates the opening of Ca^{2+} channels on the cell membrane (L-type Ca^{2+} channels, $I_{Ca,L}$), hence enabling Ca^{2+} ion release into the cells, which arouses the release of Ca^{2+} ions from the SR into the cytosol. The SR, the organelle that initiates this chain of events, is known as the Ca^{2+} clock. Together, the M and Ca^{2+} clocks create a coupled-clock system (Lakatta et al., 2010). The crosstalk between the two clocks is dictated by Ca^{2+} and by secondary Ca^{2+}-activated mechanisms [reviewed in Yaniv et al. (2015b)]. More specifically, Ca^{2+} activates calmodulin, which, in turn, regulates the adenylyl cyclase (AC) and Ca^{2+}/calmodulin-dependent protein kinase II (CaMKII) function. AC catalyzes the conversion of adenosine triphosphate (ATP) to cyclic adenosine monophosphate (cAMP), which exposes the phosphorylation sites on the protein kinase A (PKA) molecules. PKA signaling cascades, together with CaMKII, act on both SR [phospholamban (PLB) and the RyR2] and M-clock proteins (L-type Ca^{2+} channels and K^{+} channels). In parallel, AC-cAMP signaling regulates the binding of cAMP molecules to the funny channel. Taken together, pacemaker electro-Ca^{2+} feedback is controlled by intrinsic signaling mechanisms originating at multiple cellular (surface membrane), intracellular (phosphorylation cascades, SR, the mitochondria), and heart-brain (neurotransmitter or hormonal stimulation of surface membrane receptors) locations. cAMP/PKA signaling also links the pacemaker electro-Ca^{2+} feedback to energetics. To maintain proper electrical activity in pacemaker cells, ATP is supplied to the cell in order to produce cAMP, maintain ionic homeostasis, and pump Ca^{2+} into the SR. It has been shown that Ca^{2+}-dependent activation of cAMP/PKA signaling within pacemaker cells links ATP utilization and its production in the mitochondria; when the spontaneous AP firing rate is decreased by drugs that lead directly or indirectly to cAMP/PKA reduction, ATP in the pacemaker cells is depleted (Yaniv et al., 2011). Similar results were found when CaMKII signaling was eliminated using pharmacological drugs (Yaniv et al., 2013a). When the ATP demand increases above basal levels, the mitochondrial cAMP/PKA-CaMKII signaling and mitochondrial Ca^{2+} work together to increase the ATP supply to match the increase in energetic demand (Yaniv et al., 2013b). An additional electro-energetics link in pacemaker cells has been shown by changes in SR Ca^{2+} loading and spontaneous Ca^{2+} release in response to changes in mitochondrial Ca^{2+} flux, all of which translate into changes in cell automaticity (Yaniv et al., 2012). Similar evidence was found upon genetic manipulation of the Ca^{2+} influx channel (Wu et al., 2015). Taken together, the

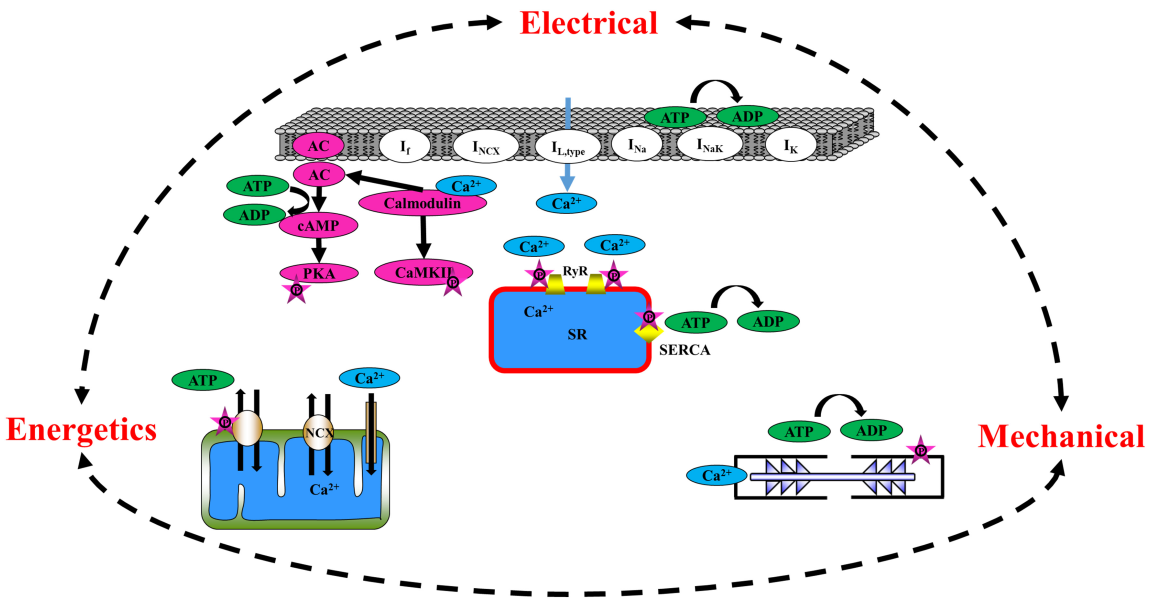

FIGURE 1 | Schematic illustration of the major players in mechano-electrical, mechano-Ca^{2+}, and mechano-metabolic feedbacks.

role of pacemaker cell mitochondria is not limited to ATP production alone, but rather, extends to the cells' coupled-clock system and its influence on the AP firing rate (i.e., reverse electro-energetic feedback). Finally, electrical-mechanical feedback also regulates pacemaker cells. Although questioned in the past, it has been firmly established that pacemaker cells possess sarcomeres, the basic contractile unit (Yaniv et al., 2011). Evidence for such feedback was demonstrated in heart failure patients presenting a distended atrial wall (the location of the SAN tissue) as a result of increased venous return post-exercise and saline loading (Andersen et al., 2015). Another study showed a strong relationship between elevated right atrial pressure and pacemaker cell dysfunction (Paul et al., 1998). Extensive research also showed that mechano-electrical feedback exists in pacemaker cells and SAN tissue. An increase in the beating rate in response to mechanical stretch of the SAN tissue (Lange et al., 1966; Kamiyama et al., 1984) and of pacemaker cells (Kohl et al., 1999) has been documented, demonstrating that the heart's positive stretch-induced chronotropic response is caused by mechanisms within the SAN tissue. However, the main regulators of this feedback have not been fully elucidated.

Propagation of the AP from the SAN ignites AP in the atria and leads to the opening of L-type Ca^{2+} channels, which induce the release of Ca^{2+} ions from the SR. The majority of the Ca^{2+} released attaches to the sarcomeres, with only a small portion entering the mitochondria (Bootman et al., 2006; Maack and O'Rourke, 2007). Similarly to pacemaker cells, atrial cells express AC type 1 and 8 (Collins and Terrar, 2012). Intracellular Ca^{2+} binds to calmodulin, which activates AC-cAMP/PKA molecules, which, in turn, increases phosphorylation activity in the cell. The cAMP produced by Ca^{2+}-stimulated ACs regulates the L-type Ca^{2+} channel and, subsequently, the calcium-induced calcium release (CICR) in the atria (Collins and Terrar, 2012). PKA also serves as a regulator of electro-Ca^{2+} feedback in atrial cells via its effect on cell membrane channels [L-type Ca^{2+} channels (Trautwein and Hescheler, 1990), K^+ channels (Freeman et al., 1992), Ca^{2+} storage within the SR (Toyofuku et al., 1993), and RyR2 (Takasago et al., 1989)]. T-tubules are extensions of the cell membrane that penetrate into the center of cardiac cells. They permit rapid transmission of APs into the cell and play an important role in regulating cellular Ca^{2+} concentrations. By synchronizing Ca^{2+} release throughout the cell (Hong and Shaw, 2017) and shifting the electro-mechanical feedback to occur in the peripheral areas of the cell, t-tubules allow cardiac cells to contract more forcefully. Atrial cells have a different t-tubule system than ventricular cells; they are termed transverse-axial tubules (TATs) and present as heterogenous sarcolemmal membrane invaginations that appear near the z-lines and assist in atrial cell contraction (Kirk et al., 2003; Hund and Mohlerp, 2016; Yue et al., 2017). When an AP is initiated, the atrial cells activate intracellular Ca^{2+} release and sarcomeric contraction through the TAT junctions (Brandenburg et al., 2018). The existence of the TATs contributes to near-synchronous Ca^{2+} transients and to synchronous subcellular depolarization and intracellular Ca^{2+} release. TATs may lead to region-specific electro-mechanical coupling and heterogeneous atrial contraction (Hund and Mohlerp, 2016; Yue et al., 2017; Brandenburg et al., 2018). There is evidence of dense and well-developed TATs in both small and large animals (Kirk et al., 2003; Glukhov et al., 2015; Yue et al., 2017; Brandenburg et al., 2018). In addition, studies have shown the existence of an atrial t-tubule system in larger mammals, such as sheep and humans (Richards et al., 2011; Trafford et al., 2013). As in the ventricles, which have a vast t-tubular system, Ca^{2+} release in atrial cells occurs simultaneously in both the central and peripheral areas of the cells. A highly efficient energy supply-and-demand matching process is essential to coordinate atrial mechano-metabolic feedback cues during permanent changes in cardiac workload. In response to an increase in electrical stimulation, frequency, or Ca^{2+} transient amplitude, Ca^{2+} accumulates in the atrial mitochondria and then activates enzymes participating in ATP production (Harada et al., 2017). It is not known whether cAMP/PKA and CaMKII signaling regulate ATP production in atrial cells, as has been seen in pacemaker cells.

In summary, cAMP and PKA signaling, together with SR and mitochondrial Ca^{2+}, are important regulators of mechano-electrical, mechano-Ca^{2+}, and mechano-metabolic feedback loops (**Figure 1**). Thus, physiologically relevant measurements of these signals are necessary to gain a comprehensive understanding of their underlying mechanisms and role. As described above, such measurements are usually conducted on cultured atrial or pacemaker cells that are placed in a sustainable culture medium for a period of at least 24–48 h.

PREVIOUS CULTURE METHODS OF PACEMAKER CELLS

Only a small number of labs have successfully established physiologically relevant methods for pacemaker cell culture. The first reported method utilized rabbit pacemaker cells (Liu et al., 1996), and while it shed light on the ionic current characteristics, it compromised several ionic channels and decreased the spontaneous beating rate. A later study from the same group demonstrated stable electrical activity in cultured rabbit pacemaker cells, but also showed a reduction in ionic currents (Muramatsu et al., 1996) in comparison to fresh cells. By modifying the culture method, Yang et al. (2012) caused pacemaker cells to generate spontaneous AP firing and rhythmical beating. However, the beating rate and the PKA-dependent phosphorylation level of PLB at site Ser^{16} and RyR2 at site Ser^{2809} were reduced in comparison to fresh cells. In addition, decreased levels of type 2 regulator of G-protein signaling (RGS2) and consequently dampened AC-cAMP/PKA signaling, were observed in comparison to fresh cells.

PREVIOUS CULTURE METHODS OF ATRIAL CELLS

Several studies have previously been conducted to characterize intrinsic atrial mechanisms (excluding heart-brain signaling) under culture conditions. In the first study, rabbit atrial cells remained viable in culture for up to 5 days (Gilliam et al., 1989). Yet cell morphology was not maintained; cells transformed from a rod-like to a spherical shape. Two additional studies (Wang et al., 1999; Rinne et al., 2010) also preserved rabbit atrial cell viability in culture for up to 48 h and showed cell stability following adenoviral infection. However, neither group was able to stimulate the cells at a rate above 0.5 Hz, a rate very far from the natural rabbit pacemaker cell beating rate of ∼3 Hz. In two additional studies on rabbit atrial cells (Hohendanner et al., 2015a,b), the researchers achieved similar results. Culture of atrial cells derived from other mammals has also been achieved. In one of the studies, rat atrial cells maintained a spindle-like morphology for a period of 3–7 days (Doupnik et al., 2001). In addition, expression of the acetylcholine-elicited inwardly rectifying potassium current ($I_{K,Ach}$) proteins was consistent with data collected from similar cells. However, functional data of the cultured cells were not shown. Finally, human atrial cells in culture (Feng et al., 1996) survived for up to 5 days, but, within 24 h, the cells assumed an oval-like shape. The voltage dependence, kinetics, and density of the sodium current were maintained in culture compared to control. While the activation properties (kinetics and voltage dependence) of the potassium transient outward current were not altered, steady potassium outward current density (current normalized to cell capacitance) was reduced in cultured compared to fresh cells. All changes in ionic currents occurred within 24 h of culture and were not altered for 4 days.

ELIMINATING MECHANO-ASSOCIATED FEEDBACK DURING CULTURE PRESERVES VENTRICULAR CELL FUNCTION IN CULTURE

Soeno et al. (1999) suggested that because the myosin-actin interaction is important for the initial phase of myofibrillogenesis, eliminating this interaction may improve the quality of the culture methods. Indeed, upon inhibition of this interaction in primary skeletal muscle cultures by application of 2,3-butanedione-monoxime (BDM), an inhibitor of myosin ATPase, culture profiles improved, as manifested by maintained cell viability and morphology. Similarly, Kivistö et al. (1995) found that BDM-treated rat ventricular myocytes maintained their shape and AP parameters and showed increased survival rates. Later, Hall et al. (Hall and Hausenloy, 2016) showed that addition of BDM to cultured mouse ventricular myocytes also reduced the number of spontaneous contractions per minute, increased survival rates, and reduced oxygen consumption. When supplementing mouse ventricular cell cultures with BDM, Ackers-Johnson et al. (2016) noted that cells survived in culture for a period of up to 7 days and retained their morphology, functionality, and Ca^{2+} handling, with optimal results observed after 2–3 days of culture. BDM has been shown to reduce the attachment of ATP to myosin, thereby reducing energy consumption in the cell (Ostap, 2002) and preserving the cellular phosphorylation status (Segal et al., 2019). Taken together, elimination of mechano-associated feedback mechanisms, specifically energetics and other phosphorylation-dependent loops, preserves cell function in culture.

Studies have indicated that BDM is a largely non-specific agent (Ostap, 2002), with effects on L-type Ca^{2+} channel conductance (Gwathmey et al., 1991) and on $I_{K,s}$ maximal conductance (Coulombe et al., 1990), and is associated with increased phosphatase activity (K_{pp1}) (Stapleton et al., 1998), and Ca^{2+} releases through RyR2 (Gwathmey et al., 1991). Due to the side effects of BDM, Kabaeva et al. (2008) sought to test other substances that eliminate mechano-associated feedbacks. Upon application of blebbistatin, to eliminate myofilament contraction in mouse ventricular myocytes during culture, the viability, membrane integrity, and morphology of ventricular myocytes were significantly increased as compared to cultures treated with BDM. Most importantly, the use of blebbistatin improved the efficiency of adenovirus-mediated gene transfer in the cultured myocytes compared to BDM (Kabaeva et al., 2008). Based on this study, use of blebbistatin to eliminate mechano-feedback has significant beneficial effects on the long-term usability of adult myocytes in primary culture, as it reduces ATP production (Kovács et al., 2004; Watanabe et al., 2010) and maintains a stable phosphorylation state in the cultured cardiomyocytes (Reddy et al., 2018; Segal et al., 2019) while avoiding the undesirable effects of BDM on adult myocytes.

ELIMINATING MECHANO-ASSOCIATED FEEDBACKS PRESERVES CULTURED PACEMAKER CELL FUNCTION

The first attempt to eliminate mechano-feedback during culture of mouse pacemaker cells (St. Clair et al., 2015) used BDM, which yielded viable and spontaneously beating pacemaker cells within 48 h. In addition, cell morphology, AP firing rate, and two tested ionic current properties were preserved. Moreover, the group successfully genetically manipulated the cells in culture, thereby expanding the range of experimental techniques available for studying the physiological and functional properties of pacemaker cells. However, these experiments were performed on mouse pacemaker cells, which are inferior to rabbit pacemaker cells, which exhibit Ca^{2+} cycling similar to that of human cells. Further, Ca^{2+} cycling and phosphorylation activity were not measured, and thus, it remains unknown whether they are maintained in culture and whether the electro-Ca^{2+} feedback is maintained. Finally, no mechanistic explanation was provided regarding the observed effects of BDM on pacemaker cells. A recent study was designed to address these open questions (Segal et al., 2019) and to characterize the electro-Ca^{2+} feedback. The study compared the effect of blebbistatin and BDM on rabbit pacemaker cells in culture and sought to uncover the mechanisms underlying improved cultured pacemaker cell function upon elimination of mechano-associated feedback. BDM and blebbistatin treatment had identical effects on cell morphology (shape and area) (**Figure 2A**), and PLB and RyR2 densities and their phosphorylation levels, as well as on adenoviral transfection efficiency (**Figures 2B,C**). Blebbistatin-supplemented pacemaker cell cultures maintained their AP firing rate and global and local Ca^{2+} properties over 48 h (**Figure 2D**). In contrast, BDM suppressed these properties. Thus, to explore electro-Ca^{2+} feedback in cultured pacemaker cell, blebbistatin should be preferred over BDM. By using tetramethylrhodamine (TMRM) intensity per cell as an indicator of mitochondrial density, the group demonstrated that the addition of either mechanical feedback inhibitor preserved the mitochondrial

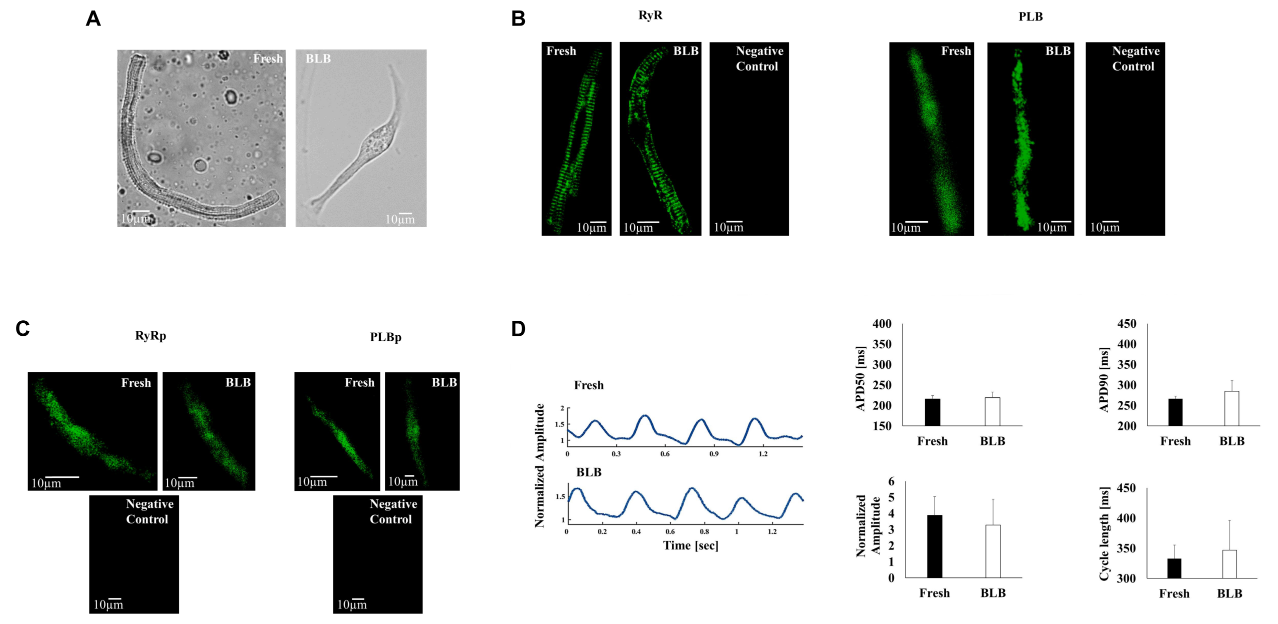

FIGURE 2 | Pacemaker cell culture. **(A)** Representative examples of fresh and cultured pacemaker cells. **(B)** Representative examples of ryanodine receptor and PLB immunolabeling in fresh and cultured pacemaker cells (No first antibody was added to the negative control). **(C)** Representative examples of the phosphorylation status immunolabeling of the ryanodine receptors and SERCA in fresh and cultured pacemaker cells. **(D)** Representative examples of action potential in fresh and cultured pacemaker cells and average data for action potential characteristics (APD50, APD90, normalized amplitude, and cycle length). Data are from Segal et al. (2019). Animals were treated in accordance with the Technion Ethics Committee. The experimental protocols were approved by the Animal Care and Use Committee of Technion (Ethics number: IL-118-10-13).

density. Yet, as mitochondrial function was not assessed, it is not clear if this culture medium is appropriate for functional mechano-metabolic studies. Using a computational model, the researchers showed that reduced cellular energy consumption following the addition of a contraction inhibitor, together with the maintenance of phosphorylation activity, allowed for the preservation of cell characteristics and function under culture conditions. Moreover, the model showed that the decreased spontaneous AP firing rate was due to non-specific BDM side effects, which involved an indirect decrease in I_{NCX} and a direct decrease in the L-type Ca^{2+} currents. The model further confirmed that blebbistatin is superior to BDM in contraction elimination in culture and is a more optimal substance for preserving mechano-Ca^{2+} feedback. The question was raised of how BDM and blebbistatin preserved the electro-Ca^{2+} feedback in cultured pacemaker cell. The authors found that by eliminating contraction, phosphorylation activity is preserved and energy is reduced. Because PKA (Yaniv et al., 2015a; Behar et al., 2016) and CaMKII (Yaniv et al., 2013a) activities correlate with AP firing rates and affect electro-Ca^{2+} feedback, maintaining these signalings is essential for pacemaker function. In previous works, it was shown that Ca^{2+} and posttranslational modification signaling are the major mechanisms that maintain ATP supply to demand in pacemaker cells (Yaniv et al., 2011, 2013a,b). Thus, a reduction in these signaling cascades during culture may limit the ATP supply, consequently reducing the spontaneous beating rate.

A similar approach using BDM was applied for culturing human SAN and atrial tissue cardiac slices (Kang et al., 2016). The cardiac slice exhibited physiological automaticity similar to that of a normal human heart rate. Moreover, AP duration and Ca^{2+} transient regions were maintained in these cardiac slices. Importantly, these cardiac slices have the potential to be transfected with an adenovirus and express exogenous protein for a period of up 96 h.

ELIMINATION OF MECHANO-ASSOCIATED FEEDBACKS DURING CULTURE PRESERVES CULTURED ATRIAL CELL FUNCTION

The first attempt to eliminate mechano-feedbacks in cultured atrial cells was documented in Kirschner-Peretz et al. (2017). Their work tested the effect of BDM on the biophysical, functional, and bioenergetic characteristics of cultured rabbit atrial cells. After 24 h in culture, their morphology and volume were similar to those of freshly isolated cells (**Figure 3A**). In the absence of BDM, the cultured atrial cells failed to maintain their morphology in comparison to fresh cells and could not be electrically paced at any stimulation rate. Importantly, the cells were successfully infected by an adenovirus by using exogenous proteins. Moreover, the mechano-Ca^{2+} feedback was sustained, with Ca^{2+} transients and local Ca^{2+} releases and intact RyR2 and SERCA structures similar to those of fresh cells (**Figure 3B**). In addition, assessment of the electro-metabolic feedback indicated that the energetic state of the cells remained constant in response to external electrical pacing at a physiological rate, a response similar to that of freshly isolated cells (**Figure 3C**). Finally, mitochondrial density, measured by TMRM average intensity, was unaffected by the inhibitor. Regarding the mechano-electrical feedback, the ability to undergo external electrical stimulation at frequencies of 1–3 Hz was maintained in the cultured cells; AP parameters were similar between fresh and cultured cells (**Figure 3D**), as was t-tubule density. Note that the authors

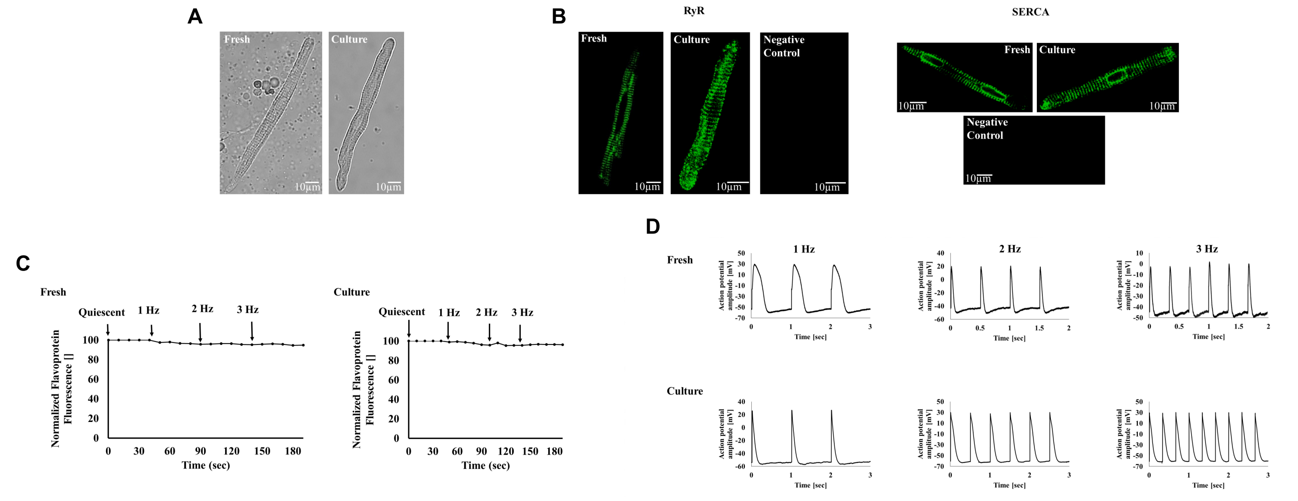

FIGURE 3 | Atrial cell culture. **(A)** Representative examples of fresh and cultured atrial cells. **(B)** Ryanodine and SERCA immunolabeling for fresh and cultured atrial cells' structures. **(C)** Representative examples of fresh and cultured atrial cell flavoprotein auto-fluorescence in response to increasing electrical stimulation (1–3 Hz). **(D)** Representative examples of fresh and cultured AP in atrial cells at 1–3 Hz of external electrical stimulation. Data from Kirschner-Peretz et al. (2017). Animals were treated in accordance with the Technion Ethics Committee. The experimental protocols were approved by the Animal Care and Use Committee of Technion (Ethics number: IL-118-10-13). **(C)** is reproduced from Kirschner-Peretz et al. (2017) with permission.

tested the effect of BDM only. While electrical-Ca^{2+} and electrical-energetic feedbacks circuits were maintained over 24 h in culture, for longer culture periods, blebbistatin may prove superior to BDM. Taken together, the elimination of electro-mechanical feedback enables cultured atrial cells to maintain physiological electrical activity and, thus, electrical-Ca^{2+} and electrical-energetic feedback mechanisms.

Summary

Optimized culture media are the key to the exploration of physiological electrical-Ca^{2+} and electrical-metabolic feedback mechanisms. Eliminating contraction during culture is critical for measuring mechano-electric, mechano-Ca^{2+}, and mechano-metabolic feedbacks. Appropriate culture methods provide an important platform for further understanding energetic, biochemical, and electrical regulatory feedbacks in healthy pacemaker and atrial cells, which could potentially provide insights into their relations to the development and maintenance of cardiac diseases involving atrial and pacemaker dysfunction.

AUTHOR CONTRIBUTIONS

All authors listed have made a substantial, direct and intellectual contribution to the work, and approved it for publication.

FUNDING

This work was supported by the Israel Science Foundation, No. 330/19 to YY. The funders had no role in study design, data collection and analysis, decision to publish, or preparation of the manuscript.

REFERENCES

Ackers-Johnson, M., Li, P. Y., Holmes, A. P., O'Brien, S. M., Pavlovic, D., and Foo, R. S. (2016). A simplified, Langendorff-free method for concomitant isolation of viable cardiac myocytes and nonmyocytes from the adult mouse heart. *Circ. Res.* 119, 909–920. doi: 10.1161/CIRCRESAHA.116.309202

Andersen, M. J., Olson, T. P., Melenovsky, V., Kane, G. C., and Borlaug, B. A. (2015). Differential hemodynamic effects of exercise and volume expansion in people with and without heart failure. *Circulation* 8, 41–48. doi: 10.1161/CIRCHEARTFAILURE.114.001731

Behar, J., Ganesan, A., Zhang, J., and Yaniv, Y. (2016). The autonomic nervous system regulates the heart rate through cAMP-PKA dependent and independent coupled-clock pacemaker cell mechanisms. *Front. Physiol.* 7:419. doi: 10.3389/fphys.2016.00419

Bers, D. M. (2008). Calcium cycling and signaling in cardiac myocytes. *Annu. Rev. Physiol.* 70, 23–49. doi: 10.1146/annurev.physiol.70.113006.100455

Bogdanov, K. Y., Vinogradova, T. M., and Lakatta, E. G. (2001). Sinoatrial nodal cell ryanodine receptor and Na+-Ca2+ exchanger: molecular partners in peacemaker regulation. *Circ. Res.* 88, 1254–1258. doi: 10.1161/hh1201.092095

Bootman, M. D., Higazi, D. R., Coombes, S., and Roderick, H. L. (2006). Calcium signalling during excitation-contraction coupling in mammalian atrial myocytes. *J. Cell Sci.* 119, 3915–3925. doi: 10.1242/jcs.03223

Brandenburg, S., Pawlowitz, J., Fakuade, F. E., Kownatzki-Danger, D., Kohl, T., Mitronova, G. Y., et al. (2018). Axial tubule junctions activate atrial Ca2+ release across species. *Front. Physiol.* 9:1227. doi: 10.3389/fphys.2018.01227

Braunwald, E. (1971). Mechanics and energetics of the normal and failing heart. *Trans. Assoc. Am. Phys.* 84, 63–94.

Collins, T. P., and Terrar, D. A. (2012). Ca2+-stimulated adenylyl cyclases regulate the L-type Ca2+ current in guinea-pig atrial myocytes. *J. Physiol.* 590, 1881–1893. doi: 10.1113/jphysiol.2011.227066

Coulombe, A., Lefevre, I. A., Deroubaix, E., Thuringer, D., and Coraboeuf, E. (1990). Effect of 2,3-butanedione 2-monoxime on slow inward and transient outward currents in rat ventricular myocytes. *J. Mol. Cell. Cardiol.* 22, 921–932. doi: 10.1016/0022-2828(90)90123-J

DiFrancesco, D., and Ojeda, C. (1980). Properties of the current If in the sinoatrial node of the rabbit compared with those of the current Ik in Purkinje fibres. *J. Physiol.* 308, 353–367. doi: 10.1113/jphysiol.1980.sp013475

Doupnik, C. A., Xu, T., and Shinaman, J. M. (2001). Profile of RGS expression in single rat atrial myocytes. *Biochim. Biophys. Acta Gene Struct. Exp.* 1522, 97–107. doi: 10.1016/S0167-4781(01)00342-6

Feng, J., Li, G. R., Fermini, B., and Nattel, S. (1996). Properties of sodium and potassium currents of cultured adult human atrial myocytes. *Am. J. Physiol. Heart Circ. Physiol.* 270, H1676–H1686. doi: 10.1152/ajpheart.1996.270.5.h1676

Freeman, L. C., Kwok, W. M., and Kass, R. S. (1992). Phosphorylation-independent regulation of cardiac Ik by guanine nucleotides and isoproterenol. *Am. J. Physiol. Heart Circ. Physiol.* 262, H1298–H1302. doi: 10.1152/ajpheart.1992.262.4.h1298

Gilliam, F. R., Starmer, C. F., and Grant, A. O. (1989). Blockade of rabbit atrial sodium channels by lidocaine: characterization of continuous and frequency-dependent blocking. *Cir. Res.* 65, 723–739. doi: 10.1161/01.RES.65.3.723

Glukhov, A. V., Balycheva, M., Sanchez-Alonso, J. L., Ilkan, Z., Alvarez-Laviada, A., Bhogal, N., et al. (2015). Direct evidence for microdomain-specific localization and remodeling of functional L-type calcium channels in rat and human atrial myocytes. *Circulation* 132, 2372–2384. doi: 10.1161/CIRCULATIONAHA.115.018131

Gwathmey, J. K., Hajjar, R. J., and Solaro, R. J. (1991). Contractile deactivation and uncoupling of crossbridges. Effects of 2,3-butanedione monoxime on mammalian myocardium. *Circ. Res.* 69, 1280–1292. doi: 10.1161/01.RES.69.5.1280

Hall, A. R., and Hausenloy, D. J. (2016). Mitochondrial respiratory inhibition by 2,3-butanedione monoxime (BDM): implications for culturing isolated mouse ventricular cardiomyocytes. *Physiol. Rep.* 4:e12606. doi: 10.14814/phy2.12606

Harada, M., Melka, J., Sobue, Y., and Nattel, S. (2017). Metabolic considerations in atrial fibrillation — Mechanistic insights and therapeutic opportunities. *Circ. J.* 81, 1749–1757. doi: 10.1253/circj.CJ-17-1058

Hohendanner, F., Maxwell, J. T., and Blatter, L. A. (2015a). Cytosolic and nuclear calcium signaling in atrial myocytes: IP3-mediated calcium release and the role of mitochondria. *Channels* 9, 129–138. doi: 10.1080/19336950.2015.1040966

Hohendanner, F., Walther, S., Maxwell, J. T., Kettlewell, S., Awad, S., Smith, G. L., et al. (2015b). Inositol-1,4,5-trisphosphate induced Ca2+ release and excitation-contraction coupling in atrial myocytes from normal and failing hearts. *J. Physiol.* 593, 1459–1477. doi: 10.1113/jphysiol.2014.283226

Hong, T. T., and Shaw, R. M. (2017). Cardiac t-tubule microanatomy and function. *Physiol. Revi.* 97, 227–252. doi: 10.1152/physrev.00037.2015

Hund, T. J., and Mohlerp, P. J. (2016). Atrial-specific pathways for control of intracellular signaling and myocyte function. *J. Clin.Investig.* 126, 3731–3734. doi: 10.1172/JCI90348

Kabaeva, Z., Zhao, M., and Michele, D. E. (2008). Blebbistatin extends culture life of adult mouse cardiac myocytes and allows efficient and stable transgene expression. *Am. J. Physiol. Heart Circ .Physiol.* 294, H1667–H1674. doi: 10.1152/ajpheart.01144.2007

Kamiyama, A., Niimura, I., and Sugi, H. (1984). Length-dependent changes of pacemaker frequency in the isolated rabbit sinoatrial node. *Jap. J. Physiol.* 34, 153–165. doi: 10.2170/jjphysiol.34.153

Kamoun, D., Behar, J., Leichner, J. M., and Yaniv, Y. (2018). Bioenergetic feedback between heart cell contractile machinery and mitochondrial 3D deformations. *Biophys. J.* 115, 1603–1613. doi: 10.1016/j.bpj.2018.08.039

Kang, C., Qiao, Y., Li, G., Baechle, K., Camelliti, P., Rentschler, S., et al. (2016). Human organotypic cultured cardiac slices: new platform for high throughput preclinical human trials. *Sci. Rep.* 6:28798. doi: 10.1038/srep28798

Kioka, H., Kato, H., Fujikawa, M., Tsukamoto, O., Suzuki, T., Imamura, H., et al. (2014). Evaluation of intramitochondrial ATP levels identifies G0/G1 switch gene 2 as a positive regulator of oxidative phosphorylation. *Proc Natl. Acad. Sci. U.S.A.* 111, 273–278. doi: 10.1073/pnas.1318547111

Kirk, M. M., Izu, L. T., Chen-Izu, Y., McCulle, S. L., Wier, W. G., Balke, C. W., et al. (2003). Role of the transverse-axial tubule system in generating calcium sparks and calcium transients in rat atrial myocytes. *J. Physiol.* 547(Pt 2), 441–451. doi: 10.1113/jphysiol.2002.034355

Kirschner-Peretz, N., Segal, S., Arbel-Ganon, L., Jehuda, R., Ben Shemer, Y., Eisen, B., et al. (2017). A method sustaining the bioelectric, biophysical, and bioenergetic function of cultured rabbit atrial cells. *Front. Physiol.* 8:584. doi: 10.3389/fphys.2017.00584

Kivistö, T., Mäkiranta, M., Oikarinen, E. L., Sellin, L. C., Karhu, S., and Weckström, M. (1995). 2,3-Butanedione Monoxime (BDM) increases initial yields and improves long-term survival of isolated cardiac myocytes. *Jap. J. Physiol.* 45, 203–210. doi: 10.2170/jjphysiol.45.203

Kohl, P., Hunter, P., and Noble, D. (1999). Stretch-induced changes in heart rate and rhythm: clinical observations, experiments and mathematical models. *Prog. Biophys. Mol. Biol.* 71, 91–138. doi: 10.1016/S0079-6107(98)00038-8

Kovács, M., Tóth, J., Hetényi, C., Málnási-Csizmadia, A., and Seller, J. R. (2004). Mechanism of blebbistatin inhibition of myosin II. *J. Biol. Chem.* 279, 35557–35563. doi: 10.1074/jbc.M405319200

Lakatta, E. G., Maltsev, V. A., and Vinogradova, T. M. (2010). A coupled system of intracellular Ca2+ clocks and surface membrane voltage clocks controls the timekeeping mechanism of the heart's pacemaker. *Circ. Res.* 106, 659–673. doi: 10.1161/CIRCRESAHA.109.206078

Lange, G., Lu, H. H., Chang, A., and Brooks, C. M. (1966). Effect of stretch on the isolated cat sinoatrial node. *Am. J. Physiol.* 211, 1192–1196. doi: 10.1152/ajplegacy.1966.211.5.1192

Li, K. L., Ghashghaee, N. B., Solaro, R. J., and Dong, W. (2016). Sarcomere length dependent effects on the interaction between cTnC and cTnI in skinned papillary muscle strips. *Arch. Biochem. Biophys.* 601, 69–79. doi: 10.1016/j.abb.2016.02.030

Liu, Z., Zou, A. R., Demir, S. S., Clark, J. W., and Nathan, R. D. (1996). Characterization of a hyperpolarization-activated inward current in cultured pacemaker cells from the sinoatrial node. *J. Mol. Cell. Cardiol.* 28, 2523–2535. doi: 10.1006/jmcc.1996.0244

Lu, X., Ginsburg, K. S., Kettlewell, S., Bossuyt, J., Smith, G. L., and Bers, D. M. (2013). Measuring local gradients of intra mitochondrial Ca2+ in cardiac myocytes during sarcoplasmic reticulum Ca2+ release. *Circ. Res.* 112, 424–431. doi: 10.1161/CIRCRESAHA.111.300501

Lyashkov, A. E., Beahr, J., Lakatta, E. G., Yaniv, Y., and Maltsev, V. A. (2018). Positive feedback mechanisms among local Ca Releases, NCX, and ICaL ignite pacemaker action potentials. *Biophys. J.* 114, 1176–1189. doi: 10.1016/j.bpj.2017.12.043

Maack, C., and O'Rourke, B. (2007). Excitation-contraction coupling and mitochondrial energetics. *Basic Res. Cardiol.* 102, 369–392. doi: 10.1007/s00395-007-0666-z

Monfredi, O., Dobrzynski, H., Mondal, T., Boyett, M. R., and Morris, G. M. (2010). The anatomy and physiology of the sinoatrial node-A contemporary review. *Pacing Clin. Electrophysiol.* 33, 1392–1406. doi: 10.1111/j.1540-8159.2010.02838.x

Muramatsu, H., Zou, A. R., Berkowitz, G. A., and Nathan, R. D. (1996). Characterization of a TTX-sensitive Na+ current in pacemaker cells isolated from rabbit sinoatrial node. *Am. J. Physiol.* 270(6 Pt 2), H2108–H2119.

Musheshe, N., Lobo, M. J., Schmidt, M., and Zaccolo, M. (2018). Targeting fret-based reporters for cAMP and PKA activity using AKAP79. *Sensors* 18:2164. doi: 10.3390/s18072164

Ostap, E. M. (2002). 2,3-Butanedione monoxime (BDM) as a myosin inhibitor. *J. Muscle Res. Cell Motil.* 23, 305–308. doi: 10.1023/A:1022047102064

Paul, T., Ziemer, G., Luhmer, L., Bertram, H., Hecker, H., and Kallfelz, H. C. (1998). Early and late atrial dysrhythmias after modified Fontan operation. *Pediatr. Medi.* 20, 9–11.

Quinn, T. A. (2014). The importance of non-uniformities in mechano-electric coupling for ventricular arrhythmias. *J. Int. Cardiac Electrophysio.* 39, 25–35. doi: 10.1007/s10840-013-9852-0

Reddy, G. R., West, T. M., Jian, Z., Jaradeh, M., Shi, Q., Wang, Y., et al. (2018). Illuminating cell signaling with genetically encoded FRET biosensors in adult mouse cardiomyocytes. *J. Gen. Physiol.* 150, 1567–1582. doi: 10.1085/jgp.201812119

Richards, M. A., Clarke, J. D., Saravanan, P., Voigt, N., Dobrev, D., Eisner, D. A., et al. (2011). Transverse tubules are a common feature in large mammalian atrial myocytes including human. *Am.J. Physiol. Heart Circ. Physiol.* 301, H1996–H2005. doi: 10.1152/ajpheart.00284.2011

Rinne, A., Kapur, N., Molkentin, J. D., Pogwizd, S. M., Bers, D. M., Banach, K., et al. (2010). Isoform- and tissue-specific regulation of the Ca2+-sensitive transcription factor NFAT in cardiac myocytes and heart failure. *Am. J. Physiol. Heart Circ. Physiol.* 298, 2001–2009. doi: 10.1152/ajpheart.01072.2009

Segal, S., Kirschner Peretz, N., Arbel-Ganon, L., Liang, J., Li, L., Marbach, D., et al. (2019). Eliminating contraction during culture maintains global and local Ca 2+ dynamics in cultured rabbit pacemaker cells. *Cell Calcium* 78, 35–47. doi: 10.1016/j.ceca.2018.12.008

Soeno, Y., Obinata, T., and Shimada, Y. (1999). BDM (2,3-butanedione monoxime), an inhibitor of myosin actin interaction, suppresses myofibrillogenesis in skeletal muscle cells in culture. *Cell Tissue Res.* 295, 307–316. doi: 10.1007/s004410051237

St. Clair, J. R., Sharpe, E. J., and Proenza, C. (2015). Culture and adenoviral infection of sinoatrial node myocytes from adult mice. *Am. J. Physiol. Heart Circ. Physiol.* 309, H490–H498. doi: 10.1152/ajpheart.00068.2015

Stapleton, M. T., Fuchsbauer, C. M., and Allshire, A. P. (1998). BDM drives protein dephosphorylation and inhibits adenine nucleotide exchange in cardiomyocytes. *Am. J. Physiol. Heart Circ. Physio.* 275, H1260–H1266. doi: 10.1152/ajpheart.1998.275.4.h1260

Takasago, T., Imagawa, T., and Shigekawa, M. (1989). Phosphorylation of the cardiac ryanodine receptor by cAMP-dependent protein kinase. *J. Biochem.* 106, 872–877. doi: 10.1093/oxfordjournals.jbchem.a122945

Toyofuku, T., Kurzydlowski, K., Tada, M., and MacLennan, D. H. (1993). Identification of regions in the Ca(2+)-ATPase of sarcoplasmic reticulum that affect functional association with phospholamban. *J. Biol. Chemi.* 268, 2809–2815.

Trafford, A. W., Clarke, J. D., Richards, M. A., Eisner, D. A., and Dibb, K. M. (2013). Calcium signalling microdomains and the t-tubular system in atrial mycoytes: potential roles in cardiac disease and arrhythmias. *Cardiovasc. Res.* 98, 192–203. doi: 10.1093/cvr/cvt018

Trautwein, W., and Hescheler, J. (1990). Regulation of cardiac L-Type calcium current by phosphorylation and G proteins. *Annu. Rev. Physiol.* 52, 257–274. doi: 10.1146/annurev.ph.52.030190.001353

Vinogradova, T. M., Bogdanov, K. Y., and Lakatta, E. G. (2002). β-adrenergic stimulation modulates ryanodine receptor Ca2+ release during diastolic depolarization to accelerate pacemaker activity in rabbit sinoatrial nodal cells. *Circ. Re.* 90, 73–79. doi: 10.1161/hh0102.102271

Wang, Z., Feng, J., Shi, H., Pond, A., Nerbonne, J. M., and Nattel, S. (1999). Potential molecular basis of different physiological properties of the transient outward K+ current in rabbit and human atrial myocytes. *Circ. Res.* 84, 551–561. doi: 10.1161/01.RES.84.5.551

Warrier, S., Belevych, A. E., Ruse, M., Eckert, R. L., Zaccolo, M., Pozzan, T., et al. (2005). β-adrenergic- and muscarinic receptor-induced changes in cAMP activity in adult cardiac myocytes detected with FRET-based biosensor. *Ame. J. Physiol. Cell Physiol.* 289, C455–C461. doi: 10.1152/ajpcell.00058.2005

Watanabe, M., Yumoto, M., Tanaka, H., Wang, H. H., Katayama, T., Yoshiyama, S., et al. (2010). Blebbistatin, a myosin II inhibitor, suppresses contraction and disrupts contractile filaments organization of skinned taenia cecum from guinea pig. *Am. J. Physiol. Cell Physiol.* 298, C1118–C1126. doi: 10.1152/ajpcell.00269.2009

Wu, Y., Rasmussen, T. P., Koval, O. M., Joiner, M. L. A., Hall, D. D., Chen, B., et al. (2015). The mitochondrial uniporter controls fight or flight heart rate increases. *Nat. Commun.* 6:6081. doi: 10.1038/ncomms7081

Yang, D., Lyashkov, A. E., Li, Y., Ziman, B. D., and Lakatta, E. G. (2012). RGS2 overexpression or Gi inhibition rescues the impaired PKA signaling and slow AP firing of cultured adult rabbit pacemaker cells. *J. Mol. Cell. Cardiol.* 53, 687–694. doi: 10.1016/j.yjmcc.2012.08.007

Yaniv, Y., Ganesan, A., Yang, D., Ziman, B. D., Lyashkov, A. E., Levchenko, A., et al. (2015a). Real-time relationship between PKA biochemical signal network dynamics and increased action potential firing rate in heart pacemaker cells. Kinetics of PKA activation in heart pacemaker cells. *J. Mol. Cell. Cardiol.* 86, 168–178. doi: 10.1016/j.yjmcc.2015.07.024

Yaniv, Y., Lakatta, E. G., and Maltsev, V. A. (2015b). From two competing oscillators to one coupled-clock pacemaker cell system. *Front, Physiol.* 6:28. doi: 10.3389/fphys.2015.00028

Yaniv, Y., Juhaszova, M., Lyashkov, A. E., Spurgeon, H. A., Sollott, S. J., and Lakatta, E. G. (2011). Ca2+-regulated-cAMP/PKA signaling in cardiac pacemaker cells links ATP supply to demand. *J. Mol. Cell.Cardiol.* 51, 740–748. doi: 10.1016/j.yjmcc.2011.07.018

Yaniv, Y., Spurgeon, H. A., Lyashkov, A. E., Yang, D., Ziman, B. D., Maltsev, V. A., et al. (2012). Crosstalk between mitochondrial and sarcoplasmic reticulum Ca2+ cycling modulates cardiac pacemaker cell automaticity. *PLoS One* 7:e37582. doi: 10.1371/journal.pone.0037582

Yaniv, Y., Spurgeon, H. A., Ziman, B. D., and Lakatta, E. G. (2013a). Ca2+/Calmodulin-Dependent Protein Kinase II (CaMKII) activity and sinoatrial nodal pacemaker cell energetics. *PLoS One* 8:e57079. doi: 10.1371/journal.pone.0057079

Yaniv, Y., Spurgeon, H. A., Ziman, B. D., Lyashkov, A. E., and Lakatta, E. G. (2013b). Mechanisms that match ATP supply to demand in cardiac pacemaker cells during high ATP demand. *Am. J. Physiol. Heart Circ. Physiol.* 304, H1428–H1438. doi: 10.1152/ajpheart.00969.2012

Yue, X., Zhang, R., Kim, B., Ma, A., Philipson, K. D., and Goldhaber, J. I. (2017). Heterogeneity of transverse-axial tubule system in mouse atria: remodeling in atrial-specific Na+-Ca2+ exchanger knockout mice. *J. Mol. Cell. Cardiol.* 108, 50–60. doi: 10.1016/j.yjmcc.2017.05.008

Conflict of Interest: The authors declare that the research was conducted in the absence of any commercial or financial relationships that could be construed as a potential conflict of interest.

frontiers
in Physiology

BRIEF RESEARCH REPORT
published: 26 March 2020
doi: 10.3389/fphys.2020.00237

Arrhythmogenic Interaction Between Sympathetic Tone and Mechanical Stretch in Rat Pulmonary Vein Myocardium

Yuriy V. Egorov[1], Leonid V. Rosenshtraukh[1] and Alexey V. Glukhov[2]*

[1] Laboratory of Heart Electrophysiology, Russian Cardiology Research Centre, Institute of Experimental Cardiology, Moscow, Russia, [2] Department of Medicine, School of Medicine and Public Health, University of Wisconsin–Madison, Madison, WI, United States

Rapid firing from pulmonary veins (PVs) frequently initiates atrial fibrillation, which is a common comorbidity associated with hypertension, heart failure, and valvular disease, i.e., conditions that pathologically increase cardiomyocyte stretch. Autonomic tone plays a crucial role in PV arrhythmogenesis, while its interplay with myocardium stretch remains uncertain. Two-microelectrode technique was used to characterize electrophysiological response of Wistar rat PV to adrenaline at baseline and under mild (150 mg of applied weight that corresponds to a pulmonary venous pressure of 1 mmHg) and moderate (10 g, ∼26 mmHg) stretch. Low concentrations of adrenaline (25–100 nmol/L) depolarized the resting membrane potential selectively within distal PV (by 26 ± 2 mV at baseline, by 18 ± 1 mV at 150 mg, $P < 0.001$, and by 5.9 ± 1.1 mV at 10 g, $P < 0.01$) suppressing action potential amplitude and resulting in intra-PV conduction dissociation and rare episodes of spontaneous activity (arrhythmia index of 0.4 ± 0.2, NS vs. no activity at baseline). In contrast, 1–10 μmol/L of adrenaline recovered intra-PV propagation. While mild stretch did not affect PV electrophysiology at baseline, moderate stretch depolarized the resting potential within distal PV (-56 ± 2 mV vs. -82 ± 1 mV at baseline, $P < 0.01$), facilitated the triggering of rapid PV firing by adrenaline (arrhythmia index: 4.4 ± 0.2 vs. 1.3 ± 0.4 in unstretched, $P < 0.001$, and 1.7 ± 0.8 in mildly stretched preparations, $P < 0.005$, at 10 μmol/L adrenaline) and induced frequent episodes of potentially arrhythmogenic atrial “echo” extra beats. Our findings demonstrate complex interactions between the sympathetic tone and mechanical stretch in the development of arrhythmogenic activity within PVs that may impact an increased atrial fibrillation vulnerability in patients with elevated blood pressure.

Keywords: pulmonary veins, stretch, arrhythmia, mechano-electrical response, adrenalin

OPEN ACCESS

Edited by:
Gentaro Iribe,
Asahikawa Medical University, Japan

Reviewed by:
Ian Findlay,
ERL7003 Laboratoire Signalisation et Transports Ioniques Membranaires (STIM), France
Tong Liu,
Tianjin Medical University, China

***Correspondence:**
Alexey V. Glukhov
aglukhov@medicine.wisc.edu

Specialty section:
This article was submitted to Cardiac Electrophysiology, a section of the journal Frontiers in Physiology

Received: *30 November 2019*
Accepted: *02 March 2020*
Published: *26 March 2020*

Citation:
Egorov YV, Rosenshtraukh LV and Glukhov AV (2020) Arrhythmogenic Interaction Between Sympathetic Tone and Mechanical Stretch in Rat Pulmonary Vein Myocardium. Front. Physiol. 11:237. doi: 10.3389/fphys.2020.00237

INTRODUCTION

Focal electrical activity from pulmonary veins (PVs) frequently initiates atrial fibrillation (Haissaguerre et al., 1998; Chen et al., 1999), which is a common comorbidity associated with hypertension, heart failure, and valvular disease (Schotten et al., 2011). These conditions cause hemodynamic atrial overload resulting in pathologically increased cardiomyocyte stretch and facilitates the arrhythmogenic activity from PVs (Tsao et al., 2001). In the setting of atrial dilatation, mechanoelectrical feedback has been linked to the development of ectopic beats that trigger atrial fibrillation. However, the precise mechanisms remain poorly understood.

We (Egorov et al., 2015, 2019) and others (Arora et al., 2003; Walters et al., 2014; Pasqualin et al., 2018) have demonstrated a significant electrophysiological heterogeneity of myocardial cells within PVs, which may form a functional substrate for focal activity and echo extra beats. This was linked to a distinct ionic channel and Ca^{2+}-handling gene repertoire in PVs that would underlie their distinct response to proarrhythmic stimuli. Our recent study revealed a tension-dependent stretch-induced depolarization of the resting membrane potential (RP) within the distal part of rat PV, which decreased action potential (AP) amplitude (APA) and triggered conduction discontinuities and both ectopic and reentrant activities within the vein (Egorov et al., 2019). One may suggest that such stretch-induced arrhythmogenesis would significantly interfere with autonomic tone that plays a crucial role in triggering rapid firing from PVs (Patterson et al., 2005; Doisne et al., 2009). It was shown that the differences in the RP and reaction to adrenergic stimulation between the PV and the left atrium leads to automatic electrical activity occurring specifically in PV (Doisne et al., 2009). Indeed, PV myocytes demonstrated a low density of the $K_{ir}2.x$ channels and the RP stabilizing inwardly rectifying current I_{K1} (Melnyk et al., 2005; Tsuneoka et al., 2017), increased resting Na^{+} permeability (Malecot et al., 2015), and enhanced chloride conductance (Okamoto et al., 2014).

In this study, we hypothesized that myocardial stretch would facilitate the development of arrhythmogenic ectopic activity induced by sympathetic stimulation in the PV. To test this, two-microelectrode technique was used to characterize a region-specific electrophysiological response of rat PV myocardium to low (25–100 nmol/L) and high (1–10 μmol/L) concentrations of adrenaline at baseline and under mild (150 mg of applied weight, which corresponds to a PV pressure of 1 mmHg) and moderate (10 g, ∼26 mmHg) stretch.

MATERIALS AND METHODS

Animals and Preparations

All methods and protocols used in these studies have been approved by the Animal Care and Use Committee of the Cardiology Research Center (Moscow, Russia) following the Guidelines for Care and Use of Laboratory Animals published by the National Institutes of Health (NIH) (publication no. 85-23, revised 1996). All animals used in this study received humane care in compliance with the Guide for the Care and Use of Laboratory Animals. Adult (8- to 12-month-old) Wistar rats ($n = 7$) of both sexes were used. Rats were anesthetized with urethane 2 g/kg with heparin (0.2 U), and the loss of pain reflex was evaluated to assure the appropriate level of anesthesia. The isolated PV preparation was performed as described previously (Egorov et al., 2015, 2019). Briefly, after mid-sternal incision, the heart with lungs was removed and placed in oxygenated (95% O_2, 5% CO_2) room-temperature Tyrode solution of the following composition (in mmol/L): 118 NaCl, 1.8 $CaCl_2$, 1.2 $MgCl_2$, 4.7 KCl, 1.2 NaH_2PO_4, 25 $NaHCO_3$, and 11 glucose (pH = 7.35 ± 0.05). The left atrium (LA) together with the LA appendage and PV region was dissected from the ventricles, right atrium, and interatrial septum. The preparation then was placed in a tissue bath (2.5 ml) and continuously superfused with oxygenated Tyrode's solution (18 ml/min) at 37 ± 0.5°C. Central PV was cleaned from fat and lung tissues, beside the LA, lanced and then positioned on a thin coat of silicon on the bottom of a tissue bath with the endocardial side facing upward. The pacing electrode was placed on the edge of the left atrial appendage. A small portion of the end—distal part of the PV was not cut open and was used to weave a silk suture (4—0) with a weight applied.

Microelectrode Recordings

Transmembrane potentials were simultaneously recorded from the endocardial surface of the distal (PV_{dis}) and the ostial (PV_{ost}) parts of the PV (Egorov et al., 2019) using two glass microelectrodes filled with 3.0 mmol/L KCl (tip resistance, ∼10–40 MΩ) and connected to high-input impedance amplifiers (WPI model KS-701, World Precision Instruments, New Haven, CT, United States). Microelectrodes were stably maintained within the tissue during all the measurements within each experimental condition (unstretched, 150 mg and stretch, 10 g; **Figure 1**). In some preparations, microelectrode stability was lost during 1-h stretch applications (i.e., between experimental conditions), and repenetration in nearby tissue was performed. Transmembrane potential signals were recorded, digitized (sampling rate of 5 kHz) using analog-digital converter (E-154, L-Card, Moscow, Russia), and then saved on a computer for offline analysis as described previously (Egorov et al., 2015). To characterize electrophysiological properties of the PV myocardium, RP and APA were measured during S1S1 = 300 ms pacing. The pacing current was at least 2× the pacing threshold.

Experimental Protocol

Experimental protocol is shown schematically in **Figure 1**. Measurements were performed 40–60 min after the isolation procedure. Three adrenaline concentrations (25–100 nmol/L, 1 and 10 μmol/L) were tested at baseline (no stretch applied), under mild stretch (150 mg of weight applied, which approximately corresponds to a physiological pulmonary venous pressure of 1 mmHg calculated as applied weight × gravity constant/cross-section area of the PV preparation) and under moderate stretch (10 g of applied weight corresponding approximately to 26 mmHg of pulmonary venous pressure) as described previously (Egorov et al., 2019). For each condition,

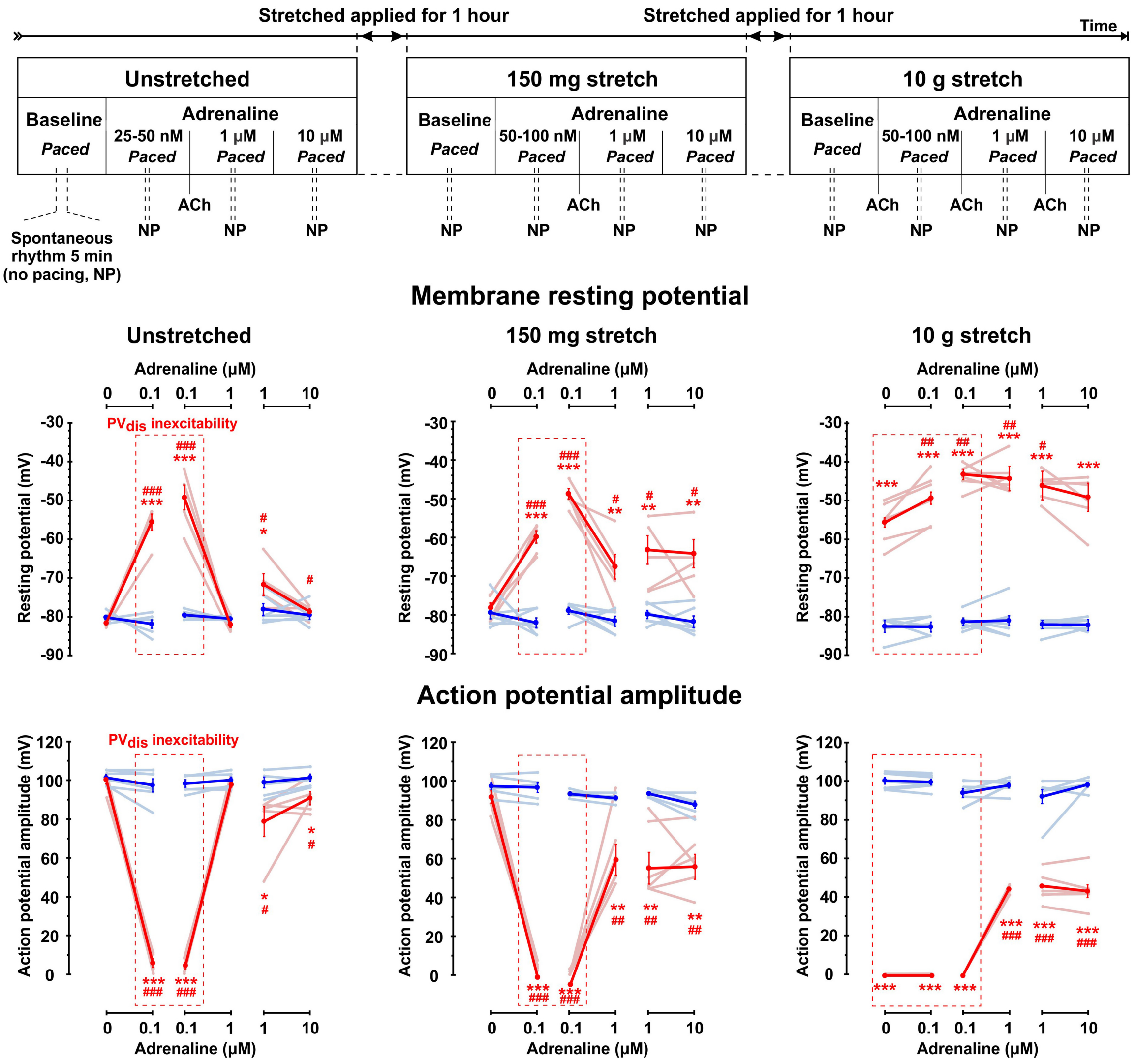

FIGURE 1 | Complex interactions between sympathetic tone and mechanical stretch in rat pulmonary vein (PV) myocardium. **Top:** Experimental protocol for testing different levels of sympathetic stimulation in unstretched and stretched PV preparations. Physiological status of PV$_{dis}$ inexcitability induced be either low concentrations of adrenaline (25–100 nmol/L), or pathological stretch (10.5 g) was tested by a brief application of acetylcholine (ACh), which was administered to hyperpolarize the RP and recover PV$_{dis}$ excitability and then washed out to continue experimental protocol. All measurements were performed during constant left atrial pacing, except brief (5–10 min) periods when pacing was stopped (no pacing, NP), and spontaneous rhythm was recorded if present. Below, changes in the resting membrane potential (middle panels) and action potential amplitude (low panels) are shown for distal (red traces) and ostium (blue traces) PV regions at baseline (no adrenaline applied) and under low (25–100 nmol/L) and high (1–10 µmol/L) concentrations of adrenaline measured in unstretched and stretched (150 mg and 10 g) preparations. Changes are shown for individual rats (light blue and light red lines) as well as mean ± SEM (solid lines). Red dashed box indicates the presence of PV$_{dis}$ inexcitability. $N = 6–7$ rats. $^{*}P < 0.05$, $^{**}P < 0.01$, $^{***}P < 0.001$ for PV$_{dis}$ vs. PV$_{ost}$; $^{\#}P < 0.05$, $^{\#\#}P < 0.01$, $^{\#\#\#}P < 0.001$ within the same group vs. baseline by repeated measurements two-way ANOVA with Bonferroni correction.

we first tested nanomolar concentrations of adrenaline (25–100 nmol/L) required to induce inexcitability within the PV$_{dis}$ (determined as a failure of excitation propagation from PV$_{ost}$ to PV$_{dis}$ under constant LA pacing and APA in PV$_{dis}$ < 20 mV, see **Figure 2A**). To test if PV$_{dis}$ inexcitability was associated with adrenaline-induced RP depolarization rather than microelectrode stability, 1 µmol/L acetylcholine was briefly applied to stimulate the acetylcholine-activated outward potassium current $I_{K,ACh}$, hyperpolarize the RP, and recover intra-PV conduction. After that, acetylcholine was washed out, and the next concentration of adrenaline was applied for 10 min. Preparations were constantly paced at stable S1S1 = 300 ms cycle length. To characterize spontaneous activity within the PV, electrical pacing was stopped for 5–10 min under each experimental condition. The protocol was repeated for 150 mg and 10 g of weight. Each weight was applied for an hour while adrenaline was washed out. The protocol was about 4–5 h long and applied to all the preparations tested. Importantly, in all experiments, PV preparations were functionally intact throughout the entire experiment as we demonstrated previously

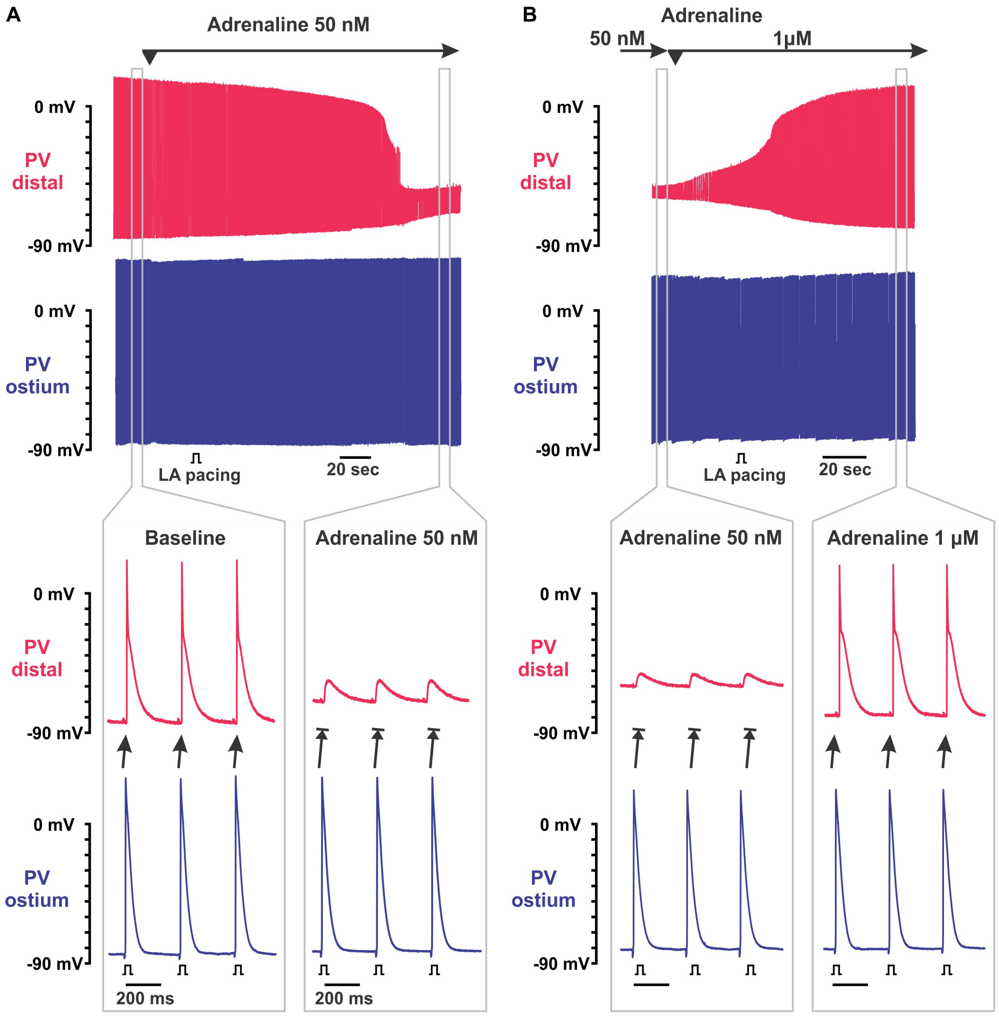

FIGURE 2 | Biphasic effect of adrenaline on intra-pulmonary vein (PV) conduction. **(A)** Application of 50 nmol/L adrenaline results in the depolarization of resting membrane potential (RP) exclusively in $\mathrm{PV}_{\mathrm{dis}}$ leading to intra-PV conduction dissociation. Two simultaneous microelectrode recordings from $\mathrm{PV}_{\mathrm{dis}}$ (top recording in red) and $\mathrm{PV}_{\mathrm{ost}}$ (bottom recording in blue) are shown. Below, selected time windows (gray rectangles) are shown enlarged before (baseline) and during $\mathrm{PV}_{\mathrm{dis}}$ inexcitability under 50 nmol/L adrenaline. Left atria (LA) was constantly paced with S1S1 = 300 ms. **(B)** Application of 1 μmol/L adrenaline recovered intra-PV conduction suppressed by 50 nmol/L adrenaline. Below, selected time windows (gray rectangles) are shown enlarged before and after the recovery of excitability of $\mathrm{PV}_{\mathrm{dis}}$.

(Egorov et al., 2019) and tested here by their response to regular applications of acetylcholine.

Arrhythmia score was defined according to a type of spontaneous electrical activity event as follows: 0, no spontaneous activity; 1, an irregular sporadic electrical activity; 2, irregular bursts of fast electrical activity; 3, irregular bursts of fast electrical activity that was suppressed by atrial pacing; 4, a stable, but slow PV rhythm that could not be suppressed by atrial pacing; and 5, a fast regular PV rhythm that could not be suppressed by atrial pacing and was complicated by echo extra beats.

Statistics

Student's *t*-test was used in two-group comparisons. Multiple groups of normally distributed data of similar variance were compared by one- or two-way ANOVA. For multiple comparisons, the Bonferroni's corrected *P* value is shown. All statistical analyses were performed using GraphPad Prism 5 or Origin version 6.1. A value of $P < 0.05$ was considered statistically significant. Values were presented as mean ± SEM.

RESULTS

Similar to what we have recently demonstrated (Egorov et al., 2019), mild stretch (150 mg) did not affect PV electrophysiology at baseline. Changes in RP, APA, and AP duration (APD) were not observed in both $\mathrm{PV}_{\mathrm{ost}}$ and $\mathrm{PV}_{\mathrm{dis}}$. In contrast, moderate (10 g) stretch significantly depolarized the RP specifically in $\mathrm{PV}_{\mathrm{dis}}$ (-56 ± 2 mV vs. -82 ± 1 mV at baseline, $P < 0.01$) suppressing APA and resulting in inexcitability of $\mathrm{PV}_{\mathrm{dis}}$ that was evident from

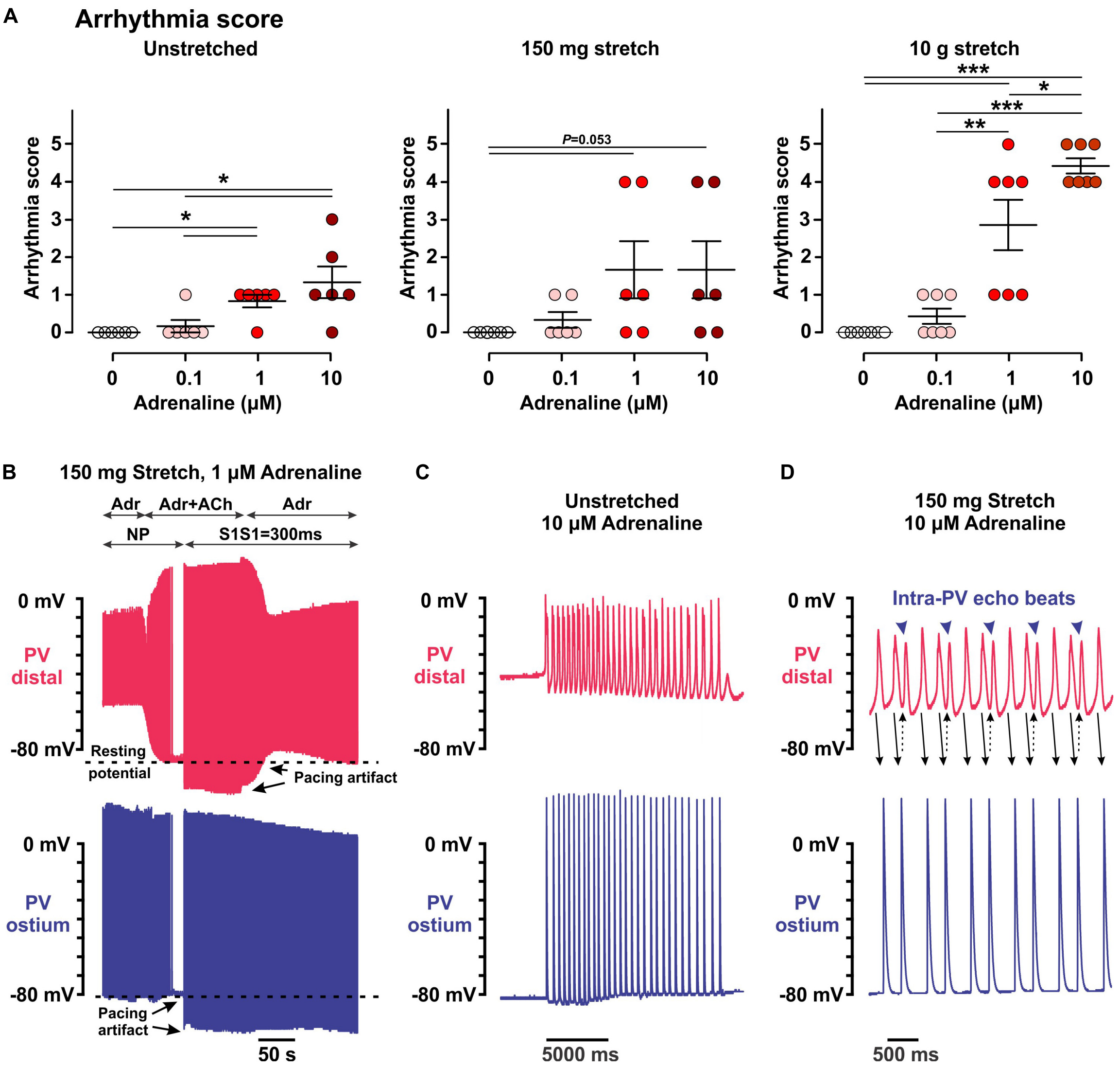

FIGURE 3 | Arrhythmic events induced within the pulmonary vein (PV) myocardium by low (25–100 nmol/L) and high (1–10 μmol/L) concentrations of adrenaline in unstretched and stretched (150 mg and 10.5 g) preparations. **(A)** Arrhythmia score calculated as described in the section "Materials and Methods." *N* = 6–7 rats. *P* values are calculated by repeated measurements two-way ANOVA with Bonferroni correction. **(B–D)** Representative examples of arrhythmic events recorded in PV preparations under different conditions. Two simultaneous microelectrode recordings from PV_{dis} (top recording in red) and PV_{ost} (bottom recording in blue) are shown for each event. **(B)** A brief application of 1 μmol/L acetylcholine (ACh) in 150 mg stretched preparation hyperpolarized the RP in PV_{dis} back to a baseline level and suppressed spontaneous PV activity (no pacing, NP) under 1 μmol/L adrenaline (Adr) application. After ACh washout, spontaneous slow PV rhythm (arrhythmia score is 3) was suppressed by atrial pacing (S1S1 = 300 ms). **(C,D)** Stable slow rhythm (arrhythmia score is 4, **C**) and fast regular rhythm (arrhythmia score is 5, **D**) induced by 10 μmol/L adrenaline in unstretched **(C)** and 150 mg stretched **(D)** PV preparations.

a failure of the propagation of excitation toward PV_{dis} (**Figure 1**). In PV_{ost}, neither RP or APA were changed at moderate stretch, while APD was significantly prolonged from 55 ± 2 ms to 84 ± 8 ms, respectively ($P < 0.01$).

Low concentrations of adrenaline (25–100 nmol/L) depolarized the RP selectively within PV_{dis} (by 26 ± 2 mV at baseline and 18 ± 1 mV at mild stretch, $P < 0.001$) and did not change the RP in PV_{ost} measured during a stable atrial stimulation of S1S1 = 300 ms (**Figure 1**). This subsequently suppressed an APA in PV_{dis} and resulted in the development of intra-PV conduction dissociation (**Figure 2A**). At moderate stretch, this further depolarized the RP in the setting of PV_{dis} inexcitability by 5.9 ± 1.1 mV at 10 g, $P < 0.01$. A brief application of acetylcholine hyperpolarized the RP back to baseline values and successfully recovered PV_{dis} excitability in all preparations (**Figure 3B**).

Subsequent application of 1 μmol/L adrenaline recovered PV_{dis} excitability and the intra-PV conduction in all the preparations tested (see representative example in **Figure 2B**). In unstretched and 150 mg stretched preparations, it was associated with significant RP hyperpolarization and recovery of the APA ($P < 0.01$) in PV_{dis}. In contrast, in 10 g stretched preparations,

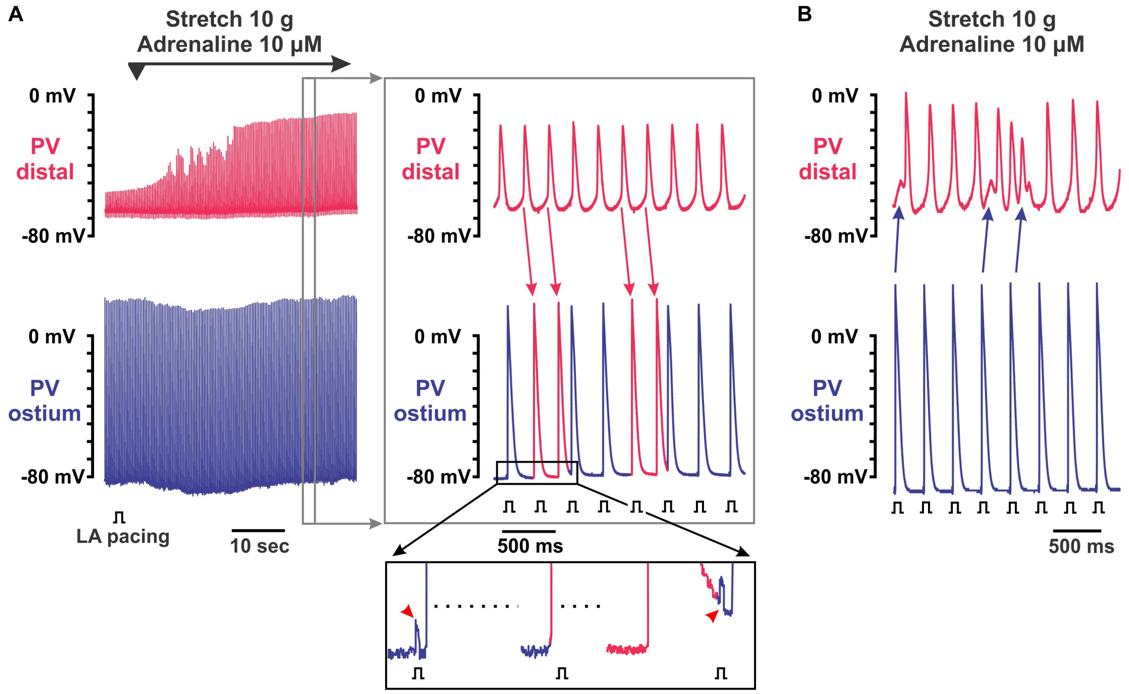

FIGURE 4 | Complex electrical activity recorded in pulmonary vein (PV) preparations under 10 μmol/L adrenaline applied during 10 g stretch. Two simultaneous microelectrode recordings from PV distal (top recording in red) and PV ostium (bottom recording in blue) are shown. **(A)** Recovery of intra-PV conduction with arrhythmogenic activity after application of 10 μmol/L adrenaline in 10 g stretched PV. Left panel shows a continuous 1-min recording of adrenaline application, while right panel represents an enlarged section of the left recording indicated by a gray rectangle. Spontaneous activity was induced in distal PV and not suppressed by left atrial (LA) pacing. Instead, a faster rhythm in distal PV interfered with a slower rate of electrical pacing resulting in frequent atrial extra beats (shown as red action potentials in PV ostium recordings; red arrows indicate propagating PV distal beats). **(B)** Burst of fast electrical activity triggered in distal PV by atrial extra beat interfered with intrinsic PV rhythm.

recovery of the intra-PV conduction was not associated with changes in the RP and only partial recovery of the APA in PV_{dis} (**Figure 1**). In PV_{ost}, neither RP or APA were changed under 1 and 10 μmol/L adrenaline in both mildly and moderately stretched preparations.

Although 25–100 nmol/L adrenaline could strongly depolarize the RP in PV_{dis}, this was not associated with the induction of automatic activity, both in unstretched and stretched preparations (arrhythmia index of 0.17 ± 0.17, $P = 0.340$ in unstretched preparations, 0.33 ± 0.21, $P = 0.145$, and 0.43 ± 0.20, $P = 0.055$, in 150 mg and 10 g stretched preparations, respectively; no spontaneous activity was observed without adrenaline; **Figure 3A**). This was opposite to higher concentrations of adrenaline (1–10 μmol/L), which evoked spontaneous activity in all preparations studied, with (unstretched and 150-mg stretched) and without (10-g stretched) concomitant hyperpolarization of the RP (**Figures 3C,D**). Moderate stretch significantly facilitated the triggering of rapid PV firing by adrenaline (arrhythmia index: 4.4 ± 0.2 vs. 1.3 ± 0.4 in unstretched, $P < 0.001$, and 1.7 ± 0.8 in mildly stretched preparations, $P < 0.005$, at 10 μmol/L adrenaline) and induced frequent episodes of intra-PV "echo" beats (**Figure 3D**) (Egorov et al., 2015; Bun et al., 2018).

Spontaneous activity induced by adrenaline in moderately stretched preparations were characterized by complex interactions between PV_{dis} and PV_{ost}. **Figure 4A** shows an example of the initiation of PV spontaneous activity by application of 10 μmol/L adrenaline in a 10-g stretched preparation that led to irregular atrial extra beats. This activity was not suppressed by LA pacing. Instead, a faster rhythm in PV_{dis} interfered with a slower rate of electrical pacing resulting in frequent atrial extra beats (shown in **Figure 4A** as red APs in PV_{ost} recordings). Atrial extra beats triggered from PV_{dis} had different morphology as shown in the enlarged insert below: while paced APs (blue in PV_{ost} recording) followed pacing artifact, triggered extra beats (red in PV_{ost} recording) were not synchronized with atrial pacing and not associated with pacing artifacts. Another example shown in **Figure 4B** demonstrates how atrial beats can initiate arrhythmogenic burst of fast electrical activity in PV_{dis}. Altogether, these findings show how spontaneous activity induced by sympathetic stimulation and facilitated by PV stretch can interfere with a stable atrial rhythm resulting in potentially arrhythmogenic atrial extra beats that can initiate atrial fibrillation.

DISCUSSION

Our findings demonstrate complex interactions between the sympathetic tone and mechanical stretch in the development of arrhythmogenic activity within PVs. First, we found a biphasic effect of adrenaline on PVs; while low concentrations of adrenaline (25–100 nmol/L) depolarized the RP and led to intra-PV conduction dissociation, high doses of adrenaline (1–10 μmol/L) led to RP hyperpolarization and the development of spontaneous electrical potentials within the PV. This biphasic effect of adrenaline could be linked to a dose-dependent activation of predominantly α- at low concentrations and both α- and β-adrenergic receptors at high concentrations (Furchgott, 1967). It was previously shown that stimulation of β-adrenergic receptors decreases the membrane stabilizing outward current I_{K1} (Braun et al., 1992) and enhances the volume-regulated inward chloride current $I_{Cl,swell}$ (Ellershaw et al., 2002) that, together, would lead the RP depolarization as observed here and previously by Doisne et al. (2009). In contrast, stimulation of β-adrenergic receptors by high concentrations of adrenaline would increase I_{K1} but decrease $I_{Cl,swell}$, hyperpolarizing the RP. Importantly, all these effects were observed under a stable atrial pacing when PV RP did not differ from that measured in the left ventricle as shown here (**Figure 1**) and previously (Doisne et al., 2009; Egorov et al., 2015).

We also found that pathological (moderate) stretch facilitated the development of arrhythmogenic ectopic activity induced by high concentrations of adrenaline in PVs. At depolarized RPs under stretch, application of adrenaline led to more regular and faster PV automaticity compared with nonstretched conditions (**Figure 3A**). Interestingly, although both moderate stretch and low concentrations of adrenaline significantly depolarized the RP, those were not associated with the induction of automatic activity and required an application of high concentrations of adrenaline. This indicate a crucial combination of pathologically depolarized RP and enhanced Ca^{2+} handling to form both a substrate [at cellular as well as tissue levels (Egorov et al., 2019)] and a trigger [in a form of early afterdepolarizations (Patterson et al., 2005)] for a stable spontaneous activity within PVs. As it was shown by Patterson et al. (2005), suppression of ryanodine receptor activity (by ryanodine) or reduction in the transmembrane gradient driving Na/Ca exchange (by increase $[Ca^{2+}]_o$ from 1.35 to 5 mM) completely suppressed spontaneous firing from PVs, without changed in RP.

Importantly, spontaneous electrical activity induced in the stretched PV by adrenaline was not suppressed by atrial pacing. Moreover, it led to frequent atrial extra beats that may potentially trigger arrhythmogenic atrial extra beats and thus initiate atrial fibrillation. It should be also noted that myocardium dilation during pressure and/or volume overload of the atria could result in heterogeneous distribution of wall stress creating regions of conduction slowing and thus facilitating the induction of atrial fibrillation by PV extra beats. Altogether, our findings highlight an arrhythmogenic impact of PV stretch in the development of atrial arrhythmias under elevated autonomic tone, which could play a critical role in patients with elevated blood pressure associated with hypertension, heart failure, and valvular disease.

DATA AVAILABILITY STATEMENT

The datasets generated for this study are available on request to the corresponding author.

ETHICS STATEMENT

The animal study was reviewed and approved by the Animal Care and Use Committee of the Cardiology Research Center (Moscow, Russia).

AUTHOR CONTRIBUTIONS

YE, LR, and AG substantially contributed to the conception and design of the work; the acquisition, analysis, or interpretation of the data and literature; drafting of the work critically for important intellectual content; providing of approval for publication of the content; and agreeing to be accountable for all aspects of the work in ensuring that questions related to the accuracy or integrity of any part of the work are appropriately investigated and resolved.

FUNDING

This work was supported by the Russian Foundation for Basic Research Grants 17-04-01634 and Scientific Research Work AAAA-A18-118022290082-7 (to LR), and NIH 1R01HL141214-01, AHA 16SDG29120011 and the Wisconsin Partnership Program (to AG).

REFERENCES

Arora, R., Verheule, S., Scott, L., Navarrete, A., Katari, V., Wilson, E., et al. (2003). Arrhythmogenic substrate of the pulmonary veins assessed by high-resolution optical mapping. *Circulation.* 107, 1816–1821.

Braun, A. P., Fedida, D., and Giles, W. R. (1992). Activation of alpha 1-adrenoceptors modulates the inwardly rectifying potassium currents of mammalian atrial myocytes. *Pflugers. Arch.* 421, 431–439.

Bun, S. S., Latcu, D. G., Wedn, A. M., and Saoudi, N. (2018). Intrapulmonary vein "echo" beats'. *HeartRhythm Case Rep.* 4, 464–465.

Chen, S. A., Hsieh, M. H., Tai, C. T., Tsai, C. F., Prakash, V. S., Yu, W. C., et al. (1999). Initiation of atrial fibrillation by ectopic beats originating from the pulmonary veins: electrophysiological characteristics, pharmacological responses, and effects of radiofrequency ablation. *Circulation.* 100, 1879–1886.

Doisne, N., Maupoil, V., Cosnay, P., and Findlay, I. (2009). Catecholaminergic automatic activity in the rat pulmonary vein: electrophysiological differences between cardiac muscle in the left atrium and pulmonary vein. *Am. J. Physiol. Heart. Circ. Physiol.* 297, H102–H108. doi: 10.1152/ajpheart.00256.2009

Egorov, Y. V., Kuz'min, V. S., Glukhov, A. V., and Rosenshtraukh, L. V. (2015). Electrophysiological Characteristics, Rhythm, Disturbances and Conduction Discontinuities Under Autonomic Stimulation in the Rat Pulmonary Vein Myocardium. *J. Cardiovasc. Electrophysiol.* 26, 1130–1139. doi: 10.1111/jce.12738

Egorov, Y. V., Lang, D., Tyan, L., Turner, D., Lim, E., Piro, Z. D., et al. (2019). Caveolae-Mediated Activation of Mechanosensitive Chloride Channels in Pulmonary Veins Triggers Atrial Arrhythmogenesis. *J. Am. Heart. Assoc.* 8, e012748. doi: 10.1161/JAHA.119.012748

Ellershaw, D. C., Greenwood, I. A., and Large, W. A. (2002). Modulation of volume-sensitive chloride current by noradrenaline in rabbit portal vein myocytes. *J. Physiol.* 542, 537–547.

Furchgott, R. F. (1967). The pharmacological differentiation of adrenergic receptors. *Annals of the New York Academy of Sciences.* 139, 553–570.

Haissaguerre, M., Jais, P., Shah, D. C., Takahashi, A., Hocini, M., Quiniou, G., et al. (1998). Spontaneous initiation of atrial fibrillation by ectopic beats originating in the pulmonary veins. *N. Engl. J. Med.* 339, 659–666.

Malecot, C. O., Bredeloux, P., Findlay, I., and Maupoil, V. (2015). A TTX-sensitive resting Na+ permeability contributes to the catecholaminergic automatic activity in rat pulmonary vein. *J. Cardiovasc. Electrophysiol.* 26, 311–319. doi: 10.1111/jce.12572

Melnyk, P., Ehrlich, J. R., Pourrier, M., Villeneuve, L., Cha, T. J., and Nattel, S. (2005). Comparison of ion channel distribution and expression in cardiomyocytes of canine pulmonary veins versus left atrium. *Cardiovasc. Res.* 65, 104–116.

Okamoto, Y., Kawamura, K., Nakamura, Y., and Ono, K. (2014). Pathological impact of hyperpolarization-activated chloride current peculiar to rat pulmonary vein cardiomyocytes. *J. Mol. Cell. Cardiol.* 66, 53–62. doi: 10.1016/j.yjmcc.2013.11.002

Pasqualin, C., Yu, A., Malecot, C. O., Gannier, F., Cognard, C., Godin-Ribuot, D., et al. (2018). Structural heterogeneity of the rat pulmonary vein myocardium: consequences on intracellular calcium dynamics and arrhythmogenic potential. *Sci. Rep.* 8, 3244. doi: 10.1038/s41598-018-21671-9

Patterson, E., Po, S. S., Scherlag, B. J., and Lazzara, R. (2005). Triggered firing in pulmonary veins initiated by in vitro autonomic nerve stimulation. *Heart Rhythm.* 2, 624–631.

Schotten, U., Verheule, S., Kirchhof, P., and Goette, A. (2011). Pathophysiological mechanisms of atrial fibrillation: a translational appraisal. *Physiol. Rev.* 91, 265–325. doi: 10.1152/physrev.00031.2009

Tsao, H. M., Yu, W. C., Cheng, H. C., Wu, M. H., Tai, C. T., Lin, W. S., et al. (2001). Pulmonary vein dilation in patients with atrial fibrillation: detection by magnetic resonance imaging. *J. Cardiovasc. Electrophysiol.* 12, 809–813.

Tsuneoka, Y., Irie, M., Tanaka, Y., Sugimoto, T., Kobayashi, Y., Kusakabe, T., et al. (2017). Permissive role of reduced inwardly-rectifying potassium current density in the automaticity of the guinea pig pulmonary vein myocardium. *J. Pharmacol. Sci.* 133, 195–202. doi: 10.1016/j.jphs.2016.12.006

Walters, T. E., Lee, G., Spence, S., Larobina, M., Atkinson, V., Antippa, P., et al. (2014). Acute atrial stretch results in conduction slowing and complex signals at the pulmonary vein to left atrial junction: insights into the mechanism of pulmonary vein arrhythmogenesis. *Circ. Arrhythm. Electrophysiol.* 7, 1189–1197. doi: 10.1161/CIRCEP.114.001894

Conflict of Interest: The authors declare that the research was conducted in the absence of any commercial or financial relationships that could be construed as a potential conflict of interest.

frontiers
in Physiology

HYPOTHESIS AND THEORY
published: 31 March 2020
doi: 10.3389/fphys.2020.00183

An Equivocal Final Link – Quantitative Determination of the Thermodynamic Efficiency of ATP Hydrolysis – Sullies the Chain of Electric, Ionic, Mechanical and Metabolic Steps Underlying Cardiac Contraction

*Christopher John Barclay[1] and Denis Scott Loiselle[1,2]**

[1] *Auckland Bioengineering Institute, The University of Auckland, Auckland, New Zealand,* [2] *Department of Physiology, The University of Auckland, Auckland, New Zealand*

Each beat of the heart completes the final step in a sequence of events commencing with electrical excitation-triggered release of Ca^{2+} from the sarcoplasmic reticulum which, in turn, triggers ATP-hydrolysis-dependent mechanical contraction. Given that *Thermodynamics* is inherently detail-independent, the heart can be thus be viewed as a mechanical pump – the generator of pressure that drives blood through the systemic and pulmonary circulations. The beat-to-beat pressure-volume work (W) of the heart is relatively straightforward to measure experimentally. Given an ability to measure, simultaneously, the accompanying heat production or oxygen consumption, it is trivial to calculate the *mechanical* efficiency: $\varepsilon = W/\Delta H$ where ΔH is the change of enthalpy: $(W + Q)$, Q representing the accompanying production of heat. But it is much less straightforward to measure the thermodynamic efficiency: $\eta = W/\Delta G_{ATP}$, where ΔG_{ATP} signifies the Gibbs Free Energy of ATP hydrolysis. The difficulty arises because of uncertain quantification of the substrate-dependent yield of ATP - conveniently expressed as the P/O_2 ratio. P/O_2 ratios, originally ("classically") inferred from thermal studies, have been considerably reduced over the past several decades by re-analysis of the stoichiometric coefficients separating sequential steps in the electron transport system – in particular, dropping the requirement that the coefficients have integer values. Since the early classical values are incompatible with the more recent estimates, we aim to probe this discrepancy with a view to its reconciliation. Our probe consists of a simple, thermodynamically constrained, algebraic model of cardiac mechano-energetics. Our analysis fails to reconcile recent and classical estimates of PO_2 ratios; hence, we are left with a conundrum.

Keywords: thermodynamics, cardiac muscle, metabolism, myothermia, stoichiometry of mitochondrial ATP production

Edited by:
Gentaro Iribe,
Asahikawa Medical University, Japan

Reviewed by:
Koji Obata,
Gifu University, Japan
Jason Bazil,
Michigan State University,
United States

***Correspondence:**
Denis Scott Loiselle
ds.loiselle@auckland.ac.nz

Specialty section:
This article was submitted to
Striated Muscle Physiology,
a section of the journal
Frontiers in Physiology

Received: 08 October 2019
Accepted: 17 February 2020
Published: 31 March 2020

Citation:
Barclay CJ and Loiselle DS (2020)
An Equivocal Final Link – Quantitative
Determination of the Thermodynamic
Efficiency of ATP Hydrolysis – Sullies
the Chain of Electric, Ionic,
Mechanical and Metabolic Steps
Underlying Cardiac Contraction.
Front. Physiol. 11:183.
doi: 10.3389/fphys.2020.00183

INTRODUCTION

Until early in the 21st Century, the accepted P/O_2 ratio for the oxidative phosphorylation of glucose had been 38 moles of ATP per 6 moles of molecular oxygen, yielding a P/O_2 ratio of 6.3. The equivalent values for palmitate (the most prevalent saturated fatty acid in the daily diet of the heart (Taegtmeyer et al., 2016) had been 129 moles of ATP per 23 moles of molecular oxygen, yielding a P/O_2 ratio of 5.6. We refer to these as "classical" estimates. Both were consistent with the existence of integer values of the stoichiometric ratios separating consecutive steps in the mitochondrial electron transport system. However, since that time, there has accumulated an extensive literature detailing the mitochondrial oxidation of glucose, in particular. It is now widely accepted, to the point of adoption in undergraduate textbooks [see, for example, Boron and Boulpaep (2009)], that the yield is considerably less than the classical value given above. Glucose oxidation is now thought to result in the generation of only 30 or 31, rather than 38, moles of ATP [for highly readable reviews, see Rich (2003) or Salway (2004). The comparable value for palmitate oxidation has been lowered from 129 to 104 (Salway, 2004)]. Since oxygen input (6 moles per mole of glucose, 24 moles per mole of palmitate) has remained unchanged, while putative ATP output has been reduced, the efficiency of cardiac *recovery metabolism* must necessarily have diminished.

Our use of the phrase "recovery metabolism" reflects the fact that the energy cost of a cardiac twitch comprises two conceptually distinct but temporally contiguous components: "initial metabolism" (I) and "recovery metabolism" (R). Initial metabolism comprises the biochemical events that occur nearly simultaneously with contraction: namely, the ATP hydrolysis-funded cycling of actin-myosin cross-bridges and ion pumps, and the rapid regeneration of ATP at the expense of a limited pool of PCr. Recovery metabolism reflects the reversal of the initial biochemical change: that is, the regeneration of PCr by ATP via oxidative phosphorylation of metabolic substrates in the mitochondria. Aerobic recovery metabolism is hence the exclusive domain of the mitochondria. Any contribution of non-mitochondrial recovery metabolism is quantitatively unimportant in myocardial tissues. Indeed, it has been recognized for over 60 years that lactate is readily metabolized by the heart (Griggs et al., 1966; Chapman and Gibbs, 1974; Drake-Holland et al., 1983).

In contrast to recovery metabolism, initial metabolism can readily be divided into two further components: activation and force development. Activation metabolism commences immediately prior to force development and continues throughout the contractile event; it funds sarcolemmal excitation and sarcoplasmic reticular Ca^{2+}- cycling – the electrical and ionic events which, acting sequentially, achieve excitation-contraction coupling.

It has been a long-standing challenge [commencing, unsurprisingly, with early investigations by AV Hill and colleagues using skeletal muscle (Hill, 1911, 1949; Hartree and Hill, 1922, 1928)], with further refinement by Bugnard (1934), to determine the ratio (r) of recovery metabolism (R) to initial metabolism (I):

$$r = \mathrm{R/I} \qquad \text{(Eq. 1)}$$

Whereas in amphibian skeletal muscle at 0°C, as typically utilized by Hill and colleagues, these two components are temporally distinct, such is not the case for cardiac muscle experiments performed between room temperature and body temperature, where other methods of separation, applicable to the thermometric technique, must be employed. Thus Mast et al. (1990), utilizing data previously published by Mast and Elzinga (1988), which had arisen from measurements of heat production by rabbit right-ventricular papillary muscles undergoing brief trains of isometric contractions at 20°C, developed a numerical correction procedure. This deconvolution procedure quantified recovery heat production that had occurred during the antecedent brief period of activity, in addition to the "pure" recovery heat observed during the subsequent exponential decline of muscle heat production to its supra-basal value.

It is important to emphasize that the separation of initial and recovery heat using the deconvolution technique was achieved by eliciting a brief train of twitches, with the accompanying heat production being recorded by rapid-response "flat-bed" thermopiles. What we now describe is a method that can be applied using data arising from steady-state contractions in a flow-through microcalorimeter (Taberner et al., 2005, 2011, 2018; Han et al., 2009; Johnston et al., 2015). The method, based on a straightforward algebraic model, yields estimates of the thermodynamic efficiencies of both cross-bridge cycling and mitochondrial ATP production, thereby allowing us to quantify the aforementioned difference between "classical" estimates of mitochondrial efficiency and more recent ones that admit non-integer mitochondrial stoichiometric coefficients.

In order to pursue that objective, we present a simple, thermodynamically consistent, algebraic model. The model aims to allow calculation of substrate-dependent P/O_2 ratios, thereby permitting comparison with the current ratios detailed above.

METHODS AND RESULTS

Since no animals were used, this study is exempt from animal ethical considerations.

We commence by defining conceptually and experimentally distinct components of overall enthalpy production (ΔH_O):

$$\Delta H_O = \Delta H_B + \Delta H_A + \Delta H_{X-b} + \Delta H_{mito} \qquad \text{(Eq. 2)}$$

Abbreviations: Glossary of symbols: ΔG_{ATP}, Gibbs free energy of ATP hydrolysis; ΔH, change of enthalpy: (W + Q); H_A, enthalpy of activating contraction; H_B, enthalpy of basal metabolism; H_{X-b}, enthalpy arising from cross-bridge cycling; H_{mito}, enthalpy of mitochondrial oxidative phosphorylation; ΔH_{PCr}, molar enthalpy change of creatine phosphate hydrolysis; δH_{x-b}, extent of PCr breakdown by cross-bridges x molar enthalpy change; W/ΔH: W/(W + Q), ε mechanical efficiency; W/ΔG, η thermodynamic efficiency; I, initial metabolism; Q, heat; Q_{X-b}, heat arising from cross-bridge cycling; $Q_{X-b(Isom)}$, heat arising from X-b cycling during the isometric phase of an auxotonic contraction; $Q_{X-b(Short)}$, heat arising from X-b cycling during the shortening phase of an auxotonic contraction; R, recovery metabolism; r, ratio of recovery metabolism to initial metabolism: R/I; W, work; X-b, cross-bridge.

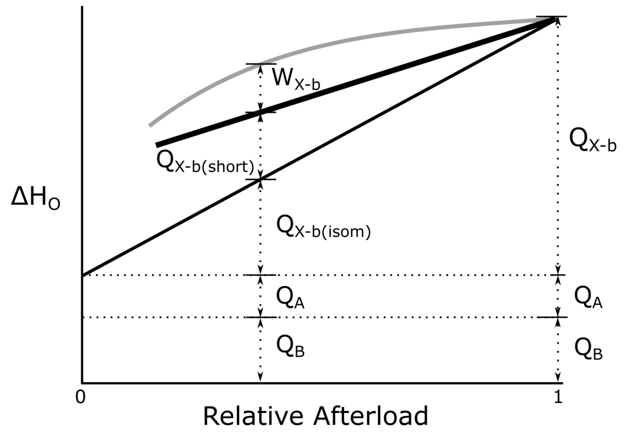

FIGURE 1 | Conceptual basis of overall cardiac enthalpy output as a function of afterload. Q_B and Q_A define basal and activation heat, respectively. Heat from cross-bridge cycling in isolated cardiac muscle preparations arises from two distinct temporal phases: isometric [$Q_{X-b(Isom)}$] and reduction of filament overlap [$Q_{X-b(short)}$] corresponding, respectively, to the isovolumic and auxotonic phases of contraction of the heart *in vivo*. *W* denotes cross-bridge work. [Modified from Tran et al. (2017) under the aegis of the Rights Link®-Copyright Clearance Center; Account Number: 3000104389; License Number: 4678431442941].

The first three variables are the enthalpy outputs arising from basal metabolism, activation and cross-bridge cycling, respectively. The enthalpy from the first two of those appears entirely as heat (denoted "Q" in **Figure 1**) whereas enthalpy from cross-bridge cycling can appear as both heat and mechanical work.

The further separation of "isometric heat" [$Q_{X-b(Isom)}$] and "shortening heat" [$Q_{X-b(Short)}$] (**Figure 1**) is again purely conceptual, reflecting the fact that, in the beating heart, a period of isovolumic contraction necessarily precedes a period of auxotonic shortening. No fundamental difference of cross-bridge energetics between the isometric and shortening phases is implied.

We next capitalize on an experimentally straightforward simplification. It is trivial to "null" the basal enthalpy contribution (ΔH_B; Eq. 2) electrically when making thermal measurements. When this is done, the magnitude of initial enthalpy production ($\Delta H_A + \Delta H_{X-b}$) is revealed.

As foreshadowed above, initial enthalpy can be further separated into its underlying components, activation enthalpy and cross-bridge enthalpy, by use of a suitable inhibitor of cross-bridge cycling. This has recently been achieved in cardiac muscle by Tran et al. (2017) and by Pham et al. (2017) using the agent blebbistatin, the effectiveness of which had previously been demonstrated in skeletal muscle (Barclay, 2012). Blebbistatin was chosen because it: (i) achieves complete inhibition of cross-bridge turnover (Kovács et al., 2004; Allingham et al., 2005), (ii) does not affect excitation-contraction coupling (Farman et al., 2008), and (iii) does not affect the Ca^{2+}-sensitivity of the contractile proteins (Dou et al., 2007). Using this cross-bridge inhibitor, Pham et al. (2017) found activation enthalpy to be both length-independent and force-independent (see **Figure 1**). These findings allow unambiguous quantification of ΔH_{X-b} at any given afterload. In the following, we focus on the afterload that maximizes cross-bridge efficiency since it too, is equally unambiguous.

Experimental quantification of cross-bridge heat (Q_{X-b}) and cross-bridge work (W) defines cross-bridge enthalpy (δH_{X-b}), thereby allowing definition of *macroscopic* cross-bridge efficiency (ε_{X-b}):

$$\varepsilon_{X-b} = \frac{W}{W + Q_{X-b}} \equiv \frac{W}{\delta H_{x-b}} \qquad \text{(Eq. 3)}$$

where δH_{x-b} is the enthalpy change, as heat plus work, associated with cross-bridge cycling. It arises from the net breakdown of PCr, subsequent to the hydrolysis of ATP, which powers cross-bridge cycling, and the subsequent rapid buffering of ATP at the expense of PCr by the creatine kinase reaction, and is distinct from *overall* efficiency (ε_o):

$$\varepsilon_o = \frac{W}{W + Q_{X-b} + Q_{mito}} \qquad \text{(Eq. 4)}$$

The biochemical correlate of the expenditure of cross-bridge enthalpy is the production of ADP and Pi which, in the presence of PCr, regenerates ATP with rapid kinetics. But the concentration of PCr in cardiac myocytes is modest (of the order of 20–30 mmol L^{-1}) so that work can be sustained only briefly from this source of ATP (see **Figure 2A**). That is, in the absence of recovery metabolism, cross-bridge cycling has but a brief existence.

Our aim is to estimate the *thermodynamic* efficiency of cross-bridge cycling (η_{X-b}), which does not depend on the enthalpy of phosphocreatine, H_{PCr}, but rather on the Gibbs Free Energy of ATP (ΔG_{ATP}), a variable whose numeric value cannot be measured by thermometric or calorimetric means:

$$\eta_{X-b} \equiv \frac{W}{\Delta G_{ATP}} = \frac{W}{\Delta H_{X-b}} \frac{\Delta H_{PCr}}{\Delta G_{ATP}} = \varepsilon_{Xb} \frac{\Delta H_{PCr}}{\Delta G_{ATP}} \qquad \text{(Eq. 5)}$$

where ΔH_{PCr} and ΔG_{ATP} are molar values, and where

$$\Delta G_{ATP} = \Delta G^{o}_{ATP} + RT \ln \left(\frac{[ADP]\ [Pi]}{[ATP]}\right), \qquad \text{(Eq. 6)}$$

as shown in the Legend of **Figure 2**. We now capitalize on an insight due to Wilkie (1974):

$$\eta_o = \eta_{X-b} \cdot \eta_{mito} \qquad \text{(Eq. 7)}$$

where the subscript "o" again signifies "overall," indicating the combined thermodynamic efficiencies of cross-bridge cycling and mitochondrial oxidative phosphorylation operating in series.

We next exploit a fortuitous *approximation*: the difference in magnitudes between ΔH and ΔG for the oxidative metabolism of each of carbohydrates, fatty acids and alcohol is negligible (Battley, 2002). The validity of this approximation is demonstrated in **Table 1**, where the rightmost column expresses the difference in magnitudes of enthalpy and Gibbs free energy, as a percentage of the former, for selected common metabolites.

Since the average difference of the entries in the right-most column of **Table 1** is −0.05%, it is evident that $\Delta G_S \approx \Delta H_S$,

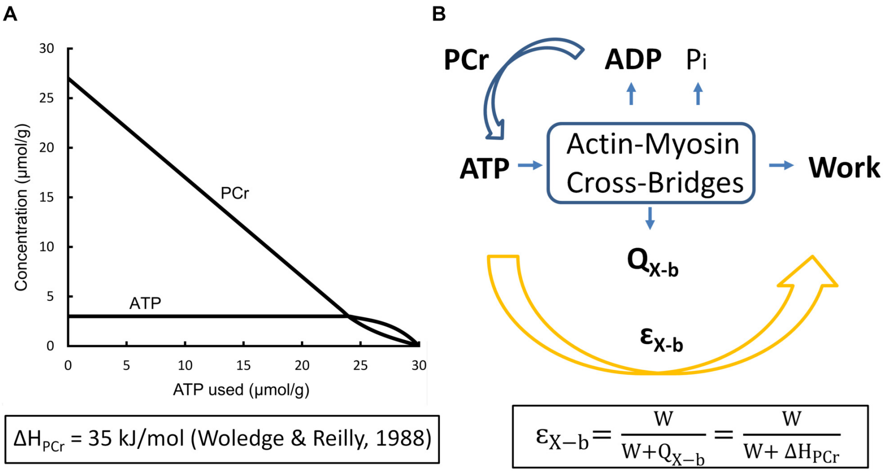

FIGURE 2 | Events underlying cross-bridge metabolism. **(A)** The creatine-phosphokinase (Lohmann) reaction. Note the relative independence of ATP and PCr concentrations until the latter is nearly exhausted [based on Figure 4.2, Page 142 of Woledge et al. (1985)] **(B)** The Gibbs Free Energy of ATP hydrolysis as a function of the progressively increasing concentration of inorganic phosphate (Pi) in the absence of mitochondrial function, reflecting events shown in **(A)**: $G_{ATP} = \Delta G^o + RT \ln([ADP]\ [Pi]/[ATP])$, where the Standard Gibbs Free Energy of ATP hydrolysis, $G^o_{ATP} = -30\ kJ/mol$, R is the Universal Gas Constant (8.31 kJ/mol), T is absolute temperature (310 K), and [ATP] and [ADP] are assumed to be 5 mmol/L and 1 μmol/L, respectively, under steady-state conditions of twitch force production. (Note the inverse scale on the ordinate).

where the subscript "S" denotes "substrate." Hence, Eq. 7 can be re-expressed as:

$$\eta_o = \eta_{X-b} \quad \eta_{mito} \quad or \quad \eta_{mito} \approx \frac{\varepsilon_o}{\eta_{X-b}} \qquad \text{(Eq. 8)}$$

where ε_o signifies *macroscopic* overall efficiency.

$$\text{But } \eta_{X-b} = \frac{\Delta H_{PCr}}{\Delta G_{ATP}} \varepsilon_{X-b} \ \& \ \eta_{mito} = \frac{\varepsilon_o}{\varepsilon_{X-b}} \frac{\Delta G_{ATP}}{\Delta H_{PCr}}$$

$$\text{so } \eta_{Xb} = \frac{\varepsilon_{X-b}}{\varepsilon_o} \frac{\Delta H_{X-b} + H_{mito}}{\Delta H_{X-b}} \qquad \text{(Eq. 9)}$$

$$\text{thus } \frac{\varepsilon_{X-b}}{\varepsilon_o} = 1 + \frac{\Delta H_{mito}}{\Delta H_{X-b}} = 1 + r, \ since\ r = \frac{\Delta H_{mito}}{\Delta H_{X-b}} \qquad \text{(Eq. 10)}$$

TABLE 1 | Difference between H° and G° for the oxidative metabolism of common metabolites at 25°C.

Metabolite	ΔH° (kJ/mol)	ΔG° (kJ/mol)	Percentage
Acetic acid	−874.54	−874.30	0.03
Glucose	−2803.03	−2881.26	−2.79
Ethanol	−1366.83	−1325.32	3.04
Glycerol	−1655.40	−1654.46	0.06
Sucrose	−5640.87	−5784.20	−2.54
Palmitic acid	−9977.83	−9789.70	1.89

Data selected from Table 6 of Battley (2002). The right-most column expresses the percentage difference between the enthalpy and Gibbs free energy for selected metabolites at 298.15 K.

$$\text{Hence, } \eta_{mito} \quad \frac{1}{1+r} \quad \frac{\Delta G_{ATP}}{\Delta H_{PCr}} \qquad \text{(Eq. 11)}$$

It is clear from Eq. 11 that estimation of the thermodynamic efficiency of recovery metabolism requires numeric estimates of r, G_{ATP}, and H_{PCr}. Very few estimates of r arising from experiments on cardiac muscle have been published. But those of which we are aware have all utilized the method developed by Woledge and described above (Mast et al., 1990). Using this technique during either single twitches or trains of ten twitches at a stimulation rate of 0.2 Hz in rabbit right-ventricular papillary muscles, these authors found the value of r to be 1.18 at 20°C. Using comparable techniques on mouse left-ventricular papillary muscles undergoing isovelocity contractions at 30°C, values of 1.16 Barclay et al. (2003) and 1.20 (Barclay and Widén, 2010) have subsequently been reported. Given the closeness of these three independent estimates, we have adopted their average value: $r = 1.18$.

The stoichiometry of ATP synthesis from PCr hydrolysis, is 1:1 and the best estimate of its enthalpy output, achieved using microcalorimetry, with both acid hydrolysis and enzymatic hydrolysis of PCr, is 35 kJ mol^{-1} (Woledge and Reilly, 1988).

Our best estimate of the Gibbs Free Energy of ATP hydrolysis, under conditions prevailing in the myocardium, probably remains that of Kammermeier et al. (1982): 60 kJ mol^{-1}, arising from experiments performed on isolated, perfused, electrically paced female Sprague-Dawley rat hearts subjected to biochemical analyses of high-energy phosphates following rapid freezing. This early value remains in remarkable agreement with the more recent determination of 59.7 kJ mol^{-1}, arising from *in situ* ATP flux measurements recorded in 17 healthy human hearts of either

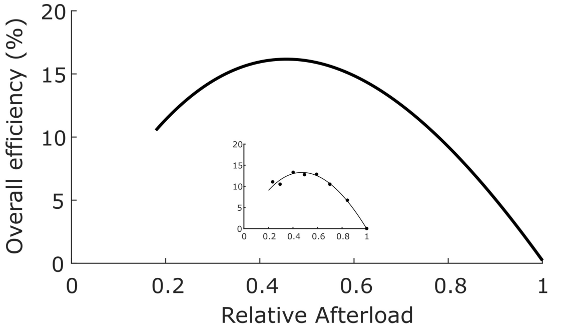

FIGURE 3 | Overall efficiency as a function of relative afterload. Average data from 56 rat left-ventricular trabecula at 32°C. Peak overall efficiency (0.155) occurred at a relative afterload of 0.45. Inset: data from a single representative trabecula; data fitted by cubic regression. [Figure modified from Tran et al. (2016) under the aegis of the Rights Link®-Copyright Clearance Center; *Permission received from The American Physiological Society*].

sex using the technique of magnetic resonance spectroscopy (Weiss et al., 2005).

Given these three required parameter values, Eq. 11 immediately returns:

$$\eta_R \approx \frac{1}{1+1.18} \cdot \frac{\frac{60kJ}{mol}}{\frac{35kJ}{mol}} \approx 0.786 \qquad \text{(Eq. 12)}$$

In order to calculate cross-bridge thermodynamic efficiency, we turn to data published by Tran et al. (2016) arising from experiments performed at 32°C using left-ventricular trabecula from Dahl salt-sensitive rats and their congenic controls. These authors apportioned 56 animals into four equal-size cohorts fed on either high- or low-salt diets. Since there were no differences of efficiency among the four groups, the results were averaged and displayed in **Figure 3**, where the mean peak value of $\varepsilon_{X-b} \pm$ SEM was found to be 0.155 ± 0.059.

Given that $\eta_{X-b} = \varepsilon_o/\eta_{mito}$ (Eq. 8), it follows that the thermodynamic efficiency of cross-bridge work performance, (η_{X-b}), is 0.155/0.786 or 0.20.

With estimates provided for the thermodynamic efficiencies of both cross-bridge energy expenditure (0.20, **Figure 3**) and mitochondrial energy expenditure (0.79, Eq. 12), we present a pictorial summary of overall thermodynamic efficiencies of cross-bridge cycling and resulting mitochondrial oxidative phosphorylation in **Figure 4**.

DISCUSSION

In order to focus on the uncertain link in the chain of events commencing with excitation-contraction and culminating with metabolic restoration of ATP, we have developed a simple and straightforward algebraic model. The model enables the separation and quantification of the thermodynamic efficiencies of cross-bridge cycling and attendant mitochondrial oxidative phosphorylation.

Critique of the Model

Whereas it contains no assumptions, the model does exploit two approximations: (i) the ratio of heat produced by the mitochondria to heat generated by cross-bridge cycling is 1.18 (the mean of three values reported in the Literature) and (ii) the quantitative differences between the enthalpies and Gibbs free energies of oxidation of common metabolic substrates is sufficiently small that they may be ignored (**Table 1**). Furthermore, with a single exception (Weiss et al., 2005), its parameter values gleaned from the literature pertain to rodent (rat or mouse) myocardial tissues. With these caveats, we conclude that the maximum thermodynamic efficiency of work generation by the myocardium (η_o) is a modest 16%. This implies (see **Figure 4**) that cross-bridges convert 20% of the free energy from ATP hydrolysis into work and mitochondrial oxidation transfers 80% of the free energy available in metabolic substrates into free energy in the form of ATP.

It is important to stress that the value of 20% efficiency is restricted to *mechanical* (i.e., cross-bridge) performance only. As shown schematically in **Figure 1**, it explicitly excludes both the basal and activation components. Inclusion of these two "overhead" metabolic costs, neither of which *directly* funds cross-bridge cycling, would, of course, reduce the overall thermodynamic efficiency of the heart even further – perhaps by as much as 40–50%. Nevertheless, our finding of 16% for the overall efficiency of cross-bridge cycling (ε_o) aligns well with the seminal values reported by Gibbs et al. (1967) for rabbit right-ventricular papillary muscles: 16% to 19%, and by Neely et al. (1967) for isolated, perfused, rat whole-heart preparations: 16% to 17%. Note that both of these estimates differ greatly from the "isoefficiency" value of 40% promoted by Khalafbeigui et al. (1979), Suga et al. (1980, 1981, 1986), Suga (1979, 1990), but which was based on a conceptual error, as revealed by Han et al. (2012).

Error Analysis of the Model

A rigorous examination of the susceptibility of a numeric model to the value of its parameters can be achieved through a formal Error Analysis. **Appendix 1** provides the relevant derivation and shows a small sample of results. Since there is a total of five input parameters [denoted by subscripted values of putative fractional errors (f), each of which has only a single constraint ($f \geq 0$)], an infinite number of Fractional Errors of Measurement are available to be modeled. Of the five input parameters, f_{PCr} may be the most likely to be in error given that its nominal value (35 kJ/mol) was obtained using a bicarbonate buffer (Woledge and Reilly, 1988), prior to the discovery of Na^+-HCO_3^- exchangers resident in the sarcolemmal membranes of cardiac myocytes, However, with respect to any potential Error of Estimate arising from this source, the authors of the study state: "*In this solution* HCO_3^- *will provide approximately 17% of the internal buffer capacity. This will have the effect of increasing the value of –*ΔH_{ob}*, by 1 kJ* mol^{-1}" - or an uncertainty of less than 3% in that parameter.

Furthermore, as shown in **Appendix Figure A1(A)**, even in a worst-case scenario, with Errors of Measurement of twice the

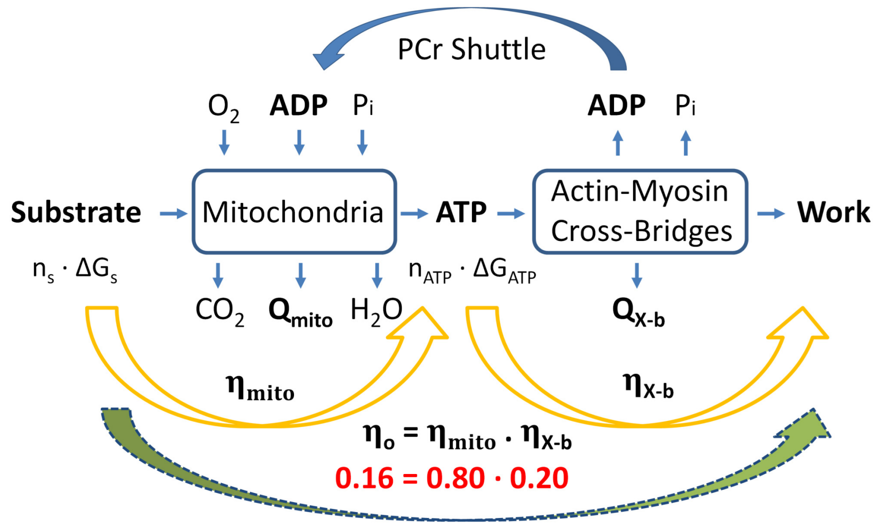

FIGURE 4 | Summary of overall "classical" thermodynamics of cardiac energetics. The right-hand orange arrow denotes the production of ATP via the Lohman reaction, which comprises cross-bridge enthalpy production (as shown in **Figure 2B**). The left-hand orange arrow denotes mitochondrial metabolism in which *n* moles of metabolic substrate are oxidizsed to provide sufficient Gibbs free energy to produce *n* moles of ATP to fund cross-bridge cycling. Overall thermodynamic efficiency (0.16) is calculated as the product of mitochondrial and cross-bridge thermodynamic efficiencies; 0.8 and 0.2, respectively. [Modified from Barclay (2017) under the aegis of Rights Link®-Copyright Clearance Center: permission received from *John Wiley and Sons*].

magnitude given above in *each* of *r*, ΔG_{ATP}, and ΔH_{PCr}, the Error of Estimate in *R* would be unlikely to exceed 10%, This would translate to an ATP yield of 35 mol_{ATP} per $mol_{glucose}$, still considerably greater than recent estimates arising from mitochondrial experiments, thereby again underscoring the "classical-mitochondrial" difference.

Appendix Figure A1(B) shows that the Error of Estimate of Initial Metabolism (I) is comparatively insensitive to errors of estimate of its input parameters (Work and Heat).

Relative Insensitivity of ε_O to Hypertension

Using the microcalorimetric technique, no difference has been found in overall cross-bridge efficiency between trabecula isolated from left and right ventricles of *healthy* rats at either room temperature (Han et al., 2013) or body temperature (Pham et al., 2017). These results in healthy cardiac tissues have been largely duplicated in heart failure models. Thus Han et al. (2014) found no difference of ε_o between trabecula dissected from the left ventricles of streptozoticin-induced Type I diabetic rats and their untreated controls. Nor were differences revealed among trabecula from Dahl salt-sensitive rats and their congenic controls, whether fed low- or high-salt diets (Tran et al., 2016). Similar results obtained in trabecula from both ventricles of hearts in which pulmonary arterial hypertension had been induced by injection of monocrotaline and untreated control trabecula (Pham et al., 2018). Hence, in each of these models overall cardiac function was compromised but the energetics of cycling cross-bridges and the associated mitochondrial energy supply were unaffected. In fact, the only hypertension-sensitive difference appeared in trabecula from spontaneously hypertensive (SHR) animals where overall cross-bridge efficiency was lower in trabecula from both failing and non-failing hearts than in those of age-matched control animals. Whereas this list is far from comprehensive, the contrast between the results of a naturally arising model (SHR), and those of three unrelated experimentally induced heart failure models, is intriguing.

Entropy Production

The modest value of thermodynamic efficiency of cross-bridge cycling (20%) shown in **Figure 4** implies a high rate of entropy production. This implication is qualitatively consistent with the conceptual "energy well" picture proffered by TL Hill and colleagues (Hill, 1974; Eisenberg and Hill, 1979; Eisenberg et al., 1980), and subsequently exploited by Barclay (1999). Under any of these authors' formulations, potential Gibbs Free Energy of ATP hydrolysis remains necessarily unused whenever a cross-bridge either attaches belatedly or detaches prematurely, rather than traversing the full descent of its parabolic Free Energy profile. Hence, by the Second Law: $-\Delta H_{ATP} = \Delta G_{ATP} + T\Delta S_{ATP}$, the entropy ($\Delta S$) so produced cannot subsequently be exchanged (Chapman and Loiselle, 2016), thereby demonstrating that the hydrolysis of an ATP molecule by actomyosin (**Figure 2B**) is an irreversible process – a conclusion reached earlier by use of a thermodynamically constrained mathematical model of the cross-bridge cycle (Loiselle et al., 2010).

In contrast to the production of entropy by cross-bridge cycling, our model predicts that the extent of inefficiency attributable to mitochondrial oxidative phosphorylation of metabolic substrates is modest; its primary source is likely to be leakage of protons back across the inner mitochondrial membrane, without contributing to ATP production via the electron transport system. An early calculation (Loiselle, 1987) suggested that this source may contribute upward of 5 mW g^{-1} to the basal component of total enthalpy production (**Figure 1**). This speculative result has subsequently been extensively investigated by Brand et al. (1994) who concluded that the increased rates of oxygen consumption at high proton motive force could be attributed to this source and that it further contributes to the basal metabolic rate of homeotherms (Brand, 1990; Porter and Brand, 1993; Rolfe and Brand, 1996).

Mitochondrial P/O$_2$ Ratios

The prediction of a modest extent (20%) of inefficiency attributable to recovery metabolism warrants further investigation. We commence by noting that, given any value of *r* (the ratio of recovery metabolism to initial metabolism, Eq. 1), then the P/O$_2$ ratio, *p*, can be calculated as:

$$p = \frac{\Delta H_S}{\Delta H_{PCr}(r+1)} \qquad \text{(Eq. 13)}$$

where ΔH_S is the substrate enthalpy per mole of oxygen consumption. Early (mid-20th Century) experiments returned values for *p* in the vicinity of *6.3* for NADH-linked metabolites [for a comprehensive Review, see Table 1 of Hinkle (2005)]. This is the value that we previously labeled "classical." As detailed above, with glucose as substrate, it generates a stoichiometric ratio of some 37–38 molecules of ATP per mole of O$_2$. With palmitate as substrate, the classical value is 129 molecules of ATP per mole of O$_2$. The equivalent current values are 30 and 104, respectively.

What value of *p* is consistent with our estimate of η_{mito}? If η_{mito} = 0.8, then 80% of ΔH_S is transferred to ΔG in ATP. In that case, then the ATP yield, per mole of glucose, would be 2802 × 0.8/60 or 37.3. This value is consistent with the classical, rather than recent, estimates of P/O$_2$ ratios. Is it possible that discrepancies of this magnitude prevailed in the muscles considered in the current investigation but were obscured by experimental uncertainties? One way in which η_{ATP} could be overestimated is if the assumed value of ΔG_{ATP} were too low. However, if n_{ATP} were 30 instead of 38, then ΔG_{ATP} would have to be an unrealistically high 76 kJ mol^{-1} to account for η_{mito} of 0.8. Recall (see Results) its re-measured and, re-confirmed, value of 59.7 kJ mol^{-1} in human hearts *in situ* (Weiss et al., 2005).

A second factor to consider (see Eq. 13) is the substrate enthalpies. Might the classical value (2800 kJ mol^{-1}) for glucose have been overestimated? Using the technique of adiabatic calorimetry, Kabo et al. (2013) found the enthalpy of α-D-glucose to be 2802.4 kJ mol^{-1}. This value is in remarkable accord with that of 2803.03 kJ mol^{-1} calculated by Battley (2002). Thus, if the Gibbs Free Energy of cytoplasmic ATP is 60 kJ mol^{-1}, there would be sufficient energy to generate 2803 × 0.8/60 or 37.4 ATP molecules per mole of glucose – a value consistent with the theoretical limit of 37–38.

Comparable stoichiometric concerns obtain for the mitochondrial oxidation of palmitate. Salway (2004) details how the classical value of 129 molecules of ATP per mole of palmitate reduces to a value of 104 when non-integral values for intermediate steps in the mitochondrial sequence are allowed. However, Levine et al. (2014), using the technique of differential scanning calorimetry, reported the enthalpy of oxidation of methyl palmitate to be 10694 kJ mol^{-1}. Correction for the presence of the methyl group, and multiplication by 0.8/60 (as above), would yield 142.6 ATP per mole, a value readily accommodating the theoretical maximum of 129 molecules of ATP per mole.

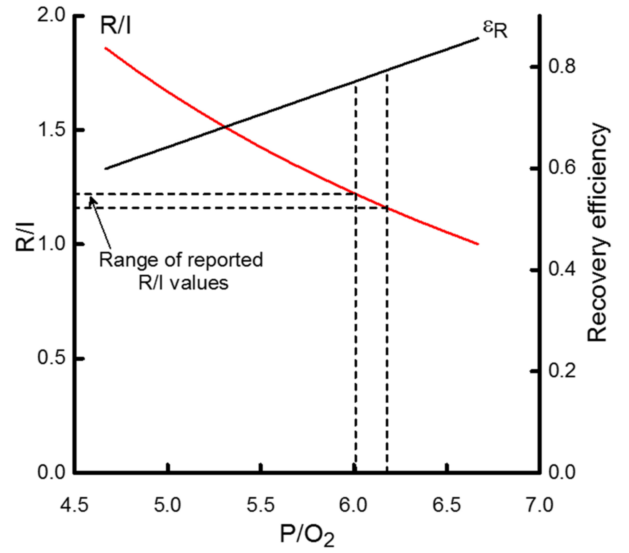

FIGURE 5 | The dependence on the P/O$_2$ ratio of the ratio of recovery heat to initial heat (R/I) and recovery efficiency (ε_R). R/I values are scaled by the left-hand *y*-axis and ε_R by the right-hand *y*- axis. The horizontal dashed lines indicate the range of reported R/I values for cardiac muscle; that range corresponds to P/O$_2$ values from approximately 6 to 6.2, indicated by the vertical dashed lines. That range of P/O$_2$ values, in turn, is consistent with ε_R values of 0.77 to 0.79, as indicated by the intersection of the vertical dashed lines and the curve relating the P/O$_2$ dependence of ε_R. If ATP yield were approximately 30 ATP/glucose, then P/O$_2$ would be 5 which would correspond to R/I and ε_R values of 1.7 and 0.64, respectively.

The third factor with potential to affect the estimated ATP yield is the value of *r*. If n_{ATP} were actually 30 instead of 38 for glucose oxidation, then the amount of substrate oxidized, and recovery heat produced, would have to be 38/30 or 1.27–times greater than assumed by acceptance of the average measured value of *r* = 1.18. That is, *r* would have to be 1.52, a value that greatly exceeds the upper 95% confidence limit arising from its experimental determinations of ∼1.22 (Barclay et al., 2003). The consequences of changed values of any of these three factors are displayed in **Figure 5**.

What could bring clarity to these disparities would be a study designed to investigate the issue by simultaneous measurement of heat production and oxygen consumption. Fortunately, such a study has been performed, albeit in skeletal muscle. Nevertheless, given the similarity of the cellular machinery between cardiac and skeletal muscles, we turn attention to the results of Mahler (1979) who, using Sartorius muscles from *Rana pipiens*." at 20°C, compared the suprabasal rate of oxygen consumption during recovery from brief tetani (0.2, 0.5, and 1.0 s) with the amount of ATP hydrolyzed (measured indirectly as the decrement of PCr concentration) during the same period. The mean ratio of the PCr decrement to the amount of suprabasal oxygen consumed, subsequently shown to obey first-order kinetics (Mahler, 1985), thereby simplifying interpretation, averaged over a total of 62 tetani, was 6.58 ± 0.55 – consistent with the "classical" P/O_2 value of 6.3.

In support of this convincing finding, Lou et al. (2000) made simultaneous measurements (at 19°C) of heat production and oxygen consumption, measured polarographically, during metabolic recovery of 10 bundles of white fibers from the dogfish. Their reported value for recovery metabolism of 84% in these skeletal muscle preparations echoes ours of 80% in cardiac muscle – in accord with the "classical" values, but again at variance with more recent estimates that yield non-integer stoichiometric coefficients.

Non-integer stoichiometric coefficients are most commonly attributed to "proton leakage." Mazat et al. (2013) provide a comprehensive discussion of this issue, emphasizing especially passive proton leak (a consequence of non-zero membrane conductance), and the role of uncoupling proteins, but considering also "slip" or "intrinsic uncoupling" as a consequence of a decrease in the efficiency of proton pumps. In a similar vein, van der Zwaard (2016) offer the timely reminder that mitochondrial inhibition may be caused by either nitric oxide production or by "methodological issues related to permeabilizing procedures or isolation." The latter, of course, is not limited to mitochondrial isolation; cardiac preparations (especially minute trabecula) can likewise be unwittingly damaged during isolation. In any case it does not seem to be unreasonable to suggest that the higher temperature at which mitochondrial experiments are conducted [37°C; see, for example (Pham et al., 2014) and accompanying commentary (Patel and McDonough, 2014)] *vis-à-vis* thermometric experiments (20–30°C; see section "Introduction") may have the unintended result that proton leakage is maximized under the former condition, thereby contributing to the disparity between "classical" and "mitochondrial" estimates of thermodynamic efficiency of cross-bridge cycling.

An Unresolved Issue Underling Mathematical Modeling of Cross-Bridge Energetics

In order for any mathematical model (independent of its complexity) in which the cross-bridge passes through a series of states from "unattached" to "detached" to be thermodynamically constrained, it must obey the following relation (Hill, 1989):

$$\frac{\prod_i f^+}{\prod_i f^-} = e^{\Delta G_{ATP}/RT} \qquad \text{(Eq. 14)}$$

That is, the ratio of the product of all forward reactions (f^+) to the product of all reverse reactions (f^-) is constrained by the Gibbs Free Energy of ATP hydrolysis (see Eq. 6). But despite the results of Mahler (1985) and Lou et al. (2000) there remains no agreement between the "Classical" and "Mitochondrial" values of ΔG_{ATP}. As noted above, if n_{ATP} were 30 (in concert with modern "Mitochondrial" estimates) instead of 38, then ΔG_{ATP} would have to be an unrealistically high 76 kJ mol^{-1} (instead of the "Classical" value of 60 kJ/mol, in order to account for η_{mito} of 0.8 as predicted by our simple model (**Figure 4**). Clearly, the yawning difference between these two estimates of n_{ATP} and, consequently, the numeric value of ΔG_{ATP} casts uncertainty on the accuracy of all mathematical models of the cross-bridge cycle.

Summary

Using a simple algebraic model, containing only three parameters (r, ΔH_{PCr}, and ΔG_{ATP}), each of which has been experimentally well-attested, we find that the thermodynamic efficiency of cross-bridge cycling is 20%, while that of mitochondrial oxidative phosphorylation is 80%, giving a value of 16% for overall thermodynamic efficiency of the mechanical activity of the heart. We show that the latter value is consistent with those measured in experiments undertaken using flow-through microcalorimetry. Nevertheless, we are left with a biophysical-biochemical conundrum. We are unable to reconcile the discrepancy between "Classical" (i.e., thermodynamically constrained) and "Mitochondrial" (i.e., stoichiometrically unconstrained) P/O_2 ratios – a situation that prevents full thermodynamic understanding of the cascade of events comprising the cardiac twitch.

DATA AVAILABILITY STATEMENT

The datasets generated for this study are available on request to the corresponding author.

AUTHOR CONTRIBUTIONS

CB and DL contributed to the conception and design of the work, acquisition, analysis, interpretation of the data, drafting the manuscript, approving the final version of the manuscript, and agreed to be accountable for all aspects of the work in ensuring that questions related to the accuracy or integrity of any part of the work have been appropriately investigated and resolved, and all persons designated as authors qualify for authorship, while all those who qualify for authorship are listed.

ACKNOWLEDGMENTS

We thank Dr. Toan Pham for converting the figures to "High Resolution" format.

REFERENCES

Allingham, J. S., Smith, R., and Rayment, I. (2005). The structural basis of blebbistatin inhibition and specificity for myosin II. *Nat. Struct. Mol. Biol.* 12, 378–379. doi: 10.1038/nsmb908

Barclay, C. J. (1999). A weakly coupled version of the Huxley crossbridge model can simulate energetics of amphibian and mammalian skeletal muscle. *J. Muscle Res. Cell Motil.* 20, 163–176.

Barclay, C. J. (2012). Quantifying Ca^{2+} release and inactivation of Ca^{2+} release in fast- and slow-twitch muscles. *J. Physiol.* 590, 6199–6212. doi: 10.1113/jphysiol.2012.242073

Barclay, C. J. (2017). The basis of differences in thermodynamic efficiency among skeletal muscles. *Clin. Exp. Pharmacol. Physiol.* 44, 1279–1286. doi: 10.1111/1440-1681.12850

Barclay, C. J., and Widén, C. (2010). "Efficiency of cross-bridges and mitochondria in mouse cardiac muscle," in *Muscle Biophysics: From Molecules to Cells, Advances in Experimental Medicine and Biology 682*, ed. D. Rassier (New York, NY: Springer Science & Business Media LLC), 267–278. doi: 10.1007/978-1-4419-6366-6_15

Barclay, C. J., Widén, C., and Mellors, L. J. (2003). Initial mechanical efficiency of isolated cardiac muscle. *J. Exp. Biol.* 206, 2725–2732. doi: 10.1242/jeb.00480

Battley, E. H. (2002). On the use of ΔQo rather than ToΔSo in the calculation of ΔGo accompanying the oxidation of fermentation of catabolic substrates of biological importance in their standard states. *Thermochim. Acta* 394, 313–327. doi: 10.1016/s0040-6031(02)00264-2

Boron, W. F., and Boulpaep, E. L. (2009). *Medical Physiology: A Cellular and Molecular Approach*, 2nd Edn. Philadelphia, PA: Saunders Elsevier.

Brand, M. D. (1990). The contribution of the leak of protons across the mitochondrial inner membrane to standard metabolic rate. *J. Theor. Biol.* 145, 267–286. doi: 10.1016/s0022-5193(05)80131-6

Brand, M. D., Chien, L.-F., and Diolez, P. (1994). Experimental discrimination between proton leak and redox slip during mitochondrial electron transport. *Biochem. J.* 297, 27–29. doi: 10.1042/bj2970027

Bugnard, L. (1934). The relation between total and initial heat in single muscle twitches. *J. Physiol.* 82, 509–519. doi: 10.1113/jphysiol.1934.sp003203

Chapman, B., and Loiselle, D. (2016). Thermodynamics and kinetics of the FoF1-ATPase: application of the probability isotherm. *R. Soc. Open Sci.* 3:150379. doi: 10.1098/rsos.150379

Chapman, J. B., and Gibbs, C. L. (1974). The effect of metabolic substrate on mechanical activity and heat production in papillary muscle. *Cardiovasc. Res.* 8, 656–667. doi: 10.1093/cvr/8.5.656

Dou, Y., Arlock, P., and Arner, A. (2007). Blebbistatin specifically inhibits actin-myosin interaction in mouse cardiac muscle. *Am. J. Physiol.* 293, C1148–C1153.

Drake-Holland, A. J., Elzinga, G., and Noble, M. I. M. (1983). The effect of palmitate and lactate on mechanical performance and metabolism of cat and rat myocardium. *J. Physiol.* 339, 1–15. doi: 10.1113/jphysiol.1983.sp014698

Eisenberg, E., and Hill, T. L. (1979). A cross-bridge model of muscle contraction. *Prog. Biophys. Molec. Biol.* 33, 55–82. doi: 10.1016/0079-6107(79)90025-7

Eisenberg, E., Hill, T. L., and Chen, Y.-D. (1980). Cross bridge model of muscle contraction: quantitative analysis. *Biophys. J.* 29, 195–227. doi: 10.1016/s0006-3495(80)85126-5

Farman, G. P., Tachampa, K., Mateja, R., Cazorla, O., Lacampagne, A., de Tombe, P. P., et al. (2008). Blebbistatin: use as inhibitor of muscle contraction. *Pflügers Arch.* 455, 995–1005. doi: 10.1007/s00424-007-0375-3

Gibbs, C. L., Mommaerts, W. F. H. M., and Ricchiuti, N. V. (1967). Energetics of cardiac contractions. *J. Physiol.* 191, 25–46. doi: 10.1113/jphysiol.1967.sp008235

Griggs, D. M. J., Nagano, S., Lipana, J. G., and Novack, P. (1966). Myocardial lactate oxidation in situ and the effect thereon of reduced coronary flow. *Am. J. Physiol.* 211, 335–340. doi: 10.1152/ajplegacy.1966.211.2.335

Han, J.-C., Taberner, A. J., Kirton, R. S., Nielsen, P. M., Smith, P., Loiselle, D. S., et al. (2009). A unique micromechanocalorimeter for simultaneous measurement of heat rate and force production of cardiac trabeculae carneae. *J. Appl. Physiol.* 107, 946–951. doi: 10.1152/japplphysiol.00549.2009

Han, J.-C., Taberner, A. J., Nielsen, P. M. F., and Loiselle, D. S. (2013). Interventricular comparison of the energetics of contraction of trabeculae carneae isolated from the rat heart. *J. Physiol.* 591, 701–717. doi: 10.1113/jphysiol.2012.242719

Han, J.-C., Taberner, A. J., Tran, K., Goo, S., Nickerson, D. P., Nash, M. P., et al. (2012). Comparison of the Gibbs and Suga formulations of cardiac energetics: the demise of "isoefficiency". *J. Appl. Physiol.* 113, 996–1003. doi: 10.1152/japplphysiol.00693.2011

Han, J.-C., Tran, K., Nielsen, P. M. F., Taberner, A. J., and Loiselle, D. S. (2014). Streptozotocin-induced diabetes prolongs twitch duration without affecting the energetics of isolated ventricular trabeculae. *Cardiovasc. Diabetol.* 13:79. doi: 10.1186/1475-2840-13-79

Hartree, W., and Hill, A. V. (1922). The recovery heat-production in muscle. *J. Physiol.* 56, 367–381. doi: 10.1113/jphysiol.1922.sp002019

Hartree, W., and Hill, A. V. (1928). The energy liberated by an isolated muscle during the performance of work. *Proc. R. Soc. Lond. Ser. B* 104, 1–27. doi: 10.1098/rspb.1928.0062

Hill, A. V. (1911). The position occupied by the production of heat, in the chain of processes constituting a muscular contraction. *J. Physiol. (Lond.)* 42, 1–43. doi: 10.1113/jphysiol.1911.sp001422

Hill, A. V. (1949). The heat of activation and the heat of shortening in a muscle twitch. *Proc. R. Soc. B* 136, 195–211. doi: 10.1098/rspb.1949.0019

Hill, T. L. (1974). Theoretical formalism for the sliding filament model of contraction of striated muscle. *Part I Prog. Biophys. Mol. Biol.* 28, 267–340. doi: 10.1016/0079-6107(74)90020-0

Hill, T. L. (1989). *Free Energy Transduction and Biochemical Cycle Kinetics*. New York, NY: Springer-Verlag, 115.

Hinkle, P. C. (2005). P/O ratios of mitochondrial oxidative phosphorylation. *Biochim. Biophys. Acta (BBA)* 1706, 1–11. doi: 10.1007/978-1-4614-3573-0_1

Johnston, C. M., Han, J.-H., Ruddy, B. P., Nielsen, P. M. F., and Taberner, A. J. (2015). A high-resolution thermoelectric-module-based calorimeter for measuring the energetics of isolated ventricular trabeculae at body temperature. *Am. J. Physiol.* 309, H318–H324. doi: 10.1152/ajpheart.00194.2015

Kabo, G. J., Voitkevich, O. V., Blokhin, A. V., Kohut, S. V., Stepurko, E. N., Paulechka, Y. U., et al. (2013). Thermodynamic properties of starch and glucose. *J. Chem. Thermodyn.* 59, 87–93.

Kammermeier, H., Schmidt, P., and Jüngling, E. (1982). Free energy change of ATP-hydrolysis: a causal factor of early hypoxic failure of the myocardium? *J. Molec. Cell Cardiol.* 14, 267–277. doi: 10.1016/0022-2828(82)90205-x

Khalafbeigui, F., Suga, H., and Sagawa, K. (1979). Left ventricular systolic pressure-volume area correlates with oxygen consumption. *Am. J. Physiol.* 237, H566–H569.

Kovács, M., Tóth, J., Hetényi, C., Málnási-Csizmadia, A., and Sellers, J. R. (2004). Mechanism of blebbistatin inhibition of myosin II. *J. Biol. Chem.* 279, 35557–35563. doi: 10.1074/jbc.m405319200

Levine, F., Kayea, R. V., Wexler, R., Sadvary, D. J., Melick, C., La Scala, J., et al. (2014). Heats of comubstion of fatty acids and fatty acid esters. *J. Am. Oil Chem. Soc.* 91, 235–249.

Loiselle, D. S. (1987). Cardiac basal and activation metabolism. *Basic Res. Cardiol.* 82(Suppl. 2), 37–50. doi: 10.1007/978-3-662-11289-2_4

Loiselle, D. S., Tran, K., Crampin, E., and Curtin, N. A. (2010). Why has reversal of the actin-myosin cross-bridge cycle not been observed experimentally? *J. Appl. Physiol.* 108, 1465–1471. doi: 10.1152/japplphysiol.01198.2009

Lou, F., van der Laarse, W. J., Curtin, N. A., and Woledge, R. C. (2000). Heat production and oxygen consumption during metabolic recovery of white muscle fibres from the dogfish *Scyliorhinus canicula*. *J. Exp. Biol.* 203, 1201–1210.

Mahler, M. (1979). The relationship between initial creatine phosphate breakdown and recovery oxygen consumption for a single Isometric tetanus of the frog sartorius muscle at 20°C. *J. Gen. Physiol.* 73, 159–174. doi: 10.1085/jgp.73.2.159

Mahler, M. (1985). First-order kinetics of muscle oxygen consumption,and an equivalent proportionality between QO2 and phosphorylcreatine level. *J. Gen. Physiol.* 86, 135–165. doi: 10.1085/jgp.86.1.135

Mast, F., and Elzinga, G. (1988). Recovery heat production of isolated rabbit papillary muscle at 20 °C. *Pflügers Arch.* 411, 600–605. doi: 10.1007/bf00580854

Mast, F., Woledge, R. C., and Elzinga, G. (1990). Analysis of thermopile records from contracting isolated cardiac muscle. *Am. J. Physiol.* 259, H1601–H1605.

Mazat, J. P., Ransac, S., Hieske, M., Devin, A., and Rigoulet, M. (2013). Mitochondrial energetic metabolism – some general principles. *Int. Union Biochem. Mol. Biol.* 65, 171–179. doi: 10.1002/iub.1138

Neely, J. R., Liebermeister, H., Battersby, E. J., and Morgan, H. E. (1967). Effect of pressure development on oxygen consumption by isolated rat heart. *Am. J. Physiol.* 212, 804–814. doi: 10.1152/ajplegacy.1967.212.4.804

Patel, H. H., and McDonough, A. A. (2014). Of mice and men: modelling cardiovascular complexity in diabtes. Focus on Mitochondral Inefficiencies and anoxic ATP hydrolysis capacities in diabetic and rat heart. *Am. J. Physiol.* 306, C497–C498.

Pham, T., Loiselle, D., Power, A., and Hickey, A. J. R. (2014). Mitochondrial inefficiencies and anoxic ATP hydrolysis capacities in diabetic rat heart. *Am. J. Physiol. Cell Physiol.* 307, C499–C507. doi: 10.1152/ajpcell.00006.2014

Pham, T., Nisbet, L., Taberner, A., Loiselle, D., and Han, J.-C. (2018). Pulmonary arterial hypertension reduces energy efficiency of right, but not left, rat ventricular trabeculae. *J. Physiol.* 596, 1153–1166. doi: 10.1113/JP275578

Pham, T., Tran, K., Mellor, K. M., Hickey, A., Power, A., Ward, M. L., et al. (2017). Does the intercept of the heat–stress relation provide an accurate estimate of cardiac activation heat? *J. Physiol. (Lond.)* 595, 4725–4733. doi: 10.1113/JP274174

Porter, R. K., and Brand, M. D. (1993). Body mass dependence of H+ leak in mitochondria and its relevance to metabolic rate. *Nature* 362, 628–630. doi: 10.1038/362628a0

Rich, P. R. (2003). The molecular machinery of Keilin's respiratory chain. *Biochem. Soc. Trans.* 31, 1095–1105. doi: 10.1042/bst0311095

Rolfe, D. F. S., and Brand, M. D. (1996). Contribution of mitocondrial proton leak to skeletal muscle respiration and to standard metabolic rate. *Am. J. Physiol.* 271, C1380–C1389.

Salway, J. S. (2004). *Metabolism At a Glance*, 3rd Edn. Oxford, UK: Blackwell Publishing Ltd, 129.

Suga, H. (1979). Total mechanical energy of a ventricle model and cardiac oxygen consumption. *Am. J. Physiol.* 236, H498–H505.

Suga, H. (1990). Ventricular energetics. *Physiol. Rev.* 70, 247–277. doi: 10.1152/physrev.1990.70.2.247

Suga, H., Hayashi, T., Shirahata, M., and Ninomiya, I. (1980). Critical evaluation of left ventricular systolic pressure volume areas as predictor of oxygen consumption rate. *Jpn. J. Physiol.* 30, 907–919. doi: 10.2170/jjphysiol.30.907

Suga, H., Hayashi, T., Shirahata, M., Suehiro, S., and Hisano, R. (1981). Regression of cardiac oxygen consumption on ventricular pressure-volume area in dog. *Am. J. Physiol. Heart Circ. Physiol.* 240, H320–H325.

Suga, H., Igarashi, Y., Yamada, O., and Goto, Y. (1986). Cardiac oxygen consumption and systolic pressure volume area. *Basic Res. Cardiol.* 81(Suppl. 1), 39–50. doi: 10.1007/978-3-662-11374-5_5

Taberner, A. J., Han, J.-C., Loiselle, D. S., and Nielsen, P. M. F. (2011). An innovative work-loop calorimeter for in vitro measurement of the mechanics and energetics of working cardiac trabeculae. *J. Appl. Physiol.* 111, 1798–1803. doi: 10.1152/japplphysiol.00752.2011

Taberner, A. J., Hunter, I. W., Kirton, R. S., Nielsen, P. M. F., and Loiselle, D. S. (2005). Characterization of a flow-through microcalorimeter for measuring the heat production of cardiac trabeculae. *Rev. Sci. Instrum.* 76, 104901–104907.

Taberner, A. J., Zgierski-Johnston, C., Han, J.-C., and Pham, T. (2018). A flow-through infusion calorimeter for measuring muscle energetics: design and performance. *IEEE Trans. Instrum. Meas.* 67, 1690–1699. Accepted: 29/12/2017, doi: 10.1109/tim.2018.2800838

Taegtmeyer, H., Young, M. E., Lopaschuk, G. D., Abel, E. D., Brunengraber, H., Darley-Usmar, V., et al. (2016). Assessing cardiac metabolism: a scientific statement from the American heart association. *Circ. Res.* 118, 1659–1701.

Tran, K., Han, J.-C., Crampin, E. J., Taberner, A. J., and Loiselle, D. S. (2017). Experimental and modelling evidence of shortening heat in cardiac muscle. *J. Physiol.* 595, 6313–6326. doi: 10.1113/JP274680

Tran, K., Han, J.-C., Taberner, A. J., Barrett, C. J., Crampin, E. J., and Loiselle, D. S. (2016). Myocardial energetics is not compromised during compensated hypertrophy in the Dahl salt-sensitive rat model of hypertension. *Am. J. Physiol.* 311, H563–H571.

van der Zwaard, S. (2016). Maximal oxygen uptake is proportional to muscle fiber oxidative capacity -from chronic heart failure patients to professional cyclists. *J. Appl. Physiol.* 121, 636–645. doi: 10.1152/japplphysiol.00355.2016

Weiss, R. G., Gerstenblith, G., and Bottomley, P. A. (2005). ATP flux through creatine kinase in the normal, stressed, and failing human heart. *PNAS* 102, 808–813. doi: 10.1073/pnas.0408962102

Wilkie, D. R. (1974). The efficiency of muscular contraction. *J. Mechanochem. Cell Motil.* 2, 257–267.

Woledge, R. C., Curtin, N. A., and Homsher, E. (1985). *Energetic Aspects of Muscle Contraction*. London: Academic Press, 163–171.

Woledge, R. C., and Reilly, P. J. (1988). Molar enthalpy change for hydrolysis of phosphorylcreatine under conditions in muscle cells. *Biophys. J.* 54, 97–104. doi: 10.1016/s0006-3495(88)82934-5

Conflict of Interest: The authors declare that the research was conducted in the absence of any commercial or financial relationships that could be construed as a potential conflict of interest.

APPENDIX

It is required to determine the Errors of Estimate of *R* and *I*. To that end, we define *f* as the fractional error in each component of *R* and *I*. For example, if $f = 0.1$, then the measurement error of ΔH_{PCr} is expressed as 48 ± 4.8 J mol^{-1}.

The Error of Estimate of η_R is given by:

$$\sqrt{\left(\frac{\partial \eta_R}{\partial r} f \cdot r\right)^2 + \left(\frac{\partial \eta_R}{\partial \Delta G_{ATP}} f \cdot \Delta G_{ATP}\right)^2 + \left(\frac{\partial \eta_R}{\partial \Delta H_{PCr}} f \cdot \Delta H_{PCr}\right)^2}$$

where the nominal values of *r*, ΔG_{ATP}, and ΔH_{PCr} are 1.2, 60, and 48, respectively (see Text).

The Error of Estimate of η_I is given by:

$$\sqrt{\left(\frac{\partial \eta_I}{\partial W} f \cdot W\right)^2 + \left(\frac{\partial \eta_I}{\partial Q} f \cdot Q\right)^2}$$

where the numeric values of W and Q arise from the original data used to construct **Figure 3** and are 1.4625 and 7.6780, respectively (Tran et al., 2016).

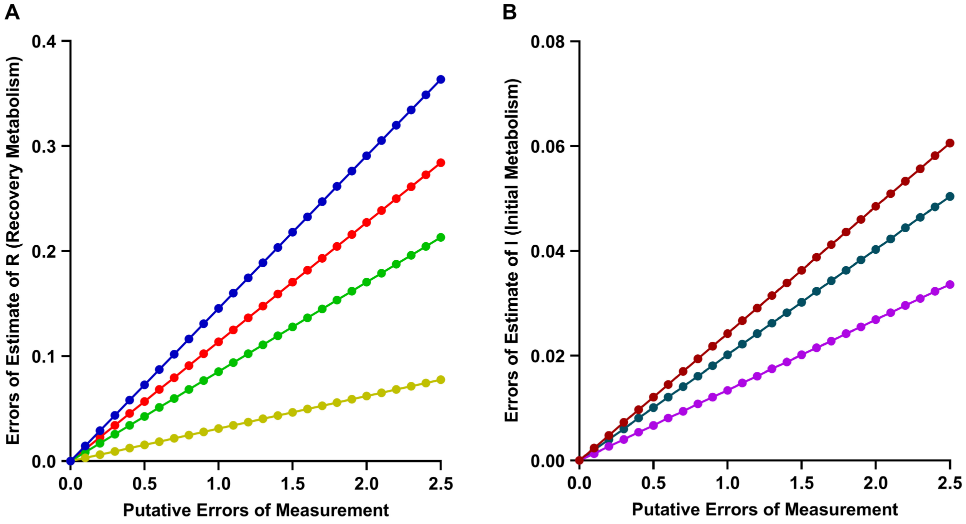

APPENDIX A1 | Relative Errors of Estimate of Recovery Metabolism (R). **(A)** Relative error in Recovery Metabolism attributable singly to *r* (red), ΔG_{ATP} (green), ΔH_{PCr} (orange) and collectively to all three input terms (blue). **(B)** Relative error in Initial Metabolism attributable to Work (purple), Heat (black) and collectively to both (red).

frontiers
in Physiology

ORIGINAL RESEARCH
published: 16 April 2020
doi: 10.3389/fphys.2020.00289

Ischemia Enhances the Acute Stretch-Induced Increase in Calcium Spark Rate in Ventricular Myocytes

Breanne A. Cameron[1]***, Hiroaki Kai***[2]***, Keiko Kaihara***[2]***, Gentaro Iribe***[2,3†] ***and T. Alexander Quinn***[1,4*†]

[1] Department of Physiology and Biophysics, Dalhousie University, Halifax, NS, Canada, [2] Graduate School of Medicine, Dentistry, and Pharmaceutical Sciences, Okayama University, Okayama, Japan, [3] Department of Physiology, Asahikawa Medical University, Asahikawa, Japan, [4] School of Biomedical Engineering, Dalhousie University, Halifax, NS, Canada

Introduction: In ventricular myocytes, spontaneous release of calcium (Ca^{2+}) from the sarcoplasmic reticulum via ryanodine receptors ("Ca^{2+} sparks") is acutely increased by stretch, due to a stretch-induced increase of reactive oxygen species (ROS). In acute regional ischemia there is stretch of ischemic tissue, along with an increase in Ca^{2+} spark rate and ROS production, each of which has been implicated in arrhythmogenesis. Yet, whether there is an impact of ischemia on the stretch-induced increase in Ca^{2+} sparks and ROS has not been investigated. We hypothesized that ischemia would enhance the increase of Ca^{2+} sparks and ROS that occurs with stretch.

Methods: Isolated ventricular myocytes from mice (male, C57BL/6J) were loaded with fluorescent dye to detect Ca^{2+} sparks (4.6 μM Fluo-4, 10 min) or ROS (1 μM DCF, 20 min), exposed to normal Tyrode (NT) or simulated ischemia (SI) solution (hyperkalemia [15 mM potassium], acidosis [6.5 pH], and metabolic inhibition [1 mM sodium cyanide, 20 mM 2-deoxyglucose]), and subjected to sustained stretch by the carbon fiber technique (∼10% increase in sarcomere length, 15 s). Ca^{2+} spark rate and rate of ROS production were measured by confocal microscopy.

Results: Baseline Ca^{2+} spark rate was greater in SI (2.54 ± 0.11 sparks·s^{-1}·100 μm^{-2}; $n = 103$ cells, $N = 10$ mice) than NT (0.29 ± 0.05 sparks·s^{-1}·100 μm^{-2}; $n = 33$ cells, $N = 9$ mice; $p < 0.0001$). Stretch resulted in an acute increase in Ca^{2+} spark rate in both SI (3.03 ± 0.13 sparks·s^{-1}·100 μm^{-2}; $p < 0.0001$) and NT (0.49 ± 0.07 sparks·s^{-1}·100 μm^{-2}; $p < 0.0001$), with the increase in SI being greater than NT (+0.49 ± 0.04 vs. +0.20 ± 0.04 sparks·s^{-1}·100 μm^{-2}; $p < 0.0001$). Baseline rate of ROS production was also greater in SI (1.01 ± 0.01 normalized slope; $n = 11$, $N = 8$ mice) than NT (0.98 ± 0.01 normalized slope; $n = 12$, $N = 4$ mice; $p < 0.05$), but there was an acute increase with stretch only in SI (+12.5 ± 2.6%; $p < 0.001$).

Conclusion: Ischemia enhances the stretch-induced increase of Ca^{2+} sparks in ventricular myocytes, with an associated enhancement of stretch-induced ROS production. This effect may be important for premature excitation and/or in the development of an arrhythmogenic substrate in acute regional ischemia.

Keywords: calcium, ischemia, myocytes, reactive oxygen species, stretch, ventricle

OPEN ACCESS

Edited by:
Remi Peyronnet,
University of Freiburg, Germany

Reviewed by:
Alexandra Zahradnikova,
Slovak Academy of Sciences, Slovakia
Wayne Rodney Giles,
University of Calgary, Canada

****Correspondence:***
T. Alexander Quinn
alex.quinn@dal.ca

† These authors have contributed equally to this work

Specialty section:
This article was submitted to Cardiac Electrophysiology, a section of the journal Frontiers in Physiology

Received: *11 October 2019*
Accepted: *16 March 2020*
Published: *16 April 2020*

Citation:
Cameron BA, Kai H, Kaihara K, Iribe G and Quinn TA (2020) Ischemia Enhances the Acute Stretch-Induced Increase in Calcium Spark Rate in Ventricular Myocytes. Front. Physiol. 11:289. doi: 10.3389/fphys.2020.00289

INTRODUCTION

In cardiac myocytes, calcium (Ca^{2+}) sparks represent the elementary release of Ca^{2+} from the sarcoplasmic reticulum (SR, the cell's primary Ca^{2+} store) via ryanodine receptors (RyR), and thus play a critical role in intracellular Ca^{2+} handling. The frequency of Ca^{2+} sparks is determined by RyR open probability, which under normal conditions is primarily influenced by the free intracellular Ca^{2+} concentration ($[Ca^{2+}]_i$) and the concentration of Ca^{2+} in the SR (Cheng and Lederer, 2008). In pathological settings, an elevation in Ca^{2+} spark rate, due to increased $[Ca^{2+}]_i$ or altered RyR function [secondary to metabolic, adrenergic, or genetic changes, or to channel phosphorylation, oxidation, or nitrosylation (Prosser et al., 2010)], has been implicated in the induction of aberrant Ca^{2+} waves and deadly cardiac arrhythmias (Ter Keurs and Boyden, 2007).

Recently, it has been shown that stretch of single ventricular myocytes can also acutely increase Ca^{2+} spark rate (Iribe et al., 2009), which has been suggested to perhaps "tune" excitation-contraction coupling in the whole heart (Prosser et al., 2013a), thus contributing to the Frank Starling mechanism (Quinn and Kohl, 2016) and acting to maintain contractile homogeneity across the ventricles by normalizing inter-cellular contractile force (Cannell, 2009; Quinn, 2015). Follow up studies have shown that the acute stretch-induced increase in Ca^{2+} sparks results from a microtubule-dependent increase in reactive oxygen species (ROS) production by NADPH oxidase 2 (NOX2) with stretch, which has been termed X-ROS (Prosser et al., 2011). Further, Ca^{2+} spark rate and X-ROS production have been shown to be enhanced by cyclic stretch (as occurs during filling with each heartbeat) and graded by stretch amplitude and frequency, which may additionally tune the mechanical activity and redox state of cardiac myocytes to changes in physiological demand (Prosser et al., 2013b).

An acute stretch-induced increase in Ca^{2+} sparks may be particularly relevant in disease states associated with heterogeneous changes in the heart's mechanical activity (Quinn, 2014). In patients suffering from acute regional ischemia, there is stretch of ischemic tissue, with the magnitude of stretch relating to the prevalence of ventricular fibrillation (Hirche et al., 1987; Barrabes et al., 1998, 2002, 2013, 2017). Moreover, there is a correlation between wall motion abnormalities and arrhythmia incidence in ischemia (Califf et al., 1978; Siogas et al., 1998), with ectopic excitation often originating from regions where systolic segment lengthening occurs (Lab, 1989; Coronel et al., 2002). In experimental models of non-uniform contraction, on the other hand, there is an increase in ROS production localized to stretched regions, which results in the activation of Ca^{2+} waves (Miura et al., 2018). Thus, in ischemia, a stretch-induced increase in Ca^{2+} sparks may act as a trigger, or contribute to the substrate, for the associated arrhythmias (Janse and Wit, 1989).

Myocardial ischemia is also associated with an increase in $[Ca^{2+}]_i$ (Baumeister and Quinn, 2016), leading to a rise in Ca^{2+}-calmodulin-dependent protein kinase II (CaMKII) activity (Mattiazzi et al., 2015b), which increases phosphorylation of RyR and the frequency of Ca^{2+} sparks (Maier and Bers, 2007). Computational modeling has suggested that an elevation in $[Ca^{2+}]_i$ associated with hyperkalemia-induced membrane depolarization, along with a consequential reduction in NCX-mediated Ca^{2+} efflux and an increase in SR Ca^{2+} content may also contribute to an increase in Ca^{2+} spark rate in ischemia (Sato et al., 2014). Ca^{2+} spark rate is further increased in ischemia by an increase in ROS (Raedschelders et al., 2012; Köhler et al., 2014), including a contribution of increased NOX2 activity (Donoso et al., 2014), which increases the open probability of RyR by *S*-glutathionylation (Sánchez et al., 2005), and sensitizes RyR to cytoplasmic Ca^{2+} (Belevych et al., 2009; Zhang et al., 2013). In fact, an increased Ca^{2+} spark rate has been shown to be a contributor to the elevation in $[Ca^{2+}]_i$ in ischemia (Mattiazzi et al., 2015a). At the same time, ischemia is associated with a reduction of the key anti-oxidant glutathione (Ferrari et al., 1985; Poluektov et al., 2019), which computational modeling has suggested may increase the effects of stretch-induced ROS on Ca^{2+} sparks by limiting cellular reducing capacity through a decrease in glutathione, resulting in a consequential increase in the open probability of RyR during stretch (Limbu et al., 2015). This combination of effects on RyR activity and its modulators suggests that ischemia may alter the response of Ca^{2+} sparks to stretch, yet the effect of ischemia on the stretch-induced increase in Ca^{2+} spark rate has not been investigated.

We hypothesized that in simulated ischemic conditions, there would be an enhancement of the stretch-induced increase in Ca^{2+} sparks, with an associated potentiation of the stretch-induced increase in ROS production. Single ventricular myocytes isolated from mice were subjected to a single controlled stretch using carbon fibers in normal or simulated ischemic conditions (Iribe et al., 2009). Fluorescent confocal microscopy was used to monitor $[Ca^{2+}]_i$ or ROS, to assess the effect of stretch on Ca^{2+} spark rate and ROS production. Our results demonstrate that ischemia enhances the stretch-induced increase of Ca^{2+} spark rate in isolated ventricular myocytes, with an associated enhancement of stretch-induced ROS production. This enhancement of the stretch-induced increase in Ca^{2+} sparks may be a contributing factor to the lethal arrhythmias that occur in the setting of ischemia.

MATERIALS AND METHODS

Experiments were performed in accordance with the Guidance Principles for the Care and Use of Animals established by the Council of the Physiological Society of Japan. The experimental protocol was reviewed and accepted by the Animal Subjects Committee of Okayama University Graduate School of Medicine, Dentistry, and Pharmaceutical Sciences. Details of experimental protocols have been reported following the Minimum Information about a Cardiac Electrophysiology Experiment (MICEE) reporting standard (Quinn et al., 2011).

Abbreviations: Ca^{2+}, calcium; CaMKII, Ca^{2+}-calmodulin-dependent protein kinase II; DCF, 2′,7′-dichlorofluorescein diacetate; $[Ca^{2+}]_i$, free intracellular calcium concentration; NOX2, NADPH oxidase 2; NT, normal Tyrode; ROS, reactive oxygen species; RyR, ryanodine receptors; SI, simulated ischemia; SEM, standard error of the mean; SR, sarcoplasmic reticulum; X-ROS, NOX2-dependent ROS.

Ventricular Myocyte Isolation

Ventricular myocytes were isolated from mice as previously described (Iribe et al., 2013, 2014). Mice (male C57BL/6J, 8–12 weeks old) were administered an intraperitoneal injection of heparin sodium (100 I.U.; Wockhardt, Mumbai, India). After 30 min, surgical anesthesia was induced by inhalation of isoflurane (IsoFlu; Abbott Laboratories, Abbott Park, USA) followed by rapid cardiac excision, aortic cannulation, and Langendorff perfusion for enzymatic cell isolation. Hearts were perfused at a rate of 4 mL/min for 3 min with Ca^{2+}-free solution (composition in mM: 128 NaCl, 2.6 KCl, 1.18 $MgSO_4$, 1.18 KH_2PO_4, 10 HEPES, 20 Taurine, 11 Glucose; pH 7.47 adjusted with NaOH), followed by 5-6 min of perfusion with 30 mL of Ca^{2+}-free solution that included 6 mg of the enzyme blend Liberase TM Research Grade (Roche, Basel, Switzerland). The ventricles were harvested by cutting along the atrioventricular border, and then cut into 1–2 mm^3 cubes and gently agitated in oxygenated Ca^{2+}-free solution. The supernatant containing ventricular cells was collected, the remaining tissue was resuspended in fresh Ca^{2+}-free solution, and the above procedure was repeated in triplicate. The collected supernatant was passed through a nylon mesh and centrifuged at 15 × g for 3 min, followed by resuspension of the resulting cell pellet in normal Tyrode's solution (NT, composition in mM: 140 NaCl, 5.4 KCl, 1.8 $CaCl_2$, 1 $MgCl_2$, 5 HEPES, 11 Glucose; pH 7.4 adjusted with NaOH). Cells were kept at room temperature (∼22°C) until ready to be used.

Single Cell Stretch

Two groups of quiescent ventricular myocytes were considered: a control group (exposed to NT) and a simulated ischemia (SI) group [exposed to an ischemic solution containing [in mM]: 140 NaCl, 15 KCl, 1.8 $CaCl_2$, 1 $MgCl_2$, 10 HEPES, 1 NaCN, 20 2-deoxyglucose, and with pH adjusted to 6.5 with NaOH (Murata et al., 2001; Khokhlova et al., 2017)], which mimicked the ∼30 min time point of ischemia (phase 1b) through hyperkalemia [15 mM extracellular potassium], extracellular acidosis [pH 6.5], and metabolic inhibition (block of oxidative phosphorylation with 1 mM NaCN and inhibition of anaerobic glycolysis with 20 mM 2-deoxyglucose). Within a 30 min window from the beginning of exposure to SI solution, healthy cells (rod-shaped with clear striations, an intact membrane with no signs of blebbing, and no spontaneous intracellular Ca^{2+} waves before stretch) were subjected to a controlled, axial stretch at a single time point using the carbon fiber technique, as has been previously described for axial stretch of single ventricular myocytes (Iribe et al., 2007, 2009). Cells were placed on coverslips coated with poly-2-hydroxyethyl methacrylate (poly-HEMA; Sigma-Aldrich, Tokyo, Japan) to prevent cellular adhesion. Carbon fibers (10 μm in diameter) mounted in glass capillaries that adhere to isolated cells through biophysical interactions (Peyronnet et al., 2017) were attached to either end of an individual cell. For experiments examining the effect of stretch on Ca^{2+} sparks, one "compliant" (1.2 mm) and one "stiff" (0.6 mm) carbon fiber were used, while for the ROS experiments two compliant (1.2 mm) carbon fibers were used (Tsukuba Material Information Laboratory, Tsukuba, Japan). Tri-axial positioning of the carbon fibers was performed by custom-made three-axis hydraulic manipulators (Narishige, Tokyo, Japan), with the compliant carbon fibers mounted on piezo-electric translators (P-621.1 CL; Physik Instrumente, Karlsruhe, Germany) and the stiff carbon fiber held stationary. While the unidirectional stretch using one stiff stationary and one compliant translating carbon fiber was sufficient for the Ca^{2+} spark experiments, this produced too much motion of the cell under the detector during stretch for ROS production to be measured. The bi-directional stretch using two compliant translating carbon fibers reduced the level of cell motion, so allowed for more accurate measurements of ROS. Whole-cell axial stretch was applied by a 20 μm increase in the separation of the piezo-electric translators and held for 15 s, controlled by custom-written LabView software and a fast analog-to-digital converter (NI USB-6259; National Instruments, Austin, USA), which has been shown previously to result in a ∼10% increase in sarcomere length (Iribe et al., 2017).

Ca^{2+} Spark Measurement

Detection of Ca^{2+} sparks in ventricular myocytes was performed similar to a previously described technique (Iribe et al., 2009). Cells were incubated with Fluo-4-AM (4.6 μM, 10 min; Invitrogen, Carlsbad, California). Confocal images (XY, 30 fps, CSU-X1; Yokogawa, Tokyo, Japan) were obtained by excitation with a 488 nm laser and fluorescence emission detection above 505 nm. Ca^{2+} sparks were detected in the cellular region between the carbon fibers using custom LabVIEW software. Ca^{2+} spark rate was calculated by counting the number of sparks detected over 5 s, excluding duplicate counts by subtracting single-coordinate spark fluorescence that exceeded one contiguous frame, and was normalized by area (to control for variability in cell size) and reported as $sparks \cdot s^{-1} \cdot 100\ \mu m^{-2}$. The rate of image acquisition limited additional measurements of spark dynamics. Ca^{2+} spark rate was measured over three 5 s intervals: immediately before stretch, during stretch (immediately after its application), and immediately following complete release of stretch. Any cell in which an intracellular Ca^{2+} wave or synchronized SR Ca^{2+} release occurred during the analysis window was excluded (8% of cells in both conditions).

ROS Measurement

The rate of intracellular ROS production was measured using 2′,7′-dichlorofluorescein diacetate (DCF) as previously described (Iribe et al., 2017). Cells were loaded with DCF (1 μm, 20 min; Life Technologies Japan, Tokyo, Japan) and confocal images (FV1000; Olympus Corporation, Tokyo, Japan) were captured (XY, 1.27 fps) by excitation with a 488 nm laser and fluorescence emission detection above 500 nm. As DCF fluorescence is known to be artificially amplified by continuous light exposure (Prosser et al., 2011, 2013b), a low laser intensity was used. The rate of ROS production was measured in the cellular region between the carbon fibers with custom LabView software as the slope of the increase in fluorescence over three 15 s intervals: immediately before stretch, during stretch, and immediately following complete release of stretch.

Statistics

Data are presented as mean ± standard error of the mean (SEM). For the Ca^{2+} spark rate measurements, as the data was not normally distributed, Kruskal-Wallis test with *pot hoc* Dunn's multiple comparisons test was used to assess Ca^{2+} spark rate over time, and Wilcoxon paired or Mann-Whitney unpaired tests were used for comparison of group means. For the ROS production measurements, two-tailed paired or unpaired Student's *t*-tests were used for comparison of group means. A $p < 0.05$ was considered statistically significant.

RESULTS

Effect of Stretch on Ca^{2+} Spark Rate

Figure 1 shows surface plots of Fluo-4 fluorescence derived from a line of pixels across the confocal images of a cell, demonstrating the effect of stretch on the occurrence of Ca^{2+} sparks in single mouse ventricular myocytes exposed to either NT (**Figure 1A**) or SI (**Figure 1B**; movies of the fluorescence in the represented cells are presented in **Supplemental Videos 1, 2**). Ca^{2+} sparks occur more frequently in SI than NT and acutely increase in both groups during stretch, with a return to normal levels after stretch release.

Figure 2 shows the Ca^{2+} spark rate before, during, and after stretch, and the change with stretch, in cells of the NT or SI group over the 30 min measurement window. Cells were subjected to stretch at a single time point and values from all cells stretched within 5 min intervals were averaged. There was no effect of time on Ca^{2+} spark rate (**Figure 2A**) or its change with stretch (**Figure 2B**) in the NT group, as values before, during, and after stretch and the change with stretch did not vary over the 30 min. There was variation of Ca^{2+} spark rate over 30 min in the SI group (**Figure 2C**; $p < 0.05$ by Kruskal-Wallis test), however values only differed between the 6-10 min and 26-30 min time points ($p < 0.01$, by *post-hoc* Dunn's multiple comparisons test), and there was no effect of time on the change in Ca^{2+} spark rate with stretch (**Figure 2D**). Thus, as the change in Ca^{2+} spark rate with stretch did not vary over the 30 min experimental window in either group, all cells in each group were averaged for further analysis.

Figure 3 shows the effect of stretch on Ca^{2+} spark rate averaged across all cells in the NT ($n = 33$ cells, $N = 9$ mice) or SI ($n = 103$ cells, $N = 10$ mice) group. The average Ca^{2+} spark rate was higher in SI than NT (**Figure 3A**), both at baseline (2.54 ± 0.11 vs. 0.29 ± 0.05 sparks·s^{-1}·100 µm^{-2}, $p < 0.0001$ by Mann-Whitney unpaired test) and during stretch (3.03 ± 0.13 vs. 0.49 ± 0.07 sparks·s^{-1}·100 µm^{-2}; $p < 0.0001$). With stretch, Ca^{2+} spark rate was acutely increased in both NT ($+0.20 \pm 0.04$ sparks·s^{-1}·100 µm^{-2}; $p < 0.0001$ by Wilcoxon paired test) and SI ($+0.49 \pm 0.04$ sparks·s^{-1}·100 µm^{-2}; $p < 0.0001$), with a larger increase in Ca^{2+} spark rate with stretch in SI compared to NT ($p < 0.0001$; **Figure 3B**).

Effect of Stretch on ROS Production

To determine whether the observed enhancement of the stretch-induced increase in Ca^{2+} sparks in SI compared to NT is associated with a concomitant enhancement of the stretch-induced increase in ROS production that has been shown by others (Prosser et al., 2011), cells were loaded with DCF to assess the rate of ROS production before and during stretch (measured as the slope of the change in DCF fluorescence over time). **Figure 4** shows the effect of stretch on the rate of ROS production in cells exposed to NT ($n = 12$ cells, $N = 4$ mice) or SI ($n = 11$ cells, $N = 8$ mice). The rate of ROS production was greater in SI than in NT both at baseline (1.01 ± 0.01 vs. 0.98 ± 0.01 normalized slope; $p < 0.05$ by two-tailed unpaired Student's *t*-test) and during stretch (1.14 ± 0.03 vs. 1.00 ± 0.03; $p < 0.01$). With stretch, the rate of ROS production was acutely increased in SI ($+12.5 \pm 2.6\%$; $p < 0.001$ by two-tailed paired Student's *t*-test), but not in NT ($+2.1 \pm 2.7\%$).

DISCUSSION

This study sought to determine the effect of ischemia on the increase in Ca^{2+} spark rate and ROS production that occurs with stretch in ventricular myocytes. It was found that in simulated ischemic conditions, the basal level of both Ca^{2+} spark rate and ROS production were greater than in control, and that the increase in spark rate with stretch was enhanced in ischemic conditions. The difference in the response of Ca^{2+} spark rate to stretch represents a potential contributing mechanism to aberrant Ca^{2+} handling in ischemia and could be a source of premature excitation and the arrhythmogenic substrate in this pathological state.

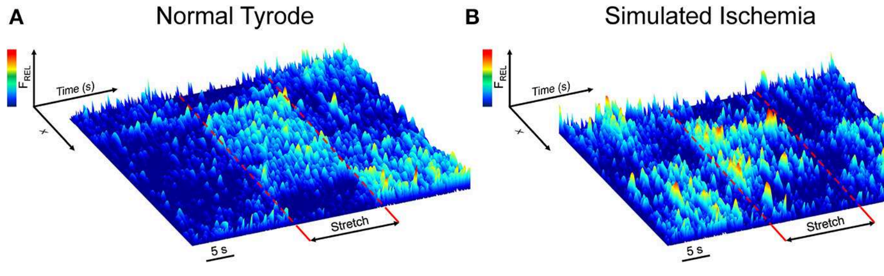

FIGURE 1 | Effect of axial stretch on the occurrence of calcium sparks in single quiescent mouse ventricular myocytes exposed to either normal Tyrode **(A)** or simulated ischemia **(B)**. Fluorescence surface plots are derived from a line of pixels across the cell, providing a temporal depiction of the relative Fluo-4 fluorescence (F_{REL}) before, during, and after 15 s of stretch (dashed red lines). Movies of the cells are provided as **Supplemental Videos 1, 2**.

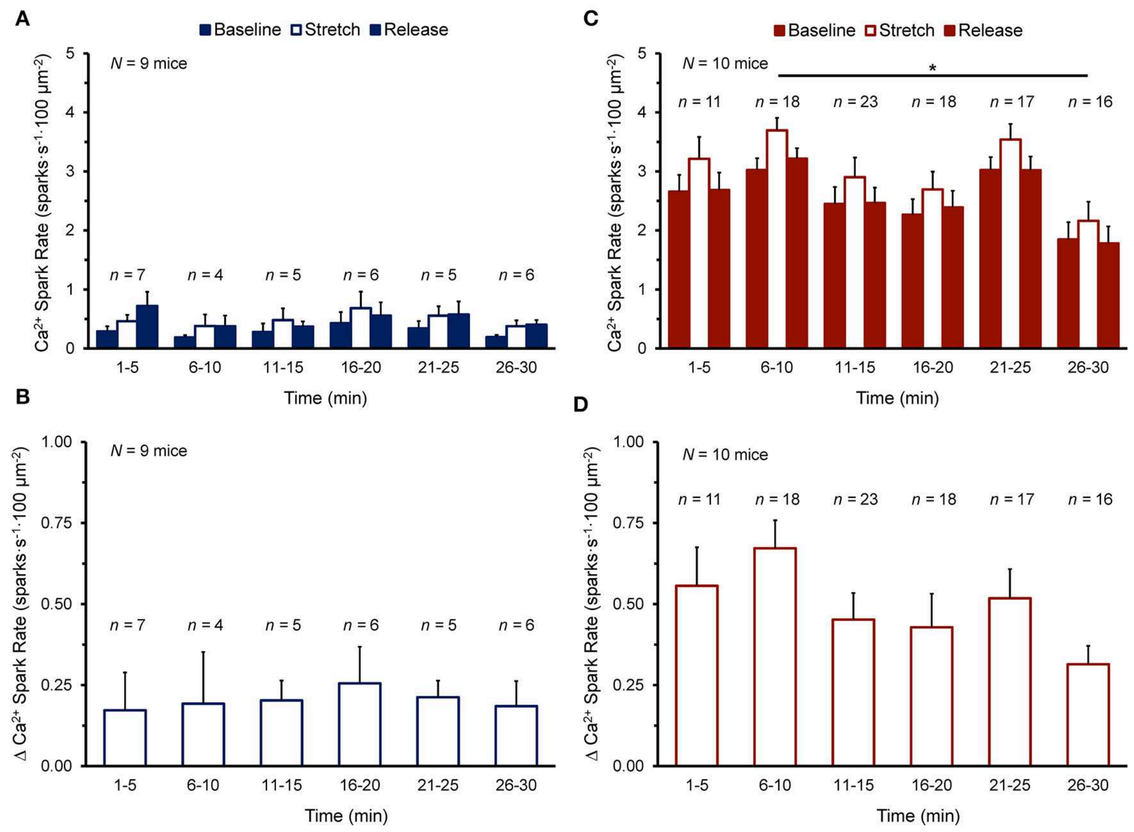

FIGURE 2 | Effect of duration of exposure of quiescent mouse ventricular myocytes to normal Tyrode **(A,B)** or simulated ischemia solution **(C,D)** on calcium (Ca^{2+}) spark rate before (Baseline), during (Stretch), and after stretch (Release) **(A,C)**, as well as the change in Ca^{2+} spark rate with stretch [Δ Ca^{2+} Spark Rate; **(B,D)**] over the 30 min measurement window. Cells were subjected to stretch at a single time point and values from all cells stretched within 5 min intervals were averaged (presented as mean ± SEM). *N* indicates the number of mice; *n* indicates the number of cells. $^{*}p < 0.01$ by *post-hoc* Dunn's multiple comparisons test.

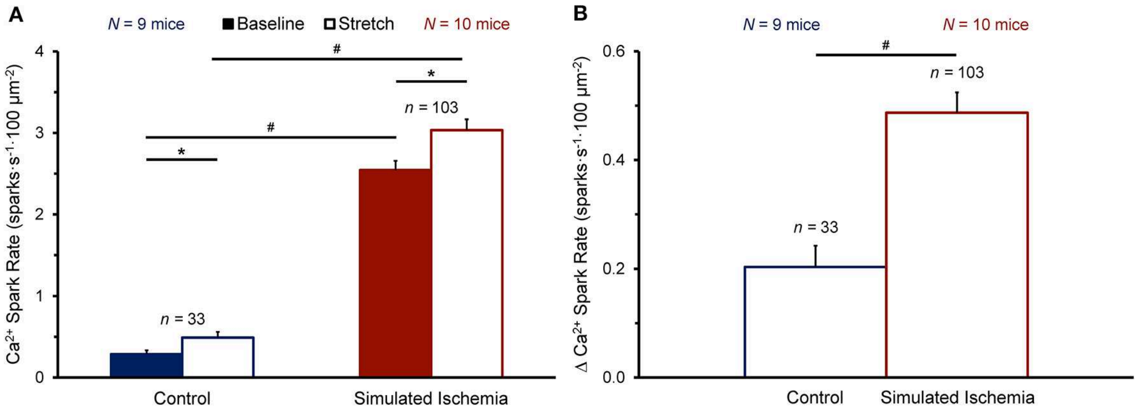

FIGURE 3 | Effect of stretch of quiescent mouse ventricular myocytes on calcium (Ca^{2+}) spark rate before (Baseline) and during stretch (Stretch; **A**) and the change in Ca^{2+} spark rate with stretch (Δ Ca^{2+} Spark Rate; **B**) averaged across all cells exposed to either normal Tyrode or simulated ischemia solution (presented as mean ± SEM). $^{*}p < 0.0001$ by Wilcoxon paired test; $^{\#}p < 0.0001$ by Mann-Whitney unpaired test. *N* indicates the number of mice; *n* indicates the number of cells.

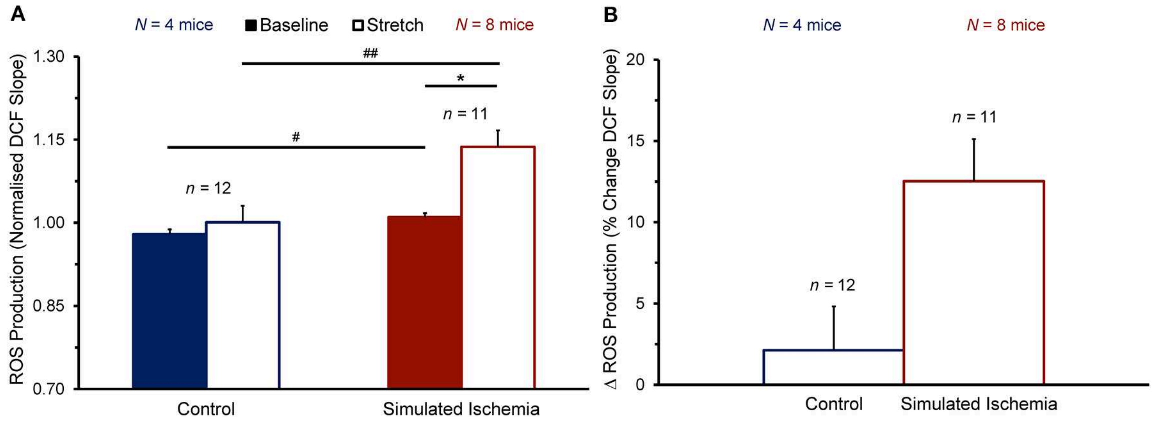

FIGURE 4 | Effect of stretch of quiescent mouse ventricular myocytes on the rate of reactive oxygen species (ROS) production (quantified as the slope of the change in 2′,7′-dichlorofluorescein diacetate, DCF, fluorescence over time) before (Baseline) and during stretch (Stretch; **A**) and the change in ROS production with stretch (Δ ROS Production; **B**) averaged across all cells exposed to either normal Tyrode or simulated ischemia solution (presented as mean ± SEM). $^{*}p < 0.001$ by two-tailed, paired Student's *t*-test; $^{\#}p < 0.05$ and $^{\#\#}p < 0.01$, by two-tailed, unpaired Student's *t*-test. *N* indicates the number of mice; *n* indicates the number of cells.

Mechanisms of Ventricular Arrhythmias in Acute Regional Ischemia

Acute regional ischemia is a major cause of sudden cardiac death (Zipes and Wellens, 1998; Rubart and Zipes, 2005), with lethal ventricular arrhythmias accounting for 80% of all cases without a prior history of heart disease (Myerburg et al., 1997). Arrhythmias in the first hour of ischemia [phase 1, during which ~50% of all sudden cardiac deaths occur (Di Diego and Antzelevitch, 2011)] are both focal and re-entrant in nature, resulting from a combination of ischemia-induced changes in electrical, mechanical, and biochemical properties of the myocardium (Janse and Wit, 1989; Carmeliet, 1999).

The arrhythmogenic changes in ventricular myocyte electrophysiology during acute ischemia have been extensively studied (Janse and Wit, 1989; Carmeliet, 1999). The most prominent effects include: (i) a decrease in ATP, pH, and the fast sodium and L-type Ca^{2+} currents; (ii) an increase in intracellular Ca^{2+} and sodium concentrations; and (iii) activation of the ATP-sensitive potassium current. At the same time, extracellular potassium concentration and catecholamine levels are also increased. All of the above changes (except for the increase in catecholamine levels), which have been shown to result in arrhythmogenic alterations of the ventricular action potential, including: (i) depolarization of the resting membrane potential; (ii) a decrease in the action potential upstroke, amplitude, and duration; and (iii) an increase in the effective refractory period, were simulated or present in the current study.

Other, poorly understood cell-level effects are thought to contribute to ventricular arrhythmias in acute ischemia, including cell stretch and changes in intracellular Ca^{2+} handling. The acute phase of ischemia is associated with tissue stretch, which may result in ectopic excitation (Lab, 1989; Coronel et al., 2002) and whose magnitude correlates with the prevalence of ventricular fibrillation (Hirche et al., 1987; Barrabes et al., 1998, 2002, 2013, 2017). At the same time, acute ischemia causes an increase in the frequency of Ca^{2+} sparks that contributes to an increase in $[Ca^{2+}]_i$ (Mattiazzi et al., 2015a). The increase in $[Ca^{2+}]_i$ in ischemia is thought to be arrhythmogenic (Baumeister and Quinn, 2016) by driving excitatory after-depolarizations (Billman et al., 1991; Xing and Martins, 2004; Wu et al., 2011). Thus, if links exist between cell stretch and altered Ca^{2+} handling in ischemia, they could represent important mechanisms for arrhythmogenesis.

Effects of Stretch on Ca^{2+} Sparks

The frequency of Ca^{2+} sparks is determined by RyR open probability, which is strongly influenced by $[Ca^{2+}]_i$ and the concentration of Ca^{2+} in the SR (Cheng and Lederer, 2008). Previous studies have shown that in healthy conditions, stretch acutely increases the frequency of Ca^{2+} sparks in ventricular cells (Iribe et al., 2009), which is the result of an increase in NOX2-dependent ROS production (X-ROS), with microtubules acting as the mechano-transducers (Prosser et al., 2011). Interestingly, Ca^{2+} spark rate and X-ROS production are further increased by cyclic stretch (compared to sustained stretch), which is more similar to what occurs in the regularly beating heart (Prosser et al., 2013b). This response is also graded by the amplitude and frequency of stretch (Prosser et al., 2013b), so may help match the $[Ca^{2+}]_i$ and redox state of cardiac myocytes to changes in physiological demand.

In many diseases, there is an increase in the frequency of Ca^{2+} sparks, often due to an increase in $[Ca^{2+}]_i$ or altered RyR function [relating to cellular changes such as membrane depolarization (Sato et al., 2014) or increased ROS (Prosser et al., 2010)], which has the potential to lead to intracellular Ca^{2+} waves and cardiac arrhythmias (Ter Keurs and Boyden, 2007). This includes diseases in which there are changes in cardiac mechanics resulting in regions of tissue stretch (Quinn, 2014). For instance, in an experimental model of non-uniform myocardial contraction, it has been shown that there is an increase in ROS production localized to stretched regions, which can result in intracellular Ca^{2+} waves (Miura et al., 2018). Interestingly, in a similar experimental model, it has been shown that Ca^{2+} waves in fact relate to the rapid shortening of muscle immediately after a period of stretch (ter Keurs et al., 2006), due to a surge in intracellular Ca^{2+} as it dissociates from troponin-C (Wakayama et al., 2005). This Ca^{2+} surge is precipitated by a length-dependent increase in the affinity of troponin-C for Ca^{2+} (Allen and Kentish, 1988) and can result in after-depolarizations, premature excitation (Miura et al., 2008), and sustained arrhythmias (Miura et al., 2010).

In the present study, we observed an acute increase in basal Ca^{2+} spark rate in ischemia, which was further increased with stretch. This increase in Ca^{2+} spark rate with stretch was greater than that seen under normal conditions, representing an enhancement of the stretch-induced effect. Further, there was a higher baseline level of ROS production in ischemia compared to control, and an increase in ROS production with stretch in ischemia, which may in part account for the higher baseline levels of Ca^{2+} sparks and the increase with stretch in ischemia (although the difference in baseline level of ROS production between ischemia and control was small [3%], so may in fact not be physiologically significant).

While it is speculated that the observed enhancement of the stretch-induced increase in Ca^{2+} sparks in ischemic conditions may represent an arrhythmogenic mechanism, we observed few stretch-induced intracellular Ca^{2+} waves or synchronized SR Ca^{2+} releases, and the amount did not differ between ischemic and control cells (1 vs. 0% occurrence of intracellular Ca^{2+} waves; 7 vs. 5% occurrence of synchronized SR Ca^{2+} releases).

Mechanisms of Enhanced Stretch Effects in Ischemic Conditions

The enhancement of the increase in Ca^{2+} sparks and ROS with stretch in ischemia may result from effects on various factors involved in the stretch-induced response (Ward et al., 2014; Joca et al., 2020). Ischemia may increase the mechano-sensitivity or responsiveness of NOX2, and mechano-transduction may be increased due to changes in microtubule properties, cell stiffness, or mechano-sensitive channel function (including transient receptor potential channels), resulting in greater X-ROS production with stretch. Alternatively (or additionally), rather than an increase in the production of X-ROS, its effect on Ca^{2+} sparks could be increased by a reduction of anti-oxidants in the cell [as suggested by computational modeling (Limbu et al., 2015)], as the key anti-oxidant glutathione is reduced in ischemia (Ferrari et al., 1985). At the same time, there could be a contribution of emergent, X-ROS-independent mechano-transduction pathways (e.g., via direct effects relating to the baseline increase in $[Ca^{2+}]_i$ or ROS with ischemia on mechano-sensitive ion channel activity, CaMKII activation, RyR sensitivity to Ca^{2+}, or mitochondrial-derived Ca^{2+} and ROS production). These possibilities warrant further investigation, as they may represent novel anti-arrhythmic targets in ischemia.

Comparison of Results to Previous Studies

In our study, under normal conditions we observed an increase in the Ca^{2+} spark rate with axial stretch of isolated mouse ventricular myocytes, as has been previously reported by others in both rat (Iribe et al., 2009; Prosser et al., 2011) and mouse (Prosser et al., 2011). We did not, however, see an associated increase in ROS production with stretch (∼2%; measured as the change in the slope of DCF fluorescence), as shown in other studies (∼70% for rat, ∼40% for mouse) (Prosser et al., 2011). In ischemic conditions we did see a statistically significant stretch-induced increase in ROS production (∼13%), along with a greater increase in Ca^{2+} spark rate than control (suggesting the increase in ROS might be involved), yet this increase was still much lower than the previously reported control values. The reason for this discrepancy is unclear. It may relate to methodological differences or differences in data handling. Our experiments involved the stretch of ventricular myocytes using 10 μm diameter compliant carbon fibers, which stick to the cells through biophysical interactions (Peyronnet et al., 2017). The previous work from Prosser et al. (2011) used 20 μm stiff glass rods adhered to the cells with a biological adhesive (Myotak, composed of laminin, entactin, heparin sulfate proteoglycan, gentamicin, Dulbecco's Modified Eagle Medium, collagen IV, Alexa Fluor-647 conjugated to bovine serum albumin, and an inert alumina silica aggregate with a diameter of 1 μm, dissolved in 100 μM BSA). While it was reported that none of these components are harmful to cells (as normal cell morphology and robust contractions are maintained for up to 2 h following cell attachment), it could be there are unappreciated effects of Myotak on ROS production, which could account for the greater effect in the previous work. Alternatively, differences in imaging methods (for instance whole cell confocal measurements in the current study vs. line scans in the previous report) or data analysis (such as measurement of DCF fluorescence slope by fitting a linear relation across the entire stretch period vs. the peak DCF slope extracted from a polynomial fit) might also be involved.

Potential Limitations of the Current Study

In the current study, ischemia was simulated by a solution which mimicked the ∼30 min time point of ischemia (phase 1b), including hyperkalemia, acidosis, and metabolic inhibition. Previous studies that exposed isolated ventricular myocytes to simulated ischemic conditions have used a similar approach but have simulated hypoxia by the use of a 90% nitrogen-10% carbon dioxide gas phase directed over the cell chamber (Cordeiro et al., 1994; O'Brien et al., 2008) or by bubbling the cell chamber with nitrogen (Tang et al., 2012) to displace oxygen from the solution. These techniques, however, are not compatible with the carbon fiber technique or our fluorescence imaging, as they cause mechanical disruption and motion artifact. As such, we simulated hypoxia with NaCN, which blocks oxidative phosphorylation, resulting in a lack of ATP generation, as reported previously by others (Murata et al., 2001; Khokhlova et al., 2017). One concern with this approach might be the effect of NaCN on cell viability. While we found that a majority of the cells exposed to our SI solution remained viable over the 30 min experimental period, to mitigate any concern that cells used were unhealthy, we included only myocytes that appeared rod-shaped with clear striations, had an intact membrane with no signs of blebbing, and displayed no spontaneous intracellular Ca^{2+} waves.

Temperature has been shown previously to affect Ca^{2+} sparks, with a higher spark rate, amplitude, and time to peak at room temperature compared to 37°C due to effects on sarcoplasmic reticulum Ca^{2+} stores and RyR function (Ferrier et al., 2003; Fu et al., 2005). While our experiments were performed at room temperature (∼22°C), this is in-line with the previous studies of the effects of stretch on Ca^{2+} sparks (Iribe et al., 2009; Prosser et al., 2011), and it is not believed that that the associated difference in baseline spark rate is responsible for the fundamental effect of stretch on the frequency of Ca^{2+} sparks, nor the difference in the response of Ca^{2+} spark rate to stretch between NT and SI cells (although it may impact the magnitude of the response). Related to this concern, the increase in Ca^{2+} spark rate in ischemia compared to control, as well as its increase with stretch could be partly related to changes in intracellular Ca^{2+}, however this was not measured in the current study (it would require the use of a ratiometric Ca^{2+}- imaging approach).

CONCLUSION

In the current study, we have demonstrated that ischemia enhances the acute increase in calcium spark rate that occurs with stretch of isolated ventricular myocytes, with an associated enhancement of stretch-induced ROS production. While the mechanism(s) of these enhancements remains unknown, they may contribute to the generation of Ca^{2+}-induced arrhythmias in acute ischemia, and thus represent potential therapeutic targets for lethal arrhythmias.

DATA AVAILABILITY STATEMENT

The datasets generated for this study are available on request to the corresponding author.

ETHICS STATEMENT

This animal study was reviewed and approved by Animal Subjects Committee of Okayama University Graduate School of Medicine, Dentistry, and Pharmaceutical Sciences.

AUTHOR CONTRIBUTIONS

BC contributed to the design of the study, performed the experimental work, analyzed the data, and wrote the manuscript. HK and KK provided technical support for the experiments. GI and TAQ contributed to the design of the study and revised the manuscript. All authors approved the final submission.

FUNDING

This work was supported through a Mitacs—Japan Society for the Promotion of Science (JSPS) Internship funded by a Mitacs Globalink Research Award and a JSPS International Research Fellowship (IT11003 to BC), by the JSPS (KAKENHI 17K01359 and 15K21745 to GI), by the Canadian Institutes of Health Research (MOP 342562 to TAQ), and by the Natural Sciences and Engineering Research Council of Canada (RGPIN-2016-04879 to TAQ). TAQ was a National New Investigator of the Heart and Stroke Foundation of Canada.

SUPPLEMENTARY MATERIAL

The Supplementary Material for this article can be found online at: https://www.frontiersin.org/articles/10.3389/fphys.2020.00289/full#supplementary-material

Supplemental Video 1 | Movie showing the effect of axial stretch on the occurrence of calcium sparks in single quiescent mouse ventricular myocytes exposed to normal Tyrode, measured by two-dimensional confocal microscopic recordings of Fluo-4AM fluorescence.

Supplemental Video 2 | Movie showing the effect of axial stretch on the occurrence of calcium sparks in single quiescent mouse ventricular myocytes exposed to simulated ischemia, measured by two-dimensional confocal microscopic recordings of Fluo-4AM fluorescence.

REFERENCES

Allen, D. G., and Kentish, J. C. (1988). Calcium concentration in the myoplasm of skinned ferret ventricular muscle following changes in muscle length. *J. Physiol.* 407, 489–503. doi: 10.1113/jphysiol.1988.sp017427

Barrabes, J. A., Figueras, J., Candell-Riera, J., Agullo, L., Inserte, J., and Garcia-Dorado, D. (2013). Distension of the ischemic region predicts increased ventricular fibrillation inducibility following coronary occlusion in swine. *Rev. Esp. Cardiol.* 66, 171–176. doi: 10.1016/j.rec.2012.08.006

Barrabes, J. A., Garcia-Dorado, D., Gonzalez, M. A., Ruiz-Meana, M., Solares, J., Puigfel, Y., et al. (1998). Regional expansion during myocardial ischemia predicts ventricular fibrillation and coronary reocclusion. *Am. J. Physiol.* 274, H1767–H1775. doi: 10.1152/ajpheart.1998.274.5.H1767

Barrabes, J. A., Garcia-Dorado, D., Padilla, F., Agullo, L., Trobo, L., Carballo, J., et al. (2002). Ventricular fibrillation during acute coronary occlusion is related to the dilation of the ischemic region. *Basic Res. Cardiol.* 97, 445–451. doi: 10.1007/s003950200051

Barrabes, J. A., Inserte, J., Rodriguez-Sinovas, A., Ruiz-Meana, M., and Garcia-Dorado, D. (2017). Early regional wall distension is strongly associated with vulnerability to ventricular fibrillation but not arrhythmia triggers following coronary occlusion *in vivo*. *Prog. Biophys. Mol. Biol.* 130(Pt B), 387–393. doi: 10.1016/j.pbiomolbio.2017.05.012

Baumeister, P., and Quinn, T. A. (2016). Altered calcium handling and ventricular arrhythmias in acute ischemia. *Clin. Med. Insights Cardiol.* 10(Suppl. 1), 61–69. doi: 10.4137/CMC.S39706

Belevych, A. E., Terentyev, D., Viatchenko-Karpinski, S., Terentyeva, R., Sridhar, A., Nishijima, Y., et al. (2009). Redox modification of ryanodine receptors underlies calcium alternans in a canine model of sudden cardiac death. *Cardiovasc. Res.* 84, 387–395. doi: 10.1093/cvr/cvp246

Billman, G. E., McIlroy, B., and Johnson, J. D. (1991). Elevated cardiac myocardial calcium and its role in sudden cardiac death. *FASEB J.* 5, 2586–2592. doi: 10.1096/fasebj.5.11.1714409

Califf, R. M., Burks, J. M., Behar, V. S., Margolis, J. R., and Wagner, G. S. (1978). Relationships among ventricular arrhythmias, coronary artery disease, and angiographic and electrocardiographic indicators of myocardial fibrosis. *Circulation* 57, 725–732. doi: 10.1161/01.cir.57.4.725

Cannell, M. B. (2009). Pulling on the heart strings: a new mechanism within Starling's law of the heart? *Circ. Res.* 104, 715–716. doi: 10.1161/CIRCRESAHA.109.195511

Carmeliet, E. (1999). Cardiac ionic currents and acute ischemia: from channels to arrhythmias. *Physiol. Rev.* 79, 917–1017. doi: 10.1152/physrev.1999.79.3.917

Cheng, H., and Lederer, W. J. (2008). Calcium sparks. *Physiol. Rev.* 88, 1491–1545. doi: 10.1152/physrev.00030.2007

Cordeiro, J. M., Howlett, S. E., and Ferrier, G. R. (1994). Simulated ischaemia and reperfusion in isolated guinea pig ventricular myocytes. *Cardiovasc. Res.* 28, 1794–1802. doi: 10.1093/cvr/28.12.1794

Coronel, R., Wilms-Schopman, F. J., and deGroot, J. R. (2002). Origin of ischemia-induced phase 1b ventricular arrhythmias in pig hearts. *J. Am. Coll. Cardiol.* 39, 166–176. doi: 10.1016/s0735-1097(01)01686-2

Di Diego, J. M., and Antzelevitch, C. (2011). Ischemic ventricular arrhythmias: experimental models and their clinical relevance. *Heart Rhythm* 8, 1963–1968. doi: 10.1016/j.hrthm.2011.06.036

Donoso, P., Finkelstein, J. P., Montecinos, L., Said, M., Sanchez, G., Vittone, L., et al. (2014). Stimulation of NOX2 in isolated hearts reversibly sensitizes RyR2 channels to activation by cytoplasmic calcium. *J. Mol. Cell. Cardiol.* 68, 38–46. doi: 10.1016/j.yjmcc.2013.12.028

Ferrari, R., Ceconi, C., Curello, S., Guarnieri, C., Caldarera, C. M., Albertini, A., et al. (1985). Oxygen-mediated myocardial damage during ischaemia and reperfusion: role of the cellular defences against oxygen toxicity. *J. Mol. Cell. Cardiol.* 17, 937–945. doi: 10.1016/s0022-2828(85)80074-2

Ferrier, G. R., Smith, R. H., and Howlett, S. E. (2003). Calcium sparks in mouse ventricular myocytes at physiological temperature. *Am. J. Physiol. Heart Circ. Physiol.* 285, H1495–H1505. doi: 10.1152/ajpheart.00802.2002

Fu, Y., Zhang, G. Q., Hao, X. M., Wu, C. H., Chai, Z., and Wang, S. Q. (2005). Temperature dependence and thermodynamic properties of ca^{2+} sparks in rat cardiomyocytes. *Biophys. J.* 89, 2533–2541. doi: 10.1529/biophysj.105.067074

Hirche, H., Hoeher, M., and Risse, J. H. (1987). Inotropic changes in ischaemic and non-ischaemic myocardium and arrhythmias within the first 120 minutes of coronary occlusion in pigs. *Basic Res. Cardiol.* 82, 301–310. doi: 10.1007/978-3-662-11289-2_29

Iribe, G., Helmes, M., and Kohl, P. (2007). Force-length relations in isolated intact cardiomyocytes subjected to dynamic changes in mechanical load. *Am. J. Physiol. Heart Circ. Physiol.* 292, H1487–H1497. doi: 10.1152/ajpheart.00909.2006

Iribe, G., Kaihara, K., Ito, H., and Naruse, K. (2013). Effect of azelnidipine and amlodipine on single cell mechanics in mouse cardiomyocytes. *Eur. J. Pharmacol.* 715, 142–146. doi: 10.1016/j.ejphar.2013.05.030

Iribe, G., Kaihara, K., Yamaguchi, Y., Nakaya, M., Inoue, R., and Naruse, K. (2017). Mechano-sensitivity of mitochondrial function in mouse cardiac myocytes. *Prog. Biophys Mol. Biol.* 130(Pt B), 315–322. doi: 10.1016/j.pbiomolbio.2017.05.015

Iribe, G., Kaneko, T., Yamaguchi, Y., and Naruse, K. (2014). Load dependency in force-length relations in isolated single cardiomyocytes. *Prog. Biophys. Mol. Biol.* 115, 103–114. doi: 10.1016/j.pbiomolbio.2014.06.005

Iribe, G., Ward, C. W., Camelliti, P., Bollensdorff, C., Mason, F., Burton, R. A., et al. (2009). Axial stretch of rat single ventricular cardiomyocytes causes an acute and transient increase in Ca^{2+} spark rate. *Circ. Res.* 104, 787–795. doi: 10.1161/CIRCRESAHA.108.193334

Janse, M. J., and Wit, A. L. (1989). Electrophysiological mechanisms of ventricular arrhythmias resulting from myocardial ischemia and infarction. *Physiol. Rev.* 69, 1049–1169. doi: 10.1152/physrev.1989.69.4.1049

Joca, H. C., Coleman, A. K., Ward, C. W., and Williams, G. S. B. (2020). Quantitative tests reveal that microtubules tune the healthy heart but underlie arrhythmias in pathology. *J. Physiol.* 598, 1327–1338. doi: 10.1113/JP277083

Khokhlova, A., Iribe, G., Yamaguchi, Y., Naruse, K., and Solovyova, O. (2017). Effects of simulated ischemia on the transmural differences in the frank-starling relationship in isolated mouse ventricular cardiomyocytes. *Prog. Biophys. Mol. Biol.* 130(Pt B), 323–332. doi: 10.1016/j.pbiomolbio.2017.05.011

Köhler, A. C., Sag, C. M., and Maier, L. S. (2014). Reactive oxygen species and excitation – contraction coupling in the context of cardiac pathology. *J. Mol. Cell. Cardiol.* 73, 92–102. doi: 10.1016/j.yjmcc.2014.03.001

Lab, M. J. (1989). Contribution of mechano-electric coupling to ventricular arrhythmias during reduced perfusion. *Int. J. Microcirc. Clin. Exp.* 8, 433–442

Limbu, S., Hoang-Trong, T. M., Prosser, B. L., Lederer, W. J., and Jafri, M. S. (2015). Modeling local X-ROS and calcium signaling in the heart. *Biophys. J.* 109, 2037–2050. doi: 10.1016/j.bpj.2015.09.031

Maier, L. S., and Bers, D. M. (2007). Role of Ca^{2+}/calmodulin-dependent protein kinase (CaMK) in excitation-contraction coupling in the heart. *Cardiovasc. Res.* 73, 631–640. doi: 10.1016/j.cardiores.2006.11.005

Mattiazzi, A., Argenziano, M., Aguilar-Sanchez, Y., Mazzocchi, G., and Escobar, A. L. (2015a). Ca^{2+} Sparks and Ca^{2+} waves are the subcellular events underlying Ca^{2+} overload during ischemia and reperfusion in perfused intact hearts. *J. Mol. Cell. Cardiol.* 79, 69–78. doi: 10.1016/j.yjmcc.2014.10.011

Mattiazzi, A., Bassani, R. A., Escobar, A. L., Palomeque, J., Valverde, C. A., Vila Petroff, M., et al. (2015b). Chasing cardiac physiology and pathology down the CaMKII cascade. *Am. J. Physiol. Heart Circ. Physiol.* 308, H1177–H1191. doi: 10.1152/ajpheart.00007.2015

Miura, M., Nishio, T., Hattori, T., Murai, N., Stuyvers, B. D., Shindoh, C., et al. (2010). Effect of nonuniform muscle contraction on sustainability and frequency of triggered arrhythmias in rat cardiac muscle. *Circulation* 121, 2711–2717. doi: 10.1161/CIRCULATIONAHA.109.907717

Miura, M., Taguchi, Y., Handoh, T., Hasegawa, T., Takahashi, Y., Morita, N., et al. (2018). Regional increase in ROS within stretched region exacerbates arrhythmias in rat trabeculae with nonuniform contraction. *Pflugers Arch.* 470, 1349–1357. doi: 10.1007/s00424-018-2152-x

Miura, M., Wakayama, Y., Endoh, H., Nakano, M., Sugai, Y., Hirose, M., et al. (2008). Spatial non-uniformity of excitation-contraction coupling can enhance arrhythmogenic-delayed afterdepolarizations in rat cardiac muscle. *Cardiovasc. Res.* 80, 55–61. doi: 10.1093/cvr/cvn162

Murata, M., Akao, M., O'Rourke, B., and Marbán, E. (2001). Mitochondrial ATP-sensitive potassium channels attenuate matrix Ca(2+) overload during simulated ischemia and reperfusion: possible mechanism of cardioprotection. *Circ. Res.* 89, 891–898. doi: 10.1161/hh2201.100205

Myerburg, R. J., Interian, A. Jr., Mitrani, R. M., Kessler, K. M., and Castellanos, A. (1997). Frequency of sudden cardiac death and profiles of risk. *Am. J. Cardiol.* 80, 10F–19F. doi: 10.1016/s0002-9149(97)00477-3

O'Brien, J. D., Ferguson, J. H., and Howlett, S. E. (2008). Effects of ischemia and reperfusion on isolated ventricular myocytes from young adult and aged Fischer 344 rat hearts. *Am. J. Physiol. Heart Circ. Physiol.* 294, H2174–H2183. doi: 10.1152/ajpheart.00058.2008

Peyronnet, R., Bollensdorff, C., Capel, R. A., Rog-Zielinska, E. A., Woods, C. E., Charo, D. N., et al. (2017). Load-dependent effects of apelin on murine cardiomyocytes. *Prog. Biophys. Mol. Biol.* 130(Pt B), 333–343. doi: 10.1016/j.pbiomolbio.2017.09.013

Poluektov, Y. M., Petrushanko, I. Y., Undrovina, N. A., Lakunina, V. A., Khapchaev, A. Y., Kapelko, V. I., et al. (2019). Glutathione-related substances maintain cardiomyocyte contractile function in hypoxic conditions. *Sci. Rep.* 9:4872. doi: 10.1038/s41598-019-41266-2

Prosser, B. L., Khairallah, R. J., Ziman, A. P., Ward, C. W., and Lederer, W. J. (2013a). X-ROS signaling in the heart and skeletal muscle: stretch-dependent local ROS regulates [Ca(2)(+)]i. *J. Mol. Cell. Cardiol.* 58, 172–181. doi: 10.1016/j.yjmcc.2012.11.011

Prosser, B. L., Ward, C. W., and Lederer, W. J. (2010). Subcellular Ca^{2+} signaling in the heart: the role of ryanodine receptor sensitivity. *J. Gen. Physiol.* 136, 135–142. doi: 10.1085/jgp.201010406

Prosser, B. L., Ward, C. W., and Lederer, W. J. (2011). X-ROS signaling: rapid mechano-chemo transduction in heart. *Science* 333, 1440–1445. doi: 10.1126/science.1202768

Prosser, B. L., Ward, C. W., and Lederer, W. J. (2013b). X-ROS signalling is enhanced and graded by cyclic cardiomyocyte stretch. *Cardiovasc. Res.* 98, 307–14. doi: 10.1093/cvr/cvt066

Quinn, T. A. (2014). The importance of non-uniformities in mechano-electric coupling for ventricular arrhythmias. *J. Interv. Card. Electrophysiol.* 39, 25–35. doi: 10.1007/s10840-013-9852-0

Quinn, T. A. (2015). Cardiac mechano-electric coupling: a role in regulating normal function of the heart? *Cardiovasc. Res.* 108, 1–3. doi: 10.1093/cvr/cvv203

Quinn, T. A., Granite, S., Allessie, M. A., Antzelevitch, C., Bollensdorff, C., Bub, G., et al. (2011). Minimum Information about a Cardiac Electrophysiology Experiment (MICEE): standardised reporting for model reproducibility, interoperability, and data sharing. *Prog. Biophys. Mol. Biol.* 107, 4–10. doi: 10.1016/j.pbiomolbio.2011.07.001

Quinn, T. A., and Kohl, P. (2016). Rabbit models of cardiac mechano-electric and mechano-mechanical coupling. *Prog. Biophys. Mol. Biol.* 121, 110–122. doi: 10.1016/j.pbiomolbio.2016.05.003

Raedschelders, K., Ansley, D. M., and Chen, D. D. Y. (2012). The cellular and molecular origin of reactive oxygen species generation during myocardial ischemia and reperfusion. *Pharmacol. Ther.* 133, 230–255. doi: 10.1016/j.pharmthera.2011.11.004

Rubart, M., and Zipes, D. P. (2005). Mechanisms of sudden cardiac death. *J. Clin. Invest.* 115, 2305–2315. doi: 10.1172/JCI26381

Sánchez, G., Pedrozo, Z., Domenech, R. J., Hidalgo, C., and Donoso, P. (2005). Tachycardia increases NADPH oxidase activity and RyR2 S-glutathionylation in ventricular muscle. *J. Mol. Cell. Cardiol.* 39, 982–991. doi: 10.1016/j.yjmcc.2005.08.010

Sato, D., Bartos, D. C., Ginsburg, K. S., and Bers, D. M. (2014). Depolarization of cardiac membrane potential synchronizes calcium sparks and waves in tissue. *Biophys. J.* 107, 1313–1317. doi: 10.1016/j.bpj.2014.07.053

Siogas, K., Pappas, S., Graekas, G., Goudevenos, J., Liapi, G., and Sideris, D. A. (1998). Segmental wall motion abnormalities alter vulnerability to ventricular ectopic beats associated with acute increases in aortic pressure in patients with underlying coronary artery disease. *Heart* 79, 268–273. doi: 10.1136/hrt.79.3.268

Tang, Q., Ma, J., Zhang, P., Wan, W., Kong, L., and Wu, L. (2012). Persistent sodium current and Na^+/H^+ exchange contributes to the augmentation of the reverse Na^+/Ca^{2+} exchange during hypoxia or acute ischemia in ventricular myocytes. *Pflugers Arch.* 463, 513–522. doi: 10.1007/s00424-011-1070-y

Ter Keurs, H. E., and Boyden, P. A. (2007). Calcium and arrhythmogenesis. *Physiol. Rev.* 87, 457–506. doi: 10.1152/physrev.00011.2006

ter Keurs, H. E., Wakayama, Y., Sugai, Y., Price, G., Kagaya, Y., Boyden, P. A., et al. (2006). Role of sarcomere mechanics and Ca^{2+} overload in Ca^{2+} waves and arrhythmias in rat cardiac muscle. *Ann. N. Y. Acad. Sci.* 1080, 248–267. doi: 10.1196/annals.1380.020

Wakayama, Y., Miura, M., Stuyvers, B. D., Boyden, P. A., and ter Keurs, H. E. (2005). Spatial nonuniformity of excitation-contraction coupling causes arrhythmogenic Ca^{2+} waves in rat cardiac muscle. *Circ. Res.* 96, 1266–1273. doi: 10.1161/01.RES.0000172544.56818.54

Ward, C. W., Prosser, B. L., and Lederer, W. J. (2014). Mechanical stretch-induced activation of ROS/RNS signaling in striated muscle. *Antioxid. Redox Signal.* 20, 929–936. doi: 10.1089/ars.2013.5517

Wu, T. J., Lin, S.-F., Hsieh, Y.-C., Lin, T.-C., Lin, J.-C., and Ting, C.-T. (2011). Pretreatment of BAPTA-AM suppresses the genesis of repetitive endocardial focal discharges and pacing-induced ventricular arrhythmia during global ischemia. *J. Cardiovasc. Electrophysiol.* 22, 1154–1162. doi: 10.1111/j.1540-8167.2011.02067.x

Xing, D., and Martins, J. B. (2004). Triggered activity due to delayed afterdepolarizations in sites of focal origin of ischemic ventricular tachycardia. *Am. J. Physiol. Heart Circ. Physiol.* 287, H2078–H2084. doi: 10.1152/ajpheart.00027.2004

Zhang, H., Gomez, A. M., Wang, X., Yan, Y., Zheng, M., and Cheng, H. (2013). ROS regulation of microdomain Ca(2+) signalling at the dyads. *Cardiovasc. Res.* 98, 248–258. doi: 10.1093/cvr/cvt050

Zipes, D. P., and Wellens, H. J. (1998). Sudden cardiac death. *Circulation* 98, 2334–2351. doi: 10.1161/01.cir.98.21.2334

Conflict of Interest: The authors declare that the research was conducted in the absence of any commercial or financial relationships that could be construed as a potential conflict of interest.

The handling editor is currently organizing a Research Topic with one of the authors (GI) and confirms the absence of any other collaboration.

frontiers in Physiology

ORIGINAL RESEARCH
published: 15 May 2020
doi: 10.3389/fphys.2020.00457

The Lectin LecA Sensitizes the Human Stretch-Activated Channel TREK-1 but Not Piezo1 and Binds Selectively to Cardiac Non-myocytes

Elisa Darkow[1,2,3,4], Eva A. Rog-Zielinska[1,2], Josef Madl[1,2], Annette Brandel[4,5], Lina Siukstaite[4,5], Ramin Omidvar[4,5], Peter Kohl[1,2,5], Ursula Ravens[1,2], Winfried Römer[3,4,5] and Rémi Peyronnet[1,2]*

[1] Institute for Experimental Cardiovascular Medicine, University Heart Center Freiburg-Bad Krozingen, Medical Center-University of Freiburg, Freiburg, Germany, [2] Faculty of Medicine, University of Freiburg, Freiburg, Germany, [3] Spemann Graduate School of Biology and Medicine (SGBM), University of Freiburg, Freiburg, Germany, [4] Faculty of Biology, University of Freiburg, Freiburg, Germany, [5] Signalling Research Centres BIOSS and CIBSS, University of Freiburg, Freiburg, Germany

Edited by:
Fabio Fernandes,
University of Lisbon, Portugal

Reviewed by:
Chilman Bae,
Southern Illinois University
Carbondale, United States
Marc Borsotto,
UMR 7275 Institut de Pharmacologie
moléculaire et Cellulaire (IPMC),
France

***Correspondence:**
Rémi Peyronnet
remi.peyronnet@
universitaets-herzzentrum.de

Specialty section:
This article was submitted to
Membrane Physiology
and Membrane Biophysics,
a section of the journal
Frontiers in Physiology

Received: 24 December 2019
Accepted: 15 April 2020
Published: 15 May 2020

Citation:
Darkow E, Rog-Zielinska EA, Madl J, Brandel A, Siukstaite L, Omidvar R, Kohl P, Ravens U, Römer W and Peyronnet R (2020) The Lectin LecA Sensitizes the Human Stretch-Activated Channel TREK-1 but Not Piezo1 and Binds Selectively to Cardiac Non-myocytes. Front. Physiol. 11:457. doi: 10.3389/fphys.2020.00457

The healthy heart adapts continuously to a complex set of dynamically changing mechanical conditions. The mechanical environment is altered by, and contributes to, multiple cardiac diseases. Mechanical stimuli are detected and transduced by cellular mechano-sensors, including stretch-activated ion channels (SAC). The precise role of SAC in the heart is unclear, in part because there are few SAC-specific pharmacological modulators. That said, most SAC can be activated by inducers of membrane curvature. The lectin LecA is a virulence factor of *Pseudomonas aeruginosa* and essential for *P. aeruginosa*-induced membrane curvature, resulting in formation of endocytic structures and bacterial cell invasion. We investigate whether LecA modulates SAC activity. TREK-1 and Piezo1 have been selected, as they are widely expressed in the body, including cardiac tissue, and they are "canonical representatives" for the potassium selective and the cation non-selective SAC families, respectively. Live cell confocal microscopy and electron tomographic imaging were used to follow binding dynamics of LecA, and to track changes in cell morphology and membrane topology in human embryonic kidney (HEK) cells and in giant unilamellar vesicles (GUV). HEK cells were further transfected with human TREK-1 or Piezo1 constructs, and ion channel activity was recorded using the patch-clamp technique. Finally, freshly isolated cardiac cells were used for studies into cell type dependency of LecA binding. LecA (500 nM) binds within seconds to the surface of HEK cells, with highest concentration at cell-cell contact sites. Local membrane invaginations are detected in the presence of LecA, both in the plasma membrane of cells (by 17 min of LecA exposure) as well as in GUV. In HEK cells, LecA sensitizes TREK-1, but not Piezo1, to voltage and mechanical stimulation. In freshly isolated cardiac cells, LecA binds to non-myocytes, but not to ventricular or atrial cardiomyocytes. This cell type specific lack of binding is observed across cardiomyocytes from mouse, rabbit, pig, and human. Our results suggest that LecA may serve as a pharmacological tool to study SAC in a cell type-preferential manner. This could aid tissue-based research into the roles of SAC in cardiac non-myocytes.

Keywords: mechano-sensitive channels, cardiomyocytes, mechanotransduction, membrane curvature, α-galactosides

INTRODUCTION

Cardiac tissue continuously experiences mechanical stimulation, and it must adjust structurally and functionally to an ever-changing mechanical environment. Key molecular players underlying mechano-sensing at the cellular level are stretch-activated ion channels (SAC). In the heart, activity and regulation of SAC are still poorly understood.

SAC are mechano-gated, i.e., their open probability can be increased by raising membrane tension (in-plane stretch) and/or curvature (Murthy et al., 2017). Bavi and co-workers, using a finite element model of cell membranes, concluded that local membrane curvature with a radius < 100 nm is required for SAC activation (Bavi et al., 2016). Under physiological conditions, membrane curvature in this order of magnitude is found at many different sites (e.g., in T-tubules, caveolae, filopodia), and in the context of various forms of cellular activity (e.g., endo- or exocytosis, cell division, migration). Under pathological conditions, membrane integrity and membrane protein functions can be adversely affected by changes in membrane curvature (e.g., Diabetes mellitus type 2, Alzheimer's and Parkinson's disease; Perlmutter et al., 2009; Kegulian et al., 2015; Sugiura et al., 2015).

SAC are conserved throughout living organisms and expressed in every human tissue tested so far, including the cardiovascular system (Peyronnet et al., 2016; Beech and Kalli, 2019; Douguet et al., 2019). SAC, both in the sarcolemma and as part of intracellular membrane systems, are believed to be indispensable molecular players in cardiac physiology, involved in the positive chronotropic response of the heart to stretch, auto-regulation of myocardial calcium balance and contractility, and vascular remodeling (Cooper et al., 2000; Youm et al., 2005; Iribe et al., 2009; Murthy et al., 2017). Perhaps even better documented is the involvement of SAC in pathological responses, contributing to the genesis of arrhythmias and fibrosis (Inoue et al., 2006; Peyronnet et al., 2016; Decher et al., 2017; Quinn et al., 2017; Abraham et al., 2018).

In mammals, two main families of SAC can be distinguished, based on their ion selectivity (Reed et al., 2014): cation non-selective channels (SAC_{NS}) such as Piezo1, and potassium (K^+) selective channels (SAC_K) such as TREK-1 (TWIK-1-related K^+ channel, where TWIK stands for "two-pore-domain weak inward rectifying K^+ channel"). Piezo1 is involved in various cellular functions, including cell migration and alignment (Li et al., 2014), and it has been associated with human diseases such as hemolytic anemia, and lymphedema (Murthy et al., 2017). Piezo1 expression has recently been reported in the mammalian heart (Liang et al., 2017), more specifically in fibroblasts (Blythe et al., 2019), but its function and relevance are still unclear. TREK-1 is also widely expressed and present in the heart, both in non-myocytes and in myocytes (Terrenoire et al., 2001; Niu and Sachs, 2003; Abraham et al., 2018). A recent study showed that a mutation affecting TREK-1 permeability may lead to ventricular tachycardia (Decher et al., 2017). The function of "normal" TREK-1 in the heart is still unclear. Cardiac SAC have recently been reviewed in detail (Peyronnet et al., 2016), highlighting the need for new SAC-selective pharmacological modulators. Taking this thought a step further, cell type-specific SAC modulators would be of high utility in exploring cellular contributors to complex responses in heterocellular tissue.

A variety of pharmacological compounds have been identified as being able to modulate SAC. The vast majority of them are non-selective inhibitors (Hamill and McBride, 1996; Peyronnet et al., 2016). Among SAC-activators, membrane curvature inducers, such as the polyunsaturated fatty acid arachidonic acid (AA), are very efficient in shifting the stretch-dependence of SAC open probability to lower mechanical stimuli amplitudes. AA has been shown to influence ion channel activity in the cardiovascular system, including effects on TREK-1 in rat cardiomyocytes (Terrenoire et al., 2001; Li et al., 2006; Zhang et al., 2008). However, fatty acids (including AA) can modify the lipid composition of the bilayer, which in its own right may alter relevant membrane properties such as fluidity (Yang et al., 2011), or affect the lipid organization in ways that may generate side effects, such as changes in the activity of integral membrane proteins, cytotoxicity and apoptosis (Chen et al., 1998; Lee, 2004).

When employing lectin proteins to enhance membrane curvature, the lipidic composition of the bilayer is not altered. Lectins link *selectively* to glycoconjugates on the extracellular surface of various cell types. Some lectins bind specifically to glycosphingolipids with α-galactose residues, such as the glycosphingolipid globotriaosylceramide (Gb_3). Gb_3 has been reported to reside mainly in highly ordered lipid nanodomains, referred to as lipid rafts (Lingwood and Simons, 2010). Some lectins are able to change membrane curvature, as exemplified by the B-subunit of Shiga toxin, which has been identified as inducing membrane curvature by binding to Gb_3 (Römer et al., 2007; Johannes and Römer, 2010; Johannes et al., 2015; Schubert and Römer, 2015; Sych et al., 2018).

The lectin LecA is a homo-tetrameric, brick-shaped lectin with four carbohydrate binding sites at two opposing ends (Schubert and Römer, 2015). LecA acts as a virulence factor of the Gram-negative bacterium *Pseudomonas aeruginosa,* an opportunistic pathogen involved in nosocomial infections which can also cause endocarditis. After binding to Gb_3, the LecA-coated bacterium is able to induce concave (negative) membrane bending, which then triggers *P. aeruginosa* uptake into the host cell by endocytosis. Thus, LecA is not merely an adhesion factor, but it promotes the bacterial invasion process (Chemani et al., 2009; Aigal et al., 2015) by triggering the formation of membrane invaginations (Eierhoff et al., 2014). Since LecA binds selectively to membrane domains exhibiting α-galactose residues, the compound could be a candidate for modulating SAC in a cell type-selective manner.

From our current knowledge of SAC modulation, and of LecA, the following hypotheses are proposed: (i) LecA binds to human embryonic kidney (HEK) cells and induces membrane invaginations, (ii) LecA-induced membrane deformation affects SAC activity, and (iii) LecA binding is cell type-dependent.

MATERIALS AND METHODS

Cell Culture

HEK 293T/17 cells (ATCC-LGC Standards, United States) were cultured in Dulbecco's modified (low glucose) Eagle medium, supplemented with 10% fetal bovine serum and 1% penicillin/streptomycin (all Sigma Aldrich, Germany) in 25 cm^2 tissue culture flasks (Techno Plastic Products, Switzerland) until 90% confluency. After washing with Dulbecco's phosphate-buffered saline (PBS; Sigma Aldrich), cells were detached with trypsin (trypsin-EDTA solution; Sigma Aldrich). The suspension was centrifuged (57 × g, 3 min; Rotina 380, Hettich, Germany), the supernatant removed, and the pellet re-suspended in the cell culture medium described above. Cells were re-seeded for subculture or for experiments at 25,000 cells per Ø 35 mm dish (tissue culture or microscopy dishes; Techno Plastic Products or ibidi, Germany, respectively). Cells were cultured for a minimum of 2 days to allow cell attachment and expression of the protein of interest before further experiments were performed.

For transient overexpression of human Piezo1 or human TREK-1, HEK cells were transfected 24 h after seeding. Plasmids were kindly provided by Fred Sachs for Piezo1-internal ribosome entry site 2 (IRES2)-enhanced green fluorescent protein (eGFP), and by Eric Honoré and Delphine Bichet for TREK-1-IRES2-eGFP. For transfection of one dish, 0.5 μg of Piezo1-IRES2-eGFP or 0.1 μg of TREK-1-IRES2-eGFP were mixed with 1.5 μL of jetPEI transfection reagent in 100 μL NaCl (150 mM; both Polyplus Transfection, France). After incubating this transfection mix for 20 min at room temperature (RT), it was added to the cells (100 μL in 2 mL). Functional analyses were performed from days 2 to 4 post-transfection. Transfection success rate was about 50% (fluorescent cells per total number of cells).

Lectins

Recombinant LecA production and purification were performed as described earlier (Blanchard et al., 2008) by transforming *Escherichia coli* BL21 (DE3) with the LecA-encoding plasmid pET25-pa1l. Cells were cultured in lysogeny broth medium (Carl Roth, Germany) with ampicillin (100 mg/mL) at 37°C under gentle agitation (for oxygenation; C25 KC, New Brunswick Scientific, United Kingdom) until the optical density of the cell suspension reached 0.8 at 600 nm (mid-logarithmic phase of cell growth). For induction of protein expression, isopropyl β-D-1-thiogalactopyranoside (1 mM) was added for 3 h at 30°C during continued gentle agitation. Then, cells were harvested and re-suspended in 10 mL loading/equilibration buffer (100 mM NaCl, 100 μM $CaCl_2$, 20 mM Tris/HCl, pH 7.5; Carl Roth). For bacterial lysis, cells were disrupted in a high-pressure cell homogenizer at 170 MPa (CF1, Constant Systems, United Kingdom). After centrifugation (5,000 × g for 30 min at 4°C; Avanti J-26 XP, Beckman Coulter, Germany), the supernatant was passed through a 6 μm vacuum filter. The supernatant was further purified by affinity chromatography on D-Galactose columns (GE Healthcare Life Sciences, Germany). Lectins were allowed to bind to the immobilized saccharides, and were then eluted with elution buffer (100 mM NaCl, 100 mM EDTA, 20 mM TRIS/HCl, pH 7.5; all Carl Roth). The purity of the recombinant proteins was determined by gel electrophoresis (Monomeric LecA shows a band at its molecular weight of around 13 kDa; material from Bio-Rad, Germany). The purified proteins were intensively dialyzed against distilled water and $CaCl_2$ (5 mM) for 3 days and against distilled water only for further 3 days. The bath solution was exchanged twice daily for sugar removal. The purified and lyophilized recombinant lectin was prepared in PBS (supplemented with 0.9 mM Ca^{2+} and 0.5 mM Mg^{2+}; $PBS^{+/+}$; Thermo Fisher Scientific) and aliquots were stored at −80°C.

The concentration at which lectins produce an effect may vary between artificial bilayer systems and cells, and it may also be different between various cell lines. On GUV, 200 nM of the B-subunit of Shiga toxin (StxB) induced tubular membrane invaginations (Römer et al., 2007). For LecA, 40-100 nM is sufficient to trigger a host cell signaling cascade (Eierhoff et al., 2014; Zheng et al., 2017). *P. aeruginosa*-induced lung injury was reproduced with 2 μM LecA (Chemani et al., 2009). Based on this, 500 nM was chosen as the target LecA concentration for HEK cells.

For imaging, labeling of purified LecA with Cyanine Dye 3 (Cy3; GE Healthcare Life Sciences) was performed according to the fluorophore manufacturer's protocol. In short, fivefold molar excess of Cy3 was used. First, Cy3 was dissolved in dimethyl sulfoxide (anhydrous, Thermo Fisher Scientific) at 10 g/L. Then, the desired amount of LecA was mixed at 1:10 with 1 M $NaHCO_3$, pH 8.7 (Carl Roth) and the calculated amount of Cy3, and the mixture was incubated for 1 h at RT with gentle agitation (Thriller Thermoshaker Incubator, Peqlab, Germany). To separate labeled LecA from non-bound Cy3, Spin Desalting Columns (Zeba, 7K MWCO, 0.5 mL, Thermo Fisher Scientific) were used. After washing with PBS (Thermo Fisher Scientific), the sample was centrifuged at 1,500 × g for 2 min at RT (Heraeus Fresco 21 Microcentrifuge, Thermo Fisher Scientific). After labeling, concentrations were determined by a spectrophotometer (NanoDrop 2000c, Thermo Fisher Scientific).

Confocal Microscopy

An inverted confocal microscope (TCS SP8 X, Leica Microsystems, Germany) was used for live cell imaging. The 540 nm line of a white light laser was used to excite Cy3; in addition, a 405 nm diode laser was used when Hoechst33342 nucleus staining was assessed. The focal plane was set at the maximal cell cross-section area. Image acquisition and analysis were performed with the Leica Application Suite X software.

To follow dynamic changes in membrane configuration induced by LecA, HEK cells were imaged either in dishes with polymer coverslip bottom (μdish Ø 35 mm, ibidi) or on round glass coverslips (Ø 30 mm, thickness N° 1.5, Bioptechs) mounted in an interchangeable coverslip dish (Bioptechs, United States). In order to reduce the volume of the measurement chamber, clean, 10 mm-high Teflon tube pieces were glued onto these coverslips with a two-component silicone adhesive (Reprorubber, United States; Madl et al., 2016). These home-built reduced volume chambers (∼200 μL instead of 1 mL) were disinfected using 70% ethanol before seeding cells.

Live cell imaging was performed 3 d after seeding of cells. Labeled LecA (500 nM, in $PBS^{+/+}$) was added to HEK cells at RT and imaged within the first minute [average delay 30 s, 63× oil objective, numerical aperture (NA) 1.4]. For time-lapse microscopy, one focal plane was imaged every 10 s. Fluorescence analyses were performed with ImageJ software. Cell maximum cross sectional area and mean fluorescence were determined. Fluorescence per cell is defined as the product of cell cross sectional area and mean fluorescence (of a cell cluster divided by the area of the cluster), and assumed to be proportional to the total amount of protein in the selected area. Cell selection criteria were: clearly defined borders in at least one channel, and cell attachment to the dish (which correlated with the presence of membrane protrusions). Only cells that could be observed throughout the entire time-lapse protocol were included in the analysis.

To determine cell type dependency of LecA binding, isolated cardiac cells were imaged in small chambered coverglass wells (μ-Slide 8 Well, ibidi). After Hoechst33342 staining of nuclei (20 μM, 7 min, in PBS$^{+/+}$; Thermo Fisher Scientific), cells were incubated with LecA (500 nM, in PBS$^{+/+}$) for 1 h at RT to maximize potential binding and avoid false negatives. To get an overview, a 40 × water objective or a dry 10 × objective were used. Only cells that appeared viable, i.e., showing a sharp and contrasted plasma membrane/sarcolemma, a well-delineated nucleus, and – in case of cardiomyocytes – clear non-contracted cross-striations (sarcomere length $\geq$ 1.7 μm), were considered.

Electron Microscopy, Tomographic Imaging, and Correlative Light-Electron Microscopy

HEK cells were grown on 6 mm sapphire discs (thickness 100 μm), and preserved by chemical fixation using iso-osmotic Karnovsky's fixative (Karnovsky, 1965; Solmedia, United Kingdom). Samples were processed to Epon-Araldite resin as described before (Rog-Zielinska et al., 2018). Imaging was performed at the Electron Microscopy (EM) Core Facility at the European Molecular Biology Laboratory in Heidelberg, using a 300 kV Tecnai TF30 microscope (FEI Company, now Thermo Fisher Scientific, Netherlands) and a 4k × 4k charge-coupled device camera (Oneview, Gatan, Germany) for dual and single-tilt 3D electron tomography (ET) of thick (300 nm) sections, or a 120 kV Biotwin CM120 microscope (Philips, Thermo Fisher Scientific) equipped with a bottom-mounted 1K CCD Camera (Keen View, SIS, Olympus, Germany) for 2D transmission EM of thin (70 nm) sections. Data were visualized and analyzed using IMOD routines, as described before (Kremer et al., 1996; Rog-Zielinska et al., 2018).

For correlative light-electron microscopy (CLEM), we used HEK293 cells, cultured on carbon- and fibronectin-coated sapphire discs (thickness 160 μm). Cells were treated with LecA for 17 min. Sapphire discs were high-pressure frozen (EM ICE, Leica Microsystems, Austria), and freeze-substituted in 0.1% uranyl acetate in acetone and embedded in Lowicryl HM20 resin (Polysciences, Germany) as described before (Santarella-Mellwig et al., 2018). Thick sections (300 nm thick) were cut, placed on carbon-coated copper mesh grids, and fluorescence-imaged using a widefield fluorescence microscope (IX81, 100× oil immersion objective, NA 1.4, Olympus) and a CCD camera (Orca-ER, Hamamatsu Photonics, Germany). Sections were then post-stained with uranyl acetate and lead citrate. ET was performed on the Tecnai TF30 microscope as described above. Fine registration was conducted using the ec-CLEM function of the Icy software (De Chaumont et al., 2012; Paul-Gilloteaux et al., 2017). As a note of caution, care must be taken when interpreting CLEM images. CLEM inherently involves the matching of datasets with vastly different resolutions (ET voxel size is $\sim 10^0$ nm^3, whereas for light microscopy a diffraction-limited voxel size is $> 10^6$ nm^3). This poses challenges in terms of different granularity of information, addressed post-acquisition using advanced image processing tools to achieve the correlation and cross-mapping of the two datasets. This, in turn, can generate an inaccurate impression of the information content in the fluorescence channel (e.g., appearing able to generate signals at a resolution well below the diffraction limit of light).

GUV Preparation and Observation

GUV were composed of 1,2-dioleoyl-sn-glycero-3-phosphocholine (DOPC), cholesterol (both Avanti Polar Lipids, United States), Atto 647N 1,2-dioleoyl-sn-glycero-3-phosphoethanolamine (DOPE; Sigma Aldrich), and purified porcine Gb$_3$ (Matreya, United States) at a molar ratio of 64.7: 30: 0.3: 5 mol%.

GUV were prepared using the electroformation technique as previously described (Madl et al., 2016). Briefly, lipids dissolved in chloroform were deposited on indium tin oxide (ITO)-coated glass slides (Präzisions Glas and Optik, Germany). After complete evaporation of chloroform solvent, lipids were hydrated with 300 mM sucrose in a pre-assembled chamber. GUV were formed by applying an alternating voltage (Vmax = 1.1 V) to the chamber for 2-3 h.

GUV were imaged on an inverted confocal microscope (Eclipse Ti-E, Nikon, Japan; with a Nikon A1R confocal laser scanning system, and 60× oil immersion objective, NA = 1.49). The software NIS-elements (Nikon) was used for image acquisition and ImageJ for analysis.

Patch-Clamp

Electrophysiological properties of SAC in the plasma membrane of HEK cells, and their response to drug application, were investigated using the patch-clamp technique in voltage clamp mode at RT. Cells were exchanged every hour.

The dish containing cells was mounted onto an inverted microscope (40× objective; DM IRB, Leica Microsystems). Transfected cells were identified by cytosolic eGFP fluorescence upon illumination with a mercury lamp (HBO100, Leica Microsystems). For measurements, cells with moderate and even fluorescence intensities were chosen. Fire-polished soda-lime glass capillaries (inner diameter: 1.15 ± 0.05 mm, outer diameter: 1.55 ± 0.05 mm; VITREX Medical, Denmark) were pulled using a two-stage vertical pipette-puller (PC-10, Narishige, Japan) to create the micropipettes required for patch-clamping. Pipette resistance depended on application (see below).

Pressure in the pipette line was recorded with a pressure monitor (PM01D, World Precision Instruments, United States). Cells were approached with positive pipette pressure (5–10 mmHg). To create a seal between the cell and the pipette upon cell contact, negative pressure (suction) was applied. Recordings were obtained in cell-attached or whole-cell configurations. A patch-clamp amplifier (Axopatch 200B, Axon Instruments, United States) and a digitizer interface (Axon Digidata 1440A, Axon Instruments) were used. Currents were acquired at 20 kHz sampling rate, and low-pass filtered at 1 kHz. Recordings were analyzed with pCLAMP 10.6 software (Axon Instruments).

For cell-attached configuration, bath solution contained (in mM): 155 KCl, 3 $MgCl_2$, 5 EGTA, 10 N-2-hydroxyethylpiperazine-N-ethanesulfonic acid (HEPES); pH buffered to 7.2 using KOH, osmolarity ∼300 mOsm L^{-1} (K-7400, Knauer, Germany), to match intracellular ionic conditions. The solution was stored at RT. Pipette solution, formulated to mimic the extracellular ionic environment, contained (in mM): 150 NaCl, 5 KCl, 10 HEPES, 2 $CaCl_2$, pH buffered to 7.4 using NaOH, ∼300 mOsm L^{-1}. Pipette solution was prepared ahead of experiments and stored in aliquots at −20°C. These ionic conditions are standard to record Piezo and TREK-1 channels (Moha ou Maati et al., 2011; Peyronnet et al., 2012, 2013). In case of application of compounds, these were added to the pipette solution before use. A delay of 2 min after seal formation was allowed for LecA effects to develop.

To test for SAC_{NS} (reversal potential ≈0 mV), voltage was clamped to −80 mV. To test for SAC_K (reversal potential ≈−80 mV), voltage was clamped to 0 mV. Average pipette resistance for cell-attached recordings was 1.36 ± 0.03 MΩ (n = 164). Seal resistances accepted were ∼1 GΩ, independent of pipette size and cell quality. Local membrane stretch was induced by applying pulses of negative pressure through the patch pipette, generated by an automated precision system (High Speed Pressure Clamp system; HSPC-1, ALA Scientific Instruments, United States). For mechanical stimulation, negative pressure was applied for 500 ms, in 5 mmHg increments from 0 to −80 mmHg (i.e., 16 sweeps), with 1.8 s at pressure = 0 mmHg between pressure steps.

Recordings obtained with the stretch protocol were analyzed in Clampfit 10.6 (Molecular Devices, United States). Baseline activity at 0 mmHg was taken as the "zero" reference (average baseline current = 0.3 ± 1.57 pA; n = 259). Peak, average and near steady-state currents were analyzed during pressure pulses. The time constant (τ) was determined according to the exponential function $f(t) = \sum_{i=1}^{n} A_i i e^{\frac{-t}{\tau_i}} + c$, where A: amplitude, τ: time constant and c: y-offset. The time constant τ (in ms) reflects the speed of inactivation after initial activation of SAC (analysis parameters illustrated in **Supplementary Figure S2A**). Averaged data were fitted by the Boltzmann equation: $y = \frac{A_1 - A_2}{1 + e^{(x-x_0)/\tau}} + A_2$ (with A_1: maximum current, A_2: current near steady-state, x_0: inflection point, τ: time constant).

For whole-cell configuration, solutions were as above, but inverted (pipette solution in cell-attached configuration constitutes the bath solution, and *vice versa*). Thereby, the pipette solution mimics the intracellular ionic milieu while the bath solution mimics extracellular ionic conditions.

A local perfusion system was installed for controlled administration of control (bath solution) or AA-containing solution (10 μM in bath solution; Meves, 2008). Flow rate was adapted by adjusting the height of reservoirs for gravity-fed flow to 1 mL min^{-1}, yielding nominally one exchange of the bath per minute. Due to the limited availability of LecA, it was added manually to the bath solution at a final concentration of 500 nM (to avoid the dead space of the perfusion system).

Average pipette resistance for whole-cell studies was 1.97 ± 0.02 MΩ; n = 124. A voltage ramp protocol (continuous change from −120 V to +40 mV within 1 s) was used for electrical stimulation (potential gradients above +40 mV were found to compromise membranes). Between application of ramps, cells were held for 5 s at −80 mV. On average, 10 min of stable recordings were obtained per cell.

To compare recordings from different cells, currents obtained in whole-cell configuration were normalized to membrane capacitance (a surrogate for cell size) and expressed as current density (in pA/pF). Currents at the maximum level of de- and hyperpolarization (+40 and −80 mV) were analyzed for each ramp acquired.

Cardiac Cell Isolation

For cell isolation, hearts were excised from animals sacrificed according to the guidelines stated in Directive 2010/63/EU of the European Parliament on the protection of animals used for scientific purposes, with approval by the local authorities in Baden Württemberg (G-16-131). Mouse and rabbit hearts were mounted on a Langendorff apparatus and perfused with collagenase-containing isolation solution (for protocols see Burton et al., 2017; Peyronnet et al., 2017). Porcine atrial and ventricular tissue was obtained with approval from the local ethics committee and the regional council of Freiburg, Baden-Württemberg, Germany (license number 35-9185.81/G-19/70). Human atrial tissue samples were obtained from patients in sinus rhythm, undergoing open heart surgery at the University Heart Center Freiburg-Bad Krozingen. All tissue is used with written informed consent and handled *via* the CardioVascular BioBank (CVBB) Freiburg, as approved by the Ethics Commission of the University of Freiburg, Freiburg, Germany (CVBB ethical approval reference 393/16 and 214/18). Human and porcine tissues were provided *via* the CardioVascular BioBank (CVBB study approval reference 214/18). Enzymatic cell isolation followed the protocol of Schmidt et al. (2017). Myocardial tissue was placed into Ca^{2+}-free "Kraftbrühe" (Isenberg and Klockner, 1982); containing (in mM): 20 KCl, 10 KH_2PO_4, 25 glucose, 40 D-mannitol, 0.1% (w/v) albumin, 70 K-glutamate, 10 β-hydroxybutyrate, 20 taurine, 10 ethylene glycol tetraacetic acid (EGTA); pH adjusted to 7.4 using KOH, ∼300 mOsm L^{-1}. Tissue was cut into pieces of 1 mm^3, and rinsed for 5 min with pre-digestion solution (in mM): 137 NaCl, 5 KH_2PO_4, 1 $MgSO_4$ ($7H_2O$), 10 glucose, 10 taurine, 5 HEPES, 0.2 EGTA; pH adjusted to 7.4 using NaOH, ∼300 mOsm L^{-1}). Solutions were oxygenated with 100% O_2 at 37°C and stirred. For digestion, tissue pieces were transferred for 10 min into digestion solution [as pre-digestion solution, but without EGTA, and supplemented with albumin (0.1%), collagenase type V (200 U mL^{-1}) and proteinase type XXIV (5.4 U mL^{-1}); all Sigma Aldrich]. After induction of enzyme activity by increasing the Ca^{2+} concentration to 0.02 mM, tissue chunks were agitated for further 20–30 min and then transferred into protease-free cell isolation solution (containing collagenase and 0.02 mM Ca^{2+})

for another 10 min. Dissociation of single cells was checked under a light microscope. The last dissociation step was repeated until cardiomyocytes with clear cross striations appeared. Digestion was stopped by removing the supernatant when 2–3 cross-striated cells per field of view were observed at high magnification (40× objective). Cell suspensions were centrifuged (2 min at 7 × g; PK121R, ALC, United Kingdom), and myocytes were re-suspended in Kraftbrühe without EGTA at RT, until use. If enrichment in non-myocytes was needed, centrifugation at 260 × g for 5 min was performed, to spin down cardiomyocytes and to enrich the supernatant in non-myocytes.

Statistics

If not specified otherwise, data are presented as mean ± standard error of the mean. For statistical analysis, Origin 2019 software (OriginLab Corporation, United States) was used; graphic representations were made using Origin and Canvas X software (ACD Systems, United States). "N" indicates the number of independent experiments (e.g., the number of animals or tissue donors); "n" is the number of cells studied. In general, control data are shown in black, interventions in red.

Significance of the difference between two independent and normally distributed groups was tested with a two-tailed Student's *t*-test if $n \geq 20$, or with the non-parametric Mann–Whitney-test if $n < 20$. Prior to *t*-tests, each sample was tested for variance. If paired experiments were conducted (whole-cell configuration), means were compared using the paired *t*-test. To compare the presence or absence of membrane rupture, the Chi-square test was used if $n \geq 20$, and Fisher's exact test if $n < 20$. One asterisk indicates a *p*-value $p \leq 0.05$ and this was considered indicative of a statistically significant difference between means; two asterisks: $p < 0.01$; three asterisks: $p < 0.001$; n.s. indicates that no significant differences are seen ($p > 0.05$).

Statistical power analysis was performed with GPower 3.1 software to identify the necessary sample size.

RESULTS

LecA Binding Dynamics and Effects on Membrane Topology

Cy3-labeled LecA started to binds at the surface of HEK cells by the first time-point we could image after addition to the bath solution (**Figures 1A–D**), i.e., within less than 30 s (hereafter referred to as the first 1 min-bin). LecA binding was quantified as fluorescence per cell (a.u.) and amounted to 1,169.0 ± 140.3 at 1 min, rising to 1,753.6 ± 188.86 at 2 min ($n = 63$; $N = 6$; $p = 0.014$; **Figure 1E**). At 15 min, LecA intensity was 2,487.8 ± 190.4 ($n = 63$; $N = 6$; $p = 0.007$ compared to 2 min). At this time-point, the first internalized LecA vesicles were detected, and tubular invaginations or single labeled endosomes started to appear (arrows in **Figures 1D,F**). LecA accumulated preferentially at cell-cell contact sites compared to patches of membrane facing the bath solution (**Figures 1G,H**). Accumulation of LecA on the surface of HEK cells was clustered after 1 min of incubation (**Figures 1B–D,F**). Similar uneven distribution was also observed on GUV after the initial binding phase where LecA also induced concave membrane deformations (**Figure 1I**).

EM and ET of cells chemically fixed after 17 min of LecA exposure revealed concave membrane invaginations; compatible in their shape with caveolae-like structures, while others are more tubular. These invaginations are not seen in time-matched controls (tmControl) in the absence of LecA (**Figures 2A,B**).

CLEM further demonstrated (i) the preferential localization of the fluorescent signal at cell-cell interfaces (**Figure 2C**), and the association of membrane invaginations with LecA fluorescence (**Figure 2D**). Membrane invaginations at cell-cell interfaces often presented as paired in/ex-vagination events of the two apposing cell membranes. While all membrane invaginations were associated with LecA fluorescence, LecA signal was also seen in membranes containing no curved domains, possibly owing to the fact that membrane curvature induction by LecA is a non-synchronized process that takes place over time.

LecA Effect on SAC

In patch-clamp experiments, HEK cells transfected with Piezo1 or TREK-1 exhibited significantly higher SAC activity than non-transfected tmControl cells (for Piezo1 at all suction levels more negative than −10 mmHg; for TREK-1 even at rest; **Supplementary Figure S1**), indicating effective functional expression of the channels. Moreover, channel kinetics were similar to those published previously (Patel et al., 1998; Coste et al., 2010).

Piezo1 activity was not affected by LecA, neither in cell-attached, nor in whole-cell configurations. As an example: at a holding potential of −80 mV, the average current at −35 mmHg was −14.3 ± 2.8 pA in tmControl ($n = 37$) and −12.4 ± 2.2 pA in LecA-exposed cells ($n = 37$, $p = 0.574$; **Figure 3A**). Current-pressure relationships were not different in the two conditions (**Figure 3B**). The same held true for the time-constants of inactivation, peak current and near steady-state current (**Supplementary Figures S2B–D**). At a holding potential of +40 mV, current-pressure relationships were also not different between both groups ($n = 23$ each for LecA and the tmControl group, data not shown). The voltage ramp protocols applied in whole-cell configuration upon LecA exposure did not reveal any changes in Piezo1 current either. The ratio of current after LecA application to pre-drug control did not change from 0 to 80 s. Analyzed at +40 mV of the ramp pulse and after 80 s of LecA exposure, ratios were 1.04 ± 0.02 with LecA ($n = 7$) and 1.00 ± 0.01 in tmControl ($n = 7$, $p = 0.371$; **Supplementary Figures S2E,F**). At −80 mV, there was also no difference between both groups (data not shown).

In contrast to Piezo1, TREK-1 was sensitized to mechanical stimulation by LecA. In cell-attached configuration, this was significant for pressures more negative than −20 mmHg (**Figures 3C,D**). The average current at −40 mmHg was 27.6 ± 7.0 pA in tmControl ($n = 37$) and 87.6 ± 23.3 pA in cells exposed to 500 nM LecA for 2 min ($n = 46$, $p = 0.007$). Individual average currents measured at −40 and −60 mmHg are depicted in **Figures 3E,F**. Current-pressure curves for peak and near steady-state current were also significantly different with and without LecA, while the time constants of peak current decay

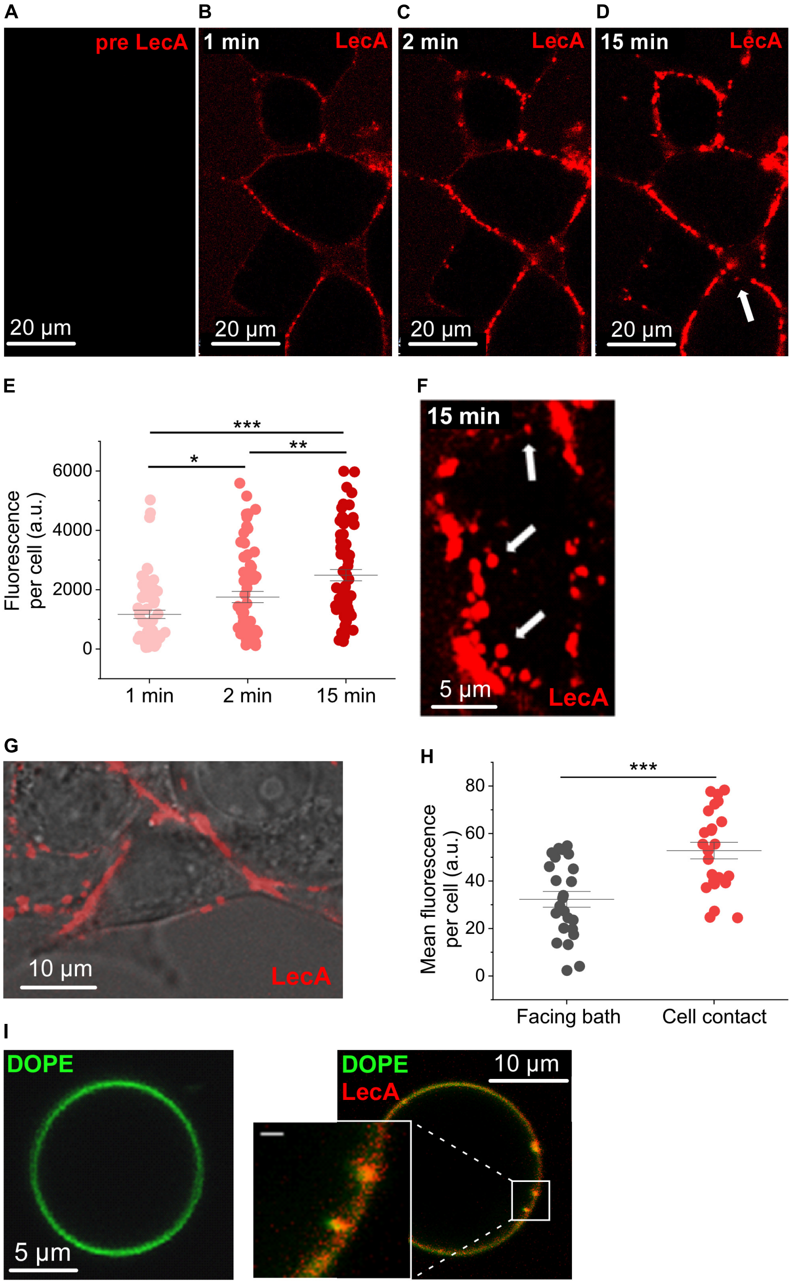

FIGURE 1 | LecA binding to HEK cells and giant unilamellar vesicles. Representative confocal microscopy images (one plane) of HEK cells incubated with LecA (in red). **(A)** Before application of 500 nM LecA. **(B)** LecA within the first minute after application. **(C)** LecA accumulation at 2 min. **(D,F)** appearance of first endosomes at 15 min (arrows). **(E)** Quantification of the fluorescence of LecA per cell at 1, 2, and 15 min ($n = 63$; $N = 6$). Significance was assessed by the t-test. **(G)** Overlay of transmission light and fluorescence microscopy, illustrating LecA accumulation at cell-cell contact site and less LecA staining at the cell membrane facing the bath. **(H)** Quantification of the mean fluorescence of LecA per cell at membranes facing the bath or facing a neighboring cell (cell contact; $n = 24$; $N = 6$). Significance was assessed by the t-test. **(I)** Gb3-decorated giant unilamellar vesicle (Atto 647N 1,2-dioleoyl-sn-glycero-3-phosphoethanolamine (DOPE), green) without (left) and with (right) 500 nM of LecA (red). LecA (500 nM) binds to Gb_3 and induces tubular membrane invaginations (inset, scale bar = 1 µm). $^*p \leq 0.05$, $^{**}p < 0.01$, and $^{***}p < 0.001$.

were not (**Supplementary Figure S3**). At a holding potential of −120 mV, the current-pressure relationships were not different between both groups ($n = 23$ for the tmControl group and $n = 23$ cells in presence of LecA; data not shown).

The concentration-dependence of LecA effects on TREK-1 was tested in cell-attached configuration at a holding potential of 0 mV. While 45 and 100 nM of LecA had no effect after 2 min, 225 and 500 nM increased the TREK-1

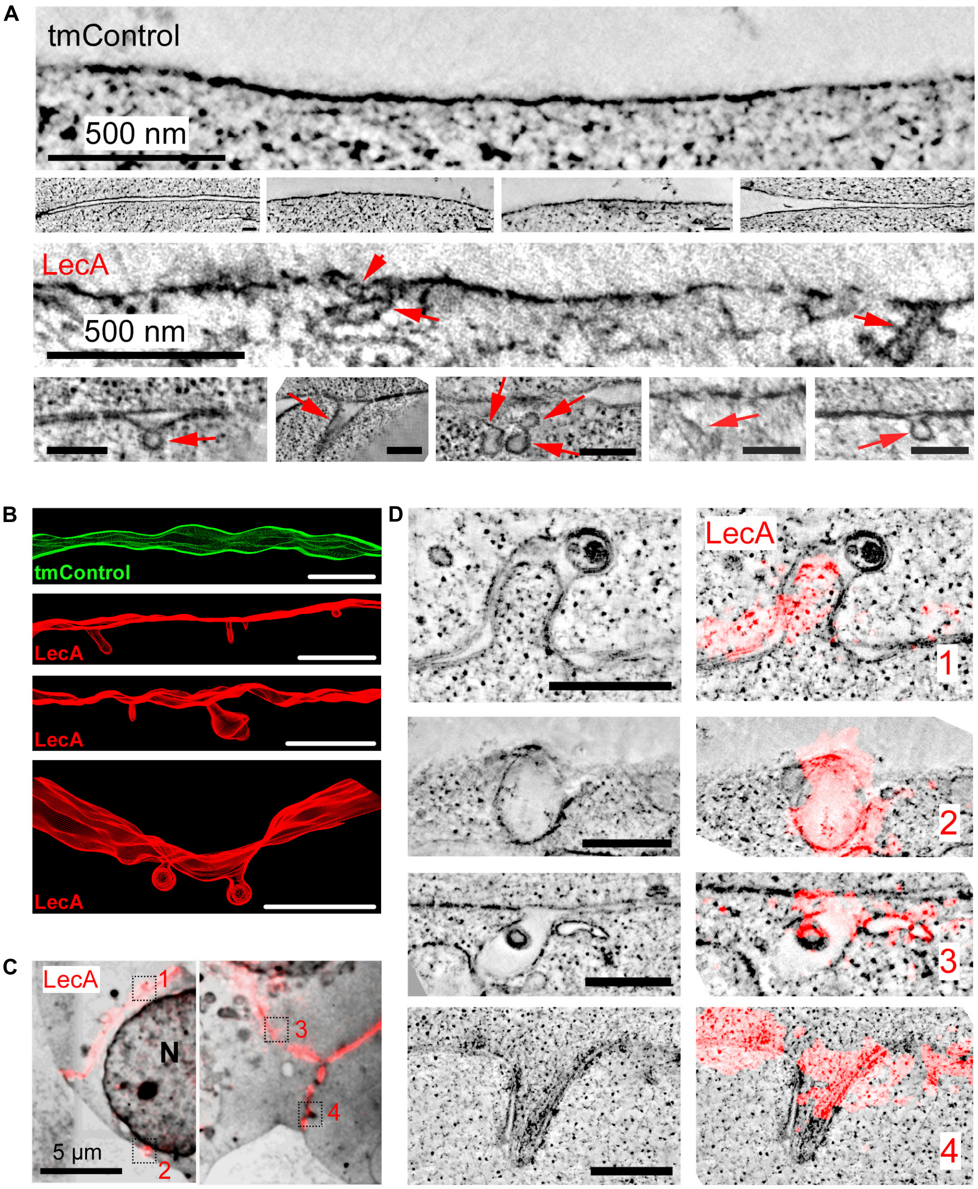

FIGURE 2 | LecA-associated changes in membrane ultrastructure in HEK cells. **(A)** Representative 2D electron tomographic slices (maximum projection over 50 nm) of tmControl cells (top rows) and cells exposed for 17 min to 500 nM LecA (bottom rows), demonstrating the morphology of LecA-associated surface membrane invaginations. If not otherwise stated, scale bars = 200 nm. **(B)** Representative 3D electron tomographic reconstructions of surface plasma membrane in tmControl (top, green) and LecA-exposed cells (red), demonstrating numerous membrane invaginations. Reconstructed volume: $(4{,}190 \times 4{,}190 \times 300)\ \mathrm{nm}^3$; scale bars = 500 nm. **(C)** CLEM overview maps of LecA-exposed cells, demonstrating the preferential localization of the fluorescent signal at the cell-cell interfaces. The median free gap width between adjacent cells in areas of high fluorescence signal is 8.8 nm. Squares highlight the location of larger resolution images in **(D)**. N, nucleus. **(D)** Representative 2D electron tomographic slices (left) and corresponding CLEM images (right) of LecA-exposed cells. The slices demonstrate the colocalization of LecA staining (red) with plasma membrane invaginations on neighboring and single (second panel from above) cells. Scale bar = 500 nm.

response to stretch. As for the fold change (LecA/tmControl) in average current, the half maximal effective pressure was −46.6 mmHg at 45 nM, −39.1 mmHg at 100 nM, −45.0 mmHg at 255 nM, and −18.3 mmHg at 500 nM of LecA with $n = 13, 50, 25, 46$, respectively (a total of $n = 133$ tmControl recordings were conducted; **Figure 3G**). At −20 mmHg, the concentration-response curve is shown **Figure 3H**. In whole-cell configuration, the effect of LecA on TREK-1 during the first 80 s of exposure was determined with voltage ramp pulses. The LecA-induced current showed outward rectification (**Figure 4A**). The activity of TREK-1, relative to pre-drug control, increases with exposure time to LecA, with significant difference for all time points exceeding 55 s (**Figure 4B**). As an example, after 80 s and +40 mV of the ramp pulse, corresponding values were 1.13 ± 0.04 with LecA ($n = 12$) and 1.01 ± 0.04 in tmControl ($n = 11$, $p = 0.039$; **Figure 4C**). The propensity toward increasing

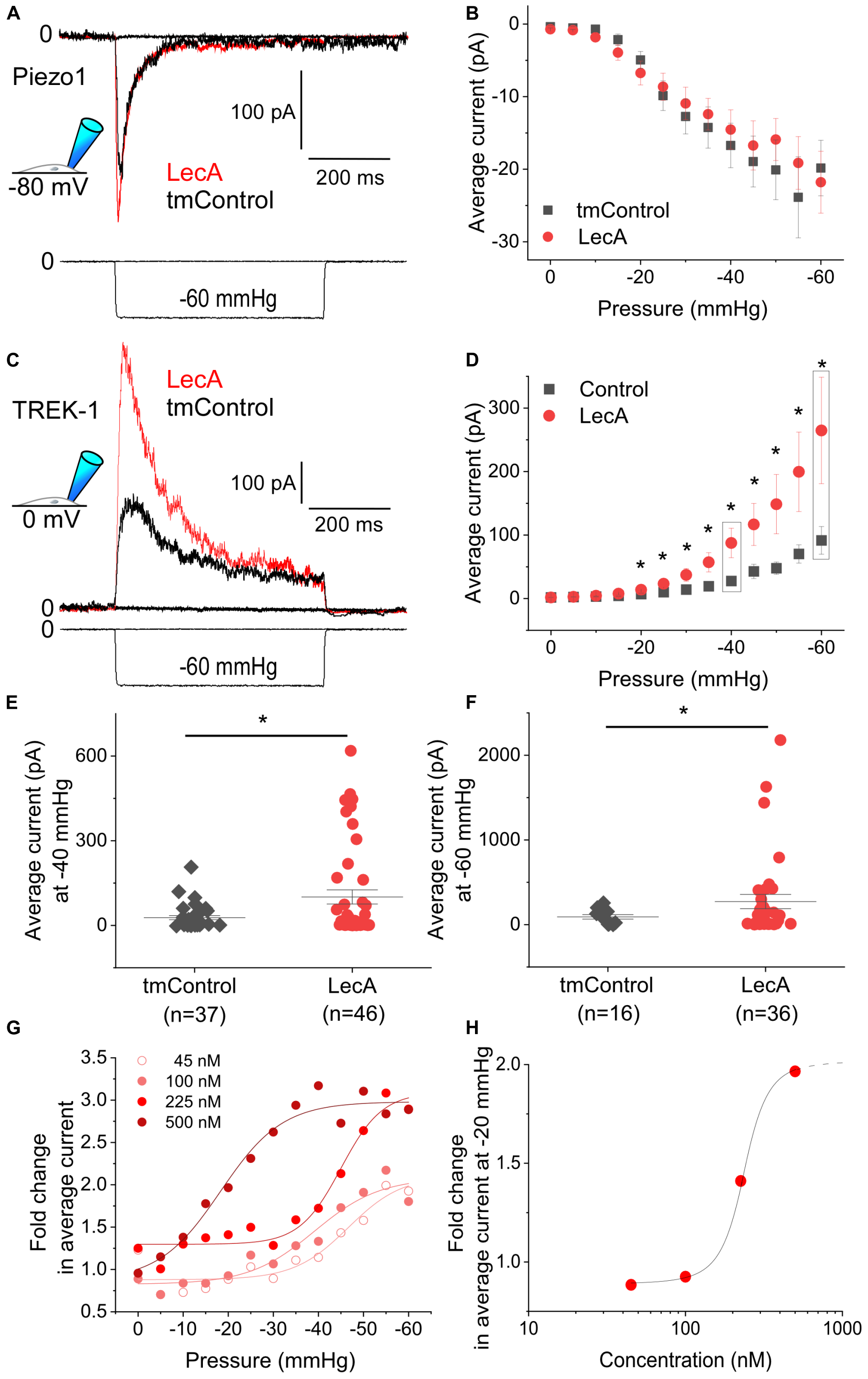

FIGURE 3 | Mechanically-induced Piezo1 and TREK-1 activity in absence or presence of LecA in HEK cells. Patch-clamp measurements in cell-attached configuration showing Piezo1 **(A,B)** and TREK-1 **(C–H)** activity, at holding potentials of −80 and 0 mV, respectively, after 2 min of exposure to 500 nM LecA (red), compared to time-matched controls (tmControl, black). **(A)** Representative Piezo1 recording during application of negative pressure (mechanical activation) of −35 mmHg. **(B)** Quantification of Piezo1 activity in the absence or presence of LecA at 0 mmHg (*n* = 38 and 38, respectively) and −60 mmHg (*n* = 23 and 23, respectively, lower n-numbers in tmControl cells are caused by patches that did not withstand −60 mmHg suction levels). Significance assessed by the *t*-test. **(C)** Representative TREK-1 recording during application of negative pressure (mechanical activation) of −60 mmHg. **(D)** Quantification of TREK-1 activity in the absence and presence of LecA at 0 mmHg (*n* = 43 and 46, respectively) and −60 mmHg (*n* = 16 and 36, respectively; lower n-numbers in tmControl as above). Significance assessed by the *t*-test. **(E,F)** Single data points and means ± SEM of TREK-1 at −40 and −60 mmHg. Significance was assessed by the *t*-test. **(G)** Fold change (LecA/tmControl) in TREK-1 average current at suction levels from 0 to −60 mmHg for different LecA concentrations (45, 100, 225, and 500 nM). The averaged data were fitted with a Boltzmann function. **(H)** Concentration-response curve, the stretch-induced fold change (LecA/tmControl) in TREK-1 average current at −20 mmHg is presented as a function of LecA concentration. $^{*}p \leq 0.05$.

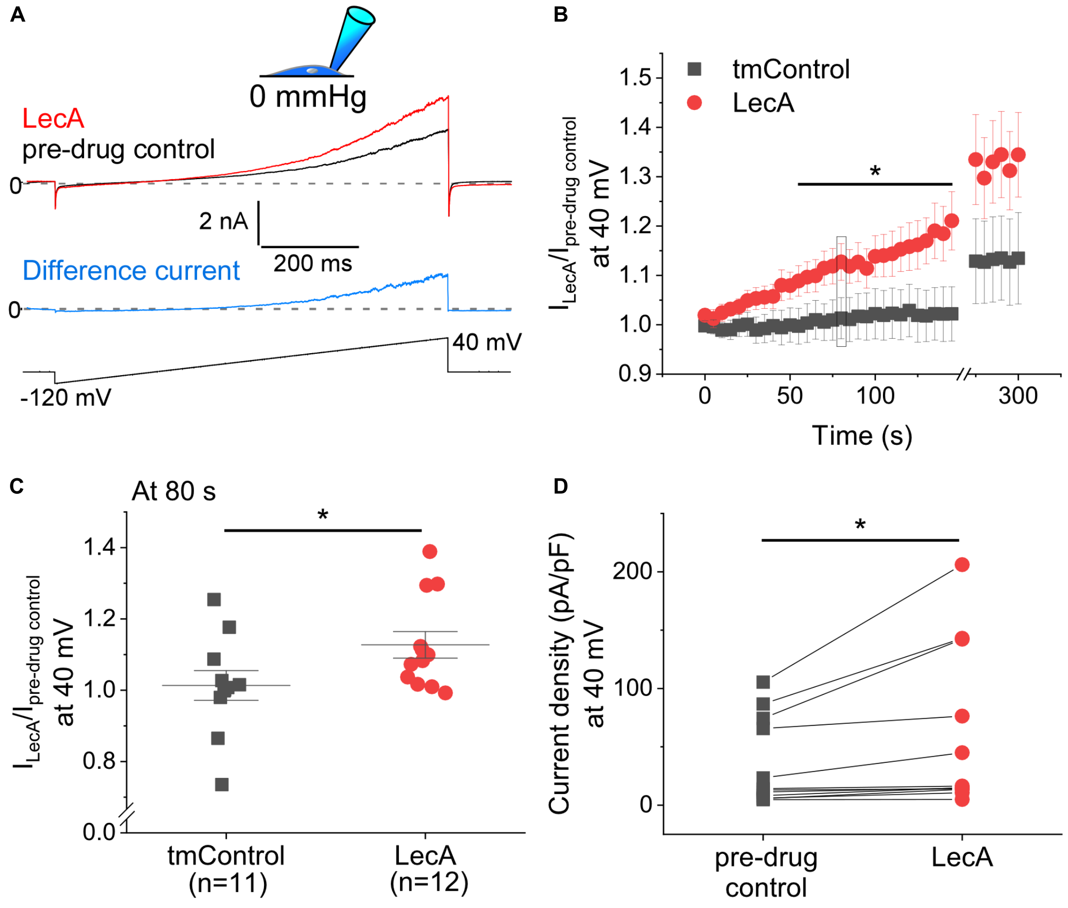

FIGURE 4 | Voltage-induced TREK-1 activity in absence or presence of LecA in HEK cells. Patch-clamp measurements in whole-cell configuration (pipette pressure 0 mmHg). **(A)** Representative recording; Top: LecA at 80 s after onset of LecA exposure; pre-drug control 10 s before LecA exposure; Middle: Difference current (blue); pre-drug control activity subtracted from LecA activity; Bottom: voltage ramp applied from −80 to +40 mV. **(B)** Quantification of the activity induced by LecA vs. tmControl (n = 12 at 0 and 80 s in both groups). **(C)** Single data points (tmControl vs. LecA) at 80 s are shown. Significance was assessed by the Mann–Whitney-test. **(D)** Single paired data points (pre-drug control vs. LecA). The maximum density of LecA-induced current is shown. Significance was assessed by the paired t-test. $^*p \leq 0.05$.

TREK-1 current was visible on a cell-by-cell basis (p = 0.031) (**Figure 4D**). At −80 mV, there was no difference between both groups (data not shown).

Since the known membrane curvature inducer AA had been shown previously to reversibly activate TREK-1 (Fink et al., 1998), we also tested its effect. As expected, 10 μM of AA produced robust activation of TREK-1 in whole-cell recordings, which reversed slowly upon wash-out (**Supplementary Figure S4**). Interestingly, AA, like LecA, did not alter Piezo1 activity (**Supplementary Figure S5**).

LecA Effect on Patch Stability

Suction pulses of high negative pressure can destabilize a membrane patch and cause sudden loss of the current trace. We investigated the influence of LecA on the maximum negative pressure that patched cell membranes can withstand (Piezo1 and TREK-1 cell-attached recordings, pooled). In tmControl conditions, sudden loss of recordings started to occur at −35 mmHg. In the presence of LecA, higher negative pressure values were tolerated, so that first losses were observed at −45 mmHg. At −80 mmHg, only 14.5% of tmControl patches (n = 61) remained intact, whereas 53.7% of patches in the presence of LecA were sustained (n = 71; **Figure 5**). This difference was statistically significant for all pressure levels more negative than −45 mmHg (p = 0.021; chi-square test). This difference was maintained for in- and outward currents for both channels (data not shown).

Cell Type Dependency of LecA Binding

In freshly isolated cardiac cell suspensions from mouse, rabbit, pig and human, no LecA binding to cardiomyocytes was observed (0%, n = 30 for pig and 300 for the other species, **Figures 6A–C**). In contrast, non-myocytes exhibited intense membrane staining (66, 75, 61, and 44%; n > 450 for each group; **Figure 6C**). This differential binding is illustrated in **Figures 6A,B**; note: T-tubules are visible due to diffusion of labeled LecA into their lumen.

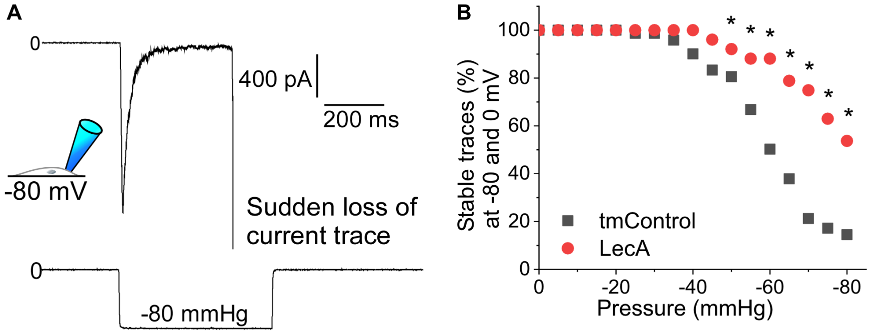

FIGURE 5 | Patch stability in response to negative pressure in the absence or presence of LecA in HEK cells. Patch-clamp measurements in cell-attached configuration (data pooled from Piezo1 and TREK-1 recordings) after 2 min of LecA exposure. **(A)** Exemplary recording of a sudden loss of the current trace at −80 mmHg suction; here voltage clamped to −80 mV. **(B)** Quantification of the maximum pressure levels that were sustained in tmControl (*n* = 61 at 0 mmHg; *n* = 11 at −80 mmHg) vs. LecA (*n* = 71 at 0 mmHg; *n* = 38 at −80 mmHg). Significance was assessed by the chi-square test. $^{*}p \leq 0.05$.

DISCUSSION

The present study shows that LecA binds to non-myocytes (but not to cardiomyocytes), inducing changes in surface membrane topology, and enhancing the stretch-sensitivity of TREK-1 but not of Piezo1.

LecA Binding Dynamics and Effects on Membrane Topology

LecA binds to the plasma membrane of HEK cells within seconds. In confocal microscopy, first LecA-positive intracellular structures, compatible with endosomes, are detected 15 min after the start of LecA exposure. This time period determined the window for subsequent electrophysiological investigations.

LecA forms clusters at the cell surface. This binding pattern may be explained by the heterogeneous distribution of Gb_3 within specific plasma membrane domains (Kovbasnjuk et al., 2001; Nutikka and Lingwood, 2003).

LecA becomes enriched over time at the interfaces between adjacent cells. This confirms a recently published observation that LecA crosslinks protocells to form prototissues (Villringer et al., 2018; Omidvar and Römer, 2019). One LecA, crosslinking two neighboring cells, might encounter less steric hindrance than binding to up to four Gb_3 on the flat surface of a single cell. The opposing binding pockets of LecA are approximately 7 nm apart (Schubert and Römer, 2015). This distance is assumed to be large enough for crosslinking neighboring plasma membranes at points of close cell-to-cell contact. Our EM data is compatible with this possibility (just under half of the intercellular gaps are narrow enough to be bridged by LecA), and suggestive of the presence of additional mechanism(s) in regions where LecA accumulation is present in spite of inter-cellular gaps exceeding LecA size; these remain to be assessed.

Plasma membrane invaginations, colocalizing with LecA staining in our CLEM data, are highly curved membrane domains and, in places, resemble structures such as either caveolae or toxin-induced membrane tubules (Römer et al., 2007). As the voxel size of the fluorescent channel is more than 6 orders of magnitude larger than that of ET, we cannot unequivocally relate the fluorescent signal to specific ultrastructures. Beyond the in-plane resolution differences, one must bear in mind that the fluorescent signal can be generated in planes below or above the ET slices shown. That said, all membrane invaginations observed in ET occurred in membrane areas rich in LecA signal. This supports the ability of LecA (without the need for presence of LecA-producing bacteria) to trigger membrane deformations. Since such invaginations are also observed on synthetic GUV membranes, we conclude that they are not confined to cells. HEK cells endogenously express only low levels of caveolin1 (Jung et al., 2004; Pérez-Verdaguer et al., 2016) and hence lack caveolae (**Figure 2A**), additionally confirming the concept that LecA generates the observed membrane invaginations.

Taken together, in confocal microscopy, we observed two main LecA binding patterns: first, there are clusters (patchy pattern), possibly accounting for local negative membrane curvature (in accordance with EM data). Second, there is accumulation of LecA at cell-cell contact sites, possibly leading to cell crosslinking.

LecA Effect on SAC

Patch-clamp recordings were performed from 2 min until 15 min after the start of LecA exposure. Electrical and mechanical stimulation protocols were applied to pre-strained membrane patches (in cell-attached configuration, membrane tension is ∼30–40% of the membrane lytic tension; Sachs, 2010), while electrical recordings were also conducted on membranes with a less disturbed mechanical environment (whole-cell configuration).

Neither AA, a well-known inducer of negative membrane curvature, nor LecA, which also causes membrane invagination, activates Piezo1. Piezo1 itself induces negative curvature in membranes, because of its curved transmembrane region (Murthy et al., 2017; Saotome et al., 2018). Stretch-activation of Piezo1 has been proposed to be due to flattening of the Piezo-related local concave dome structure (Haselwandter and MacKinnon, 2018). Thus, compounds that stabilize or enhance negative membrane curvature may prevent Piezo1 activation. Of course, membrane domains exhibiting Gb_3, to which LecA binds, may not co-localize with domains exhibiting Piezo1.

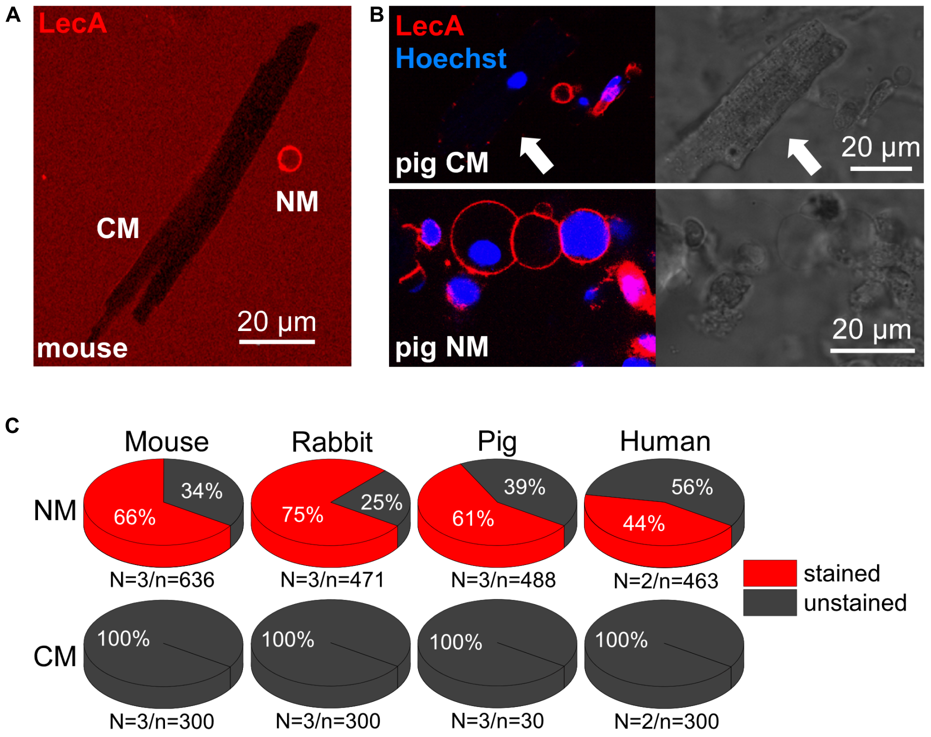

FIGURE 6 | LecA binding to cardiac myocytes vs. non-myocytes. **(A,B)** Confocal images of murine **(A)** and porcine **(B)** cardiac cells (LecA: red; nuclei: blue). In contrast to non-myocytes (NM), LecA does not bind to the sarcolemma of cardiomyocytes (CM). **(C)** Quantification of LecA binding to NM (top) and CM (bottom) from mouse, rabbit, pig and human. N/n-numbers indicated below pie charts.

In contrast, TREK-1 currents are increased by LecA and AA, both in response to mechanical and electrical stimulation. In cell-attached configuration, LecA effects are highly variable. This may be explained by the irregular (patchy) binding pattern of LecA to α-galactose residues. This may have given rise to substantial differences in LecA presence in any given patch clamp investigation.

The effect of LecA is modest in comparison to the activity induced by AA. This may have several explanations. Firstly, the focal effects of LecA, promoting rapid endocytosis of highly curved membrane domains, might start happening before detection with confocal microscopy. This may lead to an underestimation of its effect on the channel in case a fraction of TREK-1 is located in excised invaginations and, hence, no longer detectable in the plasma membrane-dominated electrophysiological read-outs. Secondly, the membrane curvature induced by LecA (remotely via α-galactose residues) might be less efficient in activating SAC compared to the curvature induced by changes in lipid packing generated by AA. LecA was applied at a concentration 20 times lower than AA: 500 nM for LecA (above what is required to trigger host cell signaling; see section Lectins) vs. 10 µM for AA (most commonly used concentration in publications). However, we suggest that the concentration may not be a limiting factor in LecA membrane binding as free LecA is still present in the bath solution (high fluorescence level compared to pre-LecA application) even after 30 min.

The mechanism by which LecA modifies TREK-1 activity remains an open question. The most likely scenario is mechano-activation *via* the highly curved membrane domains generated by LecA. Their presence and dimensions, with curvature radii in the range of 100 nm (which matter for SAC gating; Bavi et al., 2016) have been confirmed by our ET findings. Even though membrane topology is altered by LecA, other mechanisms could also play a role. LecA may bind directly to the channel protein or trigger secondary signaling cascades, sensitizing TREK-1. The increased response to voltage stimulation by a change in membrane mechanics is in agreement with data published for AA (Kim and Duff, 1990; Kirber et al., 1992; Fink et al., 1998), and the mechanisms underlying these matching responses to LecA and AA remain to be assessed.

To sum up, we reproduced TREK-1 activation by AA upon electrical stimulation. We also show that TREK-1 activity is increased by LecA exposure, both upon mechanical and electrical stimulation, while no effect of AA or LecA on Piezo1 was observed.

LecA Effect on Patch Stability

Patch stability quantification reveals that LecA protects the plasma membrane, or the seal, from failure during high levels of suction. In the presence of LecA in the cell-attached configuration, recordings of Piezo1 and TREK-1 could be conducted at higher-amplitudes of negative pressure. Possible mechanisms explaining the increased stability of the patch in the presence of LecA may be stiffening of the membrane, coating of the membrane with LecA-crosslinks, or improved adhesion between glass pipette and cell membrane.

Cell Type Selectivity of LecA Binding

Cell-preferential binding of LecA is of interest for assessment of heterocellular organs, where cell composition may vary between regions, or change as a consequence of remodeling. We observed that LecA does not bind to cardiomyocytes of four mammalian species (mouse, rabbit, pig, and human), but to non-myocytes. It may be explained by the fact that the glycocalyx composition varies between cell types (Tsimbouri et al., 2014).

LecA, or similar compounds, could provide interesting tools for cell-selective targeting in heterocellular tissue. For example, one may be able to optimize protocols where separation between cardiac myocytes and non-myocytes has been challenging so far, such as in mechano-biology research. Furthermore, being endocytosed, LecA may operate as a cell type selective transfection reagent *in vivo*.

From a pathophysiological point of view, sensitization of TREK-1 by LecA might be a starting point for novel therapeutic targeting of atrial fibrillation or heart failure – two pathologies where TREK-1 has been reported to be suppressed (Lugenbiel et al., 2017). Furthermore, TREK-1 inhibits proliferation of neuronal stem cells, astrocytes, osteoblasts, Chinese hamster ovary cells, and neonatal cardiomyocytes (Hughes et al., 2006; Xi et al., 2011; Wang et al., 2012; Yang et al., 2014; Zhang et al., 2016), but increases the proliferation of prostate cancer cell lines (Voloshyna et al., 2008). A compound that enhances TREK-1 opening might help controlling pathological tissue remodeling associated with non-myocyte proliferation in the heart. Finally, non-myocytes can be electrically coupled to cardiac myocytes (Quinn et al., 2016; Hulsmans et al., 2017). If LecA favors TREK-1 opening in cardiac non-myocytes, these cells will be more polarized, which may affect excitability of electrotonically connected cardiac myocytes.

Limitations

LecA is a virulence factor of *P. aeruginosa* that has been shown to have cytotoxic effects in epithelial cells (Bajolet-Laudinat et al., 1994; Chemani et al., 2009), so its toxicity in cardiac non-myocytes will have to be explored. This will also determine whether the time-window, restricted in this study to ∼15 min from exposure to LecA, may be extended, which would be helpful for many experimental designs. For electrophysiological translation to the heterocellular tissue, a compound with prolonged binding to the surface membrane and reduced membrane bending effect is needed. This said, compared to traditional SAC modulators, such as lipids that insert into one leaf of the bilayer to induce curvature, LecA offers the advantage of not directly altering membrane lipid composition, limiting potential side effects.

Outlook

In a further study, the localization of the channels (especially TREK-1) relatively to LecA and curved membrane domains will be performed. Membrane invaginations associated to LecA might colocalize with the channels. In this case, local curvature would explain the effect on the channel gating. In the opposite case, if there is no colocalization, this would suggest that an increase in the global in-plane membrane tension sensitizes the channels. Long-term effects of LecA will address whether the endocytosis observed leads to a decrease of the number of TREK-1 channels at the plasma membrane.

CONCLUSION

This study demonstrates that LecA binds to non-myocytes, but not to cardiomyocytes, and changes plasma membrane topology in HEK cells. LecA increases the activity of human TREK-1 in HEK cells, in response to both mechanical and electrical stimulation, but not of human Piezo1. The here identified differential SAC modulator is potentially capable of acting in a cell type-dependent manner. It offers promise as a potential experimental tool to explore mechanotransduction in heterocellular tissues, including comparative assessments of normal and physiologically remodeled cardiac tissue.

DATA AVAILABILITY STATEMENT

The datasets generated for this study are available on request to the corresponding author.

ETHICS STATEMENT

The studies involving human participants were reviewed and approved by Ethics Commission of the University of Freiburg, reference: 393/16 and 214/18. The patients/participants provided their written informed consent to participate in this study. The animal study was reviewed and approved by Local authorities in Baden Württemberg (X-16/10R).

AUTHOR CONTRIBUTIONS

PK, RP, UR, WR, JM, and ED contributed to the conception and design of the study. AB supplied the lectins and supported their experimental application. ED performed and analyzed the experiments. LS and RO performed and analyzed the GUV experiments. ER-Z acquired and analyzed the EM images. ED drafted the manuscript. All authors contributed to manuscript revision and approved the submitted version.

FUNDING

This research was supported by the European Research Council (Advanced Grant CardioNECT, Project ID: #323099, PK) and a research grant from the Ministry of Science, Research and Arts Baden-Württemberg (MWK-BW Sonderlinie Medizin, #3091311631). WR acknowledges support by the Deutsche Forschungsgemeinschaft (DFG, German Research Foundation) under Germany's Excellence Strategy (EXC-2189 – Project ID: 390939984 and EXC-294), by the DFG-funded grants RTG 2202 (Transport across and into membranes) and RO4341/3-1, by the Ministry of Science, Research and the Arts of Baden-Württemberg (Az: 33-7532.20), and by the European Union's Horizon 2020 Research and Innovation Programme under the Marie Skłodowska-Curie grant agreement synBIOcarb (No. 814029). ER-Z is an Emmy Noether Fellow and acknowledges support by the German Research Foundation (396913060). The article processing charge was funded by the University of Freiburg Open Access Publishing programme.

ACKNOWLEDGMENTS

We thank Cinthia Buchmann and Pia Iaconianni for their excellent technical support. Isolated cells from different species were kindly provided by Ramona Kopton, Diana Aria, Ana Simon-Chica and Marbely del Carmen Calderón Fernández (all IEKM, Freiburg). We thank the staff and patients of the Department for Cardiovascular Surgery of the University Heart Centre Freiburg – Bad Krozingen for access to human tissue. We are grateful to the staff of CVBB for providing human and porcine tissue samples. We thank Eric Honoré and Delphine Bichet for the gift of the TREK-1-IRES2-eGFP plasmid, and Frederick Sachs for the Piezo1-IRES2-eGFP plasmid. We would like to acknowledge the microscopy facility SCI-MED (Super-Resolution Confocal/Multiphoton Imaging for Multiparametric Experimental Designs at IEKM) for providing access to and support with confocal microscopy, and the EM Core Facility at the European Molecular Biology Laboratory Heidelberg for providing advice, assistance, and access to electron microscopy.

SUPPLEMENTARY MATERIAL

The Supplementary Material for this article can be found online at: https://www.frontiersin.org/articles/10.3389/fphys.2020.00457/full#supplementary-material

FIGURE S1 | Characterization of background activity and SAC currents in Piezo1 and TREK-1 transfected HEK cells. Patch-clamp measurements in cell-attached configuration (holding potential −80 mV for Piezo1 and 0 mV for TREK-1. **(A,C)** Representative patch-clamp recordings of non-transfected cells (top), and Piezo1 **(A)** or TREK-1 **(C)** transfected cells (middle); pressure pulses applied are 0 and −70 mmHg (bottom). **(B)** Quantification of endogenous activity at −80 mV (squares; $n = 8$ at 0 mmHg; $n = 6$ at −60 mmHg) vs. Piezo1-transfected cells (circles; $n = 38$ at 0 mmHg; $n = 25$ at −60 mmHg. **(D)** Quantification of endogenous activity at 0 mV (squares; $n = 16$ at 0 mmHg; $n = 5$ at −60 mmHg) vs. TREK-1-transfected cells (circles; $n = 32$ at 0 mmHg; $n = 13$ at −60 mmHg). Lower n-numbers at higher suction levels are caused by patches that did not withstand large pressure pulses.

FIGURE S2 | Piezo1 activity in presence or absence of LecA in HEK cells. Patch-clamp measurements in cell-attached configuration (holding potential −80 mV; **A–C**) and whole-cell configuration (holding pressure 0 mmHg; **D,E**). **(A)** Analyzed parameters (applies also to TREK-1), obtained for one pulse of pressure (vertical dashed lines). From the recorded trace (black) the peak, near steady-state (green) and average (blue) current amplitudes are deduced. The exponential fit (red) yields the time constant of current inactivation. **(B–D)** Quantification of the activity induced by LecA (2 min; $n = 37$) vs. tmControl ($n = 38$). **(E)** Quantification of the activity induced by LecA over 200 s of LecA exposure ($n = 7$ for all data). **(F)** Single data points at 80 s are shown. Significance was assessed by the Mann–Whitney-test.

FIGURE S3 | TREK-1 activity in the absence or presence of LecA in HEK cells. Patch-clamp measurements in cell-attached configuration (holding potential 0 mV). **(A–C)** Quantification of the activity induced by LecA (2 min; $n = 46$; in red) vs. tmControl ($n = 43$; in black). $^{*}p \leq 0.05$.

FIGURE S4 | TREK-1 activity in the absence of presence of arachidonic acid (AA) in HEK cells. Patch-clamp measurements in whole-cell configuration (holding pressure 0 mmHg); control: black, AA (10 μM) in the extracellular bath solution: red, wash-out: green. **(A)** Representative recording; Top: 80 s after onset of AA perfusion; pre-drug control at 10 s before onset of AA perfusion; After 90 s of wash-out; Middle: Difference current (blue); pre-drug control activity subtracted from AA activity; Bottom: voltage ramp applied from −80 to +40 mV. **(B)** Quantification of the TREK-1 activation normalized to the pre-drug control, for AA ($n = 9$ at 0 s; $n = 5$ at 80 s) vs. tmControl ($n = 4$ at 0 and 80 s), 0 s corresponds to the onset of AA perfusion. **(C)** Single data points at 55 s are shown. Significance was assessed by the Mann–Whitney-test. **(D)** Quantification of the reversibility of the AA effect. The current during wash-out ($I_{\text{wash-out}}$) is normalized to the peak current reached during AA perfusion (I_{AApeak}), for wash-out effect at 5 s ($n = 8$) vs. 90 s ($n = 3$), 0 s corresponds to the onset of wash-out perfusion. **(E)** Single data points at 5 and 90 s are shown. Significance was assessed by the Mann–Whitney-test. $^{*}p \leq 0.05$.

FIGURE S5 | Piezo1 activity in the absence or presence of arachidonic acid (AA) in HEK cells. Patch-clamp measurements in whole-cell configuration (holding pressure 0 mmHg); AA (10 μM) in the bath solution: red, tmControl: black. **(A)** Quantification of Piezo1 activity during AA exposure ($n = 6$ at 0 s; $n = 3$ at 80 s) vs. tmControl ($n = 4$ at 0 s; $n = 3$ at 80 s). **(B)** Single data points at 80 s are shown. Significance was assessed by the Mann–Whitney-test.

REFERENCES

Abraham, D. M., Lee, T. E., Watson, L. J., Mao, L., Chandok, G., Wang, H.-G., et al. (2018). The two-pore domain potassium channel TREK-1 mediates cardiac fibrosis and diastolic dysfunction. *J. Clin. Invest.* 128, 4843–4855. doi: 10.1172/JCI95945

Aigal, S., Claudinon, J., and Römer, W. (2015). Plasma membrane reorganization: a glycolipid gateway for microbes. *Biochim. Biophys. Acta* 1853, 858–871. doi: 10.1016/j.bbamcr.2014.11.014

Bajolet-Laudinat, O., Bentzmann, S. G., Tournier, J. M., Madoulet, C., Plotkowski, M. C., Chippaux, C., et al. (1994). Cytotoxicity of *Pseudomonas aeruginosa* internal lectin PA-I to respiratory epithelial cells in primary culture. *Infect. Immun.* 62, 4481–4487.

Bavi, O., Cox, C. D., Vossoughi, M., Naghdabadi, R., Jamali, Y., and Martinac, B. (2016). Influence of global and local membrane curvature on mechanosensitive ion channels: a finite element approach. *Membranes* 6:14. doi: 10.3390/MEMBRANES6010014

Beech, D. J., and Kalli, A. C. (2019). Force sensing by piezo channels in cardiovascular health and disease. *Arterioscler. Thromb. Vasc. Biol.* 39, 2228–2239. doi: 10.1161/ATVBAHA.119.313348

Blanchard, B., Nurisso, A., Hollville, E., Tétaud, C., Wiels, J., Pokorná, M., et al. (2008). Structural basis of the preferential binding for globo-series glycosphingolipids displayed by *Pseudomonas aeruginosa* Lectin I. *J. Mol. Biol.* 383, 837–853. doi: 10.1016/j.jmb.2008.08.028

Blythe, N. M., Muraki, K., Ludlow, M. J., Stylianidis, V., Gilbert, H. T. J., Evans, E. L., et al. (2019). Mechanically activated Piezo1 channels of cardiac fibroblasts stimulate p38 mitogen-activated protein kinase activity and interleukin-6 secretion. *J. Biol. Chem.* 294, 17395–17408. doi: 10.1074/jbc.RA119.009167

Burton, R. A. B., Rog-Zielinska, E. A., Corbett, A. D., Peyronnet, R., Bodi, I., Fink, M., et al. (2017). Caveolae in rabbit ventricular myocytes: distribution and dynamic diminution after cell isolation. *Biophys. J.* 113, 1047–1059. doi: 10.1016/J.BPJ.2017.07.026

Chemani, C., Imberty, A., de Bentzmann, S., Pierre, M., Wimmerová, M., Guery, B. P., et al. (2009). Role of LecA and LecB lectins in *Pseudomonas aeruginosa*-induced lung injury and effect of carbohydrate ligands. *Infect. Immun.* 77, 2065–2075. doi: 10.1128/IAI.01204-08

Chen, Q., Galleano, M., and Cederbaum, A. I. (1998). Cytotoxicity and apoptosis produced by arachidonic acid in HepG2 cells overexpressing human cytochrome P-4502E1. *Alcohol. Clin. Exp. Res.* 22, 782–784. doi: 10.1111/j.1530-0277.1998.tb03868.x

Cooper, P. J., Lei, M., Cheng, L.-X., and Kohl, P. (2000). Selected contribution: axial stretch increases spontaneous pacemaker activity in rabbit isolated sinoatrial node cells. *J. Appl. Physiol.* 89, 2099–2104. doi: 10.1152/jappl.2000.89.5.2099

Coste, B., Mathur, J., Schmidt, M., Earley, T. J., Ranade, S., Petrus, M. J., et al. (2010). Piezo1 and Piezo2 are essential components of distinct mechanically activated cation channels. *Science* 330, 55–60. doi: 10.1126/science.1193270

De Chaumont, F., Dallongeville, S., Chenouard, N., Hervé, N., Pop, S., Provoost, T., et al. (2012). Icy: an open bioimage informatics platform for extended reproducible research. *Nat. Methods* 9, 690–696. doi: 10.1038/nmeth.2075

Decher, N., Ortiz-Bonnin, B., Friedrich, C., Schewe, M., Kiper, A. K., Rinné, S., et al. (2017). Sodium permeable and "hypersensitive" TREK-1 channels cause ventricular tachycardia. *EMBO Mol. Med.* 9, 403–414. doi: 10.15252/emmm.201606690

Douguet, D., Patel, A., Xu, A., Vanhoutte, P. M., and Honoré, E. (2019). Piezo ion channels in cardiovascular mechanobiology. *Trends Pharmacol. Sci.* 40, 956–970. doi: 10.1016/j.tips.2019.10.002

Eierhoff, T., Bastian, B., Thuenauer, R., Madl, J., Audfray, A., Aigal, S., et al. (2014). A lipid zipper triggers bacterial invasion. *Proc. Natl. Acad. Sci. U.S.A.* 111, 12895–12900. doi: 10.1073/pnas.1402637111

Fink, M., Lesage, F., Duprat, F., Heurteaux, C., Reyes, R., Fosset, M., et al. (1998). A neuronal two P domain K^+ channel stimulated by arachidonic acid and polyunsaturated fatty acids. *EMBO J.* 17, 3297–3308. doi: 10.1093/emboj/17.12.3297

Hamill, O. P., and McBride, D. W. (1996). The pharmacology of mechanogated membrane ion channels. *Pharmacol. Rev.* 48, 231–252.

Haselwandter, C. A., and MacKinnon, R. (2018). Piezo's membrane footprint and its contribution to mechanosensitivity. *eLife* 7:e41968. doi: 10.7554/eLife.41968

Hughes, S., Magnay, J., Foreman, M., Publicover, S. J., Dobson, J. P., and El Haj, A. J. (2006). Expression of the mechanosensitive 2PK+ channel TREK-1 in human osteoblasts. *J. Cell. Physiol.* 206, 738–748. doi: 10.1002/jcp.20536

Hulsmans, M., Clauss, S., Xiao, L., Aguirre, A. D., King, K. R., Hanley, A., et al. (2017). Macrophages facilitate electrical conduction in the heart. *Cell* 169, 510–522.e20. doi: 10.1016/j.cell.2017.03.050

Inoue, R., Jensen, L. J., Shi, J., Morita, H., Nishida, M., Honda, A., et al. (2006). Transient receptor potential channels in cardiovascular function and disease. *Circ. Res.* 99, 119–131. doi: 10.1161/01.RES.0000233356.10630.8a

Iribe, G., Ward, C. W., Camelliti, P., Bollensdorff, C., Mason, F., Burton, R. A. B., et al. (2009). Axial stretch of rat single ventricular cardiomyocytes causes an acute and transient increase in Ca^{2+} spark rate. *Circ. Res.* 104, 787–795. doi: 10.1161/CIRCRESAHA.108.193334

Isenberg, G., and Klockner, U. (1982). Calcium tolerant ventricular myocytes prepared by preincubation in a "KB Medium". *Pflugers Arch.* 395, 6–18. doi: 10.1007/bf00584963

Johannes, L., Parton, R. G., Bassereau, P., and Mayor, S. (2015). Building endocytic pits without clathrin. *Nat. Rev. Mol. Cell Biol.* 16, 311–321. doi: 10.1038/nrm3968

Johannes, L., and Römer, W. (2010). Shiga toxins — from cell biology to biomedical applications. *Nat. Rev. Microbiol.* 8, 105–116. doi: 10.1038/nrmicro2279

Jung, N.-H., Kim, B.-R., Kim, H.-W., Kwak, J.-O., and Cha, S. H. (2004). Evidence for Cyclooxygenase-1 association with Caveolin-1 and -2 in cultured human embryonic kidney (HEK 293) cells. *IUBMB Life* 56, 221–227. doi: 10.1080/15216540410001699312

Karnovsky, M. J. (1965). *A Formaldehyde-Glutaraldehyde Fixative of High Osmolality for use in Electron-Microscopy*. Available at: https://www.scienceopen.com/document?vid=9c8c8016-abb1-41e6-9894-c433b9a26bb5 (accessed December 9, 2019).

Kegulian, N. C., Sankhagowit, S., Apostolidou, M., Jayasinghe, S. A., Malmstadt, N., Butler, P. C., et al. (2015). Membrane curvature-sensing and curvature-inducing activity of islet amyloid polypeptide and its implications for membrane disruption. *J. Biol. Chem.* 290, 25782–25793. doi: 10.1074/jbc.M115.659797

Kim, D., and Duff, R. A. (1990). Regulation of K^+ channels in cardiac myocytes by free fatty acids. *Circ. Res.* 67, 1040–1046. doi: 10.1161/01.RES.67.4.1040

Kirber, M. T., Ordway, R. W., Clapp, L. H., Walsh, J. V., and Singer, J. J. (1992). Both membrane stretch and fatty acids directly activate large conductance Ca^{2+}-activated K^+ channels in vascular smooth muscle cells. *FEBS Lett.* 297, 24–28. doi: 10.1016/0014-5793(92)80319-C

Kovbasnjuk, O., Edidin, M., and Donowitz, M. (2001). Role of lipid rafts in Shiga toxin 1 interaction with the apical surface of Caco-2 cells. *J. Cell Sci.* 114, 4025–4031.

Kremer, J. R., Mastronarde, D. N., and McIntosh, J. R. (1996). Computer visualization of three-dimensional image data using IMOD. *J. Struct. Biol.* 116, 71–76. doi: 10.1006/jsbi.1996.0013

Lee, A. G. (2004). How lipids affect the activities of integral membrane proteins. *Biochim. Biophys. Acta* 1666, 62–87. doi: 10.1016/J.BBAMEM.2004.05.012

Li, J., Hou, B., Tumova, S., Muraki, K., Bruns, A., Ludlow, M. J., et al. (2014). Piezo1 integration of vascular architecture with physiological force. *Nature* 515, 279–282. doi: 10.1038/nature13701

Li, X. T., Dyachenko, V., Zuzarte, M., Putzke, C., Preisig-Müller, R., Isenberg, G., et al. (2006). The stretch-activated potassium channel TREK-1 in rat cardiac ventricular muscle. *Cardiovasc. Res.* 69, 86–97. doi: 10.1016/j.cardiores.2005.08.018

Liang, J., Huang, B., Yuan, G., Chen, Y., Liang, F., Zeng, H., et al. (2017). Stretch-activated channel Piezo1 is up-regulated in failure heart and cardiomyocyte stimulated by AngII. *Am. J. Transl. Res.* 9, 2945–2955.

Lingwood, D., and Simons, K. (2010). Lipid rafts as a membrane-organizing principle. *Science* 327, 46–50. doi: 10.1126/science.1174621

Lugenbiel, P., Wenz, F., Syren, P., Geschwill, P., Govorov, K., Seyler, C., et al. (2017). TREK-1 ($K_{2P}2.1$) K^+ channels are suppressed in patients with atrial fibrillation and heart failure and provide therapeutic targets for rhythm control. *Basic Res. Cardiol.* 112:8. doi: 10.1007/s00395-016-0597-7

Madl, J., Villringer, S., and Römer, W. (2016). "Delving into lipid-driven endocytic mechanisms using biomimetic membranes," in *Chemical and Synthetic Approaches in Membrane Biology*, ed. A. K. Shukla (New York, NY: Humana Press), 17–36. doi: 10.1007/8623_2016_7

Meves, H. (2008). Arachidonic acid and ion channels: an update. *Br. J. Pharmacol.* 155, 4–16. doi: 10.1038/bjp.2008.216

Moha ou Maati, H., Peyronnet, R., Devader, C., Veyssiere, J., Labbal, F., Gandin, C., et al. (2011). A human TREK-1/HEK cell line: a highly efficient screening tool for drug development in neurological diseases. *PLoS One* 6:e25602. doi: 10.1371/journal.pone.0025602

Murthy, S. E., Dubin, A. E., and Patapoutian, A. (2017). Piezos thrive under pressure: mechanically activated ion channels in health and disease. *Nat. Rev. Mol. Cell Biol.* 18, 771–783. doi: 10.1038/nrm.2017.92

Niu, W., and Sachs, F. (2003). Dynamic properties of stretch-activated K^+ channels in adult rat atrial myocytes. *Prog. Biophys. Mol. Biol.* 82, 121–135. doi: 10.1016/s0079-6107(03)00010-5

Nutikka, A., and Lingwood, C. (2003). Generation of receptor-active, globotriaosyl ceramide/cholesterol lipid 'rafts' in vitro: a new assay to define factors affecting glycosphingolipid receptor activity. *Glycoconj. J.* 20, 33–38. doi: 10.1023/B:GLYC.0000016740.69726.fb

Omidvar, R., and Römer, W. (2019). Glycan-decorated protocells: novel features for rebuilding cellular processes. *Interface Focus* 9:20180084. doi: 10.1098/rsfs.2018.0084

Patel, A. J., Honoré, E., Maingret, F., Lesage, F., Fink, M., Duprat, F., et al. (1998). A mammalian two pore domain mechano-gated S-like K^+ channel. *EMBO J.* 17, 4283–4290. doi: 10.1093/emboj/17.15.4283

Paul-Gilloteaux, P., Heiligenstein, X., Belle, M., Domart, M. C., Larijani, B., Collinson, L., et al. (2017). EC-CLEM: flexible multidimensional registration software for correlative microscopies. *Nat. Methods* 14, 102–103. doi: 10.1038/nmeth.4170

Pérez-Verdaguer, M., Capera, J., Martínez-Mármol, R., Camps, M., Comes, N., Tamkun, M. M., et al. (2016). Caveolin interaction governs Kv1.3 lipid raft targeting. *Sci. Rep.* 6:22453. doi: 10.1038/srep22453

Perlmutter, J. D., Braun, A. R., and Sachs, J. N. (2009). Curvature dynamics of alpha-synuclein familial Parkinson disease mutants: molecular simulations of the micelle- and bilayer-bound forms. *J. Biol. Chem.* 284, 7177–7189. doi: 10.1074/jbc.M808895200

Peyronnet, R., Bollensdorff, C., Capel, R. A., Rog-Zielinska, E. A., Woods, C. E., Charo, D. N., et al. (2017). Load-dependent effects of apelin on murine cardiomyocytes. *Prog. Biophys. Mol. Biol.* 130(Pt B), 333–343. doi: 10.1016/j.pbiomolbio.2017.09.013

Peyronnet, R., Martins, J. R., Duprat, F., Demolombe, S., Arhatte, M., Jodar, M., et al. (2013). Piezo1-dependent stretch-activated channels are inhibited by Polycystin-2 in renal tubular epithelial cells. *EMBO Rep.* 14, 1143–1148. doi: 10.1038/embor.2013.170

Peyronnet, R., Nerbonne, J. M., and Kohl, P. (2016). Cardiac mechano-gated ion channels and arrhythmias. *Circ. Res.* 118, 311–329. doi: 10.1161/CIRCRESAHA.115.305043

Peyronnet, R., Sharif-Naeini, R., Folgering, J. H. A., Arhatte, M., Jodar, M., El Boustany, C., et al. (2012). Mechanoprotection by polycystins against apoptosis is mediated through the opening of stretch-activated K2P channels. *Cell Rep.* 1, 241–250. doi: 10.1016/J.CELREP.2012.01.006

Quinn, T. A., Camelliti, P., Rog-Zielinska, E. A., Siedlecka, U., Poggioli, T., O'Toole, E. T., et al. (2016). Electrotonic coupling of excitable and nonexcitable cells in the heart revealed by optogenetics. *Proc. Natl. Acad. Sci. U.S.A.* 113, 14852–14857. doi: 10.1073/pnas.1611184114

Quinn, T. A., Jin, H., Lee, P., and Kohl, P. (2017). Mechanically induced ectopy via stretch-activated cation-nonselective channels is caused by local tissue deformation and results in ventricular fibrillation if triggered on the repolarization wave edge (Commotio Cordis). *Circ. Arrhythm. Electrophysiol.* 10:e004777. doi: 10.1161/CIRCEP.116.004777

Reed, A., Kohl, P., and Peyronnet, R. (2014). Molecular candidates for cardiac stretch-activated ion channels. *Glob. Cardiol. Sci. Pract.* 2014, 9–25. doi: 10.5339/gcsp.2014.19

Rog-Zielinska, E. A., Kong, C. H. T., Zgierski-Johnston, C. M., Verkade, P., Mantell, J., Cannell, M. B., et al. (2018). Species differences in the morphology of transverse tubule openings in cardiomyocytes. *EP Europace* 20(Suppl._3), iii120–iii124. doi: 10.1093/europace/euy245

Römer, W., Berland, L., Chambon, V., Gaus, K., Windschiegl, B., Tenza, D., et al. (2007). Shiga toxin induces tubular membrane invaginations for its uptake into cells. *Nature* 450, 670–675. doi: 10.1038/nature05996

Sachs, F. (2010). Stretch-activated ion channels: what are they? *Physiology* 25, 50–56. doi: 10.1152/physiol.00042.2009

Santarella-Mellwig, R., Haselmann, U., Schieber, N. L., Walther, P., Schwab, Y., Antony, C., et al. (2018). Correlative light electron microscopy (CLEM) for tracking and imaging viral protein associated structures in cryo-immobilized cells. *J. Vis. Exp.* 2018:e58154. doi: 10.3791/58154

Saotome, K., Murthy, S. E., Kefauver, J. M., Whitwam, T., Patapoutian, A., and Ward, A. B. (2018). Structure of the mechanically activated ion channel Piezo1. *Nature* 554, 481–486. doi: 10.1038/nature25453

Schmidt, C., Wiedmann, F., Zhou, X.-B., Heijman, J., Voigt, N., Ratte, A., et al. (2017). Inverse remodelling of K2P 3.1 K^+ channel expression and action potential duration in left ventricular dysfunction and atrial fibrillation: implications for patient-specific antiarrhythmic drug therapy. *Eur. Heart J.* 38, 1764–1774. doi: 10.1093/eurheartj/ehw559

Schubert, T., and Römer, W. (2015). How synthetic membrane systems contribute to the understanding of lipid-driven endocytosis. *Biochim. Biophys. Acta* 1853, 2992–3005. doi: 10.1016/J.BBAMCR.2015.07.014

Sugiura, Y., Ikeda, K., and Nakano, M. (2015). High membrane curvature enhances binding, conformational changes, and fibrillation of Amyloid-β on lipid bilayer surfaces. *Langmuir* 31, 11549–11557. doi: 10.1021/acs.langmuir.5b03332

Sych, T., Mély, Y., and Römer, W. (2018). Lipid self-assembly and lectin-induced reorganization of the plasma membrane. *Philos. Trans. R. Soc. Lond. Ser. B Biol. Sci.* 373:20170117. doi: 10.1098/rstb.2017.0117

Terrenoire, C., Lauritzen, I., Lesage, F., Romey, G., and Lazdunski, M. (2001). A TREK-1–Like potassium channel in atrial cells inhibited by β-Adrenergic stimulation and activated by volatile anesthetics. *Circ. Res.* 89, 336–342. doi: 10.1161/hh1601.094979

Tsimbouri, P. M., McNamara, L. E., Alakpa, E. V., Dalby, M. J., and Turner, L.-A. (2014). Cell–material interactions. *Tis. Eng.* 2014, 217–251. doi: 10.1016/B978-0-12-420145-3.00007-9

Villringer, S., Madl, J., Sych, T., Manner, C., Imberty, A., and Römer, W. (2018). Lectin-mediated protocell crosslinking to mimic cell-cell junctions and adhesion. *Sci. Rep.* 8:1932. doi: 10.1038/s41598-018-20230-6

Voloshyna, I., Besana, A., Castillo, M., Matos, T., Weinstein, I. B., Mansukhani, M., et al. (2008). TREK-1 is a novel molecular target in prostate cancer. *Cancer Res.* 68, 1197–1203. doi: 10.1158/0008-5472.CAN-07-5163

Wang, M., Song, J., Xiao, W., Yang, L., Yuan, J., Wang, W., et al. (2012). Changes in lipid-sensitive two-pore domain potassium channel TREK-1 expression and its involvement in astrogliosis following cerebral ischemia in rats. *J. Mol. Neurosci.* 46, 384–392. doi: 10.1007/s12031-011-9598-z

Xi, G., Zhang, X., Zhang, L., Sui, Y., Hui, J., Liu, S., et al. (2011). Fluoxetine attenuates the inhibitory effect of glucocorticoid hormones on neurogenesis in vitro via a two-pore domain potassium channel, TREK-1. *Psychopharmacology* 214, 747–759. doi: 10.1007/s00213-010-2077-3

Yang, X., Guo, P., Li, J., Wang, W., Xu, S., Wang, L., et al. (2014). Functional study of TREK-1 potassium channels during rat heart development and cardiac ischemia using RNAi techniques. *J. Cardiovasc. Pharmacol.* 64, 142–150. doi: 10.1097/FJC.0000000000000099

Yang, X., Sheng, W., Sun, G. Y., and Lee, J. C.-M. (2011). Effects of fatty acid unsaturation numbers on membrane fluidity and α-secretase-dependent amyloid precursor protein processing. *Neurochem. Int.* 58, 321–329. doi: 10.1016/j.neuint.2010.12.004

Youm, J. B., Han, J., Kim, N., Zhang, Y.-H., Kim, E., Leem, C. H., et al. (2005). "Role of stretch-activated channels in the heart: action potential and Ca^{2+} transients," in *Mechanosensitivity in Cells and Tissues- Academia*, eds A. Kamkin, and I. Kiseleva (Moscow: Academia).

Zhang, H., Shepherd, N., and Creazzo, T. L. (2008). Temperature-sensitive TREK currents contribute to setting the resting membrane potential in embryonic atrial myocytes. *J. Physiol.* 586, 3645–3656. doi: 10.1113/jphysiol.2008.153395

Zhang, M., Yin, H. J., Wang, W. P., Li, J., and Wang, X. L. (2016). Over-expressed human TREK-1 inhibits CHO cell proliferation via inhibiting PKA and p38 MAPK pathways and subsequently inducing G1 arrest. *Acta Pharmacol. Sin.* 37, 1190–1198. doi: 10.1038/aps.2016.65

Zheng, S., Eierhoff, T., Aigal, S., Brandel, A., Thuenauer, R., de Bentzmann, S., et al. (2017). The *Pseudomonas aeruginosa* lectin LecA triggers host cell signalling by glycosphingolipid-dependent phosphorylation of the adaptor protein CrkII. *Biochim. Biophys. Acta* 1864, 1236–1245. doi: 10.1016/J.BBAMCR.2017.04.005

Conflict of Interest: The authors declare that the research was conducted in the absence of any commercial or financial relationships that could be construed as a potential conflict of interest.

frontiers in Physiology

ORIGINAL RESEARCH
published: 26 May 2020
doi: 10.3389/fphys.2020.00464

High-Resolution Optical Measurement of Cardiac Restitution, Contraction, and Fibrillation Dynamics in Beating vs. Blebbistatin-Uncoupled Isolated Rabbit Hearts

*Vineesh Kappadan[1], Saba Telele[1,2], Ilija Uzelac[3], Flavio Fenton[3], Ulrich Parlitz[1,2,4], Stefan Luther[1,2,5] and Jan Christoph[1,2,6]**

[1] Research Group Biomedical Physics, Max Planck Institute for Dynamics and Self-Organization, Göttingen, Germany, [2] German Center for Cardiovascular Research (DZHK e.V.), Partnersite Göttingen, Göttingen, Germany, [3] School of Physics, Georgia Institute of Technology, Atlanta, GA, United States, [4] Institute for the Dynamics of Complex Systems, University of Göttingen, Göttingen, Germany, [5] Department of Pharmacology, University Medical Center Göttingen, Göttingen, Germany, [6] Department of Cardiology and Pneumology, University Medical Center Göttingen, Göttingen, Germany

OPEN ACCESS

Edited by:
Olga Solovyova,
Institute of Immunology and
Physiology (RAS), Russia

Reviewed by:
Crystal M. Ripplinger,
University of California, Davis,
United States
Matthew W. Kay,
George Washington University,
United States

***Correspondence:**
Jan Christoph
jan.christoph@med.uni-goettingen.de

Specialty section:
This article was submitted to
Cardiac Electrophysiology,
a section of the journal
Frontiers in Physiology

Received: *30 December 2019*
Accepted: *16 April 2020*
Published: *26 May 2020*

Citation:
Kappadan V, Telele S, Uzelac I, Fenton F, Parlitz U, Luther S and Christoph J (2020) High-Resolution Optical Measurement of Cardiac Restitution, Contraction, and Fibrillation Dynamics in Beating vs. Blebbistatin-Uncoupled Isolated Rabbit Hearts. Front. Physiol. 11:464. doi: 10.3389/fphys.2020.00464

Optical mapping is a high-resolution fluorescence imaging technique, that uses voltage- or calcium-sensitive dyes to visualize electrical excitation waves on the heart surface. However, optical mapping is very susceptible to the motion of cardiac tissue, which results in so-called *motion artifacts* in the fluorescence signal. To avoid motion artifacts, contractions of the heart muscle are typically suppressed using pharmacological excitation-contraction uncoupling agents, such as Blebbistatin. The use of pharmacological agents, however, may influence cardiac electrophysiology. Recently, it has been shown that numerical motion tracking can significantly reduce motion-related artifacts in optical mapping, enabling the simultaneous optical measurement of cardiac electrophysiology and mechanics. Here, we combine ratiometric optical mapping with numerical motion tracking to further enhance the robustness and accuracy of these measurements. We evaluate the method's performance by imaging and comparing cardiac restitution and ventricular fibrillation (VF) dynamics in contracting, non-working vs. Blebbistatin-arrested Langendorff-perfused rabbit hearts ($N = 10$). We found action potential durations (APD) to be, on average, $25 \pm 5\%$ shorter in contracting hearts compared to hearts uncoupled with Blebbistatin. The relative shortening of the APD was found to be larger at higher frequencies. VF was found to be significantly accelerated in contracting hearts, i.e., $9 \pm 2Hz$ with Blebbistatin and $15 \pm 4Hz$ without Blebbistatin, and maintained a broader frequency spectrum. In contracting hearts, the average number of phase singularities was $N_{PS} = 11 \pm 4$ compared to $N_{PS} = 6 \pm 3$ with Blebbistatin during VF on the anterior ventricular surface. VF inducibility was reduced with Blebbistatin. We found the effect of Blebbistatin to be concentration-dependent and reversible by washout. Aside from the electrophysiological characterization, we also measured and analyzed cardiac motion. Our findings may have implications for the interpretation of optical mapping data, and highlight that physiological conditions, such as oxygenation and metabolic demand, must be carefully considered in *ex vivo* imaging experiments.

Keywords: fluorescence imaging, optical mapping, motion tracking, motion correction, computer vision, ventricular fibrillation, electromechanics, Blebbistatin

1. INTRODUCTION

Optical mapping is a high-resolution fluorescence imaging technique, which has been used in numerous studies to visualize electrical impulse phenomena, such as action potential waves, on the surface of intact isolated hearts. Due to its high spatial resolution, the technique has several advantages over contact-electrode measurements, including the ability to resolve APD dispersion and heterogeneity (Wu et al., 2002; Mironov et al., 2008) and visualize electrophysiological vortex waves during arrhythmias (Davidenko et al., 1992; Gray et al., 1998; Witkowski et al., 1998). Optical mapping has furthermore been used to measure cardiac electrical restitution at high spatial resolutions (Banville et al., 2004; Choi et al., 2004). However, until recently, one of the major drawbacks of optical mapping has been the necessity to uncouple cardiac excitation from contraction in order to avoid so-called motion artifacts. To avoid these artifacts, optical mapping studies have relied on pharmacological excitation-contraction uncoupling agents such as Blebbistatin (Dou et al., 2007; Fedorov et al., 2007; Farman et al., 2008). Blebbistatin inhibits actin-myosin interactions in cardiomyocytes, thereby decoupling electrophysiology from mechanics and suppressing the heart's contractile motion. Blebbistatin has been used extensively in the field because of its ease-of-use and efficacy in preventing motion artifacts; however, also in large part out of necessity, as the only alternative approach to reduce motion-artifacts involved mechanical restriction of the heart's motion. With the adaptation of computer vision techniques, with which motion in optical mapping videos can be tracked and compensated numerically, motion artifacts no longer pose a limitation in optical mapping and the imaging technique has been used to measure simultaneously cardiac electrophysiology and surface mechanics (Zhang et al., 2016; Christoph et al., 2017, 2018; Christoph and Luther, 2018). Moreover, optical mapping has recently been used in conjunction with high-speed 3D ultrasound to study electromechanical tissue dynamics during ventricular arrhythmias (Christoph et al., 2018). Nevertheless, despite the advances, further validation is required. For instance, it has yet to be determined whether the technique is sufficiently accurate to measure electrophysiological parameters such as action potential durations, and consequently cardiac electrical restitution on the strongly deforming heart surface.

Here, we combine optical mapping, using voltage-sensitive fluorescent dyes, with marker-free numerical motion tracking and ratiometric imaging. Firstly, we reduced motion artifacts to the greatest possible extent by tracking the motion of the heart wall and retrieving electrophysiological signals in a co-moving coordinate system. Secondly, we further reduced residual motion artifacts by using ratiometric imaging, exciting the voltage-sensitive dye Di-4-ANEPPS at two wavelengths, and retrieving and analyzing optical signals from two separate emission bandwidths, effectively compensating undesired effects caused by inhomogeneous illumination post-tracking. We used the imaging technique to measure cardiac APD restitution and fibrillation dynamics in Langendorff-perfused isolated rabbit hearts with and without Blebbistatin. Overall, we provide a comparison of contracting and non-contracting isolated hearts in a Langendorff-perfusion environment, and discuss the imaging technique's performance in measuring motion artifact-free optical maps and optical traces of cardiac electrophysiology.

2. MATERIALS AND METHODS

2.1. Tissue Preparation

New Zealand White rabbits ($N = 10$, female, 6–10 months old, $2.5 - 3.5$kg) were heparinized and anesthesized using 4.0ml Trapanal (single intraveneous injection, Thiopental-sodium solution, 50 mg/kg) diluted in 10.0 ml isotonic sodium chloride (NaCl). The hearts were excised rapidly and inserted into cardioplegic solution for temporary cessation of cardiac activity before being transferred into the experimental setup. All procedures regarding care and use of animals were carried out in accordance with German animal welfare laws and the recommendations of the Lower Saxony State Office for Customer Protection and Food Safety (LAVES) and the Federation of European Laboratory Animal Science Associations (FELASA). The protocol was approved by the Lower Saxony State Office for Customer Protection and Food Safety (LAVES).

2.2. Experimental Setup

Isolated rabbit hearts were positioned at the center of an eight-sided bath with 4 large (10×16 cm^2) and 4 small (4×16 cm^2) glass walls (see **Figure 1A**). The hearts were connected to a retrograde Langendorff-perfusion system with an aortic block and a bubble trap (Hugo-Sachs Apparatus, March-Hugstetten, Germany). Any fixation or mechanical pressure to the hearts was avoided to prevent compression of the coronary arteries. The hearts were only held in place by being connected with their aorta to the perfusion outflow. The bath was filled with $\sim$ 2l of warm, oxygenated Tyrode solution (see **Appendix** for details), such that the hearts were completely immersed. In total, 15l of Tyrode solution was provided from a pre-heated reservoir, from where it was pumped into the heart and then constantly reperfused. The flow rate of the perfusion pump was set to 30 ml min^{-1}. The perfusion pressure was set constantly to 50 ± 5mmHg and was regulated using a

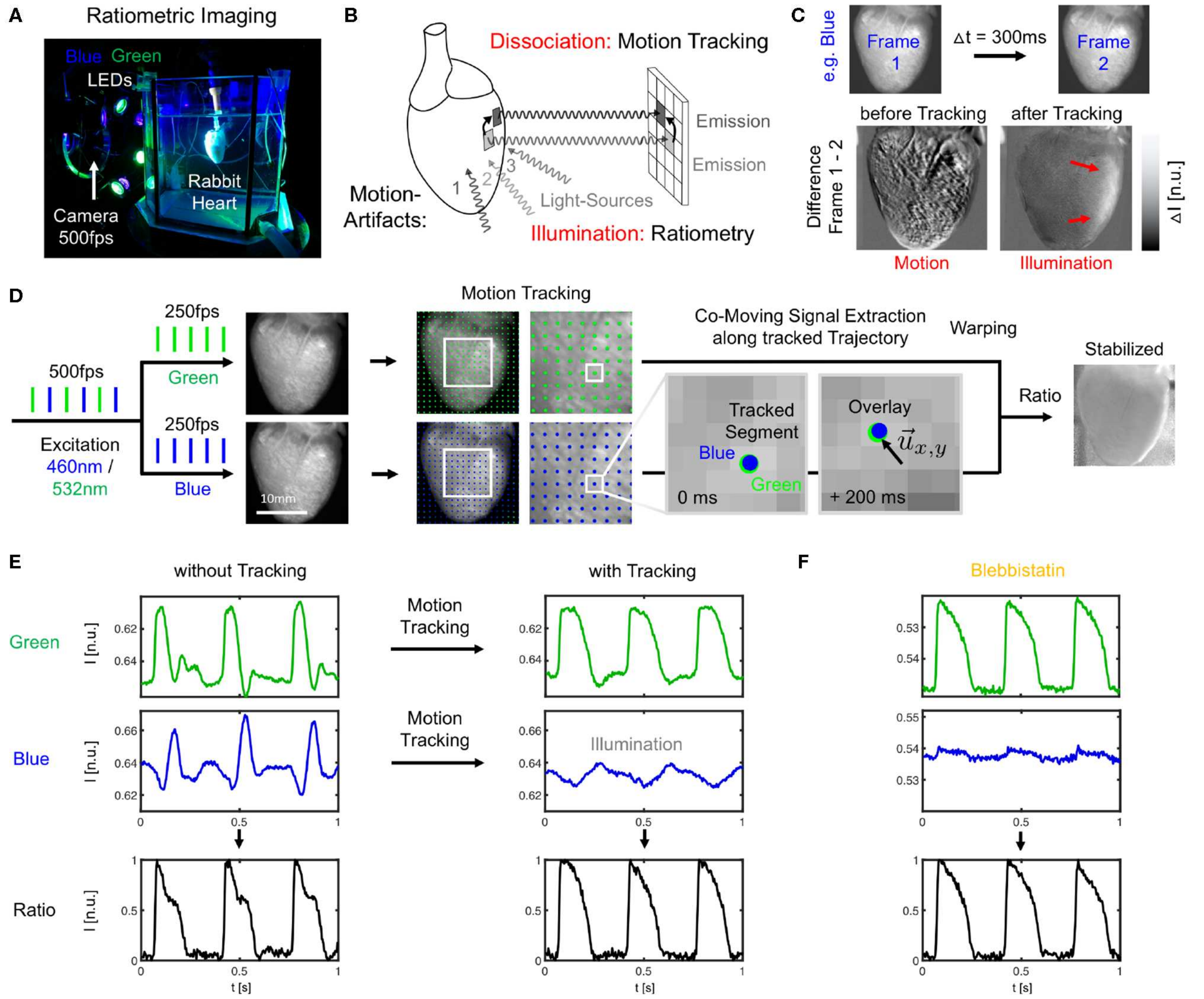

FIGURE 1 | Dual-channel ratiometric optical mapping in combination with marker-free numerical motion tracking and motion-stabilization for imaging action potential waves on the contracting surface of isolated hearts. **(A)** *Ex-vivo* optical mapping setup with a single camera. **(B)** Sources for motion artifacts: dissociation-related and illumination-related motion artifacts are compensated with motion tracking and ratiometry, respectively. **(C)** Two types of motion artifacts visible when computing the difference between video frames. Before tracking, motion creates dissociation-related motion artifacts. After tracking, relative motion between heart surface and light sources (which now move in motion-stabilized video) causes residual intensity fluctuations or illumination-related motion artifacts (red arrows). **(D)** Imaging scheme with alternating blue (460 nm) and green (523 nm) illumination for excitation of Di-4-ANEPPS and exposure of consecutive video frames at 2 × 250 or 500 fps. Separate motion tracking in each channel (every *n*-th displacement vector shown, shifts are tracked in every pixel). Overlay of tissue coordinates tracked in blue and green channel, respectively, shows congruent motion through the video images, see also **Supplementary Video 1**. Combination of warped green and blue video images yields motion-stabilized ratiometric video image. **(E)** Optical traces (from 3 × 3 pixels) before and after tracking and/or ratiometry (pacing *CL* = 350 ms) in blue and green (inverted) channel, respectively. Ratiometry alone cannot completely remove all motion artifacts (bottom left), but only illumination-related motion artifacts. Numerical motion-stabilization alone cannot completely inhibit all motion artifacts (top right), but only dissociation-related motion artifacts. After tracking, ratiometric combination of green and blue signals yields an optical signal with very little residual motion artifacts. Due to the particular dye and filter properties, the relevant electrophysiological signal is in the green channel, whereas eventual intensity fluctuations in the blue channel (after tracking) are caused mostly by motion through an inhomogeneously illuminated scene. **(F)** Optical traces obtained with Blebbistatin in same heart. Ratiometry improves the signal with very little residual contractile motion, or after numerical motion-stabilization as in **(E)**.

starling resistor and monitored throughout the experiment. The temperature of the Tyrode inside the bath was kept at a constant temperature of 37 ± 0.5°C (custom-made temperature control).

2.3. Blebbistatin

In the first half of the experiments, contracting hearts were imaged without administering Blebbistatin (see **Figure 2A**). In the second half of the experiments, Blebbistatin was administered to repeat the same measurements in uncoupled contraction-inhibited hearts. In all experiments, we used the Blebbistatin variant (−)/−Blebbistatin (Cayman Chemical Inc., USA). Prior to administering Blebbistatin, it was pre-diluted and stirred for at least 10 min in 300ml pre-heated 40°C warm Tyrode and then pumped directly into the aortic block's bubble trap (reaching 37°C) and from there into the heart. To avoid crystallization or the formation of precipitate that is associated with Blebbistatin (Swift et al., 2012), the Tyrode was filtered (5μm filter pore size) before being pumped into the heart. In some experiments ($N = 2$; see **Figure 7**), the concentration of Blebbistatin was step-wise increased from 0.7, 1.4, 2.1 to 2.8μM by adding in each step a bolus of 1ml of Blebbistatin directly to the 15l reservoir, see **Figure 2B**. After each increase of the concentration, we waited for about 30 min before starting the next measurement. In some experiments ($N = 2$), Blebbistatin was washed out toward the end of the experiment by perfusing hearts with Blebbistatin-free Tyrode for at least 60 min (see **Figures 2A**, **7D**).

2.4. Ratiometric Optical Mapping

Optical mapping was performed using a single high-speed EMCCD camera (Evolve, 128 × 128 pixels, 16 bit dynamic range, Photometrics Inc., USA) and a wide-aperture lens (0.95/25 mm, Navitar, Japan) imaging field of views of about 1.5 × 1.5 cm^2 at frame rates of 500Hz. The potentiometric dye Di-4-ANEPPS (500μl bolus injection into the bubble trap above the aortic block) was used for voltage-sensitive ratiometric imaging. Fluorescent emission light was filtered using a bandpass filter (590 ± 55nm, Omega Optical Inc., USA) mounted onto the lens in front of the camera. Ratiometric imaging (Knisley et al., 2000) was performed using two sets of high-power light-emitting diodes (LED; 3 blue LEDs: 460nm center wavelength, model LZ4-40B208; 3 green LEDs: 523nm center wavelength, model LZ4-40G108, both by LED Engin Inc., USA), and switching rapidly between the blue and green excitation light in every other frame (excitation ratiometry), similarly as previously described (Bachtel et al., 2011; Bourgeois et al., 2011). The synchronized, rapid switching was achieved using a custom-made electronic driver. The triggering of the two sets of LEDs was synchronized with the camera acquisition, such that odd and even video frames were illuminated with blue and green light, respectively (**Figures 1A,D**), resulting in a frame rate for each channel of $f_{B/G} = 250$Hz. The blue and green excitation light was further filtered by two sets of narrow bandpass filters (blue: 460 ± 5nm, Thorlabs, USA; green: 540 ± 12.5nm, Chroma Technology Corp., USA) and collimated with plano convex lenses (LA1951-A, Thorlabs, USA). To provide an even illumination of the heart surface, the light-emitting diodes were mounted (green, blue, green, …) on a ring-shaped post around the camera lens and were directed through one of the large glass walls of the aquarium at the tissue (see **Figure 1A**). All hearts were facing the camera with their anterior left ventricular surface. The camera's field of view covered the entire heart (see **Figures 1**, **3**). The camera was controlled and optical mapping recordings were acquired using custom-made software. The videos were stored as two separate green and blue videos.

2.5. Motion Tracking and Motion-Stabilization

Two-dimensional in-plane motion was numerically tracked within the fluorescence video images with sub-pixel precision using optical flow-based algorithms, as previously described (Christoph et al., 2017; Christoph and Luther, 2018). The motion was tracked in the blue and green videos separately (see **Figure 1D** and **Supplementary Video 1**). Tissue displacements were computed in every pixel with respect to the first frame as the reference frame in each video $I_b(1) = I_{r,b}$ or $I_g(1) = I_{r,g}$, respectively. During pacing, the reference frame shows the tissue at the end of the diastolic interval shortly before the application of a pacing stimulus. During ventricular fibrillation, the reference frame shows the tissue in an arbitrary deformed state. Due to the illumination scheme, both reference frames $I_{r,b}$ and $I_{r,g}$ correspond to two consecutive frames with a temporal offset of 2ms in the interleaved video. Before tracking, the green and blue videos were normalized by their minimal and maximal values. Next, the local image contrast in the green and blue videos was enhanced, as described previously (Christoph and Luther, 2018). This pre-processing step ensures that tissue features can be reliably tracked throughout the image sequence, even as the action potential activity causes intensity in- or decreases. After tracking the contrast-enhanced green and blue videos, the original normalized blue and green videos were warped using the motion tracking data, as described previously (Christoph and Luther, 2018). The difference between pre- and post-tracking is illustrated in **Figures 1C,E**, **3A,B**. Motion tracking was performed in the absence of markers attached to the heart surface and without user interaction, once a reference frame had been selected. The motion-stabilized green and blue videos were then combined by dividing one video by the other [green by blue, each individual pixel value $I_g(x, y, t)$ by the corresponding other pixel value $I_b(x, y, t)$], and normalizing the videos by their minimal and maximal values, yielding motion-stabilized ratiometric videos.

2.6. Restitution Protocol and Arrhythmia Induction

A monophasic needle electrode (FHC Inc., USA) was inserted slightly into the epicardium of the right ventricle, firstly, to be able to apply pacing stimuli, and, secondly, to hold the heart roughly in place (with the possibility to move given the flexibility of the electrode). Restitution curves were measured using a dynamic rapid pacing protocol (Goldhaber et al., 2005) with pacing frequencies starting at $f_p = 2.0$Hz ($CL = 500$ms) and then gradually increasing until $f_p = 10.0$Hz ($CL = 100$ms). The increments were 50ms for $CL = 500 - 350$ms, then 25ms for $CL = 350 - 260$ms and 5ms for $CL < 260$ms. At each cycle length, 50 pacing stimuli were applied and the last 30 elicited action potentials were analyzed. Each restitution curve measurement lasted < 7 min. Typically, at the end of the pacing the hearts fibrillated. VF was terminated using an electrical defibrillation shock. A single, long optical mapping video was recorded throughout the restitution measurement. The recording was later split into individual recordings, each showing 50 action potential waves at the individual cycle lengths.

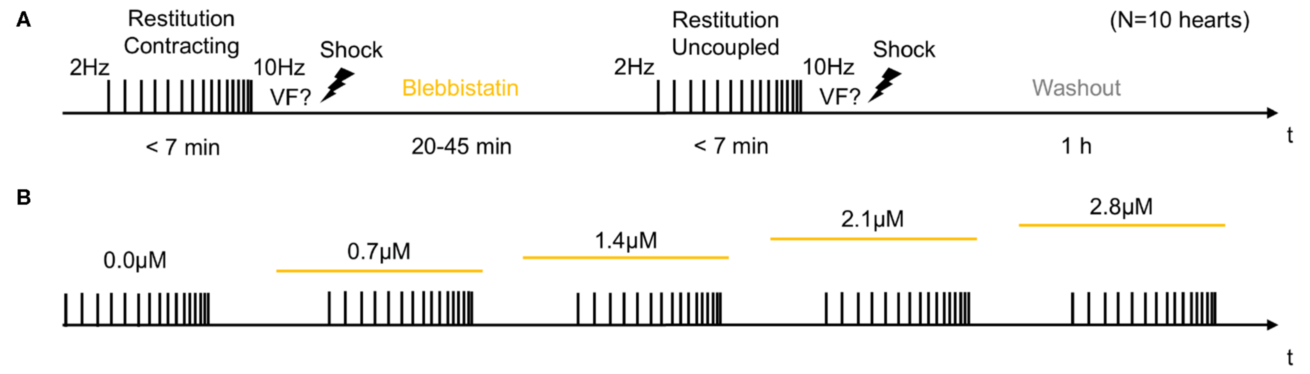

FIGURE 2 | Experimental protocol for measurements of cardiac restitution using a dynamic pacing protocol in contracting and contraction-inhibited hearts uncoupled with Blebbistatin. **(A)** Measurement pre- and post-Blebbistatin in the same heart (total $N = 10$ hearts). Pacing from $f_p = 2.0$ to $f_p = 10.0$ Hz with progressively decreasing step size. After the first restitution measurement in the contracting heart, Blebbistatin was added at concentrations of up to 2.8μM. After 20–45 min, when Blebbistatin typically had suppressed all contractile motion, the second restitution measurement was performed in the contraction-inhibited heart. The reversal of the effect of Blebbistatin was verified in a washout experiment (after 1 h). **(B)** Subsequent increase of Blebbistatin concentration (0.0, 0.7, . . . , 2.8μM). The restitution measurement from **(A)** was performed for baseline and then repeated for all four concentrations in the same heart. The concentration was immediately increased after the previous measurement, and the next measurement was started after 30 min.

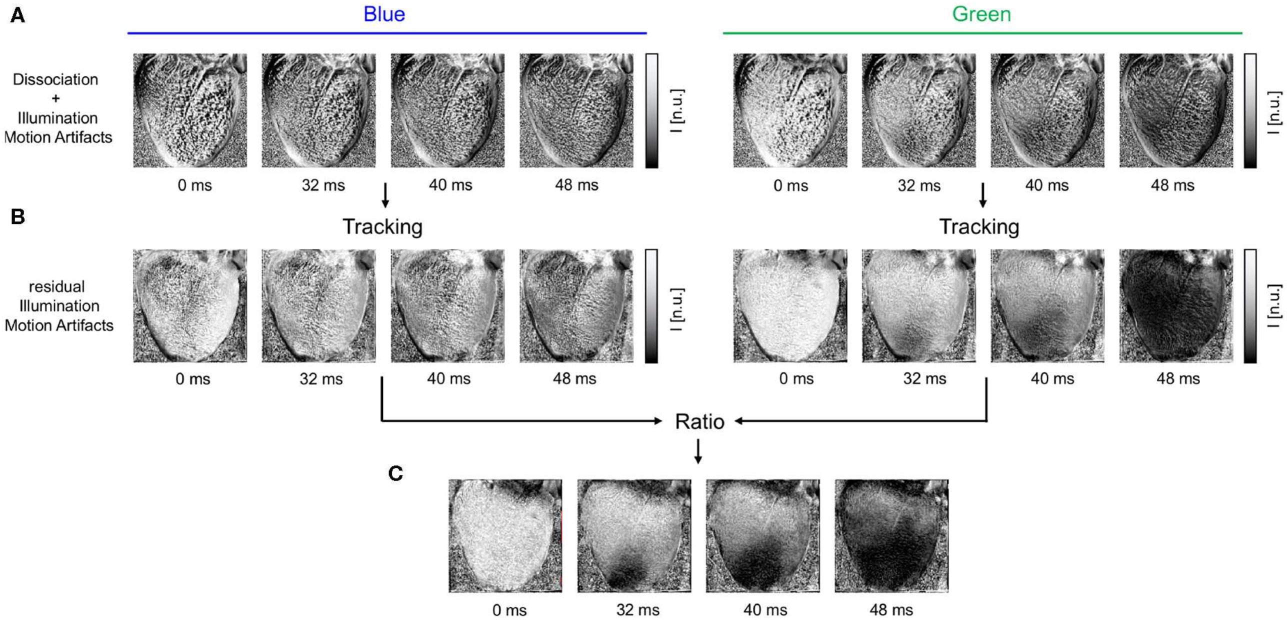

FIGURE 3 | Motion artifacts and motion artifact reduction obtained through the combination of numerical motion tracking and dual channel excitation ratiometry using blue and green excitation light. **(A)** Optical maps showing mostly motion artifacts before tracking in uncompensated videos in blue and green channels, respectively. **(B)** Optical maps after motion tracking and stabilization. Dissociation-related motion artifacts are compensated and substantially reduced. The blue channel contains no electrophysiology-related signal, and the optical maps exhibit merely residual intensity modulations caused by relative motion between tissue and light sources, which persists after tracking (see also **Figure 1C**). The green channel exhibits an action potential wave propagating across the ventricular surface (dark: depolarized tissue). **(C)** Both dissociation- and illumination-related motion artifacts are compensated due to the combined, subsequent use of tracking and ratiometry. The optical maps show an essentially artifact-free action potential wave propagating across the deforming heart surface (dark: depolarized tissue). In all optical maps, the optical signal was normalized in each pixel over time (normalized units [n.u.], pixel-wise normalization) as the last processing step after numerical motion correction and ratiometry.

2.7. Post-processing

After motion tracking, warping and ratiometric combination of the green and blue videos, the resulting optical mapping videos were processed and analyzed as conventional optical mapping videos. To amplify the optical signals that correspond to action potentials, the videos were normalized using a pixel-wise, sliding-window normalization. To measure action potential durations (APDs) during pacing, time-series were extracted across the heart

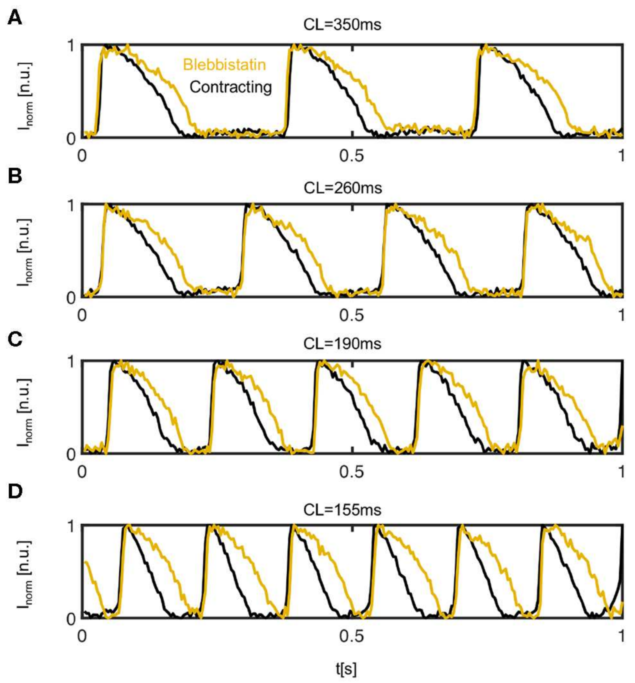

FIGURE 4 | Comparison of action potentials measured optically on the left ventricular epicardium of contracting (black) vs. contraction-inhibited (yellow) isolated rabbit heart uncoupled with Blebbistatin. Representative time series obtained from 3 × 3 pixels measured in the same location on the surface of the same heart during pacing at a cycle length of **(A)** $CL = 350ms$ (or pacing frequency $f_p = 2.86$ Hz), **(B)** $CL = 260$ ms, **(C)** $CL = 190$ ms, and **(D)** $CL = 155$ ms. The time-series were inverted and normalized ($I \in [0\ 1]$) using a sliding-window normalization.

surface (usually averaged from 3 × 3 pixels), and the durations of 30 consecutive action potentials were measured by detecting the up- and down-strokes of each action potential at 50% or 30% height of the action potential for deriving APD_{50} and APD_{70} values, respectively. The APD was then averaged from the 30 individual APD values. To detect alternans, the durations of even and odd action potentials were measured separately from 2 × 15 action potentials. The error bars in **Figure 6F** show the uncertainty (standard deviation of 30 consecutive APDs in single pixel) of these measurements.

3. RESULTS

The combination of numerical motion tracking and ratiometric imaging significantly reduced motion artifacts allowing high-resolution contact-free optical measurements of action potentials on the strongly deforming heart surface (see **Figures 1C,E**, **3**, **4**). While we found significant differences in the ventricular electrophysiology comparing contracting with Blebbistatin-arrested hearts ($N = 10$ hearts), see following sections, during sinus rhythm we found both de- and increases in the heart rate.

3.1. Action Potential Shortening in Contracting Hearts

Figure 4 shows four representative time-series of action potentials (AP) measured optically on the contracting and non-contracting left ventricular epicardium before (black) and after (yellow) the administration of Blebbistatin at pacing cycle lengths of $350, 260, 190$, and $155\,ms$, respectively. For all pacing cycle lengths, APs exhibit a different morphology and are significantly shorter on the contracting than on the non-contracting heart surface. On the contracting heart surface, the AP morphology becomes increasingly triangular-shaped with increasing pacing rates (see **Figure 4D**). While APD shortens with decreasing pacing cycle lengths, the relative shortening between non-contracting and contracting hearts becomes more pronounced at shorter pacing cycle lengths.

3.2. APD-Restitution in Contracting Hearts

To further characterize the frequency-dependence of the APD, we measured and compared APD restitution curves of contracting vs. non-contracting hearts uncoupled with Blebbistatin (see **Figure 5**). A representative APD restitution measurement is shown in **Figure 5A**. The restitution curve measured on the contracting heart surface (black/gray) is consistently lower by about $20 - 30$ms than the one obtained with Blebbistatin (yellow/orange). The relative shortening of the APD is larger at higher frequencies ($\sim$ 27% at 5Hz vs. $\sim$ 13% at 2Hz). The measurement error is larger when hearts contract. Furthermore, in contracting hearts it was possible to measure the restitution curve up to cycle lengths of $CL = 100$ms, whereas with Blebbistatin the restitution curve exhibits cardiac alternans at cycle lengths shorter than $CL < 160$ms. At cycle lengths shorter $CL < 140$ms the pacing induced ventricular fibrillation (VF). **Figure 5C** shows exemplary APD-maps that were generated for each cycle length from the restitution measurement data.

Generally, we observed in all hearts that the overall amount of motion decreases with faster pacing rates. We also observed very strong contractions and mechanical resonance phenomena (see **Figure 5B**) for pacing frequencies ranging in between 3 and 4 Hz (or $CL = 250 - 350$ms). In this mid-frequency range, translational and rotational motion became large, likely due to the particular attachment and preparation of the hearts in the bath. A brief discussion of the measurement accuracy in this regime is provided in section 3.7.

Figure 6 shows averaged restitution curves, as well as restitution curves obtained from APD_{50} and APD_{70} measurements, and from single hearts and single pixels for comparison, all for both pre- (black) and post-Blebbistatin (yellow). We observed a large variability across hearts in their individual restitution characteristics. **Figure 6A** shows the mean restitution curves averaged from $N = 5$ hearts. The mean and uncertainty of each data point was computed as the average and standard deviation of APDs across all pixels from all 5 hearts (pooled), respectively. Correspondingly, the error bars are large, as they include the variability across different hearts. **Figures 6D,E** show two exemplary individual restitution curves

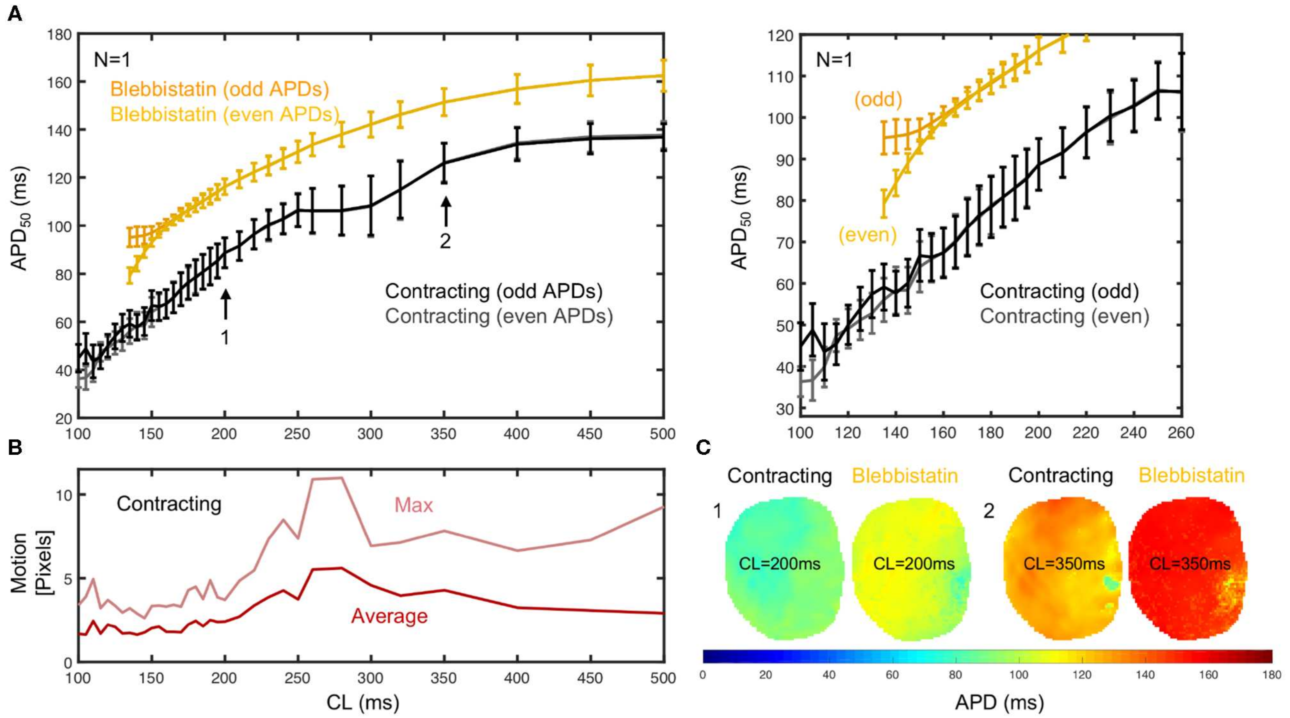

FIGURE 5 | APD_{50} restitution in contracting vs. contraction-inhibited isolated rabbit heart ($N = 1$, representative example) uncoupled with Blebbistatin (at 2.8μM concentration), optical measurement on left ventricular surface. **(A)** APD_{50} restitution before (black/gray) and after (yellow/orange) administration of Blebbistatin with APD_{50} measured from $2 \times 15 = 30$ (even and odd) consecutive action potentials at each cycle length CL (black/gray or yellow/orange = measured separately to detect alternans). Error bars indicate standard deviation of all APD_{50} in APD-maps **(C)**, or all APD_{50} measured in each pixel on heart surface. Right: Close-up of region with cardiac alternans ($CL \leq 160\,ms$). With Blebbistatin, pacing with $CL \leq 140ms$ induced (non-sustained) VF. **(B)** Motion decreases with increasing pacing frequencies. Strong motion (10–20% of heart size) at $CL = 250 - 350\,ms$. **(C)** APD_{50} maps from the same heart with and without Blebbistatin for cycle lengths $CL = 200\,ms$ and $CL = 350\,ms$ (different heart than in **A**).

from two different hearts, indicating a $\Delta APD \sim$ 10ms between hearts. **Figures 6B,C** show the average restitution curves derived from $N = 5$ hearts based on APD_{50} and APD_{70}, respectively. The curves in **Figures 6B,C** show that APD_{70} provides APD values that are on average more than $\Delta APD >$ 10ms longer than measuring APD_{50}. Correspondingly, the actual APD, which could be measured for instance at APD_{90}, might be about 20ms longer than the APD_{50} values presented mostly throughout this study. Due to noise and residual motion artifacts, we did not measure APD_{90} (see also section 3.7). In contrast to **Figure 6A**, the error bars in **Figures 6B,C** were computed individually per heart (standard deviation of individual APD-maps with $\sim 3,000$ - $5,000$ values) and then averaged. The error bars could both suggest that either the measurement on the contracting heart surface is less precise than with Blebbistatin, and/or that the APD variability on the contracting heart surface is greater than with Blebbistatin. However, the APD-maps in **Figure 5C** do not indicate stronger APD heterogeneity or gradients on the contracting heart surface, at least not within the uncertainties of the measurement. **Figure 6F** shows restitution curves from a single pixel, the error bars and the smoothness of the curve demonstrating the reproducibility of the measurement within a single pixel for APD_{50} and APD_{70}, respectively. In summary, we found that APDs are on average 25 ± 5% shorter on the left ventricular surface of contracting than in Blebbistatin-arrested isolated rabbit hearts.

3.3. Blebbistatin Concentration and Washout During Pacing

We found that the effect of Blebbistatin during pacing is concentration dependent, as increasing concentrations of Blebbistatin increasingly prolong the action potential (see **Figures 7A–C**). **Figures 7A,C** both show that for step-wise increases of Blebbistatin concentrations to 0.7 and 1.4μM the action potential becomes subsequently prolonged, until for concentrations of 2.1 or 2.8μM the prolongation effect appears to saturate. Interestingly, the contractile motion, which is shown in **Figure 7B** for the different concentrations at the same cycle length as in **Figure 7A**, has decreased the most between 1.4 and 2.1μM, suggesting that the prolongation effect becomes smaller at higher Blebbistatin concentrations, because most of the contractile motion is already largely inhibited. Note that the Blebbistatin concentration was increased consecutively, and that the measurement might contain cumulative effects. The motion was computed by averaging over the displacements in each frame

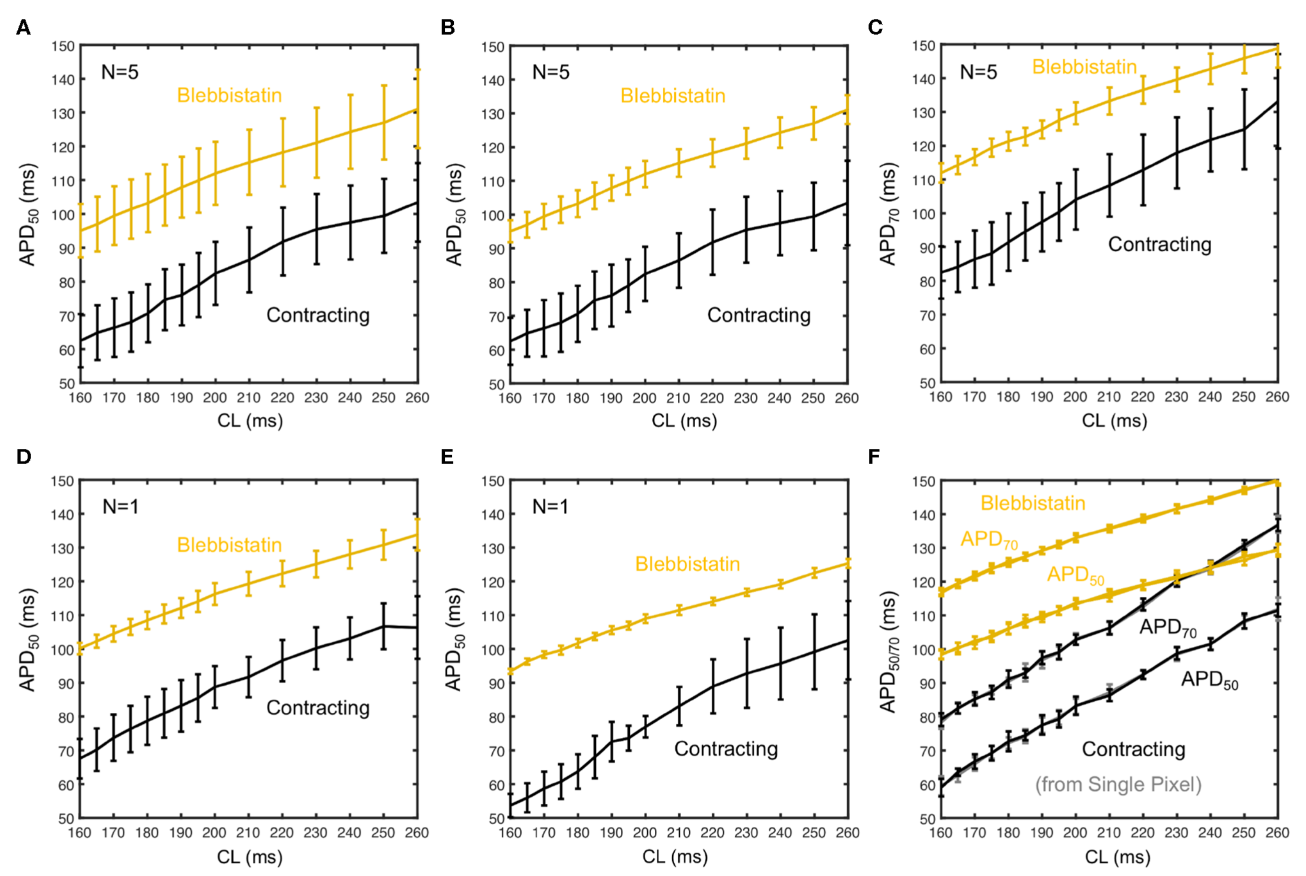

FIGURE 6 | Measurement uncertainty during optical cardiac restitution measurements on left ventricular surface of contracting (black) and contraction-inhibited hearts (Blebbistatin, yellow) for $CL = 160 - 260$ ms. **(A)** Average restitution curves including variability across hearts (means and standard deviations calculated from pooled APD_{50} of $N = 5$ hearts). **(B)** Standard deviation calculated individually for each heart, mean from pooled APD_{50} as in **(A)**. Error bars indicate higher APD variability and potentially APD dispersion on the contracting heart surface. **(C)** Average APD_{70} restitution curve ($N = 5$ hearts, derived as in **B**). **(D,E)** APD_{50} restitution curves from two individual hearts, respectively. **(F)** Restitution curve measured in a single pixel (central region of field of view) from 30 consecutive action potentials (error bars: standard deviation of the 30 APDs).

and then computing either the maximum or the average over the video sequence for each concentration.

The Blebbistatin-mediated APD prolongation is reversible since APDs shorten after washout of Blebbistatin (see **Figure 7D**). The action potentials were measured at a pacing frequency of $f_p = 3.7$Hz ($CL = 270$ms), at first on the surface of a Blebbistatin-arrested heart (yellow) at a concentration of 2.8μM, and subsequently in the same heart after replacing the Tyrode with Blebbistatin-free Tyrode (gray). The Tyrode was completely replaced and washed out for at least 1h with Blebbistatin-free Tyrode before the second measurement was conducted. The Tyrode containing Blebbistatin was not recirculated.

3.4. Electromechanical Response During Pacing

We measured the mechanical response of the heart to the electrical activation during pacing. **Figure 8** shows both the electrical activity as well as the mechanical motion of the heart measured optically in response to different pacing frequencies. The time-series were calculated by averaging the optical signals or displacements from all pixels in each video frame. The data shows in agreement with **Figure 5B** that the amplitude of the motion decreases with higher pacing frequencies, but that there is a resonant peak between 3 and 4 Hz where the motion becomes maximal. We observed this behavior in all hearts. We typically observed displacement magnitudes of about 10 pixels (~ 10% heart size) at lower frequencies as shown in **Figures 8A,C**, and larger displacements in between 10 and 15 pixels at frequencies in between 3 and 4 Hz, as shown in **Figure 8C**. At frequencies higher than 5Hz the motion typically decreased to below 5 pixels, as shown in **Figures 8D,E**.

However, more importantly, the data shows how the contractile motion of the heart stays synchronized or entrained with the electrical activation for all pacing frequencies or cycle lengths up to a frequency of about 8Hz. Electrically, there is no loss of capture. For all pacing frequencies from 2 to 10 Hz, each pacing stimulus triggers equally an action potential wave. The sequence of action potentials does not exhibit electrical alternans and fully matches with the pacing. Correspondingly, the power spectra calculated from the electrical time-series

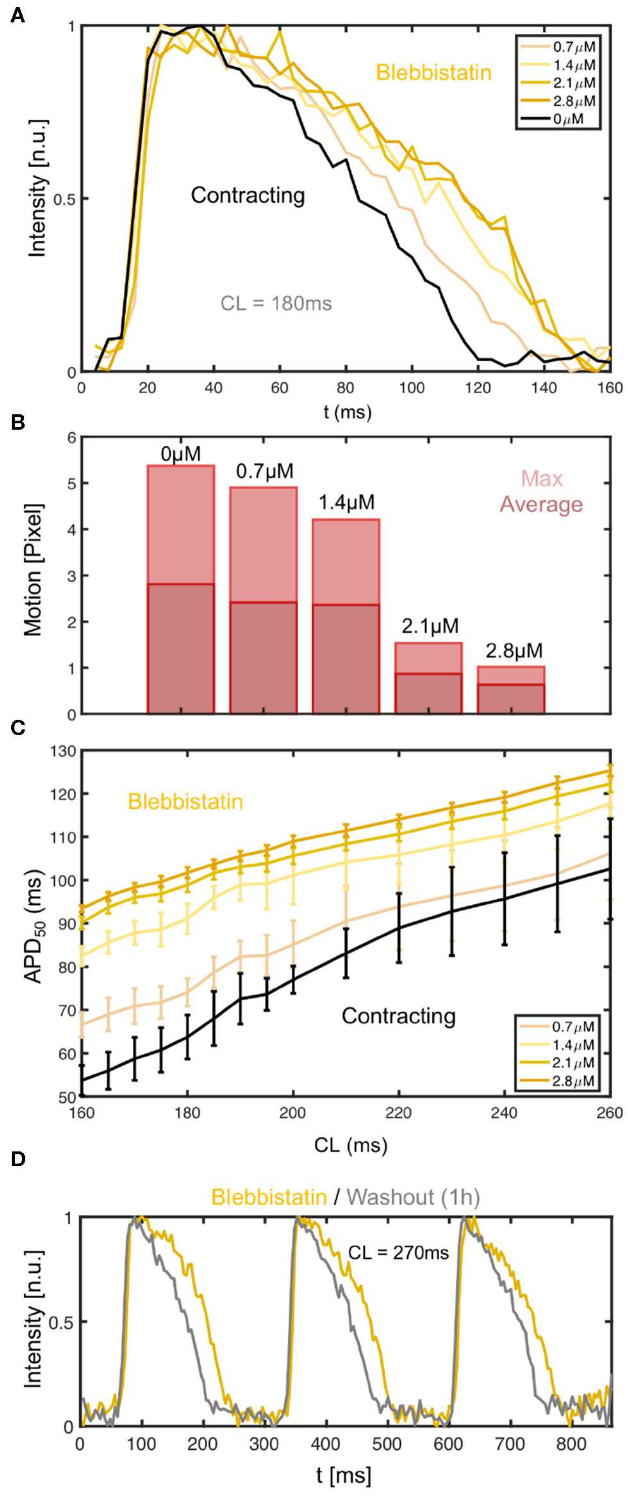

FIGURE 7 | Dependence of action potential duration (APD) and restitution curve on Blebbistatin concentration. **(A)** APD prolongation with increasing Blebbistatin concentrations (black: 0μ*M* contracting, light to dark yellow: 0.7 − 2.8μ*M* Blebbistatin) at a cycle length of *CL* = 180*ms*. Optical traces obtained from 3 × 3 pixels (spatial averaging), single action potentials without temporal averaging. **(B)** Contractile motion at different Blebbistatin

(Continued)

FIGURE 7 | concentrations: baseline 0μ*M* at *CL* = 180*ms*, decreasing contractility with 0.7 − 2.8μM. **(C)** Blebbistatin concentration-dependence of restitution curves: increasing Blebbistatin concentrations prolong the APD over all cycle lengths (*N* = 1 heart, APD$_{50}$, black: 0μM contracting, light to dark yellow: 0.7 − 2.8μM Blebbistatin). The error bars become smaller with increasing Blebbistatin concentrations and decreasing contraction magnitudes. **(D)** Shortening of action potential after washout (1h) of Blebbistatin (gray) at cycle length of *CL* = 270ms on left ventricular surface.

exhibit a single peak matching the pacing frequency. The power spectra calculated from the mechanical time-series also exhibit single peaks that match both the pacing frequency and the corresponding peaks in the electrical power spectra, however, only up to a frequency of about $f_p = 8.0$Hz. Beyond 8Hz every pacing stimulus leads to a corresponding synchronous electrical activation of the ventricles, but only every second pacing pulse causes a fully noticeable mechanical response. In this regime, the mechanical power spectrum exhibits two peaks, one at the pacing frequency and one at half the pacing frequency, while the electrical power spectrum exhibits only one peak still at the pacing frequency (see **Figure 8E**). The data suggests the existence of calcium alternans or mechanical resonance phenomena (sub-harmonics) in this regime.

3.5. Accelerated Vortex Wave Dynamics During Ventricular Fibrillation in Contracting Hearts

We found that the action potential vortex wave dynamics during ventricular fibrillation (VF) become significantly altered when administering Blebbistatin. On average, contracting hearts fibrillate faster than Blebbistatin-arrested hearts (see **Figure 9**). **Figure 9A** shows two series of raw optical maps displaying and comparing the action potential wave dynamics on the surface of the same rabbit heart during VF, once contracting (top) and once Blebbistatin-arrested (bottom) see also **Supplementary Video 2**. To ensure comparability, the optical maps show in both cases the heart surface after numerical motion tracking and motion-stabilization, the signals being equally normalized in each pixel over time (normalized units [n.u.] ∈ [0,1], black: depolarized tissue, white: repolarized tissue). One can immediately notice that the fibrillatory waves on the contracting heart surface (top) are smaller and more fragmented than the waves on the uncoupled non-contracting heart surface (bottom), which are larger and have longer wavelengths (see also **Figure 10**). Correspondingly, the two exemplary optical traces or time-series in **Figure 9C** show shorter and more irregular action potentials on the contracting compared to the uncoupled heart surface.

We confirmed that contracting hearts typically fibrillate much faster than with Blebbistatin in $N = 10$ hearts (see **Figures 9D–G**). We observed frequencies ranging in the order of $f_c = 13.1 \pm 4.9$Hz across the 10 hearts as they contracted, and frequencies of $f_B = 7.9 \pm 2.1$Hz after they had been contraction-inhibited. The example shown in **Figure 9A** is typical (heart 4). However, we also observed a significant variability across hearts. While we saw a similar behavior in six hearts with frequencies

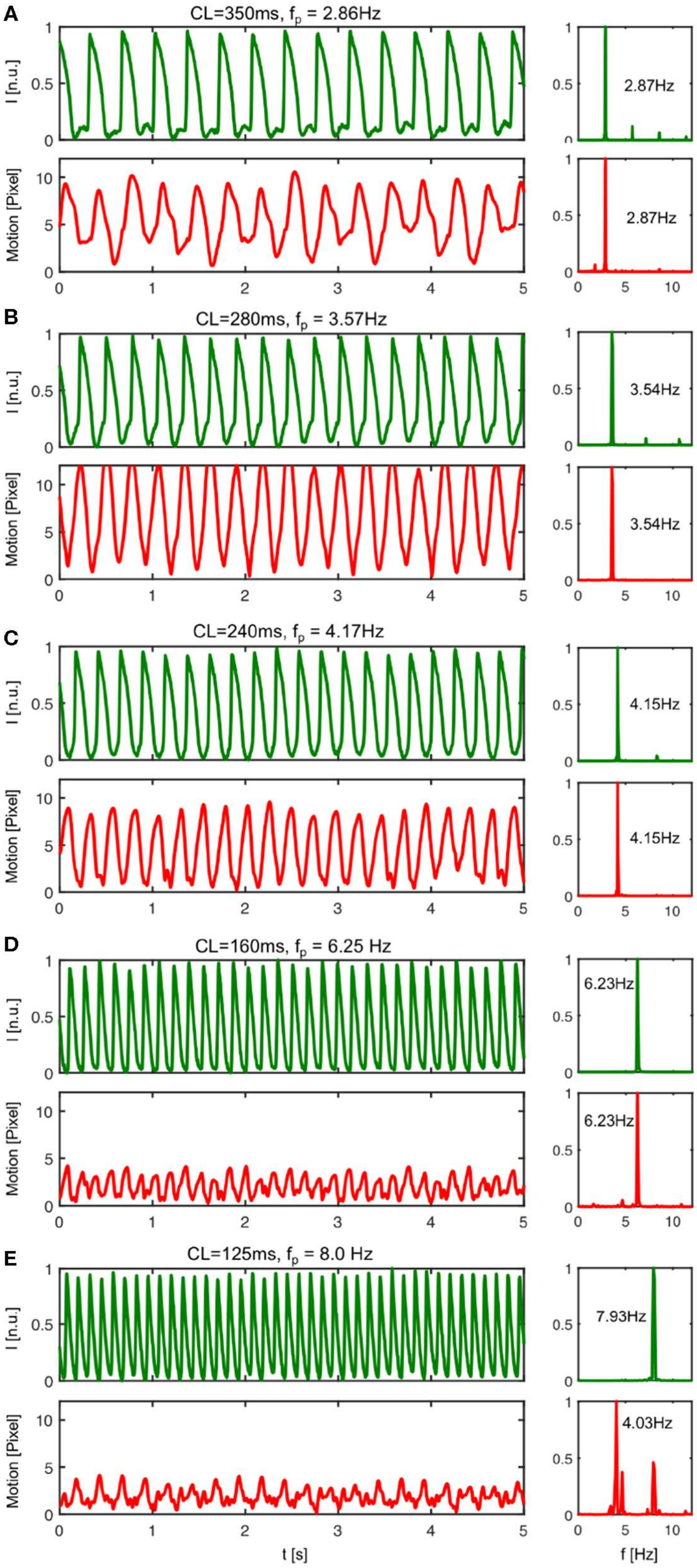

FIGURE 8 | Mechanical response to electrical activation during pacing. The pacing fully captures both electrical and mechanical activation of the heart up to a frequency of about $f_p < 8$Hz. In particular, for pacing frequencies below $f_p < 8$Hz the mechanical contraction and motion of the heart is enslaved to the electrical

(Continued)

FIGURE 8 | pacing. Each electrical pacing stimulus leads to a contraction and equally a mechanical forth and back motion. **(A)** At pacing frequencies below $f_p = 3$Hz (here $CL = 350$ms or $f_p = 2.86$Hz) the electrical activation leads to moderately strong motion. **(B)** The motion amplitude becomes maximal for pacing frequencies ranging in between $3 - 4$Hz (see also **Figure 5B**). At pacing frequencies above $f_p = 4$Hz (here $CL = 240$ms or $f_p = 4.17$Hz) the rapid periodic electrical activation leads to a highly correlated back and forth motion of the heart. A similar behavior can be observed until $f_p < 8$Hz. The powerspectrum is mono-modal. **(D)** At a pacing frequency of $f_p = 6.25$Hz both powerspectra are mono-modal and exhibit a single dominant frequency. **(E)** With pacing frequencies > 8Hz, the pacing still fully captures electrically, but the mechanical powerspectrum is no longer mono-modal.

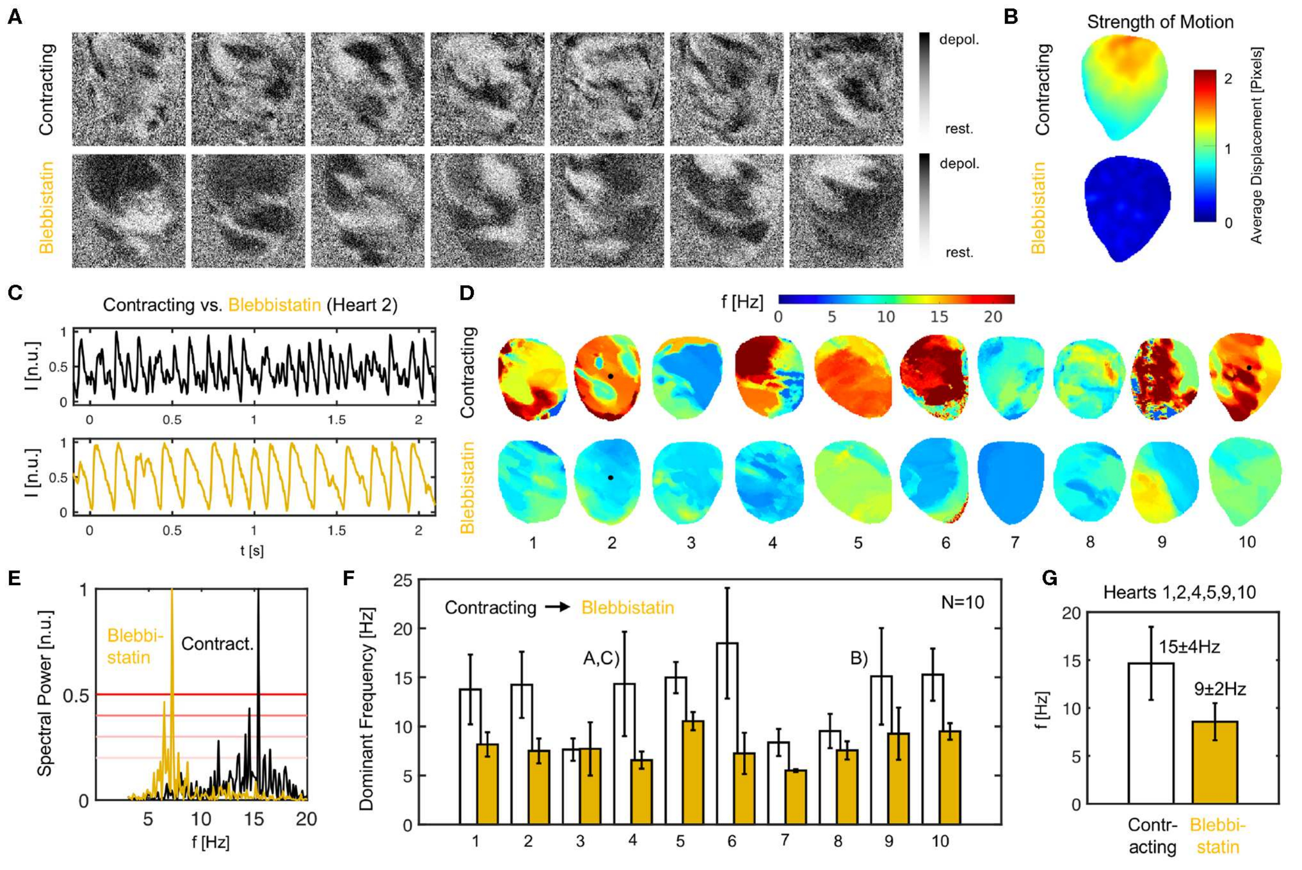

FIGURE 9 | Ventricular fibrillation (VF) is faster in contracting than in Blebbistatin-arrested isolated rabbit hearts. **(A)** Raw optical mapping data (pixel-wise normalized) showing action potential waves during VF on contracting (top) and contraction-inhibited (bottom) ventricular surface, see also **Supplementary Video 2**. **(B)** Contractile motion without (top) and with (bottom) Blebbistatin during VF measured with numerical motion tracking (time-averaged). **(C)** Exemplary time-series (averaged from 5×5 pixels, inverted) showing action potential sequence on contracting heart surface (black) and with Blebbistatin (yellow). **(D)** Dominant frequency maps. **(E)** Exemplary power spectrum (cumulative from all pixels, heart 2) with and without Blebbistatin. **(F)** Frequencies in $N = 10$ hearts during 8 sec. long VF episodes without (white) and with Blebbistatin (yellow). Mean values and standard deviations computed from data in **(D,E)** including at least $5,000$ pixels containing time-series as shown in **(C)**. 4th and 9th bar plot pairs correspond to data shown in **(A–C)**, respectively. **(G)** Typical dominant frequencies during VF with and without Blebbistatin (averaged from $N = 6$ hearts).

decreasing from around 14.7 ± 3.8Hz down to 8.6 ± 1.9Hz with Blebbistatin (hearts 1, 2, 4, 5, 9, 10), in three cases the frequencies were already below $10Hz$ as the hearts contracted (hearts 3, 7, 8). Of these three cases, two cases (hearts 7, 8) decreased slightly further and one remained the same (heart 3). In one case, the heart did not exhibit VF but monomorphic VT with Blebbistatin (heart 7). In another case, the heart fibrillated very rapidly while contracting ($\sim 20Hz$) and then the frequency fell below 10Hz with Blebbistatin (heart 6). However, in summary, in almost all cases frequencies were higher and the frequency contents were broader when hearts were contracting, as seen in **Figure 9F**). The frequency maps in **Figure 9D** show a higher spatial heterogeneity in contracting hearts and a homogenization of the activity with Blebbistatin.

It is important to point out that the VF data contains episodes that were either induced after the restitution measurements, in which the rapid pacing at the end (final pacing frequency/cycle length of 10Hz/100ms after 390 s or 6.5 min long pacing) had induced ventricular arrhythmias (hearts 1–4, 6, 9, 10), or after rapid pacing ($30 - 50$Hz for 30 s) with biphasic pulses (10V) during sinus rhythm (hearts 5, 7, 8). Therefore, the findings are independent from the particular pacing protocol with which the

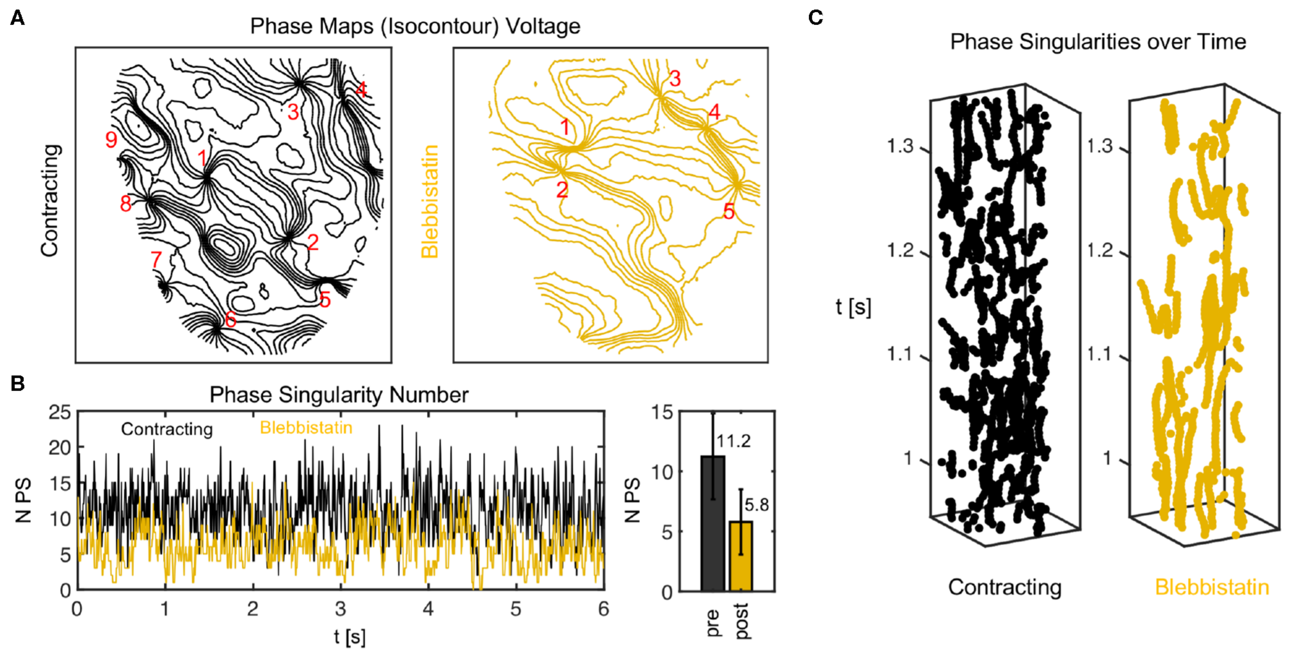

FIGURE 10 | Phase singularity dynamics of action potential vortex waves on contracting and contraction-inhibited ventricular heart surface. **(A)** Phase maps showing phase singularities as nodal points. **(B)** Number of phase singularities N_{PS} over time. Right: mean of N_{PS} and standard deviation (6 s). **(C)** Space-time plots (vertical axis: time) indicating trajectories of phase singularities across heart surface.

arrhythmia was induced. The perfusion pump was not turned off during the experiments.

Figure 10 shows a comparison of phase maps (isocontour lines indicating lines of equal phase) and phase singularity dynamics (nodal points) during VF without (black) and with Blebbistatin (yellow) at a concentration of 2.7µMol. The number of phase singularities is higher on the surface of the contracting than the contraction-inhibited heart, confirming the impression given by the optical maps in **Figure 9A**. **Figure 10B** shows the automatically tracked number of phase singularities over time. Overall, the number of phase singularities fluctuates strongly. However, the average number of phase singularities is higher on the contracting heart surface with $PS_N = 11.2 \pm 3.6$, compared to $PS_N = 5.8 \pm 2.7$ on the motion-inhibited, uncoupled surface of the same heart (over $6.0s$ or $1,500$ video frames). Note that the actual number of phase singularities on the entire surface of the heart is larger since one camera can image only $30 - 50\%$ of the heart surface. **Figure 10C** shows phase singularity dynamics on the heart surface (vertical axis: time).

3.6. Blebbistatin Concentration and Washout During VF

We found that the decelerating effect of Blebbistatin during VF is reversible. We performed washout experiments in $N = 2$ hearts and observed that the VF dynamics accelerate again when Blebbistatin is washed out. **Figure 11A** shows that when administering Blebbistatin (1.4µM concentration for 15 min) VF decelerates, and after washout with Blebbistatin-free Tyrode accelerates again (lower time-series, 100 min after starting washout). The central time-series in **Figure 11A** was measured 75 min after the first, and the last was measured 100 min after the central time-series. Blebbistatin was effective at suppressing contractile motion during VF at concentrations as low as 0.7µM. At 2.8µM the motion was completely suppressed (see **Figure 9B**). The dominant frequency during VF (computed from dominant frequency maps) decreased from about 15Hz to approximately 10Hz for all concentrations (30 min in between each measurement) (see **Figure 11B**).

3.7. Efficacy of Motion Artifact Compensation

In this study, we assumed that motion artifacts are generated mainly by two mechanisms: firstly, the dissociation or deallocation of particular tissue segments with particular pixels on the sensor, and, secondly, relative motion between tissue and light sources. Dissociation-related motion artifacts can be compensated by introducing numerical motion tracking and -stabilization, and the efficacy of the tracking was validated previously (Christoph and Luther, 2018). Illumination-related motion artifacts can be compensated using ratiometric optical mapping (Knisley et al., 2000; Bachtel et al., 2011). In this section, we discuss the advantages of the combined use of numerical motion tracking and ratiometry over numerical motion tracking and stabilization alone.

We found that the combination of numerical motion tracking and ratiometric imaging was not always and unrestrictedly effective in compensating motion artifacts. With excessive motion even the combination of numerical motion stabilization

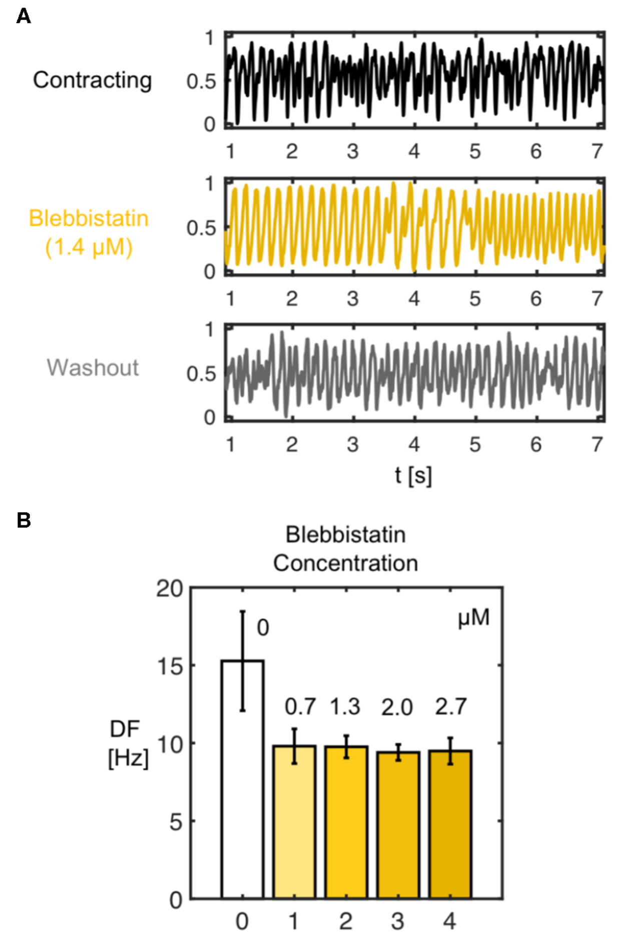

FIGURE 11 | (A) Deceleration of VF by Blebbistatin and acceleration of VF after washout demonstrating reversibility of decelerating effect of Blebbistatin. The frequency and complexity of the electrocardiogram (shown) and optical traces measured during VF decreases with Blebbistatin (here 1.4μM after 15 min) and increases after washout of Blebbistatin (100 min), respectively. **(B)** Frequency decrease after administration of Blebbistatin (from 15.3 ± 3.2Hz to 9.6 ± 0.8Hz, data from $N = 1$ heart) to constant level for various concentrations. Frequency spectra become narrower with Blebbistatin. Confirmed for $N = 2$ hearts.

and ratiometry faces limitations. For instance, during restitution curve measurements, we typically found a regime in which excessive motion occurred (pacing at $3 - 4$Hz, displacements as large as $10-30\%$ of the heart size, > 10 pixels) (see also **Figure 5**), and which in turn appeared to cause large measurement errors. Shows that two restitution curves that were computed from the same measurement data can strongly differ from each other and retain large uncertainties in between pacing rates of $3 - 4$Hz. One curve was computed from APD_{50} and the other from APD_{70} values. **Figure A1C** in the **Appendix** illustrates how baseline modulations and deflections in the optical data may produce this under- or over-estimation (only in site B). The data suggests that either the efficacy of excitation ratiometry (different green and blue illumination fields) is limited in the presence of very strong relative (light source–tissue) motion, or other sources generating motion artifacts start to emerge with very strong contractile motion and deformation (e.g., absorption and emission changes of dye). The data demonstrates that it is yet a challenge to derive reliable restitution curves from APD_{90} values in the presence of strong motion. However, the strong translational and rotational motion that we observed in our experiments is in part caused by the specific experimental configuration, and could be avoided in future experiments (mechanical stabilization: e.g., intraventricular inflatable ballons or artificial pericard sacks).

During VF, subsequent ratiometric imaging does not necessarily improve the accuracy of the measurement substantially over numerical motion tracking alone, as can be seen in **Figure 12**. The phase maps in **Figures 12A,B** show fibrillatory wave dynamics measured, firstly, using numerical motion tracking and -stabilization alone (green), and secondly, using a combination of numerical motion tracking and -stabilization with ratiometry (black). Therefore, the green phase maps contain illumination-related motion-artifacts, but no or little dissociation-related motion-artifacts, whereas the black phase maps should contain neither dissociation- nor illumination-related motion-artifacts (both maps superimposed within the non-moving material coordinate frame). The high similarity between the green and the black phase maps (in $70 - 80\%$ almost congruent and vortex cores coincide almost perfectly, see **Figure 12D**), in $20 - 30\%$ subtle to moderate differences, see red arrows in **Figure 12B** and box in **Figure 12D** indicates that motion tracking is largely sufficient in suppressing motion artifacts and, vice versa, that ratiometric imaging does not necessarily improve the accuracy of the measurement much further during VF. The compensated raw optical maps (see **Figure 12C**), are visually nearly indistinguishable (aside from few exceptions, red box). **Figure 12D** shows the distribution of the mismatches (shortest distances) between the phase singularities (green-black) obtained without (green) and with (black) ratiometry (in 71% mismatches $<\ 5$ pixels, in 78% mismatches < 10 pixels, in 22% mismatches comparatively large $>\ 10\%$ pixels, average distance between both green-green or black-black phase singularities 17.5 ± 2.5 pixels). The space-time plot shows the motion of a subset of phase singularities across the heart surface (rectangular region of interest on LV to facilitate visualization) over time (y-axis, left: $1.1s$) and illustrates that phase singularities imaged in mono-channel mode (green) represent the “true” phase singularities (black) sufficiently accurate (exception indicated by red box). The phase singularity density is almost equal (9.4 ± 4.0 without and 10.9 ± 4.0 with ratiometry in 8.0 sec. or $2,000$ video frames). The data shows that, with small amounts of contractile motion during VF, illumination artifacts become negligible and therefore tracking and numerical motion correction alone is sufficient and ratiometric imaging is not necessarily needed.

4. DISCUSSION

In this study, we used marker-free numerical motion tracking and -stabilization together with ratiometric optical mapping

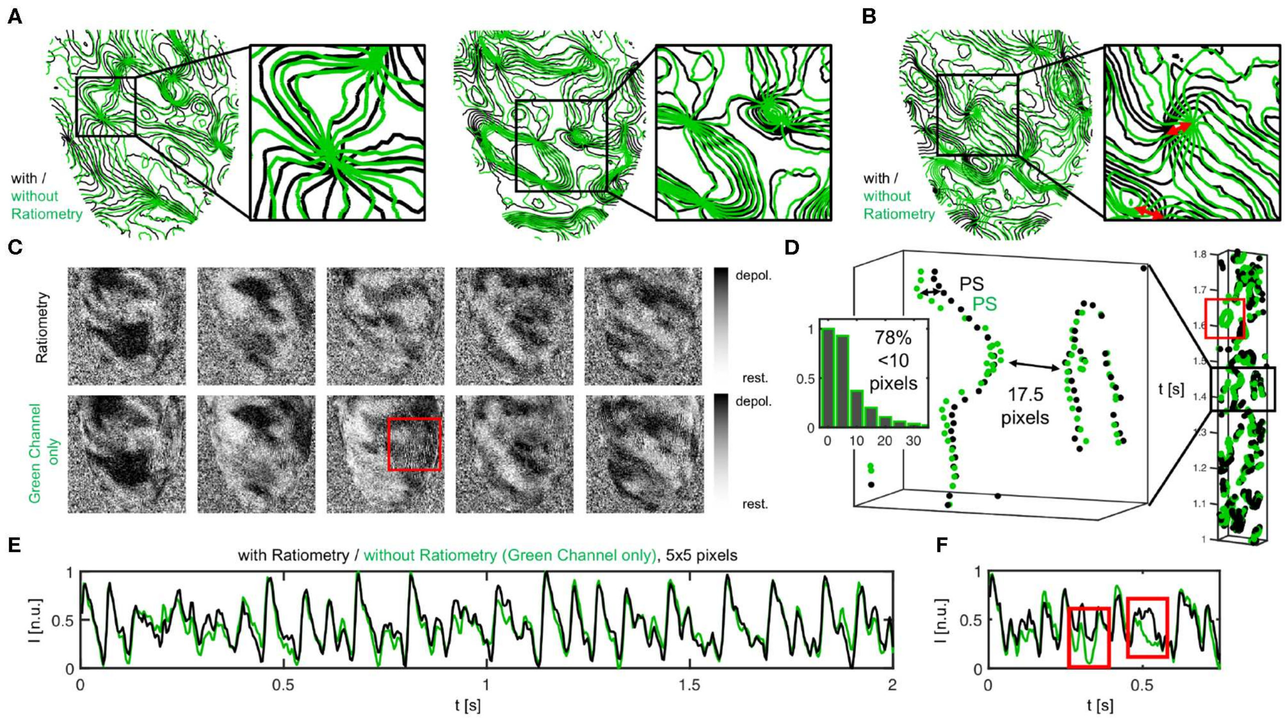

FIGURE 12 | Vortex wave and phase singularity dynamics measured during VF on the contracting heart surface with numerical motion tracking and -stabilization alone (green) compared to with numerical motion tracking and -stabilization and ratiometry (black), respectively. **(A)** Good agreement between phase maps obtained with or without ratiometry, both equally showing vortex waves and vortex cores in the same locations. Phase maps are displayed as isocontour lines indicating lines of equal phase. Vortex cores or phase singular points are displayed as nodal points. **(B)** Slight mismatches and subtle differences between vortex waves and vortex core positions with and without ratiometry. **(C)** Optical maps with and without ratiometry are visually nearly indistinguishable (except for few occasions, see red box). **(D)** Space-time plot showing motion of phase singularities across heart surface over time (y-axis), once from green channel alone and with ratiometry (black). Distribution of green-black phase singularity distances ($> 17,000$ phase singularities in $1,800$ video frames over duration of 7.2 s). **(E,F)** Optical traces obtained during VF with (black) and without (green) ratiometry.

to perform high-resolution measurements of action potential durations on the beating surface of intact Langendorff-perfused hearts, and have consequently compared the ventricular electrophysiology in beating vs. contraction-inhibited hearts uncoupled with Blebbistatin during both paced rhythms and arrhythmias. As discussed in section 3.7, we were able to retrieve largely artifact-free optical traces from high-resolution optical maps, measuring action potential waves in a co-moving frame of reference propagating across the contracting and strongly deforming heart surface. The combination of numerical motion tracking with ratiometric imaging inhibited motion artifacts substantially, enabling optical action potential duration (APD) measurements across the heart surface with uncertainties in the order of the temporal resolution of the camera. We were able to detect changes in APD in response to small changes in Blebbistatin concentrations, and we expect that we would similarly also be able to detect other physiological changes caused by, for instance, pharmacological agents. However, we observed substantial APD measurement uncertainties during excessive motion of the hearts (see **Figure A1** in **Appendix**).

One of our main findings shows that the duration of the action potential becomes shorter in beating isolated rabbit hearts, or is prolonged in contraction-inhibited rabbit hearts uncoupled with Blebbistatin. Moreover, we found that, in agreement with the shorter APD, VF dynamics are faster and more complex in contracting rabbit hearts. Our findings confirm previous findings by Brack et al. (2013) and Lee et al. (2019), who found that ventricular electrophysiology is significantly different in beating vs. contraction-inhibited isolated rabbit and pig hearts uncoupled with Blebbistatin, respectively. More specifically, Brack et al. (2013) found that Blebbistatin substantially prolonges ($\sim 17-25\%$) the ventricular action potential in isolated New Zealand White rabbit hearts ($N = 39$), and increases the ventricular fibrillation threshold, or reduces the likeliness of inducing VF, at a concentration of $5\mu M$. Our study confirms the findings both directly and indirectly and we found that VF appears to be less aggressive and decelerated in uncoupled hearts, which could in principle explain higher VF thresholds. More recently, Lee et al. (2019) reported a substantial prolongation of the ventricular action potential ($\sim 15\%$), as well as a substantial decrease of the conduction velocity ($\sim 25\%$) in

TABLE 1 | Overview over studies investigating the effect of Blebbistatin onto cardiac electrophysiology.

Study	Δ APD	N	Conc. [μM]	Species	Preparation
Fedorov et al. (2007)	Yes	$N = 6$	5–10	Rabbit	Isolated Heart (Ventr.)
	No	$N = 5$	5–10	Rabbit	Wedge Prep. (Atria)
	No	$N = 5$	5–10	Rabbit	Wedge Prep. (SAN)
	NA	NA	5–10	Rat	Cardiomyocyte (Ventr.)
Dou et al. (2007)	NA	NA	NA	Mouse	Papillary Muscle
	No	$N = 11$	10	Mouse	Cardiomyocyte (Ventr.)
Jou et al. (2010)	No	$N = 4$	10	Zebrafish	Atria
	No	$N = 4$	10	Zebrafish	Ventricles
Fenton et al. (2008)	No	$N = 1$	10–15	Horse	Isolated Heart (Atria)
	No	$N = 1$	10–15	Horse	Isolated Heart (Ventr.)
Zhang et al. (2016)	No	$N = 1$	20	Pig	Isolated Heart (Ventr.)
Brack et al. (2013)	Yes	$N = 39$	5	Rabbit	Isolated Heart (Ventr.)
Lee et al. (2019)	Yes	$N = 5$	NA	Pig	Isolated Heart (Ventr.)
Kappadan et al.	Yes	$N = 10$	3	Rabbit	Isolated Heart (Ventr.)

Overall, the findings regarding APD difference (Δ APD) with and without Blebbistatin remain inconclusive and seem to depend on preparations and species.

($N = 5$) pig hearts *ex vivo* comparing hearts pre- and post-Blebbistatin (concentration unknown). The findings by Brack et al. (2013) and Lee et al. (2019) are in agreement with our study. Fedorov et al. (2007) reported that Blebbistatin does *not have any effect onto electrical activity*. More specifically, they found no effect onto the calcium transient morphology in single rat ventricular cardiomyocytes, and no effect onto the action potential morphology in the atria ($N = 5$) and the sinoatrial node ($N = 5$), but a slight prolongation of the action potential in the right ventricles ($N = 6$) in isolated New Zealand White rabbit hearts with Blebbistatin concentrations of $5 - 10\mu$M at a pacing cycle length of $400ms$. Dou et al. (2007) reported that Blebbistatin did not alter APD in single mice cardiomyocytes ($N = 11$) at a Blebbistatin concentration of 10μM. Fenton et al. (2008) found no significant change in APD in isolated equine hearts ($N = 1$) in both atria and ventricles uncoupled with Blebbistatin at concentrations of $10 - 15\mu$M. Jou et al. (2010) reported that the action potential morphology did not get altered significantly in the atria or the ventricles of embryonic zebrafish hearts ($N = 4$) at Blebbistatin concentrations of 10μM. Lou et al. (2012) studied the electrophysiological differences between New Zealand White rabbit hearts ($N = 7$) uncoupled with BDM (10mM) vs. Blebbistatin (10μM) using panoramic optical mapping, and found that BDM produces shorter APDs than Blebbistatin. They concluded that Blebbistatin does not alter APD restitution, however, without comparing directly to a contracting heart as baseline. On the other hand, Bourgeois et al. (2011) found in isolated pig hearts ($N = 7$) *ex vivo* that BDM produces shorter APDs than when the heart contracts. Together, the findings suggest that APDs in contracting hearts are longer than with BDM, but shorter than with Blebbistatin. Lastly, Zhang et al. (2016) found at a Blebbistatin concentration of 20μM a *very similar action potential morphology* pre- and post-Blebbistatin in an isolated pig heart ($N = 1$) *ex vivo*.

A shortening of the action potential in beating isolated hearts was previously associated with a higher metabolic demand and oxygen consumption of the contracting heart muscle, which can not be sufficiently met using standard aqueous crystalloid perfusates (e.g., Tyrode) during Langendorff-perfusion (Gillis et al., 1996; Wengrowski et al., 2014; Kuzmiak-Glancy et al., 2015, 2018; Garrot et al., 2017; Ruiz and Comtois, 2018). More specifically, Gillis et al. (1996) found that APDs are shorter and ventricular fibrillation thresholds lower in crystalloid buffer-perfused vs. blood-perfused contracting rabbit hearts. Our data confirms that action potentials in beating buffer-perfused rabbit hearts become progressively triangular-shaped with faster beating rates (see **Figure 4**), triangularity being a hallmark of hypoxia or ischemia (Pinto and Boyden, 1999). Our data therefore strongly suggests that the beating heart's oxygen consumption becomes larger, and, consequently, an undersupply with oxygen more severe at faster beating rates. Our data is in agreement with previous findings by Garrot et al. (2017), who measured oxygen consumption to be larger and APD shorter in working than in unloaded contracting Langendorff-perfused rabbit hearts. Garrot et al. (2017) furthermore linked hypoxia and hypoxia-induced APD shortening to K_{ATP}-channel activation, suggesting that the channel regulates contractile function in response to available oxygen and energy levels. Lastly, it was shown that crystalloid-perfused working hearts are oxygen limited and have reduced cardiac performance (Kuzmiak-Glancy et al., 2018). Other potential side-effects that seem to be associated with the use of Blebbistatin need to be considered very carefully. Brack et al. (2013) discussed potential other secondary effects of Blebbistatin that could affect APD, including vasodilatory and -constrictory phenomena that could alter perfusion and oxygen supply. Swift et al. (2012) found that Blebbistatin can form precipitate, which may block microcirculation in the cardiac muscle. In summary, the question whether Blebbistatin affects cardiac electrophysiology—directly or indirectly—remains controversial, see also **Table 1**, and further research is needed. As of today, it appears that one has to choose between two unphysiological conditions when performing *ex vivo* optical mapping studies in a Tyrode-based Langendorff-perfusion environment: either one can image hearts treated with Blebbistatin, which resultantly do not contract (as they are intended to), or one can renounce Blebbistatin and image beating hearts, which seem to have a higher metabolic demand than the experimental *ex vivo* environment can provide. In the future, the oxygenation problem in Langendorff experiments with contracting hearts could be addressed by using blood-based perfusion, perfusates enriched with red blood cells (or blood), or, more ideally, by using optically clear, aqueous perfusates that provide a higher oxygen carrying capacity (Kuzmiak-Glancy et al., 2018).

Electrophysiological differences between beating and contraction-inhibited hearts could also be mechanically-induced and result from physiological processes unrelated to oxygenation or potential side-effects of pharmacological agents. For instance, it was observed in bypass surgery patients that APD shortens during recurring contractile work of the heart muscle when switching from "nonworking" to "working" conditions during reperfusion (Taggart et al., 1988), suggesting that mechano-electrical feedback phenomena may also influence APD. Thompson et al. (2011) found in cardiac cell cultures that using mechanosensitive channel blockers, which suppress the influence of tissue deformation on cardiac electrophysiology, similarly results in an increase of action potential conduction velocity as using Blebbistatin, suggesting that the suppression of mechanical deformation itself as well as the heart's mechano-sensitivity to it may also play a role in altering cardiac electrophysiology. Contractile work, or the absence of it, could affect various interactions between the contractile machinery, calcium handling, and excitability of cardiac cells, and strongly influence coupling and feedback mechanisms between voltage, calcium and mechanics on cellular and tissue levels.

5. CONCLUSIONS

We demonstrated that ratiometric electromechanical optical mapping can be used to reliably measure action potential durations on a broad range of pacing frequencies and at very high spatial and temporal resolutions on the surface of contracting isolated hearts. We found that action potential durations are shorter in contracting isolated rabbit hearts than in Blebbistatin-arrested isolated rabbit hearts perfused with standard Tyrode in Langendorff experiments. During ventricular fibrillation, the dominant frequency and the number of phase singularities are increased in contracting vs. non-contracting hearts. These observations are consistent with the assumption that contracting hearts experience mild hypoxia in the Langendorff-perfusion. Our findings may have important implications for future optical mapping studies.

DATA AVAILABILITY STATEMENT

The datasets generated for this study are available on request to the corresponding author.

ETHICS STATEMENT

The animal study was reviewed and approved by the Lower Saxony State Office for Customer Protection and Food Safety (LAVES) and the Federation of European Laboratory Animal Science Associations (FELASA). The protocol was approved by the Lower Saxony State Office for Customer Protection and Food Safety (LAVES).

AUTHOR CONTRIBUTIONS

VK performed the experiments. VK and JC analyzed the data. JC wrote the initial and revised versions of the manuscript, drafted the figures, and supervised the experiments. JC, SL, and UP set the scientific agenda and supervised the research. ST contributed to the experiments and data analysis. IU and FF contributed to the experiments. All authors reviewed and approved the manuscript.

FUNDING

This research was funded by the German Center for Cardiovascular Research (DZHK e.V.), partnersite Göttingen (to SL and JC), the European International Training Network Be-Optical (ITN) (to UP and SL), the Max Planck Society (to SL), NIH 1R01HL143450-01 (to FF), and NSF CMMI-1762553 (to FF).

ACKNOWLEDGMENTS

We would like to thank M. Kunze and S. Berg for technical assistance.

SUPPLEMENTARY MATERIAL

The Supplementary Material for this article can be found online at: https://www.frontiersin.org/articles/10.3389/fphys.2020.00464/full#supplementary-material

REFERENCES

Bachtel, A. D., Gray, R. A., and Rogers, J. M. (2011). A novel approach to dual excitation ratiometric optical mapping of cardiac action potentials with di-4-anepps using pulsed led excitation. *IEEE Trans. Biomed. Eng*. 58, 2120–2126. doi: 10.1109/TBME.2011.2148719

Banville, I., Chattipakron, N., and Gray, R. A. (2004). Restitution dynamics during pacing and arrhythmias in isolated pig hearts. *J. Cardiovasc. Electrophysiol*. 15, 455–463. doi: 10.1046/j.1540-8167.2004.03330.x

Bourgeois, E. B., Bachtel, A. D., Huang, J., Walcott, G. P., and Rogers, J. M. (2011). Simultaneous optical mapping of transmembrane potential and wall motion in isolated, perfused whole hearts. *J. Biomed. Opt*. 16:096020. doi: 10.1117/1.3630115

Brack, K. E., Narang, R., Winter, J., and Ng, G. A. (2013). The mechanical uncoupler blebbistatin is associated with significant electrophysiological effects in the isolated rabbit heart. *Exp. Physiol*. 98, 1009–1027. doi: 10.1113/expphysiol.2012.069369

Choi, B.-R., Liu, T., and Salama, G. (2004). Adaptation of cardiac action potential durations to stimulation history with random diastolic intervals. *J. Cardiovasc. Electrophysiol*. 15, 1188–1197. doi: 10.1046/j.1540-8167.2004.04070.x

Christoph, J., Chebbok, M., Richter, C., Schröder-Schetelig, J., Bittihn, P., Stein, S., et al. (2018). Electromechanical vortex filaments during cardiac fibrillation. *Nature* 555, 667–672. doi: 10.1038/nature26001

Christoph, J., and Luther, S. (2018). Marker-free tracking for motion artifact compensation and deformation measurements in optical mapping videos of contracting hearts. *Front. Physiol*. 9:1483. doi: 10.3389/fphys.2018.01483

Christoph, J., Schröder-Schetelig, J., and Luther, S. (2017). Electromechanical optical mapping. *Prog. Biophys. Mol. Biol*. 130, 150–169. doi: 10.1016/j.pbiomolbio.2017.09.015

Davidenko, J. M., Pertsov, A. V., Salomonsz, R., Baxter, W., and Jalife, J. (1992). Stationary and drifting spiral waves of excitation in isolated cardiac muscle. *Nature* 355, 349–351. doi: 10.1038/355349a0

Dou, Y., Arlock, P., and Arner, A. (2007). Blebbistatin specifically inhibits actin-myosin interaction in mouse cardiac muscle. *Am. J. Physiol*. 293, C1148–C1153. doi: 10.1152/ajpcell.00551.2006

Farman, G. P., Tachampa, K., Mateja, R., Cazorla, O., Lacampagne, A., and de Tombe, P. P. (2008). Blebbistatin: use as inhibitor of muscle contraction. *Pflügers Archiv*. 455, 995–1005. doi: 10.1007/s00424-007-0375-3

Fedorov, V., Lozinsky, I., Sosunov, E., Anyukhovsky, E., Rosen, M., Balke, C., et al. (2007). Application of blebbistatin as an excitation-contraction uncoupler for electrophysiologic study of rat and rabbit hearts. *Heart Rhythm* 4, 619–626. doi: 10.1016/j.hrthm.2006.12.047

Fenton, F. H., Cherry, E. M., and Kornreich, B. G. (2008). Termination of equine atrial fibrillation by quinidine: an optical mapping study. *J. Vet. Cardiol.* 10, 87–103. doi: 10.1016/j.jvc.2008.10.002

Garrot, K., Kuzmiak-Glancy, S., Wengrowski, A., Zhang, H., Rogers, J. M., and Kay, M. W. (2017). Katp channel inhibition blunts electromechanical decline during hypoxia in left ventricular working rabbit hearts. *J. Physiol.* 595, 3799–3813. doi: 10.1113/JP273873

Gillis, A. M., Kulisz, E., and Mathison, H. J. (1996). Cardiac electrophysiological variables in blood-perfused and buffer-perfused, isolated, working rabbit heart. *Heart Circ. Physiol.* 40, 784–789. doi: 10.1152/ajpheart.1996.271.2.H784

Goldhaber, J. I., Xie, L., Duong, T., Motter, C., Khuu, K., and Weiss, J. (2005). Action potential duration restitution and alternans in rabbit ventricular myocytes - the key role of intracellular calcium cycling. *Circ. Res.* 96, 459–466. doi: 10.1161/01.RES.0000156891.66893.83

Gray, R. A., Pertsov, A. M., and Jalife, J. (1998). Spatial and temporal organization during cardiac fibrillation. *Nature* 392, 75–78. doi: 10.1038/32164

Jou, C. J., Spitzer, K. W., and Tristani-Firouzi, M. (2010). Blebbistatin effectively uncouples the excitation- contraction process in zebrafish embryonic heart. *Cell. Physiol. Biochem.* 25, 419–424. doi: 10.1159/000303046

Knisley, S. B., Justice, R. K., Kong, W., and Johnson, P. L. (2000). Ratiometry of transmembrane voltage-sensitive fluorescent dye emission in hearts. *Am. J. Physiol.* 279, 1421–1433. doi: 10.1152/ajpheart.2000.279.3.H1421

Kuzmiak-Glancy, S., Covian, R., Femnou, A. N., Glancy, B., Jaimes, R., Wengrowski, A. M., et al. (2018). Cardiac performance is limited by oxygen delivery to the mitochondria in the crystalloid-perfused working heart. *Am. J. Physiol. Heart Circul. Physiol.* 314, H704–H715. doi: 10.1152/ajpheart.00321.2017

Kuzmiak-Glancy, S., Jaimes, R. III, Wengrowski, A. M., and Kay, M. W. (2015). Oxygen demand of perfused heart preparations: how electromechanical function and inadequate oxygenation affect physiology and optical measurements. *Exp. Physiol.* 100, 603–616. doi: 10.1113/EP085042

Lee, P., Quintanilla, J. G., Alfonso-Almazán, J. M., Galán-Arriola, C., Yan, P., Sánchez-González, J., et al. (2019). *In-vivo* ratiometric optical mapping enables high-resolution cardiac electrophysiology in pig models. *Cardiovasc. Res.* 115, 1659–1671. doi: 10.1093/cvr/cvz039

Lou, Q., Li, W., and Efimov, I. R. (2012). The role of dynamic instability and wavelength in arrhythmia maintenance as revealed by panoramic imaging with blebbistatin vs. 2,3-butanedione monoxime. *Am. J. Physiol. Heart Circul. Physiol.* 302, H262–H269. doi: 10.1152/ajpheart.00711.2011

Mironov, S., Jalife, J., and Tolkacheva, E. G. (2008). Role of conduction velocity restitution and short-term memory in the development of action potential duration alternans in isolated rabbit hearts. *Circulation* 118, 17–25. doi: 10.1161/CIRCULATIONAHA.107.737254

Pinto, J. M., and Boyden, P. A. (1999). Electrical remodeling in ischemia and infarction. *Cardiovasc. Res.* 42, 284–297. doi: 10.1016/S0008-6363(99)00013-9

Ruiz, M., and Comtois, P. (2018). The heart in lack of oxygen? A revisited method to improve cardiac performance *ex vivo*. *Am. J. Physiol. Heart Circul. Physiol.* 314, H776–H779. doi: 10.1152/ajpheart.00699.2017

Swift, L. M., Asfour, H., Posnack, N. G., Arutunyan, A., Kay, M. W., and Sarvazyan, N. (2012). Properties of blebbistatin for cardiac optical mapping and other imaging applications. *Pflugers Arch.* 464, 503–512. doi: 10.1007/s00424-012-1147-2

Taggart, P., Sutton, P. M., Treasure, T., Lab, M., O'Brien, W., Runnalls, M., et al. (1988). Monophasic action potentials at discontinuation of cardiopulmonary bypass: evidence for contraction-excitation feedback in man. *Circulation* 77, 1266–1275. doi: 10.1161/01.CIR.77.6.1266

Thompson, S. A., Copeland, C. R., Reich, D. H., and Tung, L. (2011). Mechanical coupling between myofibroblasts and cardiomyocytes slows electric conduction in fibrotic cell monolayers. *Circulation* 123, 2083–2093. doi: 10.1161/CIRCULATIONAHA.110.015057

Wengrowski, A. M., Kuzmiak-Glancy, S., Jaimes, R., and Kay, M. W. (2014). Nadh changes during hypoxia, ischemia, and increased work differ between isolated heart preparations. *Am. J. Physiol. Heart Circul. Physiol.* 306, H529–H537. doi: 10.1152/ajpheart.00696.2013

Witkowski, F. X., Leon, L. J., Penkoske, P. A., Giles, W. R., Spano, M. L., Ditto, W. L., et al. (1998). Spatiotemporal evolution of ventricular fibrillation. *Nature* 392, 78–82. doi: 10.1038/32170

Wu, T.-J., Lin, S.-F., Weiss, J. N., Ting, C.-T., and Chen, P.-S. (2002). Two types of ventricular fibrillation in isolated rabbit hearts. *Circulation* 106, 1859–1866. doi: 10.1161/01.CIR.0000031334.49170.FB

Zhang, H., Iijima, K., Huang, J., Walcott, G. P., and Rogers, J. M. (2016). Optical mapping of membrane potential and epicardial deformation in beating hearts. *Biophys. J.* 111, 438–451. doi: 10.1016/j.bpj.2016.03.043

Conflict of Interest: The authors declare that the research was conducted in the absence of any commercial or financial relationships that could be construed as a potential conflict of interest.

A. APPENDIX

A.1. Tyrode Solution

Tyrode solution was prepared with $15.0l$ distilled water, $130mMol$ or $114g$ sodium chloride (NaCl), $4mMol$ or $4.47g$ potassium chloride (KCl), $0.6mMol$ or $1.83g$ magnesium chloride hexahydrate ($MgCl_2(6H_2O)$), $2.2mMol$ or $3.36g$ calcium chloride ($CaCl_2$), $1.2mMol$ or $2.16g$ sodiumdihydrogen-phosphate ($NaH_2PO_4(H_2O)$), $24.2mMol$ or $30.45g$ sodium bicarbonate ($NaHCO_3$), $12mMol$ or $32.4g$ glucose, resulting in a pH-level of $7.36 - 7.40$.

A.2. Computation of Dominant Frequencies and Dominant Frequency Maps

Dominant frequencies and dominant frequency maps, as seen in **Figure 9D-G**), were computed from raw optical maps as seen in Fig. **Figure 9A**). Prior to the computation of power spectra from time-series data, each optical trace was normalized over time by their maximal and minimal values in the entire time-series yielding normalized time-series with values $\in [0,1]$, as shown in Fig. **Figure 9C**). Next, power spectra were computed from the time-series data independently for all pixels. The power spectra were then normalized by their maximal value or amplitude value of the dominant peak yielding a normalized power spectrum $P(f) \in [0,1]$ as shown in Fig. **Figure 9E**). Dominant frequencies were then computed by setting a threshold $p_t = 0.5, 0.4, 0.3, 0.2, \ldots$, clipping the power spectra's frequency contents below the threshold, and letting only frequencies with amplitudes greater the threshold contribute to an average dominant frequency:

$$f_d = \frac{\sum_i f_i P_i}{\sum_i P_i} \tag{A1}$$

effectively averaging the dominant frequencies f_i with an amplitude of at least $P_i \geq 50\%, 40\%, \ldots$ of the maximal peak from the power spectrum. We found that the different thresholds ($p_t = 20\% - 50\%$) equally yielded a robust computation of the dominant frequency, also accounting for multiple peaks in broader frequency spectra. All mean values and error bars shown in Fig. **Figure 9** were computed with a threshold of $p_t = 0.5$.

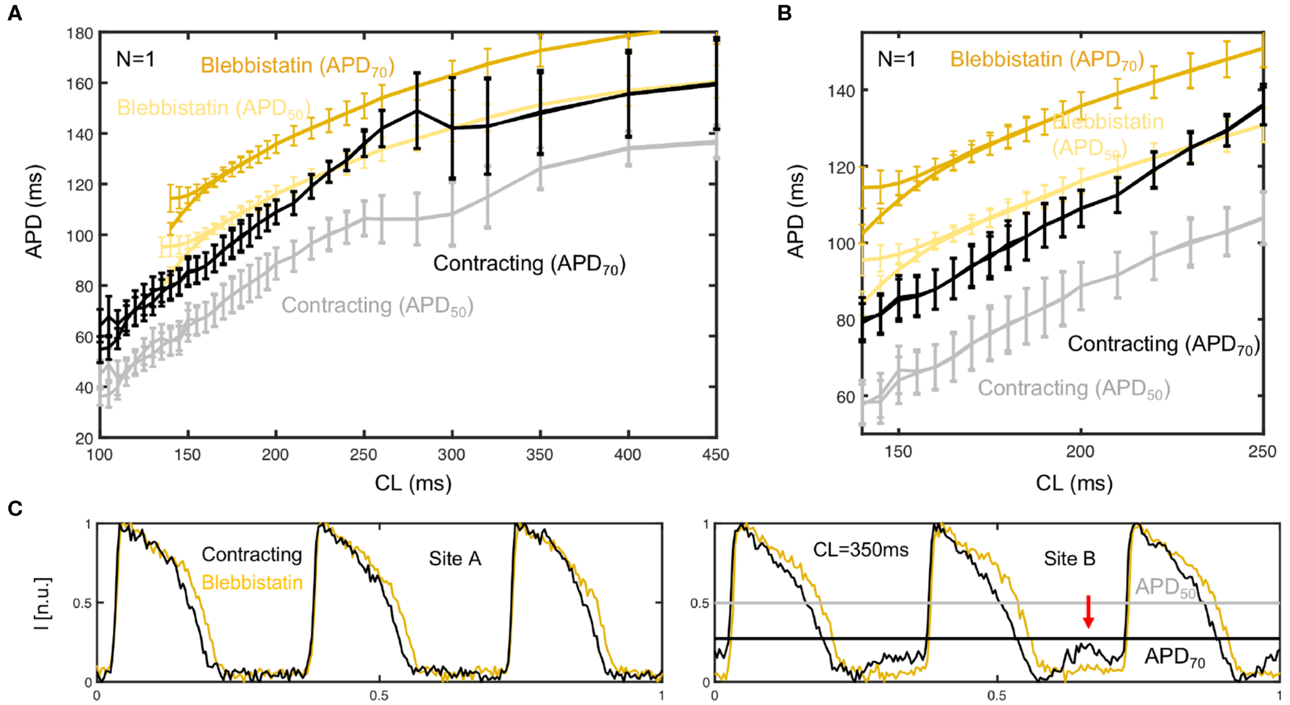

FIGURE A1 | Cardiac restitution curves determined from APD_{50} and APD_{70} measurements. At 30% of the height of the action potential (APD_{70}) the APD is longer than at 50% (APD_{50}), but also includes larger measurement errors for lower pacing frequencies. **(A)** In this mid-frequency regime with large motion, the APDs are overestimated at APD_{70} and underestimated at APD_{50}. **(B)** At higher frequencies or shorter cycle lengths $CL < 200ms$ both APD_{70} and APD_{50} values appear to provide reliable measurement data. **(C)** Corresponding time-series obtained at upper limit of mid-frequency range ($CL = 350ms$), which hint at measurement artifacts. In one site (site A) the optical traces look unobjectionable, whereas in another (site B) they exhibit motion artifacts that could be related to the under- or overestimation of APD shown in **(A)**.

frontiers
in Physiology

ORIGINAL RESEARCH
published: 29 May 2020
doi: 10.3389/fphys.2020.00587

Insights From Computational Modeling Into the Contribution of Mechano-Calcium Feedback on the Cardiac End-Systolic Force-Length Relationship

Megan E. Guidry[1], David P. Nickerson[1], Edmund J. Crampin[2,3], Martyn P. Nash[1,4], Denis S. Loiselle[1,5] and Kenneth Tran[1]*

[1] Auckland Bioengineering Institute, The University of Auckland, Auckland, New Zealand, [2] Systems Biology Laboratory, School of Mathematics and Statistics, The University of Melbourne, Melbourne, VIC, Australia, [3] ARC Centre of Excellence in Convergent Bio-Nano Science and Technology, School of Chemical and Biomedical Engineering, The University of Melbourne, Melbourne, VIC, Australia, [4] Department of Engineering Science, The University of Auckland, Auckland, New Zealand, [5] Department of Physiology, The University of Auckland, Auckland, New Zealand

Edited by:
Leonid Katsnelson,
Institute of Immunology
and Physiology (RAS), Russia

Reviewed by:
Andrey K. Tsaturyan,
Lomonosov Moscow State University,
Russia
Aurore Lyon,
Maastricht University, Netherlands

***Correspondence:**
Kenneth Tran
k.tran@auckland.ac.nz

Specialty section:
This article was submitted to
Striated Muscle Physiology,
a section of the journal
Frontiers in Physiology

Received: 08 October 2019
Accepted: 11 May 2020
Published: 29 May 2020

Citation:
Guidry ME, Nickerson DP,
Crampin EJ, Nash MP, Loiselle DS
and Tran K (2020) Insights From
Computational Modeling Into
the Contribution of Mechano-Calcium
Feedback on the Cardiac
End-Systolic Force-Length
Relationship. Front. Physiol. 11:587.
doi: 10.3389/fphys.2020.00587

In experimental studies on cardiac tissue, the end-systolic force-length relation (ESFLR) has been shown to depend on the mode of contraction: isometric or isotonic. The isometric ESFLR is derived from isometric contractions spanning a range of muscle lengths while the isotonic ESFLR is derived from shortening contractions across a range of afterloads. The ESFLR of isotonic contractions consistently lies below its isometric counterpart. Despite the passing of over a hundred years since the first insight by Otto Frank, the mechanism(s) underlying this protocol-dependent difference in the ESFLR remain incompletely explained. Here, we investigate the role of mechano-calcium feedback in accounting for the difference between these two ESFLRs. Previous studies have compared the dynamics of isotonic contractions to those of a single isometric contraction at a length that produces maximum force, without considering isometric contractions at shorter muscle lengths. We used a mathematical model of cardiac excitation-contraction to simulate isometric and force-length work-loop contractions (the latter being the 1D equivalent of the whole-heart pressure-volume loop), and compared Ca^{2+} transients produced under equivalent force conditions. We found that the duration of the simulated Ca^{2+} transient increases with decreasing sarcomere length for isometric contractions, and increases with decreasing afterload for work-loop contractions. At any given force, the Ca^{2+} transient for an isometric contraction is wider than that during a work-loop contraction. By driving simulated work-loops with wider Ca^{2+} transients generated from isometric contractions, we show that the duration of muscle shortening was prolonged, thereby shifting the work-loop ESFLR toward the isometric ESFLR. These observations are explained by an increase in the rate of binding of Ca^{2+} to troponin-C with increasing force. However, the leftward shift of the work-loop ESFLR does not superimpose on the isometric ESFLR, leading us to conclude that while mechano-calcium feedback does indeed contribute to the difference between the two ESFLRs, it does not completely account for it.

Keywords: end-systolic force-length relations, cardiac calcium transient, thin filament activation, calcium-troponin binding affinity, cardiac excitation-contraction model, mechano-calcium feedback

INTRODUCTION

The end-systolic force-length (or pressure-volume) relationships (ESFLRs) occupy a special place in cardiovascular physiology, often used as a proxy for cardiac contractility. Two distinct relationships are commonly reported, one for isometric (or isovolumic) contractions and a separate one for isotonic (or ejecting) contractions. It is sobering to reflect that the existence of these two distinct ESFLRs has been recognized since the 1899 publication by Otto Frank (1899) but remains incompletely explained. Frank's findings arose from experiments performed on the isolated heart of the frog and clearly reveal the existence of two distinct protocol-dependent end-systolic relations. Despite Frank's insight, and more than 100 years of research since, the mechanisms responsible for the protocol-dependence of the ESFLRs remain incompletely understood. This absence of a definitive explanation stands in stark contrast to the many experimental affirmations of the phenomenon, commencing with Brady (1967) and Gibbs et al. (1967), who independently demonstrated that the isometric ESFLR of isolated papillary muscles lies to the left of the equivalent isotonic (or work-loop) curve.

This phenomenon can be readily replicated and a variety of explanations have been proffered. These include the contribution of strain rate-dependent transitions between strong and weak cross-bridge conformations (Landesberg, 1996), velocity-dependent shortening deactivation of thin filaments (Iribe et al., 2014), and sarcomeric force-length dynamic interactions (Pironet et al., 2013). Perhaps the most germane of which was that of Brady (1967): "the time-course of the active state," which focused attention on the duration of the Ca^{2+} transient. But it was Housmans et al. (1983) who demonstrated that active shortening retards the decline of the Ca^{2+} transient, a phenomenon that their group boldly attributed to the affinity of Ca^{2+} for troponin-C, hinting at the role of mechano-calcium feedback. Their insight has been corroborated by many others, in both intact (ter Keurs et al., 1980; Lab et al., 1984; Kentish and Wrzosek, 1998) and skinned (Hibberd and Jewell, 1982) cardiac muscle preparations, and in both relaxed and rigor states, thereby demonstrating the requirement that cross-bridges be attached for the phenomenon to instantiate (Hofmann and Fuchs, 1987; Kurihara et al., 1990). The encompassing phrase "myofilament length-dependent activation" includes the now widely accepted notion of force-dependent binding of Ca^{2+} to troponin (Rice and de Tombe, 2004; de Tombe et al., 2010; Solaro and Kobayashi, 2011; de Tombe and ter Keurs, 2016; Li et al., 2016), where force-dependence arises primarily from the consequence of length-dependent overlap of the thick and thin contractile filaments. At the core of this mechanism is the role of Ca^{2+} as an activator of contraction and as a target for force feedback—the mechano-calcium mechanism.

A shortcoming of previous experimental studies has been the comparison of isotonic contractions to an isometric contraction at the unique length (L_o) that maximizes force (Housmans et al., 1983; Lab et al., 1984). While such studies have uncovered a number of key properties of actively shortening muscle, the failure to compare isotonic contractions to isometric contractions of equivalent force has hindered the development of a satisfactory explanation to explain their different ESFLRs.

This perceived shortcoming has prompted us to investigate the role of mechano-calcium feedback in the mode-dependence of the ESFLR and to ask whether the Ca^{2+} transients of isometric- and work-loop-derived ESFLRs are different under equivalent force conditions. If that were to transpire, then a second question would arise: could the activation of work-loop contractions using Ca^{2+} transients derived from isometric contractions reconcile these two ESFLRs? To that end, we undertook the assembly of a mathematical model of cardiac excitation-contraction. The model tightly couples three existing components—one for each of electrical excitation (Rogers and McCulloch, 1994), Ca^{2+} dynamics (Hinch et al., 2004) and cross-bridge mechanics (Tran et al., 2017). The latter module, which is based on a three-state model of cross-bridge cycling (Rice et al., 2008), is capable of generating both isometric and afterloaded isotonic contractions under either fixed or variable Ca^{2+} transients. It thus provides a tool with which to address the two questions raised above.

MATERIALS AND METHODS

Model Development

A novel integrated model of cardiac cellular excitation-contraction was developed to investigate the protocol-dependence of the isometric and work-loop ESFLRs. The model was designed to encapsulate sufficient biophysical detail for the purposes of the current study, with a focus on computational efficiency to permit integration into large scale tissue modeling studies.

The Tran et al. (2017) mechano-energetics model forms the basis of the coupled model, since it captures the detailed biophysical interdependencies of thin filament activation and cross-bridge cycling. It has been previously parameterized to simulate a wide range of experimentally observed cardiac myofilament behavior, including steady-state, force-length, and force-Ca^{2+} relations, as well as dynamic force transients and

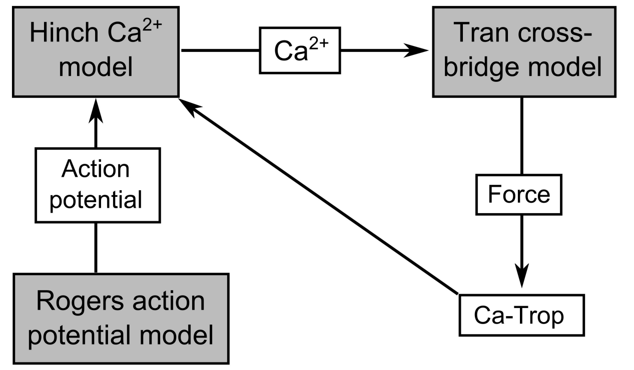

FIGURE 1 | Schematic of the THR excitation-contraction model. The connections indicate the coupling between the Tran et al. (2017) cross-bridge model, the Hinch et al. (2004) Ca^{2+} model, and the Rogers and McCulloch (1994) action potential model. Ca-Trop represents Ca^{2+} bound to troponin-C, which is modulated by active force, and therefore mediates the mechano-calcium feedback pathway.

metabolite dependence (Rice et al., 2008; Tran et al., 2010). The force-dependent binding of Ca^{2+} to troponin-C is also explicitly captured allowing cross-bridge force production to modify the intracellular Ca^{2+} transient. The total force generated by the model is composed of an active and a passive component. To enable the required range of simulations, the cross-bridge model was coupled to the Hinch et al. (2004) model of Ca^{2+}-induced-Ca^{2+}-release (CICR), which simulates Ca^{2+} fluxes across the sarcolemmal and sarcoplasmic reticular membranes. The CICR model was driven by a simplified model of the cardiac action potential. Since our study did not require detailed cellular electrophysiology, we parameterized the phenomenological Rogers and McCulloch (1994) model to simulate a rat cardiac action potential and used it to drive the cellular contraction cycle. The mechano-calcium feedback between the cross-bridge and CICR models was implemented using equations 56–64 of Rice et al. (2008). All three components of the model were previously parameterized for rat cardiomyocyte, and were not modified from their original values in this study. The Rogers and McCulloch (1994) action potential model is not temperature dependent, while the Hinch et al. (2004) model was parameterized using data at 22°C and the Tran et al. (2017) cross-bridge model is appropriate over the temperature range of 23–37°C. We, therefore, set the temperature of the Tran et al. (2017) cross-bridge model to 23°C to be consistent with that of Hinch et al. (2004). A schematic of the integrated Tran-Hinch-Rogers (THR) model is presented in **Figure 1**. The simulated calcium transient therefore arises from interactions between the dynamics of the CICR model and the mechano-calcium feedback of the cross-bridge model.

Each of the Rogers and McCulloch (1994); Hinch et al. (2004), and Tran et al. (2017) models is available in the Physiome Model Repository.[1] We took advantage of the modular features of the CellML standard (Cuellar et al., 2003) and the software tool OpenCOR (Garny and Hunter, 2015) to integrate these disparate models to construct the coupled THR model of cardiac excitation-contraction (see Nickerson and Buist, 2008; Terkildsen et al., 2008 for detailed demonstrations of such model integration). The CellML models, descriptions of simulation experiments, and parameters for reproducing the figures in this study are available from: https://models.physiomeproject.org/workspace/4ca.

Isometric and Work-Loop Protocols

The THR model was used to simulate isometric and work-loop contractions. Isometric simulations consisted of holding the sarcomere length constant throughout the duration of a contraction. Initial sarcomere lengths were varied between 1.95 and 2.3 μm, the length (L_o) at which maximum force is produced. At each sarcomere length, twitches were simulated at 1 Hz frequency until a beat-to-beat steady-state was reached (20 beats). The isometric ESFLR was derived by plotting the peak force as a function of sarcomere length. All forces in the simulations were normalized to the peak L_o-isometric force.

The work-loop protocol was designed to mimic the whole-heart pressure-volume loop (Taberner et al., 2011), and was simulated using four contraction phases.

Phase 1: Isometric Contraction

Starting at an initial sarcomere length of L_o, stimulation by an action potential initiates CICR and force generation. Muscle length is held constant as force develops. Isometric contraction continues until the total muscle force (the sum of active and passive forces) exceeds a user-specified afterload.

Phase 2: Isotonic Contraction

Following Phase 1, once the muscle force exceeds the afterload, the muscle shortens isotonically against the constant afterload. The shortening velocity is calculated using Equation 38 from Rice et al. (2008). The simulation continues in this phase for as long as the force generated by the muscle matches or exceeds the user-specified afterload.

Phase 3: Isometric Relaxation

When the force generated by the muscle falls below that of the afterload, it is declared to have reached end-systole. The muscle length is held constant while the force decreases until Ca^{2+} declines to diastolic levels.

Phase 4: Re-stretch

When Ca^{2+} reaches diastolic levels, the now-quiescent muscle is re-stretched, at constant velocity, to its initial length of L_o.

Work-loops were simulated using afterloads between 0.2 and 1 (normalized to isometric force at L_o). Work-loops at a normalized afterload of 1 produced contractions that were identical to an L_o-isometric contraction, because the afterload exceeded the threshold for muscle shortening. Similar to the isometric protocol, a train of work-loop contractions was generated to attain steady-state at a frequency of 1 Hz. The work-loop-derived ESFLR was given by the force and length of the muscle at the end of Phase 2 (end-systole) for each work-loop

---

[1] https://models.physiomeproject.org

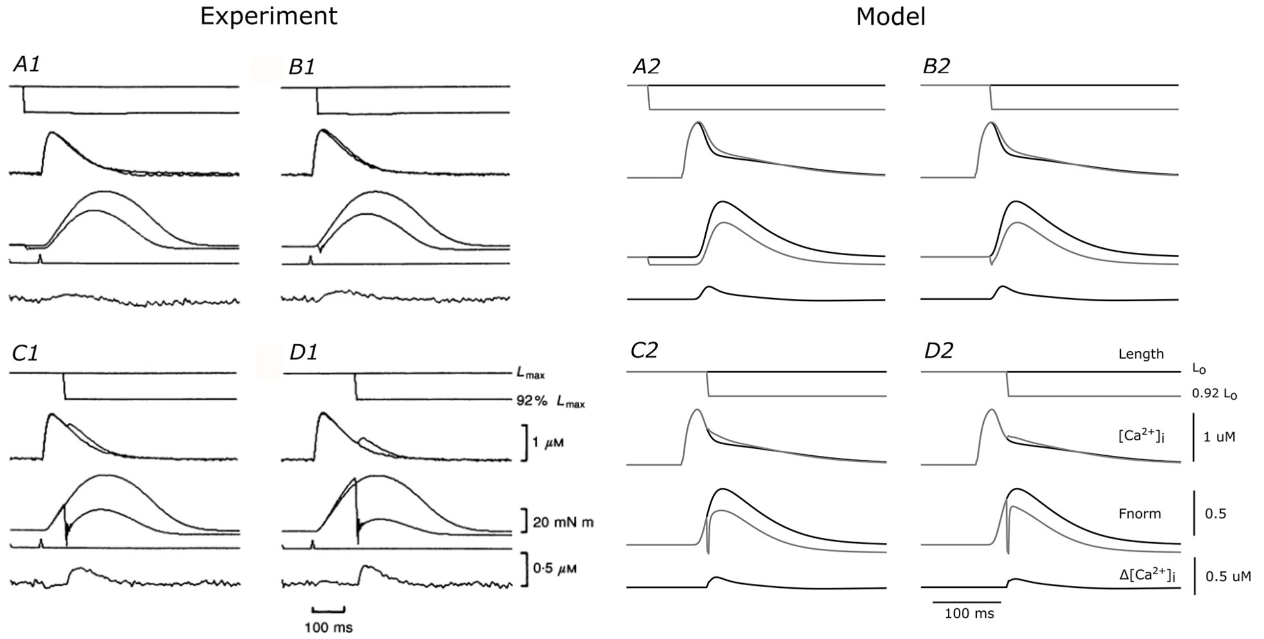

FIGURE 2 | Comparison of THR model simulations with experimental quick-release data. Experimental quick-release shortening of ferret papillary muscle by Kurihara and Komukai (1995) (left) at 30°C and equivalent simulations from the THR model (right). Each of the four panels for the experimental (A1–D1) and model (A2–D2) outputs represent different timings of the quick release. Within each panel are traces of outputs from isometric (black lines) and quick-release protocols (gray lines). From top to bottom, the traces represent muscle length, intracellular Ca^{2+} concentration, total force development, and difference of Ca^{2+} between the two protocols. (A1–D1 were reproduced with permission from John Wiley and Sons).

contraction. The sarcomere lengths for the isometric contractions and afterloads for the work-loop contractions were chosen so that they formed pairs of force-equivalent contractions. This allowed the comparison of force profiles and Ca^{2+} dynamics for the two modes of contraction at the same level of force production.

RESULTS

Model Validation

We used the coupled THR model to examine the role of Ca^{2+} in the ESFLR of cardiac muscle contraction. The Ca^{2+} and force dynamics of the model were validated by comparing simulated output to quick-release shortening experiments reported by Kurihara and Komukai (1995). In those experiments, isolated cardiac muscles were initially held at a length (L_o) that produced maximum force, and then was rapidly shortened to a new length (0.92 L_o) at four different predetermined times following the stimulus. The resulting force and Ca^{2+} transients were measured and compared to those of an isometric contraction where the length was held constant at L_o throughout the duration of the twitch (**Figure 2**). The sudden length change due to the quick-release caused an immediate drop in developed force and a near-simultaneous increase of intracellular Ca^{2+}, evidenced by the extra surge of Ca^{2+} during the declining phase of the Ca^{2+} transient. The magnitude of the extra Ca^{2+} elicited by the quick-release twitch is shown in the lower-most trace in each panel of **Figure 2**.

We simulated the quick-release protocol in our THR model and semi-quantitatively reproduced the experimental data from Kurihara and Komukai (1995). Note that none of the parameters in the THR model were optimized to reproduce the experimental data. The quick release from L_o to 0.92 L_o caused a decrease in force and an increase in intracellular Ca^{2+}. The rates of force redevelopment in the model simulations were greater than those of the experiments, as is evident in panels C1 and D1 (experiment) versus C2 and D2 (model) of **Figure 2**, where the length change was applied after the peak of the Ca^{2+} transient. This may be due to the inherently faster cross-bridge cycling rates of the rat (model) versus those of other larger mammalian species, such as the ferret (Hasenfuss et al., 1991; Palmer and Kentish, 1998). The Ca^{2+} surges in panels C2 and D2 were smaller than those recorded in the experiments (panels C1 and D1), because the recovery force was much larger. Nevertheless, the force recovery and Ca^{2+} surge were semi-quantitatively similar to the experimental data in panels A1 and B1, thereby validating the ability of the THR model to mimic force-dependent binding of Ca^{2+} from troponin-C and the consequent effect on the simulated Ca^{2+} transient.

Simulating Isometric and Work-Loop ESFLRs Using Dynamic Ca^{2+}

The ESFLRs for isometric and work-loop contractions were simulated using the THR model following the protocols outlined in Section "Materials and Methods" (**Figure 3A**). The isometric ESFLR was derived from isometric contractions at different

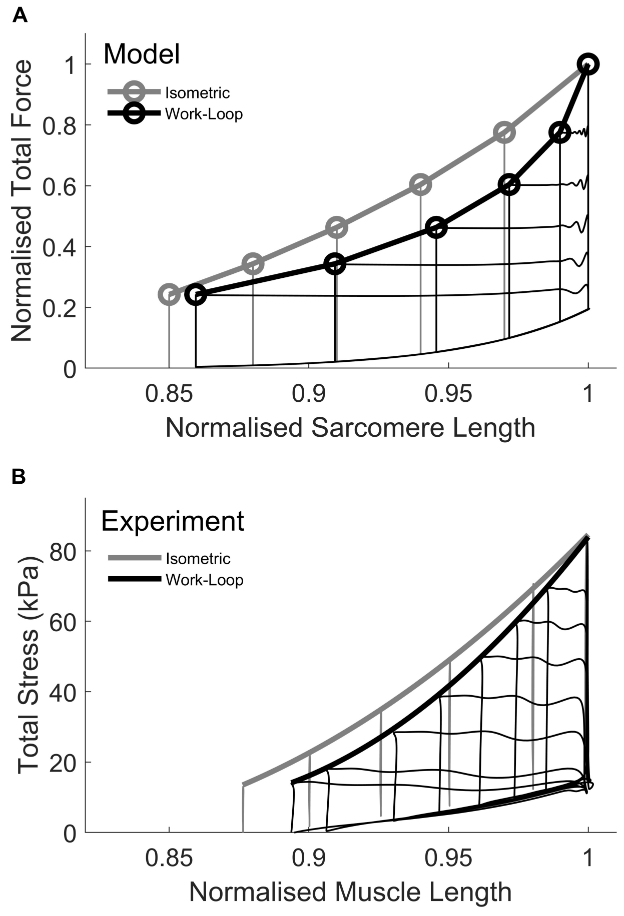

FIGURE 3 | Simulation of isometric and work-loop end-systolic force-length relations (ESFLR). **(A)** The isometric ESFLR (gray) was simulated from six isometric contractions at sarcomere lengths ranging from 1.95 to 2.3 μm (L$_o$). Sarcomere lengths were normalized to L$_o$. The work-loop ESFLR was simulated from five work-loop contractions commencing at an initial sarcomere length of L$_o$. Each work-loop contraction is matched by an isometric contraction of equivalent force. Note that the work-loop contraction at the highest afterload is identical to the L$_o$-isometric contraction. **(B)** Experimental data depicting the isometric ESFLR and work-loop ESLFR from left ventricular rat trabeculae. Reproduced from data reported in Tran et al. (2016).

sarcomere lengths while the work-loop ESFLR was derived from afterloaded shortening contractions, all of which commenced at the same initial length (L$_o$). These simulation results compare well with the experimental data from rat trabeculae (Tran et al., 2016) in **Figure 3B** and are consistent with other previous studies on rat cardiac myocytes (Iribe et al., 2014), rat trabeculae (Han et al., 2014a,b), rabbit papillary (Sørhus et al., 2000), ferret papillary (Hisano and CooperIV, 1987), and rat papillary (Gülch, 1986), the simulated work-loop ESFLR lies to the right of its isometric counterpart. In **Figure 3A**, the afterloads for the simulated work-loop contractions (black circles) correspond to isometric contractions of equivalent peak force (gray circles). For a given afterload, a work-loop contraction did not shorten to the sarcomere length of its force-equivalent isometric contraction. Previous studies have attributed this difference to mechano-calcium feedback, a phenomenon whereby active shortening of a muscle during a contraction reduces the affinity of Ca^{2+} for troponin-C, thus offloading Ca^{2+} into the cytosol and reducing the level of activation of the cross-bridges (Housmans et al., 1983; Lab et al., 1984; Baan et al., 1992). The principal mechanism for this phenomenon is attributed to the force-dependent binding of Ca^{2+} to the troponin-C complex, whereby the affinity of Ca^{2+} for troponin-C increases with increasing force (Hibberd and Jewell, 1982; Hofmann and Fuchs, 1987). For our simulated work-loop contractions, shortening during the isotonic phase (Phase 2) is expected to offload Ca^{2+} from troponin-C and enhance the descending portion of the intracellular Ca^{2+} transient. The level of enhancement is also predicted to increase with decreasing afterload.

Model simulations of the Ca^{2+} transients associated with work-loop contractions are presented in **Figure 4**. The work-loop contractions (black lines) did indeed prolong the Ca^{2+} transient compared to the isometric contraction at L$_o$. The Ca^{2+} transients widened with decreasing afterload, but the extent of widening was small relative to the effect of decreasing sarcomere length on the isometric contractions (**Figure 4**, gray lines). The narrowest of the isometric Ca^{2+} transients corresponds to an isometric contraction at L$_o$ (gray line in **Figure 4** inset). Note that because all of the work-loop contractions originated at L$_o$, the Ca^{2+} transients for the work-loop contractions matched those of the L$_o$-isometric contraction up to the onset of Phase 2 (i.e., up to t = 45 ms). Decreasing the muscle length of the isometric contractions resulted in a more significant widening of the Ca^{2+} profile relative to the effect of decreasing afterload in the work-loop contractions. For clarity, the Ca^{2+} transients for the L$_o$-isometric contraction and the work-loop contraction at the lowest afterload are shown in the inset of **Figure 4**. Additional simulations of work-loop ESFLRs at initial sarcomere lengths below L$_o$ were consistent with recent experimental data on rat cardiac trabeculae showing the preload dependence of work-loop contractions (Han et al., 2019), and simulation of associated Ca^{2+} transients were consistent with the trends observed in **Figure 4** (**Supplementary Material**).

The variation of the Ca^{2+} transients within and between the two modes of contraction (**Figure 4**) is a result of the interaction between cross-bridge force production and the force-dependent affinity of Ca^{2+} for troponin-C. In **Figure 5**, the intracellular Ca^{2+} concentration, force, and the flux of Ca^{2+} binding to troponin (Ca-troponin) as functions of time are presented for the L$_o$-isometric contraction, as well as for a selected pair of isometric and work-loop contractions at equivalent peak forces. The force-equivalent isometric contraction was simulated at SL = 0.91 L$_o$, while the force-equivalent work-loop was simulated at a normalized afterload of approximately 0.45. The narrowest of the three Ca^{2+} transients was generated by the L$_o$-isometric contraction, while the widest was generated by the 0.91 L$_o$-isometric contraction. The variations in the Ca^{2+} profiles were directly due to the differential responses of the Ca-troponin fluxes to the contractions.

The Ca-troponin fluxes began diverging at t = 20 ms when the active force in each of the three contractions started to rise

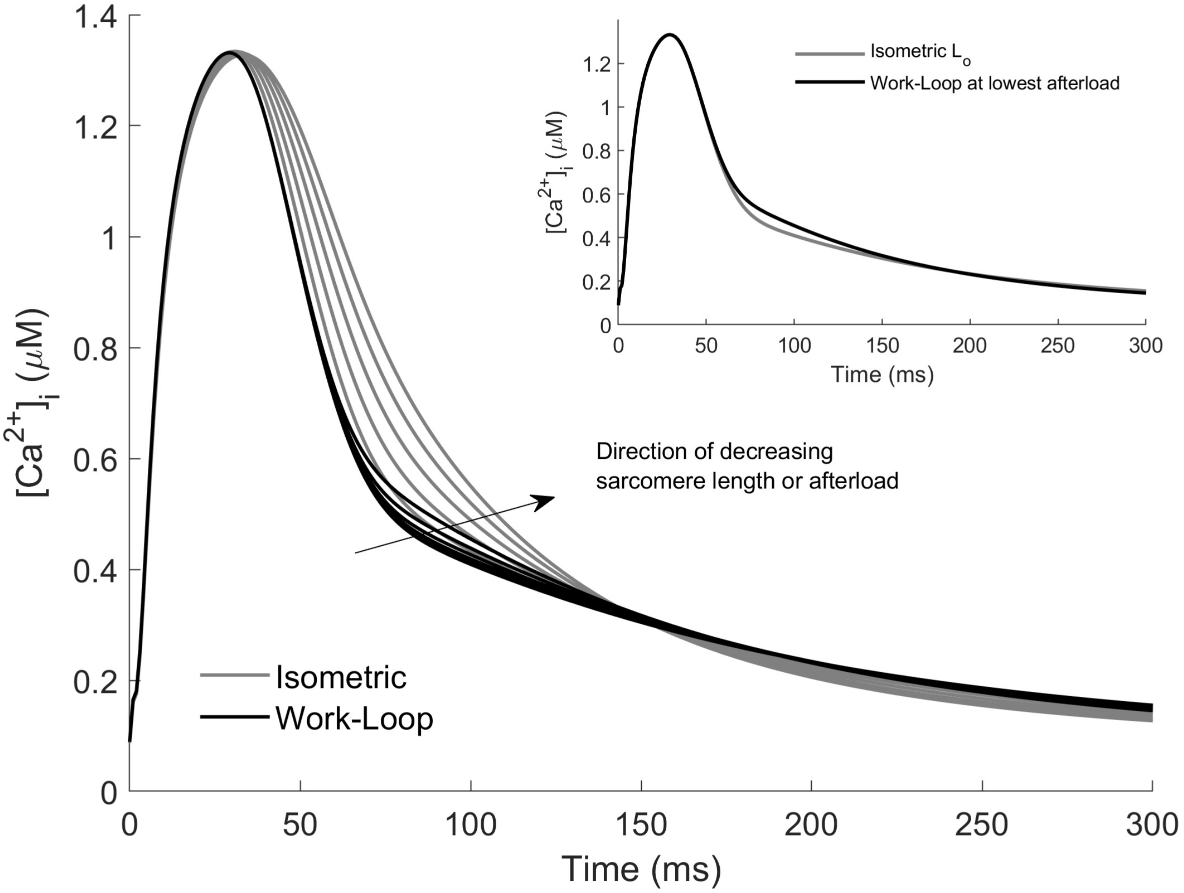

FIGURE 4 | Simulated Ca^{2+} transients arising from isometric and work-loop contractions. Isometric contractions (gray) as functions of initial sarcomere length and work-loop contractions (black) as functions of afterload. The arrow indicates the direction of decreasing sarcomere length for the isometric simulations, and decreasing afterload for the work-loop simulations. Inset: Ca^{2+} transients of the L_o-isometric contraction (gray) and the work-loop contraction (black) at the lowest afterload.

(**Figure 5**; t_1). The faster rate of force development in the L_o-isometric and work-loop contractions transiently increased the Ca-troponin flux above that of the 0.91 L_o-isometric contraction, which had a lower rate of force development over that initial period. As a result, less Ca^{2+} was bound to troponin for the 0.91 L_o-isometric contraction, which was reflected in the widening of its Ca^{2+} transient. Intracellular Ca^{2+} concentration directly affects the level of cross-bridge activation and the ability of the muscle to maintain force. For given equivalent peak forces, the model simulations reveal that isometric contractions were characterized by wider Ca^{2+} transients, relative to those of work-loop contractions (**Figure 4**). We hypothesized that driving work-loop contractions with wider Ca^{2+} transients would result in greater isotonic shortening and a leftward shift of the work-loop derived ESFLR toward the isometric ESFLR.

Simulating Work-Loop ESFLRs Using Fixed Ca^{2+} Transients

Figure 6 shows simulation results whereby Ca^{2+} transients associated with isometric contractions (**Figure 4**) were used to drive force-equivalent work-loop contractions. The activation of work-loop contractions using the wider Ca^{2+} transients derived from isometric contractions caused a leftward-shift of the work-loop derived ESFLRs (**Figure 6**). Specifically, the greater level of activation increased the proportion of cross-bridges in force-producing states, leading to greater force production at lower sarcomere lengths.

The extent of the shift increased with decreasing afterloads. At high afterloads, the wider Ca^{2+} transients were not sufficient to shift the work-loop end-systolic point to coincide with its isometric counterpart. However, at afterloads below approximately 0.4 normalized total force, the work-loop end-systolic point was shifted beyond its isometric counterpart. The two ESFLRs therefore crossed over at around the midpoint. These simulations demonstrate that the work-loop derived ESFLR can be shifted toward the isometric ESFLR by increasing the duration of the Ca^{2+} transient to prolong the shortening phase. But the contraction-mode difference in the Ca^{2+} transients cannot completely explain the discrepancy between the isometric and work-loop ESFLRs.

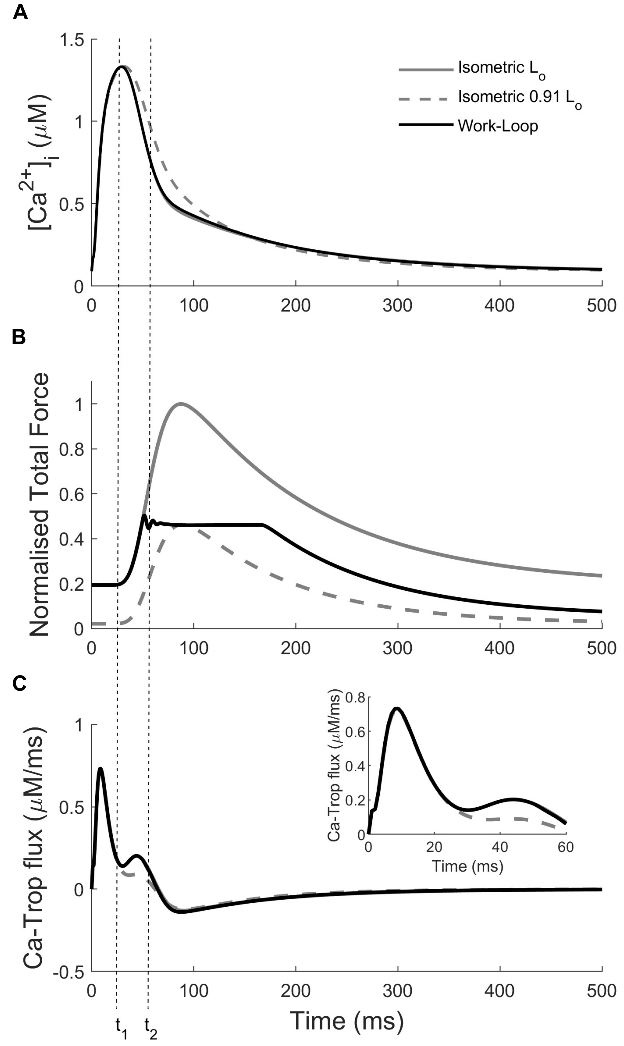

FIGURE 5 | Simulations highlighting the mechano-calcium feedback mechanism. Simulated intracellular Ca^{2+} transient **(A)**, total force production **(B)**, and Ca-troponin flux **(C)** for an L_o-isometric contraction, and a pair of isometric (SL = 0.91 L_o) and work-loop (normalized afterload at 0.45) contractions at the same peak force. Inset: close-up of the Ca-troponin flux at the start of the twitch. The dotted vertical lines indicate the times at the start of force production (t_1) and at the start of the isotonic phase in the work-loop contraction (t_2).

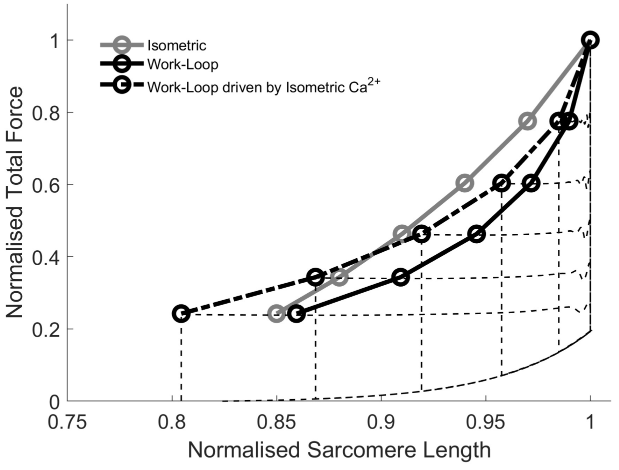

FIGURE 6 | Simulations of work-loops driven by Ca^{2+} transients generated from isometric contractions. The isometric and work-loop ESFLR are replotted from **Figure 4**. Driving work-loops with Ca^{2+} transients generated from force-equivalent isometric contractions leads to a left-ward shift of the work-loop end-systolic force-length relation (ESFLR; dashed line) but it does not superimpose on the isometric ESFLR.

DISCUSSION

Using computational modeling, we have demonstrated that mechano-calcium feedback in cardiac muscle produces Ca^{2+} transients, which are dependent on the mode of contraction. We compared the force and Ca^{2+} dynamics of work-loop contractions with their force-equivalent isometric counterparts (**Figure 5**) and revealed that the Ca^{2+} transients generated by isometric contractions were of longer duration (**Figure 4**). Our computational modeling approach enabled the application of a novel "cross-over" technique wherein work-loops are driven with Ca^{2+} transients generated by force-equivalent isometric contractions (**Figure 6**), a feat which has yet to be realized experimentally. However, the difference in the duration of Ca^{2+} transients is insufficient to completely explain the protocol-dependent difference between the isometric- and work-loop-derived ESFLRs. At higher afterloads, the increase in the Ca^{2+} transient duration was insufficient to overcome the shortening deactivation that is present in the cross-bridge model (Rice et al., 2008). Specifically, muscle shortening reduces cross-bridge distortion, which promotes cross-bridge detachment and leads to a loss of activation and a reduction in tension. At lower afterloads, the Ca^{2+} transients generated by force-equivalent isometric contractions were longer, overcompensating for the shortening deactivation, resulting in a shift of the work-loop end-systolic points past those generated from isometric contractions.

The mechanism of force-dependent affinity of Ca^{2+} to troponin-C is responsible for the prolongation of the Ca^{2+} transient duration for both modes of contraction (**Figure 5**). Model simulations revealed that reducing the initial muscle length of an isometric contraction produced a much more significant widening of the Ca^{2+} transient than decreasing the afterload for a work-loop contraction. Isometric contractions therefore operate at a greater level of Ca^{2+} activation, explaining the leftward-shift of the isometric ESFLR. Our conclusion is in accord with the study of De Tombe and Little (1994) on rat cardiac trabeculae at 27°C, which showed that the ESFLR of shortening contractions is left-shifted with respect to isosarcometric contractions when the duration of activation is prolonged by substitution of Ca^{2+} with Sr^{2+}. Our simulations reveal that the difference in the ESFLR of these two modes of contraction cannot be solely explained by the differing levels of activation elicited through the mechanism of force-dependent affinity of Ca^{2+} binding to troponin-C.

Force-Equivalent Contractions

Previous experimental studies investigating the protocol-dependence of the ESFLR compared isotonic contractions to a single isometric contraction at L_o (Housmans et al., 1983; Lab et al., 1984). Housmans et al. (1983) initially hypothesized that: "The rightward location of work-loop end-systolic points is due to sarcomere shortening abbreviating the Ca^{2+} transient responsible for excitation-contraction coupling" but rejected this hypothesis when their experimental data showed that the isotonic contraction actually exhibited a wider Ca^{2+} transient than the isometric case. Instead, they proffered the hypothesis that the "extra" Ca^{2+} released during the relaxation phase of the Ca^{2+} transient appears too late in the twitch cycle to have an effect on prolongation of force development.

Our simulation results are consistent with these two studies provided that we replicate their protocol by comparing the Ca^{2+} transient from an afterloaded work-loop contraction to that of a single isometric contraction at L_o (**Figure 4** inset). The Ca^{2+} transient of the work-loop contraction was indeed wider than that of the L_o-isometric contraction. Compared to the experimental results of Housmans et al. (1983) and Lab et al. (1984), the magnitude of the increase of Ca^{2+} in our simulations was less pronounced. This is likely to be because the lowest afterload of our work-loop simulations is not as low as those achieved in the experiments owing to the lower passive force component in experimental preparations relative to that of our model. But this reveals only part of the story, since we showed that the greater prolongation of the Ca^{2+} transient for a work-loop contraction holds only when compared to the L_o-isometric contraction. For isometric contractions at reduced muscle lengths, the predicted Ca^{2+} transient is of a longer duration than that of the work-loop contractions (**Figure 4**). In other words, a work-loop *does* have an abbreviated Ca^{2+} transient when compared to an isometric contraction that is of equivalent peak force (**Figure 5**).

Time-Course of Isometric and Work-Loop Twitches

The end-systolic point of an isometric contraction coincides with the peak force of the twitch, whereas the end-systolic point of a work-loop contraction is defined as the point where the muscle can no longer shorten. As a result, the end-systolic point of a work-loop contraction always occurs later in the time-course of the Ca^{2+} transient when its intracellular Ca^{2+} concentration is lower (**Figure 5**). Therefore, the width of the Ca^{2+} transient, governed by the rate at which it declines, is a key factor that determines the positioning of the work-loop derived ESFLR. By widening the Ca^{2+} transient, more time is available for shortening to occur before Ca^{2+} levels fall too low (**Figure 6**).

The different time-courses of isometric and work-loop contractions also explain their varying effects on the width of the Ca^{2+} transient. Decreasing the afterload of a work-loop contraction has a relatively small impact on the Ca^{2+} transient compared to decreasing the initial length of an isometric contraction (**Figure 4**). Every work-loop starts Phase 1 at an initial length of L_o and behaves like an L_o-isometric contraction during Phase 1. The mechanical feedback of isotonic shortening onto the affinity of Ca^{2+} for troponin-C does not occur until Phase 2, which is approximately 45 ms after the start of the Ca^{2+} transient (**Figure 5**; t_2). This time point is well into the declining phase of the Ca^{2+} transient; hence, the enhancement of the transient from this point on is relatively small. In contrast, for an isometric contraction, the muscle length is changed prior to stimulation of the muscle. The commencement of the twitch takes place 25 ms after the start of the Ca^{2+} transient (**Figure 5**; t_1). Hence, for isometric contractions at reduced initial muscle lengths, the mechanical feedback begins to affect the Ca^{2+} transient from an earlier time point, leading to a greater increase in the width of the Ca^{2+} transient relative to decreasing the afterload in work-loop contractions. Mechanical feedback from isometric contractions arises from the positive relationship between muscle length and the initial rate of tension development. At decreasing muscle lengths, the rate of rise of tension development also decreases (Han et al., 2014a,b; Tran et al., 2016), which lowers the Ca-troponin flux, allowing enhancement of the entire declining phase of the Ca^{2+} transient (**Figure 5**).

Time-Course of Ca^{2+} Transients

The duration of our simulated Ca^{2+} transients increased with decreasing sarcomere length and decreasing afterload for isometric and work-loop contractions, respectively (**Figure 4**). The prolongation of the Ca^{2+} transient associated with isometric contractions at shorter muscle lengths is consistent with experimental studies on isolated rat cardiac tissues (Allen and Kurihara, 1982; Kentish and Wrzosek, 1998). At shorter muscle lengths, the affinity of Ca^{2+} for troponin-C is lower, hence less Ca^{2+} is bound to troponin-C, resulting in a wider Ca^{2+} transient. The effect of an afterloaded contraction on the Ca^{2+} transient has typically been compared only to an L_o-isometric contraction, as has been discussed above.

Despite a prolongation of the Ca^{2+} transient due to either a reduction of initial muscle length in isometric contractions or a reduction of afterload in work-loop contractions, the peaks of the simulated Ca^{2+} transients remained relatively constant for both modes of contraction. Studies on rat cardiac trabeculae have reported no change in the peak Ca^{2+} transient in isometric contractions at different muscle lengths (Allen and Kurihara, 1982; Backx and Ter Keurs, 1993; Kentish and Wrzosek, 1998). Studies on the effect of a shortening contraction on the peak of the Ca^{2+} transient are not so clear. Peak Ca^{2+} has been shown to be higher for a shortening contraction compared to an isometric contraction in rat cardiac myocytes (Yasuda et al., 2003) and trabeculae (Janssen and de Tombe, 1997). In contrast, no differences were reported for either guinea pig myocytes (White et al., 1995), or for papillary muscles of either ferret (Lab et al., 1984) or cat (Housmans et al., 1983). In rat cardiomyocytes undergoing auxotonic contractions, Hongo et al. (1996) showed no change in the Ca^{2+} transient peak immediately after a stretch, but a gradual increase in peak force and peak Ca^{2+} transient 3 min later.

In our simulations, the peak of the Ca^{2+} transient remained relatively constant, because only a fraction of peak force development had occurred at the time of peak Ca^{2+} (**Figure 5**). The completion of force development occurs after the peak Ca^{2+}

has passed and is reflected in the prolongation of the declining phase of the Ca^{2+} transient (Allen and Kurihara, 1982).

Comparison to Previous Computational Modeling Studies

A number of studies have developed computational approaches to investigate the ESFLR of cardiomyocytes (Iribe et al., 2014) and the end-systolic pressure-volume relation (ESPVR) of the whole heart (Landesberg and Sideman, 1994; Landesberg, 1996; Shimizu et al., 2002). Iribe et al. (2014) were able to reconcile their protocol-dependent ESFLR data collected from rat cardiomyocytes by modifying an excitation-contraction model to include a term that represents the shortening velocity-dependent inactivation of the thin filament. However, despite the absence of this mechanism in our THR model, we were still able to produce the contraction-mode dependence of the ESFLR, suggesting that velocity-dependent inactivation of thin filaments is not the sole mechanism. In our THR model, the protocol-dependence of the ESFLR was attributed to force-dependent affinity of Ca^{2+} to troponin-C, a mechanism that is in accord with that of many other modeling studies that describe thin filament activation and cross-bridge force generation (Katsnelson et al., 1990; Izakov et al., 1991; Markhasin et al., 2003; Niederer et al., 2006; Syomin and Tsaturyan, 2017).

Our model simulations of the mode-dependency of the ESFLR (**Figure 3**) and the effect of changing initial sarcomere length on the Ca^{2+} transient from isometric contractions (**Figure 4**) are consistent with the model simulations of Landesberg and Sideman (1994), which incorporated force-dependent affinity of troponin-C for Ca^{2+} as well as velocity-dependent transitions between weak and strong cross-bridge states in their four-state model of cross-bridge contraction. In subsequent work, Landesberg (1996) showed that the ESPVR of work-loop contractions could be shifted by varying the scale of the velocity-dependence parameter. However, in that model, the effect of changing initial sarcomere length on the Ca^{2+} transient from isometric contractions was reversed, i.e., longer initial sarcomere lengths resulted in wider, rather than narrower, Ca^{2+} transients. We are unable to determine why the behavior of the Ca^{2+} transient is inconsistent between those two publications by Landesberg except to point out that in Landesberg (1996), a simple thin-wall model of the LV was added.

In experiments on canine hearts, Shimizu et al. (2002) reported a single ESPVR for isovolumic and ejection contractions and invariant shape of the Ca^{2+} transient for both modes of contraction. As such, they used a single Ca^{2+} transient to drive their model of cross-bridge force development. They concluded that length-dependence of the Ca^{2+} binding affinity for troponin-C was not an important factor in the canine heart, which is at odds with our findings using the THR model of rat myocardium. This disparity is likely due to the peculiarity of canine hearts, which have been reported to exhibit an ESPVR that is independent of contraction protocol (Taylor et al., 1969; Suga and Sagawa, 1974; Weber et al., 1976; Suga et al., 1981). Contraction-mode independence of the ESPVR is likely an artifact arising from performance of work-loop contractions at low diastolic left ventricular volumes (Han et al., 2019). These findings stand in contrast to those from the hearts of other smaller mammalian species (ferret, rabbit, and rat) (Hisano and CooperIV, 1987; Sørhus et al., 2000; Han et al., 2014a,b; Tran et al., 2016), all of which show contraction-mode dependence.

Model Limitations

The THR model of excitation-contraction utilizes a simple phenomenological model of rat cardiac electrophysiology to capture the action potential waveform, and couples it to detailed biophysical models of Ca^{2+} handling and cross-bridge kinetics. The phenomenological nature of the action potential waveform means that electrophysiological length-dependent pathways, such as stretch-activated channels (SACs) which underlie the slow force response (Calaghan and White, 2004; Niederer and Smith, 2007; Dowrick et al., 2019), are not explicitly captured. But despite their absence, the THR model is able to reproduce the widely observed difference in isometric and work-loop ESFLRs, suggesting that length-dependent electrophysiological pathways play a minor role, if any, in eliciting this phenomenon.

The contraction-mode dependence of the cardiac ESFLR has been observed to be independent of experimental temperature (Gülch, 1986; Hisano and CooperIV, 1987; Sørhus et al., 2000; Han et al., 2014a,b; Tran et al., 2016), providing confidence in the predictions of our model, which was parameterized using data at room temperature. Experimental reports from cat papillary (Downing and Sonnenblick, 1964) and frog myocytes (Parikh et al., 1993) at room temperature, which purported to show contraction-mode independence of the ESFLR, was recently refuted in a re-examination of the data using a novel end-systolic zone framework (Han et al., 2019).

Implications for Cardiac Physiology

The mechanical loading experienced by individual cardiomyocytes in the heart wall during a contraction cycle is heterogeneous. The tension-time-courses generated by cardiomyocytes vary transmurally from endocardial to the epicardial surfaces (Khokhlova et al., 2020). Mechanical feedback mechanisms allow communication of, and adaptation to, changing loading conditions across individual cells and over regions of myocardium. In the case of mechano-calcium feedback, facilitated by binding of calcium to troponin C, this mechanism allows modulation of twitch dynamics in response to changes in local loading conditions.

The impact of pathological changes on mechano-calcium feedback on cardiac function, in particular, on the ESFLR is not well known. Our recent work demonstrates that in healthy cardiac tissues, the end-systolic zone (defined as the region enclosed by isometric and work-loop ESFLRs; see Han et al., 2019) increases in the presence of isoproterenol-induced enhancement of contractility (Tran et al., 2020). We would expect the end-systolic zone to also be impacted in a disease setting. We note that mutations in the gene that encodes for cardiac troponin C (TNNC1) have been associated with hypertrophic cardiomyopathy (Liang et al., 2008; Pinto et al., 2009; Parvatiyar et al., 2012), restrictive cardiomyopathy (Parvatiyar et al., 2010), and ventricular fibrillation (Parvatiyar et al., 2012). While these pathologies are associated with the role of troponin C as an activator of contraction, changes in Ca^{2+} binding and unbinding kinetics can lead to modification of the calcium transient.

DATA AVAILABILITY STATEMENT

Publicly available datasets were analyzed in this study. These data can be found here: Kurihara and Komukai (1995). Tension-dependent changes of the intracellular Ca^{2+} transients in ferret ventricular muscles. J Physiol 489 (Pt 3), 617–625.

AUTHOR CONTRIBUTIONS

KT, MN, DL, and MG conceived and designed the experiments. MG and DN performed the computational simulations. All authors provided critical feedback on simulation results and manuscript revision, and all approved the final manuscript.

FUNDING

This work was supported in part by: the Whitaker International Program (MG); the Australian Government through the Australian Research Council's Discovery Projects funding scheme (project DP170101358) (EC); a Marsden Fast-Start award (UOA1703) from the Royal Society of New Zealand (KT); a Research Fellowship (1692) (KT); a Project Grant (1601) (DL) from the Heart Foundation of New Zealand; an Aotearoa Foundation Fellowship (DN); and a Health Research Council of New Zealand programme grant (17/608) (MN).

SUPPLEMENTARY MATERIAL

The Supplementary Material for this article can be found online at: https://www.frontiersin.org/articles/10.3389/fphys.2020.00587/full#supplementary-material

REFERENCES

Allen, D. G., and Kurihara, S. (1982). The effects of muscle length on intracellular calcium transients in mammalian cardiac muscle. *J. Physiol.* 327, 79–94. doi: 10.1113/jphysiol.1982.sp014221

Baan, J., van der Velde, E. T., and Steendijk, P. (1992). Ventricular pressure-volume relations in vivo. *Eur. Heart J.* 13(Suppl. E), 2–6. doi: 10.1093/eurheartj/13.suppl_e.2

Backx, P. H., and Ter Keurs, H. E. (1993). Fluorescent properties of rat cardiac trabeculae microinjected with fura-2 salt. *Am. J. Physiol.* 264, H1098–H1110.

Brady, A. J. (1967). Length-tension relations in cardiac muscle. *Am. Zool.* 7, 603–610. doi: 10.1093/icb/7.3.603

Calaghan, S., and White, E. (2004). Activation of Na+–H+ exchange and stretch-activated channels underlies the slow inotropic response to stretch in myocytes and muscle from the rat heart. *J. Physiol.* 559(Pt 1), 205–214. doi: 10.1113/jphysiol.2004.069021

Cuellar, A. A., Lloyd, C. M., Nielsen, P. F., Bullivant, D. P., Nickerson, D. P., and Hunter, P. J. (2003). An overview of CellML 1.1, a biological model description language. *Simulation* 79, 740–747. doi: 10.1177/0037549703040939

De Tombe, P. P., and Little, W. C. (1994). Inotropic effects of ejection are myocardial properties. *Am. J. Physiol.* 266, H1202–H1213.

de Tombe, P. P., Mateja, R. D., Tachampa, K., Ait Mou, Y., Farman, G. P., and Irving, T. C. (2010). Myofilament length dependent activation. *J, Mol. Cell Cardiol.* 48, 851–858. doi: 10.1016/j.yjmcc.2009.12.017

de Tombe, P. P., and ter Keurs, H. E. D. J. (2016). Cardiac muscle mechanics: sarcomere length matters. *J. Mol. Cell Cardiol.* 91, 148–150. doi: 10.1016/j.yjmcc.2015.12.006

Downing, S. E., and Sonnenblick, E. H. (1964). Cardiac muscle mechanics and ventricular performance: force and time parameters. *Am. J. Physiol.* 207, 705–715. doi: 10.1152/ajplegacy.1964.207.3.705

Dowrick, J. M., Tran, K., Loiselle, D. S., Nielsen, P. M. F., Taberner, A. J., Han, J.-C., et al. (2019). The slow force response to stretch: controversy and contradictions. *Acta Physiol.* 226:e13250. doi: 10.1111/apha.13250

Frank, O. (1899). Die Grundform des arteriellen Pulses. *Z. Biol.*37, 483–526.

Garny, A., and Hunter, P. J. (2015). OpenCOR: a modular and interoperable approach to computational biology. *Front. Physiol.* 6:26. doi: 10.3389/fphys.2015.00026

Gibbs, C. L., Mommaerts, W. F., and Ricchiuti, N. V. (1967). Energetics of cardiac contractions. *J. Physiol.* 191, 25–46. doi: 10.1113/jphysiol.1967.sp008235

Gülch, R. W. (1986). "The concept of "end-systolic" pressure-volume and length-tension relations of the heart from a muscle physiologist's point of view," in *Controversial Issues in Cardiac Pathophysiology*, ed. R. Jacob, (Heidelberg: Steinkopff), 51–57. doi: 10.1007/978-3-662-11374-5_6

Han, J.-C., Pham, T., Taberner, A. J., Loiselle, D. S., and Tran, K. (2019). Solving a century-old conundrum underlying cardiac force-length relations. *Am. J. Physiol. Heart Circ. Physiol.* 316, H781–H793. doi: 10.1152/ajpheart.00763.2018

Han, J.-C., Tran, K., Johnston, C. M., Nielsen, P. M. F., Barrett, C. J., Taberner, A. J., et al. (2014a). Reduced mechanical efficiency in left-ventricular trabeculae of the spontaneously hypertensive rat. *Physiol. Rep.* 2:e12211. doi: 10.14814/phy2.12211

Han, J.-C., Tran, K., Nielsen, P. M. F., Taberner, A. J., and Loiselle, D. S. (2014b). Streptozotocin-induced diabetes prolongs twitch duration without affecting the energetics of isolated ventricular trabeculae. *Cardiovasc. Diabetol.* 13:79. doi: 10.1186/1475-2840-13-79

Hasenfuss, G., Mulieri, L. A., Blanchard, E. M., Holubarsch, C., Leavitt, B. J., Ittleman, F., et al. (1991). Energetics of isometric force development in control and volume-overload human myocardium. Comparison with animal species. *Circ. Res.* 68, 836–846. doi: 10.1161/01.res.68.3.836

Hibberd, M. G., and Jewell, B. R. (1982). Calcium- and length-dependent force production in rat ventricular muscle. *J. Physiol.* 329, 527–540. doi: 10.1113/jphysiol.1982.sp014317

Hinch, R., Greenstein, J. L., Tanskanen, A. J., Xu, L., and Winslow, R. L. (2004). A simplified local control model of calcium-induced calcium release in cardiac ventricular myocytes. *Biophys. J.* 87, 3723–3736. doi: 10.1529/biophysj.104.049973

Hisano, R., and Cooper, G. IV (1987). Correlation of force-length area with oxygen consumption in ferret papillary muscle. *Circ. Res.* 61, 318–328. doi: 10.1161/01.res.61.3.318

Hofmann, P. A., and Fuchs, F. (1987). Evidence for a force-dependent component of calcium binding to cardiac troponin C. *Am. J. Physiol.* 253, C541–C546.

Hongo, K., White, E., Le Guennec, J.-Y., and Orchard, C. H. (1996). Changes in [Ca2+]i, [Na+]i and Ca2+ current in isolated rat ventricular myocytes following an increase in cell length. *J. Physiol.* 491, 609–619. doi: 10.1113/jphysiol.1996.sp021243

Housmans, P. R., Lee, N. K., and Blinks, J. R. (1983). Active shortening retards the decline of the intracellular calcium transient in mammalian heart muscle. *Science* 221, 159–161. doi: 10.1126/science.6857274

Iribe, G., Kaneko, T., Yamaguchi, Y., and Naruse, K. (2014). Load dependency in force-length relations in isolated single cardiomyocytes. *Prog. Biophys. Mol. Biol.* 115, 103–114. doi: 10.1016/j.pbiomolbio.2014.06.005

Izakov, V. Y., Katsnelson, L. B., Blyakhman, F. A., Markhasin, V. S., and Shklyar, T. F. (1991). Cooperative effects due to calcium binding by troponin and their consequences for contraction and relaxation of cardiac muscle under various conditions of mechanical loading. *Circ. Res.* 69, 1171–1184. doi: 10.1161/01.res.69.5.1171

Janssen, P. M., and de Tombe, P. P. (1997). Uncontrolled sarcomere shortening increases intracellular Ca2+ transient in rat cardiac trabeculae. *Am. J. Physiol.* 272, H1892–H1897.

Katsnelson, L. B., Izakov, V. Y., and Markhasin, V. S. (1990). Heart muscle: mathematical modelling of the mechanical activity and modelling of mechanochemical uncoupling. *Gen. Physiol. Biophys.* 9, 219–243.

Kentish, J. C., and Wrzosek, A. (1998). Changes in force and cytosolic Ca2+ concentration after length changes in isolated rat ventricular trabeculae. *J. Physiol.* 506(Pt 2), 431–444. doi: 10.1111/j.1469-7793.1998.431bw.x

Khokhlova, A., Konovalov, P., Iribe, G., Solovyova, O., and Katsnelson, L. (2020). The effects of mechanical preload on transmural differences in mechano-calcium-electric feedback in single cardiomyocytes: experiments and mathematical models. *Front. Physiol.* 11:171. doi: 10.3389/fphys.2020.00171

Kurihara, S., and Komukai, K. (1995). Tension-dependent changes of the intracellular Ca2+ transients in ferret ventricular muscles. *J. Physiol.* 489(Pt 3), 617–625. doi: 10.1113/jphysiol.1995.sp021077

Kurihara, S., Saeki, Y., Hongo, K., Tanaka, E., and Sudo, N. (1990). Effects of length change on intracellular Ca2+ transients in ferret ventricular muscle treated with 2,3-butanedione monoxime (BDM). *Jpn J. Physiol.* 40, 915–920. doi: 10.2170/jjphysiol.40.915

Lab, M. J., Allen, D. G., and Orchard, C. H. (1984). The effects of shortening on myoplasmic calcium concentration and on the action potential in mammalian ventricular muscle. *Circ. Res.* 55, 825–829. doi: 10.1161/01.res.55.6.825

Landesberg, A. (1996). End-systolic pressure-volume relationship and intracellular control of contraction. *Am. J. Physiol.* 270, H338–H349.

Landesberg, A., and Sideman, S. (1994). Mechanical regulation of cardiac muscle by coupling calcium kinetics with cross-bridge cycling: a dynamic model. *Am. J. Physiol.* 267, H779–H795.

Li, K.-L., Ghashghaee, N. B., Solaro, R. J., and Dong, W. (2016). Sarcomere length dependent effects on the interaction between cTnC and cTnI in skinned papillary muscle strips. *Arch. Biochem. Biophys.* 601, 69–79. doi: 10.1016/j.abb.2016.02.030

Liang, B., Chung, F., Qu, Y., Pavlov, D., Gillis, T. E., Tikunova, S. B., et al. (2008). Familial hypertrophic cardiomyopathy-related cardiac troponin C mutation L29Q affects Ca2+ binding and myofilament contractility. *Physiol. Genomics* 33, 257–266. doi: 10.1152/physiolgenomics.00154.2007

Markhasin, V. S., Solovyova, O., Katsnelson, L. B., Protsenko, Y., Kohl, P., and Noble, D. (2003). Mechano-electric interactions in heterogeneous myocardium: development of fundamental experimental and theoretical models. *Prog. Biophys. Mol. Biol.* 82, 207–220. doi: 10.1016/s0079-6107(03)00017-8

Nickerson, D., and Buist, M. (2008). Practical application of CellML 1.1: the integration of new mechanisms into a human ventricular myocyte model. *Prog. Biophys. Mol. Biol.* 98, 38–51. doi: 10.1016/j.pbiomolbio.2008.05.006

Niederer, S. A., Hunter, P. J., and Smith, N. P. (2006). A quantitative analysis of cardiac myocyte relaxation: a simulation study. *Biophys. J.* 90, 1697–1722. doi: 10.1529/biophysj.105.069534

Niederer, S. A., and Smith, N. P. (2007). A mathematical model of the slow force response to stretch in rat ventricular myocytes. *Biophys. J.* 92, 4030–4044. doi: 10.1529/biophysj.106.095463

Palmer, S., and Kentish, J. C. (1998). Roles of Ca2+ and crossbridge kinetics in determining the maximum rates of Ca2+ activation and relaxation in rat and guinea pig skinned trabeculae. *Circ. Res.* 83, 179–186. doi: 10.1161/01.res.83.2.179

Parikh, S. S., Zou, S. Z., and Tung, L. (1993). Contraction and relaxation of isolated cardiac myocytes of the frog under varying mechanical loads. *Circ. Res.* 72, 297–311. doi: 10.1161/01.res.72.2.297

Parvatiyar, M. S., Landstrom, A. P., Figueiredo-Freitas, C., Potter, J. D., Ackerman, M. J., and Pinto, J. R. (2012). A mutation in TNNC1-encoded cardiac troponin C, TNNC1-A31S, predisposes to hypertrophic cardiomyopathy and ventricular fibrillation. *J. Biol. Chem.* 287, 31845–31855. doi: 10.1074/jbc.M112.377713

Parvatiyar, M. S., Pinto, J. R., Dweck, D., and Potter, J. D. (2010). Cardiac troponin mutations and restrictive cardiomyopathy. *J. Biomed. Biotechnol.* 2010:350706. doi: 10.1155/2010/350706

Pinto, J. R., Parvatiyar, M. S., Jones, M. A., Liang, J., Ackerman, M. J., and Potter, J. D. (2009). A functional and structural study of troponin C mutations related to hypertrophic cardiomyopathy. *J. Biol. Chem.* 284, 19090–19100. doi: 10.1074/jbc.M109.007021

Pironet, A., Desaive, T., Kosta, S., Lucas, A., Paeme, S., Collet, A., et al. (2013). A multi-scale cardiovascular system model can account for the load-dependence of the end-systolic pressure-volume relationship. *Biomed. Eng. Online* 12:8. doi: 10.1186/1475-925X-12-8

Rice, J. J., and de Tombe, P. P. (2004). Approaches to modeling crossbridges and calcium-dependent activation in cardiac muscle. *Prog. Biophys. Mol. Biol.* 85, 179–195. doi: 10.1016/j.pbiomolbio.2004.01.011

Rice, J. J., Wang, F., Bers, D. M., and de Tombe, P. P. (2008). Approximate model of cooperative activation and crossbridge cycling in cardiac muscle using ordinary differential equations. *Biophys. J.* 95, 2368–2390. doi: 10.1529/biophysj.107.119487

Rogers, J. M., and McCulloch, A. D. (1994). A collocation–Galerkin finite element model of cardiac action potential propagation. *IEEE Trans. Biomed. Eng.* 41, 743–757. doi: 10.1109/10.310090

Shimizu, J., Todaka, K., and Burkhoff, D. (2002). Load dependence of ventricular performance explained by model of calcium-myofilament interactions. *Am. J. Physiol. Heart Circ. Physiol.* 282, H1081–H1091.

Solaro, R. J., and Kobayashi, T. (2011). Protein phosphorylation and signal transduction in cardiac thin filaments. *J. Biol. Chem.* 286, 9935–9940. doi: 10.1074/jbc.r110.197731

Sørhus, V., Sys, S. U., Natåns, A., Demolder, M. J., and Angelsen, B. A. (2000). Controlled auxotonic twitch in papillary muscle: a new computer-based control approach. *Comput. Biomed. Res.* 33, 398–415. doi: 10.1006/cbmr.2000.1551

Suga, H., Hayashi, T., Shirahata, M., Suehiro, S., and Hisano, R. (1981). Regression of cardiac oxygen consumption on ventricular pressure-volume area in dog. *Am. J. Physiol.* 240, H320–H325.

Suga, H., and Sagawa, K. (1974). Instantaneous pressure-volume relationships and their ratio in the excised, supported canine left ventricle. *Circ. Res.* 35, 117–126. doi: 10.1161/01.res.35.1.117

Syomin, F. A., and Tsaturyan, A. K. (2017). A simple model of cardiac muscle for multiscale simulation: passive mechanics, crossbridge kinetics and calcium regulation. *J. Theor. Biol.* 420, 105–116. doi: 10.1016/j.jtbi.2017.02.021

Taberner, A. J., Han, J.-C., Loiselle, D. S., Nielsen, P. M. F., and Nielsen, P. M. F. (2011). An innovative work-loop calorimeter for in vitro measurement of the mechanics and energetics of working cardiac trabeculae. *J. Appl. Physiol.* 111, 1798–1803. doi: 10.1152/japplphysiol.00752.2011

Taylor, R. R., Covell, J. W., and Ross, J. Jr. (1969). Volume-tension diagrams of ejecting and isovolumic contractions in left ventricle. *Am. J. Physiol.* 216, 1097–1102. doi: 10.1152/ajplegacy.1969.216.5.1097

ter Keurs, H. E., Rijnsburger, W. H., van Heuningen, R., and Nagelsmit, M. J. (1980). Tension development and sarcomere length in rat cardiac trabeculae. Evidence of length-dependent activation. *Circ. Res.* 46, 703–714. doi: 10.1161/01.res.46.5.703

Terkildsen, J. R., Niederer, S., Crampin, E. J., Hunter, P., and Smith, N. P. (2008). Using Physiome standards to couple cellular functions for rat cardiac excitation-contraction. *Exp. Physiol.* 93, 919–929. doi: 10.1113/expphysiol.2007.041871

Tran, K., Han, J.-C., Crampin, E. J., Taberner, A. J., and Loiselle, D. S. (2017). Experimental and modelling evidence of shortening heat in cardiac muscle. *J. Physiol.* 595, 6313–6326. doi: 10.1113/JP274680

Tran, K., Han, J.-C., Taberner, A. J., Barrett, C. J., Crampin, E. J., and Loiselle, D. S. (2016). Myocardial energetics is not compromised during compensated hypertrophy in the Dahl salt-sensitive rat model of hypertension. *Am. J. Physiol. Heart Circ. Physiol.* 311, H563–H571.

Tran, K., Smith, N. P., Loiselle, D. S., and Crampin, E. J. (2010). A metabolite-sensitive, thermodynamically constrained model of cardiac cross-bridge cycling: implications for force development during ischemia. *Biophys. J.* 98, 267–276. doi: 10.1016/j.bpj.2009.10.011

Tran, K., Taberner, A. J., Loiselle, D. S., and Han, J.-C. (2020). Energetics equivalent of the cardiac force-length end-systolic zone: implications for contractility and economy of contraction. *Front. Physiol.* 10:1633. doi: 10.3389/fphys.2019.01633

Weber, K. T., Janicki, J. S., and Hefner, L. L. (1976). Left ventricular force-length relations of isovolumic and ejecting contractions. *Am. J. Physiol.* 231, 337–343. doi: 10.1152/ajplegacy.1976.231.2.337

White, E., Boyett, M. R., and Orchard, C. H. (1995). The effect of mechanical loading and changes of length on single guinea-pig ventricular myocytes. *J. Physiol.* 482, 93–107. doi: 10.1113/jphysiol.1995.sp020502

Yasuda, S.-I., Sugiura, S., Yamashita, H., Nishimura, S., Saeki, Y., Momomura, S.-I., et al. (2003). Unloaded shortening increases peak of Ca2+ transients but accelerates their decay in rat single cardiac myocytes. *Am. J. Physiol. Heart Circ. Physiol.* 285, H470–H475.

Conflict of Interest: The authors declare that the research was conducted in the absence of any commercial or financial relationships that could be construed as a potential conflict of interest.

frontiers in Physiology

ORIGINAL RESEARCH
published: 22 July 2020
doi: 10.3389/fphys.2020.00809

Sinoatrial Node Structure, Mechanics, Electrophysiology and the Chronotropic Response to Stretch in Rabbit and Mouse

Eilidh A. MacDonald[1], Josef Madl[2], Joachim Greiner[2], Ahmed F. Ramadan[3], Sarah M. Wells[4], Angelo G. Torrente[5], Peter Kohl[2], Eva A. Rog-Zielinska[2]† and T. Alexander Quinn[1,3]*†*

[1] Department of Physiology and Biophysics, Dalhousie University, Halifax, NS, Canada, [2] Institute for Experimental Cardiovascular Medicine, University Heart Center Freiburg - Bad Krozingen, and Faculty of Medicine, University of Freiburg, Freiburg, Germany, [3] Department of Electrical and Computer Engineering, Dalhousie University, Halifax, NS, Canada, [4] School of Biomedical Engineering, Dalhousie University, Halifax, NS, Canada, [5] Department of Physiology, Institut de Génomique Fonctionnelle, Montpellier, France

Edited by:
Leonid Katsnelson,
Institute of Immunology and Physiology (RAS), Russia

Reviewed by:
Victor A. Maltsev,
National Institute on Aging, National Institutes of Health (NIH), United States
Ed White,
University of Leeds, United Kingdom

***Correspondence:**
Eva A. Rog-Zielinska
eva.rog-zielinska@uniklinik-freiburg.de
T. Alexander Quinn
alex.quinn@dal.ca

†These authors have contributed equally to this work

Specialty section:
This article was submitted to Cardiac Electrophysiology, a section of the journal Frontiers in Physiology

Received: *18 December 2019*
Accepted: *18 June 2020*
Published: *22 July 2020*

Citation:
MacDonald EA, Madl J, Greiner J, Ramadan AF, Wells SM, Torrente AG, Kohl P, Rog-Zielinska EA and Quinn TA (2020) Sinoatrial Node Structure, Mechanics, Electrophysiology and the Chronotropic Response to Stretch in Rabbit and Mouse. Front. Physiol. 11:809. doi: 10.3389/fphys.2020.00809

The rhythmic electrical activity of the heart's natural pacemaker, the sinoatrial node (SAN), determines cardiac beating rate (BR). SAN electrical activity is tightly controlled by multiple factors, including tissue stretch, which may contribute to adaptation of BR to changes in venous return. In most animals, including human, there is a robust increase in BR when the SAN is stretched. However, the chronotropic response to sustained stretch differs in mouse SAN, where it causes variable responses, including decreased BR. The reasons for this species difference are unclear. They are thought to relate to dissimilarities in SAN electrophysiology (particularly action potential morphology) between mouse and other species and to how these interact with subcellular stretch-activated mechanisms. Furthermore, species-related differences in structural and mechanical properties of the SAN may influence the chronotropic response to SAN stretch. Here we assess (i) how the BR response to sustained stretch of rabbit and mouse isolated SAN relates to tissue stiffness, (ii) whether structural differences could account for observed differences in BR responsiveness to stretch, and (iii) whether pharmacological modification of mouse SAN electrophysiology alters stretch-induced chronotropy. We found disparities in the relationship between SAN stiffness and the *magnitude* of the chronotropic response to stretch between rabbit and mouse along with differences in SAN collagen structure, alignment, and changes with stretch. We further observed that pharmacological modification to prolong mouse SAN action potential plateau duration rectified the *direction* of BR changes during sustained stretch, resulting in a positive chronotropic response akin to that of other species. Overall, our results suggest that structural, mechanical, and background electrophysiological properties of the SAN influence the chronotropic response to stretch. Improved insight into the biophysical determinants of stretch effects on SAN pacemaking is essential for a comprehensive understanding of SAN regulation with important implications for studies of SAN physiology and its dysfunction, such as in the aging and fibrotic heart.

Keywords: mechano-electric coupling, heart rate, tissue stiffness, collagen, caveolae, second-harmonic generation microscopy, electron tomography, computational modeling

INTRODUCTION

The heart's intrinsic pacemaker, the sinoatrial node (SAN), generates spontaneous action potentials (AP) through a system of coupled oscillators whose common output initiates each normal heartbeat. The rate of SAN firing, and, thus, cardiac beating rate (BR), is determined by multiple subcellular mechanisms whose interaction and mutual entrainment form a robust system that drives SAN automaticity (Jalife, 1984; Noble et al., 1992; Lakatta et al., 2010). SAN automaticity is modulated by multiple factors, including the autonomic nervous system and various endocrine, paracrine, and autocrine agents, allowing adaptation of BR to changes in physiological demand (MacDonald et al., 2017, 2020). The SAN also responds to altered hemodynamic load through the Bainbridge response: an increase in BR upon right atrial distention, which may help in matching cardiac output to venous return (Bainbridge, 1915). This response was initially thought to be neurally mediated; however, mechanically induced changes in BR have since been demonstrated in isolated heart, atria, SAN, and single SAN cells, indicating the involvement of mechano-sensitive mechanisms (Quinn and Kohl, 2020) intrinsic to pacemaker cells (Quinn and Kohl, 2012). Here, we investigate how structural and mechanical properties of the SAN relate to amplitude and directionality of stretch-induced changes in BR, including a comparison between rabbit and mouse as important species-specific differences may exist (Cooper and Kohl, 2005).

Pacemaker cells in the SAN are interspersed with fibroblasts and embedded within a matrix of fibrous connective tissue, predominately consisting of collagen and elastin (Monfredi et al., 2010; Ho and Sánchez-Quintana, 2016). SAN cells are smaller than surrounding atrial cardiomyocytes (Boyett et al., 2000), and their sarcolemma shows less pronounced invaginations at Z-disks, which are thought to convey a "spare membrane pool" that, together with sarcolemmal caveolae, allows working cardiomyocytes to adapt to mechanically induced changes in volume:surface ratio that arise as a consequence of aspect ratio dynamics during the cycle of contraction and relaxation (Dulhunty and Franzini-Armstrong, 1975; Kohl et al., 2003). Interestingly, SAN cells appear to have more caveolae than working cardiomyocytes (reports range from a twofold to fivefold difference; Masson-Pévet et al., 1980; Kordylewski et al., 1993; Burton et al., 2017). In ventricular cardiomyocytes, stretch-induced sarcolemmal membrane-incorporation of caveolae has been observed during myocardial stretch, both in rabbit (Kohl et al., 2003) and mouse (Pfeiffer et al., 2014). Caveolae have been shown to play important roles in spatial compartmentalization of proteins, ion channels, and G-protein complexes that contribute to automaticity of SAN cells (Lang and Glukhov, 2018). Yet whether their presence in SAN cells is affected by the mechanical environment is as yet unknown.

SAN stretch has been most widely studied in the rabbit (Quinn and Kohl, 2016), and the structure and composition of rabbit SAN are well established. The volume of rabbit SAN tissue is comprised of ~50% extracellular matrix and fibroblasts and ~50% pacemaker cells (Bleeker et al., 1980; Opthof et al., 1987) with pacemaker cells having diverse cell volumes, morphologies, and ion current densities (Verheijck et al., 1998; Monfredi et al., 2018). The central SAN contains a dense arrangement of small, spindle-shaped pacemaker cells, interwoven and embedded in a dense collagen network, whereas in peripheral regions, cell arrangement is more ordered with a large proportion of pacemaker cells oriented parallel to the *Crista* terminalis (CT; Bleeker et al., 1980). Mouse SAN also contains a compact central region with densely packed pacemaker cells. However, unlike rabbit, these cells are generally well aligned and oriented perpendicular to the CT (Liu et al., 2007). There is proportionately less extracellular matrix, and there are fewer fibroblasts in mouse SAN, comprising ~25% of volume (Hao et al., 2011; Glukhov et al., 2015). In the mouse SAN periphery, cells are loosely packed and – like in the rabbit – arranged parallel to the CT (Liu et al., 2007).

Investigating and comparing the importance of structural and mechanical SAN properties for the chronotropic response to stretch using rabbit and mouse is favorable as they both have thin endo- and epicardial layers, comprised primarily of connective tissue with most of the thickness between the outer layers composed of a mix of pacemaker cells and connective tissue (Opthof et al., 1987; Verheijck et al., 2001), whereas larger animals have thicker endo- and epicardial covers (Opthof, 1988; Kalyanasundaram et al., 2019). Yet, although there is a robust increase in BR when stretch of the SAN is sustained over the entire cardiac cycle in most species (including human, dog, cat, rabbit, guinea pig, and zebrafish; summarized in Quinn and Kohl, 2012), the response to sustained SAN stretch in mouse differs, causing a variable response that includes decreases in BR (Cooper and Kohl, 2005). This is an important consideration as mouse is a commonly utilized model for studies of SAN electrophysiology and its regulation.

The reason(s) for this difference in the chronotropic response of the SAN to sustained stretch between mouse and other animals has remained elusive. It has been suggested that it may not be due to a fundamental difference in subcellular stretch-activated mechanism(s), but rather to the fact that the same mechanism(s) result in different outcomes in mice compared to other species (Cooper and Kohl, 2005). Specifically, it is thought that current flowing through cation non-selective stretch-activated channels ($I_{SAC,NS}$) may generate varying outcomes due to species-specific differences in SAN AP morphology (Cooper and Kohl, 2005). The reasoning for this is as follows. Activation of $I_{SAC,NS}$ in cardiac cells causes their membrane potential to be "pulled toward" the $I_{SAC,NS}$ reversal potential ($E_{SAC,NS}$), which is between -20 and 0 mV in cardiomyocytes, including SAN pacemaker cells (Guharay and Sachs, 1984; Craelius et al., 1988; Cooper et al., 2000). For those phases of the SAN AP during which their dynamically changing membrane potential is moving *toward* $E_{SAC,NS}$ (i.e., during spontaneous diastolic depolarization and during early AP repolarization; see green panels in **Figure 3A**), activation of $I_{SAC,NS}$ would be expected to *accelerate* the intrinsic change in membrane polarization, thus causing more rapid diastolic

---

Abbreviations: 4-AP, 4-aminopyridine; AP, action potential; BR, beating rate; CT, *Crista terminalis*; $E_{SAC,NS}$, reversal potential of the cation non-selective stretch-activated channel; ET, electron tomography; $I_{SAC,NS}$, cation non-selective stretch activated current; IVC, inferior (caudal) *vena cava*; SAN, sinoatrial node; SHGM, second-harmonic generation microscopy; SVC, superior (cranial) *vena cava*.

depolarization or faster early repolarization, thereby increasing BR. Contrarily, during phases of the SAN AP during which the membrane potential is moving *away* from $E_{SAC,NS}$ (i.e., late AP upstroke and late repolarization; see pink panels in **Figure 3A**), $I_{SAC,NS}$ activation would oppose the intrinsic change, resulting in a slowed upstroke or delayed final repolarization, thus potentially contributing to a decrease in BR. Consequently, the chronotropic response to stretch that is sustained over the entire SAN cycle would be expected to arise as the net effect of both positive and negative chronotropic contributions of $I_{SAC,NS}$ during different phases of the SAN AP. Species-specific differences in SAN AP morphology affect this balance of positive and negative chronotropic contributions. In rabbit, periods with a potentially positive chronotropic effect dominate the SAN AP–$I_{SAC,NS}$ interrelation. In mouse, in contrast, diastolic depolarization and AP plateau are both proportionately shorter than in rabbit and other species (Verheijck et al., 2001), such that periods during which $I_{SAC,NS}$ could act to increase or decrease BR are near-evenly balanced. We, therefore, tested whether prolonging the plateau of mouse SAN AP by exposure to 4-aminopyridine (4-AP, a blocker of rapidly activating potassium currents important for early repolarization in mouse SAN cells; Golovko et al., 2015) would result in a more consistent response of mouse SAN BR to stretch rather than the previously reported variable outcome (Cooper and Kohl, 2005).

We further hypothesize that the chronotropic response to stretch may be influenced by structural and mechanical properties of the SAN and that dissimilarities between rabbit and mouse exist. To test this, we assessed maximum changes in BR of rabbit and mouse isolated SAN upon sustained stretch and compared them to measured SAN stiffness. This was combined with second-harmonic generation microscopy (SHGM) for visualization of collagen in stretched and non-stretched SAN to investigate structural components, such as collagen fiber alignment, crimp wavelength, and fiber tortuosity, that may account for interspecies differences in passive tissue mechanics, and to explore their potential relation to stretch-induced changes in BR. Finally, using electron tomography (ET), we examined stretch effects on SAN membrane ultra-structure that could potentially affect mechano-transduction by membrane tension or alter the integrity of signaling hubs, such as contained in sub-sarcolemmal caveolae.

MATERIALS AND METHODS

All experimental procedures were approved by the Dalhousie University Committee for Laboratory Animals or the local Institutional Animal Care and Use Committee in Freiburg, Germany (Regierungspraesidium Freiburg, X-16/10R) and followed the guidelines of the Canadian Council on Animal Care or German animal welfare laws and guidelines (TierSchG and TierSchVersV), compatible with Directive 2010/63/EU of the European Parliament on the protection of animals used for scientific purposes. Details of experimental protocols have been reported following the Minimum Information about a Cardiac Electrophysiology Experiment (MICEE) reporting standard (Quinn et al., 2011).

SAN Isolation

Female rabbits (New Zealand White, 2.1 ± 0.2 kg) were euthanized by ear vein injection of pentobarbital (140 $mg \cdot kg^{-1}$), followed by rapid excision of the heart, aortic cannulation, and Langendorff perfusion (20 $mL \cdot min^{-1}$) with 37°C, carbogen (95% O_2, 5% CO_2) saturated Krebs-Henseleit solution (containing, in mM: 120 NaCl, 4.7 KCl, 24 $NaHCO_3$, 1.4 NaH_2PO_4, 1.0 $MgCl_2$, 1.8 $CaCl_2$, and 10 Glucose, with an osmolality of 300 ± 5 mOsm and a pH of 7.40 ± 0.05). The atria were removed and placed in a bath of Krebs-Henseleit solution. Adult female mice (C57BL/6J, 8–12 weeks) were sacrificed by cervical dislocation, followed by rapid excision of the heart, which was placed in a bath with Krebs-Henseleit solution for removal of the atria. For both species, the atria were separated from the ventricles by cutting along the atrio-ventricular valve plane and pinned down at the appendages in a Sylgard-lined dish (DC 170; Dow Corning, Midland, United States) with the surface that normally rests against the ventricle facing up, taking care to not stretch the tissue. The SAN was exposed by incisions from the cut right atrio-ventricular junction along the frontal surface of the superior (cranial) and inferior (caudal) *Venae cavae* (SVC, IVC, respectively). The rabbit SAN was further trimmed by dissection along the auricular side of the medial edge of the CT to remove the large (>200 mg) atrial appendage and the (much smaller) interatrial septum. When cutting along the CT, mouse SAN has previously been shown to demonstrate irregularities in BR (Verheijck et al., 2001), so for the mouse, the much smaller (∼3 mg) right atrial appendage and the tiny inter-atrial septum were left in place.

SAN Stretch

Following SAN isolation, insect pins were woven through the cut edges of the SVC and IVC above and below the SAN tissue (**Figure 1**). A clip hanging from an isometric force transducer (PY2 72-4491, Harvard Apparatus, Holliston, United States) was attached to the SVC pin. A clip coupled to a computer-controlled linear DC-servomotor (LM 1247-02-01; FAULHABER MICROMO, Clearwater, United States) was attached to and supported the IVC pin with bipolar electrodes at either end of the pin connected to an ECG amplifier (Animal Bio Amp; ADInstruments, Colorado Springs, United States) for measurement of SAN electrical activity. This arrangement allowed for simultaneous stretch and measurement of force and BR (calculated from the peaks of the ECG or force signal; **Supplementary Figure S1**) in a water-jacketed imaging chamber, containing 37°C Krebs-Henseleit solution bubbled with carbogen.

After isolation and mounting, SAN preparations with irregular (n = 0) or low baseline BR (<290 $beats \cdot min^{-1}$) were excluded (n = 1 out of 14). The non-stretched SAN was lengthened in 10 μm steps of the linear motor until a baseline force of ∼0.2 g for rabbit (measured force = 0.21 ± 0.02 g) or ∼0.05 g for mouse (measured force = 0.07 ± 0.01 g) was applied to the tissue (based on preliminary experiments and

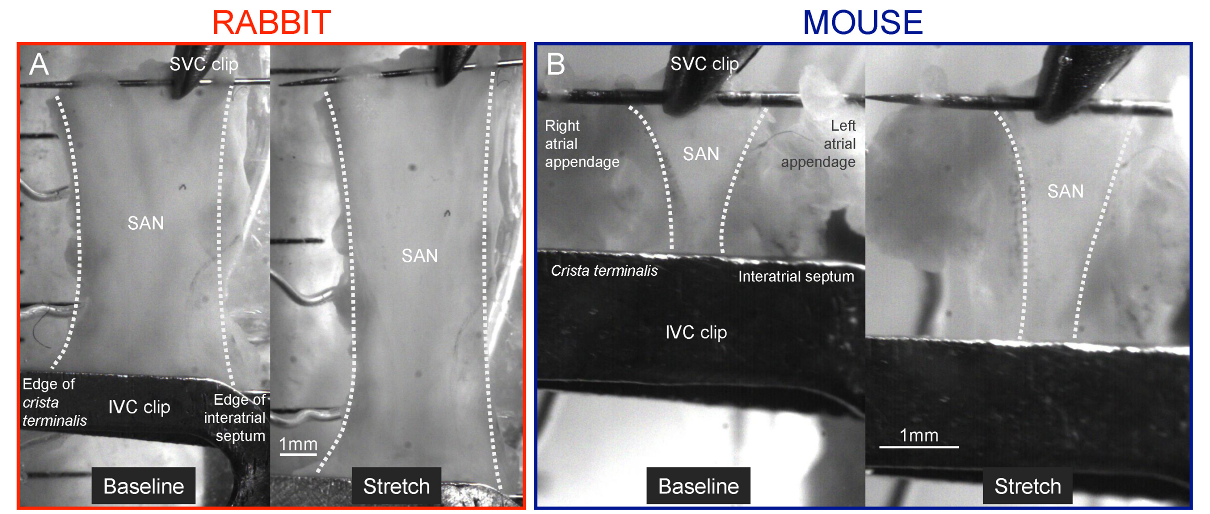

FIGURE 1 | Isolated sinoatrial node (SAN) preparation. Representative images of isolated SAN before and during stretch from rabbit (40% stretch, **A**) and mouse (50% stretch, **B**). IVC, inferior (caudal) *vena cava*; SVC, superior (cranial) *Vena cava*.

previous studies by others (Kamiyama et al., 1984; Cooper and Kohl, 2005). Baseline tissue length (distance between the pins; 12.1 ± 0.6 mm for rabbit, 2.7 ± 0.2 mm for mouse) was measured as the distance between the SVC and IVC clips from video images (DMK 23UP1300; The Imaging Source, Charlotte, United States) with custom routines in Matlab (MathWorks, Natick, United States). Length was increased by 10% at a rate of 25 $\text{mm}\cdot\text{s}^{-1}$ with the linear motor, maintained for 30 s, and returned to baseline length at the same rate. After 120 s of rest, the 10% stretch/relengthening protocol was repeated once, followed by repetitions of the procedure with an increase in the amount of stretch by 10% for each iteration until either 50% stretch was applied or SAN BR became unstable (due to over-stretch).

Force and ECG signals were continuously recorded at 2 kHz using a data acquisition device (PowerLab, controlled by LabChart; ADInstruments). Force was measured in diastole (passive force) and converted to stress by dividing by the baseline cross-sectional area (perpendicular to the direction of stretch) of each SAN [rabbit = 1.45 ± 0.09 mm^2, mouse = 0.28 ± 0.01 mm^2; estimated as SAN width (measured from the video images with Matlab) multiplied by average SAN thickness for each species (294 μm for rabbit, 191 μm for mouse; measured from SHGM images of three isolated SAN from each species, embedded in agarose and sliced crosswise)]. Stretch was expressed as strain by dividing by baseline tissue length before stretch and values of BR and force from the two repeated stretches at each strain were averaged. An index of overall tissue stiffness (β) was calculated from the stress-strain data for each SAN by fitting the relationship: stress = $\alpha \times e^{\beta \times strain}$, where α indicates the y-axis intercept (Burkhoff et al., 2005; Garofalo et al., 2006).

Experimental and Computational Modulation of Mouse SAN AP

SAN from mouse, prepared as described above, were subjected to two 30 s periods of 40% stretch, interspersed with 120 s of rest. 4-AP (275875; Sigma-Aldrich, St. Louis, United States; made freshly from a 25 mM stock solution in distilled water; pH titrated to 7.4 using HCl) was added to the chamber at final concentrations of 50, 100, and 500 μM, which had been shown previously to increase mouse SAN AP plateau duration without affecting the rate of diastolic depolarization or baseline BR (Golovko et al., 2015). After 2 min incubation at each of the target 4-AP concentrations as well as after a 20 min washout, the 40% stretch protocol was repeated.

The results of the above 4-AP experiments were further explored in computational simulations (Quinn and Kohl, 2013), using a mouse SAN cell AP model (Kharche et al., 2011). To simulate the electrophysiological effect of SAN stretch, a Hodgkin-Huxley formulation for an instantly activating, non-inactivating SAC_{NS} current with a linear current-voltage relationship as proposed by Healy and McCulloch (2005), was added to the model. This current was defined as $I_{SAC,NS} = g_{SAC,NS} \times (V_m(\text{t}) - E_{SAC,NS})$, where $E_{SAC,NS} = -10$ mV (in keeping with SAN; Cooper et al., 2000). V_m is the time-varying membrane potential, and $g_{SAC,NS} = 0.000248$ nS/pF is the maximum whole cell SAC_{NS} conductance (which caused a 10% reduction in the absolute value of the maximum diastolic potential upon simulated cell stretch). Application of 4-AP was simulated by a reduction in the conductance of rapidly activating potassium currents in the model (with the transient outward potassium current set to zero and the delayed rectifier potassium current reduced by 25%). Simulations were run to steady state (10 s of simulated SAN activity) in Dev-C++ , using a standard explicit Euler integration method with a constant time step of 0.1 ms.

Collagen Imaging and Characterization in SAN Tissue

SAN from rabbit and mouse, prepared as above, were left at baseline length (n = 3 for each species) or subjected to 40%

stretch (n = 3 for each species) and immediately fixed with 4% paraformaldehyde in phosphate-buffered saline. After 1 h, samples were washed in phosphate-buffered saline and used for imaging. Collagen was visualized by SHGM on an upright microscope (TCS SP8 DIVE; Leica Microsystems, Wetzlar, Germany) using a 25×, 1.0 NA, water immersion objective (IRAPO L 25x/1.00 W; Leica Microsystems) with 920 nm illumination from a pulsed laser (InSight X3 Dual; Spectra-Physics, Santa Clara, United States). 3-D imaging was performed by recording tiled z-stacks (442.9 × 442.9 μm^2 in x-y, between 100 and 200 μm in z, with six to nine tiled z-stacks per SAN). Stitching and image processing were done in Leica LAS-X (Leica Microsystems).

Collagen orientation was analyzed in the central SAN at the epicardial surface and in the middle layers of SAN tissue by tracing the skeleton of 50 representative fibers in each of the acquired SHGM stacks, using the "Simple Neurite Tracer" (Longair et al., 2011) plugin within Fiji (Schindelin et al., 2012). To enable interactive tracing, image stacks were first laterally binned four times. Principal component analysis of each fiber was performed to define the principal eigenvectors with the largest eigenvalue, indicating fiber direction. Polar orientation plots displaying the measured fiber directions were then generated using the Python package Matplotlib (Hunter, 2007). For characterization of collagen fibers, crimp wavelength and fiber tortuosity were measured by a blinded observer using ImageJ (Schneider et al., 2012). Wavelength was measured as the linear distance between two adjacent collagen fiber wave peaks (Pierlot et al., 2014). Eight wavelength measurements were made in three SHGM images for each layer (surface or middle) for a total of 48 measurements per preparation (non-stretched or stretched in mouse and rabbit). Tortuosity was calculated as the ratio of the collagen path length traced directly along the fiber between two points divided by the linear distance between those points (Jan et al., 2018). Three tortuosity values were calculated in three images for each layer for a total of nine measurements per preparation.

Caveolae Imaging and Characterization in SAN Cells

For ET imaging of sub-sarcolemmal caveolae, SAN isolated from rabbit or mouse (as described above) were cut longitudinally (from the SVC to IVC) into two strips. One strip was left non-stretched, and the other was stretched, resulting in a change in SAN pacemaker cell sarcomere length from 1.76 ± 0.03 to 2.16 ± 0.04 μm for rabbit and from 1.75 ± 0.02 to 2.09 ± 0.05 μm for mouse. Immediately after application of stretch, strips were immersion-fixed in iso-osmotic (300 mOsm) Karnovsky's fixative (2.4% sodium cacodylate, 0.75% paraformaldehyde, 0.75% glutaraldehyde; Solmedia, Shrewsbury, United Kingdom). Tissue fragments were excised from fixed SAN strips and prepared for ET (Rog-Zielinska et al., 2016). Briefly, fragments were washed with 0.1 M sodium cacodylate, post-fixed for 1 h in 1% OsO_4, dehydrated in graded acetone, and embedded in Epon-Araldite resin. Semithick (275 nm) sections were placed on formvar-coated slot-grids, poststained with 2% aqueous uranyl acetate and Reynold's lead citrate. Colloidal gold particles (15 nm; BBI Solutions, Crumlin, United Kingdom) were added to both surfaces of the sections to serve as fiducial markers for tilt series alignment.

Imaging was performed in the Electron Microscopy Core Facility of the European Molecular Biology Laboratory (EMBL) in Heidelberg, using a transmission electron microscope (Tecnai TF-30 300 KV; formerly FEI Company, now Thermo Fisher Scientific, Waltham, United States) and a 4 K × 4 K charge-coupled device camera (OneView; Gatan, Munich, Germany). Isotropic voxel size was $(1.55\ nm)^3$. Double-tilt tomograms were processed and analyzed using IMOD software, which was also used to generate 3-D models of relevant structures. The number of sub-sarcolemmal caveolae per unit of cell surface area was calculated, and surface membrane convolution was assessed as the total surface area (including folds) relative to a flat projection.

Statistical Analysis

Data are presented as mean ± standard error of the mean (SEM). Unpaired Student's t-test and mixed-effects analysis or one-way ANOVA were used for comparison of means, when appropriate, and *post hoc* comparisons were performed using Sidak's or Tukey's multiple comparison test, respectively. Linear regression was used to assess the relationship between variables. A p-value of less than 0.05 was considered to indicate a statistically significant difference between means.

RESULTS

Chronotropic Response to Stretch and Its Relation to SAN Stiffness

After isolation and mounting, all SAN demonstrated regular spontaneous beating. In the first set of experiments involving stretch in physiological saline only, baseline BR at the start of the experimental protocol in rabbit SAN was 192 ± 7 $\text{beats}\cdot\text{min}^{-1}$ (n = 9), and in mouse SAN, it was 407 ± 22 $\text{beats}\cdot\text{min}^{-1}$ (n = 8). Baseline BR did not change significantly throughout the entire experimental investigation (up to 2 h). Stretch of rabbit SAN caused an increase in BR at strain levels of 20% or greater ($p < 0.05$ by mixed-effects analysis) with BR returning to baseline between each stretch application and with the magnitude of the change in BR correlating with the amount of strain (**Figure 2A** and **Supplementary Figure S2A**). Stretch of mouse SAN resulted in a more variable chronotropic response: BR increased in three mice, decreased in one mouse, and varied between increase and decrease in four mice (**Supplementary Figure S2B**). There was no correlation between the magnitude of the stretch-induced change in BR and baseline BR prior to stretch application in either species (**Supplementary Figure S3**).

Individual stress-strain curves (whose slopes represent tissue stiffness) were generated for each SAN preparation. There was no difference between mean stress-strain behavior in rabbit and mouse (**Figure 2B**). To determine the relationship between the magnitude of electrophysiological responses to stretch and SAN stiffness, the largest *absolute* percentage change in BR observed in each individual SAN preparation was identified and plotted

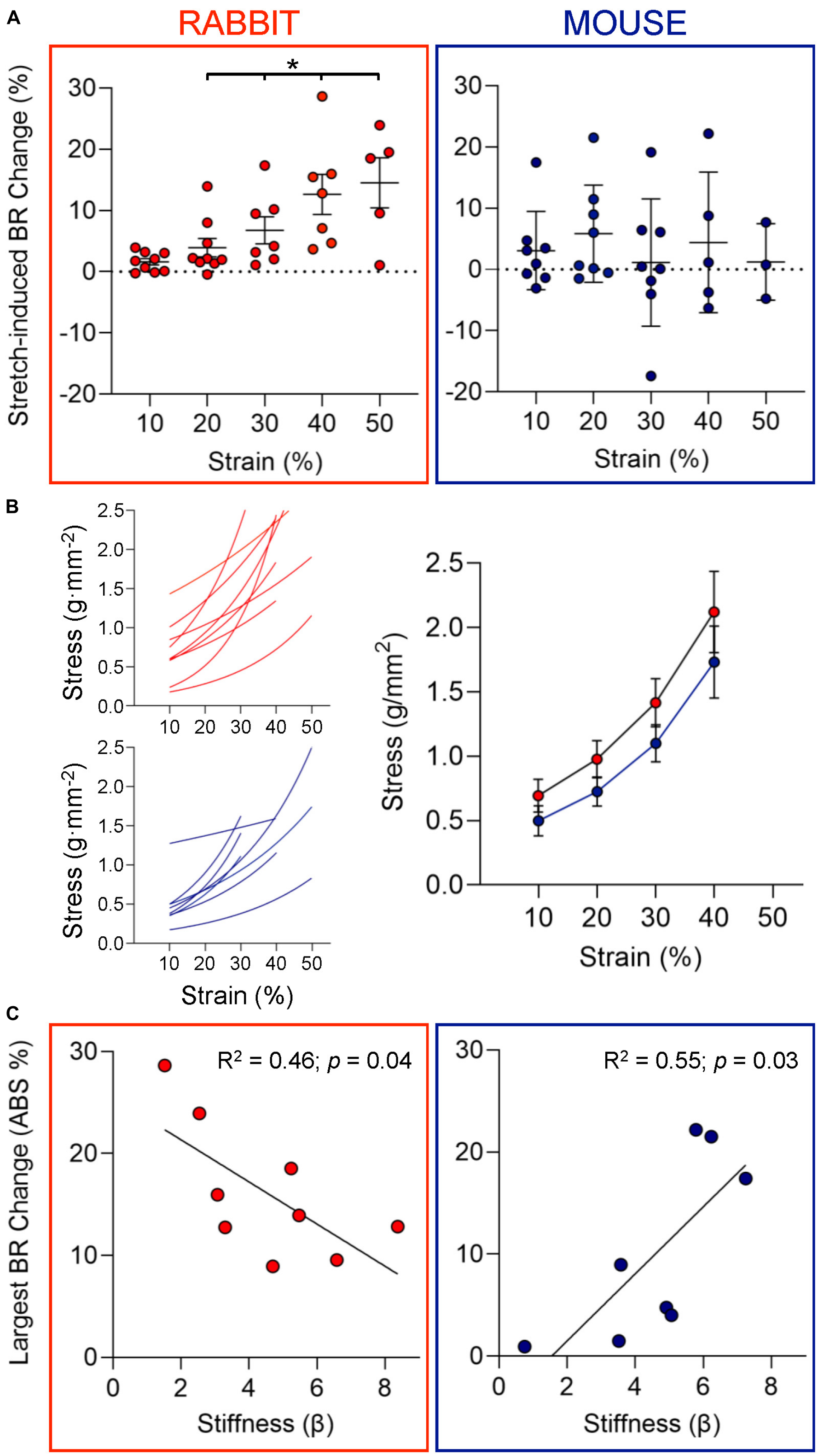

FIGURE 2 | Chronotropic response to stretch and mechanical properties of SAN. **(A)** Change in beating rate (BR) of rabbit (left, $n = 9$) and mouse (right, $n = 8$) SAN upon strain application of increasing magnitude. **(B)** Individual and average stress-strain curves for rabbit (red) and mouse (blue) SAN. **(C)** The relationship between the largest absolute (ABS) percentage change in BR observed upon SAN stretch and tissue stiffness (β) of the individual sinoatrial node studied for rabbit (left) and mouse (right). $^*p < 0.05$ indicates a significant increase in BR by mixed-effects analysis.

against SAN tissue stiffness (β, **Figure 2C**; note: absolute values of BR change were used to assess responsiveness independently of directionality of change). Interestingly, for rabbits, there was an inverse relationship between the chronotropic responsiveness to stretch and SAN stiffness although for mice the relationship was positive ($p < 0.05$ for both by linear regression).

Effect of 4-AP on the Chronotropic Response to Stretch in Mouse

In further experiments ($n = 5$), 40% stretch of the mouse SAN again resulted in a variable chronotropic response with BR increasing in two of the SAN tested and decreasing in the other three (**Figure 3B** and **Supplementary Figure S2C**). After application of increasing concentrations of 4-AP, there was a shift in the stretch-induced change in BR toward a positive chronotropic response with a significant difference seen at a concentration of 500 μM ($p < 0.05$, mixed-effects analysis). After 20 min washout, there was no longer a difference in stretch-induced BR changes compared to the initial control. As in the first set of experiments, the magnitude of stretch-induced BR changes was not related to baseline BR before stretch (**Supplementary Figure S4**). Baseline BR was not affected by 4-AP (in agreement with previous findings in mouse SAN; Golovko et al., 2015) and did not change significantly over the course of the experiment.

In the computational simulations (AP presented in **Supplementary Figure S5**), stretch in control conditions resulted in a 10% decrease in BR (even though the rate of diastolic depolarization was increased by 20%), which is within the range of stretch-induced changes in BR seen in control experiments. Simulation of 4-AP application by reducing the magnitude of rapidly activating potassium currents resulted in a 32% increase in APD_{20} with little effect on BR (-1%) similar to previous reports (Golovko et al., 2015). In the presence of 4-AP, the negative chronotropic response to simulated stretch was nearly abolished (BR changed by -3% instead of -10% compared to prestretch values).

SAN Microstructure and the Effect of Stretch: Collagen

Collagen was visualized with SHGM in both the surface and middle layers of the central SAN of rabbit and mouse at baseline and at 40% stretch (**Figure 4A**; $n = 3$, for both baseline and stretch in each species).

In the dense epicardial surface layers of non-stretched SAN, collagen fiber alignment differed between rabbit and mouse: fibers were highly aligned in parallel to the CT in rabbit but were less organized with a more distributed orientation in mouse (see surface layers at baseline in **Figure 4B**). During 40% stretch, collagen fibers were highly aligned parallel to the CT in the surface layers both of rabbit and mouse SAN. Thus, the less organized collagen fibers in the surface layers of mouse SAN rotated in the direction of stretch and became highly aligned with the CT. In both species, surface collagen was tightly crimped (as indicated by relatively low wavelength) and tortuous (**Figure 4C**). Counterintuitively, there was no difference in crimp wavelength between stretched and non-stretched SAN from either species, presumably indicative of a rotational reorientation of collagen that may precede stretching. Tortuosity was also not different in stretched versus non-stretched SAN from mouse but was lower in stretched versus non-stretched rabbit SAN (for which collagen rotation would be less pronounced than in mice as it is already aligned in parallel to CT before application of stretch).

In the less-dense middle layers of non-stretched SAN from both species, collagen fibers were disorganized (with a distributed orientation; **Figure 4B**), crimped, and tortuous (**Figure 4C**). In stretched SAN, collagen fibers rotated in the direction of stretch to become highly aligned with the CT (∼2–3-fold increase; **Figure 4B**), and they were less tortuous than in non-stretched SAN (**Figure 4C**). Crimp wavelength was not different between stretched and non-stretched SAN of the mouse but were greater in stretched compared to non-stretched rabbit SAN (**Figure 4C**). Crimp wavelength in stretched rabbit SAN was also greater in middle versus surface layers.

SAN Nanostructure and the Effect of Stretch: Caveolae

Sub-sarcolemmal caveolae were abundant in SAN cells at baseline in both species (**Figure 5A**; $n = 18$ cells for rabbit, $n = 17$ cells for mouse), and there were nearly twice as many caveolae per unit of cell surface area in rabbit SAN than in mouse ($p < 0.05$ by one-way ANOVA; **Figure 5C**). Upon stretch, both in rabbit ($n = 5$ cells) and mouse ($n = 6$ cells) SAN, there was a significant reduction in the presence of caveolae with almost complete sarcolemmal membrane incorporation at sarcomere lengths ≥ 2 μm (**Figure 5B**; total membrane surface area analyzed was: baseline = 19.5 μm^2, stretch = 3.2 μm^2 for rabbit; baseline = 12.3 μm^2, stretch = 6 μm^2 for mouse). The difference in sub-sarcolemmal caveolae content between rabbit and mouse in SAN cells, observed at baseline, thus disappeared during stretch (**Figure 5C**).

Concurrently, the surface membrane was significantly more convoluted at baseline in mouse SAN cells compared to rabbit, providing an excess surface compared to a 2-D "flat projection" of the cell surface, of 10.9 ± 1.7% in rabbit versus 31.8 ± 4.4% in mouse ($p < 0.05$ by one-way ANOVA), a difference that was also abolished with stretch (**Figure 5D**).

Taking into account *both* membrane convolution and caveolae, the total "spare membrane" reserve at baseline (as compared to a 2-D flat projection) is higher in rabbit compared to mouse SAN cells (excess sarcolemmal surface at rest was 141 ± 3.7% in rabbit versus 118 ± 7.3% in mouse; $p < 0.05$, unpaired Student's *t*-test).

DISCUSSION

In this study, we demonstrate (i) a correlation between SAN stiffness and the magnitude of the stretch-induced change in BR, which differs between rabbit and mouse; (ii) species differences in SAN tissue structure and sub-sarcolemmal caveolae density as well as their change with stretch; and (iii) a shift of stretch-induced changes in mouse SAN BR toward positive chronotropy in the presence of 4-AP.

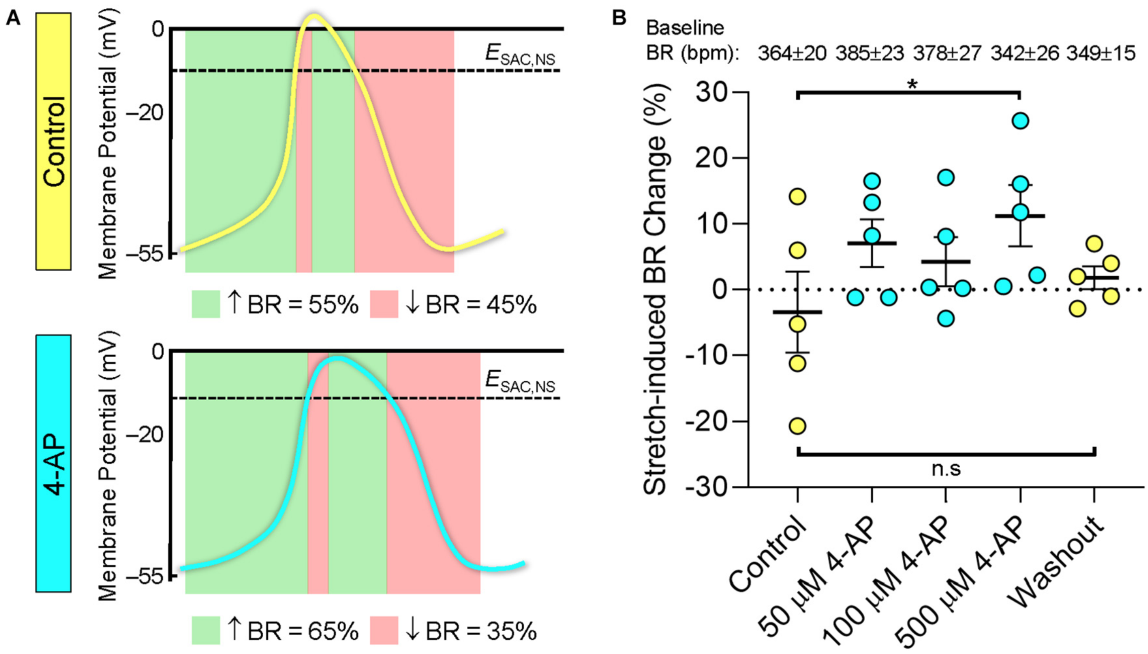

FIGURE 3 | Relationship between action potential morphology and the chronotropic response to stretch of the mouse SAN. **(A)** Theoretical effects of stretch, sustained over the cardiac cycle, on BR of the mouse SAN in control conditions (top) and during application of 4-aminopyridine (4-AP, bottom). Green panels indicate phases during which activation of a cation non-selective stretch activated current ($I_{SAC,NS}$) would accelerate intrinsic changes in SAN membrane potential and, hence, increase BR, and red panels indicate phases during which $I_{SAC,NS}$ activation would decrease BR. Mouse action potentials redrawn from microelectrode recordings in Figure 2 from Golovko et al., 2015. **(B)** Experimentally observed changes in BR of mouse SAN upon 40% stretch before (Control), during (X µM 4-AP), and after (Washout) application of increasing levels of 4-AP (n = 5). Baseline BR in the absence of stretch for each concentration of 4-AP is indicated at the top of the figure (in beats·min^{-1}, bpm). $E_{SAC,NS}$, reversal potential of $I_{SAC,NS}$. $^{*}p < 0.05$ indicates a significant increase in BR compared to control by mixed-effects analysis; n.s. indicates no significant difference.

Species Difference in the Chronotropic Response to Stretch and Their Relation to SAN Stiffness

The stretch-induced increase in BR of rabbit SAN and the variable response of mouse SAN observed in the current study (**Figure 2A**) are consistent with previous reports (Deck, 1964; Golenhofen and Lippross, 1969; Ushiyama and Brooks, 1977; Kamiyama et al., 1984; Arai et al., 1996; Cooper and Kohl, 2005). Yet little is known about the mechanical determinants of the chronotropic response to SAN stretch. Although some previous studies have suggested that the amount of strain is a key input parameter (Sanders et al., 1979; Kamiyama et al., 1984), others have proposed that stress levels (Brooks et al., 1966; Chiba, 1977; Arai et al., 1996) or a combination of both (Lange et al., 1966), determine mechanical effects on BR.

We observed that the largest absolute changes in BR upon stretch show an inverse correlation with SAN tissue stiffness in rabbit (i.e., the least stiff SAN preparations show the largest responses) although in mouse there is a positive correlation (i.e., the stiffest SAN respond most; **Figure 2C**). This suggests that rabbit SAN pacemaker cells may respond primarily to strain, and mouse SAN pacemaker cells may be more sensitive to stress. This would mean that effects of mechanical loading on SAN BR may depend on the mode of load application (i.e., whether a specific magnitude of stretch or a specific magnitude of force is applied), perhaps explaining some of the previous lack of agreement between experimental studies. One caveat of all these studies (including ours) is that sustained mechanical stimulation has been used, applied throughout systole and diastole. This differs from the *in vivo* setting, in which the right atrium is cyclically stretched during atrial diastole by ventricular contraction (valve plane shift) and accumulation of venous return.

Species Differences in SAN Microstructure and Changes With Stretch

Species-specific responses of the SAN to stretch may also be modulated by differences in SAN structure and its stretch-induced alteration. At the epicardial surface of the non-stretched rabbit SAN, we observed aligned (**Figure 4B**), tightly crimped, and tortuous collagen fibers (**Figure 4C**), running parallel to the CT. In non-stretched mouse SAN, collagen fibers in the surface layer are also highly crimped and tortuous (**Figure 4C**) but poorly aligned (**Figure 4B**) and less dense, consistent with previous studies (Hao et al., 2011; Glukhov et al., 2015). During 40% stretch, collagen fibers in the surface layer of rabbit SAN became less tortuous (**Figure 4C**) although in mouse SAN fibers were rotated in the stretch direction (so became parallel to the CT; **Figure 4B**) without a change in crimp or tortuosity. In the middle layer of non-stretched SAN in both species, collagen fibers

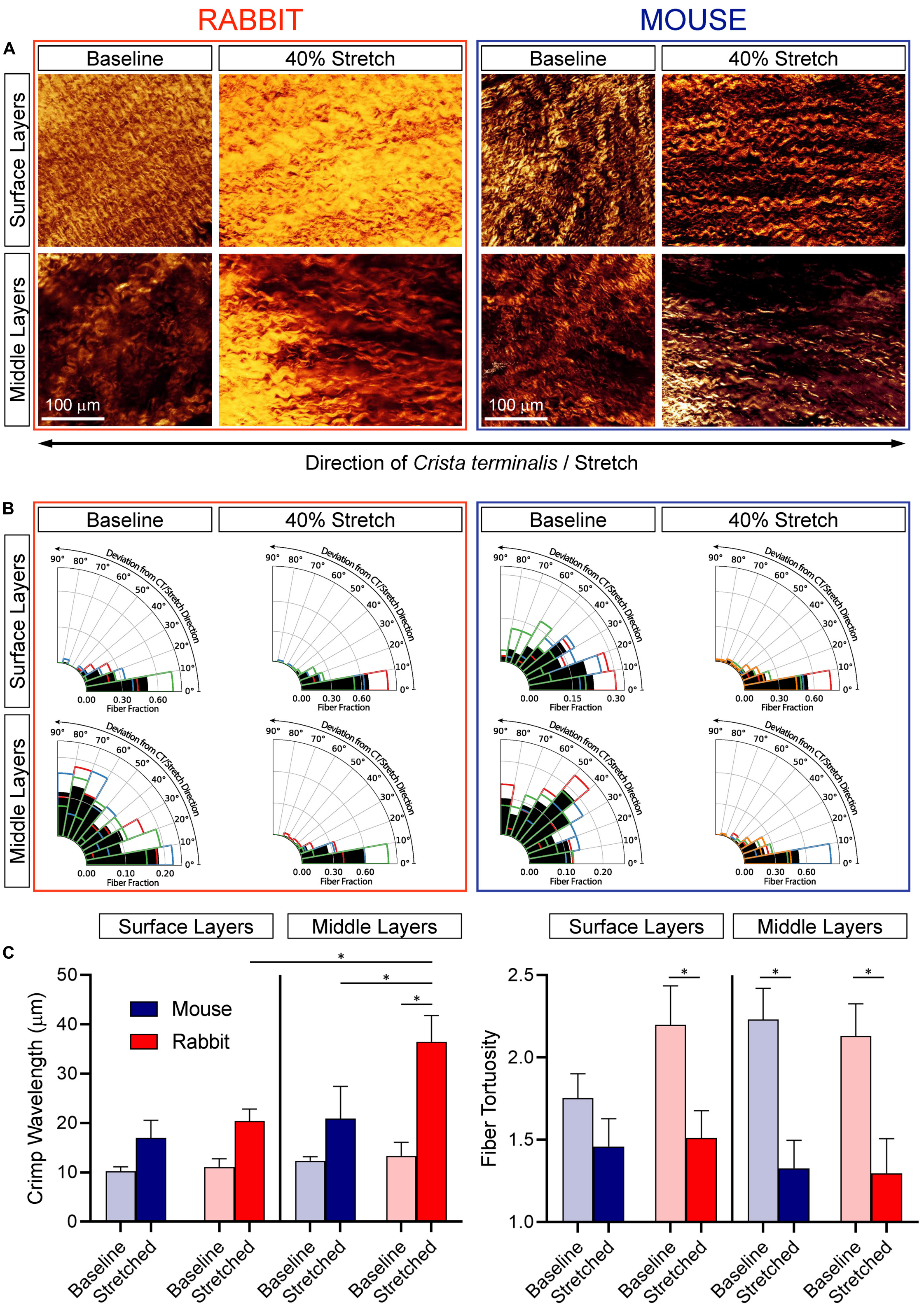

FIGURE 4 | Effect of SAN stretch on collagen alignment and crimp characteristics. **(A)** Representative second-harmonic generation images of collagen at the epicardial surface and in the middle layers of the central SAN of rabbit (left) and mouse (right) at baseline and during 40% stretch. **(B)** Collagen orientation analysis for all samples ($n = 3$ for each). Black bars represent the fraction of fibers averaged across all samples and colored outlines represent the average fraction of fibers from individual samples. **(C)** Collagen crimp wavelength (left) and fiber tortuosity (right). *$p < 0.05$ indicates a difference between the means by one-way ANOVA.

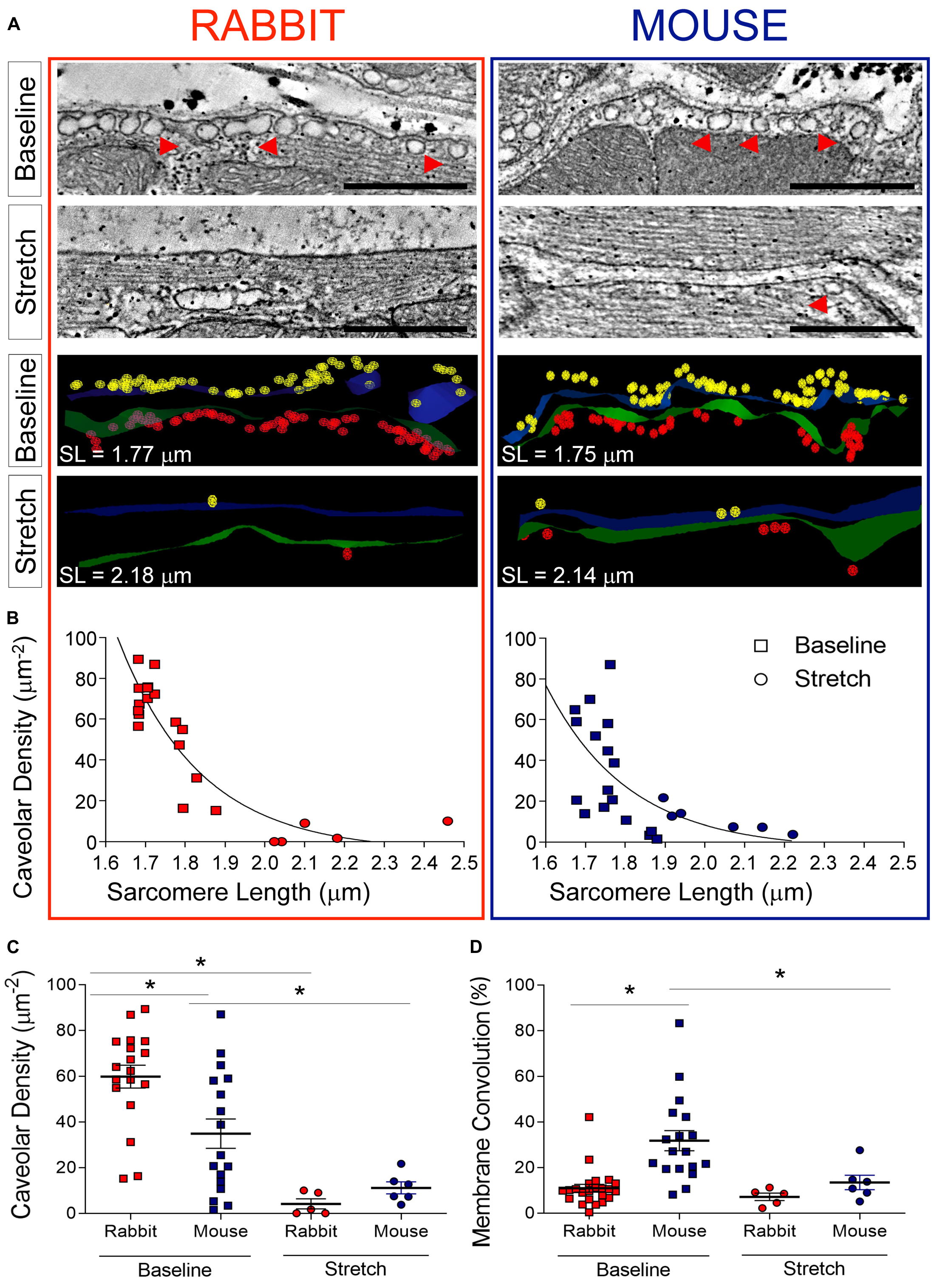

FIGURE 5 | Effect of stretch on SAN nanostructure. **(A)** Representative electron tomography slices and three-dimensional segmentations of the sarcolemma and sub-sarcolemmal caveolae (examples indicated by red arrowheads) in rabbit (left) and mouse (right) SAN cells. **(B)** Relationship between caveolar density and sarcomere length (SL) across all preparations at baseline (square symbols; *n* = 18 cells for rabbit, *n* = 17 cells for mouse) and during stretch (round symbols; *n* = 5 cells for rabbit, *n* = 6 cells for mouse). **(C)** Average values of caveolar density for rabbit and mouse at baseline and during stretch. **(D)** Average values of surface membrane convolution for rabbit and mouse at baseline and during stretch. Green/blue, surface membranes of two opposing SAN cells; yellow/red, caveolae in the two cells. *$p < 0.05$ indicates a difference between the means, by one-way ANOVA.

were crimped, tortuous (**Figure 4C**), and irregularly oriented (**Figure 4B**). This is in agreement with previous reports from rabbit (Bleeker et al., 1980). When SAN were stretched, collagen fibers aligned with the stretch direction (**Figure 4B**) and became less tortuous in both species. In the rabbit SAN, crimp of fibers in the middle layer was also reduced (**Figure 4C**). Interestingly, in the surface layers of the rabbit SAN and middle layers of the mouse SAN, collagen fiber tortuosity was reduced during stretch without a change in crimp wavelength. This apparent disparity suggests that, in addition to crimp, there is a "bowing" of collagen fibers, which is straightened first during stretch to reduce tortuosity before altering crimp wavelength. Overall, these results demonstrate that collagen fibers in rabbit and mouse SAN differ in their arrangement and in their response to stretch. In the rabbit SAN, collagen fibers predominantly straighten with stretch (with some rotation in the middle layer), and in the mouse SAN, collagen fibers predominantly rotate (with some straightening in the middle layer). Interestingly, despite their differing structures and their change with stretch, no species differences in SAN tissue stiffness or in average stress-strain relations were observed (**Figure 2B**).

Noting the potential importance of differences in collagen architecture of rabbit and mouse SAN, it is worth considering the cells responsible for its production. Like pacemaker cells in the SAN (Cooper et al., 2000), fibroblasts are mechano-sensitive and display $I_{SAC,NS}$ (Stockbridge and French, 1988). Non-myocytes have recently been shown to electrically connect to myocytes in the ventricles (Quinn et al., 2016; Rubart et al., 2018) and to atrio-ventricular node cells (Hulsmans et al., 2017). This may be true also for pacemaker cells in the SAN (Camelliti et al., 2004), and it could account for at least some of the chronotropic response to stretch (Kohl et al., 1994). Presence, mechano-sensitivity, and electrical connectivity of cardiac non-myocytes may differ between species and contribute to the species dependence of BR responses to stretch. To comprehensively consider the role that collagen architecture might play in stretch responses, these findings should be followed up by experiments using biaxial or concentric stretch of isolated SAN or 3-D atrial volume manipulation (rather than in-plane or uniaxial stretch), where collagen fiber rotation will be less pronounced. This would also be closer to the stretch experienced by the SAN *in vivo*.

Species Differences in SAN Nanostructure and Changes With Stretch

At the subcellular level, we observed an abundance of caveolae in non-stretched SAN cells (**Figures 5A,B**) as reported previously for rabbit (Bleeker et al., 1980). Caveolar density in the absence of stretch was twice as high in rabbit compared to mouse SAN, and the membrane area contained in caveolae adds an additional 117% of surface sarcolemma in rabbit and 66% in mouse when compared to a smoothly traced cell surface outline (in other words, membrane contained within caveolae constitutes roughly 54 and 40% of total surface sarcolemma in mice and rabbit, respectively). Cell surface membranes were less undulated in non-stretched SAN of rabbit compared to mouse. Upon stretch, surface membranes were flattened (**Figure 5A**: compare green and blue surfaces in the representative models of juxtaposed cells at baseline and during stretch; **Figure 5D** for quantitative data) and caveolar density was reduced in both species to the extent that differences were no longer apparent (**Figure 5C**). Membrane straightening and a reduction in caveolae, presumably by incorporation into the surface membrane (Kohl et al., 2003; Pfeiffer et al., 2014), is thought to relieve membrane tension as originally proposed for skeletal muscle (Dulhunty and Franzini-Armstrong, 1975). In ventricular myocytes, caveolar membrane integration into the surface sarcolemma has been shown to also alter passive electrophysiological membrane properties (increased capacity), reducing conduction velocity in response to stretch (Pfeiffer et al., 2014). Whether this mechanism contributes to stretch-induced changes in BR is unclear although it may be involved in stretch-mediated ion channel activation (Egorov et al., 2019). As chemical disruption of caveolar integrity in SAN cells alters pacemaking (Lang and Glukhov, 2018), it is not unreasonable to suspect that reconfiguration of caveolae by stretch, altering spatial compartmentalization of important signaling pathways, may affect SAN pacemaking. Whether or not this occurs on a beat-by-beat basis remains to be determined as the temporal offset between stretch and onset of tissue fixation – in our experiments about 1–2 s – is at least an order of magnitude slower than normal BR and any associated mechanical changes.

Despite more undulated surface membranes of non-stretched mouse SAN, given the lower presence of caveolae, murine cells have less spare membrane reserves to relieve membrane tension during stretch, so stress (rather than strain) could be a primary input parameter for mechano-sensitive responses in that species. This differs from rabbit and may be a result of adaptation to different intrinsic BR in the two species. At the high BR of mouse hearts, stroke volume will be relatively small compared to rabbit hearts with a much lower BR. Given that the relation between the changes in surface area and volume of a cardiac chamber, simplistically approximating it as a sphere, is linear (as surface area = 3 × volume/radius), small volume changes will result in small changes of surface area in the mouse and, therefore, less SAN stretch than in rabbit. This could involve a reduced requirement for "spare membrane" in mouse compared to rabbit.

Species Differences in Stretch Responsiveness and SAN Stiffness

Even though the passive stress-strain relationships of rabbit and mouse SAN tissue were not significantly different, the difference in the relation of the change in BR to tissue stiffness suggests that pacemaker cells in the SAN of rabbit and mouse may experience or respond to different key mechanical stimuli during tissue stretch. In rabbit, stretch-induced changes in SAN BR appear to correlate with the amount of strain. This would be in keeping with our observation that stretch of rabbit SAN straightens collagen fibers at the epicardial surface and intramurally, which would result in stretch of interspersed pacemaker cells (Rego et al., 2016). In contrast, collagen fibers in mouse SAN rotate in the stretch direction but maintain their crimp wavelength, thereby potentially protecting associated pacemaker cells from themselves being stretched. Again, this should be assessed in future studies with biaxial, concentric, or *in situ* mechanical stimulation.

The Importance of SAN Background Electrophysiology for the Chronotropic Response to Stretch

The difference in the chronotropic response to SAN stretch in rabbit (increase in BR) versus mouse (varied responses, including decreased BR) may be explained conceptionally by differences in their SAN AP shape with respect to $E_{SAC,NS}$ (as described in the Introduction and schematically illustrated in **Figure 3A**). If applicable, an increased plateau duration of mouse SAN AP at unchanged baseline BR should shift the stretch-induced change in BR toward positive chronotropy. This effect was indeed observed in our study, using 4-AP at concentrations that had previously been shown to lengthen the plateau of mouse SAN AP by up to 50% without affecting the slope of final SAN repolarization or spontaneous diastolic depolarization (Golovko et al., 2015). This was observed in all cells tested, and the response disappeared upon washout, supporting the critical importance of intrinsic AP morphology for the chronotropic response of the SAN to stretch. Computational simulations, using an "out-of-the-box" model[1], failed to reproduce the 4-AP induced shift toward an actual positive chronotropic response to stretch. It did reproduce, however, main features, such as the 4-AP induced prolongation of APD_{20} in the absence of changes in BR. This changed the chronotropic response of the SAN cell model to stretch from a reduction in BR (by 10%) to a much less pronounced effect (reduction by 3%; **Supplementary Figure S5**). This "positive shift" in the BR response to stretch after block of rapidly activating potassium currents agrees with the notion that AP shape matters for the extent and direction of the SAN stretch response.

That said, activation of $I_{SAC,NS}$ by cyclic stretch exclusively during diastolic depolarization (to mimic the *in vivo* setting), would be expected to cause an even more pronounced and potentially species-independent increase in BR. So the Bainbridge response that speeds up initiation of the next wave of cardiac excitation if venous return from the systemic circulation is high may well be active in all species – another relevant target for follow-up experimental research, using dynamic stretch protocols.

Study Limitations

The general anatomy of rabbit and mouse SAN is principally similar, and we made every effort to prepare the SAN from these two species and from each individual heart within each species in a matching manner. The fact that the "cut tissue" surface on the auricular side of the SAN would have been further away from the SAN in mouse compared to rabbit (2–3 mm instead of 1–2 mm) may have contributed to interspecies (but not to intersubject) differences in the chronotropic response to stretch. That said, the steady (no significant change over 2 h), low-variability, and relatively high (for isolated tissue) spontaneous BR of preparations indicate relatively well-sustained background activity of the SAN. Furthermore, although our 4-AP results support the idea that AP morphology is indeed a critical factor for differences in the directionality of chronotropic responses, this hypothesis has not been corroborated directly in the current study. This would have required AP assessment by microelectrode-based or optical voltage mapping from the *leading* SAN pacemaker site (which may shift during stretch) yet still be unable to address an ill-posed problem (in the presence of electrotonic entrainment of individual SAN cells). For this reason, we targeted ensemble properties using a pharmacological intervention known to modify SAN AP shape, but not duration. Although our computational simulations of 4-AP application support the quantitative plausibility of the proposed explanation, they do not prove it (Quinn and Kohl, 2011). It is difficult to ascertain, based on the type of data available and the constraints of the model, whether underlying mechanisms indeed match one another (for example, we are unable to relate the amount of SAC_{NS} activation in the experiments and model, and we cannot confirm the SAN AP shape in the leading pacemaker site of the preparation, which furthermore may change during stretch). This is compounded by the fact that the computational mouse SAN cell AP model used depicts only one of many AP morphologies occurring in the mouse SAN. Finally, it is important to note that the current study should not be used to construe a lack of physiological relevance of stretch for murine SAN BR regulation as this will require further work using cyclic stretch, applied during right atrial diastole.

CONCLUSION

The current study illustrates the potential importance of SAN structural, mechanical, and background electrophysiological properties for the magnitude and direction of the chronotropic response to stretch in rabbit and mouse. A thorough understanding of the effects of the biophysical environment on SAN pacemaking is important for basic science, conceptual and mechanistic modeling with potentially important implications for further research into SAN dysfunction in the aging and/or fibrotic heart.

DATA AVAILABILITY STATEMENT

The datasets generated for this study are available on request to the corresponding authors.

ETHICS STATEMENT

The animal study was reviewed and approved by the Dalhousie University Committee for Laboratory Animals or the local Institutional Animal Care and Use Committee in Freiburg, Germany (Regierungspraesidium Freiburg, X-16/10R).

---

[1] We specifically abstained from "tweaking" the model even though the simulated SAN AP shape differs from that observed, for example, by Golovko et al. (2015), as to support replication and to avoid unintended user bias. The principally matching direction of 4-AP induced changes is, under these conditions, a conservative estimate of responses.

AUTHOR CONTRIBUTIONS

EM contributed to the design of the study, performed SN stretch experiments, analyzed data, and drafted the manuscript. JM performed light imaging work and analyzed data. JG developed image analysis tools for collagen quantification and analyzed data. AR performed the computational simulations. SW contributed to the design of the study, developed image analysis tools for collagen quantification, and revised the manuscript. AT contributed to the design of the study, performed sample preparation, and revised the manuscript. PK contributed to the design of the study, performed sample preparation, and revised the manuscript. ER-Z contributed to the design of the study, performed light and electron imaging work, analyzed data, and revised the manuscript. TAQ contributed to the design of the study and revised the manuscript. All authors approved the final submission.

FUNDING

This work was supported by a Mitacs Globalink Research Award Internship (IT11003 to EM), the European Research Council (Advanced Grant CardioNECT, Project ID: #323099 to PK), a Deutsche Forschungsgemeinschaft (DFG) Emmy Noether Fellowship (RO5694/1-1 to ER-Z), the Natural Sciences and Engineering Research Council of Canada (RGPIN-2016-04879 to TAQ), and the Canadian Institutes of Health Research (MOP 342562 to TAQ). ER-Z and PK are members of the DFG-funded Collaborative Research Centre CRC1425 (DFG #422681845). TAQ was a National New Investigator of the Heart and Stroke Foundation of Canada.

ACKNOWLEDGMENTS

We would like to acknowledge the microscopy facility SCI-MED (Super-Resolution Confocal/Multiphoton Imaging for Multiparametric Experimental Designs at the Institute for Experimental Cardiovascular Medicine, Freiburg) for advice and access to second-harmonic generation microscopy, and the Electron Microscopy Core Facility at the European Molecular Biology Laboratory in Heidelberg for advice and access to electron microscopy. The article processing fee was covered by the University of Freiburg Open Access Publishing programme.

SUPPLEMENTARY MATERIAL

The Supplementary Material for this article can be found online at: https://www.frontiersin.org/articles/10.3389/fphys.2020.00809/full#supplementary-material

FIGURE S1 | Representative measurements of force and beating rate (BR) during sinoatrial node (SAN) stretch from the rabbit (**left**) and mouse, showing both a stretch that caused a decrease (**middle**) and a stretch that caused an increase (**right**) in BR.

FIGURE S2 | (A) Change in BR of individual rabbit (**left**) and mouse (**middle**) SAN upon strain application of increasing magnitude and of individual mouse SAN (**right**) during application of various concentrations of 4-aminopyridine (4-AP) and after 20 min of washout. Each color represents an individual preparation (which are different in each panel).

FIGURE S3 | (A) The relationship between change in BR of rabbit (**left**) and mouse (**right**) SAN with application of stretch of increasing magnitude and the baseline BR before stretch. **(B)** Comparison (green boxes cover matching areas in BR space) of the above relationship with the experiments by Cooper and Kohl (2005) in guinea pig and mouse SAN (at 27 or 37°C).

FIGURE S4 | The relationship between the change in BR of mouse SAN upon application of 40% stretch and the baseline BR before stretch during exposure to various concentrations of 4-AP and after 20 min of washout.

FIGURE S5 | Computational simulations of mouse SAN cell stretch with ("4-AP") and without ("Control") reduction of rapidly activating potassium currents (complete block of transient outward potassium current and 25% reduction in delayed rectifier potassium current) using the mouse SAN cell action potential model of Kharche et al. (2011). $E_{SAC,NS}$, reversal potential of $I_{SAC,NS}$.

REFERENCES

Arai, A., Kodama, I., and Toyama, J. (1996). Roles of Cl^- channels and Ca^{2+} mobilization in stretch-induced increase of SA node pacemaker activity. *Am. J. Physiol.* 270(5 Pt 2), H1726–H1735. doi: 10.1152/ajpheart.1996.270.5.h1726

Bainbridge, F. A. (1915). The influence of venous filling upon the rate of the heart. *J. Physiol.* 50, 65–84. doi: 10.1113/jphysiol.1915.sp001736

Bleeker, W. K., Mackaay, A. J. C., Masson-Pevet, M., Bouman, L. N., and Becker, A. E. (1980). Functional and morphological organization of the rabbit sinus node. *Circ. Res.* 46, 11–22. doi: 10.1161/01.RES.46.1.11

Boyett, M. R., Honjo, H., and Kodama, I. (2000). The sinoatrial node, a heterogeneous pacemaker structure. *Cardiovasc. Res.* 47, 658–687. doi: 10.1016/S0008-6363(00)00135-8

Brooks, C. M., Lu, H. H., Lange, G., Mangi, R., Shaw, R. B., and Geoly, K. (1966). Effects of localized stretch of the sinoatrial node region of the dog heart. *Am. J. Physiol.* 211, 1197–1202. doi: 10.1152/ajplegacy.1966.211.5.1197

Burkhoff, D., Mirsky, I., and Suga, H. (2005). Assessment of systolic and diastolic ventricular properties via pressure-volume analysis: A guide for clinical, translational, and basic researchers. *Am. J. Physiol.* 289, H501-H512. doi: 10.1152/ajpheart.00138.2005

Burton, R. A. B., Rog-Zielinska, E. A., Corbett, A. D., Peyronnet, R., Bodi, I., Fink, M., et al. (2017). Caveolae in rabbit ventricular myocytes: distribution and dynamic diminution after cell isolation. *Biophys. J.* 113, 1047–1059. doi: 10.1016/j.bpj.2017.07.026

Camelliti, P., Green, C. R., LeGrice, I., and Kohl, P. (2004). Fibroblast network in rabbit sinoatrial node: structural and functional identification of homogeneous and heterogeneous cell coupling. *Circ. Res.* 94, 828–835. doi: 10.1161/01.RES.0000122382.19400.14

Chiba, S. (1977). Pharmacologic analysis of stretch-induced sinus acceleration of the isolated dog atrium. *JPN. Heart J.* 18, 398–405. doi: 10.1536/ihj.18.398

Cooper, P. J., and Kohl, P. (2005). Species- and preparation-dependence of stretch effects on sino-atrial node pacemaking. *Ann. N. Y. Acad. Sci.* 1047, 324–335. doi: 10.1196/annals.1341.029

Cooper, P. J., Lei, M., Cheng, L. X., and Kohl, P. (2000). Selected contribution: axial stretch increases spontaneous pacemaker activity in rabbit isolated sinoatrial node cells. *J. Appl. Physiol.* 89, 2099–2104. doi: 10.1152/jappl.2000.89.5.2099

Craelius, W., Chen, V., and El-Sherif, N. (1988). Stretch activated ion channels in ventricular myocytes. *Biosci. Rep.* 8, 407–414. doi: 10.1007/BF01121637

Deck, K. A. (1964). Dehnungseffekte am spontanschlagenden, isolierten Sinusknoten. *Pflugers Arch. Gesamte Physiol. Menschen Tiere* 280, 120–130. doi: 10.1007/BF00363751

Dulhunty, A. F., and Franzini-Armstrong, C. (1975). The relative contributions of the folds and caveolae to the surface membrane of frog skeletal muscle fibres at different sarcomere lengths. *J. Physiol.* 250, 513–539. doi: 10.1113/jphysiol.1975.sp011068

Egorov, Y. V., Lang, D., Tyan, L., Turner, D., Lim, E., Piro, Z. D., et al. (2019). Caveolae-mediated activation of mechanosensitive chloride channels in pulmonary veins triggers atrial arrhythmogenesis. *J. Am. Heart Assoc.* 8, e012748. doi: 10.1161/JAHA.119.012748

Garofalo, C. A., Cabreriza, S. E., Quinn, T. A., Weinberg, A. D., Printz, B. F., Hsu, D. T., et al. (2006). Ventricular diastolic stiffness predicts perioperative morbidity and duration of pleural effusions after the fontan operation. *Circulation* 114(1 Suppl), I56-I61. doi: 10.1161/CIRCULATIONAHA.105.001396

Glukhov, A. V., Kalyanasundaram, A., Lou, Q., Hage, L. T., Hansen, B. J., Belevych, A. E., et al. (2015). Calsequestrin 2 deletion causes sinoatrial node dysfunction and atrial arrhythmias associated with altered sarcoplasmic reticulum calcium cycling and degenerative fibrosis within the mouse atrial pacemaker complex. *Eur. Heart J.* 36, 686–697. doi: 10.1093/eurheartj/eht452

Golenhofen, K., and Lippross, H. (1969). Der effekt dynamischer und statischer dehnung auf die spontanfrequenz des isolierten herzschrittmachers. *Pflügers Arch. Eur. J. Physiol.* 309, 145–158. doi: 10.1007/BF00586964

Golovko, V., Gonotkov, M., and Lebedeva, E. (2015). Effects of 4-aminopyridine on action potentials generation in mouse sinoauricular node strips. *Physiol. Rep.* 3, 1–8. doi: 10.14814/phy2.12447

Guharay, F., and Sachs, F. (1984). Stretch-activated single ion channel currents in tissue-cultured embryonic chick skeletal muscle. *J. Physiol.* 352, 685–701. doi: 10.1113/jphysiol.1984.sp015317

Hao, X., Zhang, Y., Zhang, X., Nirmalan, M., Davies, L., Konstantinou, D., et al. (2011). TGF-β1-mediated fibrosis and ion channel remodeling are key mechanisms in producing the sinus node dysfunction associated with SCN5A deficiency and aging. *Circ. Arrhythm. Electrophysiol.* 4, 397–406. doi: 10.1161/CIRCEP.110.960807

Healy, S. N., and McCulloch, A. D. (2005). An ionic model of stretch-activated and stretch-modulated currents in rabbit ventricular myocytes. *Europace* 7, S128–S134. doi: 10.1016/j.eupc.2005.03.019

Ho, S. Y., and Sánchez-Quintana, D. (2016). Anatomy and pathology of the sinus node. *J. Interv. Card. Electrophysiol.* 46, 3–8. doi: 10.1007/s10840-015-0049-6

Hulsmans, M., Clauss, S., Xiao, L., Aguirre, A. D., King, K. R., Hanley, A., et al. (2017). Macrophages facilitate electrical conduction in the heart. *Cell* 169, 510–522. doi: 10.1016/j.cell.2017.03.050

Hunter, J. D. (2007). Matplotlib: A 2D graphics environment. *Comput. Sci. Eng.* 9, 99–104. doi: 10.1109/MCSE.2007.55

Jalife, J. (1984). Mutual entrainment and electrical coupling as mechanisms for synchronous firing of rabbit sino-atrial pace-maker cells. *J. Physiol.* 356, 221–243. doi: 10.1113/jphysiol.1984.sp015461

Jan, N. J., Brazile, B. L., Hu, D., Grube, G., Wallace, J., Gogola, A., et al. (2018). Crimp around the globe; patterns of collagen crimp across the corneoscleral shell. *Exp. Eye Res.* 172, 159–170. doi: 10.1016/j.exer.2018.04.003

Kalyanasundaram, A., Li, N., Hansen, B. J., Zhao, J., and Fedorov, V. V. (2019). Canine and human sinoatrial node: differences and similarities in the structure, function, molecular profiles, and arrhythmia. *J. Vet. Cardiol.* 22, 2–19. doi: 10.1016/j.jvc.2018.10.004

Kamiyama, A., Niimura, I., and Sugi, H. (1984). Length-dependent changes of pacemaker frequency in the isolated rabbit sinoatrial node. *JPN. J. Physiol.* 34, 153–165. doi: 10.2170/jjphysiol.34.153

Kharche, S., Yu, J., Lei, M., and Zhang, H. (2011). A mathematical model of action potentials of mouse sinoatrial node cells with molecular bases. *Am. J. Physiol. Heart Circ. Physiol.* 301, H945–H963. doi: 10.1152/ajpheart.00143.2010

Kohl, P., Cooper, P. J., and Holloway, H. (2003). Effects of acute ventricular volume manipulation on in situ cardiomyocyte cell membrane configuration. *Prog. Biophys. Mol. Biol.* 82, 221–227. doi: 10.1016/S0079-6107(03)00024-5

Kohl, P., Kamkin, A., Kiseleva, I., and Noble, D. (1994). Mechanosensitive fibroblasts in the sino-atrial node region of rat heart: interaction with cardiomyocytes and possible role. *Exp. Physiol.* 79, 943–956. doi: 10.1113/expphysiol.1994.sp003819

Kordylewski, L., Goings, G. E., and Page, E. (1993). Rat atrial myocyte plasmalemmal caveolae in situ: Reversible experimental increases in caveolar size and in surface density of caveolar necks. *Circ. Res.* 73, 135–146. doi: 10.1161/01.RES.73.1.135

Lakatta, E. G., Maltsev, V. A., and Vinogradova, T. M. (2010). A coupled SYSTEM of intracellular Ca^{2+} clocks and surface membrane voltage clocks controls the timekeeping mechanism of the heart's pacemaker. *Circ. Res.* 106, 659–673. doi: 10.1161/CIRCRESAHA.109.206078

Lang, D., and Glukhov, A. V. (2018). Functional microdomains in heart's pacemaker: a step beyond classical electrophysiology and remodeling. *Front. Physiol.* 9:1686. doi: 10.3389/fphys.2018.01686

Lange, G., Lu, H. H., Chang, A., and Brooks, C. M. (1966). Effect of stretch on the isolated cat sinoatrial node. *Am. J. Physiol.* 211, 1192–1196. doi: 10.1152/ajplegacy.1966.211.5.1192

Liu, J., Dobrzynski, H., Yanni, J., Boyett, M. R., and Lei, M. (2007). Organisation of the mouse sinoatrial node: structure and expression of HCN channels. *Cardiovasc. Res.* 73, 729–738. doi: 10.1016/j.cardiores.2006.11.016

Longair, M. H., Baker, D. A., and Armstrong, J. D. (2011). Simple Neurite Tracer: open source software for reconstruction, visualization and analysis of neuronal processes. *Bioinformatics* 27, 2453–2454. doi: 10.1093/bioinformatics/btr390

MacDonald, E. A., Rose, R. A., and Quinn, T. A. (2020). Neurohumoral control of sinoatrial node activity and heart rate: insight from experimental models and findings from humans. *Front. Physiol.* 11:170. doi: 10.3389/fphys.2020.00170

MacDonald, E. A., Stoyek, M. R., Rose, R. A., and Quinn, T. A. (2017). Intrinsic regulation of sinoatrial node function and the zebrafish as a model of stretch effects on pacemaking. *Prog. Biophys. Mol. Biol.* 130, 198–211. doi: 10.1016/j.pbiomolbio.2017.07.012

Masson-Pévet, M., Gros, D., and Besselsen, E. (1980). The caveolae in rabbit sinus node and atrium. *Cell Tissue Res.* 208, 183–196. doi: 10.1007/BF00234869

Monfredi, O., Dobrzynski, H., Mondal, T., Boyett, M. R., and Morris, G. M. (2010). The anatomy and physiology of the sinoatrial node - a contemporary review. *PACE* 33, 1392–1406. doi: 10.1111/j.1540-8159.2010.02838.x

Monfredi, O., Tsutsui, K., Ziman, B., Stern, M. D., Lakatta, E. G., and Maltsev, V. A. (2018). Electrophysiological heterogeneity of pacemaker cells in the rabbit intercaval region, including the SA node: Insights from recording multiple ion currents in each cell. *Am. J. Physiol.* 314, H403–H414. doi: 10.1152/ajpheart.00253.2016

Noble, D., Denyer, J. C., Brown, H. F., and DiFrancesco, D. (1992). Reciprocal role of the inward currents I(b,Na) and I(f) in controlling and stabilizing pacemaker frequency of rabbit sino-atrial node cells. *Proc. R. Soc. B Biol. Sci.* 250, 199–207. doi: 10.1098/rspb.1992.0150

Opthof, T. (1988). The mammalian sinoatrial node. *Cardiovasc. Drugs Ther.* 1, 573–597. doi: 10.1007/BF02125744

Opthof, T., de Jonge, B., Jongsma, H. J., and Bouman, L. N. (1987). Functional morphology of the mammalian sinuatrial node. *Eur. Heart J.* 8, 1249–1259. doi: 10.1093/oxfordjournals.eurheartj.a062200

Pfeiffer, E. R., Wright, A. T., Edwards, A. G., Stowe, J. C., McNall, K., Tan, J., et al. (2014). Caveolae in ventricular myocytes are required for stretch-dependent conduction slowing. *J. Mol. Cell. Cardiol.* 76, 265–274. doi: 10.1016/j.yjmcc.2014.09.014

Pierlot, C. M., Lee, J. M., Amini, R., Sacks, M. S., and Wells, S. M. (2014). Pregnancy-induced remodeling of collagen architecture and content in the mitral valve. *Ann. Biomed. Eng.* 42, 2058–2071. doi: 10.1007/s10439-014-1077-6

Quinn, T. A., Camelliti, P., Rog-Zielinska, E. A., Siedlecka, U., Poggioli, T., O'Toole, E. T., et al. (2016). Electrotonic coupling of excitable and nonexcitable cells in the heart revealed by optogenetics. *Proc. Natl. Acad. Sci. U.S.A.* 113, 14852–14857. doi: 10.1073/pnas.1611184114

Quinn, T. A., Granite, S., Allessie, M. A., Antzelevitch, C., Bollensdorff, C., Bub, G., et al. (2011). Minimum information about a cardiac electrophysiology experiment (MICEE): Standardised reporting for model reproducibility, interoperability, and data sharing. *Prog. Biophys. Mol. Biol.* 107, 4–10. doi: 10.1016/j.pbiomolbio.2011.07.001

Quinn, T. A., and Kohl, P. (2011). Systems biology of the heart: hype or hope? *Ann. N. Y. Acad. Sci.* 1245, 40–43. doi: 10.1111/j.1749-6632.2011.06327.x

Quinn, T. A., and Kohl, P. (2012). Mechano-sensitivity of cardiac pacemaker function: Pathophysiological relevance, experimental implications, and conceptual integration with other mechanisms of rhythmicity. *Prog. Biophys. Mol. Biol.* 110, 257–268. doi: 10.1016/j.pbiomolbio.2012.08.008

Quinn, T. A., and Kohl, P. (2013). Combining wet and dry research: experience with model development for cardiac mechano-electric structure-function studies. *Cardiovasc. Res.* 97, 601–611. doi: 10.1093/cvr/cvt003

Quinn, T. A., and Kohl, P. (2016). Rabbit models of cardiac mechano-electric and mechano-mechanical coupling. *Prog. Biophys. Mol. Biol.* 121, 110–122. doi: 10.1016/j.pbiomolbio.2016.05.003

Quinn, T. A., and Kohl, P. (2020). Cardiac mechano-electric coupling: acute effects of mechanical stimulation on heart rate and rhythm. *Physiol. Rev*. Online ahead of print doi: 10.1152/physrev.00036.2019

Rego, B. V., Wells, S. M., Lee, C. H., and Sacks, M. S. (2016). Mitral valve leaflet remodelling during pregnancy: insights into cell-mediated recovery of tissue homeostasis. *J. R. Soc. Interface* 13:20160709. doi: 10.1098/rsif.2016.0709

Rog-Zielinska, E. A., Johnston, C. M., O'Toole, E. T., Morphew, M., Hoenger, A., and Kohl, P. (2016). Electron tomography of rabbit cardiomyocyte three-dimensional ultrastructure. *Prog. Biophys. Mol. Biol.* 121, 77–84. doi: 10.1016/j.pbiomolbio.2016.05.005

Rubart, M., Tao, W., Lu, X.-L., Conway, S. J., Reuter, S. P., Lin, S.-F., et al. (2018). Electrical coupling between ventricular myocytes and myofibroblasts in the infarcted mouse heart. *Cardiovasc. Res.* 114, 389–400. doi: 10.1093/cvr/cvx163

Sanders, R., Myerburg, R. J., Gelband, H., and Bassett, A. L. (1979). Dissimilar length–tension relations of canine ventricular muscle and false tendon: electrophysiologic alterations accompanying deformation. *J. Mol. Cell. Cardiol.* 11, 209–219. doi: 10.1016/0022-2828(79)90465-6

Schindelin, J., Arganda-Carreras, I., Frise, E., Kaynig, V., Longair, M., Pietzsch, T., et al. (2012). Fiji: an open-source platform for biological-image analysis. *Nat. Methods* 9, 676–682. doi: 10.1038/nmeth.2019

Schneider, C. A., Rasband, W. S., and Eliceiri, K. W. (2012). NIH Image to ImageJ: 25 years of image analysis. *Nat. Methods* 9, 671–675. doi: 10.1038/nmeth.2089

Stockbridge, L. L., and French, A. S. (1988). Stretch-activated cation channels in human fibroblasts. *Biophys J.* 54, 187–190. doi: 10.1016/S0006-3495(88)82944-8

Ushiyama, J., and Brooks, C. M. C. (1977). Interaction of oscillators: effect of sinusoidal stretching of the sinoatrial node on nodal rhythm. *J. Electrocardiol.* 10, 39–44. doi: 10.1016/S0022-0736(77)80029-0

Verheijck, E. E., Van Kempen, M. J. A., Veereschild, M., Lurvink, J., Jongsma, H. J., and Bouman, L. N. (2001). Electrophysiological features of the mouse sinoatrial node in relation to connexin distribution. *Cardiovasc. Res.* 52, 40–50. doi: 10.1016/S0008-6363(01)00364-9

Verheijck, E. E., Wessels, A., Van Ginneken, A. C. G., Bourier, J., Markman, M. W. M., Vermeulen, J. L. M., et al. (1998). Distribution of atrial and nodal cells within the rabbit sinoatrial node: Models of sinoatrial transition. *Circulation* 97, 1623–1631. doi: 10.1161/01.CIR.97.16.1623

Conflict of Interest: The authors declare that the research was conducted in the absence of any commercial or financial relationships that could be construed as a potential conflict of interest.

frontiers
in Physiology

ORIGINAL RESEARCH
published: 19 August 2020
doi: 10.3389/fphys.2020.01043

Multiscale Modeling of Cardiovascular Function Predicts That the End-Systolic Pressure Volume Relationship Can Be Targeted via Multiple Therapeutic Strategies

Kenneth S. Campbell[1]*, Brianna Sierra Chrisman[2†] and Stuart G. Campbell[2]

[1] *Division of Cardiovascular Medicine, Department of Physiology, University of Kentucky, Lexington, KY, United States,*
[2] *Department of Biomedical Engineering, Yale University, New Haven, CT, United States*

Edited by:
Gentaro Iribe,
Asahikawa Medical University, Japan

Reviewed by:
Akira Amano,
Ritsumeikan University, Japan
Vicky Y. Wang,
The University of Auckland,
New Zealand

***Correspondence:**
Kenneth S. Campbell
k.s.campbelluk@y.edu

†Present address:
Brianna Sierra Chrisman,
Department of Bioengineering,
Stanford University, Stanford, CA,
United States

Specialty section:
This article was submitted to
Computational Physiology
and Medicine,
a section of the journal
Frontiers in Physiology

Received: *16 November 2019*
Accepted: *29 July 2020*
Published: *19 August 2020*

Citation:
Campbell KS, Chrisman BS and Campbell SG (2020) Multiscale Modeling of Cardiovascular Function Predicts That the End-Systolic Pressure Volume Relationship Can Be Targeted via Multiple Therapeutic Strategies. Front. Physiol. 11:1043. doi: 10.3389/fphys.2020.01043

Most patients who develop heart failure are unable to elevate their cardiac output on demand due to impaired contractility and/or reduced ventricular filling. Despite decades of research, few effective therapies for heart failure have been developed. In part, this may reflect the difficulty of predicting how perturbations to molecular-level mechanisms that are induced by drugs will scale up to modulate system-level properties such as blood pressure. Computer modeling might help with this process and thereby accelerate the development of better therapies for heart failure. This manuscript presents a new multiscale model that uses a single contractile element to drive an idealized ventricle that pumps blood around a closed circulation. The contractile element was formed by linking an existing model of dynamically coupled myofilaments with a well-established model of myocyte electrophysiology. The resulting framework spans from molecular-level events (including opening of ion channels and transitions between different myosin states) to properties such as ejection fraction that can be measured in patients. Initial calculations showed that the model reproduces many aspects of normal cardiovascular physiology including, for example, pressure-volume loops. Subsequent sensitivity tests then quantified how each model parameter influenced a range of system level properties. The first key finding was that the End Systolic Pressure Volume Relationship, a classic index of cardiac contractility, was ~50% more sensitive to parameter changes than any other system-level property. The second important result was that parameters that primarily affect ventricular filling, such as passive stiffness and Ca^{2+} reuptake via sarco/endoplasmic reticulum Ca^{2+}-ATPase (SERCA), also have a major impact on systolic properties including stroke work, myosin ATPase, and maximum ventricular pressure. These results reinforce the impact of diastolic function on ventricular performance and identify the End Systolic Pressure Volume Relationship as a particularly sensitive system-level property that can be targeted using multiple therapeutic strategies.

Keywords: cardiac function, computer modeling, Frank-Starling, multiscale modeling, ventricular function

INTRODUCTION

Diseases caused by reduced or dysregulated contractile function are a major clinical problem. About half of the 6 million Americans who have heart failure, for example, exhibit depressed contractile function (Benjamin et al., 2018). Another 700,000 Americans have inherited genetic mutations that have been linked to myopathies (Watkins et al., 2011; Houston and Stevens, 2014). Treatment options for most of these patients remain limited. For example, the clinical guidelines for heart failure (Writing Committee et al., 2013) recommend standardized therapies (primarily β-blockers and ACE inhibitors) that were developed > 30 years ago and produce a 5-year survival rate of only 50% (Benjamin et al., 2018). Given these facts, there is a pressing need to leverage the field's ever-increasing knowledge of molecular and cellular-level processes to enhance clinical care.

Multiscaled computer modeling could accelerate this process. Indeed, a recent paper (Campbell et al., 2019) outlined a potential approach that creates patient-specific computer models that integrate genomic, proteomic, imaging, and functional data and then runs the models forward in time to predict how each patient will respond to possible therapeutic interventions. The authors went on to describe a moonshot goal of running a clinical trial to test whether implementing the model-optimized therapy helps patients more than the current standard of care. While this sort of endeavor still seems some way in the future, it captures the possible long-term impact of patient-focused modeling.

The current work describes one step in the development of multiscale models of cardiovascular function and builds on extensive prior work by many other groups including but not restricted to papers by Negroni and Lascano (1996), Shim et al. (2004), and Pironet et al. (2013). Specifically, the framework described here was constructed by linking the MyoSim model of dynamically-coupled myofilaments (Campbell et al., 2018) with the sophisticated model of myocyte electrophysiology developed by ten Tusscher et al. (2004). This created a contractile system that was based on molecular-level events (including opening of ion channels and transitions between different myosin states) that could be manipulated via numerical parameters. To the authors' knowledge, the current model is the first to simulate blood circulation using a myofilament system that incorporates transitions between the OFF and ON states of myosin (Irving, 2017). Since these transitions contribute to length-dependent Ca^{2+}-activation (Ait-Mou et al., 2016; Kampourakis et al., 2016; Zhang et al., 2017), the current model can help to improve understanding of ventricular function.

Organ-level function was simulated using the technique described by Shin et al. (Shim et al., 2004) and Campbell et al. (2008) which approximates the left ventricle as a hemisphere. In this approach, the volume of the ventricle is related to the length of a contractile element embedded circumferentially in the mid-transmural wall, while the chamber pressure is deduced from the stress in the contractile element via Laplaces's law. The circulatory system was modeled using zero-dimensional (lumped parameter) compartments (Shi et al., 2011) representing the aorta, arteries, arterioles, capillaries, and veins. Flows between the different compartments were defined by Ohm's law with one-way valves controlling the movement of blood into and out of the ventricle.

The model spans from molecular-level events to system-level properties but remains simple enough to run on a laptop. The code is open-source and available for free and unrestricted download. The results described in the following pages include sensitivity analyses that demonstrate how modulation of cell and molecular-level processes scale up to impact system-level properties. Some metrics (particularly the End Systolic Pressure Volume Relationship, ESPVR) were predicted to be particularly sensitive to molecular-level interventions while others (for example, stroke volume) were harder to modulate. These types of insights may prove useful as scientists try to translate their research toward improved clinical care.

MATERIALS AND METHODS

Electrophysiological Model

Ten Tusscher et al.'s model of the electrophysiology of a mid-myocardial human myocyte (ten Tusscher et al., 2004) was downloaded as Python source code from CellML.org (Lloyd et al., 2008). The model was based on nine channels, four pumps, and two exchangers and has 17 state variables and 46 numerical parameters. Most of the parameters were kept fixed at the published values but the code was modified to allow adjustments to the following parameters: Ca V_{leak}, Ca V_{max_up}, g_{CaL} (all related to a calcium dynamics), g_{to} (transient outward current), g_{Kr} (rapid time-dependent potassium current), and g_{Ks} (slow time-dependent potassium current).

When paced at 1 Hz with 3 ms pulses of stimulus current (−52 pA pF^{-1}), the base model took several hundred heart-beats to reach steady-state. The simulations presented in this work were initiated using the steady-state solution which was obtained by pre-calculating 1000 consecutive heart-beats.

MyoSim

The mechanical properties of dynamically-coupled myofilaments were simulated using the MyoSim framework (Campbell, 2014). As shown in **Supplementary Figure S1**, binding sites on the thin filaments were activated by Ca^{2+}. Cross-bridges transitioned between an OFF (also called super-relaxed, or interacting heads motif) state (Alamo et al., 2008; Hooijman et al., 2011; Nag et al., 2017), an ON state (that could attach to actin), and a single bound force-generating state. The bound heads contributed to cooperative activation of the thin filament. The rate of the OFF to ON transition increased linearly with force. As recently described by Campbell et al. (2018), this allows the model to exhibit length-dependent activation and reproduce the timing and magnitude of isometric twitch contractions measured at different sarcomere lengths (Campbell, 2011).

Additional details relating to the MyoSim model are provided in **Supplementary Information**.

Ventricle

The ventricle was idealized as a single hemisphere characterized by a chamber volume $V_{ventricle}$, a slack volume V_{slack} (when the passive stress in the MyoSim model was zero), a wall volume W_{volume}, and an internal radius r. The wall thickness $W_{thickness}$ was calculated as W_{volume} / (2 π r^2) with r defined as:

$$r \quad = \quad \left(\frac{3\ V_{ventricle}}{2\ \pi}\right)^{1/3} \tag{1}$$

The pressure $P_{ventricle}$ inside the ventricle was deduced from Laplace's law as:

$$P_{ventricle} \quad = \quad \frac{2\ S\ W_{thickness}}{r} \tag{2}$$

where S was the wall stress calculated by the MyoSim model.

Circulation

The systemic circulation was modeled using zero-dimensional compartments representing the aorta, arteries, arterioles, capillaries, and veins. Each compartment had a compliance C_x and a resistance R_x where x indicated the specific compartment. The pressure P_x in each compartment was calculated as $P_x = V_x/C_x$ where V_x is the compartment volume.

Ohm's law was used to calculate the blood flow into and out of each compartment. The relevant formulae are included as Eqs (S11) and (S12) in **Supplementary Information**.

Model Parameters

Base values for the parameters used in the simulations are shown in **Supplementary Table S1**. In contrast to many of the authors' prior publications, no attempt was made to constrain the parameters using new experimental data. Instead, parameters were set to plausible values based on prior experience and typical values for a human. For example, the total blood volume V_{total} was fixed at 5 liters.

Computer Code

Simulations were performed using code written in Python with non-trivial calculations performed using functions from the Numpy (van der Walt et al., 2011) and Scipy (Jones et al., 2001) libraries. Source code and documentation are available online at https://campbell-muscle-lab.github.io/PyMyoVent/. Simulations implemented with 1 ms time-steps ran in near real-time on a typical PC core. The electrophysiology model was the slowest part of the algorithm.

RESULTS

Figure 1 summarizes the multiscale model of the human cardiovascular system that was developed for this work. Heartbeats were initiated at 1 Hz by applying a pacing stimulus to a model published by ten Tusscher et al. (2004) that simulates the electrophysiology of a human mid-myocardial cell. At each time-step, the free intracellular Ca^{2+} concentration predicted by the electrophysiological model was passed to a MyoSim model of sarcomere level-contraction (Campbell, 2014; Campbell et al., 2018). The contraction model was coupled to a ventricle that was idealized as a hemisphere (Campbell et al., 2008). This approximation allowed the pressure and volume in the ventricle to be calculated from the contractile element's force per unit area and length. The ventricle was in turn coupled to a circulation

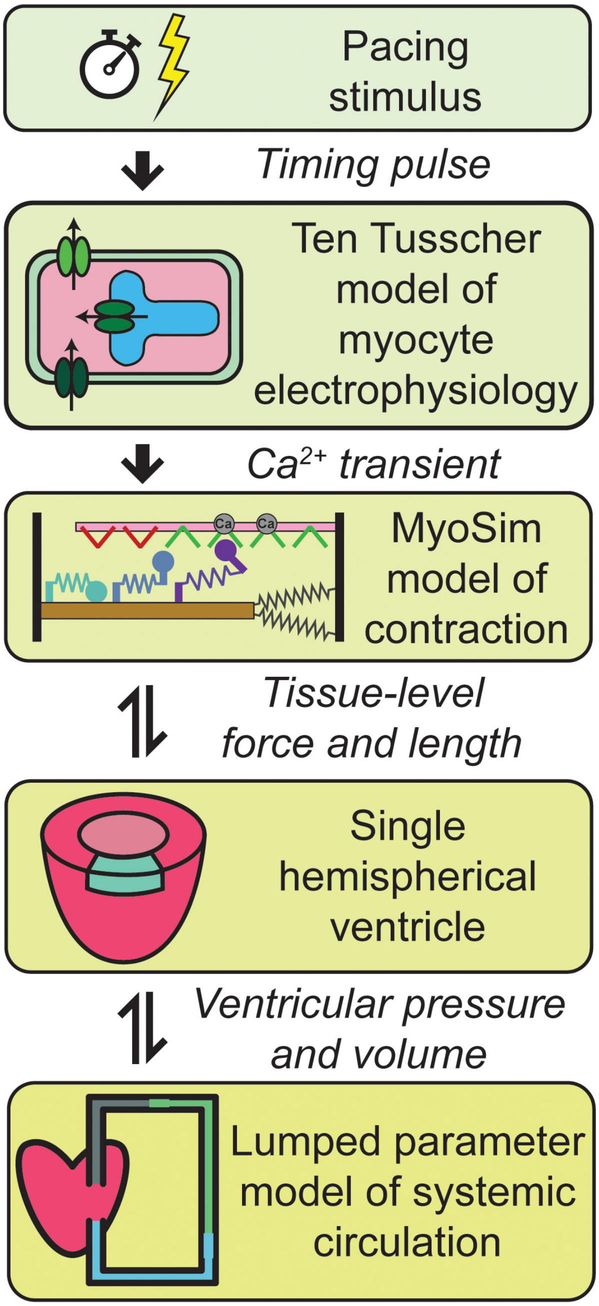

FIGURE 1 | Overview of the multiscale model of cardiovascular physiology. Ca^{2+} transients simulated using a well-established model of the electrophysiology of a human cell (ten Tusscher et al., 2004) drove a contractile model implemented using MyoSim (Campbell, 2014; Campbell et al., 2018). The pressure and volume in the hemispherical ventricle were calculated from the contractile element's force per unit area and length. The ventricle pumped blood through a systemic circulation that was mimicked using zero dimensional compartments. Additional details are provided in section "Materials and Methods."

that was mimicked using lumped parameters and valves that controlled the flow of blood into and out of the heart.

Additional details about each level of the model are provided in section "Materials and Methods."

Base Simulation

Figure 2 shows a simulation of 17 heart beats performed using the base parameters listed in **Supplementary Table S1**. The calculations were started with the ventricle filled to 150% of its slack volume and the remainder of the blood in the venous compartment. Heart beats were initiated once per second by activating a 3 ms pulse of stimulus current (-52 pA pF^{-1}) in the electrophysiological model.

Each Ca^{2+} transient activated thin filaments in the contractile model. This allowed myosin heads to transition into the force-generating state, thereby raising wall stress and ventricular pressure (Eq. 2). Once the ventricular pressure exceeded aortic pressure, blood was pumped into the aorta, and subsequently through the other circulatory components, with inter-compartmental flow rates defined by Ohm's law (Eq. S12 in **Supplementary Information**). The ventricle relaxed when the intracellular Ca^{2+} concentration declined and ventricular pressure dropped below that in the aorta. Once ventricular pressure fell below venous pressure, blood flowed back into the heart, re-stretching the ventricle and extending the contractile element.

The simulation evolved toward a steady-state as blood moved through the circulation to fill the arterial, arteriolar, capillary, and venous compartments. This required approximately seven beats with the base parameters. A volume perturbation was imposed during the second half of the simulation (**Figure 2**, double-headed arrow) to determine how the ventricle responded to reduced pre-load (ventricular filling).

Figure 3 illustrates the steady-state behavior of the system on an expanded time-scale. The heart beat was initiated by the activation pulse which triggered an action potential and an intracellular Ca^{2+} transient. N_{on} rose sharply as the thin filament was activated by the Ca^{2+} signal (see **Supplementary Figure S1** and additional details in **Supplementary Information**). This allowed some of the myosin heads in the M_{ON} state to transition into the M_{FG} state. The force developed by the attached cross-bridges accelerated the J_1 transition and pulled additional heads from M_{OFF} to M_{ON} and subsequently to M_{FG} via a positive-feedback loop that was modulated by thin filament cooperativity and force-dependent recruitment (Campbell et al., 2018). Ventricular pressure scaled with the force generated by the cross-bridges and increased quickly while the chamber remained isovolumic.

Once ventricular pressure exceeded aortic pressure, blood was pumped into the aorta, and the contractile element shortened as the ventricle started to contract. The shortening reduced the force generated by attached cross-bridges and the M_{OFF} state started to repopulate. Although half-sarcomere force decreased by ∼50% during ejection, ventricular pressure remained elevated due to the diminishing internal radius of the chamber (Eq. 2).

The final stages of relaxation progressed under isometric conditions as the thin filament deactivated and myosin heads that detached from the M_{FG} state were no longer able to re-bind to available sites.

End Systolic Pressure Volume Relationship

Figure 4 shows pressure-volume loops (ventricular pressure plotted against ventricular volume) for beats 10–15 of the simulation shown in **Figure 2**. Blood was being removed from the venous compartment during this phase of the simulation so the pressure-volume loops showed a progressive trend toward lower pressure and lower volume. The End Systolic Pressure Volume Relationship (ESPVR, an index of cardiac contractility) was calculated as the slope of a regression line fitted to the top left corner of each loop. In this example, the ESPVR was 1170 mm Hg liter^{-1}.

Sensitivity Analysis

Figure 5 shows how 12 system-level properties varied as the k_1 parameter was adjusted from 0.1 to 10 times the base value shown in **Supplementary Table S1**. Steady-state beats and single-beat estimates of the ESPVR for three of the k_1 parameter values are shown in **Supplementary Figures S2, S3**. Although the limits are somewhat arbitrary, the 0.1 to 10x range is probably large enough to encompass the functional effects that could be achieved through pharmaceutical modulation of the molecular transition. The red lines in each panel show the best-fit of a 5th order polynomial to the simulated data. The slope of each polynomial was evaluated at the base parameter value and normalized to the corresponding y value to produce relative sensitivity metrics that defined how each system-level property varied with small adjustments in k_1. For example, the relative sensitivity metric was $+0.49$ for maximum ventricular pressure (because it increased with small increases in k_1 near the base value, **Figure 5A**) but -0.17 for minimum ventricular pressure (because this property decreased as k_1 was increased, **Figure 5B**).

Note that the sensitivity metric only quantifies the effect of small changes in the model parameter. Larger changes often produced more complex effects that, in many cases, resulted in non-physiological behavior. For example, maximum ventricular pressure initially increased as k_1 was elevated above its base value because the OFF/ON thick filament equilibrium was shifted toward the ON state. This corresponds to increased cardiac contractility. However, if k_1 was increased by more than a factor of ∼3, the active contraction became so strong that the ventricle ejected most of its contents into the circulation and shrank down to a small volume. Cardiac output thus decreased to a non-physiological extent if contractility increased beyond a certain point. This effect is illustrated in **Supplementary Figure S4**.

Calculations summarizing the effects of adjusting other model parameters are shown in **Supplementary Figures S5–S34**. Note that each parameter was scaled from 0.1 to 10 times its base value in order to maintain a fixed proportional change. Non-monotonic relationships between model parameters and system-level properties (similar to the relationship between k_1 and stroke volume described above) were observed frequently.

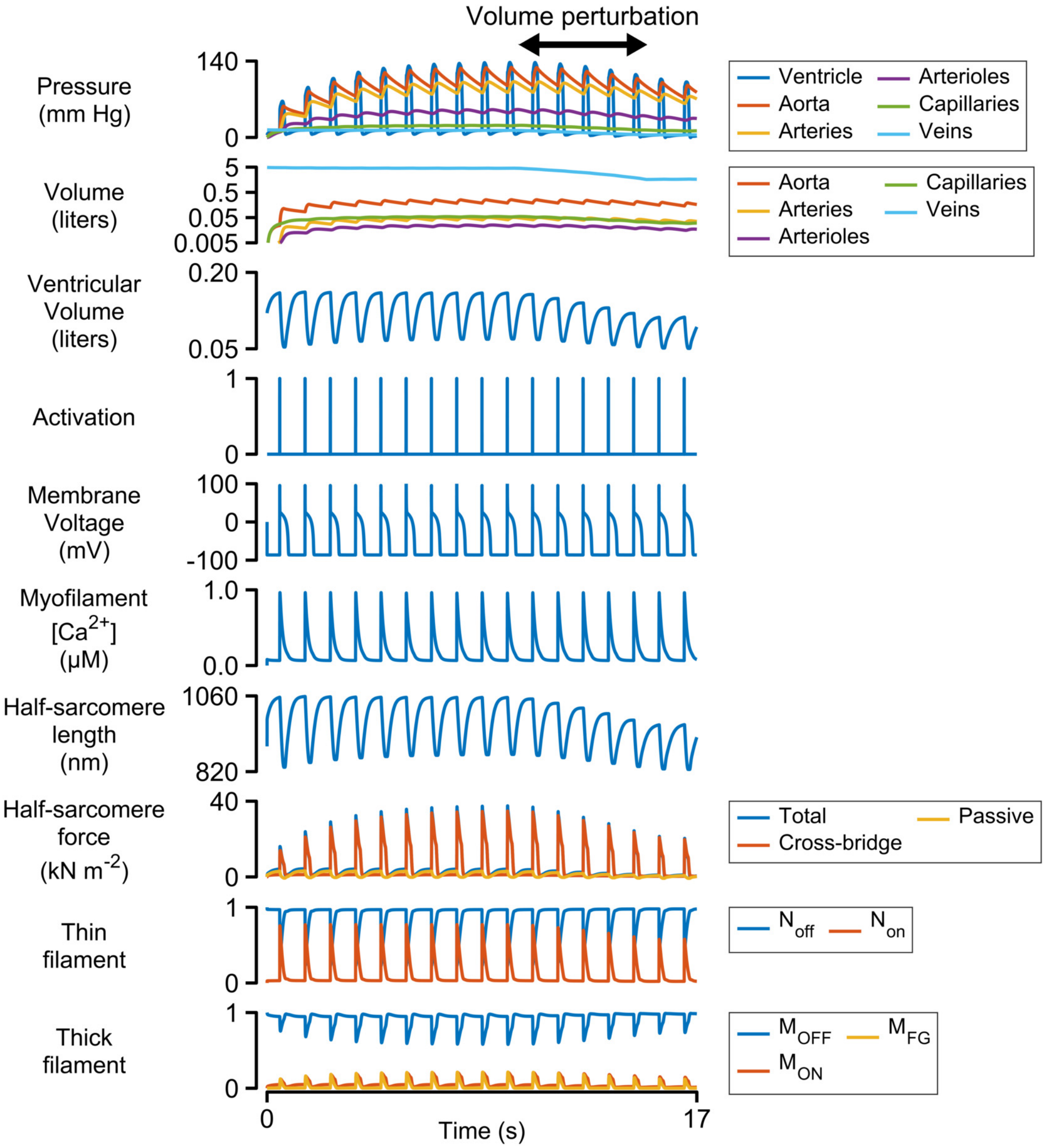

FIGURE 2 | Multiscale simulation of 17 heart-beats. The simulation took about seven beats to reach steady-state as blood was pumped through the systemic circulation. The blood volume was reduced by 60% between the 10th and 15th beats to determine how the ventricle responded to reduced pre-load. The panel showing the volumes of the circulatory compartments is plotted on a log scale. All other panels are plotted with linear scales.

Alternative strategies, including spline interpolation, could have been used to deduce sensitivity metrics but 5th order polynomials were chosen because they produced satisfactory fits to the simulated data and the calculations were straightforward to implement.

Figure 6 shows the sensitivity metrics for every combination of system-level property and model parameter as a heat-map. The first key finding from this analysis is shown by the gray bars above the matrix. These are arranged in order of size and represent the mean value of the absolute relative sensitivities for each system-level property (The absolute term prevents positive and negative relative sensitivities from canceling out). The highest bar, and thus the most sensitive property, was the ESPVR which had a mean absolute relative sensitivity of 0.52. The next most sensitive property was stroke work with a mean value of 0.35. One implication is that perturbing a randomly-chosen model parameter is likely to change the ESPVR at least 50% more than any other system-level property.

A second key finding is that both systolic and diastolic properties were sensitive to ventricular filling. The gray bars to the right of the heat-map show the mean of the absolute sensitivities for each model parameter. The bars are separated into three groups corresponding to the sarcomeric, electrophysiological, and circulatory levels of the model. The most sensitive parameters in each group were L (the length constant for the passive tension curve, equation S9), Ca

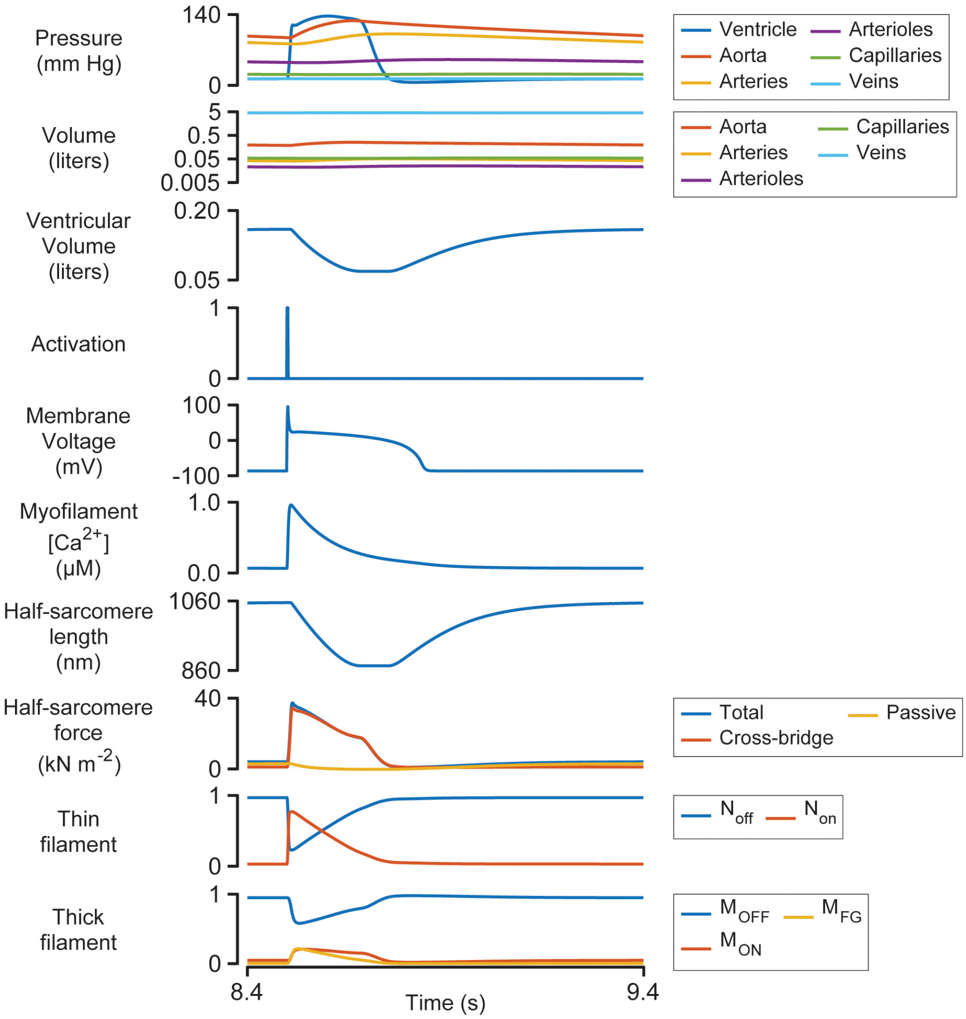

FIGURE 3 | Multiscale simulation of a heart-beat at steady-state. The figure shows the 8th beat from **Figure 2** on an expanded time-scale.

V_{maxup} (a parameter that controls how quickly Ca^{2+} is pumped into the sarcoplasmic reticulum), and V_{slack} (the volume at which passive wall stress in the ventricle is zero). Although these parameters are most obviously related to diastolic function, the sensitivity metrics show that they also influenced systolic properties. For example, all three parameters had a strong impact on ESPVR, stroke work, and minimum ventricular volume. These findings reinforce the impact of diastolic function on ventricular performance and could be interpreted as a molecular-level correlate of the Frank-Starling mechanism.

DISCUSSION

This work presents a computer model that bridges from molecular-level mechanisms (for example, opening of ion channels) to system-level cardiovascular properties (for example, blood pressure) that are measured in patients. The approach helps narrow the wide gap that currently separates myocyte biophysics from clinical cardiology and might have the potential to help accelerate translational research. For example, **Figure 6** illustrates how sensitivity analysis can be used to identify molecular-level interventions that have a particularly large impact on cardiovascular function. Similar calculations, perhaps based on more sophisticated models, might prove useful for *in silico* screens designed to identify potential therapeutic targets (Campbell et al., 2019).

Alternative Strategies for Sensitivity Analysis

The sensitivity metrics used in this work quantified the relationship between individual molecular-level parameters and a suite of system-level properties. This approach was selected because many of the molecular parameters in the model can targeted *in vivo* using current and/or potential future pharmaceutical interventions. Other mathematical approaches are possible. For example, Sobel analysis is a variance-based

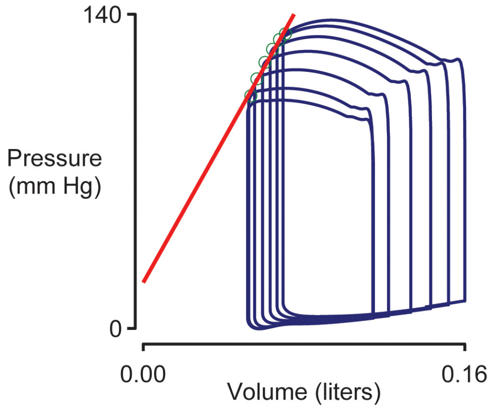

FIGURE 4 | Simulated pressure volume loops and the End Systolic Pressure Volume Relationship (ESPVR). Ventricular pressure plotted against ventricular volume for beats 10–15 of the simulation shown in **Figure 2**. The ESPVR was calculated as the slope of a regression line (shown in red) fitted to the top-left corner (green circles) of each pressure-volume loop.

sensitivity method that can quantify the effects of combinations of parameters (Sobol, 1993). It can therefore test for interactions between system inputs (Wenk, 2011).

Another option is to test how system-level function depends on chamber-level properties. For example, as shown in Eq. (S9), the passive wall stress at a given half-sarcomere length depends on three molecular-level parameters: σ (a scaling factor), L_{slack} (the half-sarcomere length at zero passive stress), and L (a parameter that defines the curvature of the passive length-tension relationship). **Supplementary Figure S35** shows how system-level properties varied as σ and L were adjusted simultaneously so that passive stress at a given half-sarcomere length was held constant. Essentially, this presentation shows how the system is influenced by the non-linear stiffness of the ventricle. Accordingly, this type of analysis might be useful for scientists and clinicians who think primarily about chamber properties rather than biophysical parameters. It could also be extended to quantify the effects of association constants (for example, k_1/k_2, Eqs S3 and S4) rather than the individual parameters.

Physiological Insights

Figure 6 showed that the End Systolic Pressure Volume Relationship (ESPVR) was ∼50% more sensitive to the model parameters than any other system-level property. Indeed, the absolute values of the ESPVR sensitivities exceeded 0.3 for 10 of the 12 sarcomere-level parameters. The sensitivities were positive for k_3, k_{cb}, k_{force}, k_1, k_{on}, and σ, and negative for L, k_{off}, and $k_{4,0}$ (see **Supplementary Information** for additional details about the mechanisms controlled by each parameter). These are important findings because the ESPVR is a classic measure of cardiac contractility and frequently depressed in patients who have heart failure (Parmley, 1985).

One interpretation of these results is that contractility is reduced in heart failure precisely because the EPSVR is impacted by so many mechanisms. A subtle deficit in nearly any aspect of sarcomere-level function could compromise contractility, with the ESPVR's high sensitivity to molecular-level function compounding the system-level problem.

An alternative, more optimistic, interpretation is that contractility can be rescued using multiple therapeutic strategies. Consider a hypothetical patient who develops heart failure because they have inherited a mutation that reduces the rate of cross-bridge binding (k_3, Eq. S5 in **Supplementary Information**). This individual could potentially be treated with a small molecule, such as omecamtiv mecarbil, that accelerates the transition and reverses the original deficit (Malik et al., 2011; Swenson et al., 2017). If this approach failed, perhaps because the mutation also altered the drug's binding pocket, **Figure 6** suggests that alternative treatment strategies could include: enhancing force-dependent recruitment (k_{force}), increasing titin-based stiffness (σ), reducing the thin filament off rate (k_{off}) and/or slowing myosin detachment ($k_{4,0}$). While the ultimate goal is, of course, to develop computer models that are specific to individual patients, even the simple analyses described here might help clinicians to weigh options in cases that are particularly challenging.

Additional physiological insights can be gained by viewing the relationships between sensitivity metrics. For example, the metrics for stroke work and stroke volume (equivalent to cardiac output in this work since heart rate was fixed) are correlated: parameter modifications that increased one, also increased the other. Unfortunately, the mean absolute relative sensitivity for stroke work was 0.35, almost double the corresponding value for stroke volume. This implies that it could be difficult to enhance cardiac output in patients without a greater than proportional change in metabolic cost. Again, this could be problematic for patients who have heart failure and who already struggling to maintain adequate circulation.

The parameter sweeps (**Figure 5** and **Supplementary Figures S5–S34**) summarize large amounts of data but the results for L (**Supplementary Figure S5**) are particularly note-worthy. This parameter controls the curvature of the passive length tension relationship (Eq. S9) and had a particularly strong effect on most system-level properties. As noted earlier, the high mean absolute relative sensitivity of L reinforces the importance of diastolic function for ventricular performance. The additional point made here is that ventricular efficiency exhibited a clear optimum near L's base parameter value (**Supplementary Figure S5I**). Ventricles with smaller values of L (stiffer chambers) or larger values (more compliant chambers) used greater amounts of ATP to perform a given amount of work.

The main sources of passive tension in myocardium are collagen, titin, microtubules, and intermediate filaments but titin is probably the most important component at physiological sarcomere lengths (Granzier and Irving, 1995). Titin's stiffness can be modulated by multiple post-translational mechanisms (Hidalgo and Granzier, 2013) and the relative expression of its isoforms changes with disease (Nagueh et al., 2004). Perhaps the relationship between titin's stiffness and ventricular efficiency is one of the driving forces underpinning these complex regulatory effects?

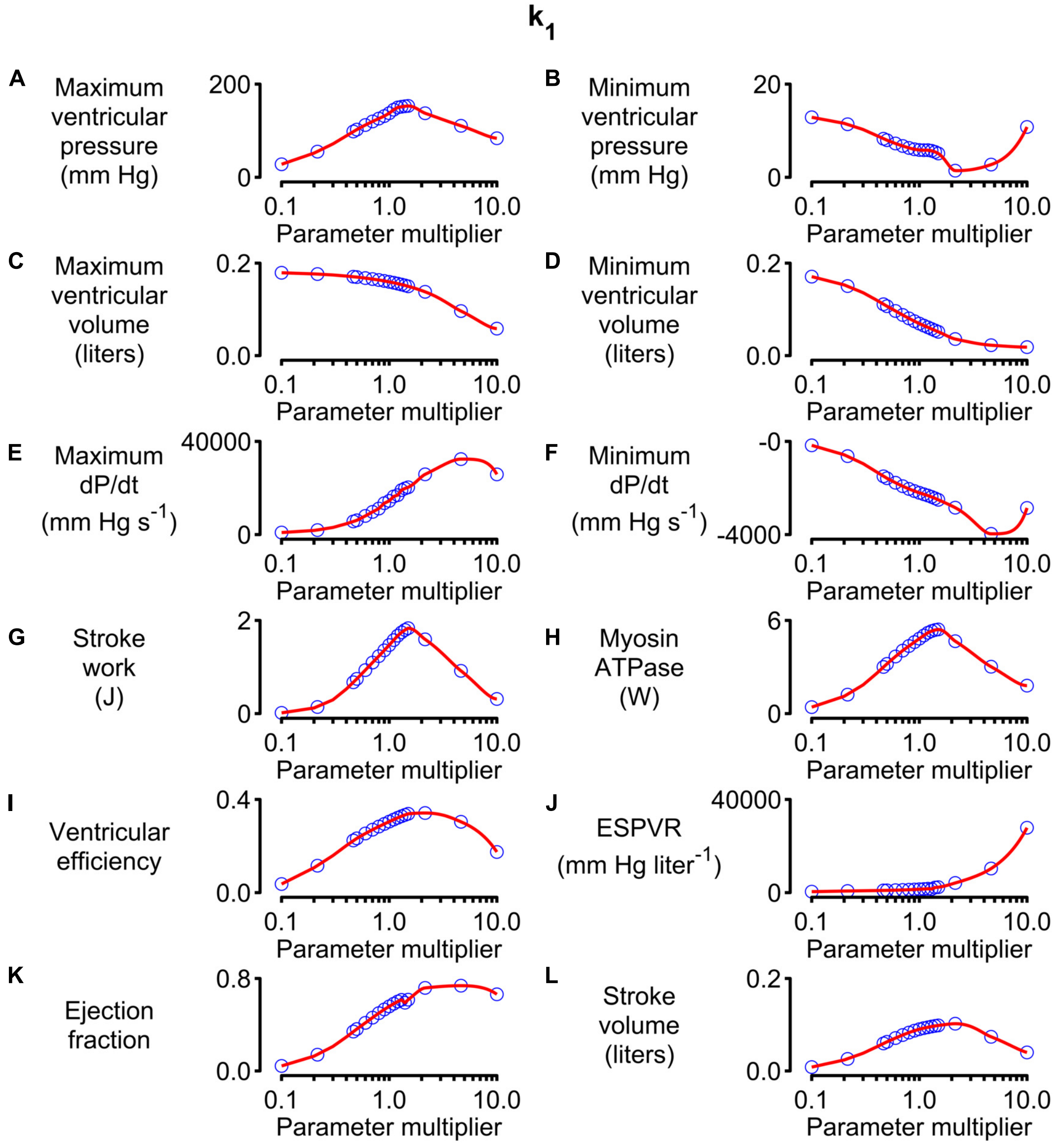

FIGURE 5 | Effects of changing k_1 on system-level properties. **(A–L)** Show values (blue circles) for 12 system-level properties (for example, maximum ventricular pressure) predicted for values of k_1 ranging from 0.1 to 10 times the value shown in **Supplementary Table S1**. The red lines show the best-fit of a 5th order polynomial to the simulated data. The relative sensitivity for each property was defined as the slope of the polynomial at the base parameter value (that is, when the multiplier was 1) divided by the corresponding y value. The division normalized the slope to facilitate comparisons between different properties.

Another parameter that deserves comment is k_1. As shown in Eq. (S3) in **Supplementary Information**, this parameter modulates the rate at which myosin heads transition from the OFF to the ON state. Since only heads in the ON state can attach to actin, k_1 has a strong influence on contractility. This is evident from the parameter sensitivities shown in **Figure 6** and the simulations shown in **Supplementary Figures S2, S3**. The last of these figures shows single-beat estimates of the ESPVR determined using the curve-fitting method described by Mirsky et al. (1987). These simulations suggest that the ESPVR increases by a factor of 2.65 as k_1 is increased from 1 to 3 s^{-1}. OFF / ON transitions in striated muscle are currently a very exciting area of research and are thought to be regulated by myosin-binding protein-C (McNamara et al., 2016) as well as being an important therapeutic target (Anderson et al., 2018). It may be useful to note that the MyoSim framework has also been used to investigate how phosphorylation of regulatory light chain accelerates the ON transition in cardiac trabeculae from rodents and thereby increases Ca^{2+} sensitivity (Kampourakis et al., 2016; Campbell et al., 2018). In the current simulations, this could be modeled as a phosphorylation dependent change in the k_1 parameter.

The final physiological insight described here relates to stroke volume. The parameter sweeps show that this system-level property has a clear optimum for about 50% of the

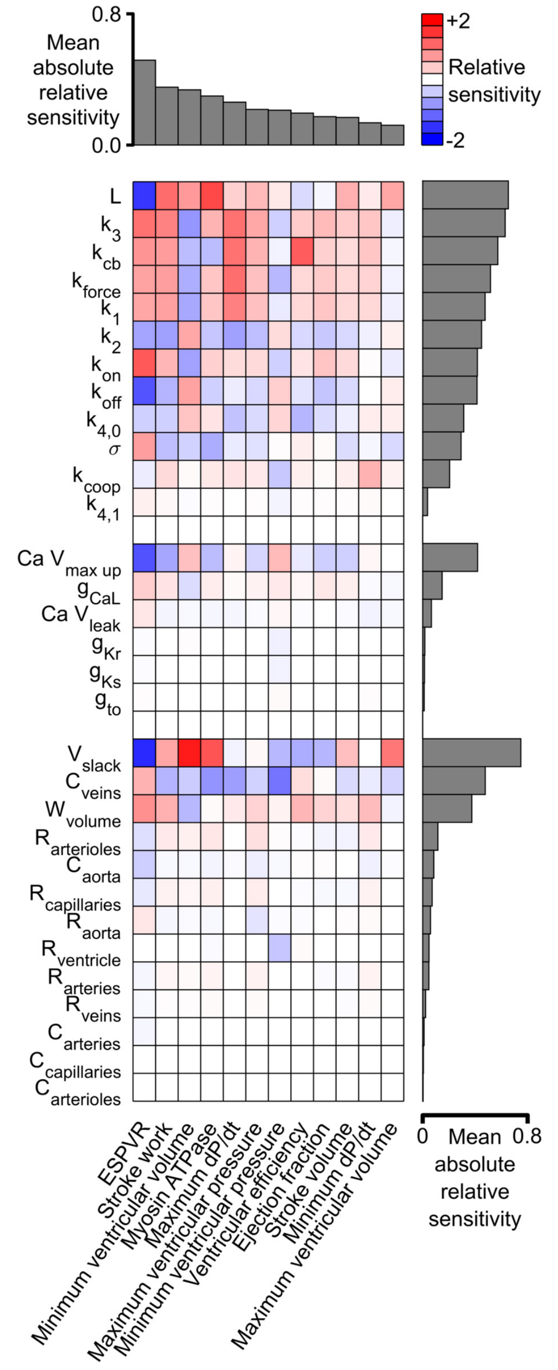

FIGURE 6 | Relative sensitivities for each combination of system-level property and model parameter. Red colors show property / parameter combinations that were positively correlated for small changes in the base parameter value. For example, stroke work, minimum ventricular pressure, and myosin ATPase all increased as L became larger (red boxes in columns 2–4 of the top row and **Supplementary Figure S5**). Blue colors show negative correlations. For example, ESPVR decreased as L became larger (blue box in column 1 of top row). The gray bars above the matrix show the mean of the absolute relative sensitivity values for each system-level property. The bars on the right show the corresponding means for each model parameter. The model parameters are clustered in three groups corresponding to the sarcomeric, electrophysiological, and circulatory levels of the model.

model parameters (including, for example, k_1, **Figure 5**, and k_{on}, **Supplementary Figure S11**). The optimum reflects the fact that weak contractions do not pump much blood while contractions that are excessively strong squeeze the ventricle dry (**Supplementary Figure S4**). Contractility seems to be a situation where you really can have too much of a good thing!

Limitations

Despite its strengths, the current model has several limitations. These include: (1) the single ventricle framework, (2) the omission of ventricular geometry and torsional effects, (3) the absence of autonomic control, and (4) the one-way coupling of the electrophysiological and contractile modules. These issues are considered in more detail in the following paragraphs.

The single ventricle framework is probably the most obvious limitation of the current model. Human hearts have two ventricles, with the left chamber pumping blood through the systemic circulation to the right side of the heart, and the right ventricle pumping blood through the pulmonary circulation to complete the circuit. Averaged over time, the flows through the systemic and pulmonary systems must be equal. However, perturbations such as a change in posture or a Valsalva maneuver, produce short-term differences in left and right ventricular output. Similarly, clinical conditions that initially effect one ventricle (for example, pulmonary hypertension) can induce long-term remodeling in the other ventricle (Vonk Noordegraaf et al., 2017). It's clearly impossible to study these types of effects with a single ventricle framework.

Lumens et al. (2009) developed the TriSeg model to overcome this issue. The approach developed by these authors is conceptually similar to the single ventricle framework presented here but uses a more sophisticated geometry. Specifically, the TriSeg model simulates a biventricular heart using three contractile elements, one in the left ventricular free wall, one in the right ventricular free wall, and one in the septum. This allows simulation of complex organ-level effects including interactions between the left and right ventricles and septal geometry dynamics. One disadvantage of Lumens et al.'s original implementation was that contractile forces were calculated using a heuristic approach, that is, from equations that linked myofiber strain and force but were not based on a molecular-level model.

More recent calculations using the TriSeg framework performed by Tewari et al. (2016) replaced the heuristic equations with a sophisticated cross-bridge model and added in an additional model of myocardial metabolism. However, Tewari et al.'s contractions were driven with experimentally-recorded Ca^{2+} transients rather than with an electrophysiological model as in this manuscript. This data-driven simulation approach is very useful because it eliminates potential uncertainties associated with the electrophysiological model. A drawback is that it makes it difficult to investigate how electrophysiological changes influence system-level behavior. For example, Tewari et al.'s model can't predict how SERCA activity influences function (**Supplementary Figure S16**) because the simulations don't include this level of molecular detail. An exciting next step would be to combine the strengths of the different frameworks and create a TriSeg model that integrates models of electrophysiology, metabolism, and contraction.

The second limitation relates to ventricular geometry. The current framework idealizes the ventricle as a thin-walled hemisphere. This is useful because it allows the ventricular volume and pressure to be calculated from the chamber's circumference and wall-stress. However, the simplification completely neglects many important features. For example, the current framework cannot reproduce cardiac torsion, the complex twisting motion of the heart (Russel et al., 2009). Nor can the model incorporate transmural (Haynes et al., 2014) or potential base to apex variation (Sharma et al., 2003) in contractile properties and fiber alignment (Streeter et al., 1969). Since the ventricle is mimicked as a hemisphere, it is also impossible to simulate the patient-specific geometries required for personalized simulations. This may be particularly limiting for studies focused on hypertrophic cardiomyopathy. This clinical condition frequently reflects a sarcomeric gene mutation and is often associated with region-specific growth, most commonly involving the basal interventricular septum (Marian and Braunwald, 2017).

The best way to simulate regional and architectural effects is to implement a finite element model. This approach deconstructs the entire heart into small interconnected blocks (the elements), calculates the physical properties (stress and dimensions) of each element, and then uses applied mathematics to integrate the block-level data to infer global function (Guccione et al., 1995). Cardiac finite element modeling is a highly evolved field and multiple groups have used the technique to investigate complex behaviors including transmural variation (Wang et al., 2016), torsion (Bagnoli et al., 2011), and regional growth (Klepach et al., 2012; Lee et al., 2016). Although many cardiac finite element models are based on phenomenological contraction laws, two recent publications have used the MyoSim model to simulate the contractile properties of each element. (Zhang et al., 2018; Mann et al., 2020). The main disadvantage of the approach is that the calculations are very involved. As a result, finite element simulations are typically run on a dedicated computer cluster and typically require hours to complete. This differentiates the technique from the current model which is simple enough to run in near real-time on a laptop.

One of the disadvantages of using the current model to screen potential therapeutic strategies is that the calculations assume that the heart is otherwise unperturbed and continues to beat once per second. A real heart would obviously be subject to autonomic control. Although beyond the scope of this work, it will be possible to reproduce autonomic control in future research by implementing a virtual baroreceptor (Kosinski et al., 2018). This could be done by monitoring the arterial blood pressure predicted by the model and adjusting the heart-rate in order to maintain pressure within pre-set limits. This chronotropic mechanism might be enough to maintain homeostasis during small perturbations but, as in the case of real hearts, additional changes in contractility would probably be required during large perturbations. These could be implemented by, for example, modulating the L-type Ca^{2+} current in the electrophysiological model (Bodi et al., 2005) or accelerating the J_1 transition (**Supplementary Figure S1**) to mimic the effects of increased phosphorylation of regulatory light chain (Kampourakis et al., 2016).

The final limitation that will be discussed is the one-way coupling of the electrophysiological and contractile models. As shown in **Figure 1**, the current framework uses ten Tusscher et al.'s electrophysiological model to predict the Ca^{2+} concentration in the myofibrillar space. More succinctly, the electrophysiology drives the contraction. Although this approach is practical, powerful, and nearly universal in current contractile modeling, it overlooks experimental data that show that quick length changes can perturb the intracellular Ca^{2+} concentration (Wakayama et al., 2001; Ter Keurs et al., 2006; Ter Keurs and Boyden, 2007). These experimental results imply that the contractile system can influence a cell's electrophysiological status (presumably through variable buffering of Ca^{2+} ions by troponin) as well as the other way around. Again, this limitation could be corrected by re-writing the computer code so that the differential equations defining the electrophysiology were solved at the same time as the equations governing the contractile system. In practice, this would be a significant technical undertaking, and again beyond the scope of the current work.

DATA AVAILABILITY STATEMENT

All datasets generated for this study are included in the article/**Supplementary Material**.

AUTHOR CONTRIBUTIONS

KC planned the project, developed the computer software, and wrote the manuscript. BC developed the first prototype of the software and edited the manuscript. SC planned the project and edited the manuscript. All authors contributed to the article and approved the submitted version.

FUNDING

KC acknowledged support from the National Institutes of Health Grant Nos. TR033173, HL133359, and HL146676. SC acknowledged support from the National Institutes of Health Grant No. HL136590.

SUPPLEMENTARY MATERIAL

The Supplementary Material for this article can be found online at: https://www.frontiersin.org/articles/10.3389/fphys.2020.01043/full#supplementary-material

REFERENCES

Ait-Mou, Y., Hsu, K., Farman, G. P., Kumar, M., Greaser, M. L., Irving, T. C., et al. (2016). Titin strain contributes to the Frank-Starling law of the heart by structural rearrangements of both thin- and thick-filament proteins. *Proc. Natl. Acad. Sci. U.S.A.* 113, 2306–2311. doi: 10.1073/pnas.1516732113

Alamo, L., Wriggers, W., Pinto, A., Bartoli, F., Salazar, L., Zhao, F. Q., et al. (2008). Three-dimensional reconstruction of tarantula myosin filaments suggests how phosphorylation may regulate myosin activity. *J. Mol. Biol.* 384, 780–797. doi: 10.1016/j.jmb.2008.10.013

Anderson, R. L., Trivedi, D. V., Sarkar, S. S., Henze, M., Ma, W., Gong, H., et al. (2018). Deciphering the super relaxed state of human beta-cardiac myosin and the mode of action of mavacamten from myosin molecules to muscle fibers. *Proc. Natl. Acad. Sci. U.S.A.* 115, E8143–E8152.

Bagnoli, P., Malagutti, N., Gastaldi, D., Marcelli, E., Lui, E., Cercenelli, L., et al. (2011). Computational finite element model of cardiac torsion. *Int. J. Artif. Organs* 34, 44–53. doi: 10.5301/ijao.2011.6313

Benjamin, E. J., Virani, S. S., Callaway, C. W., Chamberlain, A. M., Chang, A. R., Cheng, S., et al. (2018). Heart disease and stroke statistics-2018 update: a report from the American heart association. *Circulation* 137, e67–e492.

Bodi, I., Mikala, G., Koch, S. E., Akhter, S. A., and Schwartz, A. (2005). The L-type calcium channel in the heart: the beat goes on. *J. Clin. Invest.* 115, 3306–3317. doi: 10.1172/jci27167

Campbell, K. B., Simpson, A. M., Campbell, S. G., Granzier, H. L., and Slinker, B. K. (2008). Dynamic left ventricular elastance: a model for integrating cardiac muscle contraction into ventricular pressure-volume relationships. *J. Appl. Physiol.* 104, 958–975. doi: 10.1152/japplphysiol.00912.2007

Campbell, K. S. (2011). Impact of myocyte strain on cardiac myofilament activation. *Pflugers. Arch.* 462, 3–14. doi: 10.1007/s00424-011-0952-3

Campbell, K. S. (2014). Dynamic coupling of regulated binding sites and cycling myosin heads in striated muscle. *J. Gen. Physiol.* 143, 387–399. doi: 10.1085/jgp.201311078

Campbell, K. S., Janssen, P. M. L., and Campbell, S. G. (2018). Force-dependent recruitment from the myosin off state contributes to length-dependent activation. *Biophys. J.* 115, 543–553. doi: 10.1016/j.bpj.2018.07.006

Campbell, K. S., Yengo, C. M., Lee, L. C., Kotter, J., Sorrell, V. L., Guglin, M., et al. (2019). Closing the therapeutic loop. *Arch. Biochem. Biophys.* 663, 129–131.

Granzier, H. L., and Irving, T. C. (1995). Passive tension in cardiac muscles: contribution of collagen, titin, microtubules, and intermediate filaments. *Biophys. J.* 68, 1027–1044. doi: 10.1016/s0006-3495(95)80278-x

Guccione, J. M., Costa, K. D., and Mcculloch, A. D. (1995). Finite element stress analysis of left ventricular mechanics in the beating dog heart. *J. Biomech.* 28, 1167–1177. doi: 10.1016/0021-9290(94)00174-3

Haynes, P., Nava, K. E., Lawson, B. A., Chung, C. S., Mitov, M. I., Campbell, S. G., et al. (2014). Transmural heterogeneity of cellular level power output is reduced in human heart failure. *J. Mol. Cell Cardiol.* 72, 1–8. doi: 10.1016/j.yjmcc.2014.02.008

Hidalgo, C., and Granzier, H. (2013). Tuning the molecular giant titin through phosphorylation: role in health and disease. *Trends Cardiovasc. Med.* 23, 165–171. doi: 10.1016/j.tcm.2012.10.005

Hooijman, P., Stewart, M. A., and Cooke, R. (2011). A new state of cardiac myosin with very slow ATP turnover: a potential cardioprotective mechanism in the heart. *Biophys. J.* 100, 1969–1976. doi: 10.1016/j.bpj.2011.02.061

Houston, B. A., and Stevens, G. R. (2014). Hypertrophic cardiomyopathy: a review. *Clin. Med. Insights Cardiol.* 8, 53–65.

Irving, M. (2017). Regulation of contraction by the thick filaments in skeletal muscle. *Biophys. J.* 113, 2579–2594. doi: 10.1016/j.bpj.2017.09.037

Jones, E., Oliphant, T. E., and Peterson, P. (2001). *SciPy: Open source scientific tools for Python [Online]*. Available: http://www.scipy.org (accessed 11 August 2019).

Kampourakis, T., Sun, Y. B., and Irving, M. (2016). Myosin light chain phosphorylation enhances contraction of heart muscle via structural changes in both thick and thin filaments. *Proc. Natl. Acad. Sci. U.S.A.* 113, E3039–E3047.

Klepach, D., Lee, L. C., Wenk, J. F., Ratcliffe, M. B., Zohdi, T. I., Navia, J. A., et al. (2012). Growth and remodeling of the left ventricle: A case study of myocardial infarction and surgical ventricular restoration. *Mech. Res. Commun.* 42, 134–141. doi: 10.1016/j.mechrescom.2012.03.005

Kosinski, S. A., Carlson, B. E., Hummel, S. L., Brook, R. D., and Beard, D. A. (2018). Computational model-based assessment of baroreflex function from response to *Valsalva maneuver*. *J. Appl. Physiol.* 125, 1944–1967. doi: 10.1152/japplphysiol.00095.2018

Lee, L. C., Sundnes, J., Genet, M., Wenk, J. F., and Wall, S. T. (2016). An integrated electromechanical-growth heart model for simulating cardiac therapies. *Biomech. Model. Mechanobiol.* 15, 791–803. doi: 10.1007/s10237-015-0723-8

Lloyd, C. M., Lawson, J. R., Hunter, P. J., and Nielsen, P. F. (2008). The CellML Model Repository. *Bioinformatics* 24, 2122–2123. doi: 10.1093/bioinformatics/btn390

Lumens, J., Delhaas, T., Kirn, B., and Arts, T. (2009). Three-wall segment (TriSeg) model describing mechanics and hemodynamics of ventricular interaction. *Ann. Biomed. Eng.* 37, 2234–2255. doi: 10.1007/s10439-009-9774-2

Malik, F. I., Hartman, J. J., Elias, K. A., Morgan, B. P., Rodriguez, H., Brejc, K., et al. (2011). Cardiac myosin activation: a potential therapeutic approach for systolic heart failure. *Science* 331, 1439–1443.

Mann, C. K., Lee, L. C., Campbell, K. S., and Wenk, J. F. (2020). Force-dependent recruitment from myosin OFF-state increases end-systolic pressure-volume relationship in left ventricle. *Biomech. Model Mechanobiol.* [Online ahead of print]

Marian, A. J., and Braunwald, E. (2017). Hypertrophic cardiomyopathy: genetics, pathogenesis, clinical manifestations, diagnosis, and therapy. *Circ. Res.* 121, 749–770. doi: 10.1161/circresaha.117.311059

McNamara, J. W., Li, A., Smith, N. J., Lal, S., Graham, R. M., Kooiker, K. B., et al. (2016). Ablation of cardiac myosin binding protein-C disrupts the super-relaxed state of myosin in murine cardiomyocytes. *J. Mol. Cell Cardiol.* 94, 65–71. doi: 10.1016/j.yjmcc.2016.03.009

Mirsky, I., Tajimi, T., and Peterson, K. L. (1987). The development of the entire end-systolic pressure-volume and ejection fraction-afterload relations: a new concept of systolic myocardial stiffness. *Circulation* 76, 343–356. doi: 10.1161/01.cir.76.2.343

Nag, S., Trivedi, D. V., Sarkar, S. S., Adhikari, A. S., Sunitha, M. S., Sutton, S., et al. (2017). The myosin mesa and the basis of hypercontractility caused by hypertrophic cardiomyopathy mutations. *Nat. Struct. Mol. Biol.* 24, 525–533. doi: 10.1038/nsmb.3408

Nagueh, S. F., Shah, G., Wu, Y., Torre-Amione, G., King, N. M., Lahmers, S., et al. (2004). Altered titin expression, myocardial stiffness, and left ventricular function in patients with dilated cardiomyopathy. *Circulation* 110, 155–162. doi: 10.1161/01.cir.0000135591.37759.af

Negroni, J. A., and Lascano, E. C. (1996). A cardiac muscle model relating sarcomere dynamics to calcium kinetics. *J. Mol. Cell Cardiol.* 28, 915–929. doi: 10.1006/jmcc.1996.0086

Parmley, W. W. (1985). Pathophysiology of congestive heart failure. *Am. J. Cardiol.* 56, 7A–11A.

Pironet, A., Desaive, T., Kosta, S., Lucas, A., Paeme, S., Collet, A., et al. (2013). A multi-scale cardiovascular system model can account for the load-dependence of the end-systolic pressure-volume relationship. *Biomed. Eng. Online* 12:8. doi: 10.1186/1475-925x-12-8

Russel, I. K., Gotte, M. J., Bronzwaer, J. G., Knaapen, P., Paulus, W. J., and Van Rossum, A. C. (2009). Left ventricular torsion: an expanding role in the analysis of myocardial dysfunction. *JACC Cardiovasc. Imaging* 2, 648–655.

Sharma, S., Razeghi, P., Shakir, A., Keneson, B. J. II, Clubb, F., and Taegtmeyer, H. (2003). Regional heterogeneity in gene expression profiles: a transcript analysis in human and rat heart. *Cardiology* 100, 73–79. doi: 10.1159/000073042

Shi, Y., Lawford, P., and Hose, R. (2011). Review of zero-D and 1-D models of blood flow in the cardiovascular system. *Biomed. Eng. Online* 10:33. doi: 10.1186/1475-925x-10-33

Shim, E., Leem, C., and Youn, C. (2004). "System biological modeling of circulation: From cells to system," in *Proceedings of the IECON 2004 30th Annual Conference of IEEE*, Guangzhou: Industrial Electronics Society.

Sobol, I. M. (1993). Sensitivity analysis for non-linear mathematical models. *Math. Model. Comput. Exp.* 1, 407–414.

Streeter, D. D. Jr., Spotnitz, H. M., Patel, D. P., Ross, J. Jr., and Sonnenblick, E. H. (1969). Fiber orientation in the canine left ventricle during diastole and systole. *Circ. Res.* 24, 339–347. doi: 10.1161/01.res.24.3.339

Swenson, A. M., Tang, W., Blair, C. A., Fetrow, C. M., Unrath, W. C., Previs, M. J., et al. (2017). Omecamtiv mecarbil enhances the duty ratio of human beta-cardiac myosin resulting in increased calcium sensitivity and slowed force development in cardiac muscle. *J. Biol. Chem.* 292, 3768–3778. doi: 10.1074/jbc.m116.748780

ten Tusscher, K. H., Noble, D., Noble, P. J., and Panfilov, A. V. (2004). A model for human ventricular tissue. *Am. J. Physiol. Heart Circ. Physiol.* 286, H1573–H1589.

Ter Keurs, H. E., and Boyden, P. A. (2007). Calcium and arrhythmogenesis. *Physiol. Rev.* 87, 457–506. doi: 10.1152/physrev.00011.2006

Ter Keurs, H. E., Wakayama, Y., Miura, M., Shinozaki, T., Stuyvers, B. D., Boyden, P. A., et al. (2006). Arrhythmogenic Ca2+ release from cardiac myofilaments. *Prog. Biophys. Mol. Biol.* 90, 151–171. doi: 10.1016/j.pbiomolbio.2005.07.002

Tewari, S. G., Bugenhagen, S. M., Vinnakota, K. C., Rice, J. J., Janssen, P. M., and Beard, D. A. (2016). Influence of metabolic dysfunction on cardiac mechanics in decompensated hypertrophy and heart failure. *J. Mol. Cell Cardiol.* 94, 162–175. doi: 10.1016/j.yjmcc.2016.04.003

van der Walt, S., Colbert, S. C., and Varoquaux, G. (2011). The NumPy Array: a structure for efficient numerical computation. *Comput. Sci. Eng.* 13, 22–30. doi: 10.1109/mcse.2011.37

Vonk Noordegraaf, A., Westerhof, B. E., and Westerhof, N. (2017). The relationship between the right ventricle and its load in pulmonary hypertension. *J. Am. Coll. Cardiol.* 69, 236–243. doi: 10.1016/j.jacc.2016.10.047

Wakayama, Y., Miura, M., Sugai, Y., Kagaya, Y., Watanabe, J., Ter Keurs, H. E., et al. (2001). Stretch and quick release of rat cardiac trabeculae accelerates Ca2+ waves and triggered propagated contractions. *Am. J. Physiol. Heart Circ. Physiol.* 281, H2133–H2142.

Wang, H., Zhang, X., Dorsey, S. M., Mcgarvey, J. R., Campbell, K. S., Burdick, J. A., et al. (2016). Computational investigation of transmural differences in left ventricular contractility. *J. Biomech. Eng.* 138, 1145011–1145016.

Watkins, H., Ashrafian, H., and Redwood, C. (2011). Inherited cardiomyopathies. *N. Engl. J. Med.* 364, 1643–1656.

Wenk, J. F. (2011). Numerical modeling of stress in stenotic arteries with microcalcifications: a parameter sensitivity study. *J. Biomech. Eng.* 133:014503.

Writing Committee, M., Yancy, C. W., Jessup, M., Bozkurt, B., Butler, J., Casey, D. E. Jr., et al. (2013). 2013 ACCF/AHA guideline for the management of heart failure: a report of the American College of Cardiology Foundation/American Heart Association Task Force on practice guidelines. *Circulation* 128, e240–e327.

Zhang, X., Kampourakis, T., Yan, Z., Sevrieva, I., Irving, M., and Sun, Y. B. (2017). Distinct contributions of the thin and thick filaments to length-dependent activation in heart muscle. *eLife* 6:e24081.

Zhang, X., Liu, Z. Q., Campbell, K. S., and Wenk, J. F. (2018). Evaluation of a novel finite element model of active contraction in the heart. *Front. Physiol.* 9:425. doi: 10.3389/fphys.2018.00425

Conflict of Interest: The authors declare that the research was conducted in the absence of any commercial or financial relationships that could be construed as a potential conflict of interest.

frontiers in Physiology

ORIGINAL RESEARCH
published: 10 December 2020
doi: 10.3389/fphys.2020.519951

Mechano-Electric Coupling and Arrhythmogenic Current Generation in a Computational Model of Coupled Myocytes

Viviane Timmermann[1,2]* and *Andrew D. McCulloch*[2]

[1] *Simula Research Laboratory, Department of Computational Physiology, Fornebu, Norway,* [2] *Departments of Bioengineering and Medicine, University of California San Diego, La Jolla, CA, United States*

A wide range of arrhythmogenic phenotypes have been associated with heterogeneous mechanical dyskinesis. Pro-arrhythmic effects are often associated with dysregulated intra-cellular calcium handling, especially *via* the development of intra- and inter-cellular calcium waves. Experimental evidence suggests that mechanical strain can contribute to the generation and maintenance of these calcium waves *via* a variety of mechano-electric coupling mechanisms. Most model studies of mechano-electric coupling mechanisms have been focused on mechano-sensitive ion channels, even though experimental studies have shown that intra- and inter-cellular calcium waves triggered by mechanical perturbations are likely to be more prevalent pro-arrhythmic mechanisms in the diseased heart. A one-dimensional strongly coupled computational model of electromechanics in rabbit ventricular cardiomyocytes showed that specific myocyte stretch sequences can modulate the susceptibility threshold for delayed after-depolarizations. In simulations of mechanically-triggered calcium waves in cardiomyocytes coupled to fibroblasts, susceptibility to calcium wave propagation was reduced as the current through the gap junction caused current drain from the myocytes. In 1D multi-cellular arrays coupled *via* gap junctions, mechanically-induced waves may contribute to synchronizing arrhythmogenic calcium waves and after-depolarizations.

Keywords: mechno-electric feedback, intracellular calcium release, arrhythmia, calcium waves, computational model, rabbit, fibroblasts

Edited by:
Leonid Katsnelson,
Institute of Immunology and Physiology (RAS), Russia

Reviewed by:
Jieyun Bai,
Jinan University, China
Kenneth Tran,
The University of Auckland, New Zealand

***Correspondence:**
Viviane Timmermann
viviane.timmermann@universitaets-herzzentrum.de

Specialty section:
This article was submitted to Computational Physiology and Medicine, a section of the journal Frontiers in Physiology

Received: *13 December 2019*
Accepted: *10 November 2020*
Published: *10 December 2020*

Citation:
Timmermann V and McCulloch AD (2020) Mechano-Electric Coupling and Arrhythmogenic Current Generation in a Computational Model of Coupled Myocytes. Front. Physiol. 11:519951. doi: 10.3389/fphys.2020.519951

1. INTRODUCTION

Altered myocardial mechanics in disease may contribute to the triggering or maintenance of life-threatening reentrant ventricular arrhythmias *via* a variety of mechano-electric coupling mechanisms. In particular, altered myocyte mechanics may cause pro-arrhythmic perturbations to cardiomyocyte electrophysiology (Franz et al., 1992; Kohl et al., 2011). These perturbations may generate currents that trigger arrhythmias or create a heterogenous myocardial electrical substrate that supports reentry (Taggart and Lab, 2008). While most model studies of mechano-electric coupling mechanisms have focused on mechano-sensitive ion channels (Peyronnet et al., 2016), experimental studies (ter Keurs et al., 2006b), and recent mathematical simulations (Timmermann et al., 2019) suggest that intra- and inter-cellular calcium waves triggered by mechanical perturbations are likely to be more prevalent pro-arrhythmic mechanisms in the diseased heart.

To understand the mechanisms of mechanically-triggered arrhythmogenic currents, we must consider both how electrical excitation activates calcium-dependent muscle contraction [excitation-contraction coupling (ECC)] and the reverse processes by which stretch alters membrane currents [mechano-electric coupling (MEC)] (Kohl et al., 1999). Under normal conditions, both pathways are important for the electrical regulation of cardiac performance underlying mechanical changes (Kohl et al., 1999). At the organ scale, electrical dyssynchrony alters mechanical contraction and may further exacerbate pump dysfunction in disease (Pfeiffer et al., 2014). At the (sub)cellular level, dysregulated calcium handling is associated with proarrhythmia, notably *via* the development of calcium waves (Kass and Tsien, 1982; Matsuda et al., 1982; Capogrossi and Lakatta, 1985; Capogrossi et al., 1986b; Backx et al., 1989). Thus, mechanically-triggered, calcium-mediated mechanisms are likely to contribute to arrhythmogenic phenotypes. Despite intensive investigations at different levels, from single ion channels (Kohl and Sachs, 2001) to tissue (ter Keurs et al., 1998, 2006a,b; Kohl et al., 2001), the contributions of MEC to arrhythmia generation is incompletely understood.

In addition to MEC mechanisms, fibrosis and electrical remodeling are crucial modulators of long term outcomes accompanying pathological mechanical changes in the heart. Up to 70% of the total cell number in healthy rodent myocardium is comprised of fibroblasts (MacCannell et al., 2007; Maleckar et al., 2009), which are thought to electrotonically interact with myocytes *via* gap-junctions (MacCannell et al., 2007; Maleckar et al., 2009). These functional, dynamic fibroblasts-to-myocyte interactions can modulate electrical excitability and action potential (AP) waveform (MacCannell et al., 2007; Maleckar et al., 2009). Thus, fibroblast-mediated electrical remodeling together with mechanical heterogeneities might exacerbate the susceptibility to pro-arrhythmic calcium wave propagation by providing arrhythmogenic substrate (MacCannell et al., 2007; Maleckar et al., 2009).

The aim of this study is to mechanistically explore the critical role of altered myocyte mechanics, mechano-electric coupling, calcium homeostasis, and myocyte coupling in the generation and maintenance of ventricular arrhythmias, to increase the understanding of the complex interaction and balance of calcium homeostasis and contractile function. To address this goal, we simulated a one-dimensional (1D) cardiac myocyte, by strongly coupling a zero-dimensional AP model to sarcomere mechanics. The coupled model was modified to represent the cardiac myocyte as a 1D string of bi-directional end-to-end interactions between sarcomeres. We introduced mechanical heterogeneities by allowing stochastic variations in sarcomere resting length and by subjecting the model to a wide range of stretch protocols. Coupling mechanically heterogeneous myocytes by gap junctions increased the order of dynamic instability to trigger potentially arrhythmogenic delayed after-depolarizations (DADs), while coupling fibroblasts to the myocyte had a stabilizing affect.

2. MATERIALS AND METHODS

2.1. Electro-Mechanical Myocyte Models

2.1.1. 0-Dimensional Myocyte Model

We developed a strongly coupled zero-dimensional (0D) computational model of rabbit cardiomyocyte electromechanics by coupling the well-established rabbit myocyte ionic model of Shannon et al. (2004) (distributed by Bers, 2002) with the myofilament mechanics model of Rice et al. (2008b) (downloaded from Rice et al., 2008a). The calcium transient generated by the ionic model, which represents normal calcium-induced calcium release (CICR) from the sarcoplasmic reticulum (SR) at the dyadic cleft, was input to the rabbit cardiac muscle contraction model. The formulation for cytosolic calcium binding to troponin C (TnC) in the mechanics model was used as input for the mechano-electric coupling of the mechanics model to the electrophysiology (EP) model. The contractile kinetics model described thin filament activation by intra-cellular calcium binding to TnC and the resulting crossbridge (XB) cycling.

In addition to strong electromechanical coupling, we incorporated strain-dependent changes in calcium affinity to the myofilaments to empirically approximate the triggers of mechanically-induced calcium waves. Using a parameter-fitting algorithm (Bueno-Orovio et al., 2008), the on- and off-rates for calcium binding to TnC and the constants for the strain-dependence of the XB cycling were reformulated to incorporate an exponential dependence on strain-rate. (A detailed description of the 0D model can be found in Timmermann et al., 2019).

2.1.2. 1-Dimensional Myocyte Model

We extended the 0D electromechanical model of section 2.1.1 by arraying the 0D model into 50 uniform mechanically and resistively coupled units. Each unit represents a single sarcomere of the mechanical model and a single calcium-release unit (CRU) of the EP model. This linear array model was previously constructed to investigate the ability of sub-cellular mechanical perturbations to trigger and modulate calcium waves *via* strain-dependent thin filament calcium affinity (Timmermann et al., 2019). As reported by Timmermann et al. (2019), time-dependent calcium diffusion was implemented for the sub-sarcolemma (SS), SR, and cytosol. The diffusion time constants for intra-CRU diffusion in the longitudinal direction were adapted to reproduce a calcium wave velocity of $\sim 100\ \frac{\mu\mathrm{m}}{\mathrm{s}}$ at $\mathrm{Ca_o} = 4\,\mathrm{mM}$ while increasing the magnitude of the calcium transient from the originally published value by Shannon et al. (2004). In particular, the calcium diffusion between the compartments of adjacent CRUs was incorporated when calculating the calcium concentrations as follows:

$$\frac{\mathrm{dCa}_k^i}{\mathrm{dt}} = \frac{\widehat{\mathrm{dCa}_k^i}}{\mathrm{dt}} + \frac{(\mathrm{Ca}_k^{i+1} + \mathrm{Ca}_k^{i-1} - 2 \cdot \mathrm{Ca}_k^i)}{\tau_k} \qquad (1)$$

$$\forall i \in \{2, ..., 49\} \quad \text{and} \quad k \in \{\mathrm{SS}, \mathrm{SR}, \mathrm{cyto}\}$$

and for the boundaries:

$$\frac{\mathrm{dCa}_k^{1,50}}{\mathrm{dt}} = \frac{\widehat{\mathrm{dCa}_k^{1,50}}}{\mathrm{dt}} + \frac{(\mathrm{Ca}_k^{2,49} - \mathrm{Ca}_k^{1,50})}{\tau_k} \qquad (2)$$
$$k \in \{\mathrm{SS}, \mathrm{SR}, \mathrm{cyto}\}$$

with $\tau_{\mathrm{SS}} = 0.4533$ ms, $\tau_{\mathrm{SR}} = 150$ ms, $\tau_{\mathrm{cyto}} = 1.2$ ms, and $\frac{\widehat{\mathrm{dCa}_k^{1,50}}}{\mathrm{dt}}$, $k \in \{\mathrm{SS}, \mathrm{SR}, \mathrm{cyto}\}$, the time-dependent changes calcium concentrations as in Shannon et al. (2004). (A detailed description of the one dimensional (1D) model can be found in Timmermann et al., 2019).

For this study, the model was extended by calculating the membrane potential in each of the 50 CRUs to better represent the electrical conductance of a myocyte. The first CRU in the myocyte was stimulated with a 1,000 mV pulse for 3 ms, triggering a electrical stimulation of the entire cell. Using a parameter-fitting algorithm (Bueno-Orovio et al., 2008), the time constant for voltage transfer between adjacent CRUs and the electrical pulses was chosen to allow electrical propagation while retaining a similar magnitude of the AP upstroke as reported in the original ionic model (Shannon et al., 2004).

$$\begin{aligned}
\frac{\mathrm{dV}_{\mathrm{m}}^1}{\mathrm{dt}} &= -\frac{1}{\mathrm{C}_{\mathrm{m}}}\left(\mathrm{I}_{\mathrm{m}}^i + \mathrm{I}_{\mathrm{stim}}\right) + \frac{(\mathrm{V}_{\mathrm{m}}^2 - \mathrm{V}_{\mathrm{m}}^1)}{\tau_{\mathrm{V_m}}} \\
\frac{\mathrm{dV}_{\mathrm{m}}^i}{\mathrm{dt}} &= -\frac{1}{\mathrm{C}_{\mathrm{m}}}\left(\mathrm{I}_{\mathrm{m}}^i\right) + \frac{(\mathrm{V}_{\mathrm{m}}^{i+1} + \mathrm{V}_{\mathrm{m}}^{i-1} - 2 \cdot \mathrm{V}_{\mathrm{m}}^i)}{\tau_{\mathrm{V_m}}} \qquad (3) \\
\frac{\mathrm{dV}_{\mathrm{m}}^{50}}{\mathrm{dt}} &= -\frac{1}{\mathrm{C}_{\mathrm{m}}}\left(\mathrm{I}_{\mathrm{m}}^i\right) + \frac{(\mathrm{V}_{\mathrm{m}}^{49} - \mathrm{V}_{\mathrm{m}}^{50})}{\tau_{\mathrm{V_m}}} \\
&\forall i \in \{2, ..., 49\}
\end{aligned}$$

with $\mathrm{C_m}$ membrane capacitance, $\tau_{\mathrm{V_m}} = 1e^{-5}$ ms conductance propagation coefficient, $\mathrm{I_{stim}}$ the stimulus current, and I^i the total membrane current in CRU $i \in \{1, ..., 50\}$.

Furthermore, transmembrane currents with variable conductances were adapted to represent the mean experimentally reported values at the three cycle lengths 400, 600, and 1,000 ms as reported in Gemmell et al. (2016). In particular, the conductance of the transient outward potassium current (I_{to}) was increased by 30%, the conductance of slow delayed rectifier current (I_{Ks}) was decreased by 15%, the inward rectifier current (I_{K1}) was decreased by 30%, and the sodium-potassium pump current was increased by 15%.

In addition to interactions between adjacent ionic CRUs in this spatially explicit model, a single sarcomere was coupled to each EP model. We used the strong coupling approach of Timmermann et al. (2019) to represent mechanical interaction between neighboring sarcomeres. Therefore, fractional changes in length between adjacent sarcomeres were included:

$$\frac{\mathrm{dSL}_j^i}{\mathrm{dt}} = 2 \cdot \widehat{\mathrm{dSL}_j^i} - \left(\widehat{\mathrm{dSL}_j^{i+1}} + \widehat{\mathrm{dSL}_j^{i-1}}\right) \qquad (4)$$
$$\forall i \in \{2, 3, ..., 49\} \quad \forall j \in \{1, 2, 3\}$$

with $\widehat{\mathrm{dSL}_j^i}$ the isotonic length change of sarcomere i of myocyte j.

The sarcomeres at the boundaries of each myocyte, interacted only with one other sarcomere of the same myocyte. To incorporate mechanical interactions between adjacent myocytes, adjacent sarcomeres of neighboring myocytes affected each other by their scaled fractional change in length

$$\begin{aligned}
\frac{\mathrm{dSL}_1^1}{\mathrm{dt}} &= \widehat{\mathrm{dSL}_1^1} - \widehat{\mathrm{dSL}_1^2} \\
\frac{\mathrm{dSL}_j^1}{\mathrm{dt}} &= \widehat{\mathrm{dSL}_j^1} - \left(\widehat{\mathrm{dSL}_j^2} + \widehat{\mathrm{dSL}_{j-1}^{50}}\right) \\
&\forall j \in \{2, ..., n\} \qquad (5) \\
\frac{\mathrm{dSL}_j^{50}}{\mathrm{dt}} &= \widehat{\mathrm{dSL}_j^{50}} - \left(\widehat{\mathrm{dSL}_j^{49}} + \widehat{\mathrm{dSL}_{j+1}^1}\right) \\
&\forall j \in \{1, ..., n-1\} \\
\frac{\mathrm{dSL}_n^{50}}{\mathrm{dt}} &= \widehat{\mathrm{dSL}_n^{50}} - \widehat{\mathrm{dSL}_n^{49}}
\end{aligned}$$

with $\widehat{\mathrm{dSL}_j^{1,50}}$ the isotonic length change of the first (1) or the last (50) sarcomere, respectively, of the jth myocyte, and $n = 3$ or 6 for the number of coupled myocytes.

2.1.3. 1-Dimensional Multi-Cellular Model Coupled *via* Gap Junctions

To adapt the 1D electromechanical myocyte model for simulations of multi-cellular interactions, 3 myocytes were coupled *via* gap junctions. Each of the three myocytes in the coupled simulation was modeled as 1 of the 10 different single myocyte models described in section 2.1.2. Ten separate multi-cellular simulations with varying combinations of 3 of these 10 different single myocyte conditions were analyzed. The modeled combinations are given in **Supplementary Tables 6, 7**. To reproduce a conductance velocity of approximately 0.5 $\frac{\mu\mathrm{m}}{\mathrm{s}}$, the value of gap junction conductance was $\mathrm{g_{gap}} = 400$ nS. The corresponding equations for the linear gap junction current from the jth to the $(j+1)$th cell were as follows:

$$\begin{aligned}
\mathrm{I}_{\mathrm{gap}}^j &= \mathrm{g}_{\mathrm{gap}}\left(\widehat{\mathrm{V}_{\mathrm{m},j}^{50}} - \widehat{\mathrm{V}_{\mathrm{m},j+1}^1}\right) \\
\frac{\mathrm{dV}_{\mathrm{m},j}^{50}}{\mathrm{dt}} &= \frac{\widehat{\mathrm{dV}_{\mathrm{m},j}^{50}}}{\mathrm{dt}} + \mathrm{I}_{\mathrm{gap}}^j \qquad (6) \\
\frac{\mathrm{dV}_{\mathrm{m},j+1}^{50}}{\mathrm{dt}} &= \frac{\widehat{\mathrm{dV}_{\mathrm{m},j+1}^{50}}}{\mathrm{dt}} - \mathrm{I}_{\mathrm{gap}}^j \\
&\forall j \in \{1, ..., n-1\}
\end{aligned}$$

with $\frac{\widehat{\mathrm{V}_{\mathrm{m},j}^{50}}}{dt}$, $\frac{\widehat{\mathrm{V}_{\mathrm{m},j}^{1}}}{\mathrm{dt}}$, the change in membrane potential of the last CRU of myocyte j and the first CRU of myocyte $(j+1)$ in absence of the gap-junctional coupling, n, the number of myocytes, and $\frac{\mathrm{V}_{\mathrm{m},j}^{50}}{\mathrm{dt}}$, $\frac{\mathrm{V}_{\mathrm{m},j}^{1}}{\mathrm{dt}}$, the change in the potential of the membrane at last sarcomere of myocyte j and at the first sarcomere of myocyte $(j+1)$ in the presence of gap-junctional coupling.

For these multi-cellular simulations, the first CRU of the first myocyte (left boundary of the string of myocytes) was electrically stimulated with a 1,000 mV pulse for 3 ms. The adjacent myocytes were stimulated by the coupling *via* gap junctions.

2.2. Incorporation of Inter-cellular Mechanical Heterogeneities

We introduce mechanical heterogeneities by allowing sarcomeres within a single myocyte to have different resting lengths. To induce sarcomere heterogeneity, we deviated from the average resting length of 1.89 µm (Rice et al., 2008b), by 10% which are in the physiological range measured in myofibrils by Rassier et al. (2003). Therefore, for 10 random variations, the resting lengths of the 50 sarcomeres were chosen from the interval [1.701, 2.079 µm] (as shown in **Supplementary Table 1**) using a uniform random number generator (the *rand* function of MATLAB).

2.3. Incorporation of Fibroblasts

To simulate myocyte-fibroblast interactions, the active version 1 model of Maleckar et al. (2009) was incorporated to the electromechanics model. The current conductance of the fibroblasts is described by five time- and voltage-dependent equations in addition to the gap junction which allows for Na^+ and K^+-ions to move between the myocyte and the fibroblast (for a detailed description see Maleckar et al., 2009). Originating from the fibroblast model of MacCannell et al. (2007), the active model of Maleckar et al. (2009) includes the fibroblast membrane capacitance and four fibroblast ionic currents: time- and voltage-dependent fibroblast K^+ current (I_{KV}), inward-rectifying K_1^+ current (I_{K1}) which is expressed in cardiac myofibroblasts, Na^+-K^+ pump current (I_{NaK}) which has expressed K^+ channels resulting in K^+ fluxes, and background Na^+ current ($I_{b,Na}$) to balance the Na^+ efflux from the Na^+-K^+ pump activity (for a detailed description see MacCannell et al., 2007).

Each myocyte was coupled to 1, 2, or 3 fibroblasts. Each fibroblast was randomly assigned to one CRU at 1 of the last 5 CRUs at one of the ends of the myocyte due to its relatively small size compared with the myocyte since fibroblast locate close to the gap junctions between myocytes (Goldsmith et al., 2004; Ongstad and Kohl, 2016). For each coupled fibroblast the value of the linear, fixed resistance ($G_{f,gap}$) varied randomly in the interval between the low and high ends of the range of $G_{f,gap}$, 0.5 and 8.0 nS as reported in Maleckar et al. (2009). Each of the 10 myocytes described in section 2.2, we assigned a random variation of the fibroblast locations (as shown in **Supplementary Table 2**).

2.4. Pacing and Stretch Protocols

In the electromechanics model we mimic various heterogeneities by subjecting the model to a wide range of stretch protocols. Myocyte stretch was modeled as an increase in sarcomere length. All stretch protocols of single cell and multi-cellular simulations were run for 200 beats to reach limit cycle. The limit cycle was ascertained by comparing the upstroke, plateau, and repolarization phase of the last two APs by calculating the mean squared error over time between both curves until mean squared error <0.01.

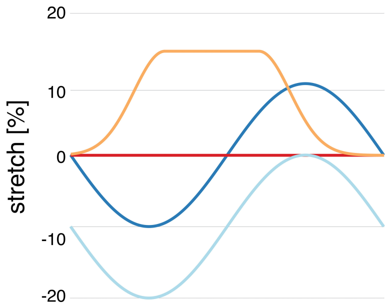

FIGURE 1 | Myocyte stretch protocols. Stretch pattern H (light blue) approximates normal isotonic myocyte shortening with a sinusoidal function. Protocol I (red) is sarcomere isometric contraction. Protocol S (dark blue) simulates late systolic stretch by shifting the sine wave upwards. Protocol P (orange) simulates systolic lengthening such as occurs in acutely ischemic regions.

Under calcium overload conditions, calcium sparks may be more likely to trigger propagated waves (Backx et al., 1989; Cheng et al., 1996). Therefore, to study calcium sparks and propagating calcium waves, all simulations were performed by increasing extracellular calcium concentration in 0.1 mM steps from $Ca_o = 2.0$ mM to $Ca_o = 4.5$ mM, which results in increased calcium transient in all our simulations from the reported values of Shannon et al. (2004). Spontaneous calcium waves with wave velocities of $\sim 100\ \frac{\mu m}{s}$ have been reported at low extracellular calcium concentrations as 1.8–2.0 mM (Takamatsu and Wier, 1990; Wier and Blatter, 1991) while others reported wave velocities of $\sim 72\ \frac{\mu m}{s}$ at $Ca_o = 2$ mM, $\sim 80\ \frac{\mu m}{s}$ at $Ca_o = 5$ mM, and $\sim 90\ \frac{\mu m}{s}$ at $Ca_o = 15$ mM (Capogrossi et al., 1986a; Cheng et al., 1996).

We refer to normal healthy contraction as protocol H, a sinusoidal function decreasing to 20% compression, and isometric contraction as protocol I. Pathophysiological stretches were represented by a sinusoidal function decreasing to 10% compression in diastole and increasing to 10% stretch in systole (protocol S) and an exponentially increasing function, increasing from 0 to 15% at the start of contraction, and then kept constant until it decreased exponentially at the time of relaxation (protocol P) (as shown in **Figure 1**). These protocols were used both for simulations of single and coupled myocytes both with and without coupled fibroblasts. Additionally, all four stretch protocols were applied to the 10 different single myocyte models generated in section 2.2 as well as the 10 different single myocyte models with 1, 2, or 3 coupled fibroblasts as described in section 2.3.

All single cell simulations were run in MATLAB R2018a using *ode15s* to solve the ordinary differential equation system, while multi-myocyte simulations were run in C++ using *odeint*.

2.5. Data Analysis

The statistical tests are presented as mean ± standard deviation calculated in MATLAB R2018a using the functions *mean* and *std*. The data was analyzed in MATLAB R2018a with the functions *anova1* and *multicompare*, a one-way analysis of variance with pairwise comparison of the group means preconditioned by the Bonferroni method. A data point was assumed to be an outlier if it did not lie within three standard deviations of the mean (three-sigma rule). Significant differences between were illustrated by asterisks with three asterisks indicating a $p < 0.01$, two a $p < 0.05$, and one a $p < 0.1$. Statistical tests were assessed for all simulations, even though some significant differences are far below the accuracy of experimental measurement techniques. To measure the inter-cellular dyssynchrony of intra-cellular calcium dynamics, we evaluated the standard deviation between cells of the mean time-to-peak of the intra-cellular calcium transient within each cell.

2.6. Data Availability

The datasets for this study can be found in the repository: https://github.com/cmrglab/1D_MEC.git.

3. RESULTS

3.1. The Occurrence of Calcium Waves and Wave Velocity Is Dependent on the Stretch Pattern and Ca_o

For all single myocyte simulations, we examined susceptibility to the generation of calcium waves after both pacing and stretching were stopped.

Even though some studies (Takamatsu and Wier, 1990; Wier and Blatter, 1991) have reported propagating calcium waves at low calcium concentrations as $Ca_o = 1.8$–2.0 mM, we did not observe spontaneous calcium waves in our model at $Ca_o = 2.0$ mM. Therefore, we increased the extracellular calcium concentration in 0.1 mM steps until in 3 of 10 control experiments (no stretch, stretch pattern I) spontaneously propagating calcium waves were observed at $Ca_o = 4.1$ mM. These findings are largely consistent with many experimental reports of calcium waves, in which the extracellular calcium concentrations varied between ∼2.0 mM (Takamatsu and Wier, 1990; Wier and Blatter, 1991) and 15 mM (Capogrossi et al., 1986a; Cheng et al., 1996).

Figure 2B shows that no calcium waves were observed for the control experiments at $Ca_o = 2.0$ mM (indicated by red daggers). For isotonic stretch simulations, the first calcium waves occurred at $Ca_o = 4.3$ mM, while all for all other stretch patterns lower calcium concentrations were sufficient to trigger spontaneously propagating calcium waves (see **Figure 2B**). At $Ca_o = 4.2$ mM, stretch pattern P generated the fastest calcium waves which always triggered an additional beat (indicated by the red star in **Figure 2B**) and propagated with a mean velocity of $4596.1 \pm 408.22 \ \frac{\mu m}{s}$. This additional beat was followed by a slow calcium wave which propagated with a $175.58 \pm 37.98 \ \frac{\mu m}{s}$ (shown in **Supplementary Table 3**). Even though the extracellular calcium concentration at which a calcium wave occurred for the different stretch patterns varied between $Ca_o = 3.7$ and 4.3 mM, the wave velocity was $\sim 100 \ \frac{\mu m}{s}$ for all stretch patterns. While the velocity of the first calcium wave was similar between stretch patterns, the maximal calcium wave amplitude (shown in **Figure 2A**) varied depending on the stretch pattern due to the extracellular calcium concentration. The lowest mean of the maximal calcium wave amplitude was observed for stretch pattern H with a magnitude of 0.15 ± 0.0 μM and the highest maximal calcium wave amplitude for stretch pattern P with a magnitude of 4.46 ± 0.13 μM.

At $Ca_o = 4.2$ mM, the greatest variation in calcium wave velocity was observed for stretch pattern P with a velocity of $4005.5 \pm 408.8 \ \frac{\mu m}{s}$. For all simulations at $Ca_o = 4.2$ mM, the resulting calcium waves induced suprathreshold DADs. For stretch pattern P in all 10 myocytes, a fast calcium wave triggered an extra beat followed by a slow propagating calcium wave, while for stretch pattern S in 6 of 10 myocytes, an additional beat and slow wave was observed in only two simulations. An example for the different calcium-mediated effects on AP are shown in **Figure 3A** and the associated calcium waves responsible for the changes in AP are illustrated in **Figure 3B**. At $Ca_o = 4.2$ mM a fast propagating wave triggered an additional beat, which was followed by a slower propagating wave. As described in Timmermann et al. (2019), calcium waves arose from spontaneous calcium release from the SR as a result of SR calcium overload. SR calcium overload resulted from stretch-dependent myofilament calcium dissociation that was sufficient to alter cytosolic calcium dynamics.

Figure 2B shows that an increase in calcium wave velocity is associated with an increase in maximal calcium wave amplitude. For control (stretch protocol I), the calcium wave amplitude significantly ($p < 0.01$) increased for experiments at $Ca_o = 4.1$ mM to $Ca_o = 4.2$ mM from $1246.0 \pm 819.0 \ \frac{\mu m}{s}$ to $1896.3 \pm 52.0 \ \frac{\mu m}{s}$ (see **Figure 2A**). Similarly, the maximal calcium wave amplitude for simulations for stretch patterns S and P increased significantly ($p < 0.01$) for experiments at which calcium waves first occurred to $Ca_o = 4.2$ mM by 637.25, 217.33%, respectively. (Mean and standard deviation of the maximal calcium wave amplitude magnitude and calcium wave velocity can be found in **Supplementary Table 3**).

3.2. Fibroblasts Function as Current Drains in Simulations of Spontaneous Calcium Waves

Owing to the large number of fibroblasts in the myocardium, we investigated their role in modulating electrophysiological instabilities. For all stretch patterns of myocytes with coupled fibroblasts, the current through the gap junction provided a drain of electric charge from the cardiomyocyte. Therefore, we were able to replicate a significant ($p < 0.01$) shortening of APD_{90} (see **Figure 4** and in **Supplementary Table 4**) as reported by MacCannell et al. (2007).

For simulations of calcium-mediated DADs the current through the gap junction between the fibroblast and the myocyte supplied an electric discharge from the cardiomyocyte as illustrated by the significantly ($p < 0.01$) decreasing maximal calcium wave amplitude in **Figure 5A**. Associated with decreased maximal calcium wave amplitude magnitude, the velocity of the induced calcium wave decreased significantly ($p < 0.01$) as more fibroblasts were coupled to the myocyte (see **Figure 5B**). For no stretch, in simulations with 3 coupled fibroblasts in 1 of 10 myocytes, no wave occurred, while for simulations of stretch patterns P and S, calcium waves were present. However, for simulations of stretch pattern P with three coupled fibroblasts

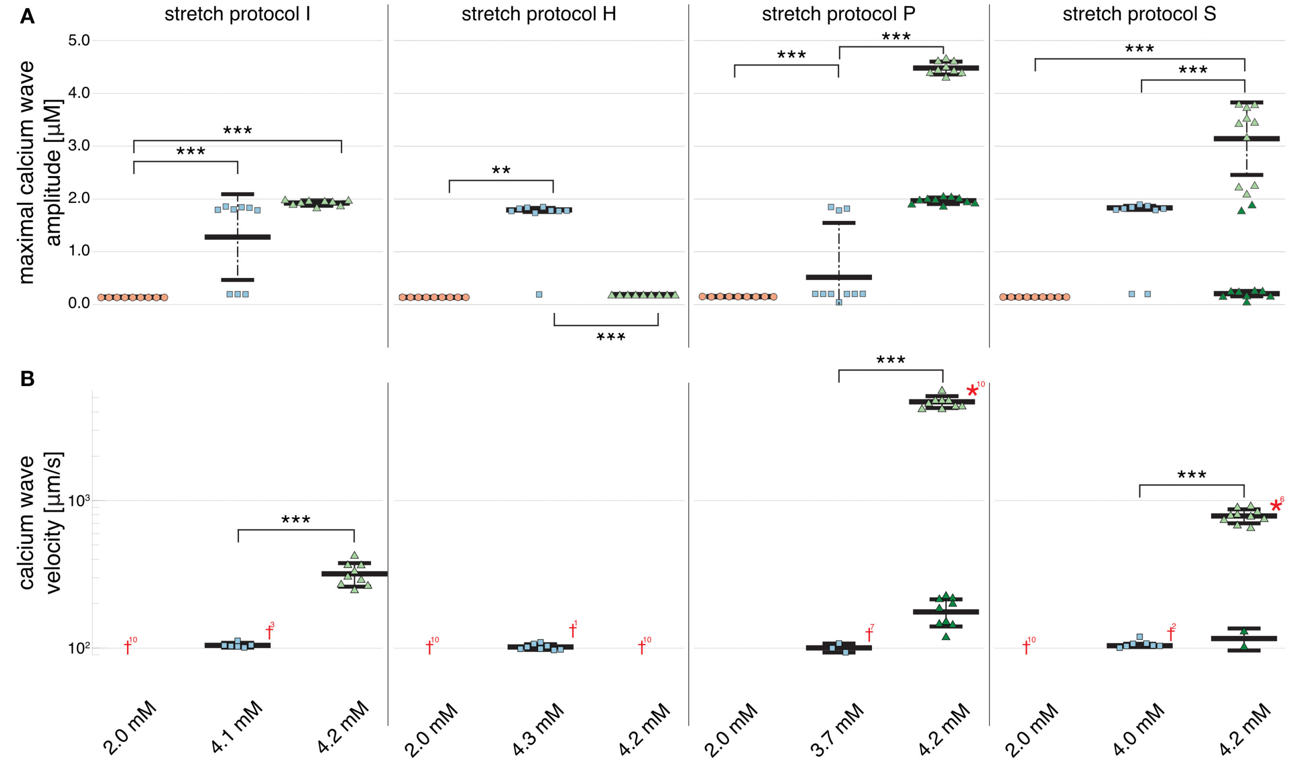

FIGURE 2 | Maximal calcium wave amplitude magnitude and calcium wave velocity in cardiomyocyte simulations at different extracellular calcium concentrations for control (no stretch protocol I), and stretch patterns H, S, and P. **(A)** The magnitude of the measured maximal calcium wave amplitude increased significantly for all stretch patterns from $Ca_o = 2.0$ mM (red data points) to the extracellular calcium concentration at which a calcium wave occurred (blue data points), and 4.2 mM (green data points). Red daggers indicate that no calcium waves occurred in the data set, while red asterisks indicate that the calcium waves triggered additional beats. The related numbers specifies the amount of occurrences within the data set. The data points in light colors specify the first spontaneous event and dark colors are used for the following spontaneous event. **(B)** The calcium wave velocity increased for all simulations from $Ca_o = 2.0$ mM (no waves) to 4.2 mM and from control, to stretch patterns H, to S, and to P. **, *** indicate the statistical significance with $p < 0.05$ and $p < 0.1$, respectively.

no slow calcium waves occurred after the triggered beat. calcium waves in myocytes coupled to three fibroblasts did not elicit extra beats in simulations of stretch pattern S.

The calcium waves in our computational model are triggered through spontaneous calcium release from the SR, which in turn triggers an increase in membrane potential and potentially, a DAD. Therefore, the coupled fibroblasts not only drain electrical charge and reduce the APD_{90} during normal pacing, but also slow calcium waves as charge is drained from the associated calcium-mediated suprathreshold DAD.

3.3. Calcium Waves Are More Synchronized in Multi-Cellular Simulations

In simulations of 3 and 6 cardiomyocytes coupled *via* gap junctions, calcium wave velocity and calcium wave amplitude of the multi-cellular simulation are given as the mean of the individually measured observed calcium wave velocities and calcium wave amplitudes of each single, coupled cell. Calcium wave velocity slightly decreased for all stretch patterns and for fibroblast coupling compared to single myocytes (see **Figures 5**, **6**, respectively). The results shown here were computed for three coupled myocytes but no differences were observed when we repeated these calculations with six coupled cells (shown in **Supplementary Figure 1**). Coupled myocytes behaved similarly to single myocytes. Maximal calcium wave amplitude varied between simulations of no stretch, and stretch patterns P and H with the highest maximal calcium wave amplitude occurring for stretch pattern P, which coincides with the fastest observed wave velocity (as shown in **Figure 6**). With stretch pattern S, fewer additional beats were triggered in the coupled myocyte simulations, showing how multi-cellular tissue can be less susceptible to extra beats than isolated cells due to the slowing and synchronization of calcium waves by electrotonic coupling effects.

Electrotonic coupling of cardiomyocytes reduced inter-cellular dyssynchrony of intra-cellular calcium dynamics for all 10 coupled cell replicates. As shown in **Figure 7B**, we measured more synchronized DAD rise times in multi-cellular compared with isolated cell simulations (see **Figure 7A**). Current conduction of triggered suprathreshold DADs *via* gap junctions triggered calcium waves with synchronized time-to-peak calcium and wave propagation velocities in all three cells. For coupled cells, the inter-cellular dyssynchrony of intra-cellular calcium dynamics was 0 within the numerical range. By contrast, the dyssynchrony of calcium wave velocity and the DAD rise times of isolated cells varied up to 378.56 ± 170.71 $\frac{\mu m}{s}$ and 36.46 ±

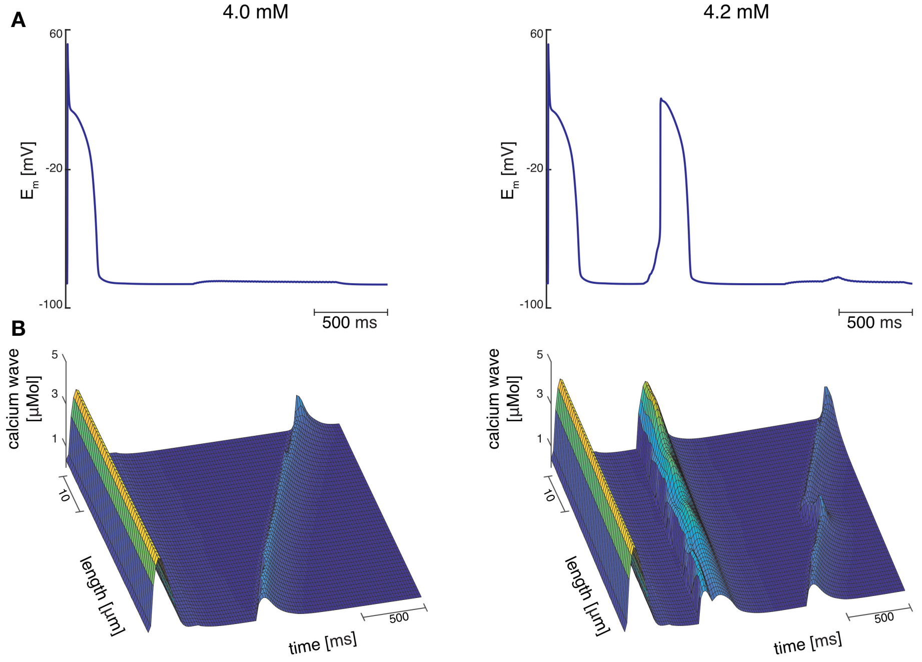

FIGURE 3 | (A) Membrane potential for stretch pattern S of myocyte 3 at $Ca_o = 4.0$ mM and $Ca_o = 4.2$ mM (from left to right). After one stimulated beat, at $Ca_o = 4.0$ mM a calcium-mediated suprathreshold DAD occurred and at $Ca_o = 4.2$ mM a calcium-mediated additional beat occurred followed by a calcium wave. **(B)** Associating calcium wave for the supratheshold DAD, and the additional beat followed by a calcium wave (from left to right) at $Ca_o = 4.0$ mM and $Ca_o = 4.2$ mM, respectively.

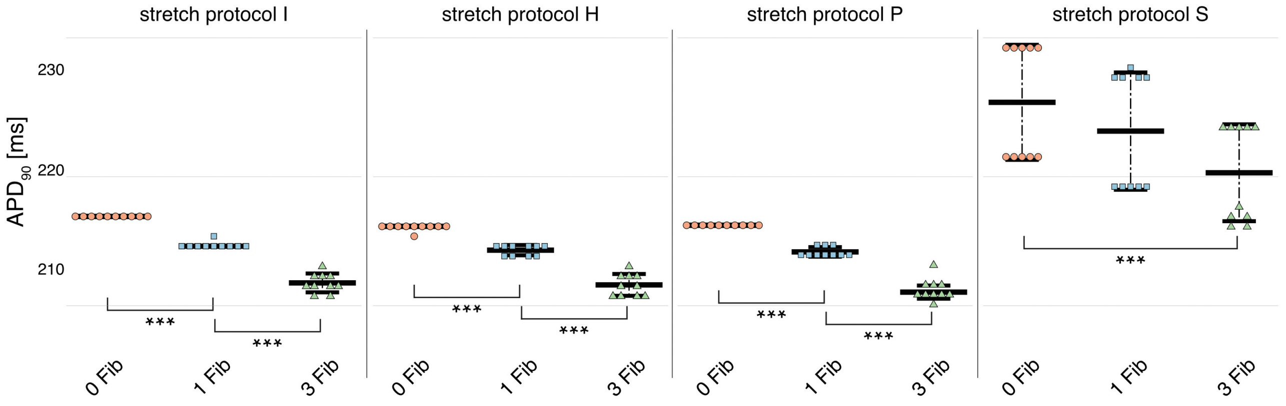

FIGURE 4 | APD_{90} for simulations of myocytes with no (red data points), 1 (blue data points), and 3 coupled fibroblast (green data points) compared with control (no coupled fibroblast) for no contraction and stretch patterns H, S, and P. APD_{90} was significantly reduced for all simulations of myocytes with coupled myocytes for the different stretch patterns.

23.45 ms, respectively. However, DAD magnitude decreased in coupled cell simulations compared with isolated myocytes due to the greater synchrony.

4. DISCUSSION

This computational study examined the importance of MEC, and particular, myofilament-triggered calcium release in the context of chronic stretch. We have assessed the arrhythmogenic potential of four different stretch patterns at cellular and multi-cellular scales with and without coupled fibroblasts. Our results support the hypothesis that MEC might be pro-arrhythmic but only under specific conditions of stretch and calcium overload.

Our model suggests that healthy, isotonically contracting myocytes may be less susceptible to generating propagating calcium waves than isometric contracting myocytes, while stretched myocytes are the most susceptible to calcium waves. For myocytes that do not contract but only stretch over the duration of the twitch (stretch pattern P), the extracellular calcium concentration necessary to trigger propagating waves was 16% lower than in isotonically contracting myocytes. Nevertheless, an

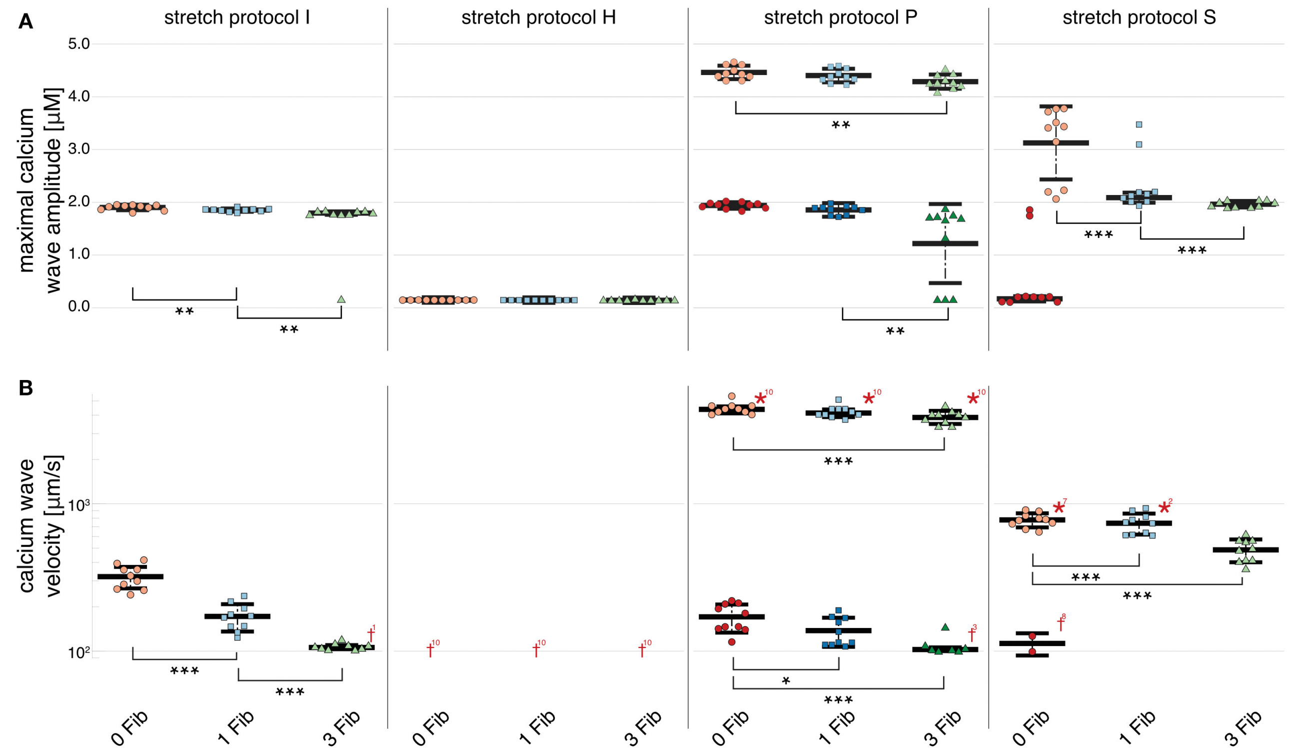

FIGURE 5 | Maximal calcium wave amplitude and calcium wave velocity for simulations for control (red data points), and myocytes with one (blue data points) and two (green data points) coupled fibroblasts. The data points in light colors specify the first spontaneous event and dark colors are used for the following spontaneous event. **(A)** For stretch patterns I (control), S, and P the maximal calcium wave amplitude significantly ($p < 0.01$) decreased the more fibroblasts were coupled to the myocyte. **(B)** The wave velocity significantly ($p < 0.01$) decreased for stretch patterns I (control), S, and P for no fibroblast coupled to three coupled fibroblasts. *, **, *** indicate the statistical significance with $p < 0.01$, $p < 0.05$, and $p < 0.1$, respectively.

increase in extracellular calcium concentration ($\mathrm{Ca_o} \geq 3.7$ mM) was necessary for all stretch patterns to trigger calcium waves. When fibroblasts were coupled to myocytes, electrical charge was drained from the myocytes reducing APD_{90} during normal pacing and slowing calcium waves.

In simulations of myocytes coupled *via* gap junctions, the calcium wave was synchronized between cells but at a lower amplitude compared with those in the single cell simulations. Cell-cell coupling reduced DAD magnitudes, but synchronized the rise times of the triggered suprathreshold DADs due to current conduction *via* gap junctions.

4.1. Sub-cellular Structure and Calcium Handling

Spontaneous calcium release events have not only been associated with a calcium overloaded SR (Takamatsu and Wier, 1990; Williams et al., 1992; Cheng et al., 1993, 1996; Satoh et al., 1997; Cheng and Lederer, 2008) but also as the site of calcium wave initiation (Cheng et al., 1996). An increased frequency of calcium sparks is thought to contribute to the initiation of DADs and cellular triggered activity (Voigt et al., 2013). The wavefront of slowly propagating calcium waves are the result of discrete calcium releases from the SR, which recruit other sparks during propagation (Cheng et al., 1996). The incidence of calcium sparks, and thus propagating waves, has also been associated with mechanical heterogeneities (Miura et al., 1993, 1999; Wakayama et al., 2001; ter Keurs et al., 2006a, 2008). Experiments in damaged cardiac muscle discovered that mechanical strain can modify calcium wave velocity resulting in an increase in the propagation velocity (ter Keurs et al., 1998). Consistent with experimental and computational observations, calcium wave velocity affects the amplitude of DADs, which can act as the initiator of arrhythmia at the tissue level (Daniels and ter Keurs, 1990; Daniels et al., 1991; Miura et al., 1993; ter Keurs et al., 2008). Indeed, experiments have shown that premature beats can result from propagating calcium waves that originate close to the border zones of mechanically-heterogeneous tissues (Boyden et al., 2003; Boyden and ter Keurs, 2005; ter Keurs and Boyden, 2007). Therefore, MEC may be an important contributor to ventricular arrhythmia in cardiac pathologies associated with mechanical perturbations.

The patterns of systolic stretch used in our simulations are similar to those described in regions of myocardial mechanical heterogeneity. Experimental studies of acute ischemia (Baumeister et al., 2018) revealed that ischemic tissue shows a similar stretches as stretch pattern P used in for this computational study. Late diastolic stretches, such as stretch pattern S, have been observed in various pathological conditions such as ischemia or heart failure (Neves et al., 2016) and isometric conditions are often used in experimental set-ups

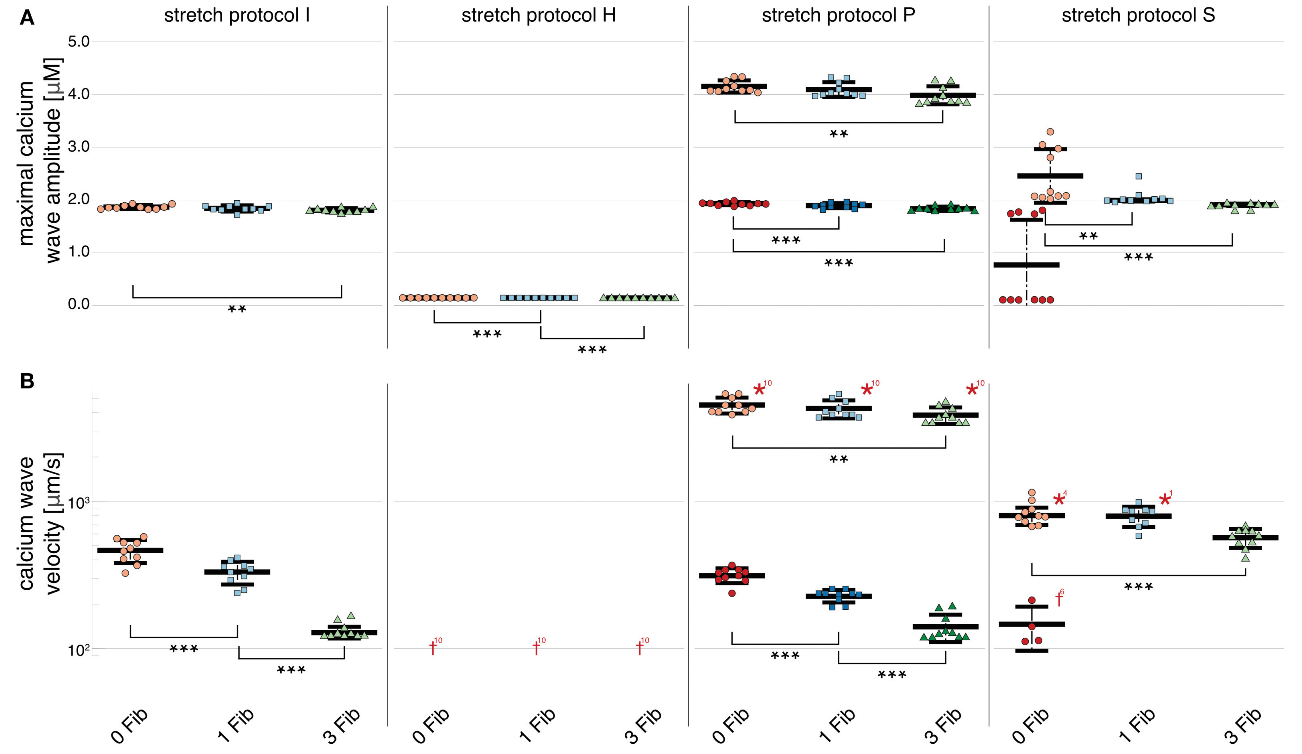

FIGURE 6 | Maximal calcium wave amplitude and calcium wave velocity for simulations of three coupled cardiomyocytes. **(A)** For all stretch patterns but H (from left to right: control, H, S, and P) the maximal calcium wave amplitude significantly ($p < 0.01$) decreased the more fibroblasts were coupled to the multi-cellular string (control red data points, 1 coupled fibroblast blue data points, and 3 coupled fibroblasts green data points; the data points in light colors specify the first spontaneous event and dark colors are used for the following spontaneous event). **(B)** The wave velocity significantly ($p < 0.01$) decreased for all stretch patterns from no coupled fibroblast to three coupled fibroblasts. *, **, *** indicate the statistical significance with $p < 0.01$, $p < 0.05$, and $p < 0.1$, respectively.

to immobilize the cells for optical mapping. In pathological conditions, such as ischemia, stretch is assumed to enhance calcium spark probability (Cameron et al., 2020), which may trigger calcium waves and DADs originating from these sites (Boyden et al., 2003; Boyden and ter Keurs, 2005; ter Keurs and Boyden, 2007). In addition to calcium waves, spontaneous contractile waves have been related to pro-arrhythmic effects in arrangements of weaker damaged regions in-series with normal muscle segments. Even though the underlying arrhythmogenic mechanism is thought to be caused by calcium release, the initiation of the calcium release has been linked to stretch and release of the myofilaments. The increase in intra-cellular calcium may be conducted to adjacent myocytes triggered by tissue-level heterogeneities in mechanical loading the resulting spontaneous contractile waves (ter Keurs et al., 1998).

4.2. Comparison With Previous Models

Cardiomyocyte function is tightly regulated by calcium signaling mechanisms that are well studied. While fibroblasts are also regulated by calcium fluxes (Feng et al., 2019), the mechanisms of calcium homeostasis in these non-excitable cells, and the role of voltage-gated calcium channels are less well studied and modeled (Feng et al., 2019). Mathematical models have not yet incorporated calcium fluxes between coupled myocytes and fibroblasts (MacCannell et al., 2007; Maleckar et al., 2009), and detailed models of calcium handling in fibroblasts are independent of membrane potential (Kotwani et al., 2014; Kotwani, 2015). Thus, there is a need for better models of fibroblast calcium fluxes and their regulation by transmembrane potential.

Spontaneous calcium release has been studied extensively in experiments (Capogrossi and Lakatta, 1985; Sasse et al., 2007; Rapila et al., 2008) as well as computational studies (Means et al., 2006; Dupont et al., 2007; Solovey et al., 2008). To study myocyte calcium handling, several computational models have been developed ranging from 0D to three-dimensional (3D) implementations and from highly detailed molecular models to common pool models (Means et al., 2006; Dupont et al., 2007; Solovey et al., 2008). Since calcium handling abnormalities are often related to cardiac diseases as heart failure, models have also focused on ryanodine receptor (RyR) and L-type channel dysfunction. Both, dysfunction or location heterogeneities of RyR clusters and L-Type channels have been associated with an impact on spontaneous calcium release events, and thus, impairment of calcium waves or pro-arrhythmic calcium waves (Zahradníková and Zahradník, 2012; Walker et al., 2014). However, to our knowledge none of these models include MEC to study the effects of mechanical heterogeneities in cells or tissues.

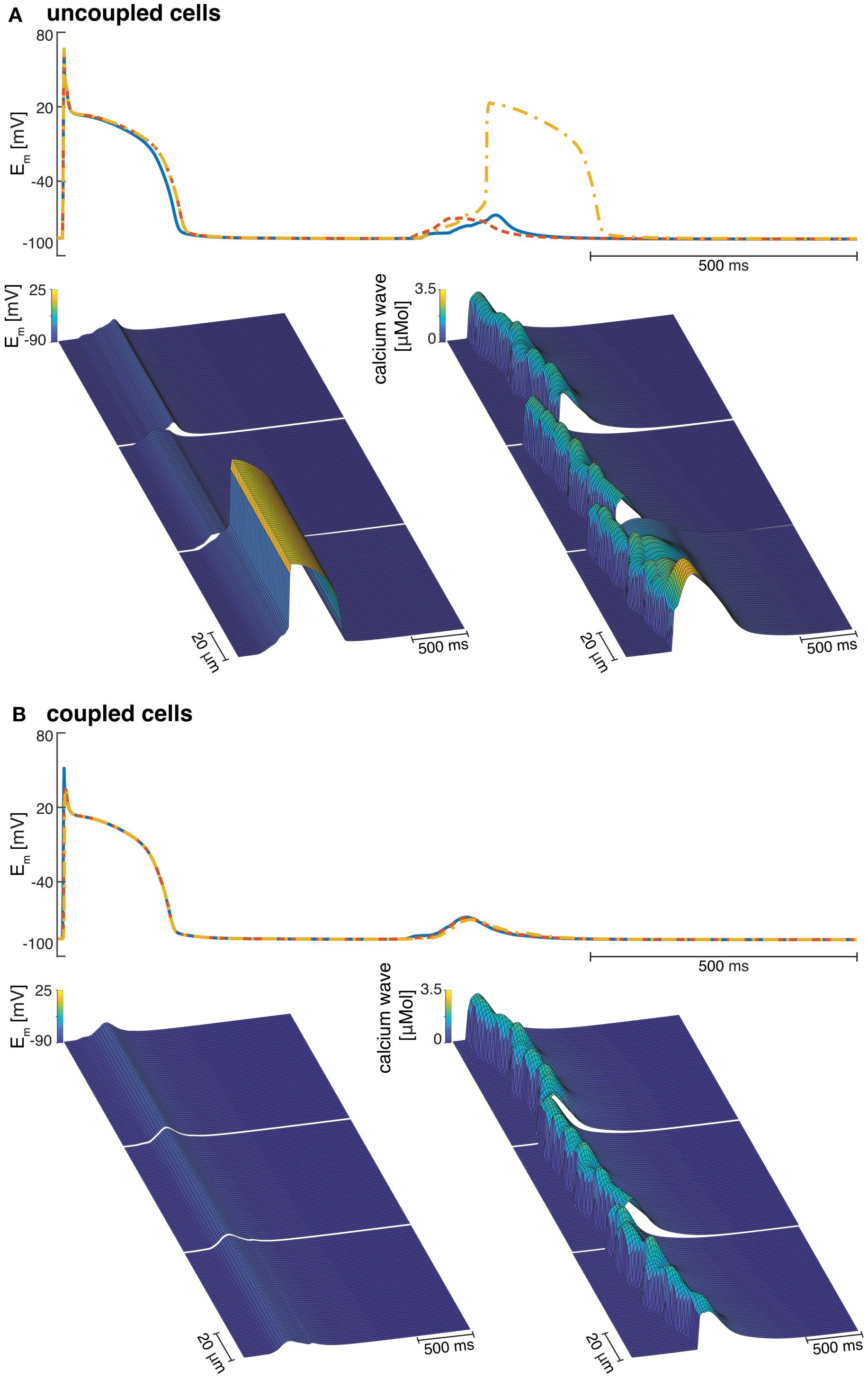

FIGURE 7 | (A) Examples of three isolated myocyte APs of the last stimulated beat and the calcium mediated DAD (top), a detailed view of the DAD (bottom left), and the calcium waves in three single cardiomyocytes coupled to three fibroblasts each (bottom right). **(B)** Example of the APs of three coupled myocytes showing the last stimulated beat and the DAD (top), a detailed view of the DAD (bottom left), and the calcium waves in three coupled cardiomyocytes coupled to three fibroblasts each (bottom right).

In larger tissue scale studies gap junctions play an important role. While our study only considered a linear gap junction model, various models of more detailed static and dynamic gap junction models have previously been developed. Vogel and Weingart (1998) developed a static model of gap junctions in which the voltage- and time-dependent conductance changes based on the voltage in myocyte pairs. A more recent dynamic model by Henriquez et al. (2001) describes each gap junction as two hemichannels in-series, which exist in either a high or low conductance state. Hence, the model assumes that the conductive gap junction channels have four conformational states regulated by nonlinear functions of the junctional voltage (Oka et al., 2006). Experimental data (Oka et al., 2006) also suggest that gap junction gating is regulated by intra-cellular calcium and protons. While a more detailed gap junction model would produce more physiological results than our linear model, they are also more computationally expensive.

4.3. Limitations

Our model was unable to elicit calcium waves at extracellular calcium concentrations below 3.7 mM, similar to some experimental studies that have used unphysiologically high extracellular calcium concentrations (Capogrossi et al., 1986a; Cheng et al., 1996). However, this is a limitation of the model because other experimental studies have observed calcium waves at concentrations as low as 1.8–2.0 mM (Takamatsu and Wier, 1990; Wier and Blatter, 1991). There are several aspects of the calcium handling mechanisms in our model that might account for the limitation that high extracellular calcium concentrations were needed to elicit propagating calcium waves. In particular, the present model does not incorporate calcium fluxes between myocytes and fibroblasts, which have been reported in experiments (Feng et al., 2019) and have been modeled mathematically by one group (Kotwani et al., 2014; Kotwani, 2015).

Our model suggests that specific chronic stretch patterns are likely to have a pro-arrhythmic effect under calcium overload conditions. However, the myocyte model only considered a 1D representation in longitudinal direction. Therefore, the model cannot give insights into cellular anisotropy and radial wave propagation (Galice et al., 2018). Additionally, we only consider sarcomeric heterogeneity but neglect possibly important details about sub-cellular distribution of RyR clusters and L-type channels, which might have a strong impact on the calcium handling (Sutanto et al., 2018). Furthermore, our conclusions are based on a deterministic model while stochastic approaches are necessary to reproduce heterogeneous systems as RyR clusters which can open spontaneously. Therefore, our model could not generate propagating waves that do not activate the whole myocyte.

The myofilament contraction model (Rice et al., 2008b) was chosen in part because of its computational efficiency compared with spatial explicit sarcomere models. It was built largely with steady-state data and a simplified representation of calcium binding to the myofilaments, while more recent models allow for a more realistic representation of this process. The parameterization of calcium diffusion in the EP model (Shannon et al., 2004) was based on ECC data and can only partially reproduce MEC.

Finally, in this study we only considered one MEC mechanism, even though mechano-sensitive ion channels and XROS are also known to contribute to mechanics-induced arrhythmia (Kohl et al., 2011). Nevertheless, mechanically-induced calcium waves have also been reported when mechano-sensitive ion channels were blocked (Wakayama et al., 2001). XROS on the other hand might be important in some context, especially during diastolic stretch (Prosser et al., 2011, 2013). But we did not explicitly simulate XROS since we used whole muscle data for the parameterization of the myofilament-triggered calcium release events.

5. CONCLUSIONS

In this study, we investigated the ability of sub-cellular mechanical transients and heterogeneity and the effects of coupled fibroblasts to modify calcium wave velocity and the resulting calcium mediated DADs. The goal was to investigate whether MEC, transient stretches, and fibroblasts contribute to pro-arrhythmic effects in calcium overloaded myocytes and multi-cellular tissues.

The present study indicates that myofilament-triggered calcium release mechanisms may modulate the susceptibility threshold for DADs. Chronic stretch may increase cytosolic calcium concentration resulting in an increase of the magnitude of the calcium-mediated DAD. In contrast, myocyte coupled to fibroblasts are less susceptible to calcium-mediated DADs as the current through the gap junction between the myocyte and the fibroblasts may provide a drain of the electric charge. Finally, at the multi-cellular scale, mechanically-induced calcium waves may trigger synchronized calcium waves and after-depolarizations. Thus, MEC may increase the susceptibility to pro-arrhythmic intra- and inter-cellular calcium wave propagation.

DATA AVAILABILITY STATEMENT

All datasets generated for this study are included in the article/**Supplementary Material**.

AUTHOR CONTRIBUTIONS

VT carried out all simulations, analyzed the data, and wrote the article. Together with VT, AM designed the research. AM commented and edited the manuscript. All authors contributed to the article and approved the submitted version.

FUNDING

This study has been supported by Simula Research Laboratory funded by the Norwegian Ministry of Education and Research. This work was also supported in part by National Institutes of Health awards (HL105242, HL137100, HL122199, HL126273) and the National Biomedical Computation Resource (P41 GM103426 to AM).

SUPPLEMENTARY MATERIAL

The Supplementary Material for this article can be found online at: https://www.frontiersin.org/articles/10.3389/fphys.2020.519951/full#supplementary-material

REFERENCES

Backx, P. H., De Tombe, P. P., Van Deen, J., Mulder, B., and Ter Keurs, H. (1989). A model of propagating calcium-induced calcium release mediated by calcium diffusion. *J. Gen. Physiol.* 93, 963–977. doi: 10.1085/jgp.93.5.963

Baumeister, P. A., Lawen, T., Rafferty, S. A., Taeb, B., Uzelac, I., Fenton, F. H., et al. (2018). Mechanically-induced ventricular arrhythmias during acute regional ischemia. *J. Mol. Cell. Cardiol.* 124, 87–88. doi: 10.1016/j.yjmcc.2018.07.021

Bers, D. M. (2002). Available online at: https://somapp.ucdmc.ucdavis.edu/Pharmacology/bers/.

Boyden, P. A., Barbhaiya, C., Lee, T., and ter Keurs, H. E. (2003). Nonuniform Ca^{2+} transients in arrhythmogenic Purkinje cells that survive in the infarcted canine heart. *Cardiovasc. Res.* 57, 681–693. doi: 10.1016/S0008-6363(02)00725-3

Boyden, P. A., and ter Keurs, H. (2005). Would modulation of intracellular Ca^{2+} be antiarrhythmic? *Pharmacol. Therap.* 108, 149–179. doi: 10.1016/j.pharmthera.2005.03.011

Bueno-Orovio, A., Cherry, E. M., and Fenton, F. H. (2008). Minimal model for human ventricular action potentials in tissue. *J. Theor. Biol.* 253, 544–560. doi: 10.1016/j.jtbi.2008.03.029

Cameron, B. A., Kai, H., Kaihara, K., Iribe, G., and Quinn, T. A. (2020). Ischemia enhances the acute stretch-induced increase in calcium spark rate in ventricular myocytes. *Front. Physiol.* 11:289. doi: 10.3389/fphys.2020.00289

Capogrossi, M. C., Kort, A. A., Spurgeon, H. A., and Lakatta, E. G. (1986a). Single adult rabbit and rat cardiac myocytes retain the Ca^{2+}-and species-dependent systolic and diastolic contractile properties of intact muscle. *J. Gen. Physiol.* 88, 589–613. doi: 10.1085/jgp.88.5.589

Capogrossi, M. C., and Lakatta, E. G. (1985). Frequency modulation and synchronization of spontaneous oscillations in cardiac cells. *Am. J. Physiol.* 248, H412–H418. doi: 10.1152/ajpheart.1985.248.3.H412

Capogrossi, M. C., Suarez-Isla, B. A., and Lakatta, E. G. (1986b). The interaction of electrically stimulated twitches and spontaneous contractile waves in single cardiac myocytes. *J. Gen. Physiol.* 88, 615–633. doi: 10.1085/jgp.88.5.615

Cheng, H., Lederer, M. R., Lederer, W., and Cannell, M. (1996). Calcium sparks and $[Ca^{2+}]_i$ waves in cardiac myocytes. *Am. J. Physiol.* 270, C148–C159. doi: 10.1152/ajpcell.1996.270.1.C148

Cheng, H., and Lederer, W. (2008). Calcium sparks. *Physiol. Rev.* 88, 1491–1545. doi: 10.1152/physrev.00030.2007

Cheng, H., Lederer, W. J., and Cannell, M. B. (1993). Calcium sparks: elementary events underlying excitation-contraction coupling in heart muscle. *Science* 262, 740–744. doi: 10.1126/science.8235594

Daniels, M. C. G., Fedida, D., Lamont, C., and ter Keurs, H. E. D. J. (1991). Role of the sarcolemma in triggered propagated contractions in rat cardiac trabeculae. *Circ. Res.* 68, 1408–1421. doi: 10.1161/01.RES.68.5.1408

Daniels, M. C. G., and ter Keurs, H. E. D. J. (1990). Spontaneous contractions in rat cardiac trabeculae; trigger mechanism and propagation velocity. *J. Gen. Physiol.* 95, 1123–1137. doi: 10.1085/jgp.95.6.1123

Dupont, G., Combettes, L., and Leybaert, L. (2007). Calcium dynamics: spatio-temporal organization from the subcellular to the organ level. *Int. Rev. Cytol.* 261, 193–245. doi: 10.1016/S0074-7696(07)61005-5

Feng, J., Armillei, M. K., Yu, A. S., Liang, B. T., Runnels, L. W., and Yue, L. (2019). Ca^{2+} signaling in cardiac fibroblasts and fibrosis-associated heart diseases. *J. Cardiovasc. Dev. Dis.* 6:34. doi: 10.3390/jcdd6040034

Franz, M. R., Cima, R., Wang, D., Profitt, D., and Kurz, R. (1992). Electrophysiological effects of myocardial stretch and mechanical determinants of stretch-activated arrhythmias. *Circulation* 86, 968–978. doi: 10.1161/01.CIR.86.3.968

Galice, S., Xie, Y., Yang, Y., Sato, D., and Bers, D. M. (2018). Size matters: ryanodine receptor cluster size affects arrhythmogenic sarcoplasmic reticulum calcium release. *J. Am. Heart Assoc.* 7:e008724. doi: 10.1161/JAHA.118.008724

Gemmell, P., Burrage, K., Rodríguez, B., and Quinn, T. A. (2016). Rabbit-specific computational modelling of ventricular cell electrophysiology: using populations of models to explore variability in the response to ischemia. *Prog. Biophys. Mol. Biol.* 121, 169–184. doi: 10.1016/j.pbiomolbio.2016.06.003

Goldsmith, E. C., Hoffman, A., Morales, M. O., Potts, J. D., Price, R. L., McFadden, A., et al. (2004). Organization of fibroblasts in the heart. *Dev. Dyn.* 230, 787–794. doi: 10.1002/dvdy.20095

Henriquez, A. P., Vogel, R., Muller-Borer, B. J., Henriquez, C. S., Weingart, R., and Cascio, W. E. (2001). Influence of dynamic gap junction resistance on impulse propagation in ventricular myocardium: a computer simulation study. *Biophys. J.* 81, 2112–2121. doi: 10.1016/S0006-3495(01)75859-6

Kass, R. S., and Tsien, R. W. (1982). Fluctuations in membrane current driven by intracellular calcium in cardiac Purkinje fibers. *Biophys. J.* 38, 259–269. doi: 10.1016/S0006-3495(82)84557-8

Kohl, P., Hunter, P., and Noble, D. (1999). Stretch-induced changes in heart rate and rhythm: clinical observations, experiments and mathematical models. *Prog. Biophys. Mol. Biol.* 71, 91–138. doi: 10.1016/S0079-6107(98)00038-8

Kohl, P., Nesbitt, A. D., Cooper, P. J., and Lei, M. (2001). Sudden cardiac death by commotio cordis: role of mechano-electric feedback. *Cardiovasc. Res.* 50, 280–289. doi: 10.1016/S0008-6363(01)00194-8

Kohl, P., and Sachs, F. (2001). Mechanoelectric feedback in cardiac cells. *Philos. Trans. R. Soc. Lond. Ser. A* 359, 1173–1185. doi: 10.1098/rsta.2001.0824

Kohl, P., Sachs, F., and Franz, M. R. (2011). *Cardiac Mechano-Electric Coupling and Arrhythmias*. Oxford: Oxford University Press. doi: 10.1093/med/9780199570164.001.0001

Kotwani, M. (2015). Modeling and simulation of calcium dynamics in fibroblast cell involving excess buffer approximation (EBA), ER flux and SERCA pump. *Proc. Comput. Sci.* 49, 347–355. doi: 10.1016/j.procs.2015.04.263

Kotwani, M., Adlakha, N., and Mehta, M. (2014). Finite element model to study the effect of buffers, source amplitude and source geometry on spatio-temporal calcium distribution in fibroblast cell. *J. Med. Imag. Health Inform.* 4, 840–847. doi: 10.1166/jmihi.2014.1328

MacCannell, K. A., Bazzazi, H., Chilton, L., Shibukawa, Y., Clark, R. B., and Giles, W. R. (2007). A mathematical model of electrotonic interactions between ventricular myocytes and fibroblasts. *Biophys. J.* 92, 4121–4132. doi: 10.1529/biophysj.106.101410

Maleckar, M. M., Greenstein, J. L., Giles, W. R., and Trayanova, N. A. (2009). Electrotonic coupling between human atrial myocytes and fibroblasts alters myocyte excitability and repolarization. *Biophys. J.* 97, 2179–2190. doi: 10.1016/j.bpj.2009.07.054

Matsuda, H., Noma, A., Kurachi, Y., and Irisawa, H. (1982). Transient depolarization and spontaneous voltage fluctuations in isolated single cells from guinea pig ventricles. Calcium-mediated membrane potential fluctuations. *Circul. Res.* 51, 142–151. doi: 10.1161/01.RES.51.2.142

Means, S., Smith, A. J., Shepherd, J., Shadid, J., Fowler, J., Wojcikiewicz, R. J., et al. (2006). Reaction diffusion modeling of calcium dynamics with realistic ER geometry. *Biophys. J.* 91, 537–557. doi: 10.1529/biophysj.105.075036

Miura, M., Boyden, P. A., and Keurs, H. E. t. (1999). Ca^{2+} waves during triggered propagated contractions in intact trabeculae: determinants of the velocity of propagation. *Circul. Res.* 84, 1459–1468. doi: 10.1161/01.RES.84.12.1459

Miura, M., Ishide, N., Oda, H., Sakurai, M., Shinozaki, T., and Takishima, T. (1993). Spatial features of calcium transients during early and delayed after depolarizations. *Am. J. Physiol. Heart Circul. Physiol.* 265, H439–H444. doi: 10.1152/ajpheart.1993.265.2.H439

Neves, J. S., Leite-Moreira, A. M., Neiva-Sousa, M., Almeida-Coelho, J., Castro-Ferreira, R., and Leite-Moreira, A. F. (2016). Acute myocardial response to stretch: what we (don't) know. *Front. Physiol.* 6:408. doi: 10.3389/fphys.2015.00408

Oka, C., Matsuda, H., Sarai, N., and Noma, A. (2006). Modeling the calcium gate of cardiac gap junction channel. *J. Physiol. Sci.* 56, 79–85. doi: 10.2170/physiolsci.R2139

Ongstad, E., and Kohl, P. (2016). Fibroblast-myocyte coupling in the heart: potential relevance for therapeutic interventions. *J. Mol. Cell. Cardiol.* 91, 238–246. doi: 10.1016/j.yjmcc.2016.01.010

Peyronnet, R., Nerbonne, J. M., and Kohl, P. (2016). Cardiac mechano-gated ion channels and arrhythmias. *Circul. Res.* 118, 311–329. doi: 10.1161/CIRCRESAHA.115.305043

Pfeiffer, E. R., Tangney, J. R., Omens, J. H., and McCulloch, A. D. (2014). Biomechanics of cardiac electromechanical coupling and mechanoelectric feedback. *J. Biomech. Eng.* 136:021007. doi: 10.1115/1.4026221

Prosser, B. L., Khairallah, R. J., Ziman, A. P., Ward, C. W., and Lederer, W. (2013). X-ROS signaling in the heart and skeletal muscle: stretch-dependent local ROS regulates $[Ca^{2+}]_i$. *J. Mol. Cell. Cardiol.* 58, 172–181. doi: 10.1016/j.yjmcc.2012.11.011

Prosser, B. L., Ward, C. W., and Lederer, W. (2011). X-ROS signaling: rapid mechano-chemo transduction in heart. *Science* 333, 1440–1445. doi: 10.1126/science.1202768

Rapila, R., Korhonen, T., and Tavi, P. (2008). Excitation-contraction coupling of the mouse embryonic cardiomyocyte. *J. Gen. Physiol.* 132, 397–405. doi: 10.1085/jgp.200809960

Rassier, D. E., Herzog, W., and Pollack, G. H. (2003). Dynamics of individual sarcomeres during and after stretch in activated single myofibrils. *Proc. R. Soc. Lond. Ser. B Biol. Sci.* 270, 1735–1740. doi: 10.1098/rspb.2003.2418

Rice, J. J., Wang, F., Bers, D. M., and de Tombe, P. P. (2008a). Available online at: https://models.cellml.org/exposure/a31519a27f4c2fe6158e04fd40eeda98/rice$_$wang$_$bers$_$detombe$_$2008.cellml/view

Rice, J. J., Wang, F., Bers, D. M., and de Tombe, P. P. (2008b). Approximate model of cooperative activation and crossbridge cycling in cardiac muscle using ordinary differential equations. *Biophys. J.* 95, 2368–2390. doi: 10.1529/biophysj.107.119487

Sasse, P., Zhang, J., Cleemann, L., Morad, M., Hescheler, J., and Fleischmann, B. K. (2007). Intracellular Ca^{2+} oscillations, a potential pacemaking mechanism in early embryonic heart cells. *J. Gen. Physiol.* 130, 133–144. doi: 10.1085/jgp.200609575

Satoh, H., Blatter, L. A., and Bers, D. M. (1997). Effects of $[Ca^{2+}]_i$, SR Ca^{2+} load, and rest on Ca^{2+} spark frequency in ventricular myocytes. *Am. J. Physiol. Heart Circul. Physiol.* 272, H657–H668. doi: 10.1152/ajpheart.1997.272.2.H657

Shannon, T. R., Wang, F., Puglisi, J., Weber, C., and Bers, D. M. (2004). A mathematical treatment of integrated ca dynamics within the ventricular myocyte. *Biophys. J.* 87, 3351–3371. doi: 10.1529/biophysj.104.047449

Solovey, G., Fraiman, D., Pando, B., and Dawson, S. P. (2008). Simplified model of cytosolic Ca^{2+} dynamics in the presence of one or several clusters of Ca^{2+}-release channels. *Phys. Rev. E* 78:041915. doi: 10.1103/PhysRevE.78.041915

Sutanto, H., van Sloun, B., Schönleitner, P., van Zandvoort, M. A., Antoons, G., and Heijman, J. (2018). The subcellular distribution of ryanodine receptors and l-type Ca^{2+} channels modulates Ca^{2+}-transient properties and spontaneous Ca^{2+}-release events in atrial cardiomyocytes. *Front. Physiol.* 9:1108. doi: 10.3389/fphys.2018.01108

Taggart, P., and Lab, M. (2008). Cardiac mechano-electric feedback and electrical restitution in humans. *Prog. Biophys. Mol. Biol.* 97, 452–460. doi: 10.1016/j.pbiomolbio.2008.02.021

Takamatsu, T., and Wier, W. (1990). Calcium waves in mammalian heart: quantification of origin, magnitude, waveform, and velocity. *FASEB J.* 4, 1519–1525. doi: 10.1096/fasebj.4.5.2307330

ter Keurs, H. E., and Boyden, P. A. (2007). Calcium and arrhythmogenesis. *Physiol. Rev.* 87, 457–506. doi: 10.1152/physrev.00011.2006

ter Keurs, H. E., Shinozaki, T., Zhang, Y. M., Zhang, M. L., Wakayama, Y., Sugai, Y., et al. (2008). Sarcomere mechanics in uniform and non-uniform cardiac muscle: a link between pump function and arrhythmias. *Prog. Biophys. Mol. Biol.* 97, 312–331. doi: 10.1016/j.pbiomolbio.2008.02.013

ter Keurs, H. E., Wakayama, Y., Miura, M., Shinozaki, T., Stuyvers, B. D., Boyden, P. A., et al. (2006a). Arrhythmogenic Ca^{2+} release from cardiac myofilaments. *Prog. Biophys. Mol. Biol.* 90, 151–171. doi: 10.1016/j.pbiomolbio.2005.07.002

ter Keurs, H. E., Wakayama, Y., Sugai, Y., Price, G., Kagaya, Y., Boyden, P. A., et al. (2006b). Role of sarcomere mechanics and Ca^{2+} overload in Ca^{2+} waves and arrhythmias in rat cardiac muscle. *Ann. N. Y. Acad. Sci.* 1080, 248–267. doi: 10.1196/annals.1380.020

ter Keurs, H. E., Zhang, Y. M., and Miura, M. (1998). Damage-induced arrhythmias: reversal of excitation-contraction coupling. *Cardiovasc. Res.* 40, 444–455. doi: 10.1016/S0008-6363(98)00263-6

Timmermann, V., Edwards, A. G., Wall, S. T., Sundnes, J., and McCulloch, A. D. (2019). Arrhythmogenic current generation by myofilament-triggered Ca^{2+} release and sarcomere heterogeneity. *Biophys. J.* 117, 2471–2485. doi: 10.1016/j.bpj.2019.11.009

Vogel, R., and Weingart, R. (1998). Mathematical model of vertebrate gap junctions derived from electrical measurements on homotypic and heterotypic channels. *J. Physiol.* 510, 177–189. doi: 10.1111/j.1469-7793.1998.177bz.x

Voigt, N., Heijman, J., Wang, Q., Chiang, D. Y., Li, N., Karck, M., et al. (2013). Cellular and molecular mechanisms of atrial arrhythmogenesis in patients with paroxysmal atrial fibrillation. *Circulation* 129, 145–156. doi: 10.1161/CIRCULATIONAHA.113.006641

Wakayama, Y., Miura, M., Sugai, Y., Kagaya, Y., Watanabe, J., ter Keurs, H. E. D. J., et al. (2001). Stretch and quick release of rat cardiac trabeculae accelerates Ca^{2+} waves and triggered propagated contractions. *Am. J. Phys.* 281, H2133–H2142. doi: 10.1152/ajpheart.2001.281.5.H2133

Walker, M. A., Williams, G. S., Kohl, T., Lehnart, S. E., Jafri, M. S., Greenstein, J. L., et al. (2014). Superresolution modeling of calcium release in the heart. *Biophys. J.* 107, 3018–3029. doi: 10.1016/j.bpj.2014.11.003

Wier, W., and Blatter, L. (1991). Ca^{2+}-oscillations and Ca^{2+}-waves in mammalian cardiac and vascular smooth muscle cells. *Cell Calc.* 12, 241–254. doi: 10.1016/0143-4160(91)90024-9

Williams, D. A., Delbridge, L. M., Cody, S. H., Harris, P., and Morgan, T. (1992). Spontaneous and propagated calcium release in isolated cardiac myocytes viewed by confocal microscopy. *Am. J. Physiol. Cell Physiol.* 262, C731–C742. doi: 10.1152/ajpcell.1992.262.3.C731

Zahradníková, A., and Zahradník, I. (2012). Construction of calcium release sites in cardiac myocytes. *Front. Physiol.* 3:322. doi: 10.3389/fphys.2012.00322

Conflict of Interest: AM is a co-founder of and has an equity interest in Insilicomed and Vektor Medical. He serves on the scientific advisory board of Insilicomed and as scientific advisor to both companies. Some of his research grants, including those acknowledged here, have been identified for conflict of interest management based on the overall scope of the project and its potential benefit to these companies.

The remaining author declares that the research was conducted in the absence of any commercial or financial relationships that could be construed as a potential conflict of interest.

Advantages of publishing in Frontiers

OPEN ACCESS
Articles are free to read
for greatest visibility
and readership

FAST PUBLICATION
Around 90 days
from submission
to decision

HIGH QUALITY PEER-REVIEW
Rigorous, collaborative,
and constructive
peer-review

TRANSPARENT PEER-REVIEW
Editors and reviewers
acknowledged by name
on published articles

Frontiers
Avenue du Tribunal-Fédéral 34
1005 Lausanne | Switzerland

Visit us: www.frontiersin.org
Contact us: frontiersin.org/about/contact

REPRODUCIBILITY OF RESEARCH
Support open data
and methods to enhance
research reproducibility

DIGITAL PUBLISHING
Articles designed
for optimal readership
across devices

FOLLOW US
@frontiersin

IMPACT METRICS
Advanced article metrics
track visibility across
digital media

EXTENSIVE PROMOTION
Marketing
and promotion
of impactful research

LOOP RESEARCH NETWORK
Our network
increases your
article’s readership